

PALEOMAGNETISM: Magnetic Domains to Geologic Terranes

Electronic Edition, September 2004

By Robert F. Butler
Department of Chemistry and Physics
University of Portland
Portland, Oregon

Preface to the Electronic Edition of
Paleomagnetism: Magnetic Domains to Geologic Terranes

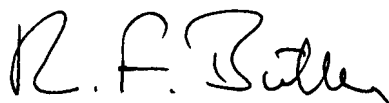
This electronic version of **Paleomagnetism: Magnetic Domains to Geologic Terranes** is made available for the use of “students of paleomagnetism.” In this context, “student” means anyone who has sufficient interest in paleomagnetism to read through this text in an effort to gain a basic understanding of the subject.

Following the decision by Blackwell Science Inc., the original publisher, to no longer make the text available in hardcopy, I obtained the copyright to the book in an effort to keep it available to interested parties. I was encouraged by several people, most notably Mark Besonen of the University of Massachusetts Amherst, to reformat the text into PDF files which could be accessed using the internet or via ftp. As with all such efforts, this operation took much longer than originally imagined, although it was relatively straightforward. As is also often the case, someone other than the author did most of the work. In this case, that someone was Norman Meader. Norm took on the task of learning PageMaker and Adobe Acrobat in order to transform the book from text and graphics files into PDF files. Many hours of Norm’s time went into this effort. All I had to do was proof the chapters as he completed the conversions. I am very grateful to Norm for his major effort on this project and his careful attention to detail. I also thank Steve Sorenson for his management of the computer system on which the files for this electronic version of the book are maintained.

Because I now hold the copyright to **Paleomagnetism: Magnetic Domains to Geologic Terranes**, it is within my legal right to permit users to make copies of this electronic version for their personal use. I hereby grant permission to anyone making a hardcopy of these PDF files to make additional hardcopies by xerography or other means for noncommercial use. The obvious importance of this permission is to allow instructors of classes or groups of students to make as many hardcopies of this book as they wish at the lowest possible cost. If you wish to have hardcopies made by a commercial firm, I recommend that you show this page to the personnel at such firms to assure them that no copyright is being violated by making hardcopies for personal use or use in formal or informal classes.

If you wish to make a citation to **Paleomagnetism: Magnetic Domains to Geologic Terranes**, you should cite the original 1992 printed version using standard citation styles.

Sincerely,



Robert F. Butler

Professor of Geosciences
University of Arizona
Tucson, AZ 85721
May 1998

TABLE OF CONTENTS

| | |
|--|------|
| PREFACE | vi |
| ACKNOWLEDGMENTS | viii |
| CHAPTER 1 INTRODUCTION TO GEOMAGNETISM | 1 |
| Some Basic Definitions | 1 |
| Geocentric Axial Dipole Model | 3 |
| The Present Geomagnetic Field | 4 |
| Geomagnetic Secular Variation | 7 |
| Origin of the Geomagnetic Field | 10 |
| Appendix 1.1: About Units | 12 |
| Suggested Readings | 15 |
| Problems | 15 |
| CHAPTER 2 FERROMAGNETIC MINERALS | 16 |
| Magnetic Properties of Solids | 16 |
| Diamagnetism | 17 |
| Paramagnetism | 17 |
| Ferromagnetism | 18 |
| Mineralogy of Ferromagnetic Minerals | 20 |
| Titanomagnetites | 20 |
| Titanohematites | 23 |
| Primary FeTi oxides | 25 |
| Exsolution | 26 |
| Deuteric oxidation | 27 |
| Low-temperature oxidation | 28 |
| Iron oxyhydroxides and sulfides | 29 |
| Suggested Readings | 29 |
| Problems | 30 |
| CHAPTER 3 ORIGINS OF NATURAL REMANENT MAGNETISM | 31 |
| Ferromagnetism of Fine Particles | 31 |
| Magnetic domains | 31 |
| Single-domain grains | 32 |
| Interaction energy | 33 |
| The internal demagnetizing field | 34 |
| Magnetocrystalline anisotropy | 36 |
| Hysteresis in single-domain grains | 36 |
| Hysteresis of multidomain grains | 39 |

| | |
|--|-----------|
| Pseudo-single-domain grains | 39 |
| Magnetic relaxation and superparamagnetism | 39 |
| Blocking temperatures | 41 |
| Natural Remanent Magnetism (NRM) | 42 |
| Thermoremanent Magnetism (TRM) | 43 |
| A theoretical model | 42 |
| Generalizing the model | 45 |
| PTRM | 47 |
| Grain-size effects | 47 |
| Chemical Remanent Magnetism (CRM) | 48 |
| Model of CRM formation | 48 |
| Detrital Remanent Magnetism (DRM) | 50 |
| Depositional DRM (the classic model) | 50 |
| Evidence for postdepositional alignment | 52 |
| Brownian motion and postdepositional alignment | 54 |
| Grain-size effects | 56 |
| Lock-in of DRM | 56 |
| Viscous Remanent Magnetism (VRM) | 56 |
| Acquisition of VRM | 57 |
| VRM in PSD and MD particles | 58 |
| Thermoviscous remanent magnetism (TVRM) | 58 |
| Caveats and summary | 61 |
| Isothermal Remanent Magnetism (IRM) | 61 |
| Suggested Readings | 62 |
| Problems | 62 |
| CHAPTER 4 SAMPLING, MEASUREMENT, AND DISPLAY OF NRM | 64 |
| Collection of Paleomagnetic Samples | 64 |
| Sample collection scheme | 64 |
| Types of samples | 66 |
| Some comments on sample collection Measurement of NRM | 68 |
| Display of NRM directions | 68 |
| Sample coordinates to geographic direction | 70 |
| Bedding-tilt correction | 71 |
| Evidences of Secondary NRM | 73 |
| Characteristic NRM | 73 |
| NRM distributions | 73 |
| Identification of Ferromagnetic Minerals | 75 |
| Microscopy | 75 |
| Curie temperature determination | 75 |
| Coercivity spectrum analysis | 77 |
| Suggested Readings | 79 |
| Problems | 79 |
| CHAPTER 5 PALEOMAGNETIC STABILITY | 81 |
| Partial Demagnetization Techniques | 81 |
| Theory of alternating-field demagnetization | 81 |

| | |
|--|------------|
| Theory of thermal demagnetization | 82 |
| Chemical demagnetization | 83 |
| Progressive demagnetization techniques | 84 |
| Graphical displays | 84 |
| Some real examples | 88 |
| Overlapping blocking temperature or coercivity spectra | 91 |
| More than two components? | 93 |
| Principal component analysis | 93 |
| Advanced techniques | 95 |
| Field Tests of Paleomagnetic Stability | 95 |
| The fold test | 95 |
| Synfolding magnetization | 96 |
| Conglomerate test | 98 |
| Reversals test | 98 |
| Baked contact and consistency tests | 99 |
| Suggested Readings | 100 |
| Problems | 101 |
| | |
| CHAPTER 6 STATISTICS OF PALEOMAGNETIC DATA | 103 |
| The Normal Distribution | 103 |
| The Fisher Distribution | 105 |
| Computing a mean direction | 106 |
| Dispersion estimates | 107 |
| A confidence limit | 108 |
| Some illustrations | 108 |
| Non-Fisherian distributions | 111 |
| Site-Mean Directions | 113 |
| Significance Tests | 115 |
| Comparing directions | 116 |
| Test of randomness | 116 |
| Comparison of precision (the fold test) | 117 |
| Suggested Readings | 118 |
| Problems | 119 |
| | |
| CHAPTER 7 PALEOMAGNETIC POLES | 121 |
| Procedure for Pole Determination | 121 |
| Types of Poles | 121 |
| Geomagnetic pole | 123 |
| Virtual geomagnetic pole | 124 |
| Paleomagnetic pole | 124 |
| Sampling of Geomagnetic Secular Variation | 126 |
| Paleosecular variation | 126 |
| Holocene lavas of western United States | 128 |
| Example Paleomagnetic Poles | 128 |
| Paleocene intrusives of north-central Montana | 128 |
| Jurassic rocks of southeastern Arizona | 131 |
| Two problem cases | 131 |

| | |
|--|------------|
| Caveats and Summary | 133 |
| Suggested Readings | 135 |
| Problems | 136 |
| CHAPTER 8 SPECIAL TOPICS IN ROCK MAGNETISM | 137 |
| Paleointensity from Thermoremanent Magnetization | 137 |
| Inclination Error of DRM | 139 |
| Biomagnetism: Birds Do It, Bees Do It | 143 |
| Marine Sediments | 143 |
| Hemipelagic sediments | 145 |
| Pelagic sediments | 146 |
| Ancient limestones | 147 |
| Magnetic Anisotropy | 147 |
| Chemical Remagnetization | 149 |
| The Red Bed Controversy | 150 |
| References | 155 |
| CHAPTER 9 GEOCHRONOLOGIC APPLICATIONS | 159 |
| Development of the Geomagnetic Polarity Time Scale | 159 |
| The Pliocene–Pleistocene | 160 |
| Extension into the Miocene | 162 |
| Marine magnetic anomalies | 162 |
| About nomenclature | 163 |
| Biostratigraphic calibrations | 165 |
| A Late Cretaceous–Cenozoic GPTS | 168 |
| The Late Mesozoic | 170 |
| Early Mesozoic, Paleozoic, and Precambrian | 171 |
| Magnetic Polarity Stratigraphy | 172 |
| Some general principles | 172 |
| The Pliocene–Pleistocene St. David Formation | 173 |
| Siwalik Group deposits | 176 |
| Siwalik sedimentology | 178 |
| References | 181 |
| CHAPTER 10 APPLICATIONS TO PALEOGEOGRAPHY | 183 |
| The Geocentric Axial Dipole Hypothesis | 183 |
| The past 5 m.y. | 183 |
| Older geologic intervals | 184 |
| Second-order deviations | 185 |
| Paleomagnetic poles and paleogeographic maps | 185 |
| Apparent Polar Wander Paths | 189 |
| Constructing APW paths | 189 |
| Paleomagnetic Euler poles | 191 |
| Paleogeographic Reconstructions of the Continents | 193 |
| Some general principles | 194 |

| | |
|---|------------|
| Europe-North America reconstruction | 196 |
| Pangea reconstructions | 197 |
| Paleozoic drift of Gondwana | 199 |
| References | 201 |
| CHAPTER 11 APPLICATIONS TO REGIONAL TECTONICS | 205 |
| Some General Principles | 205 |
| The Transverse Ranges, California: A Large, Young Rotation | 209 |
| The Goble Volcanic Series: An Older, Smaller Rotation | 212 |
| Wrangellia in Alaska: A Far-Traveled Terrane | 215 |
| Paleomagnetism of the Nikolai Greenstone | 215 |
| The hemispheric ambiguity | 217 |
| Caveats and Summary | 219 |
| References | 221 |
| APPENDIX: DERIVATIONS | 224 |
| Derivation of Magnetic Dipole Equations | 224 |
| Angle Between Two Vectors (and Great-Circle Distance Between Two Geographic Locations) | 226 |
| Law of Sines and Law of Cosines | 227 |
| Calculation of a Magnetic Pole from the Direction of the Magnetic Field | 227 |
| Confidence Limits on Poles: dp and dm | 230 |
| Expected Magnetic Field Direction | 233 |
| Rotation and Flattening in Direction Space | 235 |
| Rotation and Poleward Transport in Pole Space | 236 |
| Paleolatitudes and Confidence Limit | 237 |

PREFACE

Terms such as continental drift, seafloor spreading, and plate tectonics are understood even by nongeologists to reflect the mobility of the Earth's lithospheric plates. The revolution in the Earth sciences that took place in the 1960s has changed our view of the Earth. The former view was that of a fairly static planet with occasional mountain-building episodes of uncertain origin. Our current view is that of a dynamic system of continental and oceanic lithospheric plates with frequently changing relative motions that are largely responsible for the structural evolution of the Earth. Paleomagnetism provided some of the quantitative data about past locations of continents and oceanic plates; these observations have become cornerstones of plate tectonic theory. Today paleomagnetism is providing evidence about motion histories of suspect terranes with respect to continental interiors and is enlightening the processes by which continents grow and mountain belts form. In addition, paleomagnetism has provided major refinement of stratigraphic correlations and geochronologic calibrations of both marine and nonmarine fossil zonations. These geochronologic advances have major implications for patterns and rates of biological evolution.

In both the tectonic and geochronologic applications of paleomagnetism, there has been an explosion in scientific literature over the past 20 years. Modern paleomagnetism was initiated in a few modestly equipped laboratories in England, France, the United States, and Japan with a world population of about a dozen paleomagnetists in the late 1950s. Paleomagnetism has now grown to be a technologically sophisticated research field with scores of laboratories and several hundred scientists with a research emphasis on paleomagnetism. Because of the wide and growing influence of paleomagnetism, many Earth scientists find themselves in need of basic knowledge of paleomagnetism. But without guidance by an instructor with research experience in paleomagnetism, it is difficult to build a basic knowledge base of the subject from the existing (and rather imposing) body of paleomagnetic and rock magnetic literature. This book is intended to teach the interested Earth scientist (student or otherwise) how paleomagnetism works. An introduction to the fundamental principles of paleomagnetism is provided along with examples of tectonic and geochronologic applications.

Emphasis is placed on providing a firm foundation in the basics of the paleomagnetic technique. The building blocks are geomagnetism, rock magnetism, and paleomagnetic methods. Chapters 1 through 7 build knowledge of the paleomagnetic method to an "intermediate" level. In the early chapters (especially Chapters 2 and 3), you must learn many new concepts about physics of magnetism without really knowing how this information will eventually apply to paleomagnetism. While the physics and mathematics required to understand each individual concept are not particularly difficult, the sum of these new concepts presented in rapid succession is indeed challenging. Effort and diligence invested in these early chapters will pay back major dividends in later chapters. Invariably, students who understand and appreciate paleomagnetism have an effective working knowledge of geomagnetism and rock magnetism.

Chapters 4 through 7 develop the methodology of paleomagnetism. These chapters are the "nuts and bolts" of the paleomagnetic technique. Topics include sampling schemes, basic laboratory procedures that put the rock magnetic principles to work, and statistical treatment of paleomagnetic data. Illustrations and real examples are emphasized because this material is largely geometrical, and pictures simply work better than words in developing an intuitive feel for the principles of paleomagnetism.

Chapters 8 through 11 are the applications chapters, the rewards for learning the principles of paleomagnetism. These chapters employ a "case example" approach. A small number of research applications are discussed in some detail rather than attempting to provide a complete summary of all past and present

applications. Chapter 8 explores several topics in rock magnetism that expand on the basic rock magnetic principles introduced in Chapter 3. The development of the geomagnetic polarity time scale is briefly reviewed in Chapter 9. This review is followed by example applications of magnetic polarity stratigraphy to a variety of geochronologic problems. Chapter 10 introduces principles of paleomagnetic applications to paleogeography and investigates formation and dispersal of supercontinents during the Phanerozoic. In Chapter 11, applications to regional tectonics are introduced with emphasis on the role of paleomagnetism in the developing views of crustal mobility. In these applications chapters, special note is made of how the principles presented in early chapters are critical to classic and current applications of paleomagnetism.

In the early chapters, in which the emphasis is on developing fundamental concepts, suggested readings are listed at the ends of the chapters rather than including references within the text. But in the applications chapters, references are included to provide the accurate impression of an evolving paleomagnetic database and differences in interpretations of the observations. These references can also serve as a guide to specific research topics that the reader may wish to explore. An appendix provides the details of mathematical derivations that lead to results used in the main text. Very little about the history of paleomagnetism is presented here, mostly because others have provided excellent personal accounts (see Suggested Readings).

Throughout the text, the first occurrences of important terms or key concepts are printed in italics. This draws special attention to the definitions and concepts that must be mastered to understand paleomagnetism. At least the first occurrences of vector quantities are printed in bold type to emphasize that these quantities have both direction and magnitude. Although subsequent occurrences of these vector quantities are usually printed in regular type, it is important to keep the vector nature of these quantities in mind. A few problems are included at the ends of Chapters 1 through 7. Working these problems will help you grasp the fundamentals presented in these chapters. A solutions manual is available from the publisher to instructors adopting this book for their courses.

Given this introduction to the game plan of the book, you understand the approach that we will take. With a working knowledge of the material presented in this book, you will be able to read current paleomagnetic research articles and understand the basic objectives, methodology, and results. Now let's just do it.

SUGGESTED READINGS

W. Glen, *The Road to Jaramillo*, Stanford Univ. Press, Stanford, 459 pp., 1982.

This book covers the development of the time scale of geomagnetic polarity reversals and its role in plate tectonic theory. Excellent history of science with the personalities of the scientists left in.

E. Irving, The paleomagnetic confirmation of continental drift, *Eos Trans. AGU*, v. 69, 1001–1014, 1988.

An excellent personal account of the paleomagnetic research leading to the confirmation of Wegener's continental drift hypothesis.

R. T. Merrill and M. W. McElhinny, *The Earth's Magnetic Field*, Academic Press, London, 401 pp., 1983.

Chapter 1 provides a thorough history of geomagnetism and paleomagnetism.

N. D. Opdyke, Reversals of the Earth's magnetic field and the acceptance of crustal mobility in North America: A view from the trenches, *Eos Trans. AGU*, v. 66, 1177–1182, 1985.

A personal account of the discovery of magnetic polarity reversals in deep-sea sediment cores and events leading to acceptance of seafloor spreading by Lamont Observatory personnel.

D. H. Tarling, *Paleomagnetism*, Chapman and Hall, London, 397 pp., 1983.

Chapter 1 provides a thorough account of the history of paleomagnetism. Covers many subjects that are not treated in this book.

ACKNOWLEDGMENTS

This book could not have been completed without considerable assistance from colleagues and family. Myrl Beck is at the top of the list of helpful colleagues. Myrl arranged for my sabbatical leave at Western Washington University, which provided the time for a good start on this project. Myrl also contributed significantly to the substance of the book. He provided very thorough editing of early chapters and contributed early versions of some of the derivations that appear in the appendix. Myrl's major contribution is gratefully acknowledged.

Many colleagues read portions of the text and provided important feedback. Steve May deserves special mention for contributing editorial comments and suggestions on the entire text. Very helpful formal reviews of portions of the book were provided by Ken Kodama, Rob Coe, Jim Diehl, and Peter Shive. Numerous colleagues provided important reviews of selected chapters. These include Dave Bazard, Sue Beske-Diehl, Peter Coney, Bill Dickinson, Tekla Harms, Jack Hillhouse, Bill Lowrie, Paul Riley, Rob Van der Voo, and Ray Wells. Special contributions of photomicrographs or data for figures were provided by Steve Haggerty, Chad McCabe, Hojatollah Vali, Ken Verosub, and Ted Walker. Gary Calderone contributed several computer programs that were instrumental in producing the figures in Chapter 6.

All of the figures were prepared on Apple® Macintosh™ computers. Most of the figures were done by the author using MacDraw® II, TerraMobilis™, Stereo™, Cricketgraph™, and Wingz™ software. Paul Mirocha masterfully prepared Figures 1.4, 1.6, 1.11, 2.6, 2.9, 4.3, 5.3, and 7.1, which were beyond my capabilities. The text was prepared using Microsoft® Word™ with MathType™ 2.0 used for equation setting. I owe special thanks to Norm Meader for his meticulous assistance with text preparation.

Simon Rallison helped tremendously in his capacity as editor for Blackwell Scientific Publications. His constant encouragement and gentle reminders of things that needed attention provided me with just the right guidance.

This book is dedicated to my wife Patricia for her unflinching encouragement and support throughout the duration of this project. Expertly dealing with the logistics of a sabbatical leave and keeping the family ship afloat were just part of her contribution. In small compensation for my absences during the preparation of the manuscript, our family decided that we should take a trip in celebration of completing this book. I was hoping to see Hawaiian volcanoes. However, my son David decided that Disneyland was the place for us. I don't know what others do when they complete a book, but I'm going to Disneyland.

INTRODUCTION TO GEOMAGNETISM

The primary objective of paleomagnetic research is to obtain a record of past configurations of the geomagnetic field. Thus, understanding paleomagnetism demands some basic knowledge of the geomagnetic field. In this chapter, we begin by defining common terms used in geomagnetism and paleomagnetism. With this foothold, we describe spatial variations of the present geomagnetic field over the globe and time variations of the recent geomagnetic field. Even this elementary treatment of geomagnetism provides the essential information required for discussing magnetic properties of rocks, as we will do in the succeeding chapters. This chapter includes an appendix dealing with systems of units used in geomagnetism and paleomagnetism and describing the system of units used in this book.

SOME BASIC DEFINITIONS

New subjects always require basic definitions. Initially, we need to define magnetic moment, \mathbf{M} ; magnetization, \mathbf{J} ; magnetic field, \mathbf{H} ; and magnetic susceptibility, χ . Generally, students find developing an intuitive feel for magnetism and magnetic fields more difficult than for electrical phenomena. Perhaps this is due to the fundamental observation that isolated magnetic charges (*monopoles*) do not exist, at least for anything more than a fraction of a second. The smallest unit of magnetic charge is the magnetic dipole, and even this multipole combination of magnetic charges is more a mathematical convenience than a physical reality.

The *magnetic dipole moment* or more simply the *magnetic moment*, \mathbf{M} , can be defined by referring either to a pair of magnetic charges (Figure 1.1a) or to a loop of electrical current (Figure 1.1b). For the pair of magnetic charges, the magnitude of charge is m , and an infinitesimal distance vector, \mathbf{l} , separates the plus charge from the minus charge. The magnetic moment, \mathbf{M} , is

$$\mathbf{M} = m \mathbf{l} \quad (1.1)$$

For a loop with area A carrying electrical current I , the magnetic moment is

$$\mathbf{M} = I A \mathbf{n} \quad (1.2)$$

where \mathbf{n} is the vector of unit length perpendicular to the plane of the loop. The proper direction of \mathbf{n} (and therefore \mathbf{M}) is given by the *right-hand rule*. (Curl the fingers of your right hand in the direction of current flow and your right thumb points in the proper direction of the unit normal, \mathbf{n} .) The current loop definition of magnetic moment is basic in that all magnetic moments are caused by electrical currents. However, in some instances, it is convenient to imagine magnetic moments constructed from pairs of magnetic charges.

Magnetic force field or *magnetic field*, \mathbf{H} , in a region is defined as the force experienced by a unit positive magnetic charge placed in that region. However, this definition implies an experiment that cannot actually be performed. An experiment that you can perform (and probably have) is to observe the aligning torque on a magnetic dipole moment placed in a magnetic field (Figure 1.1c). The aligning torque, $\mathbf{\Gamma}$, is given by the vector cross product:

$$\mathbf{\Gamma} = \mathbf{M} \times \mathbf{H} = MH \sin \theta \hat{\mathbf{\Gamma}} \quad (1.3)$$

where θ is the angle between \mathbf{M} and \mathbf{H} as in Figure 1.1c and $\hat{\mathbf{\Gamma}}$ is the unit vector parallel to $\mathbf{\Gamma}$ in Figure 1.1c.

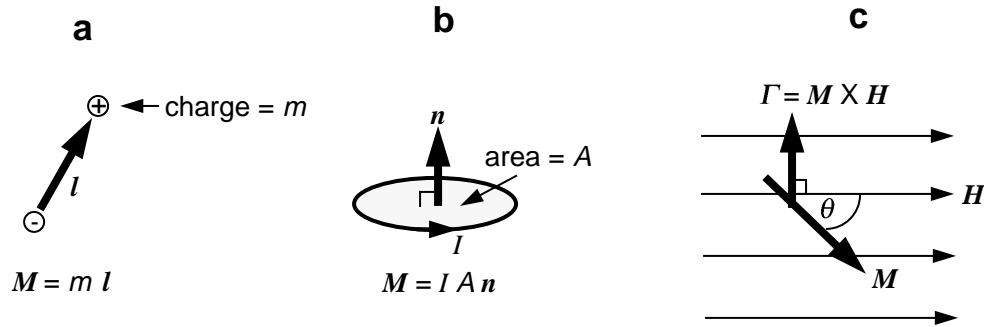


Figure 1.1 (a) A magnetic dipole constructed from a pair of magnetic charges. The magnetic charge of the plus charge is m ; the magnetic charge of the minus charge is $-m$; the distance vector from the minus charge to the plus charge is l . (b) A magnetic dipole constructed from a circular loop of electrical current. The electrical current in the circular loop is I ; the area of the loop is A ; the unit normal vector n is perpendicular to the plane of the loop. (c) Diagram illustrating the torque Γ on magnetic moment M , which is placed within magnetic field H . The angle between M and H is θ ; Γ is perpendicular to the plane containing M and H .

A magnetic moment that is free to rotate will align with the magnetic field. A compass needle has such a magnetic moment that aligns with the horizontal component of the geomagnetic field, yielding determination of magnetic azimuth.

The energy of alignment of magnetic moments with magnetic fields will be encountered often in the development of rock magnetism. This potential energy can be expressed by the vector dot product

$$E = -\mathbf{M} \cdot \mathbf{H} = -MH \cos \theta \tag{1.4}$$

The negative sign in this expression is required so that the minimum energy configuration is achieved when M is parallel to H .

The magnetic intensity, or *magnetization*, J , of a material is the net magnetic dipole moment per unit volume. To compute the magnetization of a particular volume, the vector sum of magnetic moments is divided by the volume enclosing those magnetic moments:

$$\mathbf{J} = \frac{\sum \mathbf{M}_i}{\text{volume}} \tag{1.5}$$

where M_i is the constituent magnetic moment.

There are basically two types of magnetization: induced magnetization and remanent magnetization. When a material is exposed to a magnetic field H , it acquires an *induced magnetization*, J_i . These quantities are related through the magnetic susceptibility, χ :

$$\mathbf{J}_i = \chi \mathbf{H} \tag{1.6}$$

Thus, *magnetic susceptibility*, χ , can be regarded as the *magnetizability* of a substance. The above expression uses a scalar for susceptibility, implying that J_i is parallel H . However, some materials display *magnetic anisotropy*, wherein J_i is not parallel to H . For an anisotropic substance, a magnetic field applied in a direction x will in general induce a magnetization not only in direction x , but also in directions y and z . For anisotropic substances, magnetic susceptibility is expressed as a tensor, χ , requiring a 3×3 matrix for full description.

In addition to the induced magnetization resulting from the action of present magnetic fields, a material may also possess a *remanent magnetization*, J_r . This remanent magnetization is a recording of past magnetic fields that have acted on the material. Much of the coming chapters involves understanding how rocks

can acquire and retain a remanent magnetization that records the geomagnetic field direction at the time of rock formation.

In paleomagnetism, the direction of a vector such as the surface geomagnetic field is usually defined by the angles shown in Figure 1.2. The vertical component, H_v , of the surface geomagnetic field, \mathbf{H} , is defined as positive downwards and is given by

$$H_v = H \sin I \quad (1.7)$$

where H is the magnitude of \mathbf{H} and I is the *inclination* of \mathbf{H} from horizontal, ranging from -90° to $+90^\circ$ and defined as positive downward. The horizontal component, H_h , is given by

$$H_h = H \cos I \quad (1.8)$$

and geographic north and east components are respectively,

$$H_N = H \cos I \cos D \quad (1.9)$$

$$H_E = H \cos I \sin D \quad (1.10)$$

where D is *declination*, the angle from geographic north to horizontal component, ranging from 0° to 360° , positive clockwise. Determination of I and D completely describes the direction of the geomagnetic field. If the components are known, the total intensity of the field is given by

$$H = \sqrt{H_N^2 + H_E^2 + H_v^2} \quad (1.11)$$

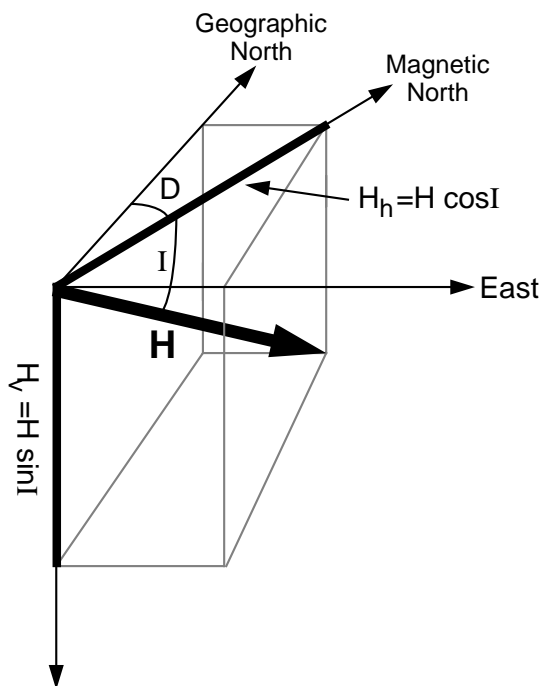


Figure 1.2 Description of the direction of the magnetic field. The total magnetic field vector \mathbf{H} can be broken into (1) a vertical component, $H_v = H \sin I$ and (2) a horizontal component, $H_h = H \cos I$; inclination, I , is the vertical angle (= dip) between the horizontal and \mathbf{H} ; declination, D , is the azimuthal angle between the horizontal component of \mathbf{H} ($= H_h$) and geographic north; the component of the magnetic field in the geographic north direction is $H \cos I \cos D$; the east component is $H \cos I \sin D$. Redrawn after McElhinny (1973).

GEOCENTRIC AXIAL DIPOLE MODEL

A concept that is central to many principles of paleomagnetism is that of the *geocentric axial dipole* (GAD), shown in Figure 1.3. In this model, the magnetic field produced by a single magnetic dipole at the center of the Earth and aligned with the rotation axis is considered. The GAD field has the following properties, which are derived in detail in the appendix on derivations:

$$H_h = \frac{M \cos \lambda}{r_e^3} \quad (1.12)$$

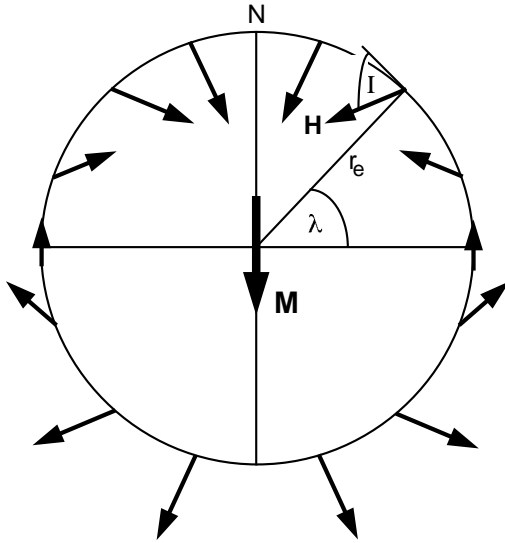


Figure 1.3 Geocentric axial dipole model. Magnetic dipole M is placed at the center of the Earth and aligned with the rotation axis; the geographic latitude is λ ; the mean Earth radius is r_e ; the magnetic field directions at the Earth's surface produced by the geocentric axial dipole are schematically shown; inclination, I , is shown for one location; N is the north geographic pole. Redrawn after McElhinny (1973).

$$H_v = \frac{2M \sin \lambda}{r_e^3} \quad (1.13)$$

$$H = \frac{M}{r_e^3} \sqrt{1 + 3 \sin^2 \lambda} \quad (1.14)$$

where M is the dipole moment of the geocentric axial dipole; λ is the geographic latitude, ranging from -90° at the south geographic pole to $+90^\circ$ at the north geographic pole; and r_e is the mean Earth radius.

The lengths of the arrows in Figure 1.3 schematically show the factor of 2 increase in magnetic field strength from equator to poles. The inclination of the field can be determined by

$$\tan I = \left(\frac{H_v}{H_h} \right) = \left(\frac{2 \sin \lambda}{\cos \lambda} \right) = 2 \tan \lambda \quad (1.15)$$

and I increases from -90° at the geographic south pole to $+90^\circ$ at the geographic north pole. Lines of equal I are parallel to lines of latitude and are simply related through Equation (1.15), which is a cornerstone of many paleomagnetic methods and is often referred to as “the dipole equation.” This relationship between I and λ will be essential to understanding many paleogeographic and tectonic applications of paleomagnetism. For a GAD, $D = 0^\circ$ everywhere.

THE PRESENT GEOMAGNETIC FIELD

The morphology of the present geomagnetic field is best illustrated with *isomagnetic charts*, which show some chosen property of the field on a world map. Figure 1.4 is an *isoclinic chart* showing contours of equal inclination of the surface geomagnetic field. The *geomagnetic equator* (line of $I = 0^\circ$) is close to the geographic equator, and inclinations are positive in the northern hemisphere and negative in the southern hemisphere. This is roughly the morphology of a geocentric axial dipole field, but there are obvious departures from that simplest configuration. The *magnetic poles* (locations where $I = \pm 90^\circ$; also called *dip poles*) are not at the geographic poles as expected for a GAD field, and the magnetic equator wavers about the geographic equator. The present geomagnetic field is obviously more complex than a GAD field, and the GAD model must be modified to better describe the field.

An *inclined geocentric dipole* is inclined to the rotation axis, as shown in Figure 1.5. The inclined geocentric dipole that best describes the present geomagnetic field has an angle of $\sim 11.5^\circ$ with the rotation axis. The poles of the best-fitting inclined geocentric dipole are the *geomagnetic poles*, which are points on

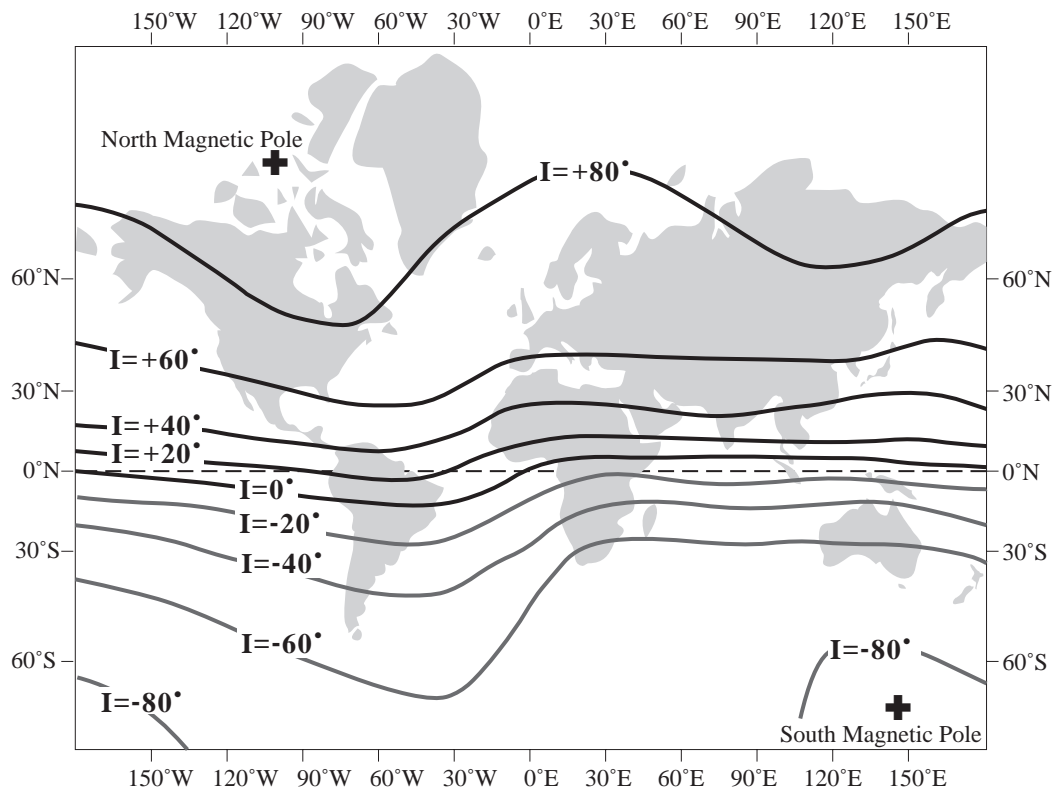


Figure 1.4 Isoclinic chart of the Earth's magnetic field for 1945. Contours are lines of equal inclination of the geomagnetic field; the locations of the magnetic poles are indicated by plus signs; Mercator map projection. Redrawn after McElhinny (1973).

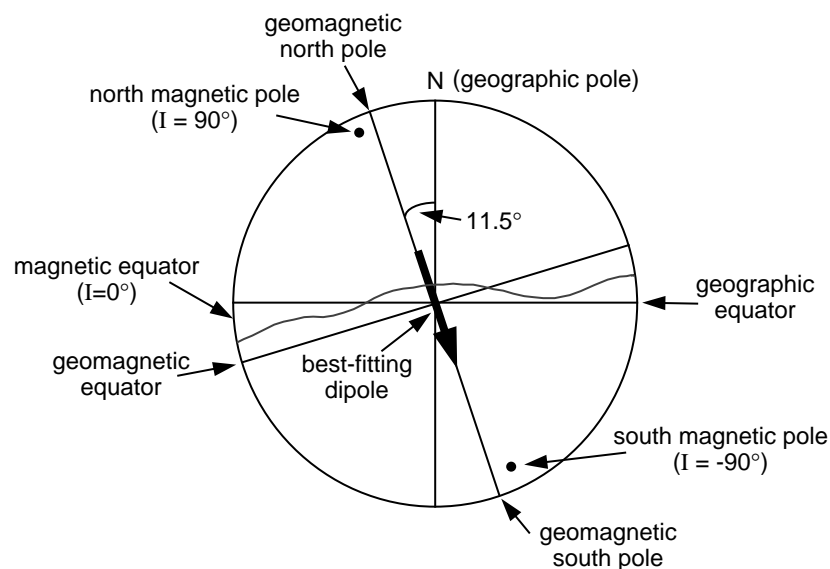


Figure 1.5 Inclined geocentric dipole model. The best-fitting inclined geocentric dipole is shown in meridional cross section through the Earth in the plane of the geocentric dipole; distinctions between magnetic poles and geomagnetic poles are illustrated; a schematic comparison of geomagnetic equator and magnetic equator is also shown. Redrawn after McElhinny (1973).

the surface where extensions of the inclined dipole intersect the Earth's surface. If the geomagnetic field were exactly that of an inclined geocentric dipole, then the geomagnetic poles would exactly coincide with the dip poles. The fact that these poles do not coincide indicates that the geomagnetic field is more complicated than can be explained by a dipole at the Earth's center. Although the inclined geocentric dipole accounts for ~90% of the surface field, the amount remaining is significant.

It is possible to further refine the fit of a single dipole to the geomagnetic field by relaxing the geocentric constraint, allowing the dipole to be positioned to best fit the field. This best-fitting dipole is the *eccentric dipole*, which describes the field only marginally better than the inclined geocentric dipole. For the present geomagnetic field, the best-fitting eccentric dipole is positioned about 500 km (~8% of Earth radius) from the geocenter, toward the northwestern portion of the Pacific Basin.

The ability of the best-fitting eccentric dipole to describe the geomagnetic field depends on location on the Earth's surface. At some locations, the best-fitting eccentric dipole perfectly describes the geomagnetic field. But at other locations, up to 20% of the surface geomagnetic field cannot be described by even the best-fitting dipole. This discrepancy indicates the presence of a higher-order portion of the geomagnetic field, which is called the *nondipole field*. This nondipole field is determined by subtracting the best-fitting dipolar field from the observed geomagnetic field. A plot of the nondipole field (for the year 1945) is shown in Figure 1.6, where the contours give the vertical component of the nondipole field and the arrows show the magnitude and direction of the horizontal component of the nondipole field.

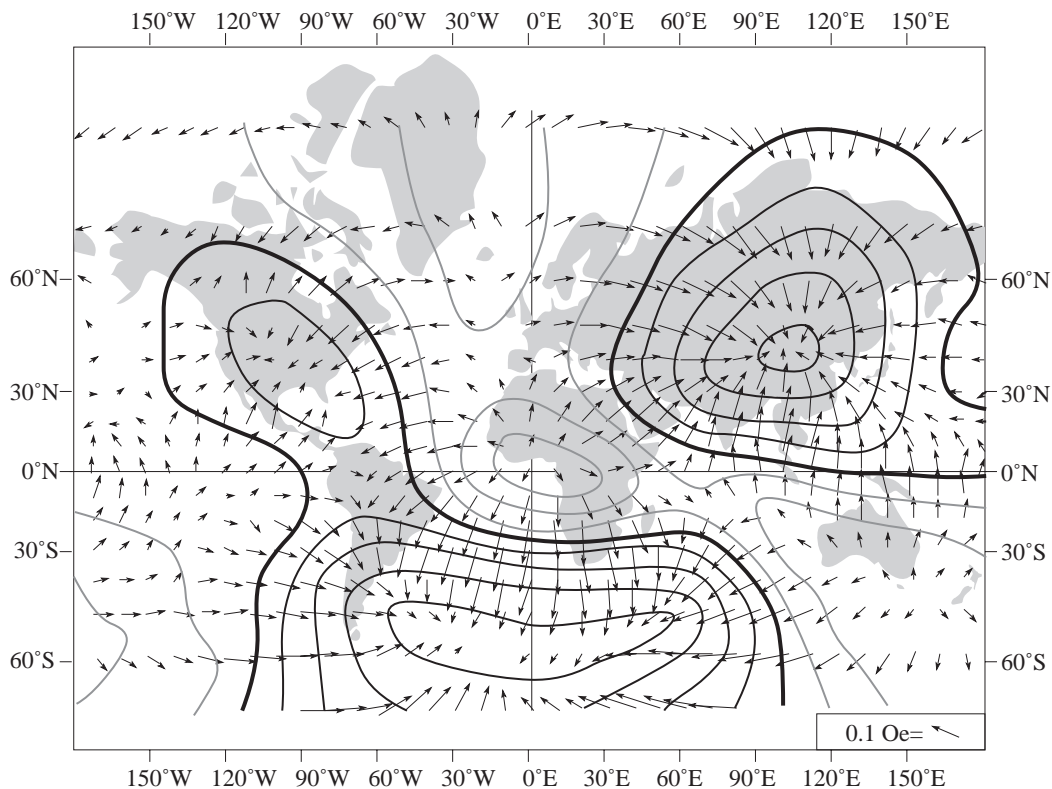


Figure 1.6 The nondipole geomagnetic field for 1945. Arrows indicate the magnitude and direction of the horizontal component on the nondipole field; the scale for the arrows is shown at the lower right corner of the diagram; contours indicate lines of equal vertical intensity of the nondipole field; heavy black lines are contours of zero vertical component; thin black lines are contours of positive (downward) vertical component, while gray lines are contours of negative vertical component; the contour interval is 0.02 Oe. Notice the clown-face appearance with the nondipole magnetic field going into the eyes and mouth and being blown out the nose. Redrawn from Bullard et al. (*Phil. Trans. Roy. Soc. London*, v. A243, 67–92, 1950).

Note that in Figure 1.6 there are six or seven continental-scale features that dominate the nondipole field. Some of these features have upward-pointing vertical field and horizontal components that point away from the center of the feature. Magnetic field lines are emerging from the Earth and radiating away from these features. Other nondipole features show the opposite pattern, with magnetic field lines pointing downward and toward the center of the feature. These patterns of the nondipole field can be modeled (at least mathematically) by placing radially pointing magnetic dipoles under each nondipole feature. (However, be advised that the physical interpretation of nondipole features is a matter of debate among geomagnetists.) These radial dipoles are (by best-fit mathematics) placed within the fluid outer core near the boundary with the overlying mantle. Opposite signs of these radial dipoles can account for the opposing field patterns of the nondipole features. This morphology and modeling of the nondipole field suggest an origin in fluid eddy currents in the outer core near the interface with the overlying solid mantle. Indeed, nondipole features are dynamic and exhibit growth, decay, and motions similar to eddy currents in turbulent fluid flow. These time variations have been measured historically and can be determined prehistorically through various paleomagnetic methods.

GEOMAGNETIC SECULAR VARIATION

The direction and magnitude of the surface geomagnetic field change with time. Changes with periods dominantly between 1 yr and 10^5 yr constitute *geomagnetic secular variation*. Even over the time of historic geomagnetic field records, directional changes are substantial. Figure 1.7 shows historic records of geomagnetic field direction in London since reliable recordings were initiated just prior to 1600 A.D. The range of inclination is 66° to 75° , and the range of declination is -25° to $+10^\circ$, so the directional changes are indeed substantial.

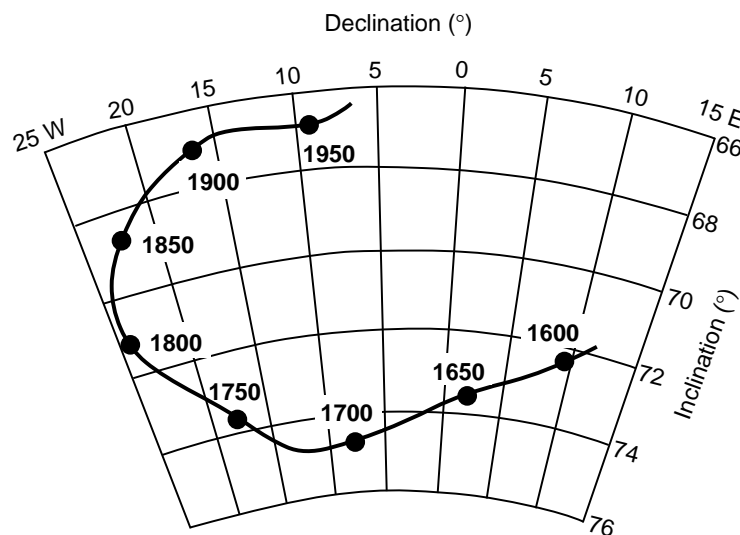


Figure 1.7 Historic record of geomagnetic field direction at Greenwich, England. Declination and inclination are shown; data points are labeled in years A.D.; azimuthal equidistant projection. Redrawn after Malin and Bullard (*Phil. Trans. Roy. Soc. London*, v. A299, 357–423, 1981.)

Patterns of secular variation are similar over subcontinental regions. For example, the pattern of secular variation observed in Paris is similar to that in London. However, from one continent to another, patterns of secular variation are very different. This observation probably reflects the size of the nondipole sources of geomagnetic field within the Earth's core.

The dominant period of the secular variation is longer than the London record, and this sometimes leads to the incorrect impression that secular variation is cyclic and predictable. One of the early objectives of

paleomagnetic investigations (and an area of active research now) was to obtain records of geomagnetic secular variation. Paleomagnetism of archeological artifacts (*archeomagnetism*), Holocene volcanic rocks, and postglacial lake sediments have provided information about secular variation.

A record of geomagnetic secular variation recorded by sediments in Fish Lake in southern Oregon is shown in Figure 1.8. Most directions are within 20° of the mean, but short-term deviations of larger amplitude are present. The observed directional changes are not cyclic. Instead, the directional change is better characterized as a *random walk* about the mean direction. There is a range of periodicities dominantly within 10^2 – 10^4 yr. Spectral analysis indicates a broad band of energy with periods in the 3000- to 9000-yr interval and maximum energy with periods in the 2500- to 3000-yr range.

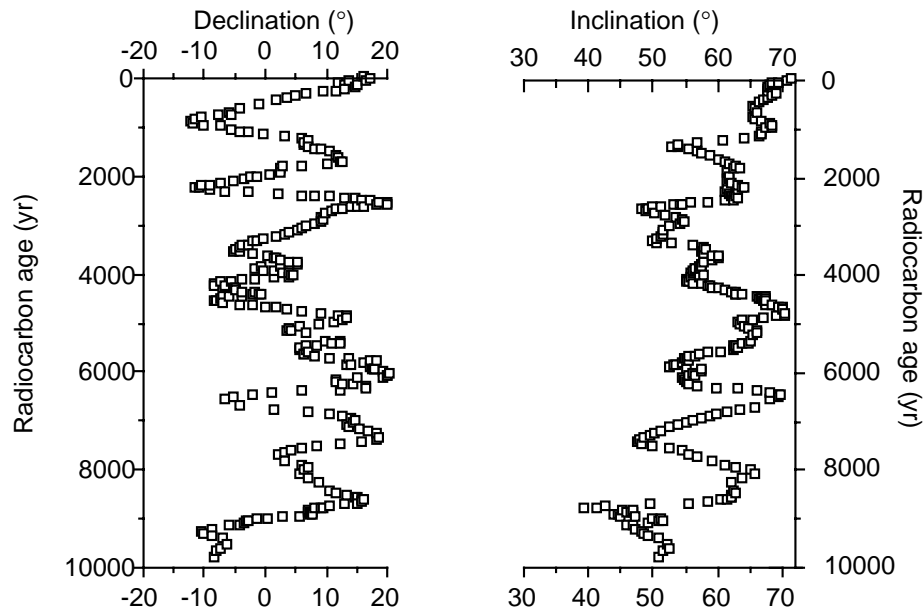


Figure 1.8 Record of Holocene geomagnetic secular variation recorded by sediments in Fish Lake in southeastern Oregon. Declination and inclination are shown against radiocarbon age. Data kindly provided by K. Verosub.

The origins of geomagnetic secular variation can be crudely subdivided into two contributions with overlapping periodicities: (1) nondipole changes dominating the shorter periods and (2) changes of the dipolar field with longer periods. Changes in the nondipole field dominate periodicities less than 3000 yr. Nondipole features appear to grow, decay, and deform with lifetimes of $\sim 10^3$ yr. Over historic time, there has been a tendency for some features of the nondipole field to undergo *westward drift*, a longitudinal shift toward the west at a rate of about 0.4° longitude per year. Other nondipole features appear to be stationary.

The dipole portion of the geomagnetic field (90% of the surface field) also changes direction and amplitude. To separate changes of the dipole and nondipole fields, historic records as well as archeomagnetic records and paleomagnetic records from Holocene volcanic rocks have been analyzed. Eight regions of the globe were defined within which mean directions of the geomagnetic field were determined at 100-yr intervals. Magnetic pole positions determined from these regional mean directions were then averaged to yield a global average geomagnetic pole for each 100-yr interval over the past 2000 yr. Results are shown in Figure 1.9.

Because this procedure has provided a global spatial average, effects of the nondipole field have been averaged out, and the secular variation evident in Figure 1.9 is that of the dipole field. The record shows the geomagnetic pole performing a random walk about the north geographic pole (the analogy is a drunk staggering around a light pole). The average position of the geomagnetic pole is indistinguishable from the

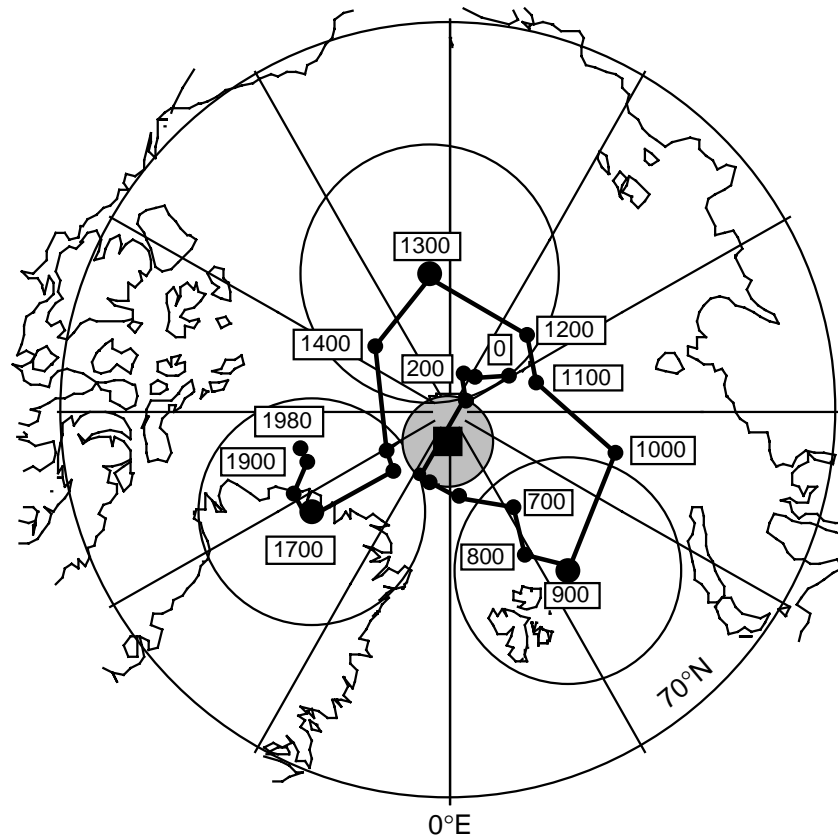


Figure 1.9 Positions of the north geomagnetic pole over the past 2000 yr. Each data point is the mean geomagnetic pole at 100-yr intervals; numbers indicate date in years A.D.; circles about geomagnetic poles at 900, 1300, and 1700 A.D. are 95% confidence limits on those geomagnetic poles; the mean geomagnetic pole position over the past 2000 yr is shown by the square with stippled region of 95% confidence. Data compiled by Merrill and McElhinny (1983).

rotation axis, indicating that the geocentric axial dipole model describes the time-averaged geomagnetic field when averaged over the past 2000 yr. This supports a crucial hypothesis about the geomagnetic field known as the *geocentric axial dipole hypothesis*. This hypothesis simply states that the time-averaged geomagnetic field is a geocentric axial dipolar field. Because this hypothesis is central to many applications of paleomagnetism, it will be explored in considerable detail later.

In addition to changes in orientation of the best-fitting dipole (depicted by changes in geomagnetic pole position shown in Figure 1.9), the amplitude of the geomagnetic dipole also changes with time. A compilation of results is shown in Figure 1.10, which shows variations in the magnitude of the dipole moment. Over the past 10^4 yr, the average dipole moment is 8.75×10^{25} G cm³ (8.75×10^{22} A m²). Changes in dipole moment appear to have a period of roughly 10^4 yr, with oscillations of up to $\pm 50\%$ of the mean value.

The picture of the geomagnetic field that emerges from examination of secular variation is one of directional and amplitude changes that are quite rapid for a geological phenomenon. Although short-term deviations of the geomagnetic field direction from the long-term mean direction can exceed 30° or so, the time-averaged field is strikingly close to that of the elegantly simple geocentric axial dipole.

On longer time scales than those considered above, the dipolar geomagnetic field has been observed to switch polarity. The present configuration of the dipole field (pointing toward geographic south) is referred to as *normal polarity*, the opposite configuration is defined as *reversed polarity*. Reversal of the polarity of the dipole produces a 180° change in surface geomagnetic field direction at all points. We shall investigate this phenomenon (especially the geomagnetic polarity time scale) in a later chapter. For now, the essential

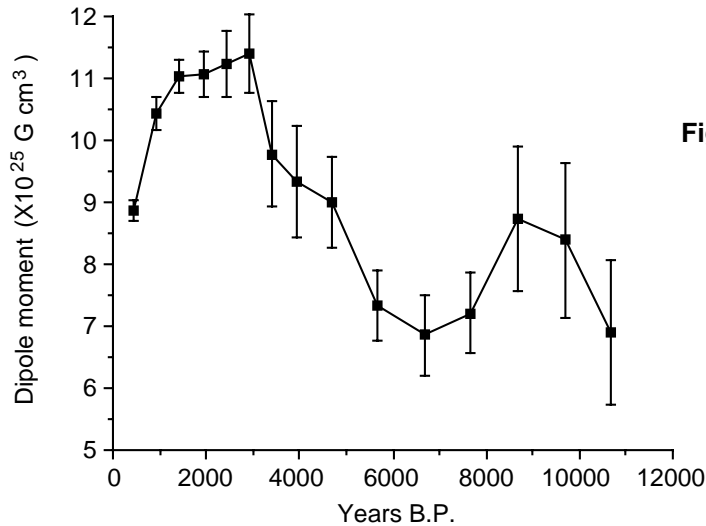


Figure 1.10 Geomagnetic dipole moment over the past 10,000 years. Means for 500-yr intervals are shown to 4000 yr B.P.; 1000-yr means are shown from 4000 to 10,000 yr B.P.; error bars are 95% confidence limits. Redrawn after Merrill and McElhinny (1983).

feature is that the geocentric axial dipole model describes the time-averaged geomagnetic field during either normal-polarity or reversed-polarity intervals.

ORIGIN OF THE GEOMAGNETIC FIELD

Measurement and description of the geomagnetic field and its spatial and temporal variations comprise one of the oldest geophysical disciplines. However, our ability to describe the field far exceeds our understanding of its origin. All plausible theories involve generation of the geomagnetic field within the fluid outer core of the Earth by some form of *magnetohydrodynamic dynamo*. Attempts to solve the full mathematical complexities of magnetohydrodynamics have driven some budding geomagnetists into useful but nonscientific lines of work. In fact, complete dynamical models have not been accomplished, although the plausibility of the magnetohydrodynamic origin of the geomagnetic field is well established.

Quantitative treatment of magnetohydrodynamics is (mercifully) beyond the scope of this book, but we can provide a qualitative explanation. The first step is to gain some appreciation for what is meant by *self-exciting dynamo*. A simple electromechanical disk-dynamo model such as that shown in Figure 1.11 contains the essential elements of a self-exciting dynamo. The model is constructed of a copper disk rotating on an electrically conducting axle. An initial magnetic induction field, \mathbf{B} (see Appendix 1.1 for definition), is present in an upward direction perpendicular to the copper disk. Electrons in the copper disk experience a *Lorenz force*, \mathbf{F}_L , when they pass through this field. The Lorenz force is given by:

$$\mathbf{F}_L = q \mathbf{v} \times \mathbf{B} \quad (1.16)$$

where q is the electrical charge of the electrons, and \mathbf{v} is the velocity of electrons. This Lorenz force on the electrons is directed toward the axle of the disk and the resulting electrical current flow is toward the outside of the disk (Figure 1.11).

Brush connectors are used to tap the electrical current from the disk, and the current passes through a coil under the disk. This coil is wound so that the electrical current produces a magnetic induction field in the same direction as the original field. The electrical circuit is a *positive feedback system* that reinforces the original magnetic induction field. The entire disk-dynamo model is a self-exciting dynamo. As long as the disk is kept rotating, the electrical current will flow, and the magnetic field will be sustained.

With this simple model we encounter the essential elements of any self-exciting dynamo:

1. A moving electrical conductor is required and is represented by the rotating copper disk.
2. An initial magnetic field is required.

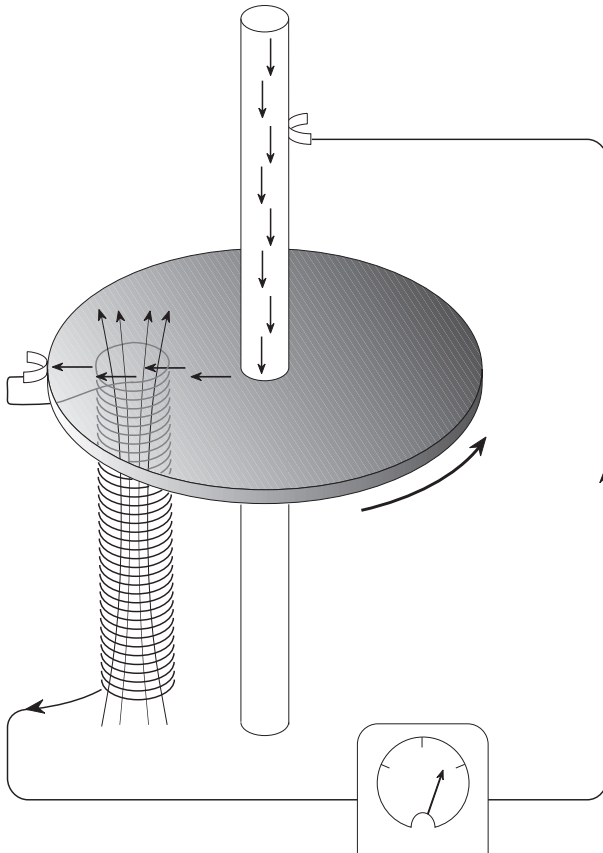


Figure 1.11 Self-exciting disk dynamo. The copper disk rotates on an electrically conducting axle; electrical current is shown by bold arrows; the magnetic field generated by the coil under the disk is shown by the fine arrows. (Adapted from *The Earth as a Dynamo*, W. Elsasser, Copyright© 1958 by Scientific American, Inc. All rights reserved.)

3. An interaction between the magnetic field and the conductor must take place to provide reinforcement of the original magnetic field. In the model, this interaction is the Lorentz force with the coil acting as a positive feedback (self-exciting) circuit.
4. Energy must be supplied to overcome electrical resistivity losses. In the model, energy must be supplied to keep the disk rotating.

Certainly no one proposes that systems of disks and feedback coils exist in the Earth's core. But interaction between the magnetic field and the electrically conducting iron-nickel alloy in the outer core can produce positive feedback and allow the Earth's core to operate as a self-exciting magnetohydrodynamic dynamo. For reasonable electrical conductivities, fluid viscosity, and plausible convective fluid motions in the Earth's outer core, the fluid motions can regenerate the magnetic field that is lost through electrical resistivity. There is a balance between fluid motions regenerating the magnetic field and loss of magnetic field because of electrical resistivity.

Apparently, fluid motions in the Earth's core are sufficient to regenerate the field, but there is enough leakage to keep the shape of the geomagnetic field fairly simple. Thus, the dominant portion of the geomagnetic field is the (simplest possible) dipolar shape with subsidiary nondipolar features probably resulting from fluid eddy currents within the core near the boundary with the overlying mantle.

Even this qualitative view of magnetohydrodynamics provides an explanation for the time-averaged geocentric axial dipolar nature of the geomagnetic field. Rotation of the Earth must be a controlling factor on the time-averaged fluid motions in the outer core. Therefore, the time-averaged magnetic field generated by these fluid motions is quite logically symmetric about the axis of rotation. The simplest such field is a geocentric axial dipolar field.

It should also be pointed out that the magnetohydrodynamic dynamo can operate in either polarity of the dipole. All the physics and mathematics of magnetohydrodynamic generation are invariant with polarity of the dipolar field. Thus, there is no contradiction between the observation of reversals of the geomagnetic

dipole and magnetohydrodynamic generation of the geomagnetic field. However, understanding the special interactions of fluid motions and magnetic field that produce geomagnetic reversals is a major challenge.

As wise economists have long observed, there is no free lunch. The geomagnetic field is no exception. Because of ohmic dissipation of energy, there is a requirement for energy input to drive the magnetohydrodynamic fluid motions and thereby sustain the geomagnetic field. Estimates of the power (energy per unit time) required to generate the geomagnetic field are about 10^{13} W (roughly the output of 10^4 nuclear power plants). This is about one fourth of the total geothermal flux, so the energy involved in generation of the geomagnetic field is a substantial part of the Earth's heat budget.

Many sources of this energy have been proposed, and ideas on this topic have changed over the years. The energy source that is currently thought to be most reasonable is gradual cooling of the Earth's core with attendant freezing of the outer core and growth of the solid inner core. This energy source is plausible in terms of the energy available from growth of the inner core and is efficient in converting energy to fluid motions of the outer core required to generate the geomagnetic field.

APPENDIX 1.1: ABOUT UNITS

Any system of units is basically an arbitrary set of names created to facilitate communication about measured or calculated quantities. These units can be broken down into fundamental quantities: mass, length, time, and electric charge. Before about 1980, most geophysical literature used the cgs system, for which fundamental units were gram (gm), centimeter (cm), seconds (s), and coulomb (C). In an effort to obtain uniformity across various disciplines of physical sciences, international committees have lately recommended usage of the *Système Internationale* (SI). The SI fundamental units are the meter (m), kilogram (kg), second (s), and coulomb (C). For basic quantities (e.g., force), both the cgs and SI systems are simple and conversions from one system to the other are by integral powers of 10.

However, things are not simple for magnetism, and for various reasons, conversion from cgs to SI has led to confusion rather than clarity. Obviously, we must have a system to follow in this book, and so we must confront the potentially confusing issue of units. In doing so, I adhere to our objective of making the paleomagnetic literature accessible and so provide a basic guide to units as they are actually used by paleomagnetists. First the cgs and SI governing equations and units are explained and a table of the units and conversions is provided. Then the current usage of units in paleomagnetism and the (we hope) simplified system used in this book are explained.

In dealing with units of magnetism, the cgs system is sometimes known as the Gaussian system or emu (electromagnetic) system. In the cgs system, the basic quantities are

\mathbf{B} = magnetic induction

\mathbf{H} = magnetic field

\mathbf{J} = magnetic moment per unit volume, or magnetization

These quantities in cgs are related by

$$\mathbf{B} = \mu_0 \mathbf{H} + 4\pi \mathbf{J} \quad (\text{A1.1})$$

where

$$\mathbf{J} = \chi \mathbf{H} \quad (\text{A1.2})$$

χ = magnetic susceptibility

and:

μ_0 = magnetic permeability of free space = 1.0

\mathbf{B} , \mathbf{H} , and \mathbf{J} all have the same fundamental units. However, common practice has been to refer to units of \mathbf{B} as gauss (G), units of \mathbf{H} as oersteds (Oe), and units of \mathbf{J} as either gauss or emu/cm^3 . Susceptibility, χ , is dimensionless.

In the SI system, \mathbf{B} , \mathbf{H} , and \mathbf{J} are also used, but an additional quantity, \mathbf{M}_v , is introduced as the magnetic moment per unit volume. (The symbol \mathbf{M}_v is used for volume density of magnetic moment in an attempt to avoid confusion with \mathbf{M} , which is used for magnetic moment.) These quantities in SI are related by

$$\mathbf{B} = \mu_0 \mathbf{H} + \mathbf{J} \quad (\text{A1.3})$$

where $\mu_0 = 4\pi \times 10^{-7}$ henries/m = permeability of free space and

$$\mathbf{J} = \frac{\chi \mathbf{H}}{\mu_0} \quad (\text{A1.4})$$

In SI, \mathbf{B} and \mathbf{J} have the same fundamental unit, given the name tesla (T), and \mathbf{M}_v and \mathbf{H} have the same fundamental unit, amperes/meter (A/m). Again, χ is dimensionless (although this is not so obvious as it was for cgs). Table 1.1 summarizes the fundamental dimensions, units, and conversions for basic quantities in cgs and SI.

Those advocating strict usage of SI would force us to use SI units throughout this book and convert all previous paleomagnetic literature according to Table 1.1. I am not going to do that, not only because I happen to be a little stubborn, but because the current paleomagnetic literature does not strictly conform to SI. I could write this book to conform strictly to SI (honest I could), but the reader would then have unnecessary difficulties in following units in past and current paleomagnetic literature.

The current usage of units in paleomagnetism has developed in the following way. Paleomagnetism and rock magnetism developed when cgs (emu) was the prevailing system. Early literature employs cgs units, and almost all instruments are calibrated in cgs. In addition, for some considerations (like energetics of interactions of magnetic dipole moments with magnetic fields), the cgs system is simply easier to deal with. However, because adherence to SI is now required by most Earth science journals, most paleomagnetists currently do their laboratory work (and thinking?) in cgs, then convert to SI at the last moment to conform with requirements for publication. The conversions used in doing so are really a perversion of the proper SI usage.

For example, let us say that a paleomagnetist does laboratory work on a suite of rocks that have intensity of magnetization, J , of 10^{-4} G. Almost invariably, this observation will get converted to SI by reporting intensity of magnetization as 10^{-1} A/m. Strict adherence to SI would require converting the observed 10^{-4} G magnetization to proper SI units of J which would yield $4\pi \times 10^{-8}$ T. But that procedure requires the dreaded 4π factor and is almost never done. To convert by simple integral powers of ten, the observed intensity of magnetization in cgs is converted (perhaps knowingly but maybe not) to an equivalent SI value of magnetic moment/unit volume, M_v , thus yielding 10^{-1} A/m.

In converting intensities of magnetic fields, H , from cgs units of Oe to SI units, a similar trick is employed. Again, strict adherence to SI would require converting an observed 100 Oe magnetic field to proper SI units of H , yielding $(1/4\pi) \times 10^5$ A/m. Once again to avoid the undesirable 4π factor, the observed magnetic field in oersteds is converted to the equivalent magnetic induction, $B = 100$ G. Then this value is converted to SI to yield a “magnetic field” (really magnetic induction) value of 10^{-2} tesla or 10 millitesla (mT). This commonly employed scheme of conversion from cgs (emu) to SI is summarized at the bottom of Table 1.1. Clearly, the confusion introduced by these conversions is considerable.

In this book, we use a system of units that is most effective for teaching paleomagnetism and for providing an introduction to the past and current paleomagnetic literature. We use definitions and governing equations for magnetic quantities that are rooted in the cgs system and provide easy conversions to SI. With any system of units, there are some pitfalls, and our system is no exception. Frankly, the primary pitfall is that even the most diligent student is likely to be bored by this discussion of units. Another pitfall is that many presentations employing SI use \mathbf{M} as the symbol for dipole moment per unit volume. But the paleomagnetic literature is full of usages of \mathbf{M} as magnetic dipole moment. In an effort to be consistent with that common usage, we also use \mathbf{M} for magnetic dipole moment. (The only known antidotes to discussions of units are undisturbed silence in a dark room for 15 minutes or a brisk walk in the park. Excess worry about systems of units may cause you to give up the quest of paleomagnetism and take up, say, modern dance.)

TABLE 1.1. Units and Conversions for Common Quantities of Magnetism

| | cgs (emu) System | | Système Internationale (SI) | | Conversion |
|------------------------------------|---|---|-----------------------------------|------------------------------|---|
| | Fundamental Units | Unit | Fundamental Units | Unit | |
| Energy | | erg | | joule (J) | $1 \text{ erg} = 10^{-7} \text{ joule}$ |
| Force (<i>F</i>) | gm cm s^{-2} | dyne | kg m s^{-2} | newton (N) | $1 \text{ dyne} = 10^{-5} \text{ newton}$ |
| Current (<i>I</i>) | 10 C s^{-1} | abampere | C s^{-1} | ampere (A) | $1 \text{ abampere} = 10 \text{ ampere}$ |
| Magnetic Induction (<i>B</i>) | $0.1 \text{ gm s}^{-1} \text{ C}^{-1}$ | gauss (G) | $\text{kg s}^{-1} \text{ C}^{-1}$ | tesla (T) | $1 \text{ gauss} = 10^{-4} \text{ tesla}$ |
| Magnetic Field (<i>H</i>) | $0.1 \text{ gm s}^{-1} \text{ C}^{-1}$ | oersted (Oe) | $\text{C s}^{-1} \text{ m}^{-1}$ | ampere m^{-1} (A/m) | $1 \text{ Oe} = (1/4\pi) \times 10^3 \text{ A/m}$ |
| Magnetization (<i>J</i>) | $0.1 \text{ gm s}^{-1} \text{ C}^{-1}$ | gauss (G) (= emu cm^{-3}) | $\text{kg s}^{-1} \text{ C}^{-1}$ | tesla (T) | $1 \text{ gauss} = 4\pi \times 10^{-4} \text{ tesla}$ |
| Magnetic Dipole Moment/Unit Volume | $0.1 \text{ gm s}^{-1} \text{ C}^{-1}$ | gauss (G) (= emu cm^{-3}) | $\text{C s}^{-1} \text{ m}^{-1}$ | A/m | $1 \text{ gauss} = 10^3 \text{ A/m}$ |
| Magnetic Moment (<i>M</i>) | $0.1 \text{ gm s}^{-1} \text{ C}^{-1} \text{ cm}^3$ | gauss cm^3 (G cm^3 = emu) | $\text{C s}^{-1} \text{ m}^2$ | A m^2 | $1 \text{ gauss cm}^3 = 10^{-3} \text{ A m}^2$ |
| Magnetic Susceptibility (χ) | Dimensionless | | Dimensionless | | $\chi \text{ (cgs)} = 4\pi \chi \text{ (SI)}$ |

Conversions commonly employed in paleomagnetism: Magnetization, $J = 10^{-3} \text{ G}$ converts to "magnetization" = 1 A/m. Magnetic field, $H = 1 \text{ Oe}$ converts to magnetic "field" = $10^{-4} \text{ T} = 0.1 \text{ mT}$.

Some Examples: Surface geomagnetic field strength: 0.24–0.66 Oe = 0.024–0.066 mT. Magnetic field generated by laboratory electromagnet: 2000 Oe = 0.2 T = 200 mT. Magnetic dipole moment of the earth: $8 \times 10^{25} \text{ G cm}^3 = 8 \times 10^{22} \text{ A m}^2$.

Natural remanent magnetization of rocks: basalt: $10^{-3} \text{ G} = 1 \text{ A/m}$; granite: $10^{-4} \text{ G} = 0.1 \text{ A/m}$; nonmarine siltstone: $10^{-5} \text{ G} = 10^{-2} \text{ A/m}$; marine limestone: $10^{-7} \text{ G} = 10^{-4} \text{ A/m}$.

SUGGESTED READINGS

- M. W. McElhinny, *Palaeomagnetism and Plate Tectonics*, Cambridge, London, 356 pp., 1973.
Chapter 1 presents an introduction to the geomagnetic field.
- R. T. Merrill and M. W. McElhinny, *The Earth's Magnetic Field*, Academic Press, London, 401 pp., 1983.
An excellent text on geomagnetism. Chapter 2 provides a thorough introduction to the geomagnetic field and historical secular variation.
- P. N. Shive, Suggestions for the use of SI units in magnetism, *Eos Trans. AGU*, v. 67, 25, 1986.
Summarizes the problems with units in magnetism.

PROBLEMS

- 1.1 The pattern of the nondipole geomagnetic field around a major feature of the nondipole field can be modeled by a magnetic dipolar source placed near the core-mantle boundary directly under the center of the feature. Figure 1.12 shows a meridional cross section through the Earth in the plane of the nondipole feature and the magnetic dipole used to model the nondipole feature. At the location directly above the model dipole, the nondipole field is directed vertically downward and has intensity 0.1 Oe. The model dipole is placed at 3480 km from the center of the Earth. Adapt the geometry of Figure 1.3 and the equations describing the magnetic field of a geocentric axial dipole to the model dipole in Figure 1.12. Calculate the magnetic dipole moment of the model dipole and compare your answer to the magnetic dipole moment of the best-fitting dipole for the present geomagnetic field ($-8.5 \times 10^{25} \text{ G cm}^3$). Remember to get all required input parameters in cgs units; then your answer will be in cgs units of magnetic moment (G cm^3); mean Earth radius = 6370 km.

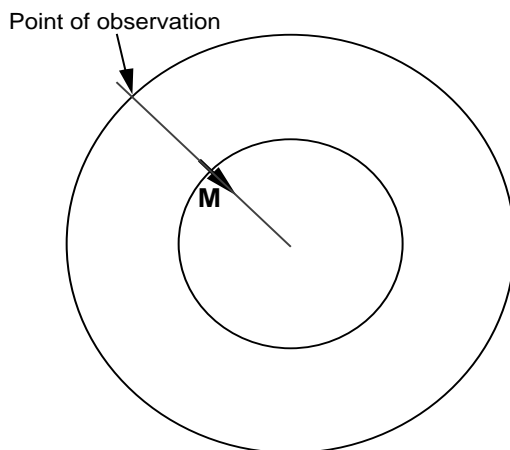


Figure 1.12 Model magnetic dipole for a nondipole feature of the geomagnetic field. The figure is a meridional cross section in the plane containing the middle of the nondipole feature (labeled “point of observation”), the center of the Earth, and the magnetic dipole used to model the nondipole feature.

- 1.2 The rate of westward drift of the nondipole geomagnetic field is about 0.4° of longitude per year. Features of the nondipole field are generally considered to originate from sources in the outer core near the boundary with the overlying mantle. Imagine a feature of the nondipole field that is centered on the geographic equator. If the source of this nondipole feature is at a distance of 3400 km from the geocenter, what is the linear rate of motion of the source with respect to the lower mantle? Calculate the linear rate in km/yr and in cm/s. (Note: On the Earth's surface at the equator, 1° of longitude ≈ 110 km. $1 \text{ yr} = 3.16 \times 10^7 \text{ s}$.)
- 1.3 Convert the following measured quantities in cgs units to SI units using the conversions generally applied in the paleomagnetic literature and described in Appendix 1.1.
- $J = 3.5 \times 10^{-5} \text{ G}$
 - $M = 2.78 \times 10^{-20} \text{ G cm}^3$
 - $H = 128 \text{ Oe}$

FERROMAGNETIC MINERALS

This chapter starts with a brief introduction to magnetic properties of solids. The bulk of the chapter concerns mineralogy and magnetic properties of iron-titanium oxides and iron sulfides, which are the dominant ferromagnetic minerals. Essential aspects (such as saturation magnetization, Curie temperature, and grain-size effects) are emphasized because these characteristics strongly affect magnetic properties. A firm grasp of the mineralogy of ferromagnetic minerals is required for understanding acquisition of paleomagnetic recordings in rocks and effects of elevated temperatures and chemical changes.

MAGNETIC PROPERTIES OF SOLIDS

Figure 2.1 illustrates the three fundamental types of magnetic properties observed in an experiment in which magnetization, J , acquired in response to application of a magnetic field, H , is monitored. In this section, these different magnetic behaviors are briefly discussed. This development uses the fact that some atoms have atomic magnetic moments because of orbital and spin motions of electrons. Atomic magnetic moments are quantized, and the smallest unit is the *Bohr magneton*, $M_B = 9.27 \times 10^{-21} \text{ G cm}^3$ ($= 9.27 \times 10^{-24} \text{ A m}^2$). Transition element solids (principally Fe-bearing) are the common solids with atoms possessing a magnetic moment because of unfilled 3d electron orbitals. Presentation of the atomic physics leading to atomic magnetic moments can be found in Chikazumi (1964).

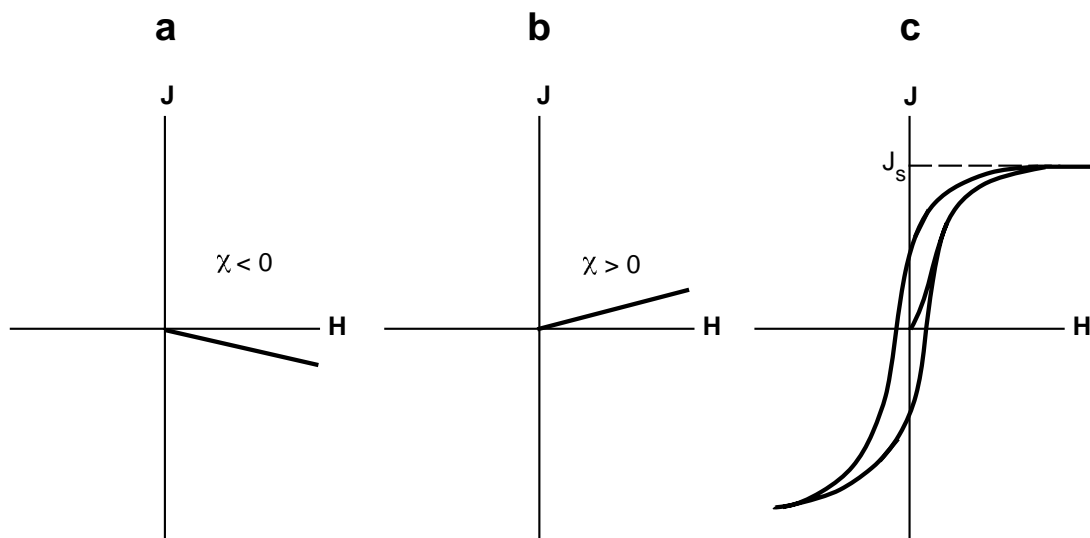


Figure 2.1 (a) Magnetization, J , versus magnetizing field, H , for a diamagnetic substance. Magnetic susceptibility, χ , is a negative constant. (b) J versus H for a paramagnetic substance. Magnetic susceptibility, χ , is a positive constant. (c) J versus H for a ferromagnetic substance. The path of magnetization exhibits hysteresis (is irreversible), and magnetic susceptibility, χ , is not a simple constant.

Diamagnetism

The *diamagnetic* response to application of a magnetic field (Figure 2.1a) is acquisition of a small induced magnetization, \mathbf{J}_i , opposite to the applied field, \mathbf{H} . The magnetization depends linearly on the applied field and reduces to zero on removal of the field. Application of the magnetic field alters the orbital motion of electrons to produce the small magnetization antiparallel to the applied magnetic field. This diamagnetic response is a property of all matter, but for substances whose atoms possess atomic magnetic moments, diamagnetism is swamped by effects of magnetic fields on the atomic magnetic moments. A material composed of atoms without atomic magnetic moments exhibits only the diamagnetic response and is classified as a diamagnetic material. Magnetic susceptibility, χ , for a diamagnetic material is negative and independent of temperature. An example of a diamagnetic mineral is quartz, SiO_2 , and a typical value of magnetic susceptibility is $\sim -10^{-6}$ in cgs units ($\sim -0.8 \times 10^{-7}$ SI).

Paramagnetism

Paramagnetic solids contain atoms with atomic magnetic moments (but no interaction between adjacent atomic moments) and acquire induced magnetization, \mathbf{J}_i , parallel to the applied field, \mathbf{H} (Figure 2.1b). For any geologically relevant conditions, J_i is linearly dependent on H . As with diamagnetic materials, magnetization reduces to zero when the magnetizing field is removed. An example of a paramagnetic mineral is fayalite, Fe_2SiO_4 , with room temperature magnetic susceptibility of $\sim 4.4 \times 10^{-4}$ cgs ($\sim 3.5 \times 10^{-5}$ SI).

In paramagnetic solids, atomic magnetic moments react independently to applied magnetic fields and to thermal energy. At any temperature above absolute zero, thermal energy vibrates the crystal lattice, causing atomic magnetic moments to oscillate rapidly and randomly in orientation. In the absence of an applied magnetic field, atomic moments are equally distributed in all directions with resultant magnetization $J_i = 0$.

Application of a magnetic field exerts an aligning torque (Equation (1.3)) on the atomic magnetic moments. The aligning energy of a magnetic moment, \mathbf{M} , in a field, \mathbf{H} , is given by Equation (1.4) as $E = -MH \cos \theta$ where θ is the angle from \mathbf{H} to \mathbf{M} . Consider an atomic magnetic moment, $M = 2M_B = 1.85 \times 10^{20}$ G cm³ ($= 1.85 \times 10^{23}$ A m²), in a magnetic field of 100 Oe ($= 10^{-2}$ T, ~ 100 times the surface geomagnetic field). The aligning energy is $MH = (1.85 \times 10^{20} \text{ G cm}^3) \times (10^2 \text{ Oe}) = 1.85 \times 10^{-18}$ erg ($= 1.85 \times 10^{27}$ J). However, thermal energy at 300°K (traditionally chosen as temperature close to room temperature, which provides easy arithmetic) is $kT = (1.38 \times 10^{-16} \text{ erg/}^\circ\text{K}) (300^\circ\text{K}) = 4.14 \times 10^{-14}$ erg, where k = Boltzmann constant. So thermal energy is 10^4 times the aligning energy; hence, magnetization is small even in this significant magnetizing field.

The *Langevin theory* provides an insightful model for paramagnetism. Consider a paramagnetic solid with N atomic moments per unit volume. The relative probability, $P(\theta)$, of an atomic moment \mathbf{M} having angle θ with the applied field \mathbf{H} is determined by statistical thermodynamics:

$$P(\theta) = \exp\left(\frac{MH \cos \theta}{kT}\right) \quad (2.1)$$

The degree of alignment depends exponentially on the ratio of aligning energy to thermal energy. Considering components of \mathbf{M} along \mathbf{H} , forcing the total number of atomic moments to equal N , and integrating over the 0 to π range of θ yield the basic result of Langevin theory:

$$J = NML(\alpha) \quad (2.2)$$

where

$$L(\alpha) = \coth(\alpha) - \frac{1}{\alpha}$$

$$\alpha = \frac{MH}{kT}$$

The function $L(\alpha)$ is the *Langevin function* plotted in Figure 2.2. Equation (2.2) predicts two intuitive results: (1) $J = 0$ for $H = 0$, because $\alpha = 0$ and $L(0) = 0$, and (2) for infinite magnetic field, $\alpha = \infty$, $L(\infty) = 1.0$, and $J = NM$, meaning that the atomic magnetic moments are completely aligned with the field.

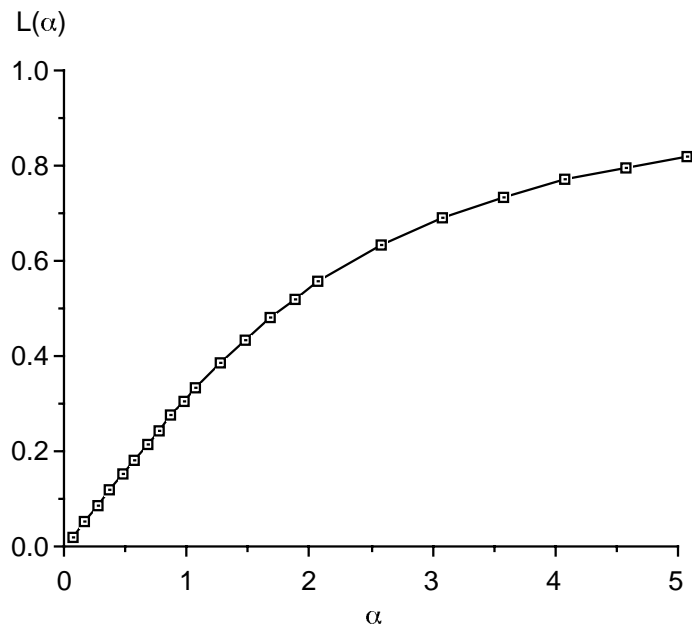


Figure 2.2 The Langevin function, $L(\alpha)$. Notice that for $\alpha < 1$, $L(\alpha) \approx \alpha/3$.

In any geologically reasonable situation, $\alpha = MH/kT$ is $< 10^{-6}$. The Langevin function is linear for $\alpha \ll 1$ with $L(\alpha) \approx \alpha/3$, and Equation (2.2) simplifies to

$$J = NML(\alpha) = \frac{NM\alpha}{3} = \frac{NM^2H}{3kT} \quad (2.3)$$

$$\chi = \frac{J}{H} = \frac{NM^2}{3kT} \quad (2.4)$$

This is the *Curie law of paramagnetic susceptibility*, which applies to any typical situation in rock magnetism. The Curie law predicts the observed constant value of paramagnetic susceptibility for a given material and temperature. In addition, the Curie law accounts for the observed $1/T$ decrease of χ with increasing temperature.

Ferromagnetism

Ferromagnetic solids have atoms with magnetic moments, but unlike the paramagnetic case, adjacent atomic moments interact strongly. The effect of interaction is to produce magnetizations in ferromagnetic solids that can be orders of magnitude larger than for paramagnetic solids in the same magnetizing field. For a given ferromagnetic material and temperature there is a maximum magnetization referred to as *saturation magnetization*, j_s (Figure 2.1c); increasing H beyond the level needed to reach j_s will not result in increased magnetization. Metallic iron is a ferromagnetic solid with saturation magnetization at room temperature $= 1.8 \times 10^3$ G (1.8×10^6 A/m).

Saturation magnetization decreases with increasing temperature, becoming zero at the *Curie temperature*, T_C , which is characteristic of the particular ferromagnetic material (580°C for magnetite and 680°C for hematite). Temperature dependences of j_s for magnetite and for hematite are shown in Figure 2.3. Above the Curie temperature, the material becomes paramagnetic.

Besides strong intensity of magnetization, the fundamental property of ferromagnetic solids that makes them the focus of our attention is their ability to record the direction of an applied magnetic field. During removal of the magnetizing field, magnetization does not return to zero but retains a record of the applied field. The path of magnetization, \mathbf{J} , as a function of applied field, \mathbf{H} , is called a *hysteresis loop*, and we will later examine hysteresis in detail. Because of hysteresis, magnetic susceptibility of ferromagnetic materials cannot be simply expressed as for diamagnetic or paramagnetic solids.

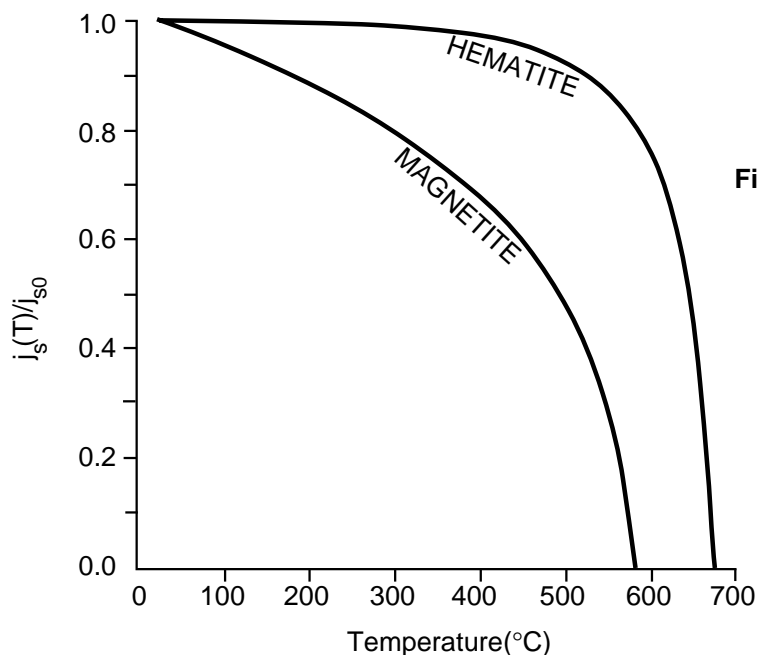


Figure 2.3 Normalized saturation magnetization versus temperature for magnetite and hematite. j_{s0} = saturation magnetization at room temperature; for hematite, $j_{s0} \approx 2$ G; for magnetite, $j_{s0} = 480$ G. Redrawn from Pullaiah et al. (*Earth Planet. Sci. Lett.*, v. 28, 133–143, 1975).

Coupling of adjacent atomic moments in a ferromagnetic material is the result of *exchange energy* of quantum mechanical nature. Classical physics does not provide an explanation for exchange energy, and rigorous understanding of exchange energy requires several years of mind-bending study. Furthermore, learning the necessary quantum mechanics has been known to disorient students. So we shall settle for a qualitative explanation of ferromagnetism.

The Pauli Principle states that only one electron per atom can have a particular set of the four quantum numbers n , l , l_z , and s_z . For an isolated atom of a transition element there is no confusion about the electron states occupied. However, for a collection of atoms within a crystal lattice, the situation can be complex. Electron orbitals are probability distributions that can have elongate shapes. Partial overlaps of electron probability distributions occur when atoms are packed together in a crystalline solid. These overlaps can develop so that electrons of adjacent atoms attempt to satisfy the Pauli Principle of both atoms simultaneously. The result is that electron states and magnetic moments of the adjacent atoms become strongly coupled. This simple view suggests how crystal structure and density of packing determine whether a solid containing transition elements is paramagnetic (no overlapping orbitals and no exchange coupling) or ferromagnetic (significant orbital overlap and resulting exchange coupling).

Because interatomic distance increases during thermal expansion, strength of exchange coupling and resultant j_s decrease with increasing temperature. At the Curie temperature, T_C , interatomic distances have increased to the point at which exchange coupling is destroyed. Atomic magnetic moments are then independent, and the material becomes paramagnetic. In general, the process is reversible, with exchange coupling and ferromagnetism again appearing when the material is cooled below T_C .

Magnetization of ferromagnetic solids to saturation is most easily achieved along certain crystallographic directions, called *magnetocrystalline easy directions*, and the crystallographic dependence of ferromagnetism is called *magnetocrystalline anisotropy*. This crystallographic directional dependence arises because electron orbitals must rotate as the atomic magnetic moments are forced to rotate. Because interatomic distances depend on crystallographic direction, the amount of orbital overlap (and resulting exchange energy) also depends on crystallographic direction. The result is magnetocrystalline anisotropy with exchange energy depending on crystallographic direction of magnetization. Magnetocrystalline anisotropy is a major source of stability for paleomagnetism in rocks and is developed more completely in Chapter 3.

Exchange energy may produce either parallel or antiparallel exchange coupling. The sense of coupling depends on the transition element involved and on crystal structure. Permutations of exchange coupling are shown in Figure 2.4. One can regard the general term *ferromagnetism* as applying to all three types of solids with coupling of atomic magnetic moments. Strictly speaking, *ferromagnetism* refers to solids with parallel coupling of adjacent atomic magnetic moments (Figure 2.4a). The situations depicted in Figure 2.4b and 2.4c involve parallel coupling within layers of atomic magnetic moments but antiparallel coupling between layers. If the layers have equal magnetic moment, opposing layers cancel, with resulting $j_s = 0$. This type of coupling is *antiferromagnetic*. If layers of unequal magnetic moment are antiparallel, the resulting j_s points in the direction of the dominant layer. Such materials are called *ferrimagnetic*, and many of the important “ferromagnetic” minerals are, in fact, ferrimagnetic. In what follows, the term “ferromagnetism” is used in the general sense to designate exchange-coupled materials. Where the exact type of coupling is important to the discussion, the terms antiferromagnetic, etc. will be used.

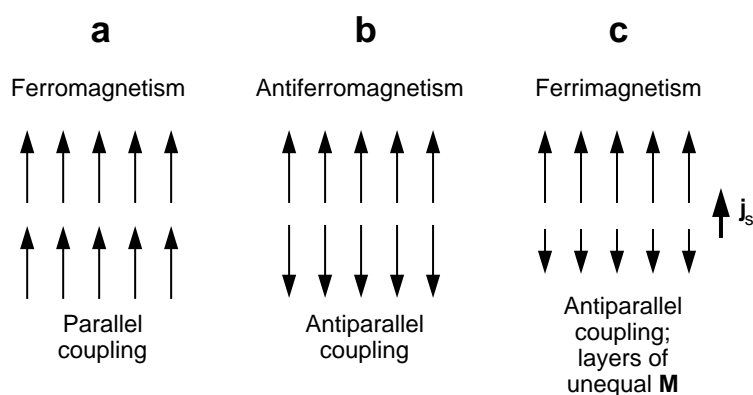


Figure 2.4 Exchange couplings for (a) ferromagnetic, (b) antiferromagnetic, and (c) ferrimagnetic materials. The net magnetization for ferrimagnetic material is shown at right; the net magnetization of antiferromagnetic material is zero.

MINERALOGY OF FERROMAGNETIC MINERALS

By far the most important ferromagnetic minerals are the *iron-titanium (FeTi) oxides*. FeTi oxides are generally opaque, and petrographic examination requires observations of polished sections in reflected light. These minerals are given little attention in standard petrology courses, which emphasize examination of thin sections in transmitted light. Accordingly, the FeTi oxides are generally an unfamiliar set of minerals. Understanding paleomagnetism requires some knowledge of the crystal chemistry and magnetic structure of FeTi oxides. This includes basic knowledge of phases formed as primary crystals from igneous melts and subsolidus reactions affecting these minerals to yield FeTi oxides encountered in igneous rocks and derivative sedimentary rocks.

Composition of the FeTi oxides are conveniently displayed on the $\text{TiO}_2\text{--FeO--Fe}_2\text{O}_3$ *ternary diagram* (Figure 2.5). Positions from left to right indicate increasing ratios of ferric (Fe^{3+}) to ferrous (Fe^{2+}) iron while positions from bottom to top indicate increasing Ti content (Ti^{4+} : total Fe). Using $(1/2)\text{Fe}_2\text{O}_3$ as the parameter for the Fe^{3+} corner normalizes the diagram to one cation, producing the convenient effect that lines of oxidation (increasing the $\text{Fe}^{3+}:\text{Fe}^{2+}$ ratio) are parallel to the base of the diagram. Two solid solution series, titanomagnetites and titanohematites, are the primary focus of our attention. Members of both series are primary crystallizing phases in igneous rocks, generally constituting from 1% to 5% by volume.

Titanomagnetites

The *titanomagnetites* are opaque, cubic minerals with compositions between end members *magnetite* (Fe_3O_4) and *ulvöspinel* (Fe_2TiO_4). The crystal structure of titanomagnetites is the *spinel structure*. A unit cell con-

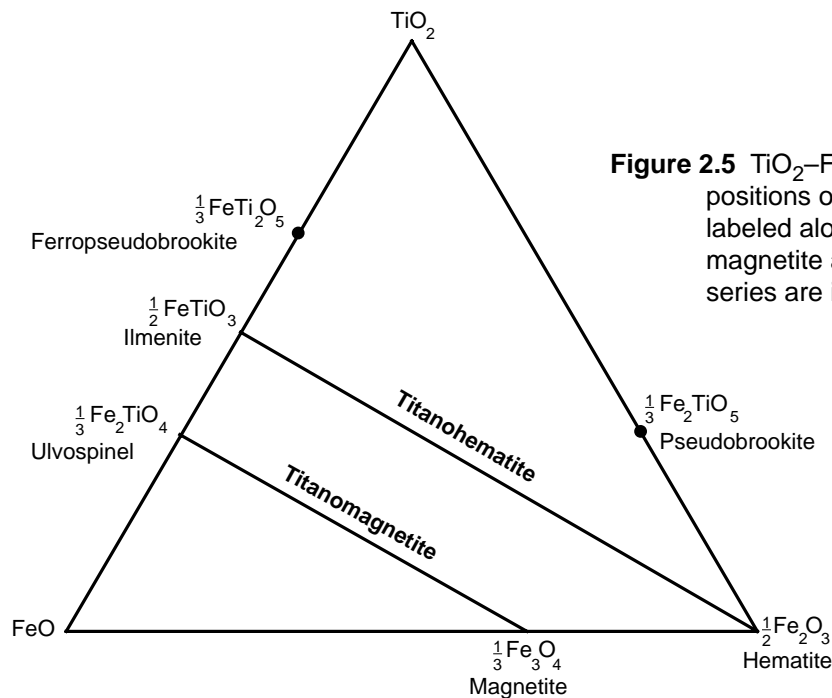


Figure 2.5 TiO_2 - FeO - Fe_2O_3 ternary diagram. Compositions of important FeTi-oxide minerals are labeled along with mineral names; titanomagnetite and titanohematite solid solution series are indicated.

tains 32 O^{2-} anions arranged in a face-centered-cubic network. These O^{2-} anions form approximately hexagonal-close-packed (111) planes orthogonal to the cube diagonal [111] direction. Within this network of O^{2-} anions, there are two types of cation sites. The *A sublattice* is made up of eight sites per unit cell in tetrahedral coordination with four surrounding O^{2-} anions. The *B sublattice* is composed of 16 sites per unit cell in octahedral coordination with six surrounding O^{2-} anions. The tetrahedral and octahedral coordinations of A and B sublattice cations are shown in Figure 2.6. Distribution of the 24 cations per unit cell within A and B sublattices and exchange coupling between these sublattices control the magnetic properties of titanomagnetites.

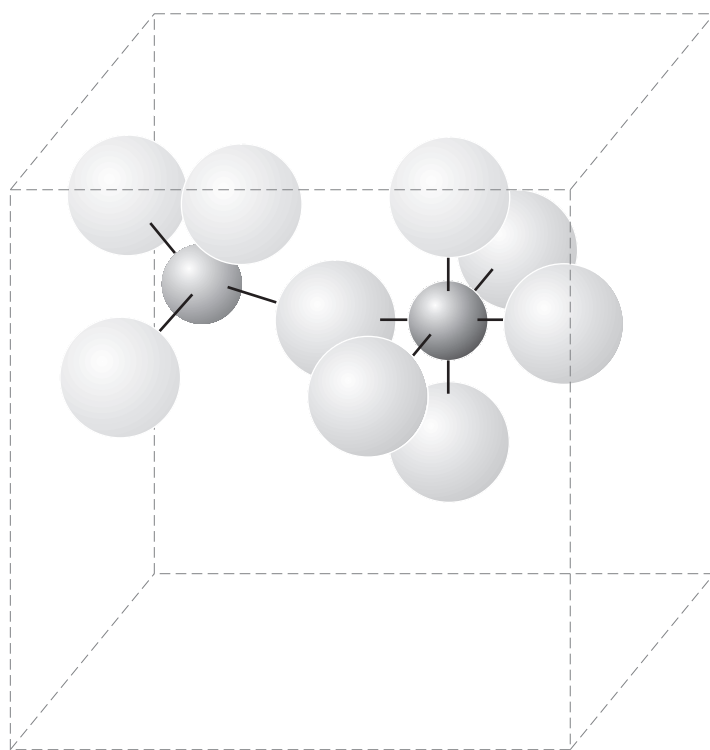


Figure 2.6 Coordinations of Fe cations with O^{2-} anions in magnetite. O^{2-} anions are lightly shaded spheres; A-sublattice cations (medium shaded spheres) are in tetrahedral coordination with four O^{2-} anions; B-sublattice cations (dark spheres) are in octahedral coordination with six O^{2-} anions; the unit cell dimension of the spinel crystal structure is shown by the dashed lines.

In magnetite, there are 16 Fe^{3+} and eight Fe^{2+} cations per unit cell. Cations distribute between the A and B sublattices in an *inverse spinel* structure. In a *normal spinel*, similar cations occupy the same sublattice. For example, ZnFe_2O_4 is a normal spinel with two Fe^{3+} cations per formula unit occupying B sites and one Zn^{2+} cation occupying the A site (Figure 2.7). In the inverse spinel structure of magnetite, the two B sites per formula unit are occupied by one Fe^{2+} and one Fe^{3+} , and the A site is occupied by the remaining Fe^{3+} .

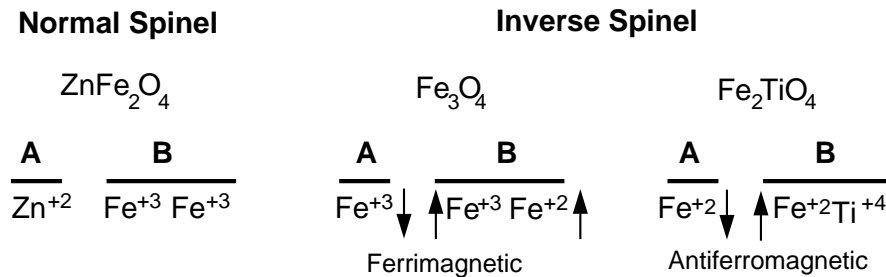


Figure 2.7 Comparison of cation distributions in normal spinel and inverse spinel. **A** and **B** indicate A sublattice and B sublattice cations, respectively; arrows indicate directions of cationic magnetic moments. Redrawn after McElhinny (*Palaeomagnetism and Plate Tectonics*, Cambridge, London, 356 pp., 1973).

Coupling of atomic magnetic moments of Fe^{2+} and Fe^{3+} cations is also shown in Figure 2.7. The exchange interaction between cations takes place through an intervening O^{2-} anion and is referred to as *super exchange* interaction. Effectively, the magnetic moments of cations within each sublattice are parallel coupled, whereas A and B sublattices are antiparallel coupled. Because the B sublattice has one Fe^{2+} and one Fe^{3+} for every Fe^{3+} cation in the A sublattice, the atomic moments of Fe^{3+} cations cancel, leaving a net magnetic moment due to Fe^{2+} cations. This antiparallel coupling of two unequal sublattices makes Fe_3O_4 ferrimagnetic. The spinel crystal structure yields a preferred direction of magnetization (= magnetocrystalline easy direction) along the cube diagonal [111]. The resulting saturation magnetization of magnetite is 480 G (4.8×10^5 A/m) (adjusted to zero thermal energy at 0°K), and the Curie temperature is 580°C.

To understand how magnetic properties vary within the titanomagnetite series, it is instructive to examine the Ti-rich end member ulvöspinel, Fe_2TiO_4 . The Ti^{4+} cations enter the inverse spinel structure in the B sublattice. Remaining Fe cations are both Fe^{2+} , as required for charge neutrality. The filled electron orbital for Ti^{4+} means that this cation does not possess an atomic magnetic moment. As illustrated in Figure 2.7, the antiparallel coupling of A and B sublattices is now between two sublattices of equal atomic moment, and ulvöspinel is antiferromagnetic. However, the Néel temperature (temperature at which antiferromagnetic coupling disappears) is -153°C , so ulvöspinel is paramagnetic at or above room temperature.

In the titanomagnetite series, Ti^{4+} substitutes for Fe^{3+} as Ti content increases. The generalized chemical formula for titanomagnetite is $\text{Fe}_{3-x}\text{Ti}_x\text{O}_4$, where x ranges from 0.0 for magnetite to 1.0 for ulvöspinel. The ionic substitution is $2\text{Fe}^{3+} \rightarrow \text{Fe}^{2+} + \text{Ti}^{4+}$, indicating that a remaining Fe cation must change valence from Fe^{3+} to Fe^{2+} for each Ti^{4+} introduced. Although it is clear that Ti^{4+} cations enter the B sublattice, the distribution of Fe^{2+} and Fe^{3+} cations between sublattices and resulting net magnetic moment for intermediate titanomagnetites is in dispute.

We use the convenient approximation (likely correct for rapidly cooled titanomagnetites) that Fe^{2+} and Fe^{3+} are equally distributed between the A and B sublattices. This yields a linear dependence of saturation magnetization, j_s , upon composition, when j_s is adjusted to 0°K. So quite sensibly, addition of Ti^{4+} (with no atomic moment) into the magnetite structure progressively decreases saturation magnetization. Equally important is the observed dependence of Curie temperature, T_C , upon Ti content. Both T_C and j_s are shown as functions of the titanomagnetite compositional parameter, x , in Figure 2.8. Any titanomagnetite with $x > 0.8$ will be paramagnetic at room temperature or above.

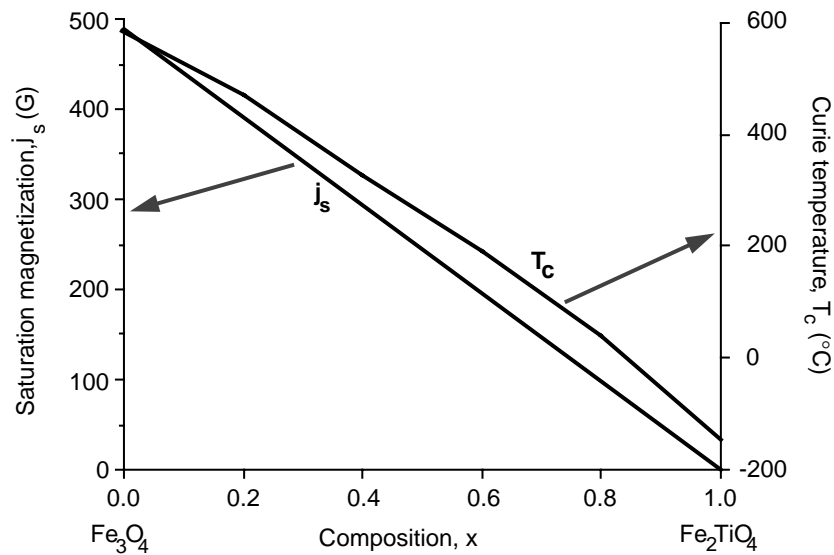


Figure 2.8 Saturation magnetization and Curie temperature for titanomagnetite series. Composition is indicated by parameter x ; the left axis indicates saturation magnetization (j_s); the right axis indicates Curie temperature (T_c). Redrawn after Nagata (1961).

Titanohematites

We wish that titanohematites were as simple as titanomagnetites, but they are not. In the presentation below, many complexities are glossed over to present essential information. (My apologies to Louis Néel, Ken Hoffman, and any other specialists in this field who might feel affronted by the simplifications employed.)

In most igneous rocks, titanohematites and their oxidation products constitute a lesser portion of ferromagnetic minerals than do titanomagnetites (and oxidation products thereof). But for highly silicic and/or highly oxidized igneous rocks, hematite can be the dominant ferromagnetic mineral. In addition, hematite is almost always the dominant or exclusive ferromagnetic mineral in red sediments, a major source of paleomagnetic data.

The titanohematites are generally opaque minerals with a magnetic structure most easily described by using the hexagonal system. Layers of approximately hexagonal-close-packed O^{2-} anions are parallel to the (0001) basal plane. For each 18 O^{2-} anions, there are 18 potential cation sites in octahedral coordination with six surrounding O^{2-} anions. In titanohematites, two thirds of these cation sites are occupied.

For hematite (denoted as $\alpha\text{Fe}_2\text{O}_3$ to avoid confusion with other forms of Fe_2O_3 introduced later), all cations are Fe^{3+} and occur in (0001) layers alternating with layers of O^{2-} anions. Atomic magnetic moments of Fe^{3+} cations lie in the basal plane orthogonal to the [0001] axis. Atomic moments are parallel coupled within (0001) planes but approximately antiparallel coupled between adjacent layers of cations. This situation is shown in Figure 2.9. However, the angle between magnetic moments of these alternate layers departs slightly from 180° , yielding a net magnetization as shown on the right side of Figure 2.9. This net magnetization lies in the basal plane nearly perpendicular to magnetic moments of the Fe^{3+} layers. Hematite ($\alpha\text{Fe}_2\text{O}_3$) is referred to as *canted antiferromagnetic* and has a saturation magnetization of ~ 2 G (2×10^3 A/m) due to this imperfect antiferromagnetism.

In addition to the magnetization from canting, some naturally occurring hematite has additional magnetization referred to as *defect ferromagnetism*, perhaps arising from (ordered structure of) lattice defects or nonmagnetic impurity cations. While the origins of the two contributions to net magnetization are complex and not fully understood, the effect is one of weak ferromagnetism with $j_s \approx 2\text{--}3$ G ($2\text{--}3 \times 10^3$ A/m). Again glossing over complications, the effective *Néel temperature* (temperature at which exchange coupling within an antiferromagnetic mineral disappears) of hematite is 680°C .

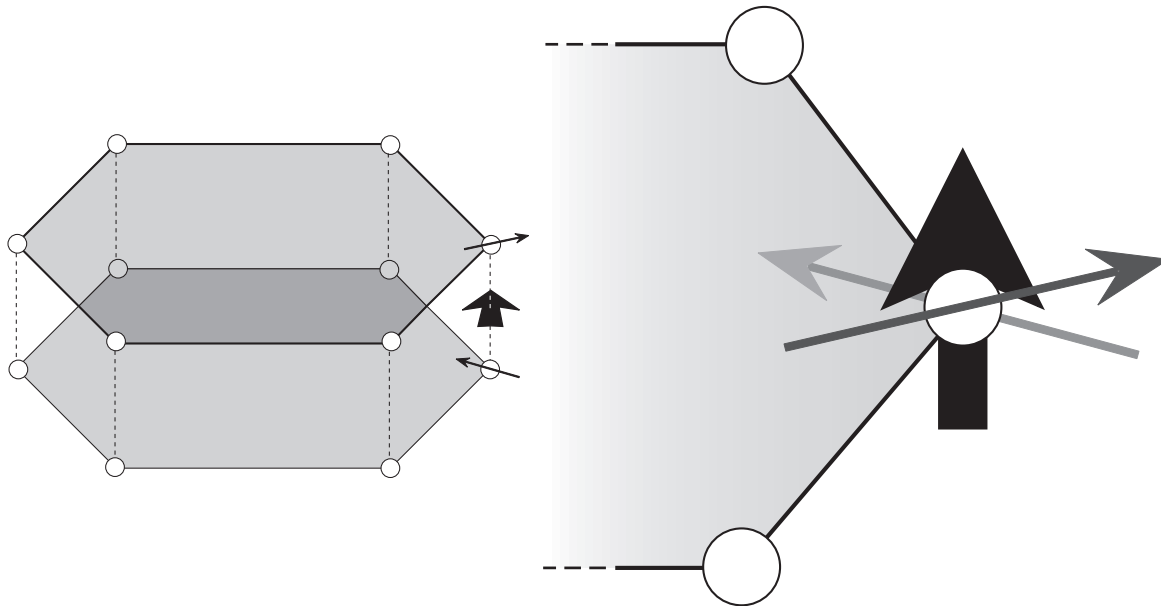


Figure 2.9 Coupling of cationic (Fe^{3+}) magnetic moments in hematite. Planes of cations are basal (0001) planes; magnetic moments are parallel within a particular basal plane; coupling of cationic (Fe^{3+}) magnetic moments between (0001) planes is shown on the right of the diagram; the magnetic moment in the upper plane is shown by the dark gray arrow; the magnetic moment in the lower plane is shown by the light gray arrow; the vector sum of these two nearly antiparallel magnetic moments is shown by the bold black arrow using a greatly expanded scale.

Turning now to *ilmenite* (FeTiO_3), Ti^{4+} layers alternate with layers of Fe^{2+} cations. Magnetic moments of Fe^{2+} cations within a particular basal plane are parallel-coupled with magnetic moment oriented along the [0001] axis. Alternating Fe^{2+} layers are antiparallel-coupled, and thus ilmenite is antiferromagnetic with Néel temperature of -218°C .

Ionic substitution in the titanohematite series is exactly as in titanomagnetites, with Ti^{4+} substituting for Fe^{3+} and one remaining Fe cation changing valence from Fe^{3+} to Fe^{2+} . The generalized formula is $\text{Fe}_{2-x}\text{Ti}_x\text{O}_3$, where x ranges from 0.0 for hematite to 1.0 for ilmenite. As shown in Figure 2.10, the “Curie” temperature has a simple linear dependence on composition. But saturation magnetization, j_s , (adjusted to 0°K) varies in a complex fashion. The explanation lies in the distribution of cations in intermediate composition titanohematites. It should be noted that titanohematites with $x > 0.8$, like titanomagnetites with high Ti content, are paramagnetic at or above room temperature.

For $0.0 < x < 0.45$, titanohematites retain the canted antiferromagnetic arrangement of hematite, with Fe and Ti cations equally distributed amongst cation layers. Over this range of compositions, saturation magnetization is approximately constant and low ($j_s \approx 2 \text{ G}$). However, for $x > 0.45$, Fe and Ti cations are no longer equally distributed; Ti cations preferentially occupy alternate cation layers. Because Ti cations have no atomic magnetic moment, antiparallel coupling of two sublattices with unequal magnetic moment develops, and titanohematites with $0.45 < x < 1.0$ are ferrimagnetic.

Intermediate titanohematites also possess an additional (mercifully) uncommon magnetic property: *self-reversal of thermoremanent magnetism*. Depending on exact composition and cooling rate, intermediate composition titanohematites can acquire remanent magnetism antiparallel to the magnetic field in which they cool below the Curie temperature. This self-reversing property is now recognized as uncommon because titanohematites of this composition are rarely the dominant ferromagnetic mineral in a rock. However, as will be discussed in Chapter 9, this self-reversing property caused confusion during early development of the geomagnetic polarity time scale.

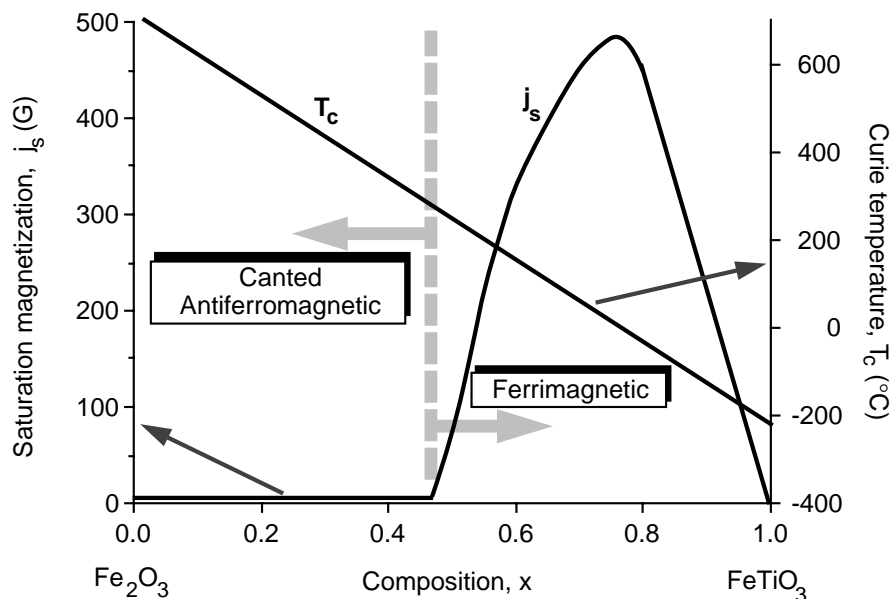


Figure 2.10 Saturation magnetization and Curie temperature for titanohematite series. Composition is indicated by parameter x ; the left axis indicates saturation magnetization (j_s); the right axis indicates Curie temperature (T_c); compositions $x < 0.45$ have canted antiferromagnetic coupling; compositions $0.45 < x < 1.0$ have ferrimagnetic coupling. Modified from Nagata (1961) and Stacey and Banerjee (1974).

Primary FeTi oxides

In this section, we discuss the grain-size distributions and composition of FeTi oxides that originally crystallize from igneous melts. These original phases are referred to as *primary FeTi oxides*.

Both titanomagnetites and titanohematites crystallize at $\sim 1300^\circ\text{C}$ and are early in the crystallization sequences of igneous rocks. Cooling rate has a major effect on grain-size distribution of FeTi oxides. Rapidly cooled volcanic rocks (such as oceanic pillow basalts) often contain titanomagnetites with a significant proportion of grains in the $1\text{-}\mu\text{m}$ or smaller sizes. These fine-grained titanomagnetites often display delicate skeletal crystalline habits. Slowly cooled intrusive rocks usually contain larger grain sizes, sometimes exceeding $100\ \mu\text{m}$. As we shall discover later, fine-grained ferromagnetic particles are the best magnetic recorders. This is one of the reasons why volcanic rocks are preferred over intrusive rocks as targets for paleomagnetic study.

As a result of magmatic differentiation processes, mafic igneous rocks tend to have a higher fraction of primary FeTi oxides (and those oxides contain higher Ti:Fe ratio) than do felsic igneous rocks. In basalts, both titanomagnetite and titanohematite are primary FeTi oxides. Compositions of primary titanomagnetites are usually within the range $0 < x < 0.8$, while primary titanohematite is almost pure ilmenite with $0.8 < x < 0.95$. Primary titanohematite is thus paramagnetic under ambient surface conditions. Total FeTi oxide content of basalts is typically 5% by volume, with approximately equal parts titanomagnetite and titanohematite.

Silicic igneous melts have higher oxygen fugacity, f_{O_2} , than mafic melts. Felsic rocks have lower content of FeTi oxides, and those FeTi oxides have lower Ti content. Primary titanomagnetites are Ti-poor approaching magnetite, and titanohematites are hematite rich. Although primary titanomagnetites of intermediate composition are common, intermediate composition titanohematites in the $0.4 < x < 0.8$ range are relatively rare. Most primary titanohematites in mafic and intermediate igneous rocks are Ti-rich, with occasional Ti-poor titanohematites in silicic rocks.

In addition to primary FeTi oxides that crystallize from igneous melts, Ti-poor titanomagnetite is often exsolved from plagioclase or pyroxene in plutonic rocks (Figure 2.11a). Although a small fraction of the total

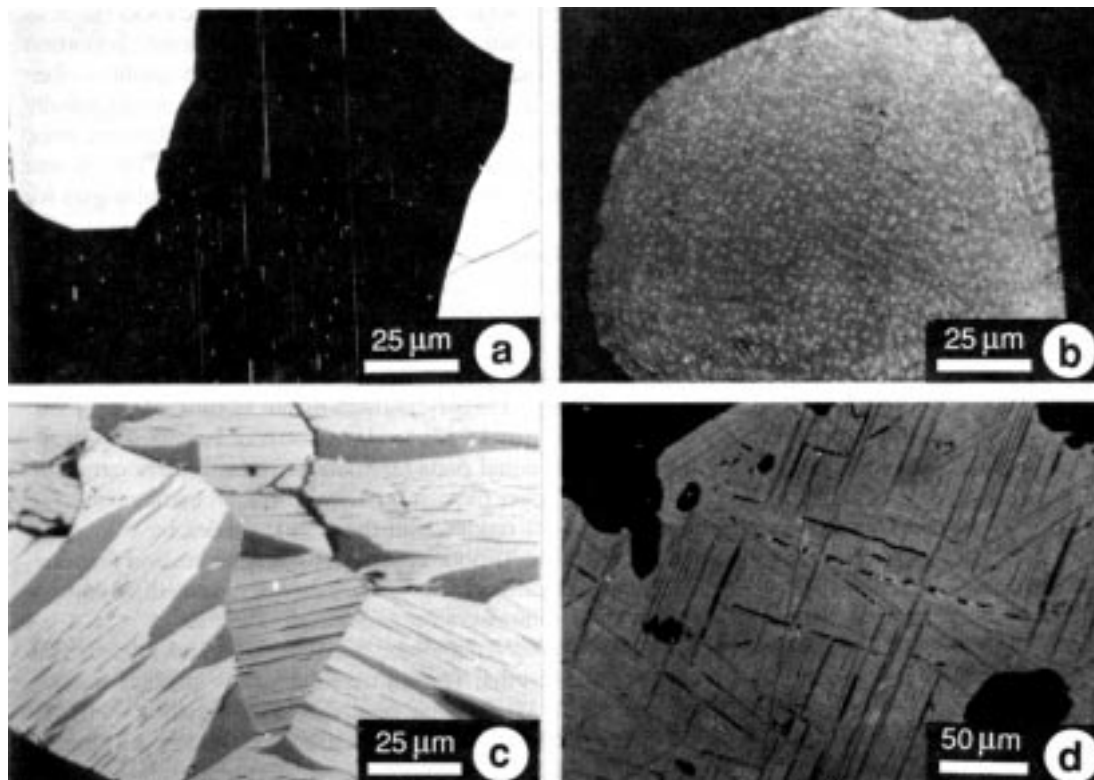


Figure 2.11 Micrographs of FeTi-oxide minerals. (a) Optical photomicrograph of exsolved rod-shaped grains of titanomagnetite (small white grains) within a plagioclase crystal. (b) Optical photomicrograph of exsolution of magnetite grains (white) within ulvöspinel (gray). (c) Optical photomicrograph of Ti-rich titanohematite (dark-gray lenses) within light-gray host Fe-rich titanohematite. (d) Optical photomicrograph of ilmenite lamellae within titanomagnetite grain; note the symmetry of the ilmenite planes that are parallel to (111) planes of the host titanomagnetite. Photomicrographs kindly provided by S. Haggerty.

FeTi oxides, these titanomagnetites are fine-grained and can be effective paleomagnetic recorders. During original cooling of igneous rocks, primary FeTi oxides can be affected by solid state exsolution and/or deuteric oxidation. Both processes can alter compositions and grain size of FeTi oxides, with profound effects on magnetic properties.

Exsolution

Both titanomagnetites and titanohematites crystallize at $\sim 1300^{\circ}\text{C}$, and solid solution is complete at these high temperatures. Thus, all compositions are possible at high temperature. However, at lower temperatures, compositional gaps develop below the curves shown in Figure 2.12. At temperatures below these curves, intermediate compositions unmix or *exsolve* into Ti-rich regions and Ti-poor regions by solid state diffusion of Fe and Ti cations. However, diffusion is sluggish at low temperatures, so rapid cooling can preserve intermediate compositions. Because titanomagnetites unmix at fairly low temperature ($\sim 600^{\circ}\text{C}$), exsolution is slow and is generally observed only in slowly cooled plutonic rocks. Compositional gaps develop at higher temperatures in the titanohematite series, and exsolution is more rapid.

Exsolution of intermediate composition titanomagnetites and titanohematites is important for two reasons:

1. Unmixing of intermediate-composition grains into composite grains with Ti-rich and Ti-poor regions alters magnetic properties such as j_s and T_C that depend on composition.
2. Exsolution dramatically decreases effective grain size.

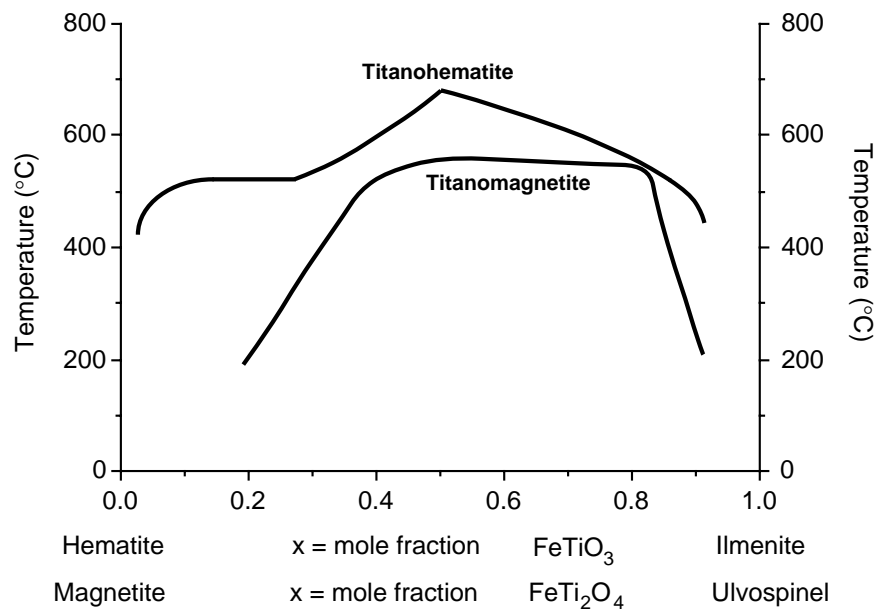


Figure 2.12 Compositional gaps for titanohematite and titanomagnetite. Compositions are indicated by parameter x for each series; solid solution is complete within each series at temperatures above the bold curves; exsolution occurs for intermediate compositions at temperatures below these curves. Adapted from Nagata (1961) and Burton (*Reviews in Mineralogy*, v. 24, in press).

By exsolution, a large homogeneous grain is transformed into a composite grain of much smaller Ti-poor (Fe-rich) regions and complementary Ti-rich (Fe-poor) regions. In titanomagnetite, exsolution yields Ti-poor crystals of cubic habit surrounded by Ti-rich regions (Figure 2.11b). The resulting composite grain will have fine-grained crystals of ferromagnetic, Ti-poor titanomagnetite surrounded by paramagnetic, Ti-rich titanomagnetite. A similar situation occurs for exsolved titanohematite, except that exsolution occurs along (0001) planes, yielding a *tiger-striped* composite grain (Figure 2.11c). As will be discussed in the following chapter, the decrease in grain size of ferromagnetic particles that accompanies exsolution has a profound influence on magnetic properties.

Deuteric oxidation

Oxidation that occurs during original cooling of an igneous rock is *deuteric oxidation*. During cooling, the primary FeTi-oxide grains are often out of equilibrium with the temperature and oxygen conditions. Deuteric oxidation almost always occurs unless the rock is rapidly cooled and/or under pressure (e.g., seafloor conditions) where degassing does not occur.

Extensive studies of deuteric oxidation in basalts indicate that typical conditions of deuteric oxidation involve temperatures of 750°C and $f\text{O}_2$ of 10^{-5} – 10^{-6} atmospheres. Deuteric oxidation occurs in the solid state but generally above the Curie temperature. Both primary titanomagnetite and primary titanohematite are affected by deuteric oxidation. As an example, consider the commonly observed effects of deuteric oxidation on primary titanomagnetite in a basalt. The path of compositional change due to oxidation is shown in Figure 2.13. Composition of primary titanomagnetite is $x = 0.6$, typical of basalts. Oxidation generally takes place along paths of constant Ti:Fe ratio parallel to the base of the ternary diagram. The $\text{Fe}^{3+}:\text{Fe}^{2+}$ ratio increases during oxidation, driving composition toward the right. However, the resulting grain is not usually homogeneous, but rather is a composite grain with ilmenite lathes along (111) planes of the host titanomagnetite (Figure 2.11d). The composition of host titanomagnetite becomes enriched in Fe and approaches pure magnetite.

The compositional change of the titanomagnetite resulting from deuteric oxidation changes the magnetic properties. An Fe-rich titanomagnetite with both higher Curie temperature and higher saturation mag-

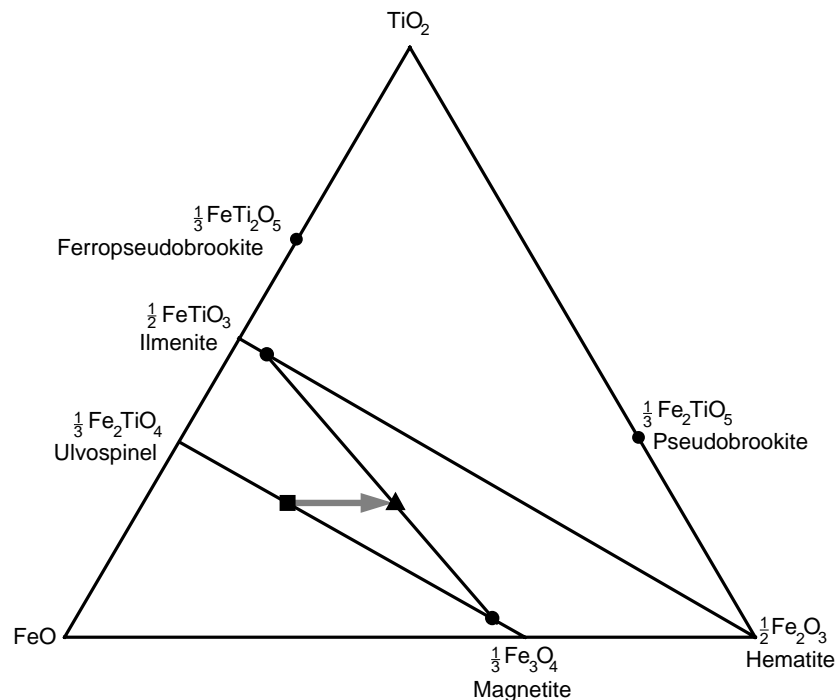


Figure 2.13 TiO_2 – FeO – Fe_2O_3 ternary diagram. Composition of primary $x = 0.6$ titanomagnetite is shown by the square; the stippled arrow shows the change in composition during deuteritic oxidation; the circles connected by solid lines show the mineral compositions resulting from deuteritic oxidation.

netization replaces primary titanomagnetite of intermediate composition. In addition, grain size is drastically decreased, the primary grain now being subdivided into many smaller grains separated by paramagnetic ilmenite. Again, this decreased grain size has a major effect on magnetic properties.

There are stages of deuteritic oxidation, and the stage to which the FeTi oxides of a particular igneous rock evolve depends on cooling rate and $f\text{O}_2$. Primary Ti-rich titanohematite also undergoes deuteritic oxidation; extreme cases yield grains that are composites of *rutile* (TiO_2), hematite ($\alpha\text{Fe}_2\text{O}_3$), and sometimes *pseudobrookite* (Fe_2TiO_5). Similarly, extreme deuteritic oxidation of primary titanomagnetite can yield rutile plus hematite. Dramatic examples of the importance of deuteritic oxidation to magnetic properties have been provided by examination of FeTi oxides and magnetic properties of samples collected from profiles through single basalt flows. Intensity and stability of paleomagnetism are commonly maximized in interior zones where deuteritic oxidation proceeded to advanced stages.

Low-temperature oxidation

Weathering of titanomagnetites at ambient surface temperatures, or hydrothermal alteration at $T < 200^\circ\text{C}$, can lead to the production of *cation deficient spinels*. The classic example is oxidation of magnetite to yield *maghemite* ($\gamma\text{Fe}_2\text{O}_3$), which is chemically equivalent to hematite ($\alpha\text{Fe}_2\text{O}_3$) but retains the spinel crystal structure.

In studying the low-temperature oxidation process, it is instructive to use a *structural formula* with brackets indicating cations in the B sublattice. For instance, magnetite can be written $\text{Fe}^{3+}[\text{Fe}^{3+}\text{Fe}^{2+}]_2\text{O}_4$, indicating that each formula unit of magnetite has one Fe^{3+} in the A sublattice and one Fe^{3+} plus one Fe^{2+} in the B sublattice. The structural formula for maghemite is $\text{Fe}^{3+}[\text{Fe}^{3+}\text{Fe}^{3+}_{2/3}\square_{1/3}]_2\text{O}_4$, indicating that magnetite is oxidized to maghemite by changing the valence state of two thirds of the original Fe^{2+} to Fe^{3+} while simultaneously removing one third of the original Fe^{2+} from the B sublattice. This removal occurs by diffusion producing *vacancies* (\square) in the spinel structure where a Fe^{2+} cation had previously resided; these vacan-

cies account for the name cation-deficient spinel. Because ferrimagnetism of magnetite results from Fe^{2+} in the B sublattice, removal of one third of these cations decreases saturation magnetization from 480 G (4.8×10^5 A/m) for magnetite to 420 G (4.2×10^5 A/m) for maghemite. Maghemite is usually metastable and irreversibly changes crystal structure to hexagonal $\alpha\text{Fe}_2\text{O}_3$ on heating to $300^\circ\text{--}500^\circ\text{C}$.

Similar low-temperature oxidation of titanomagnetites produces cation-deficient titanomaghemites. Titanomagnetite (composition $x = 0.6$) is the dominant primary FeTi oxide in oceanic pillow basalts, which comprise the upper 0.5 km of oceanic crust. During seafloor weathering, titanomagnetites oxidize to titanomaghemite with attendant decrease in intensity of magnetization, producing a major decrease in amplitude of resulting marine magnetic anomalies. Consequently, titanomaghemite is one of the most abundant FeTi oxides in the earth's crust.

It has been recognized recently that formation of maghemite is primarily responsible for increased ferromagnetic mineral content in soils. Besides the oxidation of detrital magnetite, three processes are responsible:

1. Formation of maghemite (and sometimes magnetite) from iron oxides or oxyhydroxides by repeated oxidation-reduction cycles during soil formation;
2. Natural burning in the presence of organic matter; temperatures above $\sim 200^\circ\text{C}$ aid in conversion of paramagnetic Fe-bearing minerals to maghemite;
3. Dehydration of lepidocrocite (γFeOOH), a common iron-oxyhydroxide weathering product of iron silicates.

Iron oxyhydroxides and sulfides

Oxyhydroxides of iron are common in weathered igneous and metamorphic rocks, in soils, and in sediments. The most important oxyhydroxide is goethite (αFeOOH), which is the stable form of iron oxide in soils of humid regions and also results from alteration of pyrite (FeS_2) in limestones. Goethite is orthorhombic and antiferromagnetic with a Néel temperature of 120°C , but natural goethite commonly displays weak ferromagnetism. Natural dehydration of goethite (or laboratory heating to $300^\circ\text{--}400^\circ\text{C}$) produces hematite and is an important process in formation of red sediments. Lepidocrocite (γFeOOH) is an oxyhydroxide with cubic crystal structure and is paramagnetic at room temperature (Néel temperature of -196°C). Lepidocrocite often converts to goethite or to maghemite by dehydration.

Formation of iron sulfides is a crucial concern in regard to paleomagnetic records in marine sediments, and we will return to this subject in Chapter 8. At this point, we just develop the basic magnetic properties of these minerals. Iron sulfides can occur naturally with compositions ranging from pyrite (FeS_2) to troilite (FeS), although the latter is common only in meteorites. A general chemical formula can be written FeS_{1+x} ($0 \leq x \leq 1$) and compositions of iron sulfides can be expressed by the compositional parameter x . Pyrrhotite is a ferrimagnetic iron sulfide with monoclinic crystal structure with composition in the Fe_7S_8 to Fe_9S_{10} range ($0.11 \leq x \leq 0.14$). Two antiparallel coupled sublattices containing Fe cations are present, but inequalities develop in the number of Fe cations in opposing sublattices. Thus, pyrrhotite is ferrimagnetic. The Curie temperature is 320°C , and saturation magnetization can reach 130 G (1.3×10^5 A/m). Pyrrhotite generally forms during diagenesis of marine sediments in depositional environments with abundant organic input but can also form in metamorphic aureoles surrounding igneous intrusives.

SUGGESTED READINGS

- S. Chikazumi, *Physics of Magnetism*, Wiley, New York, 554 pp., 1964.
An excellent introduction to physics of magnetism.
- D. H. Lindsley, The crystal chemistry and structure of oxide minerals as exemplified by the Fe-Ti oxides, in: *Oxide Minerals*, ed: D. Rumble, III, Mineralogical Society of America, Washington, D.C., 1976a, pp. L1–L60.
- D. H. Lindsley, Experimental studies of oxide minerals, in: *Oxide Minerals*, ed: D. Rumble, III, Mineralogical Society of America, Washington, D.C., 1976b, pp. L61–L88.

These two articles present in-depth discussion of mineralogy of Fe-Ti oxides and experimental data pertaining to exsolution.

S. E. Haggerty, Oxidation of opaque minerals in basalts, in: *Oxide Minerals*, ed: D. Rumble, III, Mineralogical Society of America, Washington, D.C., 1976a, pp. Hg1–Hg100.

S. E. Haggerty, Opaque mineral oxides in terrestrial igneous rocks, in: *Oxide Minerals*, ed: D. Rumble, III, Mineralogical Society of America, Washington, D.C., 1976b, pp. Hg101–Hg300.

These two articles present detailed observations of deuteric oxidation; they include many insightful polished section photomicrographs.

T. Nagata, *Rock Magnetism*, Maruzen Ltd., Tokyo, 350 pp., 1961.

Chapters 1–3 provide a thorough (although sometimes outdated) introduction to magnetic properties of ferromagnetic minerals.

F. D. Stacey and S. K. Banerjee, *The Physical Principles of Rock Magnetism*, Elsevier, Amsterdam, 195 pp., 1974.

Chapters 1 and 2 concern magnetic properties of solids and magnetic minerals.

R. Thompson and F. Oldfield, *Environmental Magnetism*, Allen and Unwin, London, 227 pp., 1986.

Chapters 2 through 4 discuss magnetic properties of solids and magnetic minerals.

PROBLEMS

2.1 Fayalite (Fe_2SiO_4) is a paramagnetic solid with magnetic susceptibility $\chi = 4.4 \times 10^{-4}$ emu at 0°C ($= 273^\circ\text{K}$).

a. A single crystal of fayalite has volume $= 2 \text{ cm}^3$. This crystal is placed in a magnetic field, $H = 10$ Oe, at 0°C . What is the resulting magnetic dipole moment, M , of this crystal?

b. If fayalite is placed in a magnetic field, $H = 100$ Oe, at a temperature of 500°C ($= 773^\circ\text{K}$), what is the resulting magnetization, J ?

2.2 MnS is a paramagnetic solid. At 300°K , there are 4×10^{22} molecules of MnS per cm^3 . If the cationic magnetic moment of Mn^{2+} is $5 M_B$, what is the paramagnetic susceptibility, χ , of MnS at 300°K ?

ORIGINS OF NATURAL REMANENT MAGNETISM

Of all the chapters in this book, this is “The Big Enchilada,” the one you cannot skip. The physical processes leading to acquisition of natural remanent magnetism are presented here. Perhaps the most fundamental and fascinating aspect of paleomagnetism concerns the processes by which the geomagnetic field can be recorded at the time of rock formation and then retained over geological time. We want to remove any hint of “magic” from this aspect of paleomagnetism, preferably without removing the reader’s natural astonishment that the processes actually work. Only the basic physical principles of each type of natural remanent magnetism are discussed. Some special topics in rock magnetism will be developed further in Chapter 8.

Many new concepts are presented, and some effort is required to follow the development. You will most likely have to read through this chapter more than once to see how these new concepts fit together. But effort at this point will be rewarded by ease of comprehension of principles developed in succeeding chapters. We start with a presentation of the theory of fine-particle ferromagnetism, which underlies all development of rock magnetism.

FERROMAGNETISM OF FINE PARTICLES

Rocks are assemblages of fine-grained ferromagnetic minerals dispersed within a matrix of diamagnetic and paramagnetic minerals. We are concerned with the magnetization of individual ferromagnetic grains on the one hand. But on the other hand, we must keep track of the magnetization of the rock, the entire assemblage of ferromagnetic grains plus matrix. It is useful to introduce a notation that distinguishes between magnetic parameters of individual ferromagnetic grains and magnetic parameters of entire samples. We adopt the convention that parameters for individual ferromagnetic grains are denoted by lowercase symbols, whereas parameters for the entire sample are designated by uppercase symbols. For example, the magnetization of an individual magnetite particle is designated j while the magnetization of the whole sample is designated J .

A basic principle is that ferromagnetic particles have various energies which control their magnetization. No matter how simple or complex the combination of energies may become, the grain seeks the configuration of magnetization which minimizes its total energy.

Magnetic domains

The first step is to introduce concepts and observations of magnetic domains. Consider the spherical particle of ferromagnetic material with uniform magnetization shown in Figure 3.1a. Atomic magnetic moments can be modeled as pairs of magnetic charges (as in Figure 1.1a). Magnetic charges of adjacent atoms cancel internal to the particle but produce a magnetic charge distribution at the surface of the particle. For a spherical particle, one hemisphere has positive charge and the other has negative charge. There is energy stored in this charge distribution because of repulsion between adjacent charges. This is *magnetostatic energy*, e_m .

We will soon develop an equation to determine the magnetostatic energy for a uniformly magnetized grain. At this point, all we need to know is that, for a grain with uniform magnetization j , e_m is proportional to j^2 .

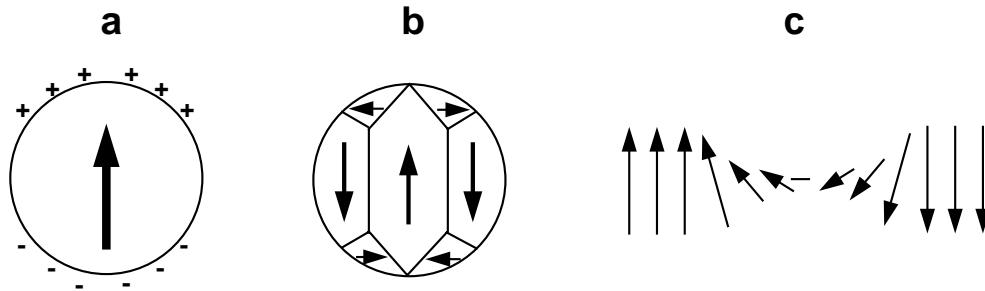


Figure 3.1 (a) Uniformly magnetized sphere of ferromagnetic material. The direction of saturation magnetization j_s is shown by the arrow; surface magnetic charges are shown by plus and minus signs. (b) Sphere of ferromagnetic material subdivided into magnetic domains. Arrows show the directions of j_s within individual magnetic domains; planes separating adjacent magnetic domains are domain walls. (c) Rotation of atomic magnetic moments within a domain wall. Arrows indicate the atomic magnetic moments which spiral in direction inside the domain wall.

A uniformly magnetized ferromagnetic grain has $j = j_s$, and magnetostatic energy is extreme for materials with high j_s .

Formation of *magnetic domains* as shown in Figure 3.1b decreases magnetostatic energy because the percent of surface covered by magnetic charges is reduced and charges of opposite sign are adjacent rather than separated. Internal to any individual domain, the magnetization is j_s , but the entire grain has net magnetization, $j \ll j_s$. Magnetite grains of diameter $d > 10 \mu\text{m}$ contain scores of domains and are referred to as *multidomain* (MD) grains. The region separating domains is the *domain wall* (Figure 3.1c). Because of exchange energy between adjacent atoms, atomic magnetic moments gradually spiral through the domain wall, which has both finite energy and finite width ($\sim 1000 \text{ \AA}$ for magnetite).

Single-domain grains

With decreasing grain size, the number of magnetic domains decreases. Eventually, the grain becomes so small that the energy required to make a domain wall is larger than the decrease in magnetostatic energy resulting from dividing the grain into two domains. Below this particle size, it is not energetically favorable to subdivide the grain into numerous domains. Instead, the grain will contain only one domain. These grains are referred to as *single-domain* (SD) grains, and magnetic properties of SD grains are dramatically different from those of MD grains.

The grain diameter below which particles are single domain is the *single-domain threshold grain size* (d_0). This size depends upon factors including grain shape and saturation magnetization, j_s . Ferromagnetic materials with low j_s have little impetus to form magnetic domains because magnetostatic energy is low. Thus, hematite (with $j_s = 2 \text{ G}$) is SD up to grain diameter (d_0) = $15 \mu\text{m}$, so a large portion of hematite encountered in rocks is single domain. However, magnetite has much higher j_s and only fine-grained magnetite is SD. Theoretical values for d_0 in parallelepiped-shaped particles of magnetite are shown in Figure 3.2.

Cubic magnetite particles must have $d < 0.1 \mu\text{m}$ to be SD, but elongated SD particles can be upward to $1 \mu\text{m}$ in length. In discussion of magnetic mineralogy in Chapter 2, examples of fine-grained magnetites were presented. So we know that fine-grained magnetites do exist and that crystals of elongate habit are common. Igneous rocks and their derivative sediments generally have some fraction of magnetite grains within the SD grain-size range.

SD grains can be very efficient carriers of remanent magnetization. To understand the behavior of SD grains, we must become familiar with energies that collectively control the direction of magnetization in a SD grain. These energies are introduced individually, then the collective effects are considered to explain hysteresis parameters.

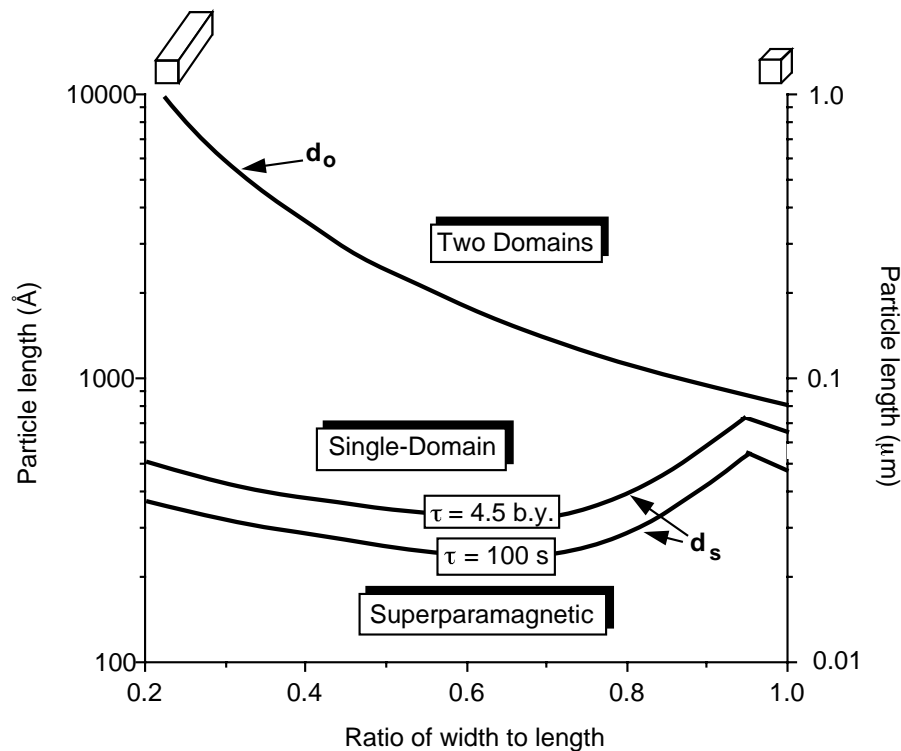


Figure 3.2 Size and shape ranges of single-domain, superparamagnetic, and two-domain configurations for parallelepipeds of magnetite at 290°K. Particle lengths are indicated in angstroms (Å) on the left ordinate and in microns (μm) on the right ordinate; shape is indicated by the ratio of width to length; cubic grains are at the right-hand side of diagram; progressively elongate grains are toward the left; the curve labeled d_0 separates the single-domain size and shape field from the size and shape distribution of grains that contain two domains; curves labeled d_s are size and shape distribution of grains that have $\tau = 4.5$ b.y. and $\tau = 100$ s; grains with sizes below d_s curves are superparamagnetic. Redrawn after Butler and Banerjee (*J. Geophys. Res.*, v. 80, 4049–4058, 1975).

Interaction energy

There is an *interaction energy*, e_H , between the magnetization of individual ferromagnetic particles, \mathbf{j} , and an applied magnetic field, \mathbf{H} . This energy essentially represents the interaction between the magnetic field and the atomic magnetic moments (Equation (1.4)) integrated over the volume of the ferromagnetic grain.

The interaction energy describes how the magnetization of a ferromagnetic grain is influenced by an externally applied magnetic field. (In detail, one has to deal with balancing torques on the magnetization, \mathbf{j} , from the external field against internal energies that resist rotation of \mathbf{j} . But a simplified approach will serve our purpose.) The interaction energy, e_H , is given by

$$e_H = \frac{-\mathbf{j} \cdot \mathbf{H}}{2} \quad (3.1)$$

This is an energy density (energy per unit volume) and applies to both SD and MD grains.

Single-domain grains have uniform magnetization with $\mathbf{j} = \mathbf{j}_s$. So application of a magnetic field cannot change the intensity of magnetization but can rotate \mathbf{j}_s toward the applied field. However, there are resistances to rotation of \mathbf{j}_s . These resistances are referred to as *anisotropies* and lead to energetically preferred directions for \mathbf{j}_s within individual SD grains. The dominant anisotropies are *shape anisotropy* and *magnetocrystalline anisotropy*.

The internal demagnetizing field

As discussed above, a surface magnetic charge results from magnetization of a ferromagnetic substance directed toward the grain surface. For a spherical SD grain, the magnetic charge distribution is shown in Figure 3.3a. The magnetic field produced by this grain can be determined from the magnetic charge distribution. For a uniformly magnetized sphere, the resulting external magnetic field is a dipole field (Equations (1.12)–(1.15)). But the magnetic charge distribution also produces a magnetic field internal to the ferromagnetic grain. This internal magnetic field is shown in Figure 3.3b and is called the *internal demagnetizing field* because it opposes the magnetization of the grain.

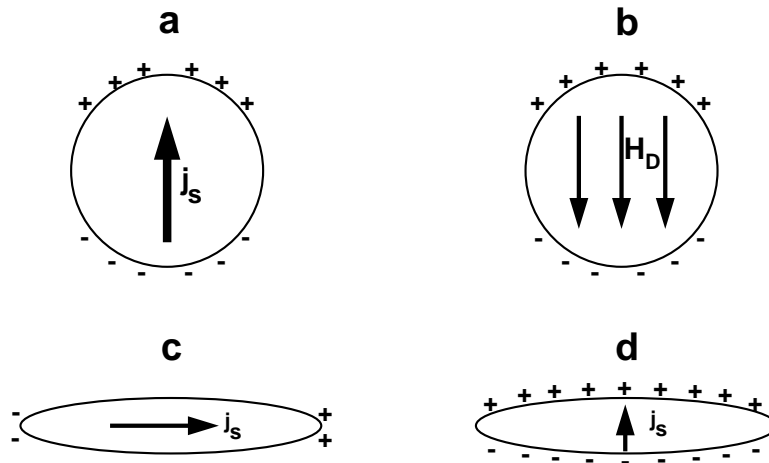


Figure 3.3 (a) Surface magnetic charge distribution resulting from uniform magnetization of a spherical ferromagnetic grain. The arrow indicates the direction of saturation magnetization j_s ; plus and minus signs indicate surface magnetic charges. (b) Internal demagnetizing field, H_D , resulting from the surface magnetic charge of a uniformly magnetized sphere. H_D is uniform within the grain. (c) Surface magnetic charge produced by magnetization of an SD grain along the long axis of the grain. The arrow indicates the direction of saturation magnetization j_s ; plus and minus signs indicate surface magnetic charges; note that magnetic charges are restricted to the ends of the grain. (d) Surface magnetic charge produced by magnetization of an SD grain perpendicular to the long axis of the grain. The arrow indicates the direction of saturation magnetization j_s ; plus and minus signs indicate surface magnetic charges; note that magnetic charges appear over the entire upper and lower surfaces of the grain.

For uniformly magnetized ellipsoids, the internal demagnetizing field, H_D , is given by

$$H_D = -N_D j \quad (3.2)$$

where j is the magnetization of the grain and N_D is the *internal demagnetizing factor*. The internal demagnetizing factor is a coefficient relating the strength of the internal demagnetizing field to the magnetization. The internal demagnetizing factor along any particular direction is proportional to the percentage of the grain surface covered by magnetic charges when the grain is magnetized in that direction. If you erect a Cartesian (x, y, z) coordinate system inside the ferromagnetic grain, the internal demagnetizing factors along the three orthogonal directions must sum to 4π .

$$N_{Dx} + N_{Dy} + N_{Dz} = 4\pi \quad (3.3)$$

where N_{Dx} is the internal demagnetizing factor along the x direction and so on.

Now consider a spherical SD grain (Figure 3.3a). No matter what direction the magnetization points, the same percentage of the grain surface gets covered by magnetic charges. This means that

$$N_{Dx} = N_{Dy} = N_{Dz} = \frac{4\pi}{3} \quad (3.4)$$

So the internal demagnetizing field for a spherical SD grain is

$$\mathbf{H}_D = -\frac{4\pi}{3} \mathbf{j} = -\frac{4\pi}{3} \mathbf{j}_s \quad (3.5)$$

With this result, we can show how to determine the magnetostatic energy. For a uniformly magnetized ellipsoid, the magnetostatic energy is the interaction energy of the internal demagnetizing field with the magnetization in the grain:

$$e_m = -\frac{\mathbf{j} \cdot \mathbf{H}}{2} = -\frac{\mathbf{j} \cdot \mathbf{H}_D}{2} = -\frac{(\mathbf{j}_s) \cdot (-N_D \mathbf{j}_s)}{2} = \frac{N_D j_s^2}{2} \quad (3.6)$$

This expression makes it clear why SD grains have high magnetostatic energy, especially if j_s is large.

Shape anisotropy

We can also use the internal demagnetizing field and magnetostatic energy to introduce *shape anisotropy*. The origin of shape anisotropy is illustrated in Figures 3.3c and 3.3d. A highly elongate ferromagnetic grain has much lower magnetostatic energy if magnetized along its length (Figure 3.3c) rather than perpendicular to its length (Figure 3.3d). This is because the percentage of surface covered by magnetic charges is small when \mathbf{j}_s points along the long dimension of the grain (Figure 3.3c). But magnetization perpendicular to the long axis leads to a substantial surface charge (Figure 3.3d). So the internal demagnetizing factor, N_{Dl} , along the long axis is much less than the internal demagnetizing factor, N_{Dp} , perpendicular to the long axis.

We can use Equation (3.6) to determine the difference in magnetostatic energy between magnetization along the long axis and magnetization perpendicular to the long axis. The difference in magnetostatic energy is

$$\Delta e_m = \frac{(N_{Dp} - N_{Dl})j_s^2}{2} = \frac{\Delta N_D j_s^2}{2} \quad (3.7)$$

where ΔN_D is the difference in demagnetizing factors between short and long axes. This difference in magnetostatic energy represents an energy barrier to rotation of \mathbf{j}_s through the perpendicular direction. In the absence of other influences, the grain will have \mathbf{j}_s along the long axis.

To force \mathbf{j}_s over the magnetostatic energy barrier, an external magnetic field must result in an interaction energy, e_H , which exceeds the energy barrier, Δe_m . By using Equations (3.1) and (3.7) the required interaction energy is

$$e_H = \frac{j_s H}{2} > \Delta e_m = \frac{\Delta N_D j_s^2}{2} \quad (3.8)$$

The required magnetic field is given by

$$h_c = \Delta N_D j_s \quad (3.9)$$

The magnetic field h_c required to force \mathbf{j}_s over the energy barrier of an individual SD grain is the *microscopic coercive force*. This microscopic coercive force is a measure of the energy barrier to rotation of \mathbf{j}_s in a SD grain and will be used extensively in models for acquisition of remanent magnetization. For elongate grains of magnetite, microscopic coercive force is dominated by shape anisotropy. Maximum shape anisotropy is displayed by needle-shaped grains for which ΔN_D in Equation (3.9) is 2π . Using $j_s = 480$ G leads to maximum coercive force for SD magnetite at room temperature of ~ 3000 Oe (300 mT).

Magnetocrystalline anisotropy

For equant SD particles (no shape anisotropy) or SD particles of ferromagnetic materials with low j_s , *magnetocrystalline anisotropy* dominates the microscopic coercive force. *Magnetocrystalline easy directions* of magnetization are crystallographic directions along which magnetocrystalline energy is minimized. An example of magnetization along different crystallographic directions in a single crystal of magnetite is shown in Figure 3.4. Magnetization is more easily achieved along the [111] magnetocrystalline easy direction. The origin of magnetocrystalline anisotropy is the dependence of exchange energy on crystallographic direction of magnetization.

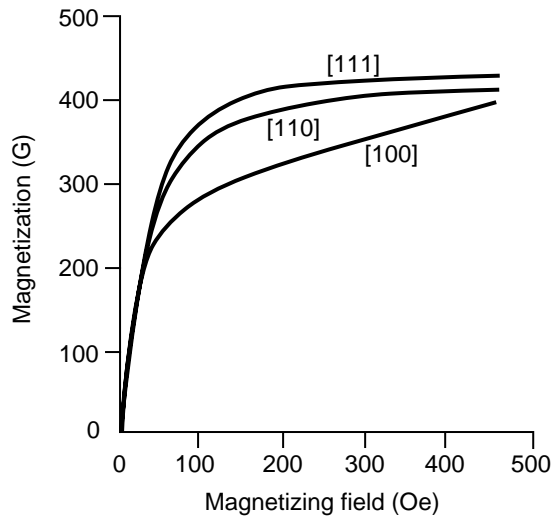


Figure 3.4 Magnetization of a single crystal of magnetite as a function of the magnetizing field. Magnetization curves are labeled indicating the crystallographic direction of the magnetizing field; [111] is the magnetocrystalline easy direction; [100] is the magnetocrystalline hard direction. Redrawn after Nagata (*Rock Magnetism*, Maruzen Ltd., Tokyo, 350 pp, 1961).

It is simplest to understand magnetocrystalline anisotropy by considering a material with *uniaxial magnetocrystalline energy*, e_a . Such a material contains one axis of minimum magnetocrystalline energy, and e_a is given by

$$e_a = K \sin^2 \theta \quad (3.10)$$

where K is the magnetocrystalline constant and θ is the angle between \mathbf{j}_s and the magnetocrystalline easy direction. There is an energy barrier to rotation of \mathbf{j}_s through the *magnetocrystalline hard direction* where $\theta = 90^\circ$ and $e_a = K$. To force \mathbf{j}_s through this energy barrier, $e_H > K$ is required. The resulting microscopic coercive force for an individual SD particle is

$$h_c = 2K / j_s \quad (3.11)$$

Magnetocrystalline anisotropy is the dominant source of microscopic coercive force in hematite because K is large and j_s is small. The resulting h_c can exceed 10^4 Oe (1 T) for SD particles of hematite.

Hysteresis in single-domain grains

Consider a synthetic sample composed of 5% by volume dispersed magnetite particles in a diamagnetic matrix. The magnetite grains are all elongate single-domain grains, and the directions of long axes of the grains are randomly distributed. Typical values of hysteresis parameters for such a sample (at room temperature) are shown in Figure 3.5a.

Magnetization of individual ferromagnetic particles, \mathbf{j}_n , adds vectorially to yield net magnetization, \mathbf{J} , for the sample given by

$$\mathbf{J} = \frac{\sum v_n \mathbf{j}_n}{\text{sample volume}} \quad (3.12)$$

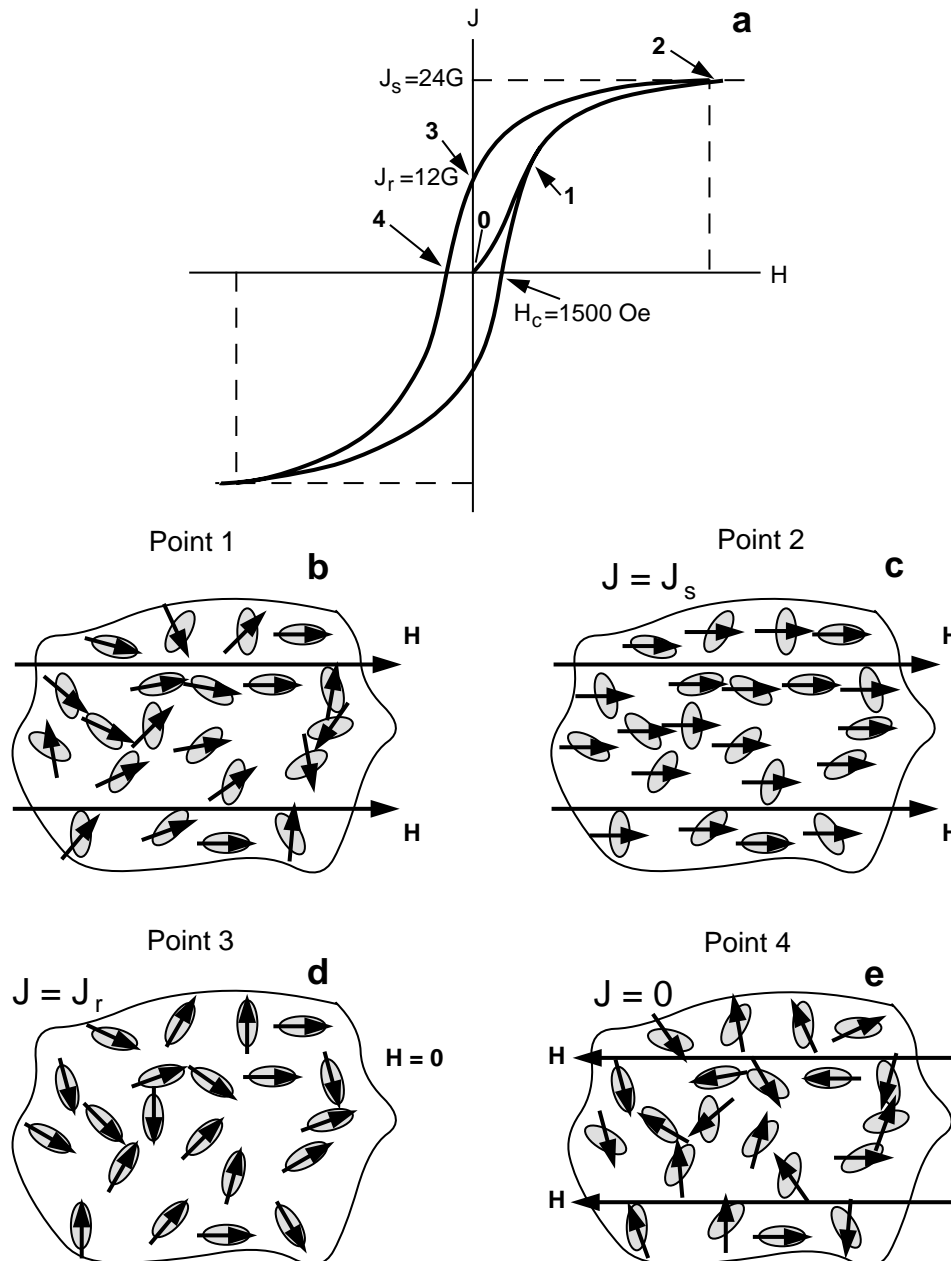


Figure 3.5 (a) Hysteresis loop for synthetic sample containing 5% by volume of dispersed elongate SD magnetite particles. The saturation magnetization of the sample is J_s ; the remanent magnetization of the sample is J_r ; the bulk coercive force is H_c ; the points labeled are referred to in text and illustrated below. (b) Magnetization directions within SD grains at point 1 on hysteresis loop. Stippled ovals are schematic representations of elongate SD magnetite grains; arrows indicate direction of j_s for each SD grain; H is the magnetizing field; note that j_s of each grain is rotating toward H . (c) Magnetization directions within SD grains at point 2 on hysteresis loop. Sample is at saturation magnetization J_s ; note that j_s of every grain is aligned with H . (d) Magnetization directions within SD grains at point 3 on hysteresis loop. The magnetizing field has been removed; sample magnetization is remanent magnetization J_r ; note that j_s of each grain has rotated back to the long axis closest to the saturating magnetic field, which was directed toward the right. (e) Magnetization directions within SD grains at point 4 on hysteresis loop. The sample has magnetization $J = 0$; note that j_s of every grain has been slightly rotated toward the magnetizing field H (now directed toward the left).

where v_n is the volume of an individual ferromagnetic particle and $v_n \mathbf{j}_n$ is the magnetic moment of an individual SD grain. It is the magnitude of this net magnetization that is measured in the hysteresis experiment. If the sample has not previously been exposed to a magnetizing field, $J = 0$ because the magnetization ($= j_s$) of SD grains is randomly directed.

Application of the initial magnetizing field (in an arbitrarily defined positive direction) leads to net magnetization acquired parallel to the field along the path 0–1–2. As the field is applied, \mathbf{j}_s of each SD grain begins to rotate toward the applied magnetic field because of the interaction energy, e_H . Directions of \mathbf{j}_s are shown schematically in Figure 3.5b for point 1 on the hysteresis loop.

If the applied field is increased to a sufficient level, all grains will have \mathbf{j}_s aligned with the field (Figure 3.5c). This is point 2 of Figure 3.5a, where the sample reaches its *saturation magnetization*, J_s . The magnetizing field required to drive the sample to saturation is that required to overcome the magnetostatic energy barrier given by Equation (3.7). For elongate SD grains of magnetite, this saturating field is ~ 3000 Oe (300 mT).

For this sample containing 5% by volume of magnetite, the saturation magnetization can be computed by using Equation (3.12):

$$\begin{aligned} J_s &= \frac{\sum_n j_s v_n}{\text{sample volume}} = \frac{j_s \sum_n v_n}{\text{sample volume}} \\ &= j_s \frac{\text{total magnetite volume}}{\text{sample volume}} \\ &= j_s (\text{volume fraction magnetite}) = (480 \text{ G}) (0.05) \\ &= 24 \text{ G } (2.4 \times 10^4 \text{ A/m}) \end{aligned}$$

So saturation magnetization of the sample depends linearly on concentration of the ferromagnetic mineral.

Removal of the magnetizing field causes J to decrease along the path 2–3. During removal of the magnetizing field, \mathbf{j}_s of individual SD grains rotates to the nearest long axis of the grain because that direction minimizes magnetostatic energy. After removal of the magnetizing field, a *remanent magnetization*, J_r , remains. Directions of \mathbf{j}_s for the SD grains at point 3 are shown schematically in Figure 3.5d. Integrating the components of \mathbf{j}_s over a random directional distribution of long axes yields $J_r = J_s/2$. The ratio J_r/J_s is often taken as a measure of efficiency in acquiring remanent magnetization and is 0.5 for this assemblage of elongate SD grains with dominant shape anisotropy. Likewise an assemblage of SD grains with dominant uniaxial magnetocrystalline anisotropy and randomly directed magnetocrystalline easy axes would have $J_r/J_s = 0.5$.

To force J back to zero, an opposing magnetic field must be applied. J decreases along the path 3–4, and the magnetic field required to drive J to zero is the *bulk coercive force*, H_c . Directions of \mathbf{j}_s for SD grains at point 4 are shown in Figure 3.5e. Integration of the effects of interaction energy and magnetostatic energy over an assemblage of randomly oriented elongate grains yields $H_c = h_c/2$, where h_c is microscopic coercive force for an individual SD grain (Equation (3.9)). For the sample with elongate SD magnetite grains, $H_c \approx 1500$ Oe (150 mT). Similarly, for an assemblage of SD grains with dominant magnetocrystalline energy, $H_c = h_c/2$, with h_c given by Equation (3.11). For an assemblage of hematite grains, H_c can reach 5000 Oe (500 mT).

Notice that H_c does not depend on the concentration of ferromagnetic material. This is because h_c depends on energy balances within individual SD grains and H_c depends only on h_c ; concentration of the grains is not involved. The hysteresis loop in Figure 3.5a is completed by driving the sample to saturation in the negative direction, then cycling back to saturation in the positive direction (Figure 3.5a). This example shows how assemblages of SD ferromagnetic grains are efficient in acquiring remanent magnetization and resistant to demagnetization; both properties are obviously desirable for paleomagnetism.

Rock samples containing titanomagnetite as the dominant ferromagnetic mineral rarely have H_c or J_r/J_s approaching the high values that we determined for this synthetic sample. Remember that rocks generally have a large percentage of MD grains and/or pseudo-single-domain grains (defined below); and these larger grains have lower h_c and lower J_r/J_s .

Hysteresis of multidomain grains

Application of a magnetic field to a MD grain produces preferential growth of domains with magnetization parallel to the field. If the applied field is sufficiently strong, domain walls are destroyed, and magnetization reaches saturation ($j = j_s$). On removal of the magnetizing field, domains re-form and move back towards their initial positions. However, because of lattice imperfections and internal strains, domain wall energy is a function of position (Figure 3.6). Rather than returning to initial positions, domain walls settle in energy minima near their initial positions, and a small remanent magnetization results. But only a small magnetic field is required to drive the domain walls back to the zero moment positions, so coercive force of MD ferromagnetic particles is modest. In addition, magnetization of MD particles tends to decay with time (domain walls can easily pass over energy barriers), and these particles are much less effective as recorders of paleomagnetism than are SD grains.

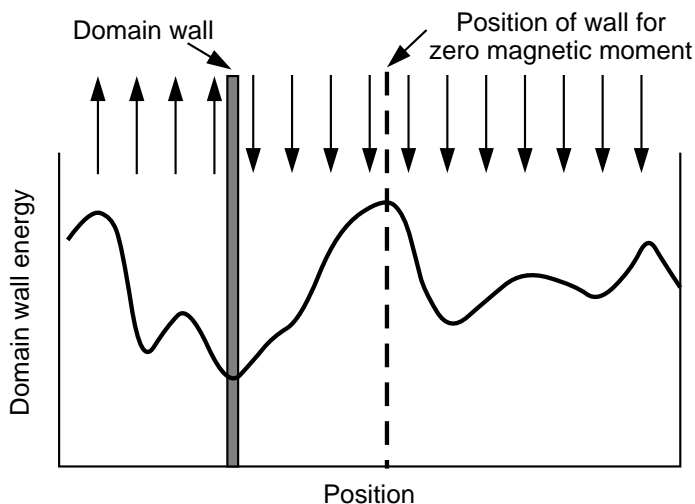


Figure 3.6 Domain wall energy versus position. The solid curve schematically represents domain wall energy; arrows show the direction of j_s within the domains; the domain wall is shown by the stippled region; the position of the domain wall that yields net $J = 0$ is shown by the dashed line. Redrawn after Stacey and Banerjee (1974).

Pseudo-single-domain grains

No sharp boundary exists between large SD grains and small multidomain grains. Instead, there is an interval of grain sizes exhibiting intermediate J_r/J_s and intermediate h_c . These grains are referred to as *pseudo-single-domain* (PSD) grains and are important in understanding magnetizations of rocks containing magnetite or titanomagnetite. The PSD grain-size interval for magnetite is approximately 1–10 μm . Grains in this size range contain a small number of domains and can have substantial magnetic moment. They can also exhibit significant coercivity and time stability of remanent magnetism. Grain-size distributions of many igneous and sedimentary rocks peak within the magnetite PSD field but have only a small percentage of particles within the true SD field. Accordingly, PSD grains can be important carriers of paleomagnetism. We will consider PSD grains at several points in our discussion of natural remanent magnetization.

Magnetic relaxation and superparamagnetism

In the above discussion, effects of magnetic fields on rotation of j_s in SD particles were considered. Thermal activation also can lead to rotation of j_s over energy barriers. *Magnetic relaxation*, in which remanent magnetization of an assemblage of SD grains decays with time, is the most straightforward effect of thermal activation. This relaxation is schematically illustrated in Figure 3.7a.

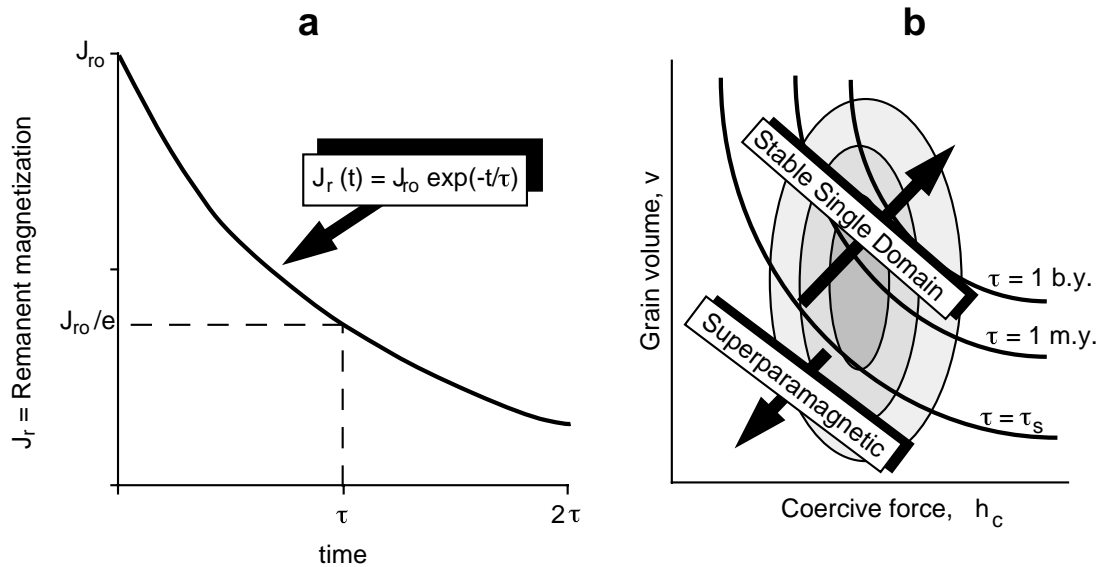


Figure 3.7 (a) Magnetic relaxation in an assemblage of SD ferromagnetic grains. Initial magnetization J_{r0} decays to J_{r0}/e in time τ . (b) Relaxation times of SD grains on diagram plotting SD grain volume, v , against SD grain microscopic coercive force, h_c . Lines of equal τ are lines of equal product vh_c ; grains with short τ plot toward the lower left; grains with long τ plot toward the upper right; superparamagnetic grains with $\tau < \tau_s$ plot to the lower left of $\tau = \tau_s$ line; stable SD grains with $\tau > \tau_s$ plot to upper right of $\tau = \tau_s$ line; the schematic contoured plot of population of SD grains is shown by the stippled regions.

Exponential decay of remanent magnetization, $J_r(t)$, after removal of the magnetizing field is

$$J_r(t) = J_{r0} \exp(-t/\tau) \tag{3.13}$$

where J_r = initial remanent magnetization
 t = time (s)
 τ = characteristic relaxation time (s), after which $J_r = J_{r0} / e$.

Magnetic relaxation was studied by Louis Néel, who showed that the characteristic relaxation time is given by

$$\tau = \frac{1}{C} \exp\left(\frac{v h_c j_s}{2kT}\right) \tag{3.14}$$

where C = frequency factor $\approx 10^8 \text{ s}^{-1}$
 v = volume of SD grain
 h_c = microscopic coercive force of SD grain
 j_s = saturation magnetization of the ferromagnetic material
 kT = thermal energy

In Equation (3.14), the product $v j_s h_c$ is an energy barrier to rotation of \mathbf{j}_s and is called the *blocking energy*. But thermal energy (kT) can cause oscillations of \mathbf{j}_s . So the relaxation time is controlled by the ratio of blocking energy to thermal energy.

Relaxation times vary over many orders of magnitude. SD grains with short relaxation times are referred to as *superparamagnetic*. A superparamagnetic grain is ferromagnetic with attendant strong magnetization. But remanent magnetization in an assemblage of these grains is unstable; it will decay to zero very soon after removal of the magnetizing field (much like paramagnetic materials that “decay” instantaneously).

From Equation (3.14) it is clear that relaxation time for SD grains of a given material at a constant temperature depends on grain volume, v , and microscopic coercive force, h_c . It is convenient to plot distributions of grains on a *volume-versus-coercive force diagram* as shown in Figure 3.7b. Grains with low product (vh_c) plot in the lower left portion of the diagram and have low relaxation time. Grains with high product (vh_c) plot in the upper right and have long relaxation time. Lines of equal τ in $v-h_c$ space are hyperbolas of equal product (vh_c). These diagrams prove useful in understanding the formation of several types of natural remanent magnetism and in understanding thermal demagnetization.

By definition, superparamagnetic grains are those grains whose remanence relaxes quickly. A convenient *critical relaxation time*, τ_s , for purposes of laboratory experiments may be taken as 100 s. It is possible to determine the size and shape of SD grains with $\tau < \tau_s$. This grain size is known as the *superparamagnetic threshold* (d_s). At 20°C (= 293°K), d_s for hematite and for equant grains of magnetite is about 0.05 μm . For elongate SD magnetite grains (with h_c controlled by shape anisotropy), size and shape of grains with $\tau = 100$ s is shown in Figure 3.2. For instance, a magnetite grain with a width:length ratio of 0.2 and length of 0.04 μm has $\tau = 100$ s and is (by definition of $\tau_s = 100$ s) at the superparamagnetic threshold.

Effective paleomagnetic recorders must have relaxation times on the order of geological time. So it might be more appropriate to choose $\tau_s = 4.5 \times 10^9$ yr as the relevant relaxation time. The size and shape dependence of elongated magnetite particles with this relaxation time is also shown in Figure 3.2. Assemblages of SD grains with $d_s < d < d_0$ are considered to be within the *stable SD grain-size range*. These grains have desirable SD properties (high J_r/J_s and high h_c) and also have the required long relaxation time. The stable SD grain-size field for magnetite (Figure 3.2) is extremely narrow for equant particles but significant for elongated grains.

For hematite, the stable SD grain-size range is large, extending from $d_s = 0.05 \mu\text{m}$ to $d_0 = 15 \mu\text{m}$. So a large percentage of hematite grains will be stable SD grains. In most rocks, a significant percentage of ferromagnetic grains will fall within the stable SD grain-size field. These grains are highly effective carriers of paleomagnetism. We will introduce many concepts of paleomagnetism by utilizing the properties of stable SD grains.

Blocking temperatures

Relaxation time has strong temperature dependence. Several parameters (besides temperature itself) appear in the argument of the exponential function in Equation (3.14). Temperature dependence of j_s (which goes to zero at T_c , the Curie temperature) is shown for both magnetite and hematite in Figure 2.3. Coercive force also depends upon temperature. For coercive force controlled by shape anisotropy, h_c is proportional to j_s , whereas coercive force controlled by magnetocrystalline anisotropy is proportional to j_s^n , with $n > 3$.

Relaxation times for an elongate SD magnetite grain with length 0.1 μm and width 0.02 μm are plotted in Figure 3.8 in semi-log format. Relaxation time is less than 1 microsecond at 575°C but exceeds the age of the earth at 510°C! If we choose 100 s as the critical relaxation time, τ_s , this grain changes behavior from superparamagnetic to stable SD at 550°C. The temperature at which this transition occurs is the *blocking temperature* (T_B). Between T_c and T_B , the grain is ferromagnetic, but remanent magnetization in an assemblage of these grains will decay quickly. Below the blocking temperature, τ exceeds τ_s and is increasing rapidly during continued cooling. Remanent magnetism formed at or below T_B can be stable, especially if temperature is decreasing.

Designation of blocking temperature depends on the choice of critical relaxation time. If we choose 10^3 yr as a more geologically relevant critical relaxation time, the corresponding blocking temperature would be 530°C rather than 550°C using $\tau_s = 100$ s. The important consideration now is that relaxation time has extraordinary dependence on temperature; SD grains that have $\tau > 10^9$ yr at 20°C can be superparamagnetic at elevated temperature.

Rocks have distributions of ferromagnetic grain sizes and shapes yielding distributions of T_B between T_c and surface temperatures. The strong dependence of relaxation time on temperature and the transition in

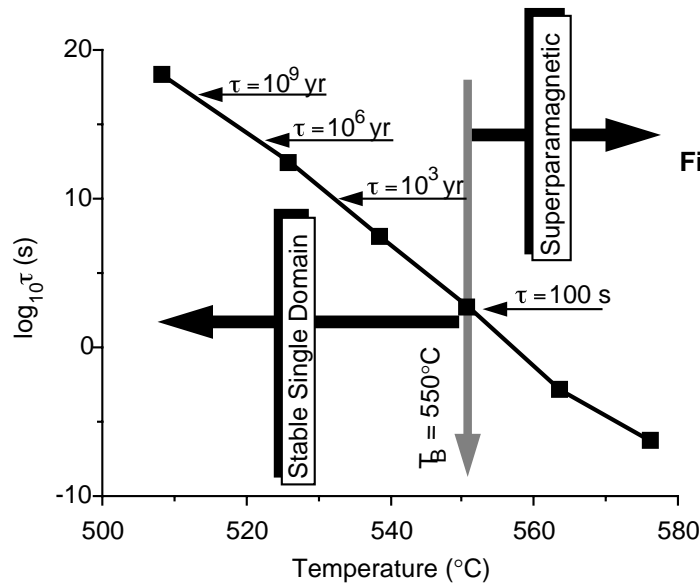


Figure 3.8 Semi-log plot of relaxation time, τ , of a SD magnetite grain as function of temperature. Key relaxation times are labeled; blocking temperature (T_B) is shown by stippled arrow; SD grain is superparamagnetic ($\tau < \tau_s = 100$ s) at $T > T_B = 550^\circ\text{C}$ and “stable” ($\tau > \tau_s = 100$ s) for $T < T_B$.

behavior from superparamagnetic above T_B to stable SD below T_B are critical to understanding acquisition of thermoremanent magnetism.

NATURAL REMANENT MAGNETISM (NRM)

In situ magnetization of rocks is the vector sum of two components:

$$\mathbf{J} = \mathbf{J}_i + \mathbf{J}_r \tag{3.15}$$

where \mathbf{J}_i is the induced magnetization and \mathbf{J}_r is the natural remanent magnetism. Bulk susceptibility, χ , is the net susceptibility resulting from contributions of all minerals but usually dominated by the ferromagnetic minerals. Presence of the local geomagnetic field, \mathbf{H} , produces the induced magnetization:

$$\mathbf{J}_i = \chi \mathbf{H} \tag{3.16}$$

This induced magnetization usually parallels the local geomagnetic field and can be the dominant component for many rock types. However, acquisition of induced magnetization is a reversible process without memory of past magnetic fields. It is the remanent magnetization that is of concern in paleomagnetism.

Natural remanent magnetization (NRM) is remanent magnetization present in a rock sample prior to laboratory treatment. NRM depends on the geomagnetic field and geological processes during rock formation and during the history of the rock. NRM typically is composed of more than one component. The NRM component acquired during rock formation is referred to as *primary NRM* and is the component sought in most paleomagnetic investigations. However, *secondary NRM* components can be acquired subsequent to rock formation and can alter or obscure primary NRM. The secondary components of NRM add vectorially to the primary component to produce the total NRM:

$$\text{NRM} = \text{primary NRM} + \text{secondary NRM} \tag{3.17}$$

The three basic forms of primary NRM are (1) *thermoremanent magnetization*, acquired during cooling from high temperature; (2) *chemical remanent magnetization*, formed by growth of ferromagnetic grains below the Curie temperature; and (3) *detrital remanent magnetization*, acquired during accumulation of sedimentary rocks containing detrital ferromagnetic minerals. In the sections below, these forms of NRM are examined. The objective is to explain how primary NRM can record the geomagnetic field present during rock formation and, under favorable conditions, retain that recording over geologic time.

Secondary NRM can result from chemical changes affecting ferromagnetic minerals, exposure to nearby lightning strikes, or long-term exposure to the geomagnetic field subsequent to rock formation. Processes of acquisition of secondary NRM must be examined to understand (1) coexistence of primary and secondary NRM in the same rock, (2) how multiple components of NRM can be recognized, and (3) how partial demagnetization procedures can preferentially erase secondary NRM, allowing isolation of primary NRM. Understanding the physics and chemistry of NRM acquisition is a prerequisite to understanding the fidelity and accuracy of primary NRM and the paleomagnetic techniques for its determination.

THERMOREMANENT MAGNETISM (TRM)

Thermoremanent magnetism (TRM) is NRM produced by cooling from above the Curie temperature (T_c) in the presence of a magnetic field. TRM is the form of remanent magnetism acquired by most igneous rocks. From the previous section, it is understood that magnetic moments of ferromagnetic grains will be stable to time decay at or below the respective blocking temperatures, T_B , which are distributed downward from the Curie temperature. As temperature decreases through T_B of an individual SD grain, that grain experiences a dramatic increase in relaxation time, τ , and changes behavior from superparamagnetic to stable single domain. It is the action of the magnetic field at the blocking temperature that produces TRM.

A significant aspect of TRM is that a small magnetic field (e.g., the surface geomagnetic field) can, at elevated temperatures, impart a small bias in the distribution of magnetic moments of the ferromagnetic grains during cooling and produce a remanent magnetization. At surface temperatures, this remanence can be stable over geologic time and resistant to effects of magnetic fields after original cooling.

A theoretical model

Here we examine a theoretical model for acquisition of TRM. The model is essentially that of French physicist Louis Néel and explains acquisition of TRM by an assemblage of single-domain ferromagnetic grains.

In this model, depicted schematically in Figure 3.9, we consider an assemblage of identical SD grains. The assemblage is assumed to have *uniaxial anisotropy*, meaning that magnetic moments of the grains can point only along some arbitrary axis, but in either direction; above T_B , they will flip rapidly between these two antiparallel directions. One could actually make such an assemblage of SD grains by distributing highly elongated SD magnetite grains in a diamagnetic matrix with long axes of the magnetite grains perfectly aligned.

Now consider a magnetic field applied along the axes of the grains. There is an interaction energy between the applied magnetic field, \mathbf{H} , and the magnetic moment, \mathbf{m} , of each SD grain (Equation (1.4)):

$$E = -\mathbf{m} \cdot \mathbf{H} \tag{3.18}$$

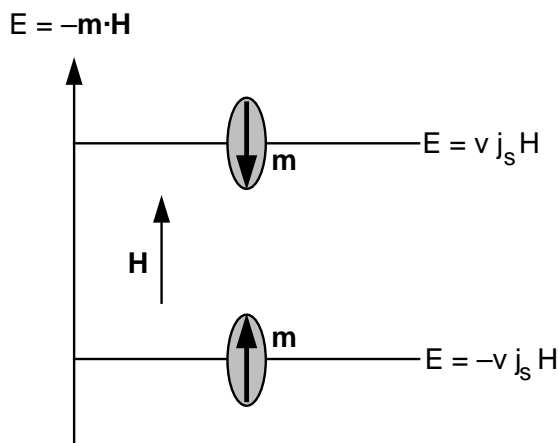


Figure 3.9 Model for TRM acquisition. SD ferromagnetic grains have uniaxial anisotropy, so magnetic moments \mathbf{m} of SD grains are parallel or antiparallel to applied magnetic field \mathbf{H} ; energies of interaction E_H between magnetic moments of SD grains and the applied magnetic field are shown for the parallel and antiparallel states; v is the SD grain volume; j_s is the saturation magnetization of ferromagnetic material.

Figure 3.9 shows the two possible orientations of magnetic moments of the SD grains and the attendant interaction energy. For grains with \mathbf{m} parallel to \mathbf{H} ,

$$E = -mH = -v j_s H \quad (3.19)$$

where v is the volume of the SD grain and j_s is the saturation magnetization. For grains with \mathbf{m} antiparallel to \mathbf{H} ,

$$E = mH = v j_s H \quad (3.20)$$

The energy difference between these two states results in a preference for occupying the state with \mathbf{m} parallel to \mathbf{H} . However, this aligning influence is countered by the randomizing influence of thermal energy, which, in the absence of a magnetizing field, will equalize the population of the two states, thereby yielding no net magnetization.

Above the blocking temperature, magnetic moments of these SD grains will flip rapidly between the parallel and antiparallel states. But because of aligning energy of the applied magnetic field, magnetic moments of individual grains will spend slightly more time in the parallel than the antiparallel state. Collectively, the assemblage will have more grains in the parallel state than in the antiparallel state. A bias of magnetic moments parallel to the applied magnetic field results.

The degree of alignment at the blocking temperature is of major importance. If the magnetic field were switched off at $T > T_B$, the population of the two stable states would quickly equalize, yielding no net magnetization. At or above T_B , the degree of alignment depend upon the ratio of aligning energy to thermal energy. At T_B , this ratio is given by

$$\left(\frac{v j_s [T_B] H}{k T_B} \right) = b \quad (3.21)$$

From statistical thermodynamics, the relative Boltzmann probability, P_+ , of a grain occupying the energy state with \mathbf{m} parallel to \mathbf{H} is given by

$$P_+ = \left(\frac{\exp[b]}{\exp[b] + \exp[-b]} \right) \quad (3.22)$$

The relative probability, P_- , of the grain occupying the antiparallel state is given by

$$P_- = \left(\frac{\exp[-b]}{\exp[b] + \exp[-b]} \right) \quad (3.23)$$

The bias of magnetic moments (degree of alignment) along H is then

$$P_+ - P_- = \left(\frac{\exp[b] - \exp[-b]}{\exp[b] + \exp[-b]} \right) = \tanh(b) \quad (3.24)$$

This bias of magnetic moments will be frozen (blocked) as the assemblage cools through T_B .

At the blocking temperature, the thermoremanent magnetization will be given by

$$\text{TRM}(T_B) = [N(T_B) m(T_B)] [P_+ - P_-] \quad (3.25)$$

where $N(T_B)$ is the number of SD grains per unit volume with blocking temperature T_B and $m(T_B)$ is the magnetic moment of an individual SD grain. Inserting $m(T_B) = v j_s(T_B)$ and Equation (3.24) for $P_+ - P_-$ yields a complete expression for TRM at the blocking temperature:

$$\text{TRM}(T_B) = N(T_B) v j_s(T_B) \tanh\left(\frac{v j_s [T_B] H}{k T_B} \right) \quad (3.26)$$

To emphasize that the degree of alignment is small, consider the expected degree of alignment of magnetic moments for an assemblage of SD magnetite grains with blocking temperature of 550°C (= 823°K). The hyperbolic tangent term in Equation (3.26) indicates the degree of alignment and the terms required are v = SD grain volume; T_B = blocking temperature (= 823°K); H = magnetizing field (we'll use 1 Oe); and $j_s(T_B)$ = saturation magnetization at T_B . To illustrate changes in relaxation time with temperature (Figure 3.8), we previously considered SD magnetite particles with $T_B = 550^\circ\text{C}$. The volume of these particles is $4.3 \times 10^{-17} \text{ cm}^3$ and j_s at $550^\circ\text{C} = 140 \text{ G}$. The argument of the hyperbolic tangent in Equation (3.26) becomes

$$\left(\frac{v j_s [T_B] H}{k T_B} \right) = 5.3 \times 10^{-2} \quad (3.27)$$

For such small arguments, $\tanh x \approx x$, so the degree of alignment = 0.053. This is indeed a small bias; only a tiny fraction more magnetic moments are aligned with the magnetic field than against it.

With the assumption of a sharp blocking temperature, no further changes in orientations of magnetic moments occur during cooling to ambient surface temperature (ca. 20°C). The only quantity which changes during cooling from T_B to 20°C is saturation magnetization of the ferromagnetic material. Thus the final TRM at 20°C is given by

$$TRM(20^\circ\text{C}) = N(T_B) v j_s(20^\circ\text{C}) \tanh\left(\frac{v j_s [T_B] H}{k T_B}\right) \quad (3.28)$$

Notice that the hyperbolic tangent term of this equation for TRM does not change upon cooling from T_B to 20°C because that term is the bias ($P_+ - P_-$) at T_B , which will not change during subsequent cooling. As shown in a previous section, relaxation time, τ , does continue to increase dramatically during cooling below T_B . The resulting TRM can have a relaxation time exceeding geologic time and can thus be stable against time decay.

This simple model illustrates essential features of TRM. It shows how a modest magnetizing field can impart a TRM during cooling through the blocking temperature and how that TRM can be retained over geological time.

Generalizing the model

There are several inadequacies in the above model. The most severe assumption is that the assemblage of SD grains has uniaxial anisotropy. This assumption provides useful simplifications in the mathematical development, but of course it is not realistic. What we expect to encounter in a rock is an assemblage of ferromagnetic grains with essentially random (isotropic) distribution of easy axes of magnetization.

A random distribution of easy axes can be dealt with by setting aligning energy for a particular grain equal to

$$E = \mathbf{m} \cdot \mathbf{H} = mH \cos \theta \quad (3.29)$$

where θ is the angle between the easy axis of magnetization and \mathbf{H} . Integration over an isotropic distribution of grains yields a TRM expression that is slightly more complicated than Equation (3.28). However, the essence of the physics is the same.

For an assemblage of SD grains with random distribution of easy axes, the resulting medium is isotropic for acquisition of TRM. This means that TRM will be parallel to the magnetizing field present during cooling. Although not unknown, igneous rocks with significant anisotropy are rare, and we expect that TRM of most igneous rocks will faithfully record the direction of the magnetic field during cooling.

The model just presented also assumes that all SD grains are identical, with only a single blocking temperature. Real rocks have a distribution of sizes and shapes of ferromagnetic grains and consequently have a distribution of T_B . With distributed blocking temperatures, TRM acquisition can be visualized by using the v - h_c diagrams of Figure 3.10. Just below the Curie temperature, microscopic coercive force, h_c , is low, and all grains are superparamagnetic (Figure 3.10a). During cooling, h_c of all grains increases, and

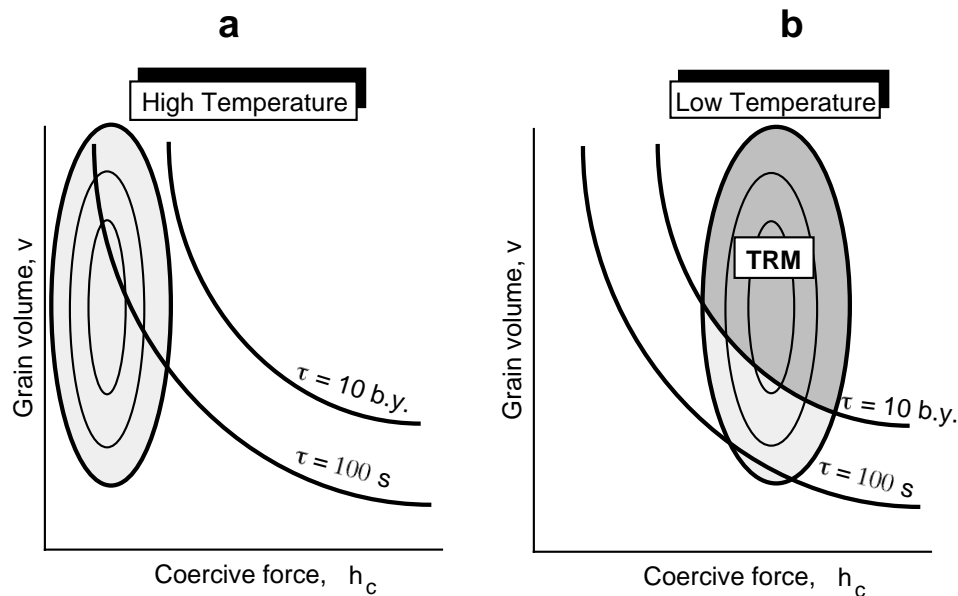


Figure 3.10 Migration of SD grain population towards increasing h_c between (a) high temperature and (b) low temperature. Lines of $\tau = 100$ s and $\tau = 10$ b.y. are schematically shown; SD grains in the dark stippled region of (b) experience blocking of their magnetic moment during cooling and acquire TRM.

the distribution of grains migrates toward increasing h_c (Figure 3.10b). At the respective blocking temperatures, grains pass through the $\tau = \tau_s$ line, change from superparamagnetic to stable SD, and acquire TRM.

The exact distribution of TB depends on the distribution of grain sizes and shapes in the rock and is routinely determined in the course of thermal demagnetization. This process erases remanent magnetization in all grains with blocking temperatures up to the maximum temperature of the laboratory heating. By this technique it is possible to determine the portion of TRM that is blocked within successive T_B intervals. A typical example is shown in Figure 3.11.

Igneous rocks with stable TRM commonly have T_B within about 100°C of the Curie temperature. Rocks with a large portion of remanent magnetization carried by grains with T_B distributed far below T_C are more likely to have complex, multiple-component magnetizations. These difficulties are explored later.

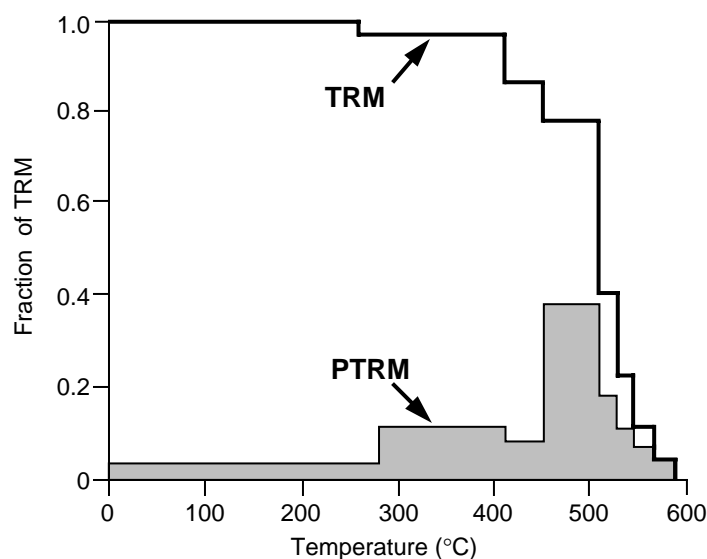


Figure 3.11 Distribution of blocking temperatures in an Eocene basalt sample. The solid line labeled TRM indicates the amount of TRM remaining after step heating to increasingly higher temperature (~75% of the original TRM has blocking temperatures between 500°C and 580°C); the stippled histogram labeled PTRM shows the amount of TRM within corresponding intervals of blocking temperature (e.g., ~40% of the original TRM has a blocking temperatures between 450°C and 510°C).

PTRM

The total TRM can be broken into portions acquired in distinct temperature intervals. For example, TRM of an igneous rock containing magnetite as the dominant ferromagnetic mineral can be broken into portions acquired within windows of blocking temperatures from $T_C = 580^\circ\text{C}$ down to 20°C . The portion of TRM blocked in any particular T_B window is referred to as “partial TRM,” often abbreviated PTRM. Each PTRM is a vector quantity, and **TRM** is the vector sum of the **PTRMs** contributed by all blocking temperature windows:

$$\mathbf{TRM} = \sum_n \mathbf{PTRM}(T_{Bn}) \quad (3.30)$$

Individual **PTRMs** depend only on the magnetic field during cooling through their respective T_B intervals and are not affected by magnetic fields applied during cooling through lower temperature intervals. This is the *law of additivity of PTRM*.

As an example of additivity of **PTRM**, again consider an igneous rock with magnetite as the dominant ferromagnetic mineral. The rock originally cooled to produce a **TRM** that is the vector sum of all **PTRMs** with T_B distributed from T_C to room temperature. If the magnetic field was constant during the original cooling, all **PTRMs** are in the same direction. Now consider that this rock is subsequently reheated for even a short time to a temperature, T_r , intermediate between room temperature and the Curie temperature and then cooled in a different magnetizing field. All **PTRMs** with $T_B < T_r$ will record the new magnetic field direction. However, neglecting time-temperature effects to be considered later, the **PTRMs** with $T_B > T_r$ will retain the **TRM** record of the original magnetizing field. This ability to strip away components of magnetization held by grains with low T_B while leaving the higher T_B grains unaffected is a fundamental element of the thermal demagnetization technique.

Grain-size effects

Perhaps the most severe simplification in the above model of TRM acquisition is that it considers only single-domain grains. Given the restricted range of grain size and shape distributions for stable SD grains of magnetite or titanomagnetite, only a small percentage of grains in a typical igneous rock are truly SD. Most grains are PSD or MD. The question then arises as to whether PSD and MD grains can acquire TRM.

Figure 3.12 shows the particle size dependence of TRM acquired by magnetite in a magnetizing field of 1 Oe (0.1 mT). Note that Figure 3.12 is a log-log plot and efficiency of TRM acquisition drops off dramatically in the PSD grain-size range from $1 \mu\text{m}$ to about $10 \mu\text{m}$. However, PSD grains do acquire TRM that can be stable against time decay and against demagnetization by later magnetic fields. The physics of PSD grains is much more complicated than for SD grains and is not fully understood. However, the basic idea of acquiring TRM by imparting a bias in directions of magnetic moments of PSD grains at the blocking temperature also applies to these inhomogeneously magnetized grains.

For grains of $d > 10 \mu\text{m}$, the acquisition of TRM is inefficient. In addition, acquired TRM in these larger grains generally decays rapidly with time, and these grains are prone to acquire viscous magnetization (discussed below). SD and PSD grains are the effective carriers of TRM, while larger MD grains are likely to carry a component of magnetization acquired long after original cooling.

It has been observed that grain-size distributions of ferromagnetic grains in igneous rocks tend to be *log normally distributed*. A histogram of number of grains versus logarithm of the grain dimension is reasonably fit by a Gaussian (bell-shaped) curve. Rapidly cooled volcanic rocks generally have grain-size distributions peaking at $d < 10 \mu\text{m}$, with a major portion of the distribution within SD and PSD ranges. Also deuteric oxidation of volcanic rocks often produces intergrowth grains with effective magnetic grain size less than the FeTi-oxide grains that crystallized from the igneous melt. Thus, volcanic rocks are commonly observed to possess fairly strong and stable TRM. A typical intensity of TRM in a basalt flow is 10^{-3} G (1 A/m). Generally, a smaller percentage of the grain-size distribution in volcanic rocks than in intrusive igneous rocks is

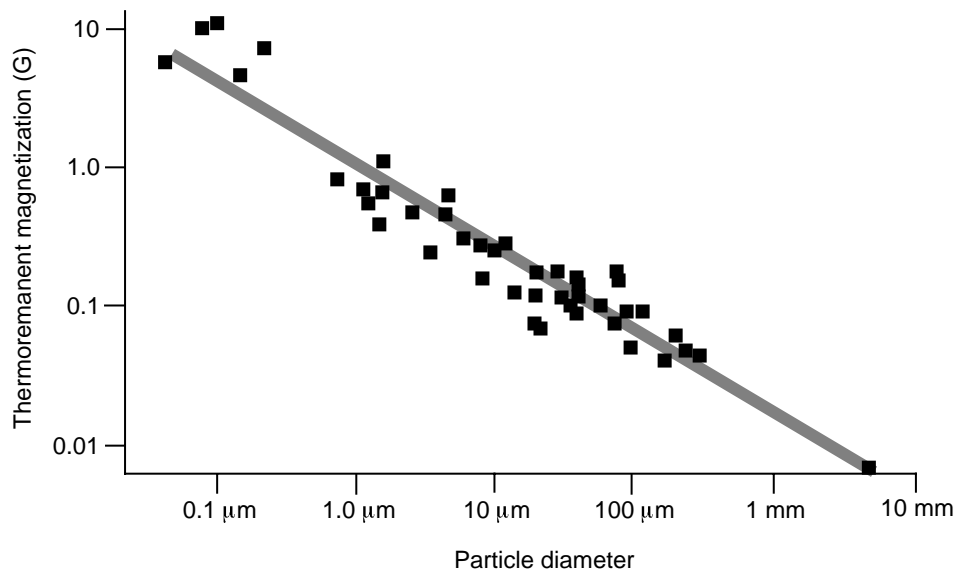


Figure 3.12 Dependence of intensity of TRM on particle diameter of magnetite. Magnetite particles were dispersed in a matrix; the intensity of TRM is determined per unit volume of magnetite to allow comparison between experiments that used varying concentrations of dispersed magnetite; the magnetizing field was 1 Oe. Redrawn after Dunlop (*Phys. Earth Planet. Int.*, v. 26, 1–26, 1981).

within the MD range. This means that secondary components of magnetization carried by MD grains are minimized in volcanic rocks.

However, for intrusive igneous rocks the opposite situation prevails. Grain-size distribution peaks at larger sizes, and a majority of the grains are within the MD range with only a small percentage within SD and PSD ranges. Accordingly, the intensity of the stable TRM component (if present at all) is diminished in comparison to volcanic rocks. More important, secondary components of magnetization carried by MD grains can dominate the magnetization. Removing this noise component to reveal the underlying stable TRM component can be a major challenge.

Mafic intrusive rocks are more likely to retain a primary TRM than are felsic intrusives. Mafic intrusives have higher Fe and Ti contents with the result that intermediate composition titanomagnetite grains often undergo exsolution during cooling. These exsolved grains are much more capable of carrying stable TRM than are homogeneous grains. In addition, many intrusive rocks containing a stable TRM component are found to contain SD magnetite grains exsolved in host plagioclase or other silicate grains (Figure 2.11a). From this discussion, it is clear that volcanic rocks are much preferred over intrusive rocks in paleomagnetic studies.

CHEMICAL REMANENT MAGNETISM (CRM)

Chemical changes that form ferromagnetic minerals below their blocking temperatures in a magnetizing field result in acquisition of *chemical remanent magnetism* (CRM). Chemical reactions involving ferromagnetic minerals include (a) alteration of a preexisting mineral (possibly also ferromagnetic) to a ferromagnetic mineral or (b) precipitation of a ferromagnetic mineral from solution. Although exceptions exist, CRM is most often encountered in sedimentary rocks. This section outlines a model of CRM acquisition that explains the basic attributes of this type of NRM.

Model of CRM formation

As in the development of a model for thermoremanent magnetism (TRM), we start with Equation (3.14) describing relaxation time, τ , of an assemblage of identical single-domain (SD) grains:

$$\tau = \left(\frac{1}{C} \right) \exp \left(\frac{v h_c j_s}{2kT} \right) \quad (3.14)$$

During TRM formation, volume (v) of the SD grains is constant, but τ increases during cooling because h_c and j_s increase as T decreases. During formation of chemical remanent magnetism, temperature is constant (usually ambient surface temperature). Accordingly, j_s and h_c are approximately constant. During chemical formation of a ferromagnetic mineral, individual grains grow from zero initial volume. Grains with small volumes have short relaxation times and are superparamagnetic. This is depicted in Figure 3.13a, with distribution of SD grains in v - h_c space compressed toward the abscissa. As growth of the ferromagnetic grains proceeds, volume of individual grains increases, and the distribution in v - h_c space migrates upward (Figure 3.13b). During grain growth, individual grains experience dramatic increase in relaxation time and change from superparamagnetic to stable single domain. The grain volume at which this transition occurs is referred to as the *blocking volume*. As assemblages of grains pass through the blocking volume, a bias of magnetic moments toward the applied magnetic field is recorded, just as with TRM. Continued grain growth following blocking of CRM can produce a chemical remanent magnetization that is stable over geological time.

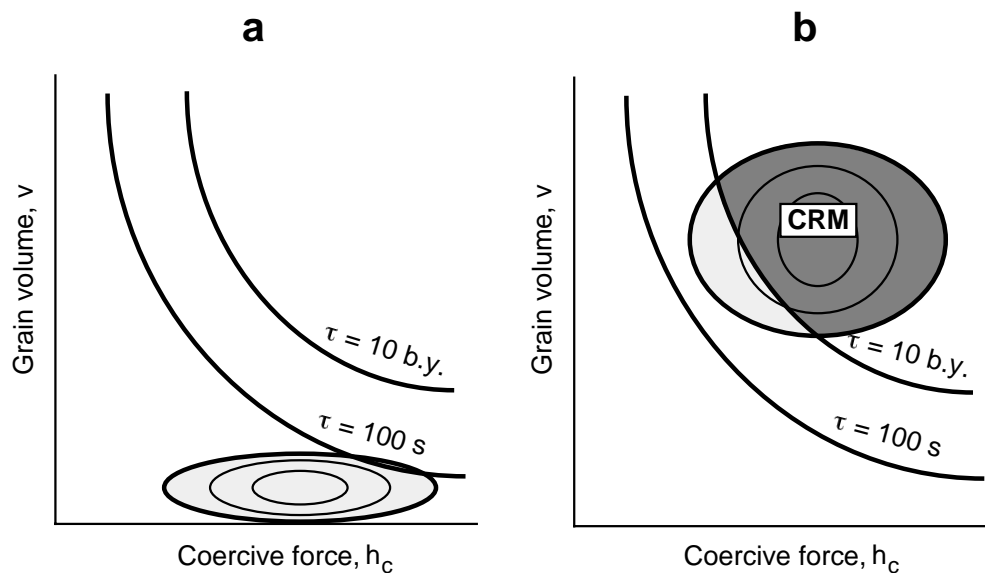


Figure 3.13 Migration of SD grain population toward increasing grain volume, v , between (a) beginning of chemical precipitation and (b) an advanced stage of grain precipitation. Lines of $\tau = 100$ s and $\tau = 10$ b.y. are schematically shown; SD grains in the dark stippled region of (b) have grown through blocking volumes and have acquired CRM.

Laboratory experiments on synthetic CRM have verified the essential elements of this model. Experiments involving precipitation of ferromagnetic minerals from solution show that CRM accurately records the direction of the magnetic field. Experiments involving alteration of one ferromagnetic mineral to another also have been performed. When the alteration involves a major change of crystal structure (e.g., magnetite to hematite), acquired CRM records the magnetic field direction during alteration and does not seem to be affected by the magnetization of the preexisting ferromagnetic mineral. However, when alteration occurs with no fundamental change of crystal structure (e.g., titanomagnetite to titanomaghemite), the resulting remanence can be controlled by the remanence direction of the original grains.

An example of natural CRM is postdepositional formation of hematite, primarily in red sediments. A typical intensity of CRM in a red siltstone is 10^{-5} G (10^{-2} A/m). A variety of postdepositional oxidation and

dehydration reactions play a role in formation of hematite. For example, goethite (αFeOOH) is an oxyhydroxide produced by alteration of Fe-bearing silicates. Goethite can dehydrate to hematite by the following reaction:



CRM is acquired during growth of the resulting hematite grains.

When hematite is produced soon after deposition, the CRM will record the magnetic field direction essentially contemporaneous with deposition and is regarded as a primary magnetization. However, the mode and timing of acquisition of remanent magnetism in red sediments are a matter of controversy. Because red sediments have been a major source of paleomagnetic data, appreciation of the processes involved in magnetization of red sediments (and attendant uncertainties) is important. Accordingly, we will discuss this red bed controversy in Chapter 8.

CRM may be regarded as a secondary component if it is acquired long after deposition. For example, diagenetic/ authigenetic formation of Fe-sulfides and MnFe-oxides in marine sediments can lead to formation of CRM. This CRM may be acquired millions of years after deposition and would be regarded as a secondary magnetization. These topics are also discussed in Chapter 8.

DETRITAL REMANENT MAGNETISM (DRM)

Detrital remanent magnetism (DRM) is acquired during deposition and lithification of sedimentary rocks. In most sedimentary environments, the dominant detrital ferromagnetic mineral is magnetite (or Ti-poor titanomagnetite). DRM is complicated because many complex processes can be involved in the formation of sedimentary rocks. There is a wide variety of initial mineralogies, and constituent minerals often are not in chemical equilibrium with each other or with the environment of deposition. Postdepositional physical processes such as bioturbation can affect magnetization. Compaction is a particularly important postdepositional process and will be a topic of special consideration in Chapter 8. Chemical processes can also alter or remove original detrital ferromagnetic minerals and/or precipitate new ferromagnetic minerals, with attendant effects on the paleomagnetic record. Because of these complexities, DRM is less well understood than is TRM, and there are more uncertainties about the accuracy of paleomagnetic recordings in sedimentary rocks.

In this section, basic physical and chemical processes affecting paleomagnetism of sedimentary rocks are outlined. We start with physical alignment occurring at the time of deposition and refer to the resulting remanence as *depositional detrital remanent magnetism*. We then discuss physical alignment processes, termed *postdepositional detrital remanent magnetism* (pDRM), that occur after deposition but before consolidation. pDRM processes can operate in the upper 10–20 cm of the accumulating sediment, where water contents are high. The combination of depositional and postdepositional magnetization processes is referred to as detrital remanent magnetism (DRM).

Depositional DRM (the classic model)

The classic model for acquisition of DRM considers only the aligning influence of a magnetic field on a ferromagnetic particle at the moment it encounters the sediment/water interface. We consider a spherical ferromagnetic grain with magnetic moment, \mathbf{m} , immersed in fluid of viscosity, η , and acted upon by magnetic field, \mathbf{H} . The angle between \mathbf{m} and \mathbf{H} is θ (Figure 3.14). The equation of motion which describes the alignment is

$$\Omega \left(\frac{d^2\theta}{dt^2} \right) + \beta \left(\frac{d\theta}{dt} \right) + mH \sin \theta = 0 \quad (3.32)$$

The first term describes inertial resistance to angular acceleration. Ω is moment of inertia of the particle given by

$$\Omega = \left(\frac{\pi d^5 \rho}{60} \right) \quad (3.33)$$

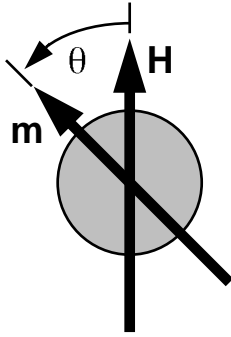


Figure 3.14 Detrital ferromagnetic grain in magnetic field. m is the magnetic moment of the ferromagnetic grain; H is magnetic field; θ is angle of m from H ; resulting aligning torque is $\Gamma = m \times H$.

where ρ is the density of the particle and d is the grain diameter. The second term in Equation (3.32) describes viscous drag between the particle and surrounding fluid. This drag resists rotation of the particle and depends upon rotation rate with β given by

$$\beta = \pi d^3 \eta \quad (3.34)$$

The last term in Equation (3.32) is the aligning torque of the magnetic field.

For values appropriate to ferromagnetic particles in sedimentary rocks, the inertial term (first term in Equation (3.32)) is negligible. This means that the grain rotates quickly and approaches small values of θ for which $\sin \theta \approx \theta$. The resulting simplifications to Equation (3.32) yield the following governing equation:

$$\frac{d\theta}{dt} = -\left(\frac{mH\theta}{\pi d^3 \eta} \right) \quad (3.35)$$

The solution to this equation will describe how the angle θ will decrease from an initial angle θ_0 . The solution describing this alignment process is

$$\theta(t) = \theta_0 \exp\left(\frac{-t}{t_0}\right) \quad (3.36)$$

where

$$t_0 = \left(\frac{\pi d^3 \eta}{mH} \right) \quad (3.37)$$

So this is an exponential alignment process in which t_0 is a characteristic alignment time during which θ decreases from θ_0 to θ_0/e .

Now we proceed by realizing that the magnetic moment of the spherical particle is simply

$$m = \frac{\pi d^3 j}{6} \quad (3.38)$$

where j is the net magnetic moment per unit volume. Substituting this expression for m back into Equation (3.37) yields t_0 , the characteristic alignment time:

$$t_0 = \frac{6\eta}{jH} \quad (3.39)$$

This result shows that t_0 is independent of particle size, d .

To gain a feeling for the magnitude of t_0 , substitute the following values into Equation (3.39):

$$\begin{aligned} \eta &= 10^{-2} \text{ poise, appropriate value for water} \\ H &= 0.5 \text{ Oe, typical surface geomagnetic field} \\ j &= 0.1 \text{ G} \end{aligned}$$

The latter value is appropriate for a large PSD grain of magnetite but is much lower than expected for a small PSD grain or an SD grain. However, even using this modest value for j , we find that Equation (3.39) yields $t_0 = 1$ s. The model implies rapid (and complete) alignment of ferromagnetic particles with the geomagnetic field at the time of deposition. Unfortunately, this theory fails a number of reality checks.

Evidence for postdepositional alignment

Laboratory redeposition experiments provide insight into DRM processes. In a number of experiments, natural sediments have been dispersed in water, then redeposited under known laboratory conditions. Results of such experiments are significantly different than predicted by the classic model.

One of the earliest laboratory redeposition experiments involved Holocene glacial varved deposits. The degree of alignment of magnetic moments (determined from resulting DRM) was found to be far less than implied by the classic model. Apparently, some (randomizing?) agent prevents the predicted high degree of alignment.

Redeposition experiments have been performed with inclination of the magnetizing field varied from one experiment to the next. Results are shown in Figure 3.15a. Inclination of the resulting DRM, I_0 , was found to be systematically shallower than inclination of the applied magnetic field, I_H , to which it was related by

$$\tan I_0 = f \tan I_H \quad (3.40)$$

The value of f in Equation (3.40) is 0.4 for redeposited glacial sediments.

One can visualize a simple explanation for this observation by examining the schematic diagram of Figure 3.15b. Because of shape anisotropy, the magnetic moment of elongated ferromagnetic grains lies along the long axis of the particle. But gravitational torques cause such particles to rotate toward the horizontal. However, in natural sediments, *inclination error* tends to be less than expected from these redeposition experiments and is often absent. The general conclusion is that the magnetization process must be in part a postdepositional detrital remanent magnetization (pDRM). Inclination error is more completely discussed in Chapter 8.

Results of an experiment that clearly demonstrated the feasibility of pDRM are shown in Figure 3.16. Dry mixtures of magnetite and quartz were made, then exposed to a magnetizing field while flooded with water and subsequently dried. Resulting pDRM was found to accurately record the inclination of the applied field. Ferromagnetic particles were able to reorient in the water-rich slurry, leading to accurate recording of the applied magnetic field direction.

Another enlightening experiment involved redeposition of deep-sea sediments (Figure 3.17). Over a number of days, sedimentary layers were redeposited under controlled magnetic field conditions. The declination of the applied magnetic field was switched by 180° on day 62. Whereas the change in declination of the applied magnetic field was essentially instantaneous, the resulting declination change in the sediment column was spread out, showing a time-integrative effect and a time lag in the magnetization process. Most significantly, the change in declination was partially recorded by sediments deposited 10 or 20 days before the change in direction of the applied magnetic field.

Natural deep-sea sediments are generally bioturbated to depths of 20 cm or more. It seems certain that any depositional DRM will be wiped out by passage of sediment through the digestive tract of a worm (if not on the intake, then certainly on the outgo). Yet bioturbated deep-sea sediments often are accurate recorders of the magnetic field present shortly after deposition. All of these laboratory experiments and natural processes emphasize the importance of postdepositional DRM. In many sediment types such as bioturbated sediments, pDRM is the only plausible mechanism for acquisition of DRM. Other sediments possess a resultant magnetization that is probably a combination of depositional and postdepositional alignment. An analysis of the pDRM process is essential to understanding detrital remanent magnetism.

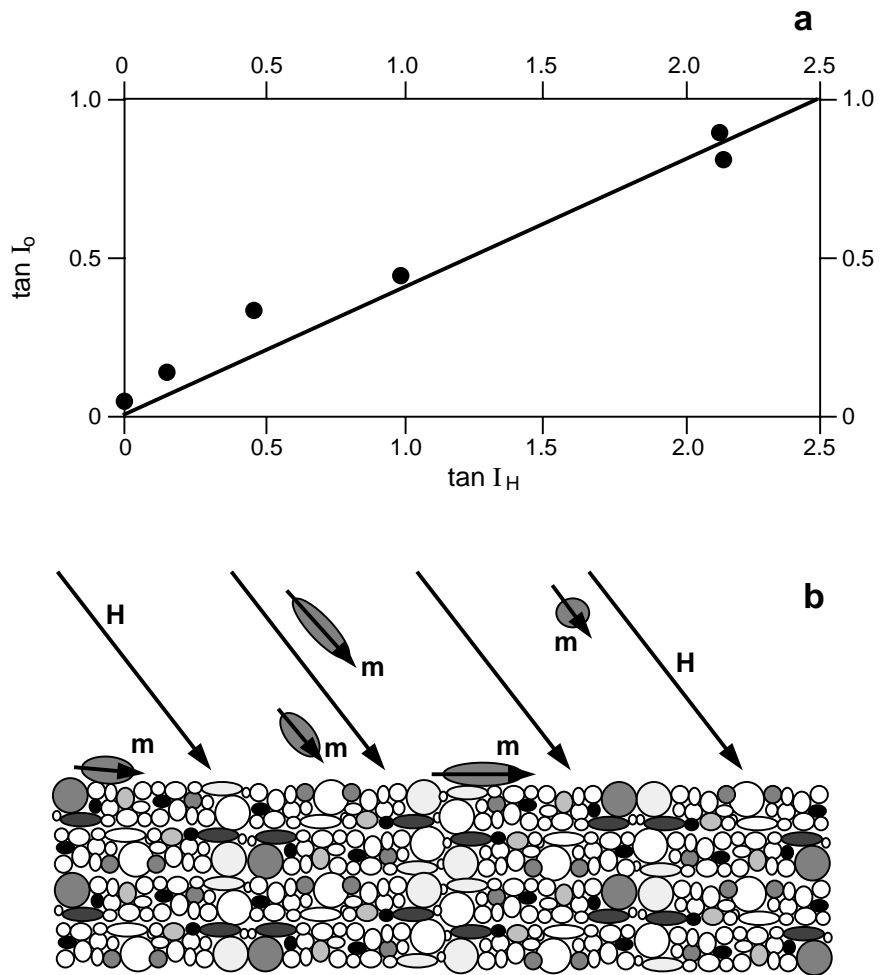


Figure 3.15 (a) The relationship between inclination (I_0) of DRM in redeposited glacial sediment and the inclination of the applied magnetic field (I_H). The solid line is the graph of $\tan I_0 = 0.4 \tan I_H$. Redrawn from Verosub (1977). (b) Schematic representation of ferromagnetic grains with magnetic moments m settling in magnetic field H . Elongate grains with m along long axis tend to rotate toward the horizontal plane, resulting in shallowed inclination of DRM.

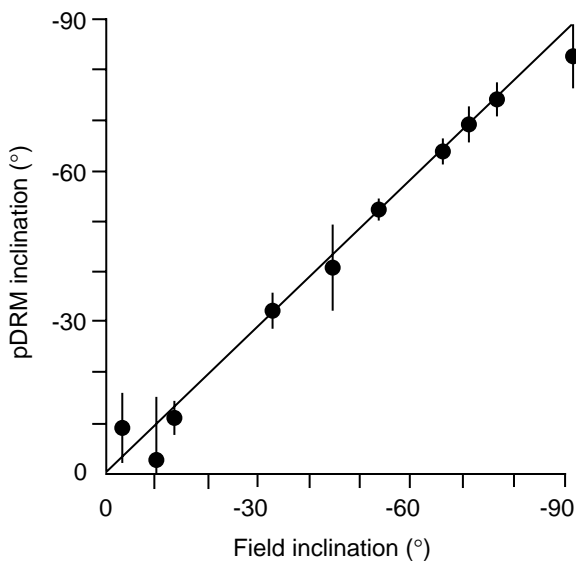


Figure 3.16 Inclination of pDRM versus inclination of applied magnetic field. Samples were dry synthetic quartz-magnetite mixtures flooded with water in a magnetic field of varying inclination; vertical error bars are confidence limits on measured pDRM inclination; the solid line is the expected result for perfect agreement between inclinations of pDRM and the applied magnetic field. Redrawn from Verosub (1977).

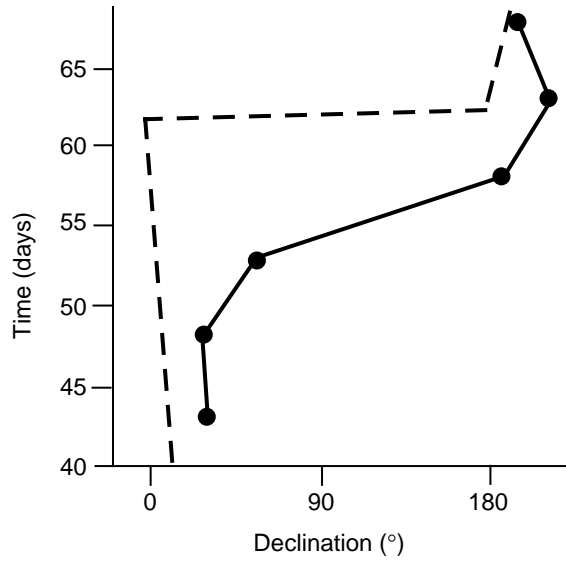


Figure 3.17 Declination of DRM recorded by redeposited deep-sea clay compared with declination of an applied magnetic field during redeposition. The ordinate indicates the number of days since commencement of the redeposition experiment; the declination of the applied magnetic field was changed by 180° on day 62; sediment deposited at least 10 days before the change in magnetic field declination partially recorded the new magnetic field direction. Redrawn from Verosub (1977).

Brownian motion and postdepositional alignment

As with thermoremanent magnetism, an important randomizing influence in DRM is thermal energy. In the postdepositional environment, thermal energy is transmitted to ferromagnetic particles by jostling from *Brownian motion* of water molecules. It is quite likely that the amount of misalignment depends on particle size; submicron particles are more severely jostled by water molecules than are 100- μm particles. Early attempts to develop a theory of pDRM likened the physical rotation of small ferromagnetic grains within water-filled pore spaces to alignment of atomic magnetic moments in a paramagnetic gas. In both situations there is an aligning torque of the magnetic field opposed by a randomizing influence of thermal energy.

First consider an assemblage of identical ferromagnetic particles with magnetic moment m . As with paramagnetism, the Langevin theory is applicable and leads to

$$\frac{\text{pDRM}}{\text{pDRM}_s} = \coth\left(\frac{mH}{kT}\right) - \left(\frac{kT}{mH}\right) \tag{3.41}$$

where pDRM is the resulting pDRM and pDRM_s is the saturation pDRM, the remanent magnetism that would result if all magnetic moments were rigidly aligned.

The *Brownian motion theory of pDRM* has been refined by considering grain magnetic moments to be distributed over a range from 0 to a maximum value, m_{max} . If the distribution of magnetic moments is uniform between these limits, integration of the above expression over the range of m yields

$$\frac{\text{pDRM}}{\text{pDRM}_s} = \left(\frac{1}{x}\right) \ln\left(\frac{\sinh x}{x}\right) \tag{3.42}$$

where
$$x = \frac{m_{\text{max}}H}{kT} \tag{3.43}$$

This expression is plotted in Figure 3.18a. For small magnetic fields and small particle magnetic moments, the value of x in Equations (3.42) and (3.43) is small. This leads to the approximation

$$\frac{\text{pDRM}}{\text{pDRM}_s} = \frac{x}{6} = \frac{m_{\text{max}}H}{6kT} \tag{3.44}$$

This result predicts the initial slope shown in Figure 3.18a.

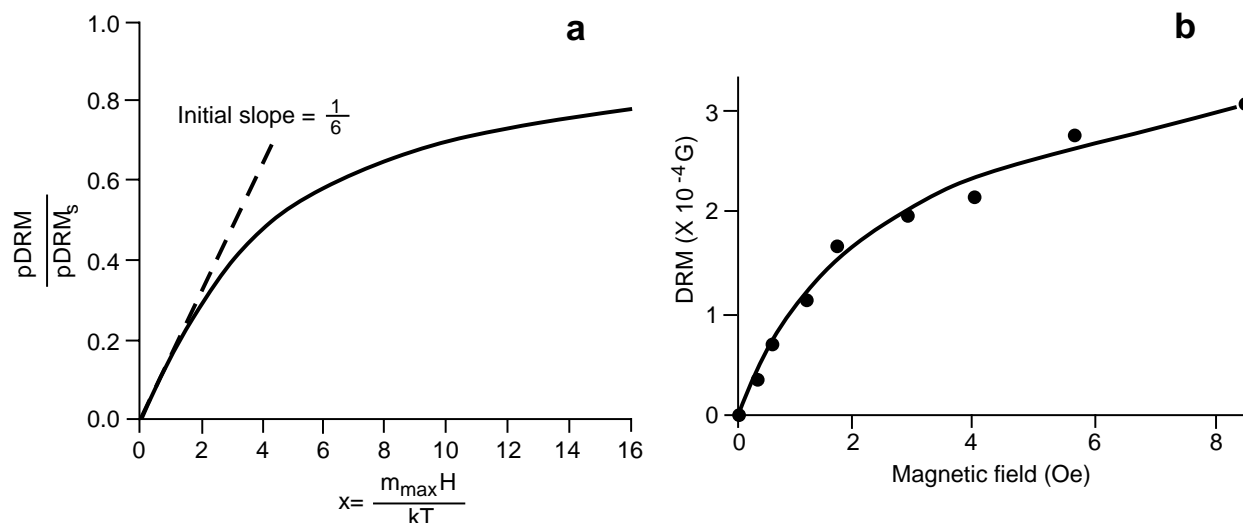


Figure 3.18 (a) Theoretical fractional saturation of pDRM in Brownian motion theory. The solid line is a plot of Equation (3.42); for small x , slope is $1/6$. (b) DRM acquired by redeposited glacial varved clay as a function of applied magnetic field. The solid line is Equation (3.42) with parameters adjusted to best fit observed DRM. Redrawn from Verosub (1977).

As with any such derivation, it is worthwhile examining whether the result is physically reasonable. Predicted pDRM for zero magnetizing field (or for $m_{\max} = 0$) is quite reasonably zero. With initial application of a magnetizing field, pDRM logically increases in a linear fashion. In strong magnetizing fields, there is an asymptotic behavior, with pDRM approaching an upper limit. This prediction is reasonable because even an infinite magnetizing field could do no more than perfectly align the constituent magnetic moments. Conversely, for any given magnetizing field, increasing temperature is predicted to decrease resulting pDRM, as expected for increased randomizing influence of Brownian motion. So, under first-order intuitive scrutiny, the governing equation for pDRM seems reasonable.

Experimental data on redeposited glacial sediments are shown by data points in Figure 3.18b, wherein Equation (3.42) was fit to the data. The form of Equation (3.42) fits the experimental data quite well, giving confidence that the theory successfully describes dependence of pDRM on field strength. The parameter for the glacial sediments adjusted to fit the form of Equation (3.42) is m_{\max} . The resulting value of m_{\max} is $7.4 \times 10^{-14} \text{ G cm}^3$ ($7.4 \times 10^{17} \text{ A m}^2$). With information about grain size of magnetite particles, it is possible to determine that intensity of magnetization is 8 G for a typical ferromagnetic grain in this sediment. This value is intermediate between the 480 G expected for SD particles and the low intensity ($<1 \text{ G}$) expected for MD grains. This result indicates the importance of PSD grains to magnetization of these silts and clays.

The Brownian motion theory of pDRM has been quite successful in describing many properties of postdepositional detrital remanent magnetism. But success of the theory does not mean that all DRM is actually pDRM. In natural sediments, a portion of DRM may be depositional, forming by action of aligning and gravitational torques at the time of deposition. The remainder is the result of postdepositional alignment. Depositional DRM can lead to inclination error, whereas pDRM realignment tends to remove inclination error. The portion of total DRM resulting from depositional alignment as opposed to pDRM processes is thus of major concern.

The ratio of depositional to postdepositional alignment depends upon a number of factors that are imperfectly understood. Some of the most important are the following:

1. *Grain size.* Small grain size enhances Brownian motion of ferromagnetic particles. Fine-grained sediments have high water contents when initially deposited and slowly decrease in water content during initial compaction and consolidation. Accordingly, there is ample time (perhaps 10^2 – 10^3 yr)

for pDRM alignment to operate. Conversely, coarse-grained sediments may have a larger portion of total DRM formed by depositional processes.

2. *Rate of deposition.* Residence time for a ferromagnetic particle within the zone of high water content depends on rate of deposition. Slow rates probably enhance postdepositional alignment.
3. *Bioturbation.* Sediments stirred by bioturbation acquire all detrital remanence by postdepositional processes. Bioturbation ensures high water content in the top of the accumulating sediment column, and high water content is known to enhance pDRM alignment.

Grain-size effects

A claystone has a maximum grain diameter of 4 μm , and virtually all magnetite particles are within the SD and PSD ranges. However, grain-size demarcation between silt and sand is 62 μm . Fine silts may have a major portion of grains within the PSD range, but almost all magnetite grains in well-sorted coarse silts or sands are MD.

These differences in grain size have dual importance. First, grains within SD or PSD ranges have relatively strong magnetization. These fine particles are more efficiently aligned by the geomagnetic field (dominantly by pDRM). Larger particles have lower intensity of magnetization and are less likely to move freely within pore spaces in newly deposited sediment. Thus, they are not effectively aligned by either depositional or postdepositional processes. Second, larger ferromagnetic particles within the MD grain-size range are more susceptible to acquisition of viscous magnetization. Thus, sandstones are less efficiently magnetized initially, and their remanent magnetization is less stable.

Other effects of grain size are also significant. For any grain size larger than medium sandstone, mechanical energies begin to outweigh aligning influence of the geomagnetic field on ferromagnetic particles. Thus, coarse sands and gravels are not likely to acquire substantial DRM. In addition, coarse sediments are generally permeable and likely to experience chemical changes due to groundwater circulation with probable effects on ferromagnetic minerals. For these reasons, claystones to fine sandstones are usually preferred in paleomagnetic studies, and larger grain-size sediments are avoided.

Lock-in of DRM

The locking-in of detrital remanent magnetism occurs when dewatering and consolidation restrains motion of sedimentary particles. Once physical contact of surrounding grains inhibits motion, DRM is mechanically locked. Lock-in is spread over the time interval of dewatering and consolidation. Estimates of lock-in time range up to 10^3 yr, depending on sedimentary environment. Larger ferromagnetic particles are probably locked before fine particles situated in interstices.

This discussion of DRM has provided a basic understanding of remanent magnetization in detrital sedimentary rocks at or soon after deposition. Considering the variations in source rocks and in depositional and postdepositional processes, it is not surprising that DRM has a wide range of intensities. Magnetite-rich continental deposits can have DRM intensities $> 10^{-4}$ G (10^{-1} A/m), while marine limestones can have DRM intensities $< 10^{-7}$ G (10^{-4} A/m).

VISCOUS REMANENT MAGNETISM (VRM)

Viscous remanent magnetism (VRM) is a remanent magnetization that is gradually acquired during exposure to weak magnetic fields. Natural VRM is a secondary magnetization resulting from action of the geomagnetic field long after formation of the rock. From the paleomagnetic viewpoint, this VRM usually is undesirable noise. In this section, we examine basic properties of viscous magnetization. By understanding the basic physics, we can discover the properties of ferromagnetic grains that are prone to acquisition of VRM. In turn, this will explain demagnetization techniques employed to erase viscous components of magnetization to reveal primary components of paleomagnetic interest. We discuss these demagnetization procedures in Chapter 5.

Acquisition of VRM

Experimental data illustrating acquisition of viscous remanence are shown in Figure 3.19. In this experiment, a synthetic sample with dispersed 2- μm grains of magnetite was placed in a magnetic field of 3.3 Oe (0.33 mT). Resulting VRM was measured periodically during exposure to the magnetic field, and the VRM acquisition experiment was repeated at various temperatures. VRM at a given temperature is acquired according to

$$\text{VRM} = S \log t \quad (3.45)$$

where t is the acquisition time (s), the time over which VRM is acquired, and S is the viscosity coefficient.

From Figure 3.19 it is clear that S increases with temperature. Because of logarithmic growth of VRM with time of exposure, viscous magnetization is dominated by the most recent magnetizing field. Rocks that have large components of VRM are usually observed to have NRM aligned with the present geomagnetic field at the sampling location.

We first consider VRM acquired by single-domain grains. For assemblages of SD particles, acquisition of VRM is essentially the inverse of magnetic relaxation. VRM acquisition involves realignment of magnetic moments of grains with short relaxation time, τ . In Figure 3.20, contours of a hypothetical distribution of SD grains are shown on a $v-h_c$ diagram. If the VRM acquisition experiment has been carried out for a length of time equal to "acquisition time," then all grains with $\tau \leq$ acquisition time (grains shown by the heavy stippled pattern in Figure 3.20) are effectively "unblocked" and can respond to the applied magnetic field. Magnetic moments of these unblocked grains seek an equilibrium distribution with resulting VRM in the direction of the applied magnetic field. As acquisition time increases, the line of $\tau =$ acquisition time sweeps through the grain distribution, and VRM increases.

The effect of increased temperature can be understood by realizing that h_c decreases with increased temperature. The distribution of grains in $v-h_c$ space migrates toward decreasing h_c (toward the left in the

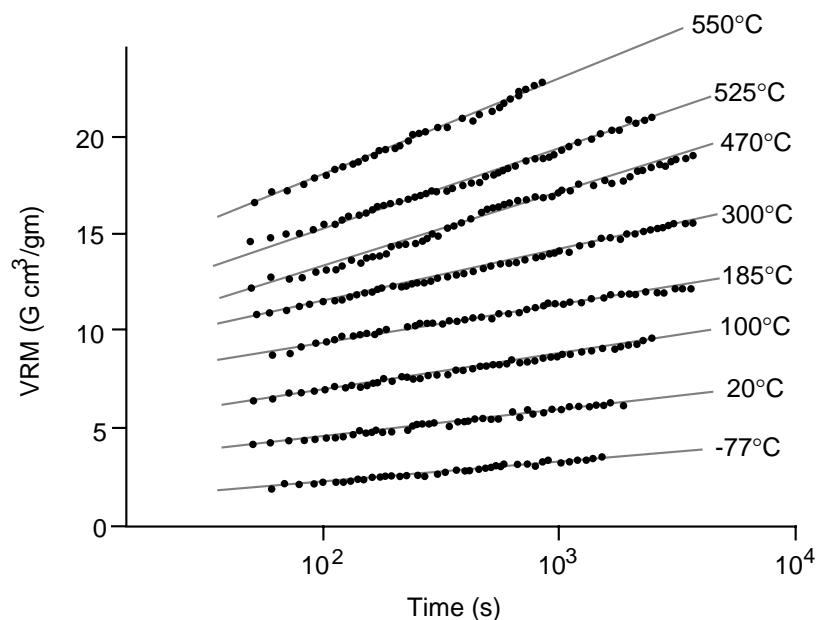


Figure 3.19 Progressive acquisition of VRM by synthetic sample of dispersed 2- μm diameter grains of magnetite. Data points show VRM acquired at corresponding time since the beginning of exposure to the magnetic field; lines show the trend of VRM for a particular VRM acquisition experiment at the temperature indicated; the magnetic field was 3.3 Oe; zero on the ordinate is arbitrary (the absolute value of VRM was adjusted so that results of all VRM acquisition experiments could be conveniently shown on a single drawing). Redrawn from Stacey and Banerjee (1974).

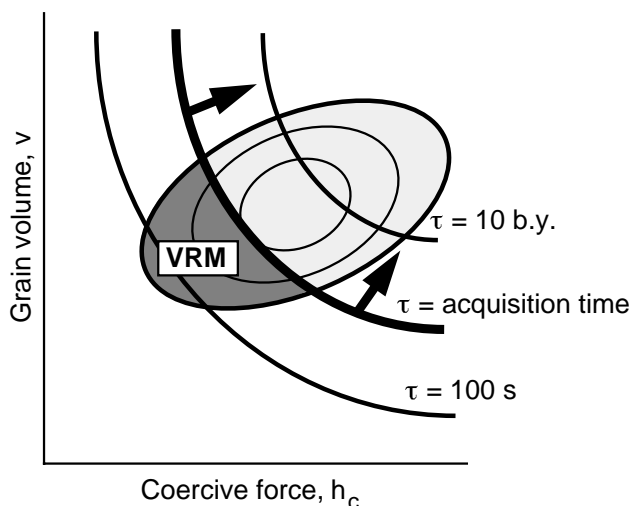


Figure 3.20 Schematic representation of VRM acquisition on a diagram of SD grain volume (v) versus microscopic coercive force (h_c). As the time of VRM acquisition increases, the bold line labeled “ τ = acquisition time” sweeps through the SD grain population from lower left to upper right; grains with progressively longer τ can acquire VRM as acquisition time increases; SD grains in the dark stippled region labeled “VRM” have acquired VRM.

v - h_c diagram) as temperature increases. Also more thermal energy means that energy barriers to rotation of the magnetic moment are more quickly overcome. Thus, for a given acquisition time, increasing temperature results in more grains becoming carriers of VRM; hence, viscosity coefficient, S , is increased. For substantially elevated temperature, the resulting VRM is referred to as *thermoviscous remanent magnetization* (TVRM).

In naturally acquired VRM, acquisition time can be up to 10^9 yr or even longer. All grains with $\tau < 10^9$ yr are potential carriers of VRM. SD grains with relaxation times $> 10^9$ yr will generally retain primary magnetization of paleomagnetic interest. On the v - h_c diagram, these stable grains with long relaxation time are in the upper right portion of the diagram.

VRM in PSD and MD particles

VRM is acquired by PSD and MD grains through thermal activation of domain walls. As shown in Figure 3.3, domain wall energy is a function of position. Thermal energy can activate domain walls over local energy barriers. Interaction energy between the applied field and the magnetization of the PSD or MD grain favors domain wall motion, resulting in increased magnetization in the direction of the applied field.

For multidomain grains, a general inverse relationship exists between coercive force and viscosity coefficient. Grains of low coercive force rapidly acquire VRM, and grains with the lowest coercive force dominate VRM. For magnetite-bearing rocks, VRM is generally carried by MD grains of low coercive force. This causal connection between low coercivity and dominance of VRM is important in explaining demagnetization of VRM in magnetite-bearing rocks.

Thermoviscous remanent magnetism (TVRM)

Rocks of paleomagnetic interest may suffer intervals of heating, possibly resulting in metamorphism. We must understand how prolonged exposure to elevated temperatures below the Curie temperature will (1) affect the ability of rocks to retain a primary NRM and (2) form thermoviscous magnetization (TVRM). In this section, we present an analysis of TVRM that employs single-domain theory to predict changes in relaxation time with temperature. This theory is quite successful in explaining acquisition of TVRM. It also explains how portions of ferromagnetic particles in rocks can potentially retain a primary paleomagnetic record despite significant metamorphism.

Initially consider an assemblage of identical SD grains. The Néel relaxation time equation with temperature dependences explicitly stated is

$$\tau(T) = \frac{1}{C} \exp\left(\frac{v j_s [T] h_c [T]}{2kT}\right) \quad (3.46)$$

which yields

$$\ln(\tau[T] C) = \left(\frac{v j_s[T] h_c[T]}{2 k T} \right) \quad (3.47)$$

For an assemblage of identical grains,

$$\frac{v}{2k} = \text{constant} = \frac{T \ln(\tau[T] C)}{j_s[T] h_c[T]} \quad (3.48)$$

Now assume that the assemblage has relaxation times τ_1 at temperature T_1 and τ_2 at temperature T_2 . Because the left side of Equation (3.48) is constant, the relationships between parameters at T_1 and T_2 becomes

$$\left(\frac{T_1 \ln[\tau_1 C]}{j_s[T_1] h_c[T_1]} \right) = \left(\frac{T_2 \ln[\tau_2 C]}{j_s[T_2] h_c[T_2]} \right) \quad (3.49)$$

To predict time-temperature relationships, we must know the temperature dependence of coercive force, $h_c(T)$. For SD magnetite, a reasonable assertion is that coercivity is dominated by shape anisotropy and will be given by

$$h_c(T) = \Delta N_D j_s(T) \quad (3.50)$$

where ΔN_D is the difference in internal demagnetizing factor between short and long axes of the SD particle. For SD hematite, coercivity is controlled by magnetocrystalline anisotropy that has more severe temperature dependence given by

$$h_c(T) = D j_s^3(T) \quad (3.51)$$

where D is a proportionality constant independent of temperature (and depends on all manner of things that are not important to this discussion). Plugging these expressions back into Equation (3.49) yields

$$\left(\frac{T_1 \ln[\tau_1 C]}{j_s^2[T_1]} \right) = \left(\frac{T_2 \ln[\tau_2 C]}{j_s^2[T_2]} \right) \quad \text{for magnetite;} \quad (3.52)$$

$$\left(\frac{T_1 \ln[\tau_1 C]}{j_s^4[T_1]} \right) = \left(\frac{T_2 \ln[\tau_2 C]}{j_s^4[T_2]} \right) \quad \text{for hematite.} \quad (3.53)$$

Using known temperature dependence of saturation magnetization, j_s , for magnetite and hematite (Figure 2.3), we can predict time-temperature stabilities.

The most useful way to display the resulting relaxation time and blocking temperature (τ , T_B) pairs is to generate *nomograms* which show the locus of points in τ - T_B space that activate the same grains. Nomograms for SD particles of magnetite and of hematite are shown in Figure 3.21. These diagrams are also known as *blocking diagrams*. An example using Figure 3.21a will reveal the utility of these nomograms.

Point 1 of Figure 3.21a labels a point in τ - T_B space corresponding to SD magnetite grains that have a relaxation time of 10 m.y. at 260°C. These grains are expected to acquire substantial VRM if held at 260°C for 10 m.y. Point 2 corresponds to $\tau = 30$ minutes at $T = 400^\circ\text{C}$ and lies on the same nomogram as point 1. This means that grains with $\tau = 10$ m.y. at 260°C also have $\tau = 30$ minutes at 400°C. The implication is that TVRM acquired by these grains during a 10 m.y. interval at 260°C could be *unblocked* by heating to 400°C for 30 minutes in zero magnetic field. Such heating would reset magnetization of these grains to zero.

Now examine points 3 and 4 in Figure 3.21a. These points are on a nomogram connecting τ - T_B conditions for identical grains. (These grains are of course very different from those described by points 1 and 2.)

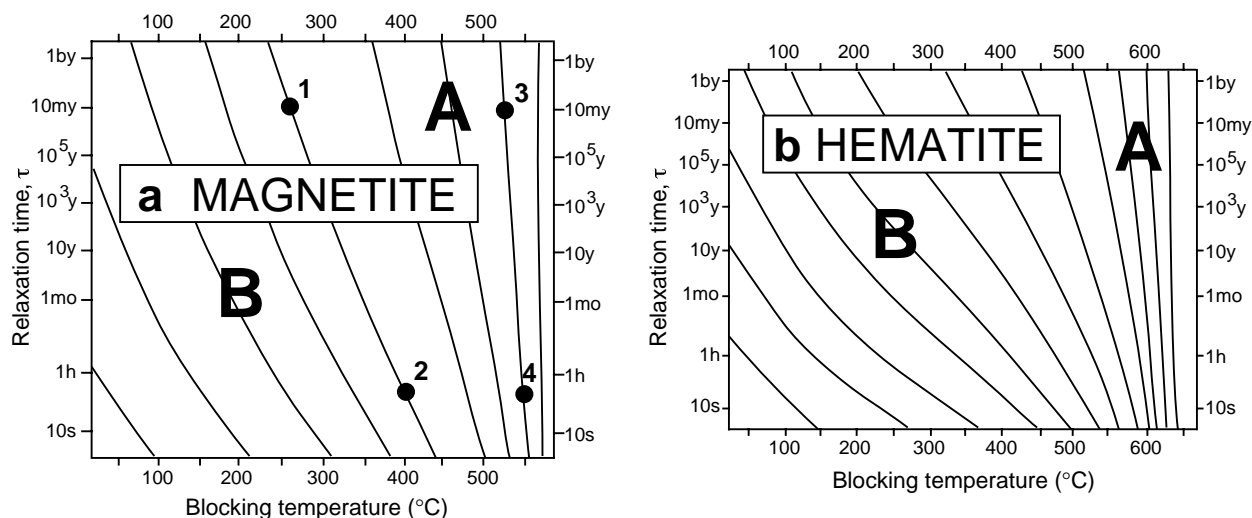


Figure 3.21 Blocking diagrams for (a) magnetite and (b) hematite. Lines on the diagrams connect combined temperature and relaxation time (τ) conditions that can unblock (reset) the magnetization in a given population of SD grains. See text for explanation. Redrawn from Pullaiah et al. (1975).

Point 3 indicates $\tau = 10$ m.y. for $T_B = 520^\circ\text{C}$, whereas point 4 indicates $\tau = 30$ minutes for $T_B = 550^\circ\text{C}$. Thus grains with a 10-m.y. relaxation time at 520°C can be unblocked by heating to only a slightly higher temperature (550°C) for 30 minutes. This is another way of expressing the rapid increase in relaxation time with decreasing temperature for grains with T_B close to the Curie temperature.

The blocking diagrams of Figures 3.21a and 3.21b have been broken into two regions. Grains in the **B** region have blocking temperatures on laboratory time scales (ca. 30 minutes) at temperatures at least 100°C below the Curie temperature. These grains could acquire TVRM at modest temperatures (ca. 300°C) if exposed to those temperatures for geologically reasonable intervals of time (ca. 10 m.y.). Grains in the **B** region are thus unstable carriers of primary components of magnetization and are likely to acquire secondary TVRM or VRM. But grains in the **A** region have laboratory blocking temperatures within 100°C of the Curie temperature. These grains are resistant to resetting of magnetization, except by heating to temperatures approaching the Curie temperature. Grains in the **B** region tend to have blocking temperatures distributed over wide intervals far below the Curie temperature, whereas grains in the **A** region have sharply defined blocking temperatures within 100°C of the Curie temperature. This explains why rocks with T_B dominantly within 100°C of the Curie temperature tend to be stable carriers of primary TRM, whereas rocks with T_B distributed far below the Curie temperature are generally unstable.

Figure 3.21 predicts that primary NRM can survive heating to the greenschist metamorphic range ($300^\circ\text{--}500^\circ\text{C}$) but not to the amphibolite range ($550^\circ\text{--}750^\circ\text{C}$). Magnetization recorded by magnetite grains with T_B in the **A** region should have magnetization blocked at approximately the same time as radiogenic argon is retained in hornblende (ca. 525°C). However, please be warned that this discussion treats only time-temperature effects. Even low-grade metamorphism is often accompanied by chemical changes that can alter the ferromagnetic minerals, sometimes destroying the primary NRM and/or chemically remagnetizing the rock.

This theory of thermoviscous remanent magnetism also provides a basic theory of thermal demagnetization of secondary NRM. SD grains that have short τ at room temperature also have low T_B while grains with long τ at room temperature have high T_B . Secondary NRM is preferentially carried by the low τ (and low T_B) grains. Thus it is possible to heat a rock to above T_B of grains carrying the secondary NRM but below T_B of grains carrying the primary NRM. This process can be used to erase secondary NRM while leaving the primary NRM essentially unaffected. Procedures for thermal demagnetization will be discussed in detail in Chapter 5.

Caveats and summary

Now for some caveats about why all this theoretical stuff that you've just learned (with some effort but, I hope, little pain) might not, in fact, exactly work. One problem that is often observed is that temperatures required to erase TVRM or VRM components are higher than those predicted by theory. Basic results still apply, but the theory might be optimistic about the predicted ease of removing secondary TVRM. Furthermore, the theory seems to work more dependably for hematite than for magnetite.

Remember that this theory applies to SD grains. A large portion of hematite is SD, while a typical magnetite-bearing rock has a significant portion of its grain-size distribution within the PSD range. It is likely that the presence of PSD grains in magnetite-bearing rocks accounts for some inadequacies of this TVRM theory. Chemical changes in ferromagnetic minerals during metamorphism were also neglected in this TVRM theory. When considering the effects of regional metamorphism or significant burial metamorphism, the strong possibility of chemical change and grain growth must be kept in mind.

Given the distribution of grain sizes and shapes for ferromagnetic grains in rocks, it is expected that some portion of these grains will acquire VRM or TVRM. These components of natural remanent magnetism are generally undesirable secondary components that we seek to destroy during partial demagnetization experiments. We have shown that SD grains with low blocking temperatures are particularly susceptible to acquisition of viscous magnetization. However, it has also been shown that grains with high blocking temperature can retain primary NRM even when other grains in the same rock have acquired VRM. So several components of NRM can reside within different populations of ferromagnetic grains in the same rock. Much paleomagnetic research is concerned with the general problem of deciphering multiple components of magnetization in rocks and uncovering the components of paleomagnetic interest.

ISOTHERMAL REMANENT MAGNETISM (IRM)

Remanent magnetism resulting from short-term exposure to strong magnetizing fields at constant temperature is referred to as *isothermal remanent magnetism* (IRM). In the laboratory, IRM is imparted by exposure (usually at room temperature) to a magnetizing field generated by an electromagnet. IRM is the form of remanence produced in hysteresis experiments and is acquired by ferromagnetic grains with coercive force less than the applied field.

Natural IRM can form as a secondary component of IRM by exposure to transient magnetic fields of lightning strikes. Electrical currents of lightning can exceed 10^4 amperes, and the magnetic field within 1 m of a lightning bolt can be 10^2 – 10^3 Oe (10–100 mT). It might seem an unlikely circumstance to collect a paleomagnetic sample within 1 m of the location where a lightning bolt has struck. However, a brief examination shows that lightning-induced IRM can be a significant problem, especially in regions of frequent thunderstorm activity.

Worldwide incidence of lightning strikes is a surprising 10^2 – 10^3 strikes/s. Substantial IRM is acquired within 2 m of a lightning strike, and a reasonable estimate of the time required to erode 2 m from a slope affording a fresh outcrop for paleomagnetic sampling is 10^4 yr. The resulting worldwide average is found to be about 0.1 lightning strike/m² over a time interval of 10^4 yr. Considering that lightning storms are concentrated in tropical regions, the probability of lightning strikes having imparted a secondary IRM to outcrops in these regions is substantial. Lightning-prone outcrops on ridges or mesas are likely to have experienced numerous strikes with virtually complete remagnetization. The obvious lesson is to avoid elevated exposures when sampling and to be thorough when examining NRM in the laboratory. Field and laboratory methods are considered in the following chapters.

SUGGESTED READINGS**THERMOREMANENT MAGNETISM:**

L. Néel, Some theoretical aspects of rock magnetism, *Adv. Phys.*, v. 4, 191–242, 1955.

The classic article on TRM.

F.D. Stacey, The physical theory of rock magnetism, *Adv. Phys.*, v. 12, 45–133, 1963.

Presents an in-depth investigation of various forms of NRM.

F.D. Stacey and S.K. Banerjee, *The Physical Principles of Rock Magnetism*, Elsevier, Amsterdam, 195 pp, 1974.

Chapters 6 and 7 treat TRM.

DETRITAL REMANENT MAGNETISM:

D.W. Collinson, Depositional remanent magnetization in sediments, *J. Geophys. Res.*, v. 70, 4663–4668, 1965.

Discusses numerous aspects of DRM acquisition.

E. Irving and A. Major, Post-depositional detrital remanent magnetization in a synthetic sediment, *Sedimentology*, v. 3, 135–143, 1964.

A classic PDRM experiment.

F.D. Stacey, On the role of Brownian motion in the control of detrital remanent magnetization of sediments, *Pure Appl. Geophys.*, v. 98, 139–145, 1972.

Treats the Brownian motion model of PDRM.

K.L. Verosub, Depositional and post-depositional processes in the magnetization of sediments, *Rev. Geophys. Space Phys.*, v. 15, 129–143, 1977.

Excellent review article on DRM.

VISCOUS REMANENT MAGNETISM:

D.J. Dunlop, Viscous magnetization of .04–100 μm magnetites, *Geophys. J. R. Astron. Soc.*, v. 74, 667–687, 1983.

A more advanced look at VRM.

G.E. Pullaiah, E. Irving, K.L. Buchan, and D.J. Dunlop, Magnetization changes caused by burial and uplift, *Earth Planet. Sci. Lett.*, v. 28, 133–143, 1975.

Develops the blocking diagram approach to TVRM.

LIGHTNING-INDUCED ISOTHERMAL REMANENT MAGNETISM:

A. Cox, Anomalous remanent magnetization of basalt, *U.S. Geol. Surv. Bull.*, v. 1083–E, 131–160, 1961.

A classic study of effects of lightning on natural remanent magnetism.

PROBLEMS

- 3.1** Consider a highly elongate rod (needle-shaped grain) of ferromagnetic material.
- Develop a simple derivation that demonstrates that $N_D \approx 0$ along the long axis of the rod and $N_D \approx 2\pi$ along the diameter of the rod (perpendicular to the long axis).
 - For a needle-shaped grain of titanomagnetite with $j_s = 400$ G, what external magnetic field is required to magnetize the rod to saturation along the diameter (perpendicular to the long axis)?
- 3.2** A sample is made up of 7% by volume of SD ferromagnetic grains randomly dispersed within a diamagnetic matrix. The coercive force of the ferromagnetic material is dominated by a uniaxial magnetocrystalline anisotropy with anisotropy constant $K = 4.5 \times 10^4$ erg/cm³. Saturation magnetization is $j_s = 100$ G.
- Determine the microscopic coercive force, h_c , of individual SD grains.
 - Consider a hysteresis experiment on this sample. Determine the following hysteresis parameters for the sample: J_s , J_r , H_c .
- 3.3** Spherical SD grains of hematite ($\alpha\text{Fe}_2\text{O}_3$) are precipitating from solution at a temperature of 280°K. The microscopic coercive force, $h_c = 10^4$ Oe; the saturation magnetization, $j_s = 2$ G; and the Boltzmann constant, $k = 1.38 \times 10^{-16}$ erg/°K.
- Use the relaxation time equation (Equation (3.14)) to determine the diameter of spherical hematite grains that have $\tau = 100$ s.

- b. Assuming that Equation (3.24) (developed to determine the bias of grain magnetic moments during blocking of TRM) can also be used for CRM formation, what is the bias ($P_+ - P_-$) of grain magnetic moments for a population of spherical hematite grains with the parameters listed above? Assume that CRM is blocked when $\tau = 100$ and that the magnetic field present during precipitation is 1 Oe. Remember that for small x , $\tanh x \approx x$.
- 3.4** Hydrothermal activity elevates the temperature of a red sandstone to 225°C for a time interval of 1000 yr and results in formation of thermoviscous remanent magnetization (TVRM). If hematite is the exclusive ferromagnetic mineral in this red sandstone, approximately what temperature of thermal demagnetization is required to unblock (remove) this TVRM? The time at maximum temperature during thermal demagnetization is approximately 30 min.

SAMPLING, MEASUREMENT, AND DISPLAY OF NRM

We now begin putting theories and observations of Chapters 1 through 3 to work. This chapter introduces data acquisition procedures by presenting techniques for sample collection, and for measurement and display of NRM. A brief discussion of methods for identifying ferromagnetic minerals in a suite of paleomagnetic samples is also included.

COLLECTION OF PALEOMAGNETIC SAMPLES

We understand from Chapter 1 that the surface geomagnetic field undergoes secular variation with periodicities up to $\sim 10^5$ yr. The average direction is expected to be that of a geocentric axial dipole, and many paleomagnetic investigations are designed to determine that average direction. Paleomagnetic samples are usually collected to provide a set of quasi-instantaneous samplings of the geomagnetic field direction at the time of rock formation. Because geomagnetic secular variation must be adequately averaged, the time interval represented by the collection of paleomagnetic samples should be $\geq 10^5$ yr. There is no clear upper limit for the time interval, but this rarely exceeds 20 m.y.

Sample collection scheme

The hierarchy of a generalized paleomagnetic sampling scheme is shown in Figure 4.1. A *rock unit* is a sequence of beds in a sedimentary sequence or cooling units in an igneous complex, usually a member of a geological formation, an entire formation, or even a sequence of formations. It is advisable to sample at several widely separated localities (perhaps separated by as much as several hundred km). This procedure avoids dependence on results from a single locality and also may provide application of field tests discussed in Chapter 5. A single locality might have been affected by undetected tectonic complications or geochemical processes that have altered the ferromagnetic minerals, whereas a region is less likely to have been systematically affected by these complications.

A *site* is an exposure of a particular bed in a sedimentary sequence or a cooling unit in an igneous complex (i.e., a lava flow or dike). If it is assumed that a primary NRM direction can be determined from the rock unit, results from an individual site provide a record of the geomagnetic field direction at the sampling locality during the (ideally short) time interval when the primary NRM was formed. Multiple sites within a given rock unit are needed to provide adequate time sampling of the geomagnetic field fundamental to most paleomagnetic applications. The proper number of sites for a paleomagnetic study is a matter of debate and is discussed in Chapter 7.

Samples are separately oriented pieces of rock. Unless prevented by logistical difficulties (e.g., lake-bottom coring, etc.), collection of multiple samples from a site is advised. A common practice is to collect six to eight separately oriented samples from a site spread over 5 to 10 m of outcrop. Comparison of NRM directions from sample to sample within a site allows within-site homogeneity of the NRM to be evaluated.

Specimens are pieces of samples prepared to appropriate dimensions for measurement of NRM. Multiple specimens may be prepared from an individual sample, and this procedure can provide additional checks on homogeneity of the NRM and experimental procedures. Often only a single specimen is pre-

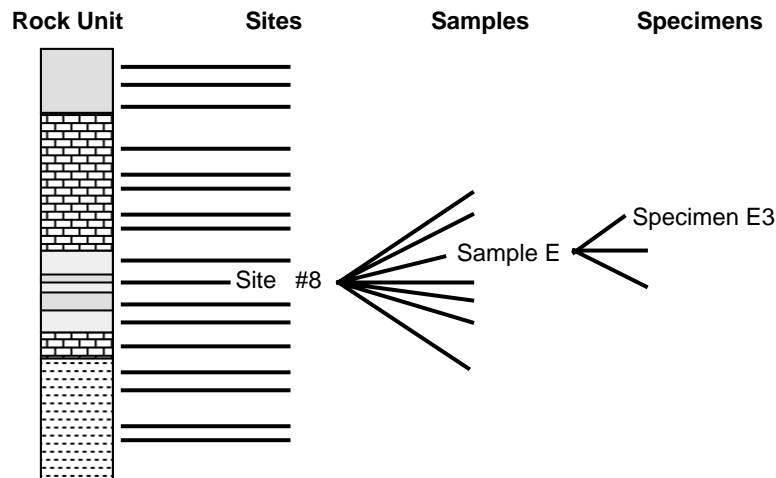


Figure 4.1 Generalized paleomagnetic sampling scheme. Multiple sampling sites are collected within the rock unit; multiple samples are collected from each site; specimens for laboratory measurements are prepared from samples.

pared from a particular sample, and little is gained by preparing more than three specimens from a sample. A typical specimen has volume $\sim 10 \text{ cm}^3$.

If the bedding at a site is other than flat-lying, the orientation of bedding must be determined so that structural corrections can be applied. Bedding orientation is determined by standard methods (usually magnetic compass and inclinometer). To the extent allowed by the exposure, the complete structural setting should be determined. If sites are collected from structures such as limbs of plunging folds, both local attitude and plunge must be determined to allow complete tectonic correction. Procedures for tectonic corrections to paleomagnetic data are discussed below.

Types of samples

Logistics of sample collection dictate strategies for obtaining oriented samples. Basic attributes of the most common sampling methods are discussed below.

1. *Samples cored with portable drill.* The most common type of paleomagnetic sample is collected by using a gasoline-powered portable drilling apparatus with a water-cooled diamond bit (Figure 4.2a). The diameter of cores is usually $\sim 2.5 \text{ cm}$. After coring of the outcrop to a depth of 6 to 12 cm (Figure 4.2b), an orientation stage is slipped over the sample while it is still attached to the outcrop at its base (Figure 4.2c). Orientation stages have an inclinometer for determining inclination (dip) of the core axis and magnetic or sun compass (or both) for determining azimuth of core axis. The accuracy of orientation by such methods is about $\pm 2^\circ$. After orientation, the core is broken from the outcrop, marked for orientation and identification (Figure 4.2d), and returned to the laboratory. Advantages of the coring technique are the ability to obtain samples from a wide variety of natural or artificial exposures and accurate orientation. Disadvantages include the necessity of transporting heavy fluids (water and gasoline) to the sampling site, dependence on performance of the drilling apparatus (often in remote locations), and herniated disks suffered by inveterate drillers.
2. *Block samples.* In some locations or with particular lithologies that are not easily drilled, logistics (or laws) might demand collection of oriented block samples. Joint blocks are often oriented (generally by determining the strike and dip of a surface) and then removed from the outcrop. For unlithified sediments, samples may be carved from the outcrop. Advantages of block sampling are freedom from reliance on coring apparatus and the ability to collect lithologies that are unsuitable for coring. There are, however, conspicuous disadvantages: limited accuracy of orientation, the need to collect joint blocks (likely more weathered than massive portions of outcrops), and the need to transport large numbers of cumbersome block samples out of the field and later subsample these to obtain specimens.

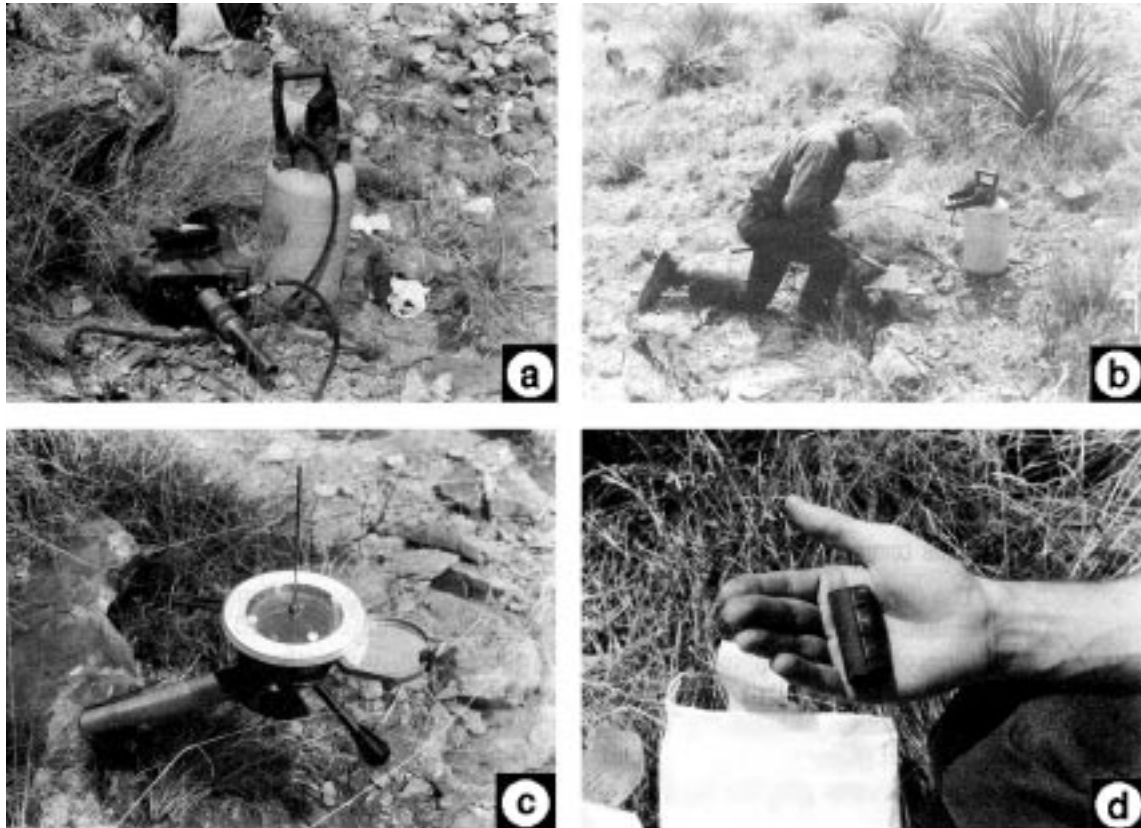


Figure 4.2 Core sample collection procedures. (a) Portable gasoline-powered drill with diamond drilling bit; a pump can is used to force cooling water through the drill bit. (b) Unskilled laborer drilling a core. (c) Orientation stage placed over in situ core. Notice the inclinometer on the side of the orientation stage; the magnetic compass is under a Plexiglas plate; the white ring on the Plexiglas plate is used to measure the azimuth of the shadow cast by the thin rod perpendicular to the plate. (d) Core sample with orientation markings.

3. *Lake-bottom or sea-bottom core samples.* Numerous devices have been developed to obtain columns of sediment from lake or sea bottom. Diameters of these coring devices are typically ~10 cm and may be of circular or square cross section. Most such cores are azimuthally unoriented and are assumed to penetrate the sediment vertically. Depth of penetration is usually ≤ 20 m. However, advances in ocean-bottom coring techniques employed by the Ocean Drilling Project now permit piston coring in advance of the rotary drill. Cores up to several hundred meters in length have been collected with almost 100% recovery. Samples for laboratory measurement are subsampled from the large sediment core.

Some comments on sample collection

The diversity of paleomagnetic investigations and applications makes it hard to generalize about sample collection, but there are some time-honored recommendations. One obvious recommendation is to collect fresh, unweathered samples. Surface weathering oxidizes magnetite to hematite or iron-oxyhydroxides, with attendant deterioration of NRM carried by magnetite and possible formation of modern CRM. Artificial outcrops (such as road cuts) thus are preferred locations, and rapidly incising gorges provide the best natural exposures.

Lightning strikes can produce significant secondary IRM, which can mask primary NRM. Although partial demagnetization in the laboratory can often erase lightning-induced IRM, the best policy is to avoid lightning-

prone areas. When possible, topographic highs should be avoided, especially in tropical regions. If samples must be collected in lightning-prone areas, effects of lightning can be minimized by two procedures.

1. Outcrops of strongly magnetic rocks such as basalts can be surveyed prior to sample collection to find areas that have probably been struck by lightning. This is done by “mapping” the areas where significant ($\geq 5^\circ$) deflections of the magnetic compass occur. If a magnetic compass is passed over an outcrop at a distance of ~ 15 cm from the rock face while the compass is held in fixed azimuth, the strong and inhomogeneous IRM produced by a lightning strike will cause detectable deflections of the compass. These regions then can be avoided during sample collection.
2. Orientations of samples should be done by sun compass in lightning-prone regions. Procedures for determining sample orientation by sun compass are straightforward, and the required calculations can be done at the outcrop on a programmable pocket calculator. This is essential in basaltic igneous complexes in which strength and inhomogeneity of outcrop magnetization can produce significant deflections of the magnetic compass. Sun-compass orientations are also required at high magnetic latitudes, where the horizontal component of the geomagnetic field is small. If cloudy conditions prevent sun-compass orientation, it is possible to determine the local deflection of the compass needle by sighting on a topographic feature at known azimuth from the collecting locality.

Procedures for orientation are varied, and no standard convention exists. However, all orientation schemes are designed to provide an unambiguous in situ geographic orientation of each sample. As an example, the right-handed Cartesian coordinate system used by the author for cored samples is illustrated in Figure 4.3. The z axis is the core axis (positive z into the outcrop); the x axis is in the vertical plane (orthogonal to z); and the y axis is horizontal (Figure 4.3a). In the field, sample orientation is determined by measuring (1) azimuth of the horizontal projection of the $+x$ axis (azimuth of x - z plane) and (2) *hade* (angle from vertical = $[90^\circ - \text{plunge}]$) of the $+z$ axis (Figure 4.3b). Laboratory measurements are made with respect to these specimen coordinate axes.

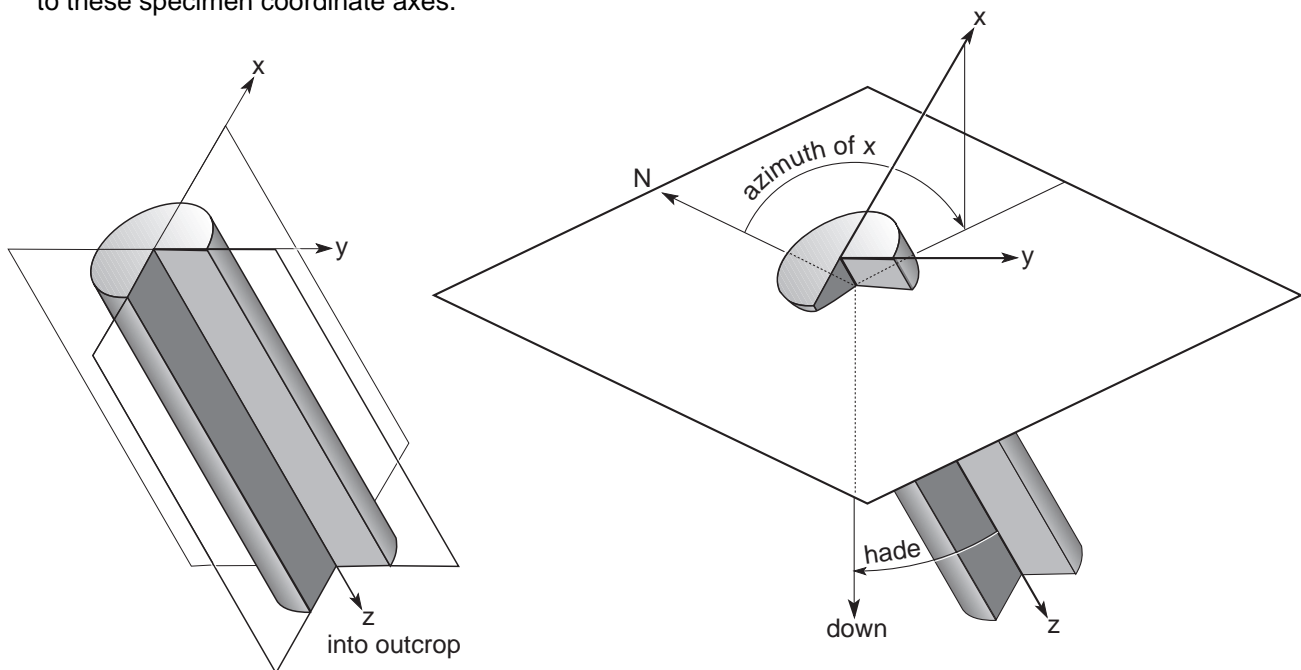


Figure 4.3 Orientation system for sample collected by portable core drill. Diagram on the left is a schematic representation of core sample in situ. The z axis points into outcrop; the x axis is in the vertical plane; the y axis is horizontal. Diagram on the right shows orientation angles for core samples. The angles measured are the hade of the z axis (angle of z from vertical) and geographic azimuth of the horizontal projection of the $+x$ axis measured clockwise from geographic north.

MEASUREMENT OF NRM

Meaningful paleomagnetic results have been obtained from rocks with NRM in the 10^{-8} G (10^{-5} A/m) range. For a standard core specimen with volume of 10 cm^3 , the magnetic moment (M) of such a sample would be 10^{-7} G cm^3 (10^{-10} A m^2), and there is genuine challenge in making reliable and rapid measurements of specimens with M of this low magnitude. During the past three decades, sensitivity of rock magnetometers has been improved by at least a factor of 1000. While early paleomagnetic studies were limited to strongly magnetized basalts and red sediments, improvements in instrumentation have allowed paleomagnetic investigations to be extended to essentially all rock types. A detailed account of instrumentation is not presented here because Collinson (see Suggested Readings) has provided a detailed book on instruments used in paleomagnetic research. Only the basics required to understand the logical development of paleomagnetic field and laboratory techniques are presented here.

During development of paleomagnetism (mostly in Britain) in the 1950s, the *astatic magnetometer* was the primary instrument for measurement of NRM. Numerous varieties were developed, but all employed a configuration of small sensing magnets suspended on a torsion fiber. The magnetic moment of the rock specimen was detected by the rotation of the torsion fiber resulting from the magnetic field of the specimen exerting torques on the sensing magnets. By clever and painstaking development, sensitive astatic magnetometers were constructed that could measure specimens with $M \leq 10^{-5}\text{ G cm}^3$ (10^{-8} A m^2). Significant drawbacks were noise problems caused by acoustic vibrations and sensitivity to changes of the magnetic field in the laboratory.

During the 1960s and early 1970s, the spinner magnetometer became the most commonly used magnetometer. Many varieties have been developed, but all involve a spinning shaft on which a rock specimen is rotated and a magnetic field sensor to detect the oscillating magnetic field produced by the rotating magnetic moment of the specimen. The signal from the sensor is passed to a phase-sensitive detector designed to amplify signals at the rotation frequency of the spinning shaft. With the development of effective phase-sensitive detectors and digital summing circuits, sensitivity of spinner magnetometers and speed of measurement have been greatly improved. Modern spinner magnetometers can reliably measure NRM of specimens with $M \approx 10^{-7}\text{ G cm}^3$ (10^{-10} A m^2). However, the measurement time increases with decreasing intensity, and measurement of a specimen with such low intensity can require in excess of 30 minutes.

In the early 1970s, cryogenic magnetometers were developed that could measure weakly magnetized specimens more quickly than spinner magnetometers. Cryogenic magnetometers use a magnetic field sensor called a SQUID (Superconducting QUantum Interference Device) magnetometer, which is superconducting at liquid helium temperatures (4°K). The SQUID is placed in a dewar containing liquid helium. A room-temperature access space is provided so that rock specimens can be placed near the SQUID, which measures the magnetic moment of the specimen. Superconducting magnetometers can routinely measure NRM of rock specimens with $M \leq 10^{-7}\text{ G cm}^3$ (10^{-10} A m^2). A major advantage is that measurement time is only about 1 minute.

Regardless of the particular magnetometer employed, measurements are made of components (M_x , M_y , M_z) of magnetic moment of the specimen (in sample coordinates). This usually entails multiple measurements of each component, allowing evaluation of homogeneity of NRM in the specimen and a measure of signal-to-noise ratio. Data are usually fed into a computer that contains orientation data for the sample, and calculation of the best-fit direction of NRM in sample coordinates and in geographic coordinates is performed. With cryogenic magnetometers, this process of measurement and data reduction can be accomplished in about 1 minute per specimen.

Display of NRM directions

Vector directions in paleomagnetism are described in terms of inclination, I , (with respect to horizontal at the collecting location) and declination, D , (with respect to geographic north) as shown in Figure 1.2. To display

such directions, a projection must be used to depict three-dimensional information on a two-dimensional page. The usual procedure is to view the NRM direction as radiating from the center of a sphere and to display the intersection of the NRM vector with this sphere. The sphere (and the points of intersection of the vectors with it) are then projected onto the horizontal plane (the plane of the page). Various projection techniques exist, and all have powers and limitations.

Two types of projections are commonly used in paleomagnetism. The *equal-angle projection* (the *stereographic* or *Wulff* projection) has the property that a cone defined by vectors that have a given angle from a central vector plot as a circle about the central vector, regardless of where the central vector plots. However, the size of the circle changes with the direction of the central vector. (It is smaller if the central vector has a steep inclination and thus plots near the center of the projection.)

The *equal-area projection* (the *Lambert* or *Schmidt* projection) has the property that the area of a cone of vectors about a central vector will remain constant regardless of the direction of the central vector. However, the cone will plot as an ellipse on the equal-area projection, except when the central vector is vertical. Because we are often concerned with the amount of directional scatter in distributions of paleomagnetic directions, the equal-area projection is usually preferred. However, be warned that no strict convention exists, and many research papers in paleomagnetism are published with paleomagnetic directions displayed using the equal-angle projection.

Mineralogists often use projections of crystal faces (or poles to those faces) to display crystal symmetries, and structural geologists use projections to display mineral lineations or planes of bedding (or poles to those planes). In both cases, the geometrical elements displayed are lines, and the upward-pointing or downward-pointing end can be displayed with no loss of information (as long as the reader knows the convention). Mineralogists generally use projections onto the upper hemisphere (they spend their lives merrily staring into space), while structural geologists use projections onto the lower hemisphere (they spend their lives on hands and knees examining mineral lineations, etc.). Paleomagnetists must be more well rounded because paleomagnetic directions are true vector quantities and therefore plot in both upper and lower hemispheres.

Projections onto the horizontal plane have the property that two vectors with equal declination but opposite inclinations (e.g., $I = 20^\circ$, $D = 340^\circ$ and $I = -20^\circ$, $D = 340^\circ$) plot at the same point. Some convention must be used to discriminate upwards-pointing directions from downward-pointing directions. The common convention is to use solid data points for directions in the lower hemisphere and open data points for directions in the upper hemisphere.

As an example, Figure 4.4 shows a direction with $I = 50^\circ$ and $D = 70^\circ$ plotted on an equal-area projection. The direction has positive inclination, so it is displayed with a filled circle. Basic familiarity with plotting

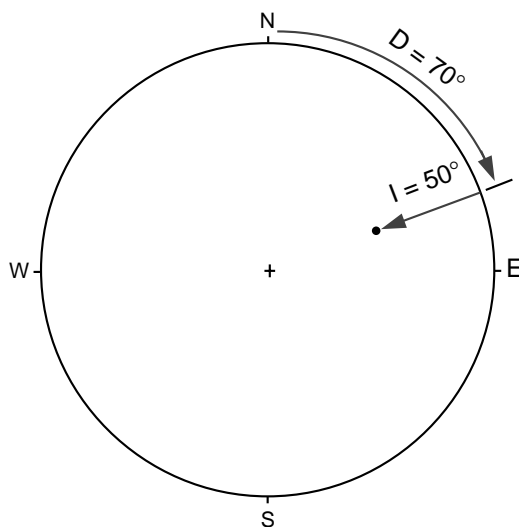


Figure 4.4 Plotting a direction on the equal-area projection. Declination is measured around the perimeter of the projection (clockwise from north); inclination is measured from 0° at the perimeter of the projection to $\pm 90^\circ$ at the center of the projection.

and rotating vectors on an equal-area projection is assumed in many discussions that follow. If these procedures are completely foreign to the reader, some time spent studying the relevant portions of Marshak and Mitra (see Suggested Readings) or another introductory structural geology text would be wise.

Sample coordinates to geographic direction

The procedure for determining a geographic direction of NRM from the measured quantities is now presented. Consider a cored sample for which orientation was determined by using the conventions of Figure 4.3. Sample orientation, volume (v) of the specimen, and the components of magnetic moment (in sample coordinates) are listed in Table 4.1.

Table 4.1 Data for Sample Coordinates to Geographic Coordinates Transformation

| |
|--|
| Sample orientation: Hade = 37°; Azimuth of +horizontal projection of +x = 25° |
| Specimen volume: 10 cm ³ |
| Components of magnetic moment: |
| $M_x = 2.3 \times 10^{-3}$ G cm ³ (2.3×10^{-6} A m ²) |
| $M_y = -1.2 \times 10^{-3}$ G cm ³ (-1.2×10^{-6} A m ²) |
| $M_z = 2.7 \times 10^{-3}$ G cm ³ (2.7×10^{-6} A m ²) |
| Sample coordinates direction: $I_s = 46^\circ$; $D_s = 332^\circ$ |
| Geographic coordinates direction: $I = 11^\circ$; $D = 6^\circ$ |

Total magnetic moment, M , of the specimen is determined by

$$M = \sqrt{M_x^2 + M_y^2 + M_z^2} \quad (4.1)$$

From the data of Table 4.1, the result is $M = 3.74 \times 10^{-3}$ G cm³ (3.74×10^{-6} A m²). The intensity of NRM is given by

$$\text{NRM} = \frac{M}{v} \quad (4.2)$$

and is found to be 3.74×10^{-4} G (3.74×10^{-1} A/m). The inclination, I_s , and declination, D_s , in sample coordinates are given by

$$I_s = \tan^{-1} \left(\frac{M_z}{\sqrt{M_x^2 + M_y^2}} \right) \quad (4.3)$$

and

$$D_s = \tan^{-1} \left(\frac{M_y}{M_x} \right)$$

Note that one must keep track of the proper quadrant for D_s . With the data of Table 4.1, the resulting direction in sample coordinates is $I_s = 46^\circ$, $D_s = -28^\circ = 332^\circ$.

To determine the direction of NRM in geographic coordinates (in situ), the sample axes (and NRM direction determined within that coordinate system) are returned to the measured in situ orientation. In practice, this is done by computing the coordinate transformations. But some insight is gained by examining the graphical procedure illustrated in Figure 4.5.

The first step is to plot the direction in sample coordinates on the equal-area projection (Figure 4.5a). The measured orientation of the +z axis of the sample was 37° (= hade). Remembering that the y axis is horizontal (according to the convention of Figure 4.3), we return the z axis to its *in situ* orientation by rotating

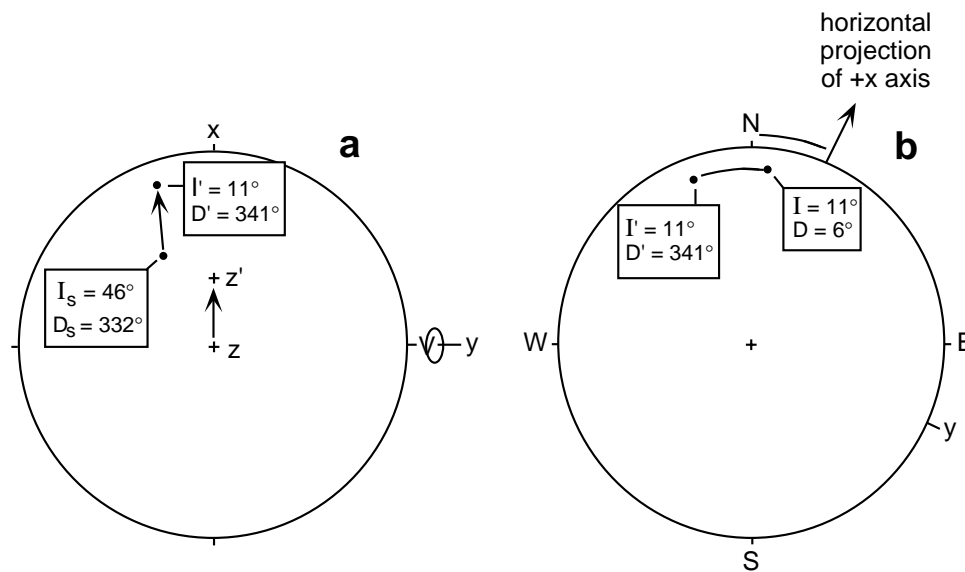


Figure 4.5 Determination of in situ (geographic) NRM direction from direction in sample coordinates. (a) Inclination and declination of NRM direction in sample coordinates (I , D) rotates to I' , D' as z axis is rotated to the in situ hade; this rotation is about the y axis of the sample; amount of rotation equals the hade of the z axis. (b) Sample axes are returned to in situ (geographic) positions by rotating the horizontal projection of the $+x$ axis to its measured azimuthal orientation; the direction of NRM is rotated along with sample coordinate system.

the coordinate system (and the NRM direction) clockwise about the $+y$ axis by 37° . This rotation is shown in Figure 4.5a and is accomplished operationally by rotating the NRM direction by 37° along a small circle of the equal-area grid centered on the y axis. Following this rotation, the direction is $I' = 11^\circ$, $D' = 341^\circ$.

The final step is to rotate the horizontal projection of the $+x$ axis, the $+y$ axis, and the NRM direction to their *in situ* (geographic) orientations. This rotation is about the vertical axis as shown in Figure 4.5b, where the horizontal projection of the $+x$ axis is rotated to the measured azimuth of 25° (thus rotating the $+y$ axis to $25^\circ + 90^\circ = 115^\circ$). With the coordinate axes properly positioned, the *in situ* (geographic) direction of NRM can be read from the equal-area projection. The resulting direction is $I = 11^\circ$, $D = 6^\circ$.

Bedding-tilt correction

If samples have been collected from sites where strata have been tilted by tectonic disturbance, a *bedding-tilt correction* is required to determine the NRM direction with respect to paleohorizontal. Structural attitude of beds at the collecting site (strike and dip, or dip angle and azimuth) must be determined during the course of field work.

The bedding-tilt correction is accomplished by rotating the NRM direction about the local strike axis by the amount of the dip of the beds. Several examples are shown in Figure 4.6, and the reader is strongly encouraged to follow through these examples. An intuitive appreciation of these geometrical operations will prove invaluable in understanding many paleomagnetic techniques and applications.

In the following discussion, it is assumed that you have access to an equal-area grid over which you place tracing paper on which graphical procedures are carried out. The graphical procedure for the bedding-tilt correction is as follows:

1. Bedding attitude is defined by azimuth of down-dip direction (the *dip azimuth*) and *dip angle*. In the example of Figure 4.6a, dip azimuth = 40° and dip angle = 20° . The azimuth of *bedding strike* (orthogonal to down-dip direction) is defined as 90° clockwise from dip azimuth (130° in the example of Figure 4.6a).

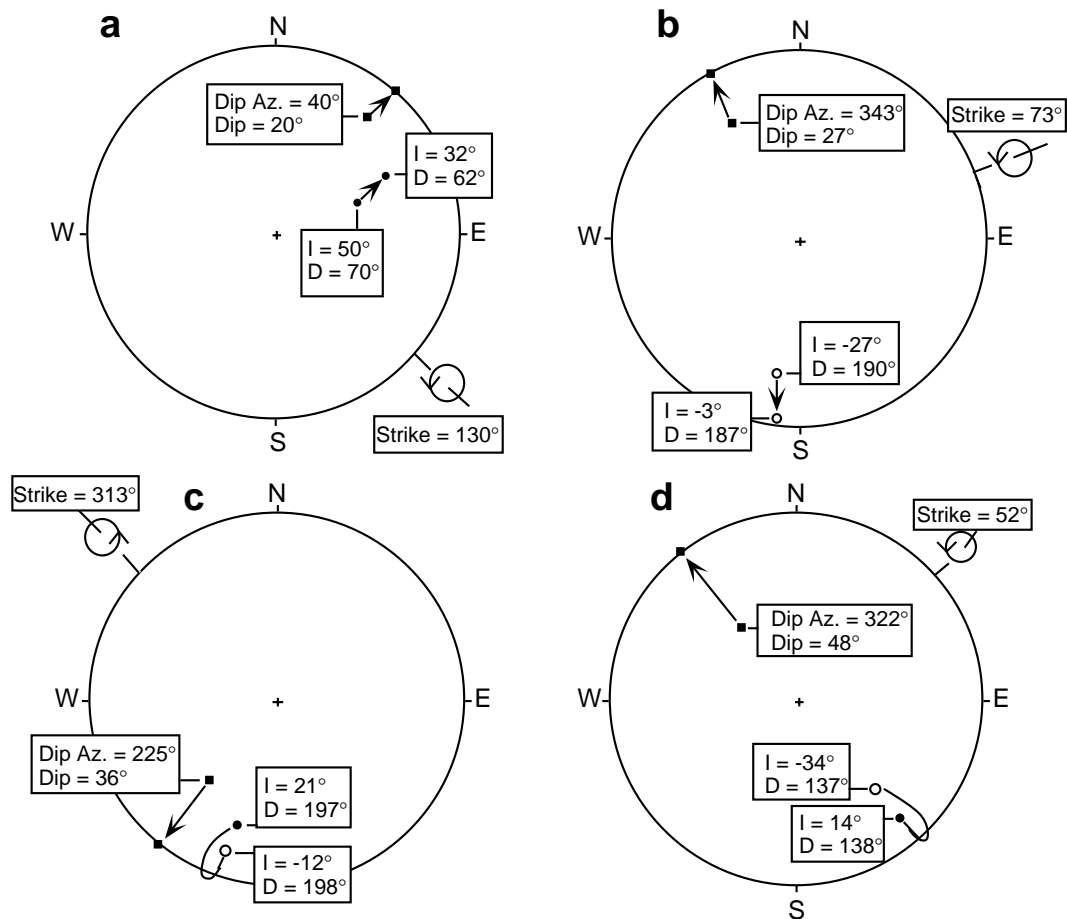


Figure 4.6 Examples of structural corrections to NRM directions. The bedding attitude is specified by dip and dip azimuth (squares on the equal-area projections); the azimuth of the strike is 90° clockwise from the dip azimuth; the rotation required to restore the bedding to horizontal (as viewed along the strike line) is clockwise (as viewed along the strike line) by the dip angle and is shown by the rotation symbol; the *in situ* NRM direction is at the tail of the arrow, and the structurally corrected NRM direction is at the head of the arrow; solid circles indicate NRM directions in the lower hemisphere of the equal-area projection; open circles indicate directions in the upper hemisphere.

- Small circles of the equal-area grid are rotated so that they are centered on the strike azimuth.
- The NRM direction is rotated clockwise about the strike azimuth (along a small circle) by an angle equaling the dip angle. Following this rotation, the *in situ* direction can be read from the equal-area projection. For the example of Figure 4.6a, the *in situ* direction is $I = 50^\circ$, $D = 70^\circ$ and the direction corrected for bedding tilt is $I = 32^\circ$; $D = 62^\circ$.

Additional examples of bedding-tilt corrections are given in Figures 4.6b, 4.6c, and 4.6d. Try these yourself to be sure that you understand the procedure. Remember that you must be able to deal with directions in the upper hemisphere ($I < 0^\circ$) as well as in the lower hemisphere ($I > 0^\circ$). The proper sense of motion of the vector should be intuitive. But it helps to do silly things like pretend that your hands are the bedding plane, wedge a pencil in your fingers approximating the NRM direction, then restore your hands to horizontal and note the direction in which the pencil rotates. (Don't do this in a crowded library. It's easy to be misunderstood.)

The above examples deal only with correction for local bedding tilt. If sites have been collected from plunging folds, a complete tectonic correction requires correction for plunge of fold axis followed by untilting of the plunge-corrected limbs of the fold.

EVIDENCES OF SECONDARY NRM

The NRM of a rock (prior to any laboratory treatment) is generally composed of at least two components: a primary NRM acquired during rock formation (TRM, CRM, or DRM) and secondary NRM components (e.g., VRM or lightning-induced IRM) acquired at some later time(s). Resultant NRM is the vector sum of primary and secondary components (Equation (3.17)). In this section, we examine how distributions of NRM directions indicate the presence of secondary NRM components and begin examination of partial demagnetization procedures.

Characteristic NRM

There is some terminology applied to components of NRM that must be introduced at the outset. *Partial demagnetization* procedures (discussed in Chapter 5) remove components of NRM. Components that are easily removed are referred to as *low-stability components*. Removal of these low-stability components by partial demagnetization will allow isolation of the more resistant *high-stability components*. In many cases, the high-stability component can logically be inferred to be a primary NRM, while the low-stability component is inferred to be a secondary NRM. However, this is not always the case, and a terminology has been introduced to deal with this potential difficulty.

The highest-stability component of NRM that is isolated by partial demagnetization is generally referred to as the *characteristic component* of NRM, abbreviated ChRM. Partial demagnetization usually can determine a ChRM direction but cannot directly determine whether it is primary; additional information is required to infer whether the ChRM is primary. The purpose of the term *characteristic component* is that this term can be applied to results of partial demagnetization experiments without the connotation of origin time attached to the term *primary NRM*. This might seem an unnecessarily picky distinction, but it is useful to separate inferences drawn from partial demagnetization experiments (determination of ChRM) from the less certain inference that the ChRM is a primary NRM.

NRM distributions

Recognition and (hopefully) erasure of secondary NRM is the major goal of paleomagnetic laboratory work. An initial step is recognition of secondary components of NRM. As the NRMs of specimens from a rock unit are initially measured, the distribution of NRM often indicates the presence of secondary NRM.

In Figure 4.7a, the NRM distribution observed in a collection of six samples from an individual site (= bed) of a Mesozoic red sediment is shown. NRM directions are distributed along a great circle through the direction of the present geomagnetic field at the collecting locality. Addition of two vectors with constant direction but variable magnitude produces resultant vectors distributed along a great circle connecting those two vectors (see the inset diagram). The inference drawn from the *streaked distribution* of Figure 4.7a is that this distribution probably results from addition of two components of NRM.

One of these two components is aligned with the present geomagnetic field at the collecting locality and is almost certainly a VRM or recently acquired CRM. The direction of the other vector is indeterminate but must lie on the great circle, probably at or beyond the end of the streaked distribution farthest from the present field direction (see Figure 4.7a). In Figure 4.7b, the cluster of ChRM directions after partial thermal demagnetization is shown. The ChRM directions are well grouped in a direction far from the present geomagnetic field direction. Partial demagnetization has successfully isolated a ChRM direction by removing the secondary NRM. For this particular case, auxiliary information indicates that the ChRM is a CRM acquired soon after deposition of this Mesozoic red sediment.

The NRM distribution from a site (= single flow) in Tertiary basalt in the Mojave–Sonora Desert region (southwestern United States) is shown in Figure 4.7c. NRM directions are scattered, and intensities of NRM for specimens from this site are anomalously high. This region is exposed to intense thunderstorms, and this distribution of NRM directions is almost certainly caused by lightning-induced IRM. Partial demagnetization

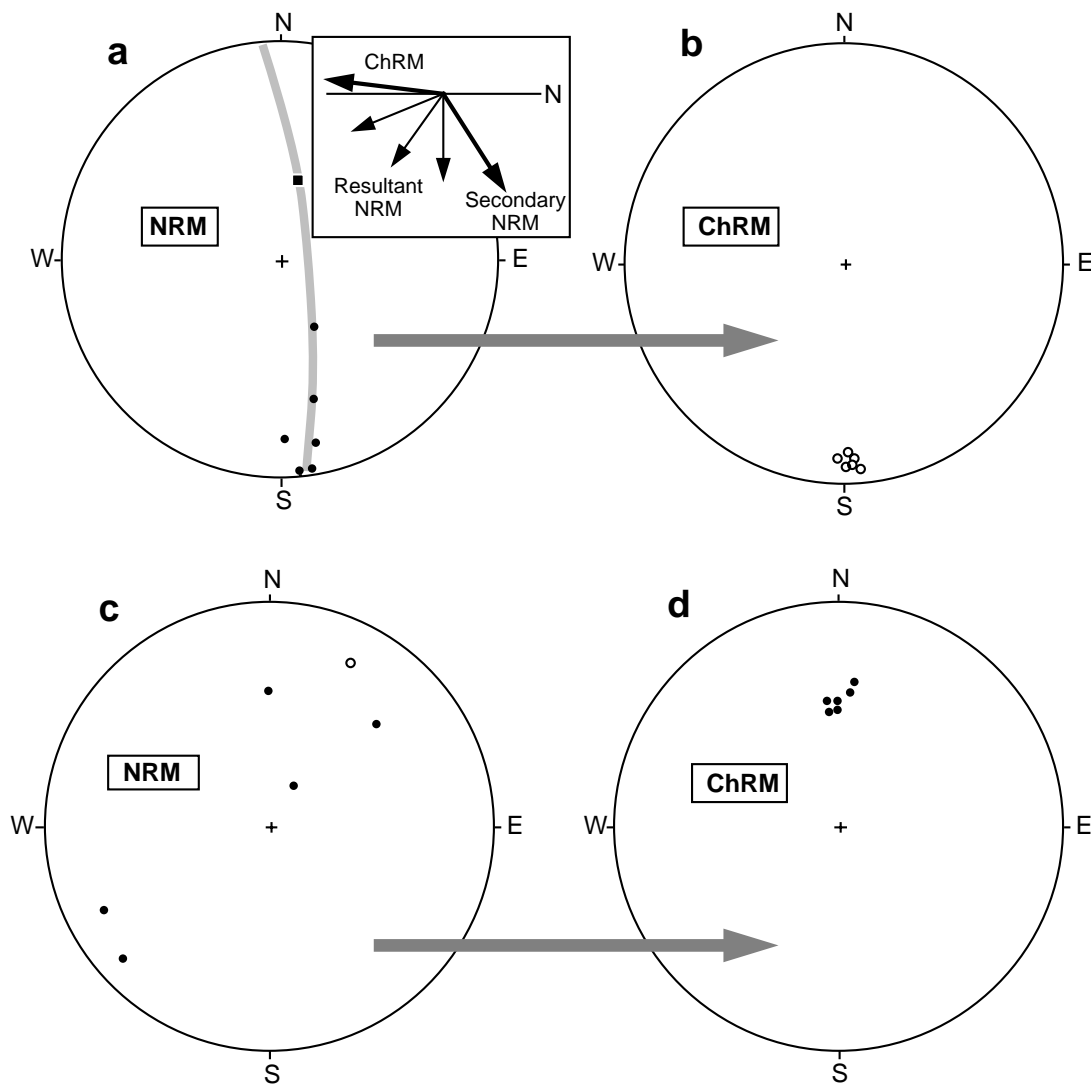


Figure 4.7 Examples of distributions of NRM directions before and after partial demagnetization. (a) Equal-area projection of NRM directions in multiple samples from a paleomagnetic site in a Mesozoic red sediment; the square shows the direction of the present geomagnetic field at the collecting locality; stippling indicates the great circle along which the NRM directions are streaked; the inset shows how the addition of varying amounts of ChRM and secondary NRM produces resultant NRM vectors distributed in the plane connecting these two component vectors. (b) ChRM directions determined from samples shown in part (a) following erasure of secondary NRM components. (c) Equal-area projection of NRM directions in multiple samples from a paleomagnetic site in Miocene basalt. (d) ChRM directions determined from samples shown in part (c) following erasure of secondary NRM components.

zation (by the alternating-field technique) was successful in isolating a ChRM in samples of this site (Figure 4.7d). Auxiliary information leads to the straightforward inference that the ChRM is a TRM acquired at the time of original cooling of the flow.

In both the above examples, partial demagnetization accomplished the desired result of isolating a characteristic NRM that is likely to be primary. Understanding paleomagnetism requires that one understands the theory, application, and analysis of partial demagnetization experiments. As a prelude to Chapter 5, laboratory procedures used for identifying the dominant ferromagnetic minerals in a suite of samples are now briefly discussed.

IDENTIFICATION OF FERROMAGNETIC MINERALS

Identification of ferromagnetic minerals in a rock can help guide the design of partial demagnetization experiments and the interpretation of results. The challenge is to associate a particular component of NRM (identified from partial demagnetization) with a particular ferromagnetic mineral. This information can often determine whether a characteristic NRM is primary or secondary. There are three families of techniques used to identify ferromagnetic minerals: (1) microscopy techniques including optical microscopy, electron microprobe, and SEM; (2) determination of Curie temperature; and (3) coercivity spectrum analysis. In the discussions below, attributes of these techniques are outlined, and some examples are provided.

Microscopy

Ferromagnetic minerals are opaque, and optical observations require reflected light microscopy. Optical and SEM observations of textures allow sequences of mineral formation to be determined. This information can sometimes determine whether minerals formed at the time of rock formation or by later chemical alteration. Direct determination of elemental abundances through electron microprobe examination can facilitate identification of ferromagnetic minerals when more than one mineral could account for optical properties. Example photomicrographs are shown in Figure 2.11.

A major difficulty in applying optical and SEM observations is the low concentration of ferromagnetic minerals and their small size (often $\leq 1 \mu\text{m}$ in SD and PSD grains). Igneous rocks generally have sufficient ferromagnetic minerals to allow optical examination of polished thin sections. However, optical examination of ferromagnetic minerals in sedimentary rocks often requires extraction of ferromagnetic minerals, which introduces uncertainties about the representative nature of the magnetic extract. For titanomagnetite, grain sizes of SD and PSD grains (dominant carriers of remanent magnetization) are often below the limit of optical resolution. It is often necessary to infer the mineralogy of SD and PSD grains from optical observations of larger MD grains. Although SEM examinations can provide pivotal information in particular cases, such examinations cannot be done as a matter of course because of the cost and time required for sample preparation.

Curie temperature determination

Curie temperatures of ferromagnetic minerals can be determined from *strong-field thermomagnetic experiments* in which magnetization of a sample exposed to a strong magnetic field ($\geq 1000 \text{ Oe} = 100 \text{ mT}$) is monitored while temperature is increased. For samples with magnetization dominated by the ferromagnetic minerals (rather than paramagnetic and/or diamagnetic minerals), measured strong-field magnetization approximates J_s of the ferromagnetic mineral(s). Curie temperatures (T_c) are determined as the points of major decrease in J_s . If ferromagnetic minerals are sufficiently concentrated, the experiment can be performed directly on a rock sample. However, for many rock types, determination of Curie temperature requires a magnetic concentrate, with attendant uncertainties about completeness of the extraction technique.

Figure 4.8 shows representative results of strong-field magnetization experiments. In Figure 4.8a, a Curie temperature of $\sim 575^\circ\text{C}$ is observed, both on heating and cooling. Because this Curie temperature could indicate either Ti-poor titanomagnetite or titanohematite of composition $x \approx 0.1$, additional information is required for complete identification. In this case, results of coercivity spectrum analysis (discussed below) indicate that the ferromagnetic mineral is Ti-poor magnetite.

Figure 4.8b illustrates a strong-field thermomagnetic result that reveals $T_c \approx 200^\circ\text{C}$. This Curie temperature could be due to either titanomagnetite or titanohematite (see Figures 2.8 and 2.10). Optical observations and electron microprobe data indicate that intermediate titanohematite is the dominant ferromagnetic mineral in this magnetic extract.

Examples in Figures 4.8a and 4.8b are simple examples with single Curie temperatures and reversible heating and cooling curves. However, irreversible chemical changes or complex combinations of ferromag-

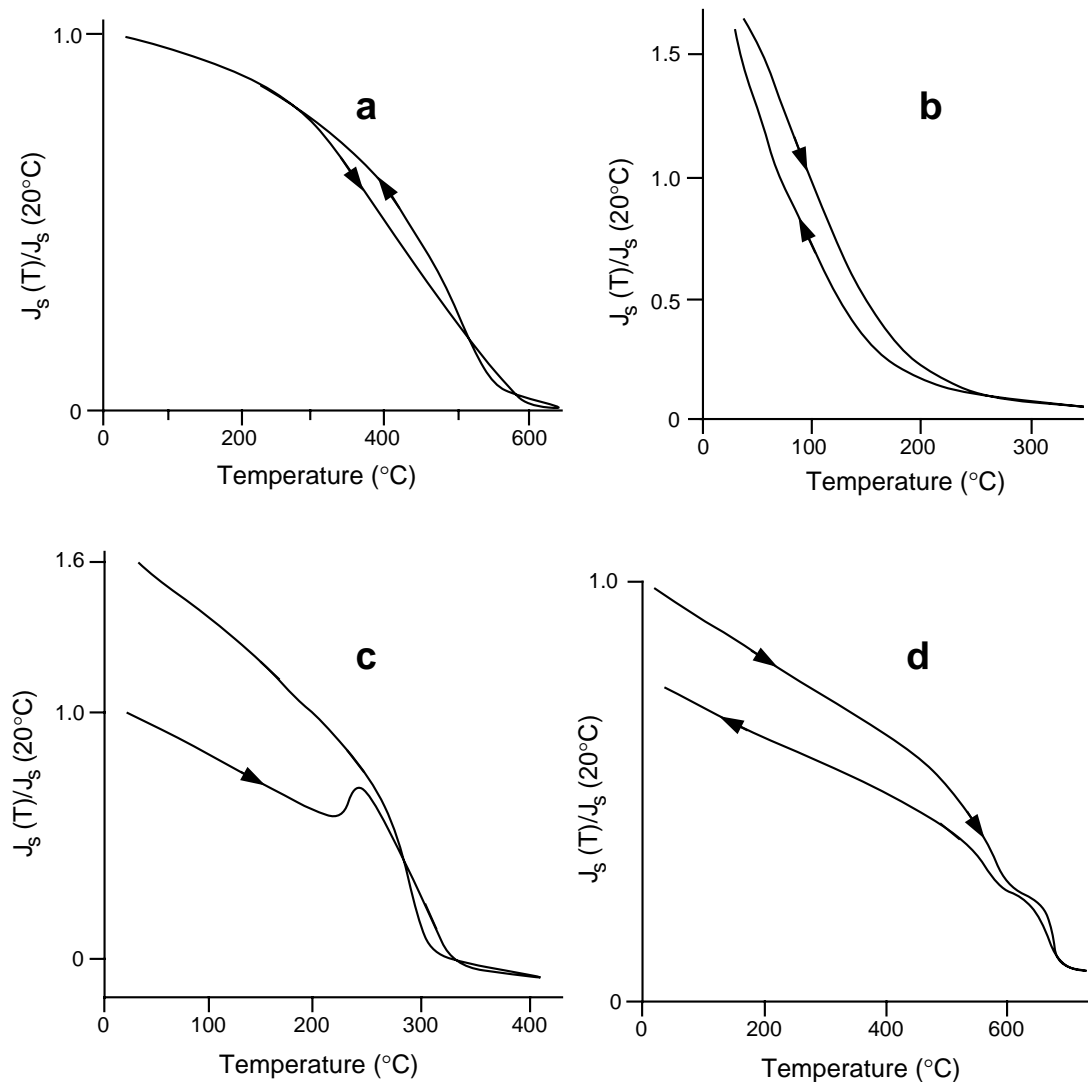


Figure 4.8 Strong-field thermomagnetic behaviors. (a) Sample is a magnetic separate from Pliocene continental sediment of northwestern Argentina; the magnetizing field was 3000 Oe; arrows indicate the direction of temperature change (heating or cooling). Redrawn from Butler et al. (*J. Geol.*, v. 92, 623–636, 1984). (b) Sample is a magnetic separate from Paleocene continental sediment of northwestern New Mexico; the magnetizing field was 2000 Oe. Redrawn from Butler and Lindsay (*J. Geol.*, v. 93, 535–554, 1985). (c) Thermomagnetic behavior of magnetic separate from Cretaceous submarine volcanic rocks of coastal Peru; the magnetizing field was 3000 Oe. Redrawn from May and Butler (*Earth Planet. Sci. Lett.*, v. 72, 205–218, 1985). (d) Sample is a magnetic separate from Berriasian marine micritic limestone from southeastern France; the magnetizing field was 3000 Oe. Redrawn from Galbrun and Butler (*Geophys. J. Roy. Astron. Soc.*, v. 86, 885–892, 1986).

netic minerals often produce complicated behaviors that can be difficult to interpret. In Figure 4.8c, heating and cooling curves are not reversible, indicating that an irreversible change in ferromagnetic minerals has resulted from heating. An increase in strong-field magnetization is observed in the 225° to 275°C interval. This sample contains a two-phase pyrrhotite (Fe_7S_8 plus Fe_9S_{10}). The Curie temperature of pyrrhotite is 320°C, and the increase in J_s at 225°C is produced by the Fe_9S_{10} changing from antiferromagnetic at $T < 225^\circ\text{C}$ to ferrimagnetic in the $225^\circ < T < 320^\circ\text{C}$ interval. Such irreversible changes in ferromagnetic minerals and combinations of ferromagnetic minerals can make identification of ferromagnetic minerals from strong-field thermomagnetic results extremely difficult.

The final example of Figure 4.8d reveals Curie temperatures of 580°C and 680°C observed in a magnetic extract. Auxiliary information indicates that these Curie temperatures are due to magnetite and hematite, respectively. This example is offered as illustration that a ferromagnetic mineral with low j_s (like hematite) can be observed in the presence of a coexisting ferromagnetic mineral with much stronger j_s (like magnetite). But this is an atypical example and highlights one of the major limitations of strong-field thermomagnetic analysis. Because measured J_s of a sample is dominated by the mineral with high j_s , coexisting ferromagnetic minerals with low j_s are often not apparent in results of strong-field thermomagnetic experiments, even though these minerals may be major contributors to the NRM. In some cases, the coercivity spectrum technique can overcome this limitation.

Coercivity spectrum analysis

Titanomagnetite has saturation magnetization, j_s , up to 480 G (4.8×10^5 A/m) and microscopic coercive force, $h_c \leq 3000$ Oe (300 mT). (Similar h_c is observed for titanohematite in the range of composition $0.5 \leq x \leq 0.8$ where it is ferrimagnetic above room temperature.) In contrast, hematite has j_s of only 2–3 G ($2\text{--}3 \times 10^3$ A/m) but can have $h_c \geq 10000$ Oe (1 T). Similar high coercivity is observed for goethite. *Coercivity spectrum analysis* uses the contrast in coercive force between titanomagnetite and hematite and goethite to detect hematite (or goethite) coexisting with more strongly ferromagnetic minerals.

The usual procedure in coercivity spectrum analysis is to (1) induce isothermal remanent magnetization (IRM) by exposing a sample to a magnetizing field, H , (2) measure resulting IRM, then (3) repeat the procedure using a stronger magnetizing field. A sample containing only titanomagnetite (or ferrimagnetic titanohematite) acquires IRM in $H \leq 3000$ Oe (300 mT), but no additional IRM is acquired in higher H . If only hematite (or goethite) is present, IRM is gradually acquired in H up to 30000 Oe (3 T). Samples containing both titanomagnetite and hematite (or goethite) rapidly acquire IRM in $H \leq 3000$ Oe (300 mT), followed by gradual acquisition of additional IRM in stronger magnetizing fields. This procedure allows detection of small amounts of hematite (or goethite) even when coexisting with more strongly ferromagnetic titanomagnetite.

It is common to follow the IRM acquisition experiment with thermal demagnetization. IRM decreases during thermal demagnetization as blocking temperatures are reached. Major decreases in IRM during thermal demagnetization allow estimation of Curie temperatures because maximum blocking temperatures are always slightly less than the Curie temperature.

The utility of coercivity spectrum analysis is illustrated in Figure 4.9. Strong-field thermomagnetic analysis of a magnetic separate from this Early Cretaceous limestone is shown in Figure 4.9c. A Curie temperature of 580°C is evident, but there is no indication of a 680°C Curie temperature due to hematite. However, IRM acquisition for a sample of this limestone (Figure 4.9a) shows a sharp rise in IRM up to 3000 Oe (300 mT) due to magnetite, followed by increased IRM in higher magnetizing fields. IRM acquired in $H \geq 3000$ Oe (300 mT) is due to the presence of a high h_c mineral (such as hematite or goethite). Thermal demagnetization of acquired IRM for this rock is illustrated in Figure 4.9b. Most IRM is removed by thermal demagnetization to the 580°C Curie temperature of magnetite. However, the portion of IRM acquired in $H \geq 3000$ Oe (300 mT) exhibits blocking temperatures up to 680°C, a clear indication that the high h_c component is hematite.

An additional example is provided in Figure 4.10. Although the shape of the IRM acquisition curves (Figures 4.10a and 4.10b) is markedly different for these two samples of Jurassic limestone, IRM is clearly dominated by a high coercivity mineral. IRM acquisition alone does not allow identification of the mineral as hematite or goethite. But thermal demagnetization of acquired IRM (Figures 4.10c and 4.10d) reveals blocking temperatures $\leq 100^\circ\text{C}$, indicating that the dominant ferromagnetic mineral is goethite (Curie temperature = 120°C).

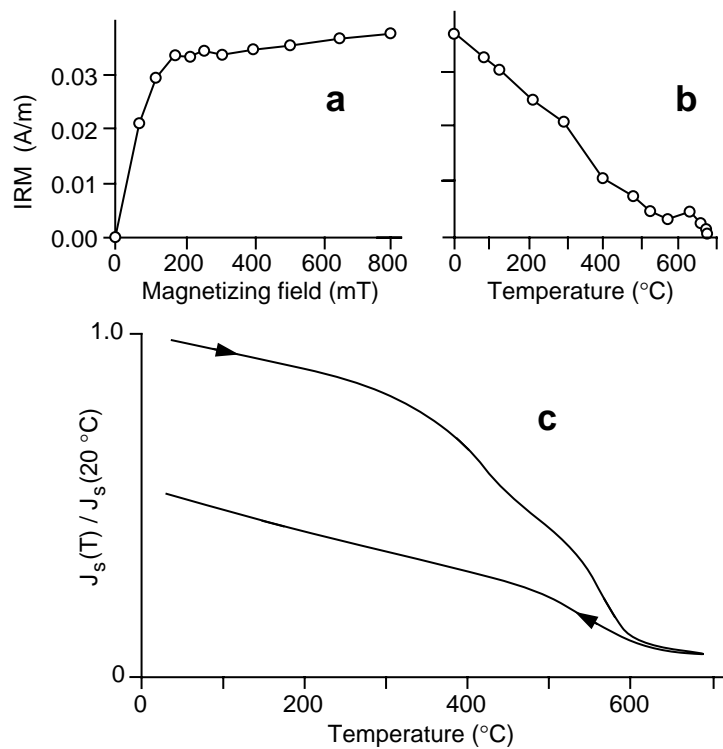


Figure 4.9 Comparison of coercivity spectrum analysis with strong-field thermomagnetic behavior. **(a)** Acquisition of IRM by sample of gray sandy marine limestone of Berriasian age from southeastern France. **(b)** Thermal demagnetization of acquired IRM. **(c)** Strong-field thermomagnetic behavior of a magnetic extract from this limestone; the magnetizing field was 2000 Oe. Redrawn from Galbrun and Butler (*Geophys. J. Roy. Astron. Soc.*, v. 86, 885–892, 1986).

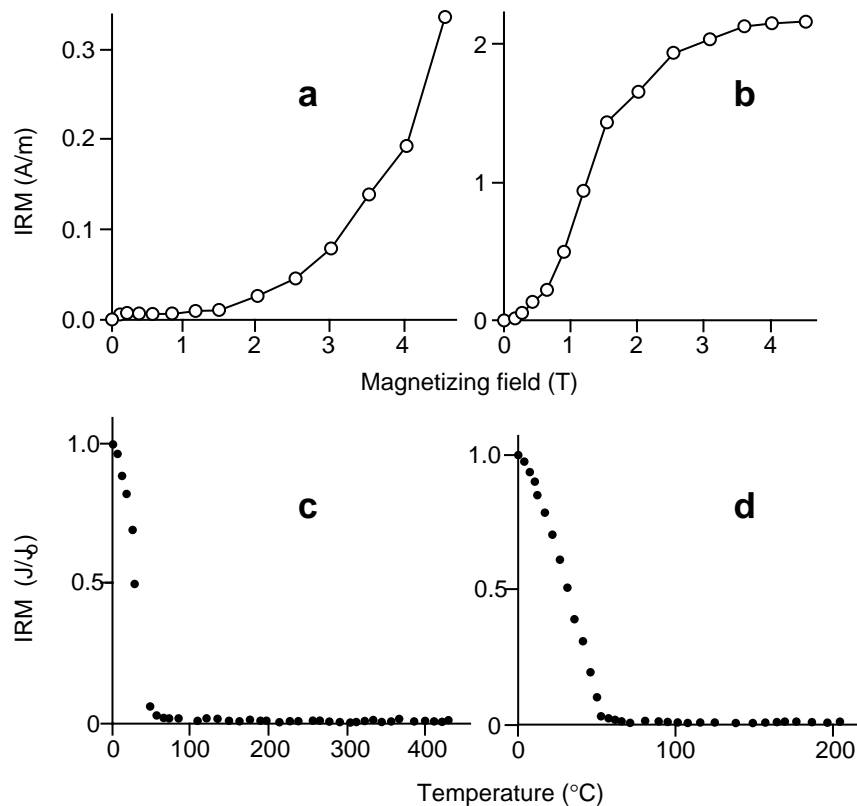


Figure 4.10 Coercivity spectrum analysis of two samples of Jurassic limestone from Bavaria. **(a and b)** Acquisition of IRM by two separate samples; note very high coercivities. **(c)** Thermal demagnetization of IRM acquired by the sample shown in part **(a)**. **(d)** Thermal demagnetization of IRM acquired by the sample shown in part **(b)**. Redrawn from Lowrie and Heller (1982).

SUGGESTED READINGS**INSTRUMENTATION AND LABORATORY TECHNIQUES:**

D. W. Collinson, *Methods in Rock Magnetism and Palaeomagnetism*, Chapman and Hall, London, 503 pp., 1983.

In-depth treatment of instruments and laboratory techniques of paleomagnetism.

GEOMETRICAL TECHNIQUES:

S. Marshak and G. Mitra, *Basic Methods of Structural Geology*, Prentice Hall, Englewood Cliffs, N. J., 446 pp., 1988.

Chapter 4 introduces stereographic and equal-area projections.

COERCIVITY SPECTRUM ANALYSIS:

D. J. Dunlop, Magnetic mineralogy of unheated and heated red sediments by coercivity spectrum analysis, *Geophys. J. Roy. Astron. Soc.*, v. 27, 37–55, 1972.

This publication introduced the technique and showed its utility.

W. Lowrie and F. Heller, Magnetic properties of marine limestones, *Rev. Geophys. Space Phys.*, v. 20, 171–192, 1982.

Numerous applications of coercivity spectrum analysis.

PROBLEMS

- 4.1** A paleomagnetic specimen has the following orientation information (using the conventions of Figure 4.3): hade of +z axis = 47°; azimuth of horizontal projection of +x axis = 310°. The specimen volume is 11.2 cm³. Laboratory measurements yield the following components of the remanent magnetic moment of this specimen:

$$\begin{aligned}M_x &= -1.2 \times 10^{-3} \text{ G}\cdot\text{cm}^3 \\M_y &= -2.3 \times 10^{-3} \text{ G}\cdot\text{cm}^3 \\M_z &= -1.8 \times 10^{-3} \text{ G}\cdot\text{cm}^3\end{aligned}$$

- a. Compute the intensity of NRM (in G) and the direction of NRM in sample coordinates (I_s , D_s).
 - b. Plot I_s , D_s on an equal-area projection.
 - c. Using the procedures shown in Figure 4.5, determine the NRM direction (I , D) in geographic coordinates.
- 4.2** In the following problems, the direction of NRM is given in geographic coordinates along with the attitude of dipping strata from which the site was collected. Plot the NRM direction on an equal-area projection. Then using the procedures shown in Figure 4.6 (or slight modifications thereof), determine the “structurally corrected” direction of NRM that results from restoring the strata to horizontal.
- a. $I = -2^\circ$, $D = 336^\circ$, bedding dip = 41°, dip azimuth = 351° (strike = 81°).
 - b. $I = 15^\circ$, $D = 227^\circ$, bedding dip = 24°, dip azimuth = 209° (strike = 299°).
- 4.3** Now consider a more complex situation in which a paleomagnetic site has been collected from the limb of a plunging fold. On the east limb of a plunging anticline, a direction of NRM is found to be $I = 33^\circ$, $D = 309^\circ$. The bedding attitude of the collection site is dip = 29°, strike = 210° (azimuth of dip = 120°, and the pole to bedding is azimuth = 300°, inclination = 61°). The trend and plunge of the anticlinal axis are trend = 170°, plunge = 20°. Determine the direction of NRM from this site following structural correction. *Hint:* First correct the NRM direction (and the pole to bedding) for the plunge of the anticline. Then complete the structural correction of the NRM direction by restoring the bedding (corrected for plunge) to horizontal.
- 4.4** Ferromagnetic minerals in two rock samples are known to be FeTi oxides and are found to have the properties described below. Using the data described below and properties of FeTi oxides described in Chapter 2, identify the ferromagnetic minerals. For titanomagnetite or titanohematite, approximate the compositional parameter x .
- a. Strong-field thermomagnetic analysis indicates a dominant Curie temperature $T_c = 420^\circ\text{C}$. IRM acquisition reveals a coercivity spectrum with $h_c < 3000$ Oe. What is this ferromagnetic mineral?

- b. Strong-field thermomagnetic analysis shows behavior identical to that of Figure 4.8b with Curie temperature $T_c = 200^\circ\text{C}$. In addition, electron microprobe data indicates abundances of FeO, Fe_2O_3 , and TiO shown in Figure 4.11. Unfortunately, electron microprobe data are not very effective in determining the Fe_2O_3 :FeO ratio (placement from left to right in the TiO – FeO – Fe_2O_3 ternary diagram). Accordingly, there is much uncertainty in the Fe_2O_3 :FeO ratio indicated by the microprobe data. But microprobe data are effective in determining the $\text{TiO}:(\text{Fe}_2\text{O}_3 + \text{FeO})$ ratio (placement from bottom to top in the TiO – FeO – Fe_2O_3 ternary diagram). With these data, identify the ferromagnetic mineral.

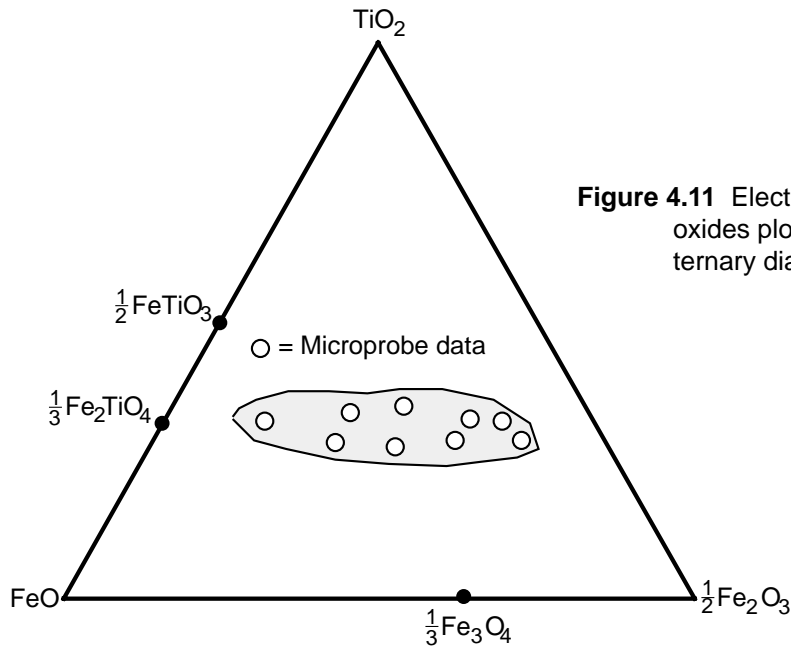


Figure 4.11 Electron microprobe data from FeTi-oxides plotted on TiO_2 – FeO – Fe_2O_3 ternary diagram.

PALEOMAGNETIC STABILITY

With the background information gained to this point, you appreciate the importance of isolating the characteristic NRM by selective removal of the secondary NRM. Theory and application of paleomagnetic stability tests are introduced here. Partial demagnetization experiments are performed in the laboratory to isolate the ChRM. Although sometimes mistaken as “magic,” these laboratory procedures are well grounded in rock magnetism theory. Field tests of paleomagnetic stability can sometimes provide crucial information about the age of a ChRM, and this question is often at the heart of paleomagnetic investigations. Lack of background in paleomagnetic stability tests often prevents interested earth scientists from understanding paleomagnetism. The material in this chapter should largely remove this obstacle. If not a “Big Enchilada,” this chapter certainly qualifies as a “Burro Grande.”

PARTIAL DEMAGNETIZATION TECHNIQUES

Theory and application of alternating-field and thermal demagnetization are introduced in this section. Although a central part of paleomagnetic investigations for some time, analysis of partial demagnetization data has become more sophisticated because of widespread availability of microcomputer systems for data analysis. Understanding modern paleomagnetism requires some familiarity with the analytical techniques that are used to decipher potentially complex, multicomponent NRM. To put the theory and techniques into practice, this section concludes with some practical examples.

Theory of alternating-field demagnetization

The fundamental AF demagnetization procedure is to expose a specimen to an alternating magnetic field. The waveform of the alternating magnetic field is a sinusoid with linear decrease in magnitude with time. Maximum value of this AF demagnetizing field can be labeled H_{AF} and the waveform is schematically represented in Figure 5.1a.

Typical instruments allow AF demagnetization to maximum H_{AF} of 1000 Oe (100 mT). The frequency of the sinusoidal waveform is commonly 400 Hz, and the time for decay of the field from maximum value to zero is ~1 minute. Most AF demagnetizing instruments use a *tumbler apparatus* that rotates the sample within several nested gears. The tumbler is designed to present in sequence all axes of the specimen to the axis of the demagnetizing coil. The tumbler thus allows demagnetization of all axes of the specimen during the course of a single demagnetization treatment.

The basic theory of AF demagnetization can be explained with the aid of Figure 5.1b, a blow-up of a portion of the AF demagnetization waveform. Imagine that the magnetic field at point 1 (Figure 5.1b) has magnitude = 200 Oe (20 mT) and that we arbitrarily define this direction as “up.” Magnetic moments of all grains in the specimen with $h_c \leq 200$ Oe (20 mT) will be forced to point in the up direction. The magnetic field then passes through zero to a maximum in the opposite direction. If the magnitude of the sinusoidal magnetic field decreases by 1 Oe every half cycle, the field at point 2 will be 199 Oe (19.9 mT) in the “down” direction, and all grains with $h_c \leq 199$ Oe (19.9 mT) will have magnetic moment pulled into the down direc-

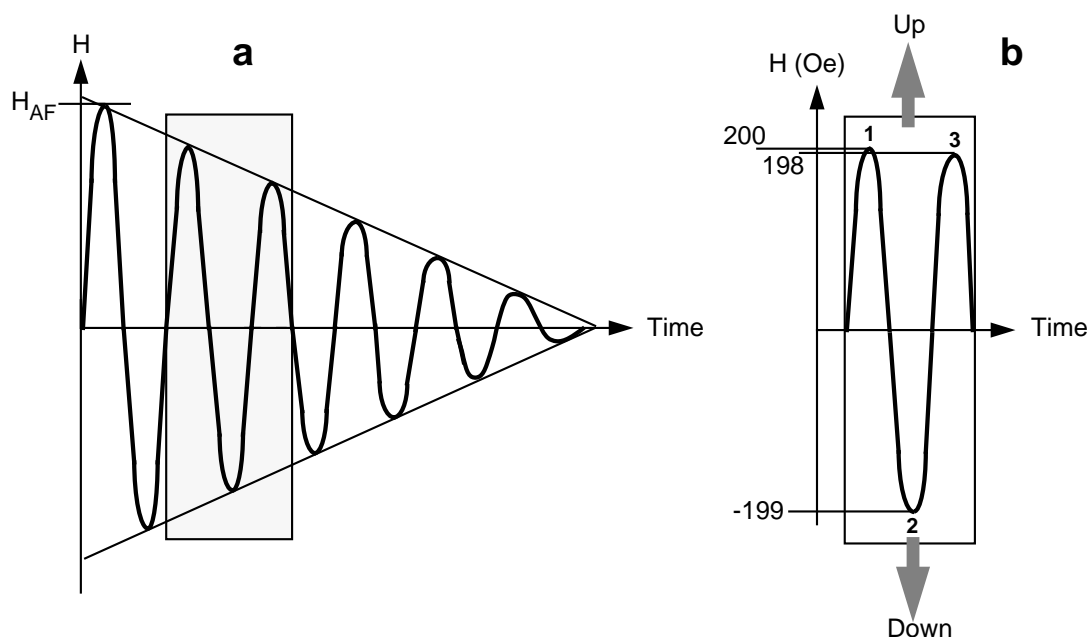


Figure 5.1 Schematic representation of alternating-field demagnetization. (a) Generalized waveform of the magnetic field used in alternating-field (AF) demagnetization showing magnetic field versus time; the waveform is a sinusoid with linear decay in amplitude; the maximum amplitude of magnetic field (= peak field) is H_{AF} ; the stippled region is amplified in part (b). (b) Detailed examination of a portion of the AF demagnetization waveform. Two successive peaks and an intervening trough of the magnetic field are shown as a function of time; the peak field at point 1 is 200 Oe; the peak field at point 2 is -199 Oe; the peak field at point 3 is 198 Oe.

tion. After point 2, the magnetic field will pass through zero and increase to 198 Oe (19.8 mT) in the up direction at point 3. Now all grains with $h_c \leq 198$ Oe (19.8 mT) have magnetic moment pointing up.

From point 1 to point 3, the net effect is that grains with h_c in the interval 199 to 200 Oe (19.9 to 20 mT) are left with magnetic moments pointing up, while grains with h_c between 198 and 199 Oe (19.8 to 19.9 mT) are left with magnetic moments pointing down. The total magnetic moments of grains in these two h_c intervals will approximately cancel one another. Thus the net contribution of all grains with $h_c \leq H_{AF}$ will be destroyed; only the NRM carried by grains of $h_c \geq H_{AF}$ will remain. Because the tumbler apparatus presents all axes of the specimen to the demagnetizing field, the NRM contained in all grains with $h_c \leq H_{AF}$ is effectively randomized. Thus, AF demagnetization can be used to erase NRM carried by grains with coercivities less than the peak demagnetizing field.

AF demagnetization is often effective in removing secondary NRM and isolating characteristic NRM (ChRM) in rocks with titanomagnetite as the dominant ferromagnetic mineral. In such rocks, secondary NRM is dominantly carried by MD grains, while ChRM is retained by SD or PSD grains. MD grains have h_c dominantly ≤ 200 Oe (20 mT), while SD and PSD grains have higher h_c . AF demagnetization thus can remove a secondary NRM carried by the low h_c grains and leave the ChRM unaffected. AF demagnetization is a convenient technique because of speed and ease of operation and is thus preferred over other techniques when it can be shown to be effective.

Theory of thermal demagnetization

The procedure for thermal demagnetization involves heating a specimen to an elevated temperature (T_{demag}) below the Curie temperature of the constituent ferromagnetic minerals, then cooling to room temperature in zero magnetic field. This causes all grains with blocking temperature (T_B) $\leq T_{demag}$ to acquire a “thermoremanent magnetization” in $H = 0$, thereby erasing the NRM carried by these grains. In other words, the

magnetization of all grains for which $T_B \leq T_{demag}$ is randomized, as with low h_c grains during AF demagnetization.

The theory of selective removal of secondary NRM (generally VRM) by partial thermal demagnetization is illustrated in the $v-h_c$ diagram of Figure 5.2. As described in discussion of VRM, SD grains with short

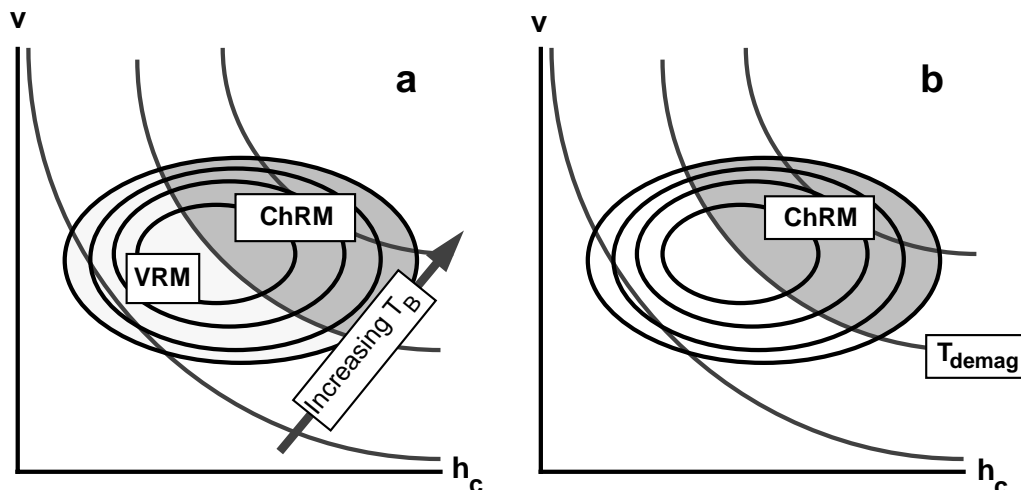


Figure 5.2 Schematic explanation of thermal demagnetization. (a) Diagram plots grain volume (v) versus microscopic coercive force (h_c) for a hypothetical population of SD grains. Solid contours are of concentration of SD grains; stippled lines are contours of τ (and T_B) with values increasing from lower left to upper right; grains with low τ and low T_B preferentially carry VRM; these grains occupy the lightly stippled region in the lower left portion of the diagram; grains with high τ and high T_B preferentially carry ChRM; these grains occupy the heavily stippled region. (b) Following thermal demagnetization to temperature T_{demag} , NRM in SD grains with $T_B < T_{demag}$ is erased. Only the ChRM in the SD grains with higher T_B remains.

relaxation time, τ , can acquire VRM, while SD grains with long τ are stable against acquisition of VRM. In the development of TVRM in Chapter 3, it was shown that SD grains with short τ also have low T_B and this is the fundamental principle underlying partial thermal demagnetization. Lines of equal τ on a $v-h_c$ diagram are also lines of equal T_B and SD grains which predominantly carry VRM also have low T_B . This situation is schematically represented in Figure 5.2a. The effectiveness of thermal demagnetization in erasing VRM can be understood by realizing that thermal demagnetization to $T_{demag} \geq T_B$ of grains carrying VRM will selectively erase VRM, leaving unaffected the ChRM carried by grains with longer τ (= higher T_B).

The above descriptions of AF and thermal demagnetization explain why AF demagnetization generally fails to remove secondary NRM components from hematite-bearing rocks. The property common to grains carrying secondary NRM in hematite-bearing rocks is low τ resulting from low product $v \cdot h_c$. Grains with high h_c but small volume, v , can carry secondary NRM. But these grains would not be erased by AF demagnetization because their coercive force could easily exceed the maximum available field H_{AF} . Therefore, in rocks with hematite as the dominant ferromagnetic mineral, removal of VRM invariably requires thermal demagnetization.

Chemical demagnetization

Leaching of rocks with dilute acids (usually hydrochloric) gradually dissolves FeTi-oxides. Acid leaching of rock specimens for progressively increasing time intervals is called *chemical demagnetization*. Because of high surface area to volume ratio for small grains, chemical demagnetization preferentially removes the small grains. The technique is effective in removing hematite pigment and microcrystalline hematite in red

sediments. This selective removal of fine-grained hematite means that chemical demagnetization can remove secondary NRM commonly carried by these grains in red sediments. Chemical demagnetization and thermal demagnetization usually accomplish the same removal of secondary NRM, leaving the ChRM. Because chemical demagnetization is an inherently messy and time-consuming process, thermal demagnetization is the preferred technique.

Progressive demagnetization techniques

In this section, we deal with the following questions:

1. How does one determine the best demagnetization technique to isolate the ChRM in a particular suite of samples?
2. What is the appropriate demagnetization level (H_{AF} or T_{demag}) for isolating the ChRM?

Progressive demagnetization experiments are intended to provide answers to these all-important questions. These experiments are usually performed following measurement of NRM of all specimens in a collection. Distributions of NRM directions provide information about likely secondary components, while knowledge of ferromagnetic mineralogy can indicate which demagnetization technique is likely to provide isolation of components of NRM.

The general procedure in progressive demagnetization is to sequentially demagnetize a specimen at progressively higher levels, measuring remaining NRM following each demagnetization. A generally adopted procedure is to apply progressive AF demagnetization to some specimens and progressive thermal demagnetization to other specimens. This procedure allows comparison of results obtained by the two techniques. The objective is to reveal *components* of NRM that are carried by ferromagnetic grains within a particular interval of coercivity or blocking temperature. Resistance to demagnetization is often discussed in terms of *stability* of NRM, with *low-stability components* easily demagnetized and *high-stability components* removed only at high levels of demagnetization.

Adequate description of components of NRM usually requires progressive demagnetization at a minimum of eight to ten levels. Exact levels of demagnetization are usually adjusted in a trial-and-error fashion. However, a general observation is that coercivities are log-normally distributed so that initially small increments in peak field of AF demagnetization are followed by larger increases at higher levels. A typical progression would be peak fields of 10, 25, 50, 100, 150, 200, 300, 400, 600, 800, and 1000 Oe.

In progressive thermal demagnetization, temperature steps are distributed between ambient temperature and the highest Curie temperature. A typical strategy is to use temperatures increasing in 50°C to 100°C steps at low temperatures but smaller temperature increments (sometimes as small as 5°C) within about 100°C of the Curie temperature. The end product of a progressive demagnetization experiment is a set of measurements of NRM remaining after increasing demagnetization levels. Analysis of these data require procedures for displaying the progressive changes in both direction and magnitude of NRM.

Graphical displays

To introduce various techniques of graphical display, consider the example of progressive demagnetization results shown in the idealized perspective diagram of Figure 5.3. Although highly simplified, this example was abstracted from actual observations and does display the fundamental observations that are typical of a common two-component NRM. Each NRM vector is labeled with a number corresponding to the demagnetization level with point 0 indicating NRM prior to demagnetization. During demagnetization at levels 1 through 3, the remaining NRM rotates in direction and changes intensity as a low-stability component is removed. This low-stability component of NRM is depicted by the dashed arrow in Figure 5.3 and can be determined by the vector subtraction

$$\mathbf{NRM}_{0-3} = \mathbf{NRM}_0 - \mathbf{NRM}_3 \quad (5.1)$$

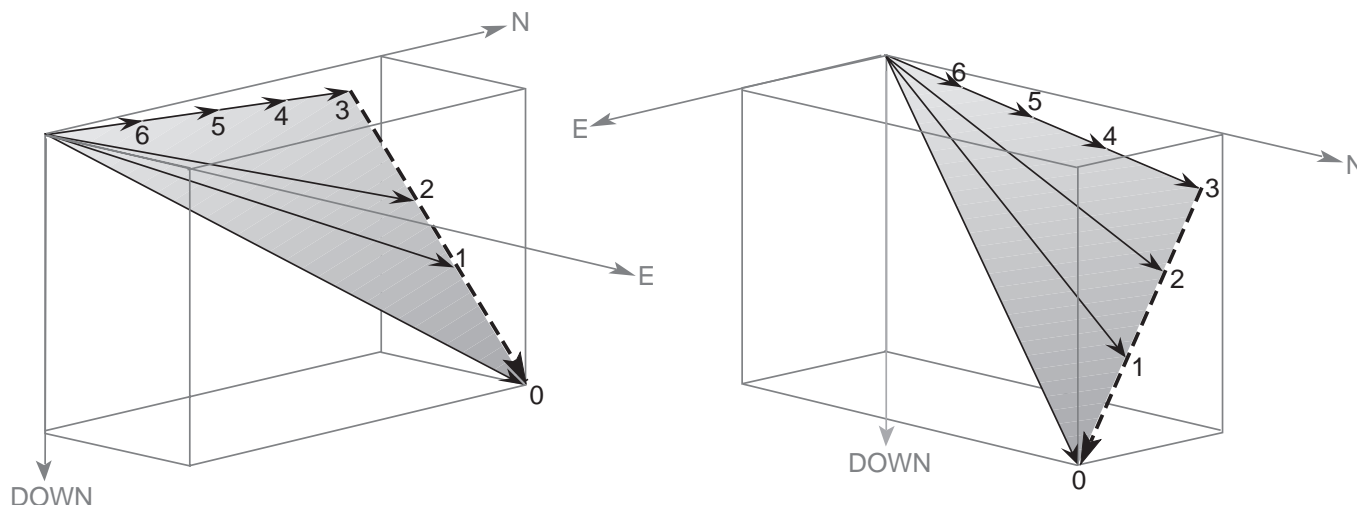


Figure 5.3 Perspective diagram of NRM vector during progressive demagnetization. Geographic axes are shown; solid arrows show the NRM vector during demagnetization at levels 0 through 6; the dashed arrow is the low-stability NRM component removed during demagnetization at levels 1 through 3; during demagnetization at levels 4 through 6, the high-stability NRM component decreases in intensity but does not change in direction.

where \mathbf{NRM}_0 and \mathbf{NRM}_3 are NRM at demagnetization levels 0 and 3.

During demagnetization at levels 4 through 6, remaining **NRM** does not change in direction but decreases in intensity. This high-stability component is successfully isolated by demagnetization to level 3 and, if observed for a number of specimens, would be taken as the ChRM. Notice that the end of the NRM vector describes a line toward the origin during demagnetization at levels 4 through 6. Observing a linear trajectory of the vector end point toward the origin is a key to recognizing that a high-stability NRM component has been isolated.

Graphical techniques that allow changes in three-dimensional vectors to be displayed on a two-dimensional page are required for analysis of progressive demagnetization results. All such graphical techniques require some sort of projection, and all have attributes and limitations.

The progressive demagnetization information of Figure 5.3 is shown in Figure 5.4, using the technique generally applied until the mid-1970s. An equal-area projection is used to display the direction of the NRM vector (Figure 5.4a), while changes in intensity of NRM are plotted separately (Figure 5.4b). The direction of NRM changes between levels 0 and 3 and is constant during subsequent demagnetization at levels 3 through 6. However, the separation of direction and intensity information makes visualization of the separate NRM components difficult.

Results of progressive demagnetization experiments are now displayed by using one of several forms of a *vector component* (*vector end point* or *orthogonal projection*) *diagram*. The technique was developed by Zijdeveld (see Suggested Readings), and the diagram is also referred to as a *Zijdeveld diagram*. The power of the vector component diagram is its ability to display directional and intensity information on a single diagram by projecting the vector onto two orthogonal planes. However, an initial investment of time and concentration is required to understand these diagrams. Almost all research articles on paleomagnetism that have been published within the past decade contain at least one vector component diagram. So understanding modern paleomagnetism requires understanding the fundamentals of this graphical technique. We're going to pause now while you go prepare a large pot of black coffee (OK, Britons may use tea). When you've got yourself suitably prepared, dive into the following explanation of vector component diagrams.

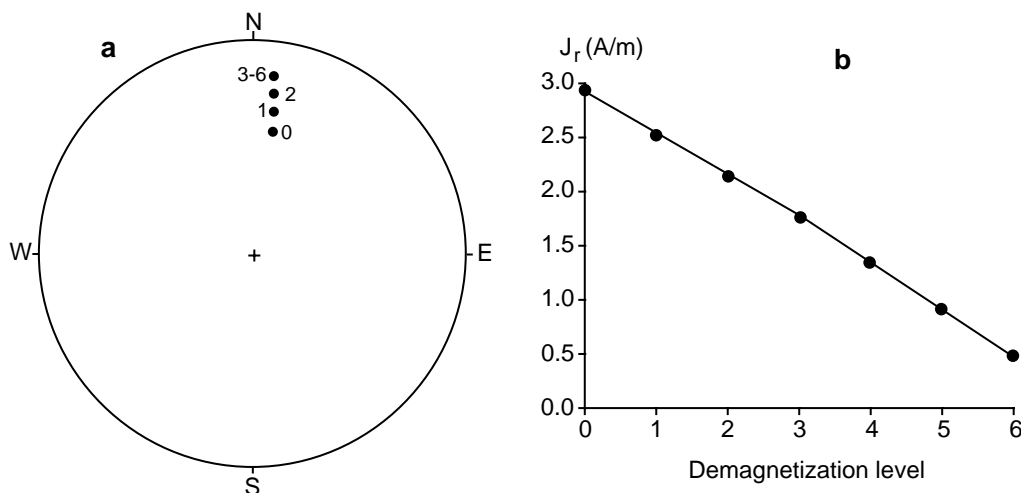


Figure 5.4 Equal-area projection and NRM intensity plot of progressive demagnetization results. (a) Equal-area projection of the direction of NRM. Numbers adjacent to NRM directions indicate the demagnetization level; the NRM direction changes between levels 0 and 3 but is constant direction between levels 3 and 6. (b) NRM intensity versus demagnetization level. A slight break in slope occurs at demagnetization level 3.

In the vector component diagram, the base of the NRM vector is placed at the origin of a Cartesian coordinate system, and the tip of the vector is projected onto two orthogonal planes. The distance of each data point from the origin is proportional to the intensity of the NRM vector projected onto that plane. To construct a vector component diagram, each NRM vector observed during the progressive demagnetization experiment is decomposed into its north (N), east (E), and vertical (Down) components:

$$N_i = \text{NRM}_i \cos I_i \cos D_i \tag{5.2}$$

$$E_i = \text{NRM}_i \cos I_i \sin D_i \tag{5.3}$$

$$Z_i = \text{NRM}_i \sin I_i \tag{5.4}$$

where NRM_i is the intensity of NRM_i , and I_i and D_i are the inclination and declination of NRM_i .

Figure 5.5 shows the construction of a vector component diagram displaying the progressive demagnetization data of Figure 5.3. In Figure 5.5a, the projection of the seven NRM vectors onto the horizontal plane is constructed by plotting N_i versus E_i ; each data point represents the end of the NRM vector projected onto the horizontal plane (hence the name vector end point diagram). As an example, the horizontal projection of NRM_3 is shown by the heavily stippled arrow. The angle between the north axis and a line from the origin to each data point is the declination of the NRM vector at that demagnetization level.

If you examine Figure 5.5a carefully, you observe that points 0 through 3 are collinear and the trajectory of those data points does not intersect the origin. Points 3 through 6 are also collinear, but the trajectory of these points does project toward the origin. These two lines on the horizontal projection of Figure 5.5a are the first indications that the progressive demagnetization data being displayed are the result of two separate components of NRM, one removed between levels 0 to 3 (= NRM_{0-3}) and one removed between levels 3 to 6. In fact, the lightly stippled arrow of Figure 5.5a is the horizontal projection of NRM_{0-3} , while the heavily stippled arrow is the horizontal projection of the ChRM isolated by demagnetization to level 3.

The second projection required to describe the progressive NRM data is on a vertical plane. In Figure 5.5b, the vertical component of the NRM vector at each demagnetization level is plotted against the north component. The actual vertical projection of NRM_0 is shown by the black arrow, while the vertical projection of NRM_3 is shown by the heavily stippled arrow. Figure 5.5b is a view looking directly westward normal to the north-south oriented vertical plane. The vertical component can be shown projected onto a vertical

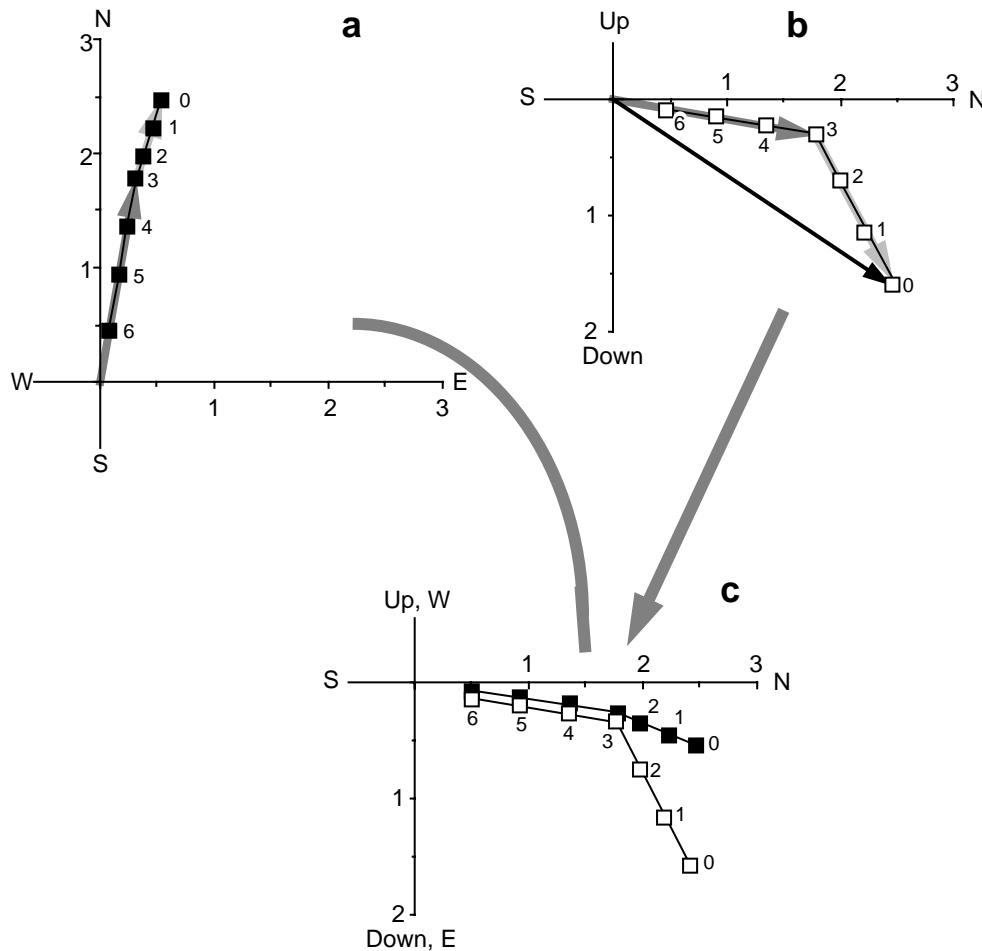


Figure 5.5 Construction of vector component diagram. (a) Projection of the NRM vector shown in Figure 5.3 onto the horizontal plane. The scale on the axes is in A/m; the lightly stippled arrow is the horizontal projection of the NRM vector removed during demagnetization at levels 1 through 3; the heavily stippled arrow is the projection of the NRM vector remaining at level 3. (b) Projection of the NRM vector onto a vertical plane oriented north-south. The solid arrow is the vertical projection of the NRM vector prior to demagnetization; the lightly stippled arrow is the projection of the NRM vector removed during demagnetization at levels 1 through 3; the heavily stippled arrow is the projection of the NRM vector remaining at level 3. (c) Horizontal and vertical projections combined into a single vector component diagram. Solid data points indicate vector end points projected onto the horizontal plane; open data points indicate vector end points projected onto the vertical plane; numbers adjacent to data points are demagnetization levels.

plane oriented north-south (as in this case) or oriented east-west. The choice of the north-south vertical plane (and north axis as abscissa) for Figure 5.5b is made because this vertical plane is closest to the vector being projected.

In Figure 5.5b, the separation of the two components of NRM is clearly displayed by the break in slope of the *end point trajectory* at level 3. Points 0 to 3 are collinear, but the line connecting these points does not include the origin. The vertical projection of the low-stability component removed in this interval is shown by the lightly stippled arrow in Figure 5.5b. Points 3 to 6 also are collinear, and the trajectory of these end points does include the origin, indicating removal of a single vector with constant direction. That vector is of course the ChRM with its vertical projection shown by the heavily stippled arrow.

The importance of observing a trajectory of vector end points that trend toward the origin of a vector component diagram cannot be overemphasized. This is the critical observation, indicating that a single

vector with constant direction is being removed (e.g., Figure 5.3, levels 3 to 6). Observation of a linear trend of end points toward the origin indicates successful removal of the low-stability NRM component allowing isolation of the high-stability ChRM.

It is possible to determine the inclination of ChRM by realizing that the angle between the N axis and the line through points 3 to 6 is the *apparent inclination*, I_{app} , which is related to the true inclination, I , by

$$\tan I = \tan I_{app} / \cos D \quad (5.5)$$

where $|\cos D|$ is the absolute value of $\cos D$. The inclination of the low-stability component could be determined similarly; it too is an apparent inclination on Figure 5.5b. The direction of the low-stability component for this example is $I \approx 60^\circ$, $D \approx 18^\circ$.

The last step in construction of the vector component diagram is to combine the two projections into a single diagram as shown in Figure 5.5c, where only end points of the projections onto the horizontal and vertical planes are shown. This diagram contains two sets of coordinate axes, both clearly labeled. Note that the caption indicates that solid data points represent projections of vector end points onto the horizontal plane, while open data points are projections on the vertical plane. This is a common form of the vector component diagram, but many variations exist. No strict conventions for vector component diagrams exist, so you must read figure captions carefully! In vector component diagrams in this book, horizontal projections are always shown with solid data points, and open data points are used for vertical projections.

From the example of Figure 5.5, the ability of the vector component diagram to reveal components of NRM is apparent. However, this technique has limitations that should be appreciated. If a component of NRM perpendicular to one of the projection planes is removed, that component is not apparent on that projection plane. However, the removed component is apparent in the projection onto the orthogonal plane. For example, if an NRM component pointing directly east is removed, the projection on a north-south oriented vertical plane degenerates to a single point. However, removal of this east-directed component is readily apparent on the horizontal projection. The lesson is that both projections must be scrutinized. Forgetting that these diagrams are geometrical constructs of three-dimensional information can lead to serious errors.

In Figure 5.6, an alternative form of the vector component diagram is shown by using the progressive demagnetization information of Figure 5.3. In this diagram, the horizontal projection (Figure 5.6a) is developed as before (Figure 5.5a). North and east axes are also drawn through point 3 in this diagram to illustrate how the declination of the low-stability component (NRM_{0-3}) can be determined from the diagram. In Figure 5.6b, the vertical plane projection is constructed by plotting the vector on the vertical plane in which it lies. This plane may change orientation for each demagnetization step. This form of the vector component diagram has the advantage that the vertical plane shows true inclination, which can be determined graphically as shown in Figure 5.6b. Also the distance of a data point from the origin of the vertical plane projection is proportional to the total intensity of NRM. However, the shifting declination of the vertical plane can be tricky (and sometimes misleading), and this form of vector component diagram is less popular than the form in Figure 5.5.

Some real examples

Actual examples of progressive demagnetization data are now examined, progressing from fairly simple to complex. Some theoretical explanations for complexities and additional techniques for analysis are introduced.

In Figure 5.7, examples of progressive demagnetization results revealing two-component NRMs of various complexity are illustrated by using vector component diagrams. Figure 5.7a illustrates results from a sample of the Moenave Formation, similar to the idealized Figures 5.3 to 5.6. Thermal demagnetization up to 508°C removes a low-stability component of NRM directed toward the north and downward. Prior to demagnetization, the distribution of sample NRM directions from this site (individual bed of red siltstone)

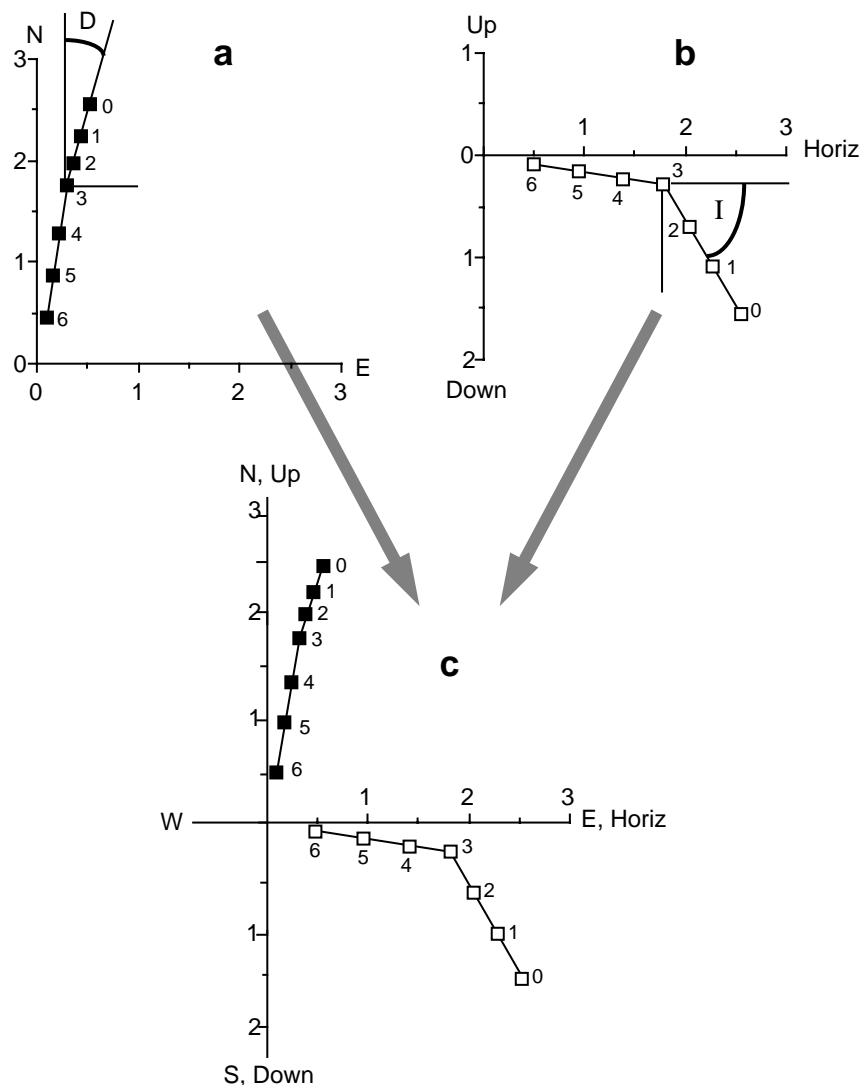


Figure 5.6 Construction of an alternative form of vector component diagram. (a) Projection of the NRM vector shown in Figure 5.3 onto the horizontal plane. This diagram is identical to Figure 5.5a; angle D is the declination of the low-stability NRM component removed during demagnetization at levels 1 through 3. (b) Projection of NRM vector onto a vertical plane cutting directly through the NRM vector. The scale on the axes is in A/m; the distance of each data point from the origin indicates the total NRM intensity; angle I is the inclination of the low-stability NRM component removed during demagnetization at levels 1 through 3. (c) Horizontal and vertical projections combined into a single vector component diagram. Solid data points indicate vector end points projected onto the horizontal plane; open data points indicate vector end points projected onto the vertical plane; numbers adjacent to data points are demagnetization levels.

shows streaking of directions along a great circle that includes the present geomagnetic field direction at the sampling locality. The low-stability component thus can be interpreted as a secondary VRM aligned with the present geomagnetic field.

For demagnetization temperatures from 508° to 690°C, the trajectory of vector end points is along a linear trend toward the origin. This ChRM points almost directly north with no significant directional change in the 508° to 690°C interval of demagnetization temperatures. Similar directions were observed during progressive demagnetization of other samples from this collecting locality. In this case, the two-components of NRM are sharply separated. The ChRM constitutes a significant portion of total NRM, and there is a

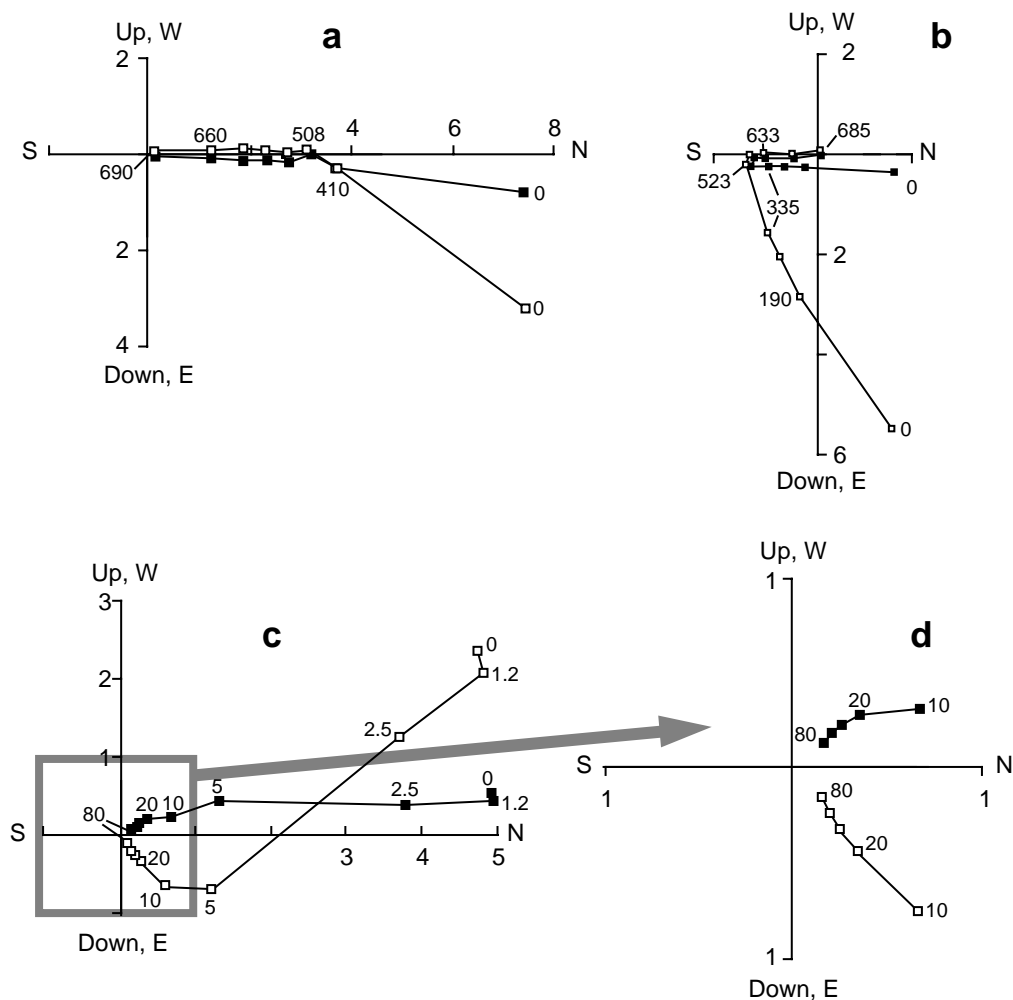


Figure 5.7 Example vector component diagrams. In all diagrams, numbers on axes indicate NRM intensities in A/m, solid data points indicate projection onto the horizontal plane, and open data points indicate projection onto the vertical plane. (a) Progressive thermal demagnetization of a sample from the Moenave Formation. Numbers adjacent to data points indicate temperature in degrees Celsius. (b) Progressive thermal demagnetization of a sample from the Chinle Formation. Numbers adjacent to data points indicate temperature in degrees Celsius. (c) Progressive AF demagnetization of a sample of Miocene basalt. Numbers adjacent to data points indicate peak demagnetizing field in mT; region of diagram outlined by stippled box is amplified in part (d).

substantial interval of demagnetization temperatures over which the ChRM can be observed. Thermal demagnetization to any temperature from about 510° to 600°C would effectively remove the low-stability component, revealing the high-stability ChRM.

In Figures 5.7c and 5.7d, results of progressive AF demagnetization of a sample of Miocene basalt are illustrated. Directions of NRM of other samples from this site are highly scattered (similar to Figure 4.7c), and intensities of NRM are anomalously high. AF demagnetization to a peak field of 20 mT (= 200 Oe) removes a large low-stability component of NRM directed toward the north with $I \approx -40^\circ$. During AF demagnetization to peak fields in the 20 to 80 mT interval (200 to 800 Oe; see the enlargement in Figure 5.7d), vector end points define a trajectory toward the origin with no significant change in direction of remaining NRM. These observations indicate that ChRM is isolated by AF demagnetization to 20 mT (200 Oe). The ChRM has a direction: $D \approx 330^\circ$, $I \approx 55^\circ$.

An additional sample from this site was thermally demagnetized following isolation of the ChRM by AF demagnetization to 20 mT (200 Oe) peak field. Blocking temperatures were dominantly between 450° and

580°C, and the direction of ChRM observed during thermal demagnetization was the same as that observed during AF demagnetization in the 20 to 80 mT interval (200 to 800 Oe). The Curie temperature determined on a sample from this locality was also 580°C, indicating that magnetite is the dominant ferromagnetic mineral. Collectively, these observations indicate that the low-stability NRM component removed by AF demagnetization to 20 mT (200 Oe) is a secondary lightning-induced IRM. The high-stability ChRM isolated during AF demagnetization to peak fields ≥ 20 mT (200 Oe) is a primary TRM acquired during original cooling of this Miocene basalt flow.

A more problematical example is presented in Figure 5.7b. During thermal demagnetization of this Late Triassic red sediment, a large component of NRM is removed during thermal demagnetization to $T \approx 600^\circ\text{C}$. This low-stability component ($D \approx 10^\circ$, $I \approx 60^\circ$) is subparallel to the geomagnetic field at the sampling locality and is interpreted as a secondary VRM (or possibly a CRM formed during recent weathering). Only at demagnetization temperatures between 633°C and 685°C is the smaller high-stability ChRM component revealed by the trajectory of vector end points toward the origin. Because the ChRM is smaller than the secondary component of NRM and is isolated only at high demagnetization levels, the ChRM direction cannot be confidently determined from a single specimen. In such cases, determination of the ChRM direction depends critically on internal consistency of results from other samples from the same site.

Overlapping blocking temperature or coercivity spectra

Rather than a sharp corner in the trajectory of vector end points (as in Figure 5.7a), end points often define a curve between the two straight-line segments on the vector component diagram. This complication is due to overlapping blocking temperature spectra (or coercivity spectra) of the ferromagnetic grains carrying the two components of NRM. Curved trajectories can be understood with the aid of Figure 5.8. In this synthetic example, NRM is composed of two components: a low-stability component \mathbf{J}_A with direction $D \approx 15^\circ$, $I \approx -25^\circ$; and a high-stability component \mathbf{J}_B with direction $D \approx 155^\circ$, $I \approx 70^\circ$. Demagnetization levels (spectra of microscopic coercivity or blocking temperature) over which these components are removed are shown on the left side of Figure 5.8.

In Figure 5.8a, demagnetization spectra of the two components do not overlap; \mathbf{J}_A is demagnetized between levels 1 and 6, while \mathbf{J}_B is demagnetized between levels 6 and 9. The resulting vector component diagram is shown in Figure 5.8b. Two linear trajectories are observed: one produced by removal of \mathbf{J}_A between levels 1 and 6, and another (which includes the origin) produced by removal of \mathbf{J}_B between levels 6 and 9. Because the demagnetization spectra of these two components are completely separated, the two trajectories are sharply separated by an acute angle at point 6.

In Figure 5.8c, demagnetization spectra overlap at levels 5 and 6. In the resulting vector component diagram of Figure 5.8d, the two linear trajectories are evident at demagnetization levels 1 to 4 and 7 to 9. However, in the interval of overlap (levels 5 and 6), both components are simultaneously removed, and a curved trajectory develops. The direction of the high-stability \mathbf{J}_B component can be determined at demagnetization levels 7 to 9 (i.e., above the overlap).

In Figure 5.8e, demagnetization spectra of the two components are completely overlapping. There is no demagnetization interval over which only one component is removed. The resulting vector component diagram (Figure 5.8f) has no linear segments, and the two components cannot be separated. Although some advanced techniques have been developed in attempts to deal with severely overlapping demagnetization spectra (see below), the situation is usually hopeless, and you might as well drown your sorrows at a local watering hole.

Fortunately, many rocks provide clear separation of components of NRM and confident determination of ChRM. One hopes to observe behaviors like those in Figures 5.7a; often one observes more difficult, but manageable, behaviors such as those in Figures 5.7b, 5.7c, and 5.7d; and one occasionally observes demagnetization behaviors that prevent isolation of a ChRM.

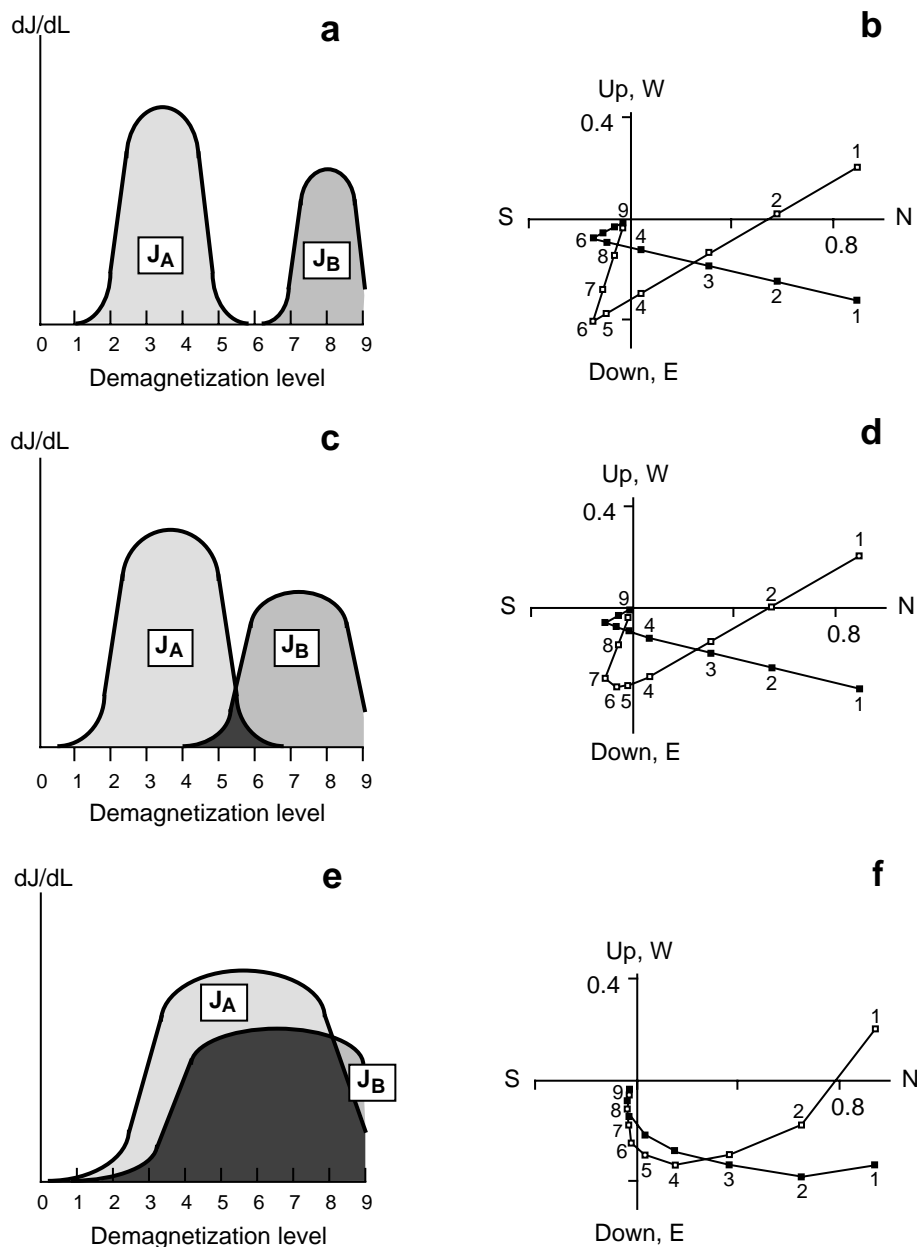


Figure 5.8 Schematic representation of effects of overlapping demagnetization spectra. A lower-stability component, J_A , has direction $I = -25^\circ$, $D = 15^\circ$. A higher-stability component, J_B , has direction $I = 70^\circ$, $D = 155^\circ$. (a) Demagnetization spectra of the two NRM components. NRM component J_A is removed during demagnetization levels 2 through 5; NRM component J_B is removed during demagnetization levels 7 through 9. (b) Vector component diagram resulting from progressive demagnetization of NRM composed of components J_A and J_B with demagnetization spectra shown in part (a). (c) Demagnetization spectra of the two NRM components with small interval of overlap. NRM component J_A is removed during demagnetization levels 2 through 6; NRM component J_B is removed during demagnetization levels 5 through 9. (d) Vector component diagram resulting from progressive demagnetization of NRM composed of components J_A and J_B with demagnetization spectra shown in part (c). (e) Demagnetization spectra of the two NRM components with large interval of overlap. NRM component J_A is removed during demagnetization levels 2 through 9; NRM component J_B is removed during demagnetization levels 3 through 9. (f) Vector component diagram resulting from progressive demagnetization of NRM composed of components J_A and J_B with demagnetization spectra shown in part (e). Modified from Dunlop (1979).

More than two components?

The majority of convincing paleomagnetic results have been obtained from rocks with no more than two components of NRM, usually a low-stability secondary NRM removed to allow isolation of a high-stability ChRM (often argued to be a primary NRM). However, a growing number of more complex NRMs with three or more components are being reported. As demagnetization procedures and analysis become more sophisticated and paleomagnetists venture into rocks with complex histories, reports of complex multicomponent NRMs will no doubt increase. It therefore seems important to show at least one example of a three-component NRM in which the components are probably interpretable.

In Figure 5.9, results of progressive demagnetization of Precambrian red argillite from the Belt Super-group are illustrated. In this study, some specimens were demagnetized by using a combination of AF demagnetization followed by thermal demagnetization (proving once again that life gets complicated when dealing with Precambrian rocks). During AF demagnetization to 50 Oe (5 mT) peak field, a component of NRM is removed with direction $I \approx 50^\circ$, $D \approx 15^\circ$, subparallel to the geomagnetic field at the sampling locality. This low-stability component is probably a VRM.

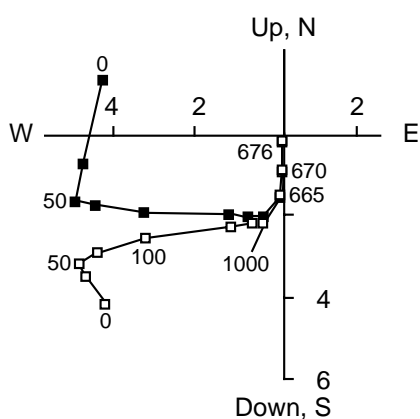


Figure 5.9 Vector component diagram on a three-component NRM. The sample is a red argillite from the Precambrian Spokane Formation of Montana; numbers on axes indicate NRM intensities in A/m; solid data points indicate projection onto the horizontal plane; open data points indicate projection onto the east-west oriented vertical plane; numbers 0 through 1000 indicate peak field (in Oe) used in alternating-field demagnetization; numbers 665 through 676 indicate temperatures (in degrees Celsius) used in subsequent thermal demagnetization. Modified from Vitorello and Van der Voo (*Can. J. Earth Sci.*, v. 14, 67–73, 1977).

During AF demagnetization between 50 Oe (5 mT) and 1000 Oe (100 mT), a component of intermediate stability is removed. The direction of this component is $I \approx 10^\circ$, $D \approx 275^\circ$. Thermal demagnetization of other samples revealed a similar intermediate-stability component with blocking temperatures in the 300° to 500°C interval. In addition, a high-stability ChRM found in many samples is isolated by thermal demagnetization in the 665° to 680°C interval. The ChRM is interpreted as a primary CRM acquired during (or soon after) deposition of these 1300 Ma argillites.

Using geological evidence for an Eocambrian metamorphic event in this region and favorable comparison of the direction of the intermediate-stability component with that predicted for Eocambrian age, this component was interpreted as the result of Eocambrian metamorphism. Although the paleomagnetists who made this observation were certainly diligent in their procedures, this example highlights the difficulty of securely interpreting multicomponent NRMs. The “degree of difficulty” in interpretation of paleomagnetic results increases as the power of the number of NRM components. Most examples discussed in this book are two-component NRMs, and we only occasionally venture into the realm of more complex multicomponent NRMs. However, it seems clear that much future paleomagnetic research will involve deciphering multicomponent NRMs that are encountered in old rocks with complex histories.

Principal component analysis

The examples of progressive demagnetization data in Figures 5.7 and 5.9 show that there is often significant scatter in otherwise linear trajectories of vector component diagrams. This is especially true for weakly

magnetized rocks and rocks for which ChRM is a small percentage of total NRM. A rigorous, quantitative technique is obviously needed to determine the direction of the best-fit line through a set of scattered observations. *Principal component analysis* (abbreviated p.c.a.) is the system that is in common use.

Consider the progressive thermal demagnetization data shown in Figure 5.10 (high temperature portion of thermal demagnetization of a Late Triassic red sediment). In the 600°C to 675°C interval, there is an obvious trend of data points toward the origin. Low-stability secondary components of NRM have been removed, and the only component remaining is the ChRM. But there is also considerable scatter. One might choose a single demagnetization level to best represent the ChRM (this was the method used until recently). However, it is preferable to use all the information from the five demagnetization temperatures by mathematically determining the best-fit line through the trajectory of those five data points. Kirschvink (see Suggested Readings) has shown how p.c.a. can provide the desired best-fit line. A qualitative understanding of p.c.a. is easily gained through the example of Figure 5.10. From a set of observations, p.c.a. determines the best-fitting line through a sequence of data points. In addition, a *maximum angular deviation* (MAD) is calculated to provide a quantitative measure of the precision with which the best-fit line is determined.

When fitting a line to data using p.c.a., there are three options regarding treatment of the origin of the vector component diagram: (1) force the line to pass through the origin (“anchored” line fit); (2) use the origin as a separate data point (“origin” line fit); or (3) do not use the origin at all (“free” line fit). For determination of ChRM, either anchored or origin line fits are commonly used because the ChRM is determined from a trend of data points toward the origin. In Figure 5.10, the anchored line fit to the data is shown. This is the best-fit line through the data determined by p.c.a. using the constraint that the line pass through the origin. The resulting line has direction $I = 6.4^\circ$, $D = 162.8^\circ$; and the MAD is 5.5° . If the data of Figure 5.10 are fit using an origin line fit, the resulting line has direction $I = 7.3^\circ$, $D = 164.7^\circ$, and the MAD is 8.0° .

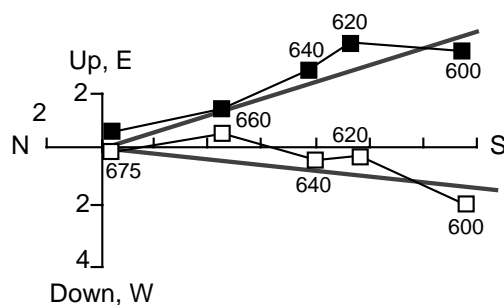


Figure 5.10 Example of best-fit line to progressive demagnetization data using principal component analysis. The sample is from the Late Triassic Chinle Formation of New Mexico; numbers on axes indicate NRM intensities in A/m; solid data points indicate projection onto the horizontal plane; open data points indicate projection onto the north-south oriented vertical plane; numbers adjacent to data points indicate temperatures of thermal demagnetization in degrees Celsius; the stippled lines show the best-fit direction ($I = 6.4^\circ$, $D = 162.8^\circ$) calculated by using the anchored option of principal component analysis applied to the data.

Note that maximum weight is put on the data points farthest from the origin because those points have maximum information content in determining the trend of the line. In an experimental context, the data points farthest from the origin are probably the best determined because the signal to noise ratio is greatest. Although no strict convention exists, line fits from p.c.a. that yield $MAD \geq 15^\circ$ are often considered ill defined and of questionable significance.

Directions of secondary NRM also can be determined by using p.c.a. The low-stability component in Figure 5.7c or the intermediate-stability component of Figure 5.9 could be determined with this technique. For secondary NRM, the free line fit would be used because the trajectory on the vector component diagram does not include the origin.

For rocks with weak NRM or noisy trajectories during progressive demagnetization, p.c.a. can provide more robust determination of ChRM than using results from a single demagnetization level. If progressive

demagnetization studies of representative samples demonstrate straightforward isolation of the ChRM, remaining samples would be treated at only one or two demagnetization levels to isolate the ChRM. This procedure is referred to as *blanket demagnetization*. However, if progressive demagnetization studies indicate weak or noisy ChRM, the remaining samples would be demagnetized at multiple demagnetization levels within the range that appears to isolate ChRM. Principal component analysis would be applied to the resulting data from all samples.

Advanced techniques

Some special techniques have been developed to deal with rocks for which ChRM cannot be isolated directly. Rocks with multiple components of NRM with severely overlapping spectra of blocking temperature or coercivity often yield arcs or *remagnetization circles* during progressive demagnetization. In special circumstances, these remagnetization circles may intersect at the direction of one of the NRM components. Several techniques for analysis of remagnetization circles have been developed and can sometimes provide important information from rocks when more straightforward analysis fails. However, these techniques are complicated, generally require special geologic situations, and often yield unsatisfying results (complex magnetizations spawn complex interpretations). Some of these advanced techniques are referenced in the Suggested Readings.

FIELD TESTS OF PALEOMAGNETIC STABILITY

Laboratory demagnetization experiments reveal components of NRM and (usually) allow definition of a ChRM. Blocking temperature and/or coercivity spectra can suggest that ferromagnetic grains carrying a ChRM are capable of retaining a primary NRM. However, laboratory tests cannot prove that the ChRM is primary. *Field tests of paleomagnetic stability* can provide crucial information about the timing of ChRM acquisition. In studies of old rocks in orogenic zones, field test(s) of paleomagnetic stability can be the critical observation.

Common field tests of paleomagnetic stability are introduced here, and examples are presented. Through these examples, the logic and power of field tests can be appreciated. It is worth noting that quantitative evaluation of field tests requires statistical techniques for analyses of directional data that are developed in the next chapter.

The fold test

The *fold test* (or *bedding-tilt test*) and the *conglomerate test* are represented in Figure 5.11. In the fold test, relative timing of acquisition of a component of NRM (usually ChRM) and folding can be evaluated. If a ChRM was acquired prior to folding, directions of ChRM from sites on opposing limbs of a fold are dispersed when plotted in geographic coordinates (in situ) but converge when the structural correction is made ("restoring" the beds to horizontal). The ChRM directions are said to "pass the fold test" if clustering increases through application of the structural correction or "fail the fold test" if the ChRM directions become more scattered. The fold test can be applied either to a single fold (Figure 5.11) or to several sites from widely separated localities at which different bedding tilts are observed.

An example of a set of ChRM directions which passes the fold test is shown in Figure 5.12. These directions are mean ChRM directions observed at five localities of the Nikolai Greenstone, part of the Wrangellia Terrane of Alaska. The ChRM directions in Figure 5.12a are uncorrected for bedding tilt (geographic coordinates), while those in Figure 5.12b are after structural correction. This is a realistic example in the sense that bedding tilts are moderate. Improvement in clustering of ChRM directions upon application of structural correction is evident, if not dramatic, and passage of the fold test indicates that ChRM of the Nikolai Greenstone was acquired prior to folding. The ChRM directions also pass a reversals test (discussed below), which helps to confirm that the ChRM of the Nikolai Greenstone is a primary TRM acquired

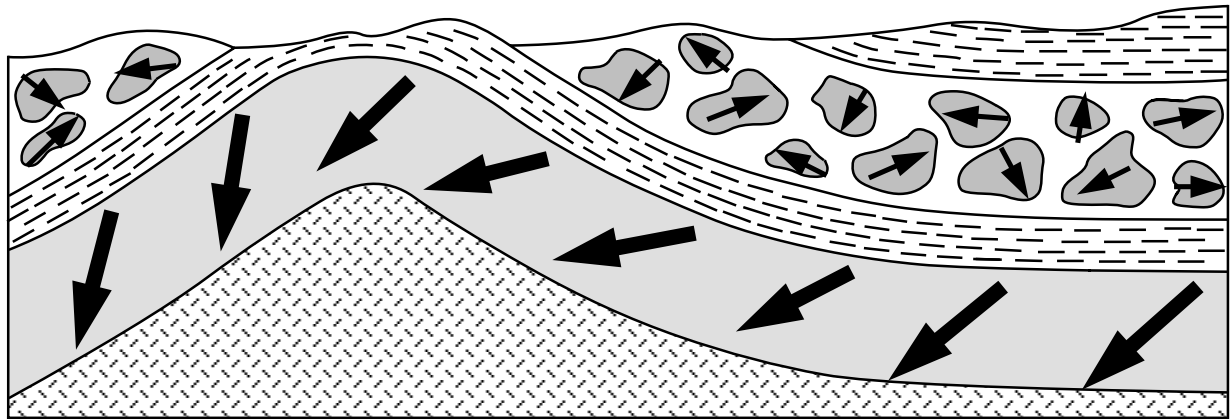


Figure 5.11 Schematic illustration of the fold and conglomerate tests of paleomagnetic stability. Bold arrows are directions of ChRM in limbs of the fold and in cobbles of the conglomerate; random distribution of ChRM directions from cobble to cobble within the conglomerate indicates that ChRM was acquired prior to formation of the conglomerate; improved grouping of ChRM upon restoring the limbs of the fold to horizontal indicates ChRM formation prior to folding. Redrawn from Cox and Doell (1960).

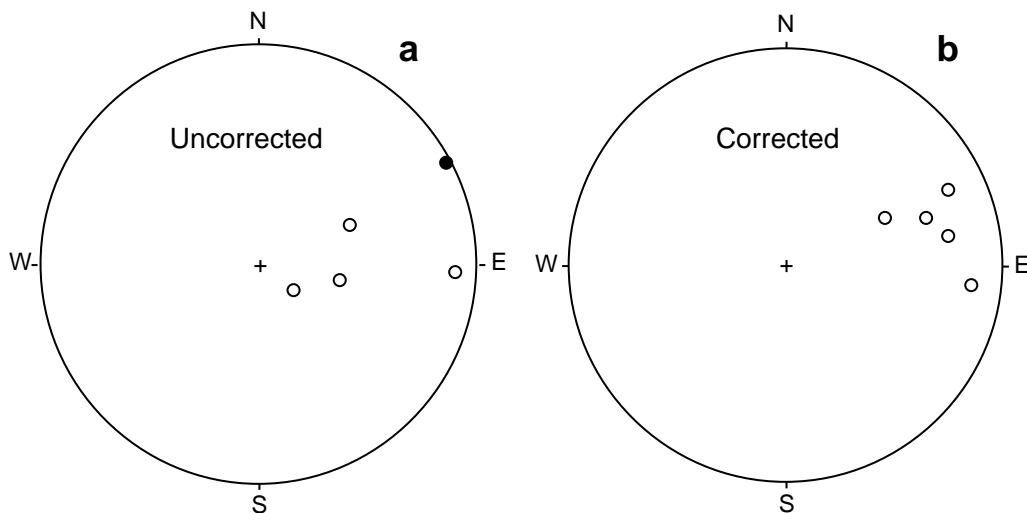


Figure 5.12 Example of ChRM directions that pass the fold test. Equal-area projections show mean ChRM directions from multiple sites at each of five collecting localities in the Nikolai Greenstone, Alaska; solid circles indicate directions in the lower hemisphere of the projection; open circles indicate directions in the upper hemisphere. (a) ChRM directions *in situ* (prior to structural correction). (b) ChRM directions after structural correction to restore beds to horizontal. Data from Hillhouse (*Can. J. Earth Sci.*, v. 14, 2578–2592, 1977).

during original cooling in the Middle–Late Triassic. This example also illustrates the necessity for a statistical test to allow quantitative evaluation of the fold test. (For example, at what level of certainty can we assert that the clustering of ChRM directions is improved by applying the structural corrections?)

Synfolding magnetization

Because an increasing number of cases of *synfolding magnetization* are being reported, the principles of synfolding magnetization are introduced, and an example is provided. In Figure 5.13a, observations expected for a prefolding magnetization are shown for a simple syncline. In Figure 5.13b, the observations

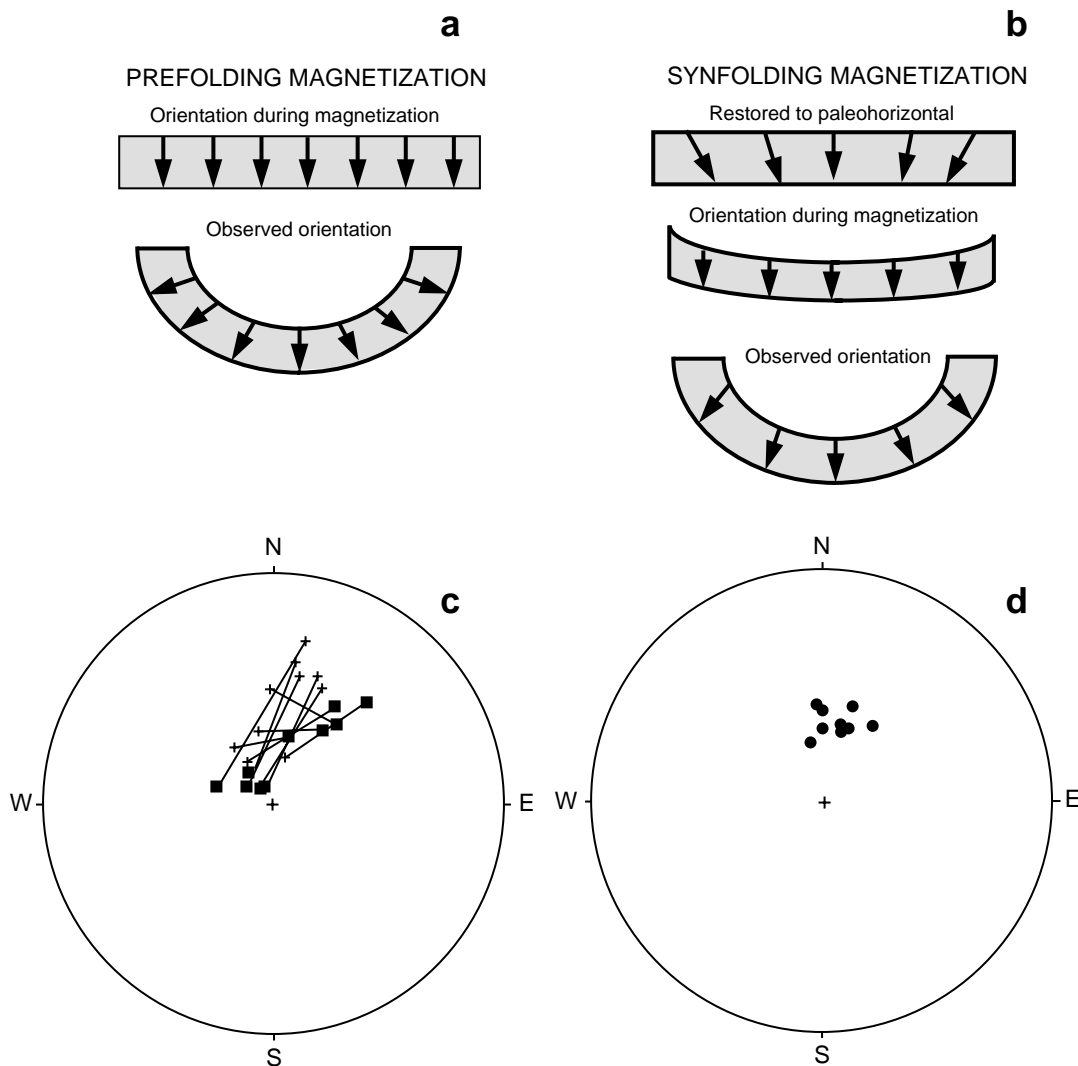


Figure 5.13 Synfolding magnetization. **(a)** Directions of ChRM are shown by arrows for pre-folding magnetization. ChRM directions are dispersed in the observed *in situ* orientation; restoring bedding to horizontal results in maximum grouping of the ChRM directions. **(b)** Directions of ChRM for synfolding magnetization. ChRM directions are dispersed in both the *in situ* orientation and when bedding is restored to horizontal; maximum grouping of the ChRM directions occurs when bedding is partially restored to horizontal. **(c)** Equal-area projection of directions of ChRM in Cretaceous Midnight Peak Formation of north-central Washington. Crosses are *in situ* site-mean ChRM directions for ten sites spread across opposing limbs of a fold; squares are site-mean ChRM directions resulting from restoring bedding at each site to horizontal; all directions are in the lower hemisphere of the projection. **(d)** Site-mean ChRM directions in Midnight Peak Formation after 50% unfolding. Data from Bazard et al. (*Can. J. Earth Sci.*, v. 27, 330–343, 1990).

expected for synfolding magnetization are represented. Observed directions of magnetization are shown in the bottom diagram of Figure 5.13b while the configuration of directions after complete unfolding is shown in the top diagram. Complete unfolding “overcorrects” the magnetization directions. The best grouping of the magnetization directions occurs when the structure is only partially unfolded, as in the middle diagram of Figure 5.13b. The inference drawn from such observations is that the magnetization was formed during formation of the syncline (synfolding magnetization).

In Figures 5.13c and 5.13d, an example of synfolding magnetization is shown. Mean directions of ChRM were determined for ten sites collected from localities spread across opposing limbs of a fold. In situ ChRM directions (geographic coordinates) are shown by crosses in Figure 5.13c, while ChRM directions after 100% unfolding are shown by squares. Inspection of Figure 5.13c reveals that ChRM directions from opposing limbs of the fold pass one another as the structural corrections are applied. Maximum clustering of ChRM directions occurs at 50% unfolding (Figure 5.13d). The conclusion is that the ChRM was most likely formed during folding. Again, quantitative assessment of the percentage of unfolding producing maximum clustering of ChRM directions requires use of a statistical method.

Conglomerate test

The *conglomerate test* is illustrated in Figure 5.11. If ChRM in clasts from a conglomerate has been stable since before deposition of the conglomerate, ChRM directions from numerous cobbles or boulders should be randomly distributed (= passage of conglomerate test). A nonrandom distribution indicates that ChRM was formed after deposition of the conglomerate (= failure of conglomerate test). Passage of the conglomerate test indicates that the ChRM of the source rock has been stable at least since formation of the conglomerate. A positive conglomerate test from an intraformational conglomerate provides very strong evidence that the ChRM is a primary NRM.

The Glance Conglomerate of southern Arizona is an interbedded sequence of silicic volcanic and sedimentary rocks including conglomerate. Randomly distributed ChRM directions observed in volcanic cobbles of a conglomerate are shown in Figure 5.14. Because this conglomerate is within the sequence of volcanic flows of the Glance Conglomerate, passage of the conglomerate test indicates that ChRM directions in the volcanic rocks are primary.

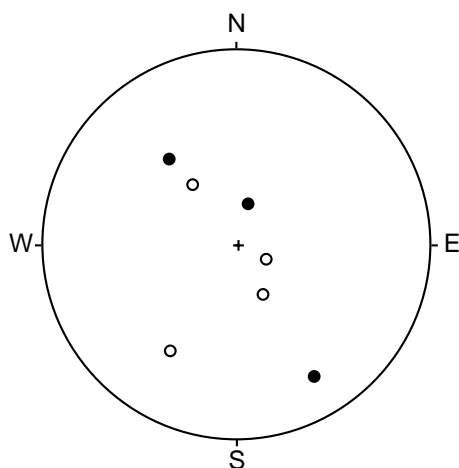


Figure 5.14 Example of ChRM directions that pass the conglomerate test. The equal-area projection shows the ChRM directions in seven volcanic cobbles in a conglomerate within a sequence of volcanic flows of the Late Jurassic Glance Conglomerate; open circles are directions in the upper hemisphere; solid circles are directions in the lower hemisphere; the ChRM directions are randomly distributed, indicating ChRM formation prior to incorporation of the cobbles in the conglomerate. Redrawn from Kluth et al. (*J. Geophys. Res.*, v. 87, 7079–7086, 1982).

If processes of weathering associated with conglomerate formation have resulted in alteration of the ferromagnetic minerals, the conglomerate test can be negative even when the source rock contains a stable ChRM. Passage of a conglomerate test thus provides strong evidence for stability, whereas failure of the test is certainly a warning, but not necessarily a clear indication that the ChRM of the source rock is secondary.

Reversals test

As explained in Chapter 1, the time-averaged geocentric axial dipolar nature of the geomagnetic field holds during both normal- and reversed-polarity intervals. At all locations, the time-averaged geomagnetic field directions during a normal-polarity interval and during a reversed-polarity interval differ by 180°. This property of the geomagnetic field is the basis for the *reversals test* of paleomagnetic stability shown schematically in Figure 5.15.

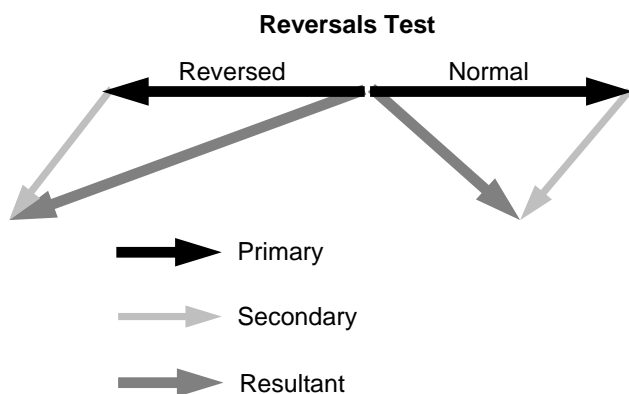


Figure 5.15 Schematic illustration of the reversals test of paleomagnetic stability. Solid arrows indicate the expected antiparallel configuration of the average direction of primary NRM vectors resulting from magnetization during normal- and reversed-polarity intervals of the geomagnetic field; an unremoved secondary NRM component is shown by the lightly stippled arrows; the resultant NRM directions are shown by the heavily stippled arrows. Redrawn from McElhinny (*Palaeomagnetism and Plate Tectonics*, Cambridge, London, 356 pp., 1973).

If a suite of paleomagnetic sites affords adequate averaging of secular variation during both normal- and reversed-polarity intervals, the average direction of primary NRM for the normal-polarity sites is expected to be antiparallel to the average direction of primary NRM for the reversed-polarity sites. However, acquisition of later secondary NRM components will cause resultant NRM vectors to deviate by less than 180° . ChRM directions are said to “pass the reversals test” if the mean direction computed from the normal-polarity sites is antiparallel to the mean direction for the reversed-polarity sites. Passage of the reversals test indicates that ChRM directions are free of secondary NRM components and that the time sampling afforded by the set of paleomagnetic data has adequately averaged geomagnetic secular variation. Furthermore, if the sets of normal- and reversed-polarity sites conform to stratigraphic layering, the ChRM is probably a primary NRM.

If a paleomagnetic data set “fails the reversals test,” the average directions for the normal and reversed polarity sites differ by an angle that is significantly less than 180° . Failure of the reversals test can indicate either (1) presence of an unremoved secondary NRM component or (2) inadequate sampling of geomagnetic secular variation during either (or both) of the polarity intervals. Because polarity reversals are characteristic of most geologic time intervals, paleomagnetic data sets often contain normal- and reversed-polarity ChRM. The reversals test of paleomagnetic stability is often applicable and, unlike the conglomerate or fold test, does not require special geologic settings.

An example of the reversals test is shown in Figure 5.16, which displays mean ChRM directions from Paleocene continental sediments of northwestern New Mexico. The mean ChRM direction from 42 normal-polarity sites is antiparallel to the mean ChRM direction of 62 reversed-polarity sites. The ChRM directions thus pass the reversals test for paleomagnetic stability. Quantitative evaluation of the reversals test involves computation of the mean directions (and confidence intervals about those mean directions) for both normal- and reversed-polarity groups and comparison of one mean direction with the antipode of the other mean direction. Statistical methods for such comparisons are developed in the next chapter.

Baked contact and consistency tests

Baked zones of country rock adjacent to igneous rocks allow application of the *baked contact test* of paleomagnetic stability. The baked country rock and igneous rock acquire a TRM that should agree in direction. Mineralogies of the igneous rock and adjacent baked country rock can be very different, with different tendencies for acquisition of secondary NRM and different demagnetization procedures required for isolation of ChRM. Agreement in ChRM direction between an igneous rock and adjacent baked country rock thus provides confidence that the ChRM direction is a stable direction that may be a primary NRM. For country rock that is much older than the igneous rock, ChRM directions in unbaked country rock are expected to be significantly different from the ChRM direction of the igneous rock. Thus similar ChRM directions for igneous rock and baked country rock but a distinct ChRM direction from unbaked country rock constitute pas-

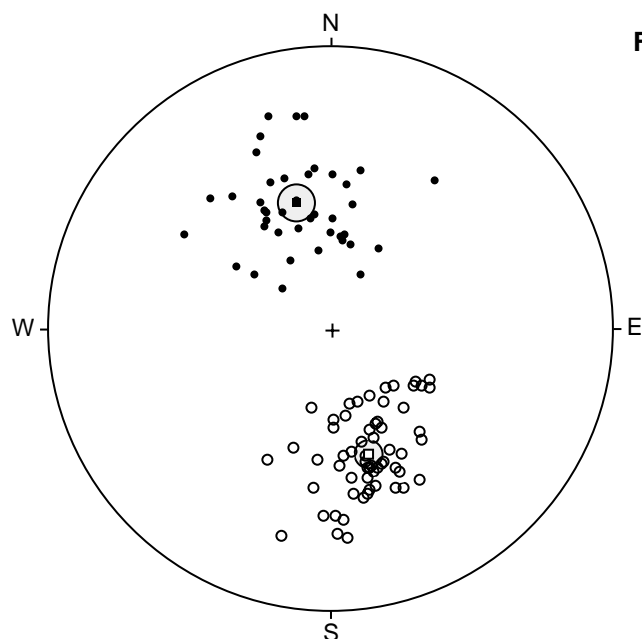


Figure 5.16 Example of ChRM directions that pass the reversals test of paleomagnetic stability. Equal-area projection of site-mean ChRM directions from 104 sites in the Paleocene Nacimiento Formation of northwestern New Mexico; solid circles are directions in the lower hemisphere of the projection; open circles are directions in the upper hemisphere; the mean of the 42 normal-polarity sites is shown by the solid square with surrounding stippled circle of 95% confidence; the mean of the 62 reversed-polarity sites is shown by the open square with surrounding stippled circle of 95% confidence; the antipode of the mean of the reversed-polarity sites is within 2° of the mean of the normal-polarity sites (within the confidence region). Redrawn from Butler and Taylor (*Geology*, v. 6, 495–498, 1978).

sage of the baked contact test. Uniform ChRM directions for igneous rock, baked zone, and unbaked country rock could indicate widespread remagnetization of all lithologies.

The *consistency test* for paleomagnetic stability involves observation of the same ChRM direction (remote from the present geomagnetic field direction) for different rock types of similar age. If mineralogies of the ferromagnetic minerals are highly variable and demagnetization procedures required for isolation of ChRM are different, but ChRM direction depends on geologic age, these observations are “consistent with the interpretation that the ChRM is a primary NRM.” Obviously, this consistency test must be accompanied by other indicators of stability of paleomagnetism because a consistent direction of ChRM could also indicate wholesale remagnetization of the region.

SUGGESTED READINGS

INSTRUMENTATION AND LABORATORY TECHNIQUES:

D. W. Collinson, *Methods in Rock Magnetism and Palaeomagnetism*, Chapman and Hall, London, 503 pp., 1983.

Theory, instrumentation, and techniques of partial demagnetization are covered in considerable detail.

CONVERGING REMAGNETIZATION CIRCLES:

H. C. Halls, A least-squares method to find a remanence direction from converging remagnetization circles, *Geophys. J. Roy. Astron. Soc.*, v. 45, 297–304, 1976.

H. C. Halls, The use of converging remagnetization circles in palaeomagnetism, *Phys. Earth Planet. Int.*, v. 16, 1–11, 1978.

Present theory and applications of remagnetization circle analysis.

VECTOR COMPONENT DIAGRAMS AND PRINCIPAL COMPONENT ANALYSIS:

D. J. Dunlop, On the use of Zijdeveld vector diagrams in multicomponent paleomagnetic samples, *Phys. Earth Planet. Sci. Lett.*, v. 20, 12–24, 1979.

Powers and limitations of vector component diagrams are discussed with many examples given.

J. D. A. Zijdeveld, A.C. demagnetization of rocks: Analysis of results, In: *Methods in Palaeomagnetism*, ed D. W. Collinson, K. M. Creer, and S. K. Runcorn, Elsevier, Amsterdam, pp. 254–286, 1967.

This paper introduces the technique of vector component diagrams.

K. A. Hoffman and R. Day, Separation of multicomponent NRM: A general method, *Earth Planet. Sci. Lett.*, v. 40, 433–438, 1978.

An advanced look at separation of components.

J. L. Kirschvink, The least-squares line and plane and the analysis of palaeomagnetic data, *Geophys. J. Roy. Astron. Soc.*, v. 62, 699–718, 1980.

Paleomagnetic applications of principal component analysis.

J. T. Kent, J. C. Briden, and K. V. Mardia, Linear and planar structure in ordered multivariate data as applied to progressive demagnetization of palaeomagnetic remanence, *Geophys. J. Roy. Astron. Soc.*, v. 75, 593–621, 1983.

An advanced treatment of statistical analysis of progressive demagnetization data.

FIELD TESTS OF PALEOMAGNETIC STABILITY:

E. Irving, *Paleomagnetism and Its Application to Geological and Geophysical Problems*, Wiley & Sons, New York, 399 pp., 1964.

Chapter 4 presents a very useful discussion of the development and application of field tests.

J. W. Graham, The stability and significance of magnetism in sedimentary rocks, *J. Geophys. Res.*, v. 54, 131–167, 1949.

A classic paper which introduces several field tests.

A. Cox and R. R. Doell, Review of Paleomagnetism, *Geol. Soc. Amer. Bull.*, v. 71, 645–768, 1960.

Several illustrations of field tests are presented.

PROBLEMS

- 5.1 A diagram (Figure 5.2) plotting SD grain volume, v , versus microscopic coercive force, h_c , was used to explain the theory of thermal demagnetization. Part of that diagram is shown in Figure 5.17. Using this $v-h_c$ diagram, develop a qualitative explanation for the observation that AF demagnetization generally fails to remove VRM from rocks with hematite as the dominant ferromagnetic mineral.

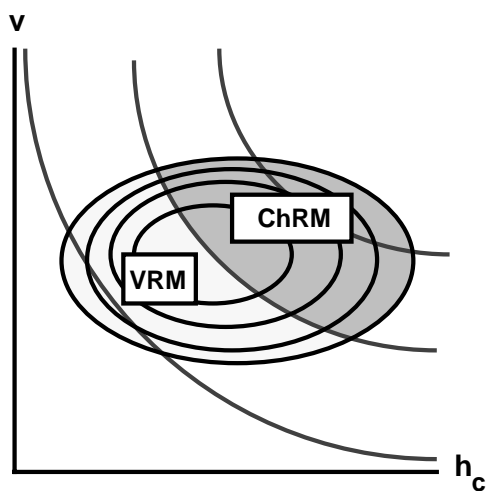


Figure 5.17 Grain volume (v) versus microscopic coercive force (h_c) for a hypothetical population of SD grains. Symbols and contours as in Figure 5.2.

- 5.2 Vector component diagrams illustrating progressive demagnetization data for two paleomagnetic samples are shown in Figure 5.18. These samples are from volcanic rocks containing magnetite as the dominant ferromagnetic mineral.
- Using a protractor to measure angles of line segments in Figure 5.18a, estimate the direction of the ChRM revealed by this progressive demagnetization experiment.
 - Applying the same procedure to Figure 5.18b, estimate the direction of the secondary component of NRM that is removed between AF demagnetization levels 2.5 mT and 10 mT.
- 5.3 Paleomagnetic samples were collected at two locations within a Permian red sedimentary unit. This unit is gently folded and overlain by flat-lying Middle Triassic limestones. There is no evidence suggesting plunging folds. The present geomagnetic field direction in the region of collection is $I = 60^\circ$, $D = 16^\circ$. At site 1, six samples were collected, and the NRM directions are listed below. Bedding at site 1 has the following attitude: dip = 15° , dip azimuth = 130° (strike = 220°). After thermal demagnetization, the ChRM directions of the samples from site 1 cluster about a direction $I = -4^\circ$, $D = 165^\circ$. At site 2, six samples were also collected, and the measured NRM directions are

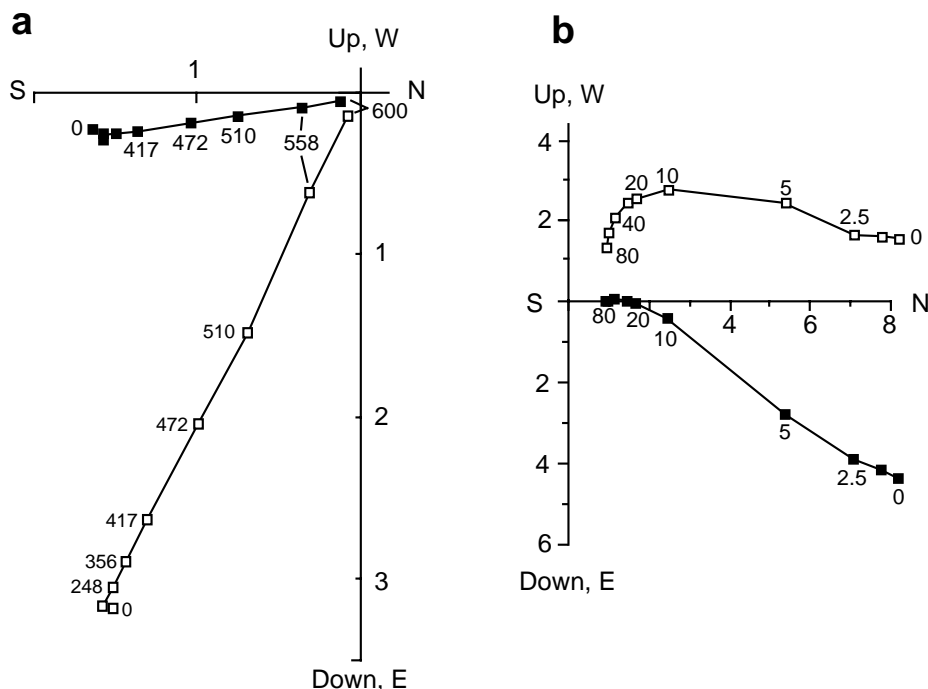


Figure 5.18 Vector component diagrams. **(a)** Progressive thermal demagnetization results for one sample; the numbers adjacent to data points are temperatures in degrees Celsius; open data points are vector end points projected onto a north-south oriented vertical plane; solid data points are vector end points projected onto the horizontal plane; numbers on axes are in A/m. **(b)** Progressive AF demagnetization results for another sample. Conventions and labels as for part **(a)**, except that numbers adjacent to the data points indicate H_{AF} (in mT); the NRM of this sample contains a large secondary lightning-induced IRM.

listed below. Bedding at site 2 has the following attitude: dip = 20°, dip azimuth = 290° (strike = 20°). After thermal demagnetization, the ChRM directions of the samples from site 2 cluster about a direction $I = -28^\circ$, $D = 174^\circ$. From these data, what can you conclude about (1) the presence of secondary components of NRM, (2) the likely origin of any secondary components of NRM, (3) the age of the ChRM? You will want to illustrate your answer by plotting directions on an equal-area projection.

| Site 1 NRM Directions: | | Site 2 NRM Directions: | |
|------------------------|---------|------------------------|---------|
| I (°) | D (°) | I (°) | D (°) |
| -2 | 164 | -27 | 174 |
| 37 | 151 | 62 | 158 |
| 10 | 162 | -20 | 175 |
| 31 | 154 | 76 | 94 |
| 69 | 46 | -11 | 175 |

STATISTICS OF PALEOMAGNETIC DATA

The need for statistical analysis of paleomagnetic data has become apparent from the preceding chapters. For instance, we require a method for determining a mean direction from a set of observed directions. This method should provide some measure of uncertainty in the mean direction. Additionally, we need methods for testing the significance of field tests of paleomagnetic stability. Basic statistical methods for analysis of directional data are introduced in this chapter. It is sometimes said that statistical analyses are used by scientists in the same manner that a drunk uses a light pole: more for support than for illumination. Although this might be true, statistical analysis is fundamental to any paleomagnetic investigation. An appreciation of the basic statistical methods is required to understand paleomagnetism.

Most of the statistical methods used in paleomagnetism have direct analogies to “planar” statistics. We begin by reviewing the basic properties of the normal distribution (Gaussian probability density function). This distribution is used for statistical analysis of a wide variety of observations and will be familiar to many readers. Statistical analysis of directional data are developed by analogy with the normal distribution. Although the reader might not follow all aspects of the mathematical formalism, this is no cause for alarm. Graphical displays of functions and examples of statistical analysis will provide the more important intuitive appreciation for the statistics.

THE NORMAL DISTRIBUTION

Any statistical method for determining a mean (and confidence limit) from a set of observations is based on a *probability density function*. This function describes the distribution of observations for a hypothetical, infinite set of observations called a *population*. The *Gaussian probability density function (normal distribution)* has the familiar bell-shaped form shown in Figure 6.1. The meaning of the probability density function $f(z)$ is that the proportion of observations within an interval of width dz centered on z is $f(z) dz$.

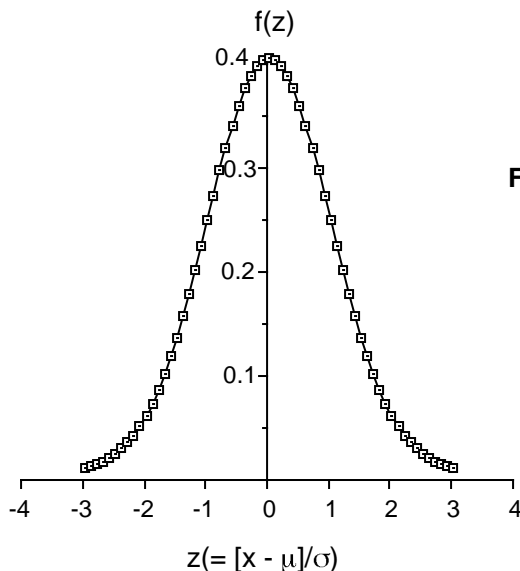


Figure 6.1 The Gaussian probability density function (normal distribution, Equation (6.1)). The proportion of observations within an interval dz centered on z is $f(z)dz$; x = measured quantity; μ = true mean; σ = standard deviation.

The normal distribution is given by

$$f(z) = \frac{1}{\sigma\sqrt{2\pi}} \exp\left(\frac{-z^2}{2}\right) \quad (6.1)$$

where

$$z = \frac{(x - \mu)}{\sigma}$$

x is the variable measured, μ is the *true mean*, and σ is the *standard deviation*. The parameter μ determines the value of x about which the distribution is centered, while σ determines the width of the distribution about the true mean. By performing the required integrals (computing area under curve $f(z)$), it can be shown that 68% of the readings in a normal distribution are within σ of μ , while 95% are within 2σ of μ .

The usual situation is that one has made a finite number of measurements of a variable x . In the literature of statistics, this set of measurements is referred to as a *sample*. By using the methods of Gaussian statistics, one is supposing that the observed sample has been drawn from a population of observations that is normally distributed. The true mean and standard deviation of the population are, of course, unknown. But the following methods allow estimation of these quantities from the observed sample.

The best estimate of the true mean (μ) is given by the mean, m , of the measured values:

$$m = \frac{\sum_{i=1}^n x_i}{n} \quad (6.2)$$

where n is the number of measurements, and x_i is an individual measurement.

The *variance* of the sample is

$$\text{var}(x) = \frac{\sum_{i=1}^n (x_i - m)^2}{(n - 1)} = s^2 \quad (6.3)$$

The *estimated standard deviation* of the sample is s and provides the best estimate of the standard deviation (σ) of the population from which the sample was drawn. The *estimated standard error of the mean*, Δm , is given by

$$\Delta m = \frac{s}{\sqrt{n}} \quad (6.4)$$

Some intuitive understanding of the effects of sampling errors can be gotten by the following theoretical results. For multiple samples drawn from the same normal distribution, 68% of the sample means will be within σ / \sqrt{n} of μ and 95% of sample means will be within $2\sigma / \sqrt{n}$ of μ . So the sample means are themselves normally distributed about the true mean with standard deviation σ / \sqrt{n} .

The estimated standard error of the mean, Δm , provides a *confidence limit* for the calculated mean. Of all the possible samples that can be drawn from a particular normal distribution, 95% have means, m , within $2\Delta m$ of μ . (Only 5% of possible samples have means that lie farther than $2\Delta m$ from μ .) Thus the 95% confidence limit on the calculated mean, m , is $2\Delta m$, and we are 95% certain that the true mean of the population from which the sample was drawn lies within $2\Delta m$ of m .

It should be appreciated and emphasized that the estimated standard deviation, s , does not fundamentally depend upon the number of observations, n . However, the estimated standard error of the mean, Δm , does depend on n and decreases as $1 / \sqrt{n}$. Because we imagine each sample as having been drawn from

a normal distribution with a definite true mean and standard deviation, it follows that our best estimate of the standard deviation does not depend on the number of observations in the sample. However, it is also reasonable that a larger sample will provide a more precise estimation of the true mean, and this is reflected in the smaller confidence limit with increasing n .

THE FISHER DISTRIBUTION

A probability density function applicable to paleomagnetic directions was developed by the British statistician R. A. Fisher and is known as the *Fisher distribution*. Each direction is given unit weight and is represented by a point on a sphere of unit radius. The Fisher distribution function $P_{dA}(\theta)$ gives the probability per unit angular area of finding a direction within an angular area, dA , centered at an angle θ from the true mean. The angular area, dA , is expressed in steradians, with the total angular area of a sphere being 4π steradians. Directions are distributed according to the probability density function

$$P_{dA}(\theta) = \frac{\kappa}{4\pi \sinh(\kappa)} \exp(\kappa \cos \theta) \tag{6.5}$$

where θ is the angle from true mean direction ($= 0$ at true mean), and κ is the *precision parameter*.

The notation $P_{dA}(\theta)$ is used to emphasize that this is a probability per unit angular area.

The distribution of directions is azimuthally symmetric about the true mean. κ is a measure of the concentration of the distribution about the true mean direction. κ is 0 for a distribution of directions that is uniform over the sphere and approaches ∞ for directions concentrated at a point. $P_{dA}(\theta)$ is shown in Figure 6.2a for $\kappa = 5, 10$, and 50 . As expected from the definition, the Fisher distribution is maximum at the true mean ($\theta = 0$), and, for higher κ , the distribution is more strongly concentrated towards the true mean.

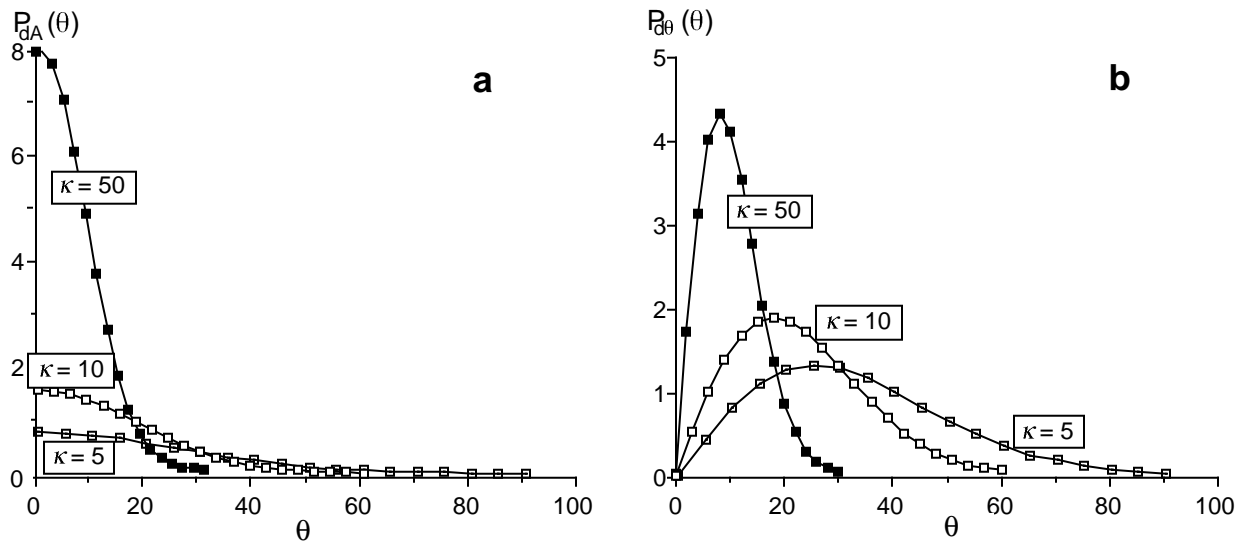


Figure 6.2 The Fisher distribution. (a) $P_{dA}(\theta)$ is shown for $\kappa = 50, \kappa = 10$, and $\kappa = 5$. $P_{dA}(\theta)$ is the probability per unit angular area of finding a direction within an angular area, dA , centered at an angle θ from the true mean; $P_{dA}(\theta)$ is given by Equation (6.5); $\kappa =$ precision parameter. (b) $P_{d\theta}(\theta)$ is shown for $\kappa = 50, \kappa = 10$, and $\kappa = 5$. $P_{d\theta}(\theta)$ is the probability of finding a direction within a band of width $d\theta$ between θ and $\theta + d\theta$. $P_{d\theta}(\theta)$ is given by Equation (6.8).

If ξ is taken as the azimuthal angle about the true mean direction, the probability of a direction within an angular area, dA , can be expressed as

$$P_{dA}(\theta)dA = P_{dA}(\theta) \sin(\theta) d\theta d\xi \tag{6.6}$$

The $\sin(\theta)$ term arises because the area of a band of width $d\theta$ varies as $\sin(\theta)$. It should be understood that the Fisher distribution is normalized so that

$$\int_{\xi=0}^{2\pi} \int_{\theta=0}^{\pi} P_{dA}(\theta) \sin(\theta) d\theta d\xi = 1.0 \quad (6.7)$$

Equation (6.7) simply indicates that the probability of finding a direction somewhere on the unit sphere must be 1.0. The probability $P_{d\theta}(\theta)$ of finding a direction in a band of width $d\theta$ between θ and $\theta + d\theta$ is given by

$$\begin{aligned} P_{d\theta}(\theta) &= \int_{\xi=0}^{2\pi} P_{dA}(\theta) dA = 2\pi P_{dA}(\theta) \sin(\theta) d\theta \\ &= \frac{\kappa}{2 \sinh(\kappa)} \exp(\kappa \cos \theta) \sin \theta d\theta \end{aligned} \quad (6.8)$$

This probability (for $\kappa = 5, 10,$ and 50) is shown in Figure 6.2b, where the effect of the $\sin(\theta)$ term is apparent.

The angle from the true mean within which a chosen percentage of directions lie can also be calculated from the Fisher distribution. The angle within which 50% of directions lie is

$$\theta_{50} = \frac{67.5^\circ}{\sqrt{\kappa}} \quad (6.9)$$

and is analogous to the *interquartile* of the normal distribution. The angle analogous to the standard deviation of the normal distribution is

$$\theta_{63} = \frac{81^\circ}{\sqrt{\kappa}} \quad (6.10)$$

This angle is often called the *angular standard deviation*. But notice that only 63% of directions lie within θ_{63} of the true mean direction, while 68% of observations in a normal distribution lie within σ of μ . The final critical angle of interest is that containing 95% of directions and given by

$$\theta_{95} = \frac{140^\circ}{\sqrt{\kappa}} \quad (6.11)$$

Computing a mean direction

The above equations apply to a population of directions that are distributed according to the Fisher probability density function. But we commonly have only a small sample of directions (e.g., a data set of ten directions) for which we must calculate (1) a mean direction, (2) a statistic indicating the amount of scatter of the directions (analogous to the estimated standard deviation in Gaussian statistics), and (3) a confidence limit for the calculated mean direction (analogous to the estimated standard error of the mean). By employing the Fisher distribution, the following calculation scheme can provide the desired quantities.

The mean of a set of directions is found simply by vector addition (Figure 6.3). To compute the mean direction from a set of N unit vectors, the direction cosines of the individual vectors are first determined by

$$l_i = \cos I_i \cos D_i \quad m_i = \cos I_i \sin D_i \quad n_i = \sin I_i \quad (6.12)$$

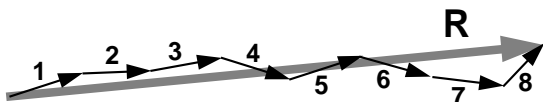


Figure 6.3 Vector addition of eight unit vectors to yield resultant vector R .

where D_i is the declination of the i vector; l_i is the inclination of the i vector; and l_i , m_i , and n_i are the direction cosines of the i vector with respect to north, east, and down directions. The direction cosines, l , m , and n , of the mean direction are given by

$$l = \frac{\sum_{i=1}^N l_i}{R} \quad m = \frac{\sum_{i=1}^N m_i}{R} \quad n = \frac{\sum_{i=1}^N n_i}{R} \quad (6.13)$$

where R is the resultant vector with length R given by

$$R^2 = \left(\sum_{i=1}^N l_i \right)^2 + \left(\sum_{i=1}^N m_i \right)^2 + \left(\sum_{i=1}^N n_i \right)^2 \quad (6.14)$$

The relationship of R to the N individual unit vectors is shown in Figure 6.3. R is always $\leq N$ and approaches N only when the vectors are tightly clustered. From the mean direction cosines given by Equations (6.13) and (6.14), the declination and inclination of the mean direction can be computed by

$$D_m = \tan^{-1}\left(\frac{m}{l}\right) \quad \text{and} \quad I_m = \sin^{-1}(n) \quad (6.15)$$

Dispersion estimates

Having calculated the mean direction, the next objective is to determine a statistic that can provide a measure of the dispersion of the population of directions from which the sample data set was drawn. One measure of the dispersion of a population of directions is the precision parameter, κ . From a finite sample set of directions, κ is unknown, but a best estimate of κ can be calculated by

$$k = \frac{N-1}{N-R} \quad (6.16)$$

Examination of Figure 6.3 provides intuitive insight into Equation (6.16). It can readily be seen that k increases as R approaches N for a tightly clustered set of directions.

By direct analogy with Gaussian statistics (Equation (6.3)), the angular variance of a sample set of directions is

$$s^2 = \frac{1}{N-1} \sum_{i=1}^N \Delta_i^2 \quad (6.17)$$

where Δ_i is the angle between the i direction and the calculated mean direction. The *estimated angular standard deviation* (often called *angular dispersion*) is simply s . As expected from Equation (6.10), s can be approximated by

$$s \approx \frac{81^\circ}{\sqrt{k}} \quad (6.18)$$

Another statistic, δ , which is often used as a measure of angular dispersion (and is often called the angular standard deviation) is given by

$$\delta = \cos^{-1}\left(\frac{R}{N}\right) \quad (6.19)$$

The advantages of using δ for an estimated angular standard deviation are ease of calculation and the intuitive appeal (e.g., Figure 6.3) that δ decreases as R approaches N and the set of directions becomes more tightly clustered. In practice (at least for reasonable values of $N \geq 10$),

$$s \approx \delta \approx \frac{81^\circ}{\sqrt{k}} \quad (6.20)$$

Although s from Equation (6.17) is the rigorously correct estimator of angular standard deviation, all of the above techniques will yield essentially the same result.

In analyzing paleomagnetic directions, it is common to report the statistic k as a measure of *within-site* scatter of directions (from multiple samples of a site). When an analysis is made of *between-site* dispersion of directions (dispersion of mean directions from one site to another), one of the above measures of angular dispersion is usually reported.

A confidence limit

We need a method for determining a confidence limit for the calculated mean direction. This confidence limit is analogous to the estimated standard error of the mean Δm of Gaussian statistics. For Fisher statistics, the confidence limit is expressed as an angular radius from the calculated mean direction. A probability level must be indicated for the confidence limit to be fully defined.

For a directional data set with N directions, the angle $\alpha_{(1-p)}$ within which the unknown true mean lies at confidence level $(1 - p)$ is given by

$$\cos \alpha_{(1-p)} = 1 - \frac{N - R}{R} \left\{ \left(\frac{1}{p} \right)^{\frac{1}{N-1}} - 1 \right\} \quad (6.21)$$

The usual choice of probability level $(1 - p)$ is 0.95 (= 95%), and the confidence limit is usually denoted as α_{95} . Two convenient approximations (reasonably accurate for both $k \geq 10$ and $N \geq 10$) are

$$\alpha_{63} \approx \frac{81^\circ}{\sqrt{kN}} \quad \text{and} \quad \alpha_{95} \approx \frac{140^\circ}{\sqrt{kN}} \quad (6.22)$$

The α_{63} is analogous to the estimated standard error of the mean, while α_{95} is analogous to two estimated standard errors of the mean.

When we calculate the mean direction, a dispersion estimate, and a confidence limit, we are supposing that the observed data came from random sampling of a population of directions accurately described by the Fisher distribution. But we do not know the true mean of that Fisherian population, nor do we know its precision parameter κ . We can only estimate these unknown parameters. The calculated mean direction of the directional data set is the best estimate of the true mean direction, while k is the best estimate of κ . The confidence limit α_{95} is a measure of the precision with which the true mean direction has been estimated. One is 95% certain that the unknown true mean direction lies within α_{95} of the calculated mean. The obvious corollary is that there is a 5% chance that the true mean lies more than α_{95} from the calculated mean.

Some illustrations

Having buried the reader in mathematical formulations, we present the following illustrations to develop some intuitive appreciation for the statistical quantities. One essential concept is the distinction between statistical quantities calculated from a directional data set and the unknown parameters of the sampled population.

The six synthetic directional data sets illustrated in Figure 6.4 were generated and analyzed in the following manner:

1. A population of directions distributed according to the Fisher probability density distribution was generated by computer. The true mean direction of this Fisherian population was $I = +90^\circ$ (directly downward) and the precision parameter was $\kappa = 20$.
2. This Fisher distribution was randomly sampled 20 times to produce a “synthetic” directional data set with $N = 20$. A total of six such data sets were produced, each being an independent random sampling of the same population of directions. These six data sets are shown on the equal-area projections of Figure 6.4.
3. For each synthetic data set, the following quantities were calculated: (a) mean direction (D_m, I_m), (b) k , and (c) the confidence limit α_{95} . These quantities are also illustrated for each data set in Figure 6.4.

There are several important observations to be taken from this example. Note that the calculated mean direction is never exactly the true mean direction ($I = +90^\circ$). The calculated mean inclination I_m varies from 85.7° to 88.8° , and at least one calculated mean declination falls within each of the four quadrants of the equal-area projection. The calculated mean direction thus randomly dances about the true mean direction and varies from the true mean by between 1.2° and 4.3° .

The calculated k statistic varies considerably from one synthetic data set to another with a range of 17.3 to 27.2 that contains the known precision parameter $\kappa = 20$. The variation of k and differences in angular variance of the data sets are simply due to the vagaries of random sampling. (Techniques for determining confidence limits for k do exist. When applied to these data sets, none of the k values is, in fact, significantly removed from the known value $\kappa = 20$ at 95% confidence. See Suggested Readings for these techniques.)

The confidence limit α_{95} varies from 6.0° to 7.5° and is shown by the stippled oval surrounding the calculated mean direction. For these six directional data sets, none has a calculated mean that is more than α_{95} from the true mean. However, if 100 such synthetic data sets had been analyzed, on average five data sets would have a calculated mean direction removed from the true mean direction by more than the calculated confidence limit α_{95} . That is, the true mean direction would lie outside the circle of 95% confidence, on average, in 5% of the cases.

It is also important to appreciate which statistical quantities are fundamentally dependent upon the number of observations N . Neither the k value (Equation (6.16)) nor the estimated angular deviation s or δ (Equation (6.18) or (6.19)) is fundamentally dependent upon N . These statistical quantities are estimates of the intrinsic dispersion of directions in the Fisherian population from which the data set was sampled. Because that dispersion is not affected by the number of times the population is sampled, the calculated statistics estimating that dispersion should not depend fundamentally on the number of observations N .

However, the confidence limit α_{95} should depend on N ; the more individual measurements there are in our sample, the greater must be the precision in estimating the true mean direction. This increased precision should be reflected by a decrease in α_{95} with increasing N . Indeed Equation (6.22) indicates that α_{95} depends approximately on $1/\sqrt{N}$.

Figure 6.5 illustrates these dependences of calculated statistics on number of directions in a data set. The following procedure was used to construct this diagram:

1. A synthetic data set of $N = 30$ was randomly sampled from a Fisherian population of directions with angular standard deviation $\theta_{63} = 15^\circ$ ($\kappa = 29.2$).
2. Starting with the first four directions in the synthetic data set, a subset of $N = 4$ was used to estimate κ and θ_{63} by calculating k and s from Equations (6.16) and (6.20), respectively. In addition, α_{95} (using Equation (6.21)) was calculated. Resulting s and α_{95} values are plotted at $N = 4$ in Figure 6.5.

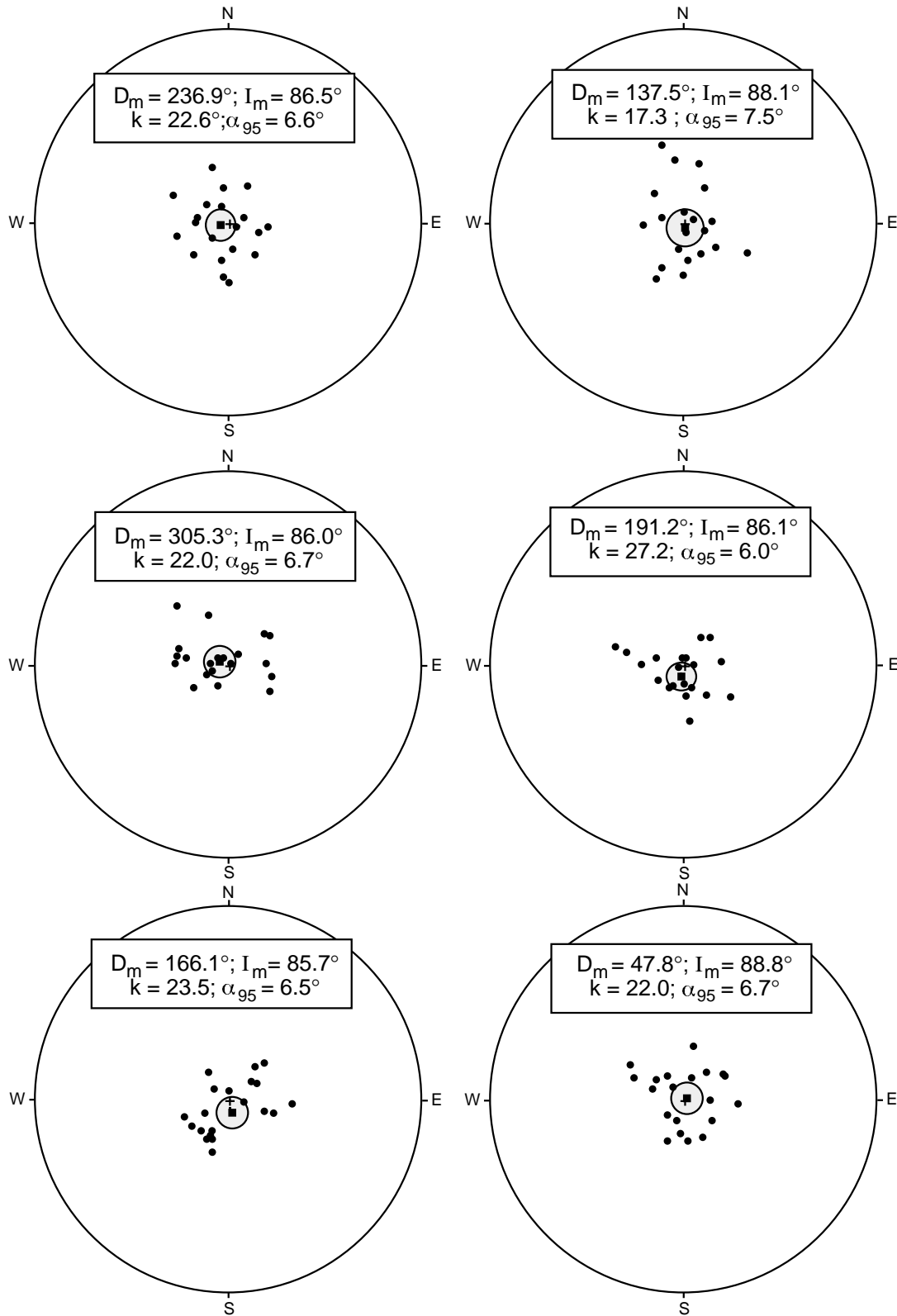


Figure 6.4 Equal-area projections of six synthetic directional data sets, mean directions, and statistical parameters. The data sets were randomly selected from a Fisherian population with true mean direction $I = +90^\circ$ and precision parameter $\kappa = 20$; individual directions are shown by solid circles; mean directions are shown by solid squares with surrounding stippled α_{95} confidence limits.

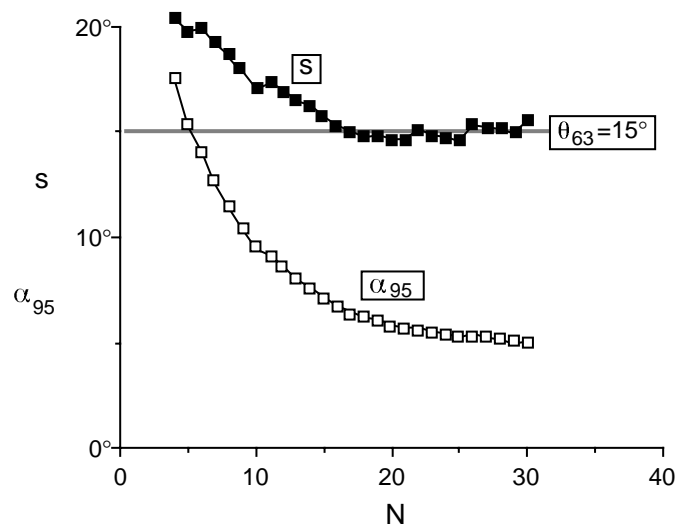


Figure 6.5 Dependence of estimated angular standard deviation, s , and confidence limit, α_{95} , on the number of directions in a data set. An increasing number of directions were selected from a Fisherian population of directions with angular standard deviation $\theta_{63} = 15^\circ$ ($\kappa = 29.2$) shown by the stippled line.

- For each succeeding value of N in Figure 6.5, the next direction from the $N = 30$ synthetic data set was added to the previous subset of directions, continuing until the full $N = 30$ synthetic data set was utilized.

The effects of increasing N are readily apparent in Figure 6.5. Although not fundamentally dependent upon N , in practice the estimated angular standard deviation, s , systematically overestimates the angular standard deviation θ_{63} for values of $N < 10$. (If uncertainties in the calculated values of s are considered, it is found that these errors become quite large for $N < 10$.) For $N > 10$, the calculated value of s approaches the known angular standard deviation $\theta_{63} = 15^\circ$. As expected, the calculated confidence limit α_{95} decreases approximately as $1/\sqrt{N}$, showing a dramatic decrease in the range $4 \leq N \leq 10$ and more gradual decrease for $N > 10$.

Another example of the effects of increasing N on the calculated statistical quantities is provided in Figure 6.6. The following procedure was used:

- Two independent synthetic directional data sets of $N = 50$ were randomly selected from a Fisherian population of directions with angular standard deviation $\theta_{63} = 15^\circ$. The true mean direction is vertically down ($I = +90^\circ$).
- Two subsets of these $N = 50$ data sets were then produced by selecting the first five directions, to yield two sets of $N = 5$, then the first ten directions, to yield two sets of $N = 10$.
- The mean of each of the six data sets was calculated along with the statistics k , s , and α_{95} as described in the example above.

The resulting data sets are illustrated in the equal-area projections of Figure 6.6. The results are arranged in two columns: the left-hand column resulting from the first $N = 50$ synthetic data set and the right-hand column resulting from the second $N = 50$ data set. As expected, the calculated mean direction provides a "better" estimation of the true mean as the number of directions, N , increases. This effect is most dramatic when the results for $N = 5$ are compared with those for $N = 10$. Notice that the mean directions calculated from the two $N = 5$ data sets are $\sim 15^\circ$ apart. For the $N = 10$ and $N = 50$ data sets, the calculated mean directions quite closely approximate the true mean direction, and the α_{95} continues to decrease.

Non-Fisherian distributions

The Fisher distribution is azimuthally symmetric about the true mean direction. Occasionally, in analysis of paleomagnetic data, a set of directions that is strongly elliptical in shape is encountered. A statistical method allowing treatment of such data is sometimes required. The *Bingham distribution* (see Suggested Read-

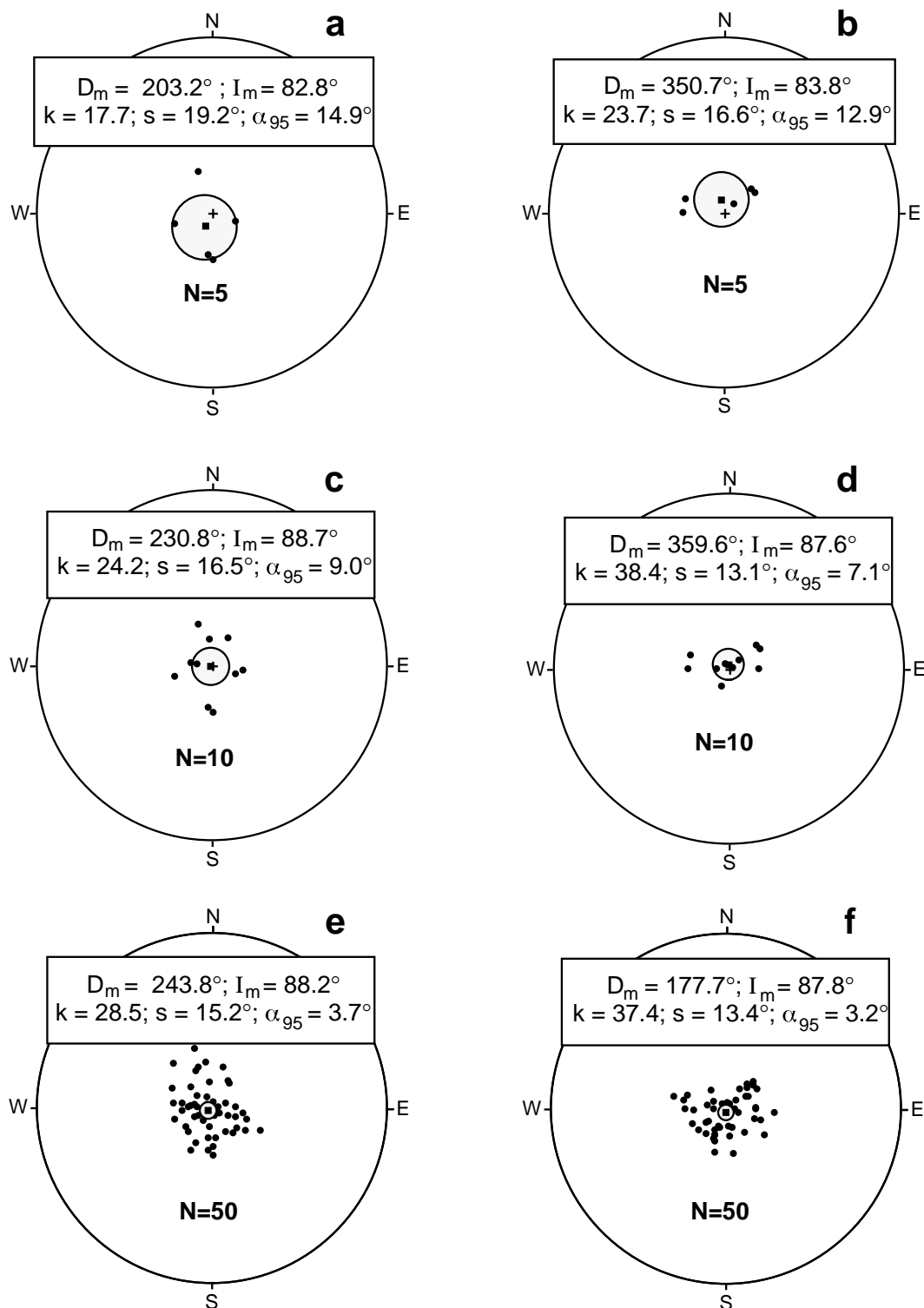


Figure 6.6 Equal-area projections showing mean directions and statistical quantities calculated from increasing numbers of directions drawn from two synthetic directional data sets. The Fisherian population had angular standard deviation $\theta_{63} = 15^\circ$ and true mean direction $I = +90^\circ$; results from one data set are shown in parts (a), (c), and (e) and for the other data set in parts (b), (d), and (f); individual directions are shown by solid circles; mean directions are shown by solid squares with surrounding stippled α_{95} confidence limits.

ings) allows for azimuthal asymmetry and is appropriate for such analyses. Some researchers prefer the Bingham distribution to the Fisher distribution for statistical analysis of all paleomagnetic data. However, the Fisher distribution remains the basis of most statistical treatments in paleomagnetism because (1) Fisher statistics provides fairly straightforward techniques for determining confidence limits, whereas the Bingham distribution does not, and (2) significance tests based on the Fisher distribution are fairly simple and have intuitive appeal, whereas significance tests based on the Bingham distribution are more complex.

SITE-MEAN DIRECTIONS

There are several levels of paleomagnetic data analysis at which mean directions must be calculated:

1. If more than one specimen was prepared from a sample, then ChRM directions for the multiple specimens must be averaged.
2. A site-mean ChRM direction is then calculated from the sample ChRM directions.
3. Generally, a paleomagnetic investigation involves numerous sites within a particular rock unit. These site-mean directions must be averaged to yield either the average ChRM direction or a paleomagnetic pole position from the rock unit.

Straightforward application of the Fisher statistical procedures (Equations (6.12)–(6.15)) is used to calculate both sample-mean directions and site-mean directions. For site-mean directions, R , k and α_{95} are often listed in a table of data. Each site-mean direction ideally provides a record of the geomagnetic field direction at a single point in time. The desired result is that site-mean directions are precisely determined. But it is important to gain an appreciation for the range of results that are actually observed.

Figure 6.7 illustrates examples of sample and site-mean ChRM directions grading from “fantastic” to “poor.” The site-mean result shown in Figure 6.7a is from a single lava flow containing essentially no secondary components of NRM. The ChRM direction for each sample was revealed over a large range of peak AF demagnetization fields. Anchored line-fits from principal component analysis (p.c.a.) were extraordinarily well defined (MAD angles $\sim 1^\circ$). For the nine samples collected from this site, the sample ChRM directions are so tightly grouped that they cannot be resolved on the equal-area plot of Figure 6.7a! The site-mean direction has $k = 2389$ and $\alpha_{95} = 1.1^\circ$. Such precisely determined site-mean directions are uncommon and generally observed only in very fresh volcanic rocks. Paleomagnetists dream about rocks like this but do not often find them.

In Figure 6.7b, a more typical “good” result from a basalt flow is shown. Minor secondary NRM components (probably lightning-induced IRM) were removed during AF demagnetization to reveal a ChRM direction for each of the seven samples. These sample ChRM directions are reasonably well clustered and yield a site-mean direction with $k = 134$ and $\alpha_{95} = 4.6^\circ$. Site-mean directions with $k \approx 100$ and $\alpha_{95} \approx 5^\circ$ would be considered good quality paleomagnetic results and are typical of fresh volcanic rocks. Well-behaved intrusive igneous rocks and red sediments also can yield paleomagnetic data of similar quality.

The clustering of sample ChRM directions shown in Figure 6.7c is only “fair.” These results are from a single bed of Mesozoic red siltstone. Substantial secondary VRM was present in samples from this site, and thermal demagnetization into the 600° to 660°C range was required to isolate the ChRM. Anchored lines (from p.c.a.) fit to four progressive thermal demagnetization results for each sample within the 600° to 660°C range had average MAD $\approx 10^\circ$. When plotted on a vector component diagram, the progressive thermal demagnetization data are similar to those of Figure 5.7b. Even with this detailed analysis, the sample ChRM directions are not particularly well clustered. The resulting site-mean direction has $k = 42.5$ and $\alpha_{95} = 11.9^\circ$. This site-mean direction was considered acceptable for inclusion in the set of site means used to calculate a paleomagnetic pole. However, this site-mean result was one of the least precise of the 23 site-mean directions considered acceptable.

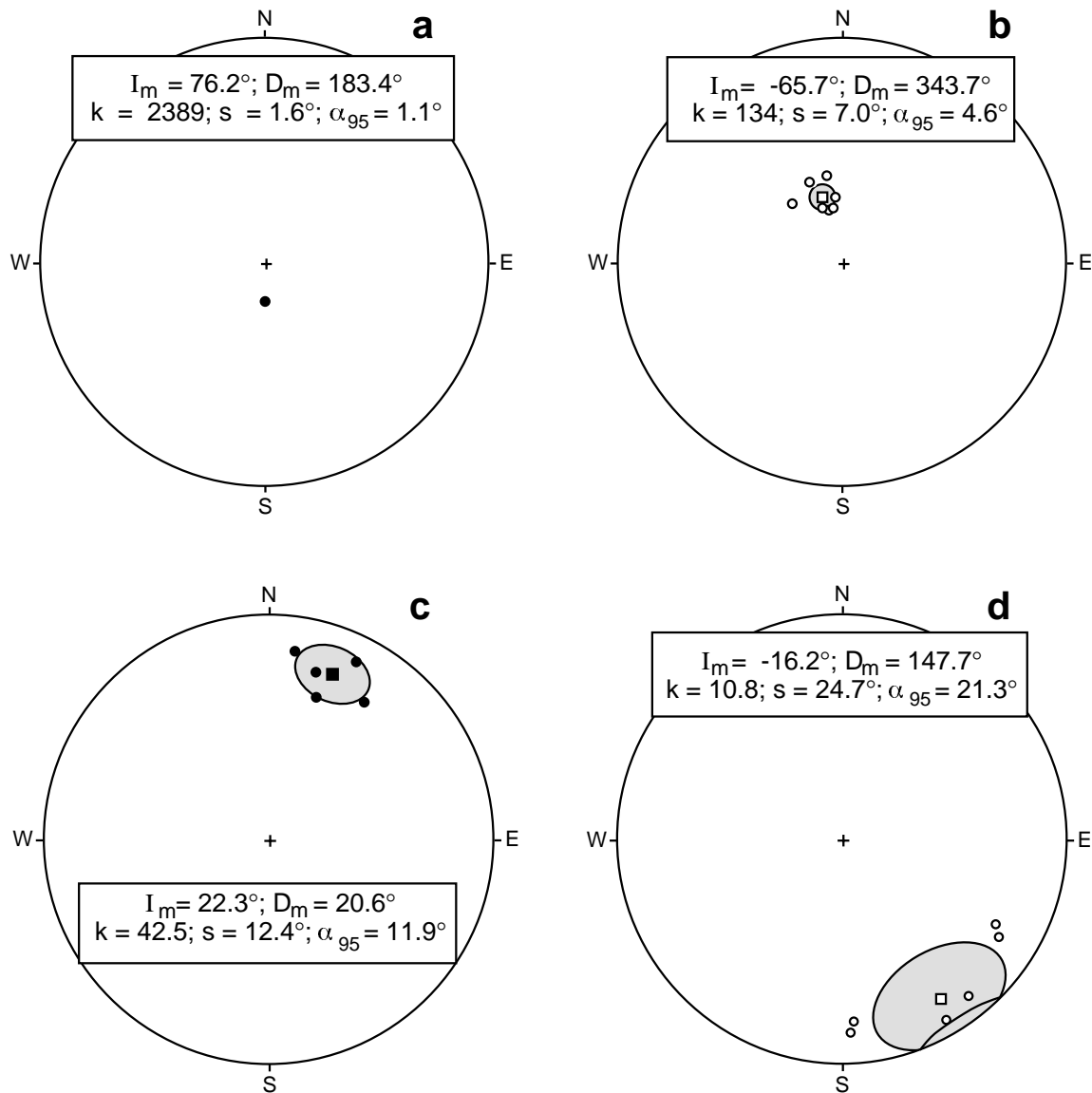


Figure 6.7 Equal-area projections showing examples of sample and site-mean ChRM directions. Sample ChRM directions are shown by circles; site-mean directions are shown by squares with surrounding stippled α_{95} confidence limits; directions in the lower hemisphere are shown by solid symbols; directions in the upper hemisphere are shown by open symbols. (a) Unusually well-determined site-mean direction from a single Late Cretaceous lava flow in southern Chile. (b) More typical “good” site-mean direction from a Late Cretaceous basalt flow in southern Argentina. (c) Site-mean direction determined with “fair” precision from a bed of red siltstone in the Early Jurassic Moenave Formation of northern Arizona. (d) A “poor”-quality site-mean direction from a bed of the Late Triassic Chinle Formation in eastern New Mexico.

In Figure 6.7d, “poor”-quality results obtained from a site in Mesozoic red sediment are shown. Despite thermal demagnetization at numerous temperatures and analysis of progressive demagnetization data using p.c.a., the ChRM directions for samples from this site are scattered. The site-mean direction is correspondingly poorly determined. Most paleomagnetists would regard the results from this site as unacceptable for inclusion in a set of site means from which a paleomagnetic pole might be determined. However, these results might still be useful for determination of polarity of ChRM.

Although no firm criteria exist for acceptability of paleomagnetic data, within-site $k > 30$ and $\alpha_{95} < 15^\circ$ would generally be regarded as minimally acceptable site-mean results from which a paleomagnetic pole could be determined. The above examples illustrate that precisely determined site-mean directions (minimal *within-site dispersion*) are desired. The situation for dispersion of site-mean directions (*between-site dispersion*) is considerably more complex. Let's defer consideration of this subject until techniques for calculation of paleomagnetic poles are presented in the next chapter.

SIGNIFICANCE TESTS

From examples of field tests of paleomagnetic stability given in Chapter 5, it is evident that techniques for quantitative evaluation of those tests are required. We must be able to give quantitative answers to such questions as the following: (1) Are two paleomagnetic directions significantly different from one another? (2) Does a set of site-mean directions pass the bedding-tilt test, as evidenced by significantly improved clustering of directions following structural correction? Quantitative evaluations of these questions require *statistical significance tests*.

There are two fundamental principles of statistical significance tests that are important to the proper interpretation:

1. Tests are generally made by comparing an observed sample with a *null hypothesis*. For example, in comparing two mean paleomagnetic directions, the null hypothesis is that the two mean directions are separate samples from the same population of directions. (This is the same as saying that the samples were not, in fact, drawn from different populations with distinct true mean directions.) Significance tests do not prove a null hypothesis but only show that observed differences between the sample and the null hypothesis are unlikely to have occurred because of sampling errors. In other words, there is probably a real difference between the sample and the null hypothesis, indicating that the null hypothesis is probably incorrect.
2. Any significance test must be applied by using a *level of significance*. This is the probability level at which the differences between a set of observations and the null hypothesis may have occurred by chance. A commonly used significance level is 5%. In Gaussian statistics, when testing an observed sample mean against a hypothetical population mean μ (the null hypothesis), there is only a 5% chance that μ is more than $2\Delta m$ from the mean, m , of the sample. If m differs from μ by more than $2\Delta m$, m is said to be "statistically significant from μ at the 5% level of significance," using proper statistical terminology. However, the corollary of the actual significance test is often what is reported by statements such as " m is distinct from μ at the 95% confidence level." The context usually makes the intended meaning clear, but be careful to practice safe statistics.

An important sidelight to this discussion of level of significance is that too much emphasis is often put on the 5% level of significance as a magic number. Remember that we are often performing significance tests on data sets with a small number of observations. Failure of a significance test at the 5% level of significance means only that the observed differences between sample and null hypothesis cannot be shown to have a probability of chance occurrence that is $\leq 5\%$. This does not mean that the observed differences are unimportant. Indeed the observed differences might be significant at a marginally higher level of significance (for instance, 10%) and might be important to the objective of the paleomagnetic investigation.

Significance tests for use in paleomagnetism were developed in the 1950s by Watson and Irving (see Suggested Readings). These versions of the significance tests are fairly simple, and an intuitive appreciation of the tests can be developed through a few examples. Because of their simplicity and intuitive appeal, we investigate these "traditional" significance tests in the development below. However, many of these tests have been revised by McFadden and colleagues (see Suggested Readings) using advances in statistical sampling theory. These revisions are technically superior to the traditional significance tests and are gener-

ally employed in modern paleomagnetic literature. However, they are more complex and less intuitive than the traditional tests.

There are two important points regarding the traditional versions of the significance tests as opposed to the revised versions:

1. Results of these versions of the significance tests differ only when the result is close to the critical value (at a specified significance level). If a result using the traditional version of the appropriate significance test just misses a critical value for being significant at the 5% significance level, it is worthwhile reformulating the test using the revised approach.
2. The revised significance tests are generally more “lenient” than the traditional tests. Results that are significant using the traditional tests will also be significant using the revised test. But some results that were not significant at the 5% significance level according to the traditional test might, in fact, be significant using the revised test.

Comparing directions

A very simple form of significance test is used to determine whether the mean of a directional data set is distinguishable from a known direction. The two directions are distinguishable at the 5% significance level if the known direction falls outside the α_{95} confidence limit of the mean direction. If the known direction is within α_{95} of the calculated mean, the two directions are not distinguishable at the 5% significance level. This test is often used to compare a site-mean direction with the present geomagnetic field or geocentric axial dipole field direction at the sampling locality.

Comparison of two mean directions is more complicated. If the confidence limits surrounding two mean directions do not overlap, the directions are distinct at that level of confidence. For example, if α_{95} circles surrounding two mean directions do not overlap, those directions are distinct at the 5% significance level. Another way of stating this result is that, with 95% probability, the directional data sets yielding these mean directions were selected from different populations with distinct true mean directions. In the case that one or both of the mean directions falls within the α_{95} circle of the other mean direction, the mean directions are not distinct at the 5% significance level.

For intermediate cases in which neither mean direction is contained within the α_{95} circle of the other mean but the α_{95} circles overlap, a further test of significance is required. In this test, the null hypothesis is that the two directional data sets are samplings of the same population and the difference between the means is due to sampling errors.

Consider two directional data sets: one has N_1 directions (described by unit vectors) yielding a resultant vector of length R_1 ; the other has N_2 directions yielding resultant R_2 . The statistic

$$F = (N - 2) \frac{(R_1 + R_2 - R)}{(N - R_1 - R_2)} \quad (6.23)$$

must be determined, where

$$N = N_1 + N_2$$

and R is the resultant of all N individual directions. This F statistic is compared with tabulated values for 2 and $2(N - 2)$ degrees of freedom. If the observed F statistic exceeds the tabulated value at the chosen significance level, then these two mean directions are different at that level of significance.

The tabulated F -distribution indicates how different two sample mean directions can be (at a chosen probability level) because of sampling errors. If the calculated mean directions are very different but the individual directional data sets are well grouped, intuition tells us that these mean directions are distinct. The mathematics described above should confirm this intuitive result. With two well-grouped directional data sets with very different means, $(R_1 + R_2) \gg R$, R_1 approaches N_1 , and R_2 approaches N_2 , so that

$(R_1 + R_2)$ approaches N . With these conditions, the F statistic given by Equation (6.23) will be large and will easily exceed the tabulated value. So this simple intuitive examination of Equation (6.23) yields a sensible result.

Comparison of mean directions is useful for examining the independence of site-mean directions in stratigraphic superposition. Implications of independence of site means will be discussed in the next chapter. Comparison of mean directions is also used in the reversals test for paleomagnetic stability. The mean of the normal-polarity sites is compared with the antipode of the mean of reversed-polarity sites. It is important to realize that this comparison really tests for failure of the reversals test because the null hypothesis is that the two means were selected from the same population. If the mean of normal-polarity sites is distinct from the antipode of the mean of reversed-polarity sites, then there is only a 5% chance that the two directions were samples of the same population (with one true mean direction). Such a result would constitute failure of the reversals test. The desired result ("passage of the reversals test") is that the two means are not distinct at the 5% significance level.

In the illustration of the reversals test shown in Figure 5.16, the mean of the normal-polarity sites is $I_m = 51.7^\circ$, $D_m = 345.2^\circ$, $\alpha_{95} = 5.4^\circ$. The mean of the reversed-polarity sites is $I_m = -51.0^\circ$, $D_m = 163.0^\circ$, $\alpha_{95} = 3.6^\circ$. When the antipode of the reversed-polarity mean is compared with the normal-polarity mean, these means are less than 2° from one another, and each is contained within the α_{95} circle of the other. These directions are not distinct at the 5% significance level, and the site means pass the reversals test.

Test of randomness

When widely scattered directions are observed, the question arises whether the observed directions could have resulted from sampling a random population of directions. (A random population is uniformly distributed over the sphere, has no mean direction, and has $\kappa = 0$.) Even for a directional data set selected from a random population, the observed data set (sample) will rarely have $k = 0$; sampling errors will yield finite R and finite k . But for a given number of directions, N , there is a critical value of R ($= R_0$) that is unlikely to result from an unusual sampling of a random population. If the 5% significance level is chosen and the observed R exceeds R_0 , then there is only a 5% chance that the observed directions resulted from sampling a random population. The corollary is that, with 95% probability, the directional data set resulted from sampling of a nonrandom population with $\kappa > 0$.

The test for randomness is often used in magnetostratigraphic investigations in which site-mean polarity of ChRM is the fundamental information sought. To ensure that a mean ChRM observed at a site is not simply the result of sampling from a random population, the randomness test is applied. For $N = 3$, the critical $R_0 = 2.62$, and $R > 2.62$ is required for 95% probability that the observed mean direction did not result from selection from a random population. In this application, $R > R_0$ is obviously the desired result.

In applying the test for randomness to the conglomerate test for paleomagnetic stability, the desired result is that the ChRM directions observed in clasts of a conglomerate are consistent with selection from a random population. For the conglomerate test shown in Figure 5.14, $N = 7$ and $R = 1.52$. But for $N = 7$, $R_0 = 4.18$ for 5% significance level. Because $R < R_0$, the test for randomness indicates that the observed set of directions could indeed have been selected from a random population. This result constitutes "passage of the conglomerate test."

Comparison of precision (the fold test)

In the fold test (or bedding-tilt test), one examines the clustering of directions before and after performing structural corrections. If the clustering improves on structural correction, the conclusion is that the ChRM was acquired prior to folding and therefore "passes the fold test." The appropriate significance test determines whether the improvement in clustering is statistically significant.

Consider two directional data sets, one with N_1 directions and k_1 , and one with N_2 directions and k_2 . If we assume (null hypothesis) that these two data sets are samples of populations with the same κ , the ratio k_1/k_2 is expected to vary because of sampling errors according to

$$\frac{k_1}{k_2} = \frac{\text{var}[2(N_2 - 1)]}{\text{var}[2(N_1 - 1)]} \quad (6.24)$$

where $\text{var}[2(N_2 - 1)]$ and $\text{var}[2(N_1 - 1)]$ are variances with $2(N_2 - 1)$ and $2(N_1 - 1)$ degrees of freedom. This ratio should follow the F -distribution if the assumption of common κ is correct. Fundamentally, one expects this ratio to be near 1.0 if the two samples were, in fact, selections from populations with common κ . The F -distribution tables indicate how far removed from 1.0 the ratio may be before the deviation is significant at a chosen probability level. If the observed ratio in Equation (6.24) is far removed from 1.0, then it is highly unlikely that the two data sets are samples of populations with the same κ . In that case, the conclusion is that the difference in the k values is significant and the two data sets were most likely sampled from populations with different κ .

As applied to the fold test, one examines the ratio of k after tectonic correction (k_a) to k before tectonic correction (k_b). The significance test for comparison of precisions determines whether k_a/k_b is significantly removed from 1.0. If k_a/k_b exceeds the value of the F -distribution for the 5% significance level, there is less than a 5% chance that the observed increase in k resulting from the tectonic correction is due only to sampling errors. There is 95% probability that the increase in k is meaningful and the data set after tectonic correction is a sample of a population with κ larger than the population sampled before tectonic correction. Such a result constitutes a “statistically significant passage of the fold test.”

As an example, consider the illustration of the bedding-tilt test shown in Figure 5.12. For the multiple collecting locations in the Nikolai Greenstone, $N = 5$, $k_b = 5.17$, $k_a = 21.51$, and $k_a/k_b = 4.16$. The degrees of freedom are $2(N - 1) = 8$ and the F -distribution value $F_{8,8}$ for 5% significance level is 3.44. With ratio $k_a/k_b > F_{8,8}$, the improvement in clustering produced by applying tectonic correction is significant at the 5% level. The bedding-tilt test is thus significant at the 5% significance level, implying that the ChRM was acquired prior to folding.

In examining the possibility of synfolding magnetization, the significance test is applied during a stepwise application of tectonic corrections. Results are usually reported as (1) percent unfolding producing the maximum k value and (2) range of unfolding percentage surrounding that producing maximum k over which the change in k is not significant at the 5% level.

These statistical significance tests are often crucial features of paleomagnetic investigations. Although specific cases can be complex, the background provided above should allow the reader to understand essential elements of the significance tests that are commonly used in paleomagnetism.

SUGGESTED READINGS

INTRODUCTIONS TO STATISTICAL METHODS APPLIED TO DIRECTIONAL DATA:

R. A. Fisher, Dispersion on a sphere, *Proc. Roy. Soc. London*, v. A217, 295–305, 1953.

The classic paper introducing the Fisher distribution.

E. Irving, *Paleomagnetism and Its Applications to Geological and Geophysical Problems*, John Wiley and Sons, New York, 399 pp., 1964.

Chapter 4 contains an excellent introduction to statistical methods in paleomagnetism.

D. H. Tarling, *Palaeomagnetism: Principles and Applications in Geology, Geophysics and Archaeology*, Chapman and Hall, 379 pp. 1983.

Chapter 6 presents a discussion of statistical methods.

G. S. Watson, *Statistics on Spheres*, Univ. Arkansas Lecture Notes in the Mathematical Sciences, Wiley, New York, 238 pp., 1983.

N. I. Fisher, T. Lewis, and B. J. J. Embleton, *Statistical Analysis of Spherical Data*, Cambridge, London, 329 pp., 1987.

More advanced texts on statistical analysis of directional data.

SIGNIFICANCE TESTS:

G. S. Watson, Analysis of dispersion on a sphere, *Monthly Notices Geophys. J. Roy. Astron. Soc.*, v. 7, 153–159, 1956.

G. S. Watson and E. Irving, Statistical methods in rock magnetism, *Monthly Notices Geophys. J. Roy. Astron. Soc.*, v. 7, 289–300, 1957.

G. S. Watson, A test for randomness of directions, *Monthly Notices Geophys. J. Roy. Astron. Soc.*, v. 7, 160–161, 1956.

M. W. McElhinny, Statistical significance of the fold test in palaeomagnetism, *Geophys. J. Roy. Astron. Soc.*, v. 8, 338–340, 1964.

The traditional approaches to statistical significance tests applied to paleomagnetism are introduced in these articles.

P. L. McFadden and F. J. Lowes, The discrimination of mean directions drawn from Fisher distributions, *Geophys. J. Roy. Astron. Soc.*, v. 67, 19–33, 1981.

P. L. McFadden and D. L. Jones, The fold test in palaeomagnetism, *Geophys. J. Roy. Astron. Soc.*, v. 67, 53–58, 1981.

Revised treatments of the significance tests.

SOME ADVANCED TOPICS:

T. C. Onstott, Application of the Bingham distribution function in paleomagnetic studies, *J. Geophys. Res.*, v. 85, 1500–1510, 1980.

T. Lewis and N. I. Fisher, Graphical methods for investigating the fit of a Fisher distribution for spherical data, *Geophys. J. Roy. Astron. Soc.*, v. 69, 1–13, 1982.

P. L. McFadden, The best estimate of Fisher's precision parameter k , *Geophys. J. Roy. Astron. Soc.*, v. 60, 397–407, 1980.

P. L. McFadden and A. B. Reid, Analysis of palaeomagnetic inclination data, *Geophys. J. Roy. Astron. Soc.*, v. 69, 307–319, 1982.

P. L. McFadden, Determination of the angle in a Fisher distribution which will be exceeded with a given probability, *Geophys. J. Roy. Astron. Soc.*, v. 60, 391–396, 1980.

PROBLEMS

6.1 The rigorous expression for α_{95} is Equation (6.21). A reasonable approximation can be obtained from Equation (6.22). Consider a directional data set with $N = 9$ and $R = 8.6800$. Investigate the accuracy of the approximation given by Equation (6.22) by determining α_{95} for this data set, using both Equation (6.21) and Equation (6.22).

6.2 Consider the table of ChRM directions given below from which a reversals test can be evaluated. Use Equation (6.22) to estimate α_{95} for the mean of the normal-polarity sites and for the mean of the reversed-polarity sites. Then use an equal-area projection to evaluate the reversals test (a simple comparison of the mean directions will suffice in this case).

| | N | I_m (°) | D_m (°) | R |
|--------------------------|-----|-----------|-----------|---------|
| Normal-polarity sites: | 16 | −46.8 | 26.6 | 15.4755 |
| Reversed-polarity sites: | 12 | 48.1 | 215.0 | 11.4836 |

6.3 A common response to inspection of Figures 6.2a and 6.2b is that the numbers on the probability axes are too large: “How can $P_{dA}(\theta) \approx 8$ for $\theta = 0^\circ$ and $\kappa = 50$?” But remember that $P_{dA}(\theta)$ is a probability *per unit angular area* of finding a direction within an angular area dA centered at angle θ from the true mean direction (at $\theta = 0^\circ$). To prove that the probabilities shown in Figures 6.2a and 6.2b are not too large but instead are intuitively reasonable, do the following calculation:

a. Determine the angular area, A (in steradians), of a spherical cap that is centered on $\theta = 0^\circ$ and extends to $\theta = 5^\circ$ (the angular radius is 5°). To do this calculation, recall that the angular area of a spherical cap centered on $\theta = 0^\circ$ is given by

$$A = \int_{\xi=0}^{\xi=2\pi} \int_{\theta} \sin \theta d\theta d\xi = 2\pi \int_{\theta} \sin \theta d\theta$$

where the integral is over the range of θ (0° to 5° in this case).

- b.** By inspection of Figure 6.2a, you can see that $P_{dA}(\theta)$ does not change dramatically between $\theta = 0^\circ$ and $\theta = 5^\circ$ (even for $\kappa = 50$). So the probability of finding a direction within a spherical cap centered on $\theta = 0^\circ$ with angular area A is approximately given by $P_{dA}(0^\circ)A$. Use the value of A determined above and the plot of $P_{dA}(\theta)$ in Figure 6.2a to calculate the approximate probability of finding a direction within a spherical cap centered on $\theta = 0^\circ$ and extending to $\theta = 5^\circ$ for a population of directions with $\kappa = 50$. Does your numerical result make intuitive sense?

PALEOMAGNETIC POLES

The basic procedure for calculating a magnetic pole position is introduced here. Definitions of types of magnetic poles are then presented, leading to a discussion of paleomagnetic sampling of geomagnetic secular variation. Here you acquire methods for judging the next level of paleomagnetic analysis: the data set of site-mean directions and the paleomagnetic pole determined from those directions. Examples of paleomagnetic poles and some common-sense criteria for judging reliability of paleomagnetic poles are offered.

PROCEDURE FOR POLE DETERMINATION

The inclination and declination of a dipolar magnetic field change with position on the globe. But the position of the *magnetic pole* of a geocentric dipole is independent of observing locality. For many purposes, comparison of results between various observing localities is facilitated by determining a *pole position*. This pole position is simply the geographic location of the projection of the negative end of the dipole onto the Earth's surface, as shown in Figure 7.1.

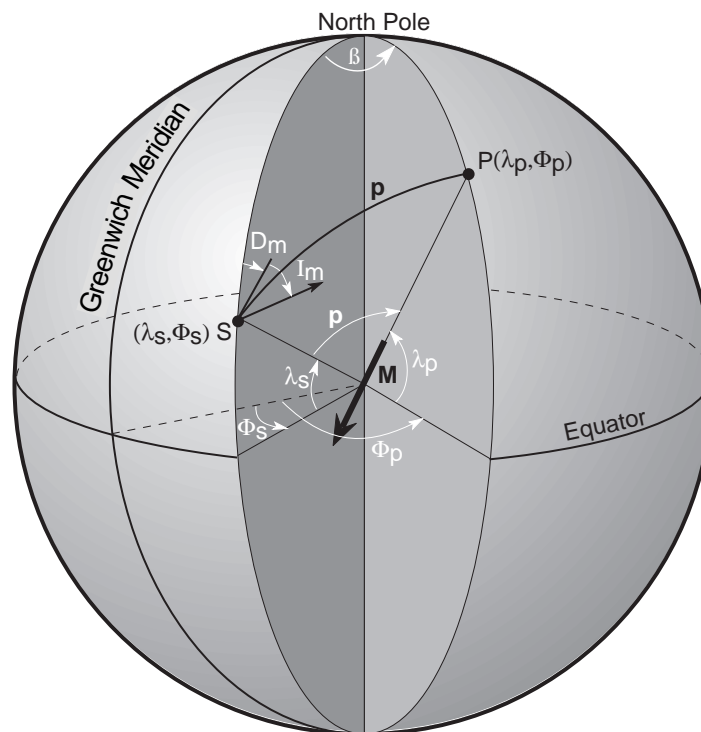


Figure 7.1 Determination of magnetic pole position from a magnetic field direction. Site location is at S (λ_s, ϕ_s); site-mean magnetic field direction is I_m , D_m ; M is the geocentric dipole that can account for the observed magnetic field direction; P is the magnetic pole at (λ_p, ϕ_p); ρ is the magnetic colatitude (angular distance from S to P); North Pole is the north geographic pole; β is the difference in longitude between the magnetic pole and the site.

Calculation of a pole position is a navigational problem in spherical trigonometry that uses the dipole formula (Equation (1.15)) to determine the distance traveled from observing locality to pole position. Details of the derivation of a magnetic pole position from a magnetic field direction are given in the Appendix. Sign conventions for geographic locations are as follows:

1. Latitudes increase from -90° at south geographic pole to 0° at equator and to $+90^\circ$ at the north geographic pole.
2. Longitudes east of the Greenwich meridian are positive, while westerly longitudes are negative.

Figure 7.1 illustrates how a pole position (λ_p, ϕ_p) is calculated from a site-mean direction (I_m, D_m) measured at a particular site (λ_s, ϕ_s). The first step is to determine the magnetic *colatitude*, p , which is the great-circle distance from site to pole. From the dipole formula (Equation (1.15)),

$$p = \cot^{-1}\left(\frac{\tan I_m}{2}\right) = \tan^{-1}\left(\frac{2}{\tan I_m}\right) \quad (7.1)$$

Pole latitude is given by

$$\lambda_p = \sin^{-1}(\sin \lambda_s \cos p + \cos \lambda_s \sin p \cos D_m) \quad (7.2)$$

The longitudinal difference between pole and site is denoted by β , is positive toward the east, and is given by

$$\beta = \sin^{-1}\left(\frac{\sin p \sin D_m}{\cos \lambda_p}\right) \quad (7.3)$$

At this point in the calculation, there are two possibilities for pole longitude. If

$$\cos p \geq \sin \lambda_s \sin \lambda_p \quad (7.4)$$

then

$$\phi_p = \phi_s + \beta \quad (7.5)$$

But if

$$\cos p < \sin \lambda_s \sin \lambda_p \quad (7.6)$$

then

$$\phi_p = \phi_s + 180^\circ - \beta \quad (7.7)$$

Any site-mean direction I_m, D_m has an associated confidence limit α_{95} . This circular confidence limit about the site-mean direction is transformed (mapped by the dipole formula) into an ellipse of confidence about the calculated pole position (see Figure 7.2). The semi-axis of the ellipse of confidence has an angular length along the site-to-pole great circle given by

$$dp = \alpha_{95} \left(\frac{1 + 3 \cos^2 p}{2} \right) \quad (7.8)$$

The semi-axis perpendicular to the great circle is given by

$$dm = \alpha_{95} \left(\frac{\sin p}{\cos I_m} \right) \quad (7.9)$$

As an example calculation, consider a site-mean direction $I_m = 45^\circ$, $D_m = 25^\circ$ with $\alpha_{95} = 5.0^\circ$ observed at location $\lambda_s = 30^\circ\text{N}$, $\phi_s = 250^\circ\text{E}$ ($= 110^\circ\text{W}$). The colatitude, p , given by Equation (7.1) is 63.4° . From

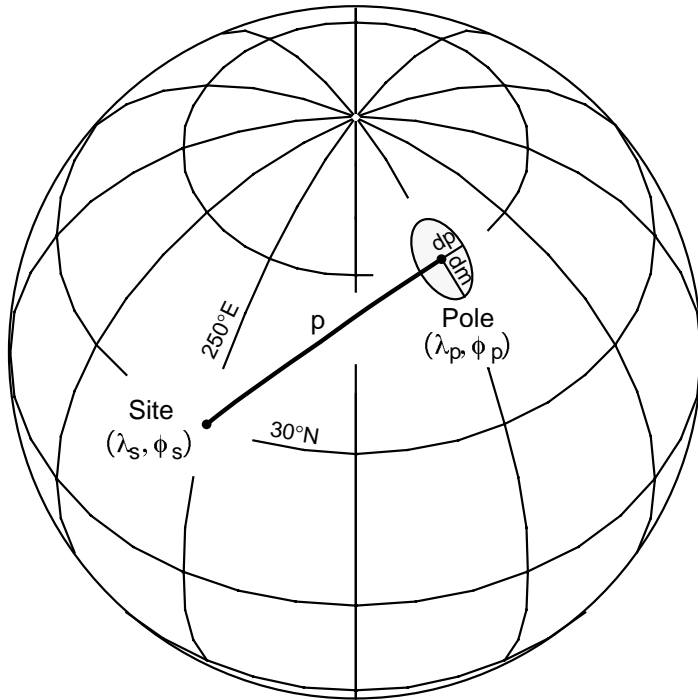


Figure 7.2 Ellipse of confidence about magnetic pole position. p is the magnetic colatitude; dp is the semi-axis of the confidence ellipse along the great-circle path from site to pole; dm is the semi-axis of the confidence ellipse perpendicular to that great-circle path. The projection (for this and all global projections to follow) is orthographic with latitude and longitude grid in 30° increments.

Equation (7.2), the pole latitude, λ_p , is $67.8^\circ N$, and the angle β from Equation (7.3) is 86.2° . The product $\sin \lambda_s \sin \lambda_p = 0.463$, while $\cos p = 0.448$, so $\cos p < \sin \lambda_s \sin \lambda_p$, and the pole longitude is given by Equation (7.7) as $\phi_p = 342.7^\circ E$. The pole is illustrated in Figure 7.2. Using Equations (7.8) and (7.9), the confidence ellipse about the pole has $dp = 4.0^\circ$ and $dm = 6.3^\circ$.

TYPES OF POLES

The calculation scheme just described yields the position of the north geomagnetic pole, assuming that the observed direction is produced by a geocentric dipole. But from Chapter 1, we know that the geomagnetic field is more complex than a simple geocentric dipole. The present geomagnetic field is composed of a dominant dipolar field and a higher-order nondipole field. In addition, we know that the geomagnetic field changes with time. To deal with these spatial and temporal complications, various types of magnetic poles have been defined. These magnetic poles are determined from different kinds of observations, and the distinctions between them are important.

Geomagnetic pole

For the present geomagnetic field, it is possible to examine globally distributed observations and determine the best-fitting geocentric dipole. The pole position of that best-fitting dipole is the *geomagnetic pole*. For the year 1980, the north geomagnetic pole was located at approximately $79^\circ N$, $289^\circ E$ in the Canadian Arctic Islands.

For determination of the geomagnetic pole position, globally distributed observations are required to “average out” the nondipole field. An observation of the magnetic field direction at a single location cannot be used because the observed direction would, in general, be affected by the nondipole field. Thus a pole position calculated on the basis of a single observation at a particular location is not expected to coincide with the geomagnetic pole. For example, the present magnetic field direction in Tucson, Arizona ($\lambda_s \approx 32^\circ N$, $\phi_s \approx 249^\circ E$) is $I \approx 60^\circ$, $D \approx 14^\circ$, and the resulting pole position is $\lambda_p \approx 76^\circ N$, $\phi_p \approx 297^\circ E$, substantially removed from the present geomagnetic pole.

Virtual geomagnetic pole

Any pole position that is calculated from a single observation of the direction of the geomagnetic field is called a *virtual geomagnetic pole* (abbreviated VGP). This is the position of the pole of a geocentric dipole that can account for the observed magnetic field direction at one location and at one point in time. As in the example above, a VGP can be calculated from an observation of the present geomagnetic field direction at a particular locality. If VGPs are determined from many globally distributed observations of the present geomagnetic field, these VGPs are scattered about the present geomagnetic pole. In paleomagnetism, a site-mean ChRM direction is a record of the past geomagnetic field direction at the sampling site location during the (ideally short) interval of time over which the ChRM was acquired. Thus a pole position calculated from a single site-mean ChRM direction is a virtual geomagnetic pole.

Paleomagnetic pole

Because of nondipole components, a site-mean VGP is not expected to coincide with the geomagnetic pole at the time the ChRM was acquired. In theory, the geomagnetic pole in ancient times could be determined by paleomagnetic investigation of globally distributed rocks of equivalent age. In practice, dating techniques are sufficiently precise to allow such geomagnetic pole determinations only for the past few thousand years (see Figure 1.9). This direct technique obviously could not be extended to rocks older than about 5 Ma because continental drift has changed the relative positions of observing localities. The only practical solution to averaging out effects of the nondipole field is to time average the field for an interval of time covering the periodicities of secular variation of the nondipole field. As discussed in Chapter 1, periodicities of secular variation of the nondipole field are dominantly less than 3000 yr.

Analyses presented in Chapter 1 also indicate that the dipolar geomagnetic field undergoes secular variation, causing the geomagnetic pole to random walk about the rotation axis with periodicities dominantly from 10^3 to 10^4 yr. The *geocentric axial dipole hypothesis* (briefly introduced in Chapter 1 and examined in detail in Chapter 10) states that, if geomagnetic secular variation has been adequately sampled, the average position of the geomagnetic pole coincides with the rotation axis. Thus a set of paleomagnetic sites magnetized over about 10^4 to 10^5 yr should yield an average pole position (average of site-mean VGPs) coinciding with the rotation axis. Pole positions calculated with these criteria satisfied are called *paleomagnetic poles*. The term paleomagnetic pole implies that the pole position has been determined from a paleomagnetic data set that has averaged geomagnetic secular variation and thus gives the position of the rotation axis with respect to the sampling area at the time the ChRM was acquired.

Procedures for calculating paleomagnetic poles have changed during the past decade. Previously, the approach was to calculate a *formation-mean direction* by using Fisher statistics to average the site-mean directions from a geological formation. The formation-mean direction then was used to calculate the paleomagnetic pole (Equations (7.1) through (7.7)). A 95% confidence ellipse for the paleomagnetic pole was determined from the α_{95} circle about the formation-mean direction (Equations (7.8) through (7.9)). This pole position was reported as the paleomagnetic pole from the formation, and the error ellipse was used as an estimate of precision.

As shown above, the α_{95} circle of confidence about a mean direction is mapped by the dipole formula into an ellipse of confidence about the calculated pole. Similarly, a circular distribution of directions is mapped into an elliptical distribution of VGPs calculated from those directions. But conversely, a circular distribution of VGPs implies that the distribution of directions yielding those VGPs is elliptical. So site-mean directions or site-mean VGPs (but not both) might be circularly distributed about their respective means. Analyses of large paleomagnetic data sets (from rocks up to a few million years in age) indicate that distributions of site-mean VGPs are more nearly circularly distributed about the mean pole position than are site-mean directions about the formation-mean direction. Consequently, most paleomagnetic poles are now determined in the following manner: (1) From each site-mean ChRM direction, a site-mean VGP is calcu-

lated. (2) The set of VGPs then is used to find the mean pole position (paleomagnetic pole) by Fisher statistics, treating each VGP as a point on the unit sphere. The procedure for determining the mean pole position is the same as for determining a mean direction (Equations (6.12) through (6.15)) except that VGP latitude is substituted for inclination and VGP longitude for declination.

Estimates of (between-site) dispersion of the site-mean VGPs are obtained by using the same procedures applied to directions (Equations (6.16) through (6.22)). But in this case, N = number of site-mean VGPs; R = vector resultant of the N site-mean VGPs; and the confidence limit applies to the calculated mean pole position. An informal convention has developed in which upper-case letters are used for dispersion estimates of VGPs. K is the best-estimate of the precision parameter κ for the observed distribution of site-mean VGPs; S is the angular dispersion of VGPs (estimated angular standard deviation of VGPs) and is usually estimated by Equation (6.18) or (6.19); A_{95} is the radius of the 95% confidence circle about the calculated mean pole (the true mean pole lies within A_{95} of the calculated mean pole with 95% confidence).

Figure 7.3 illustrates an example of a paleomagnetic pole (and A_{95} confidence circle) determined from a set of site-mean VGPs. The example is from the Early Jurassic Moenave Formation of northern Arizona

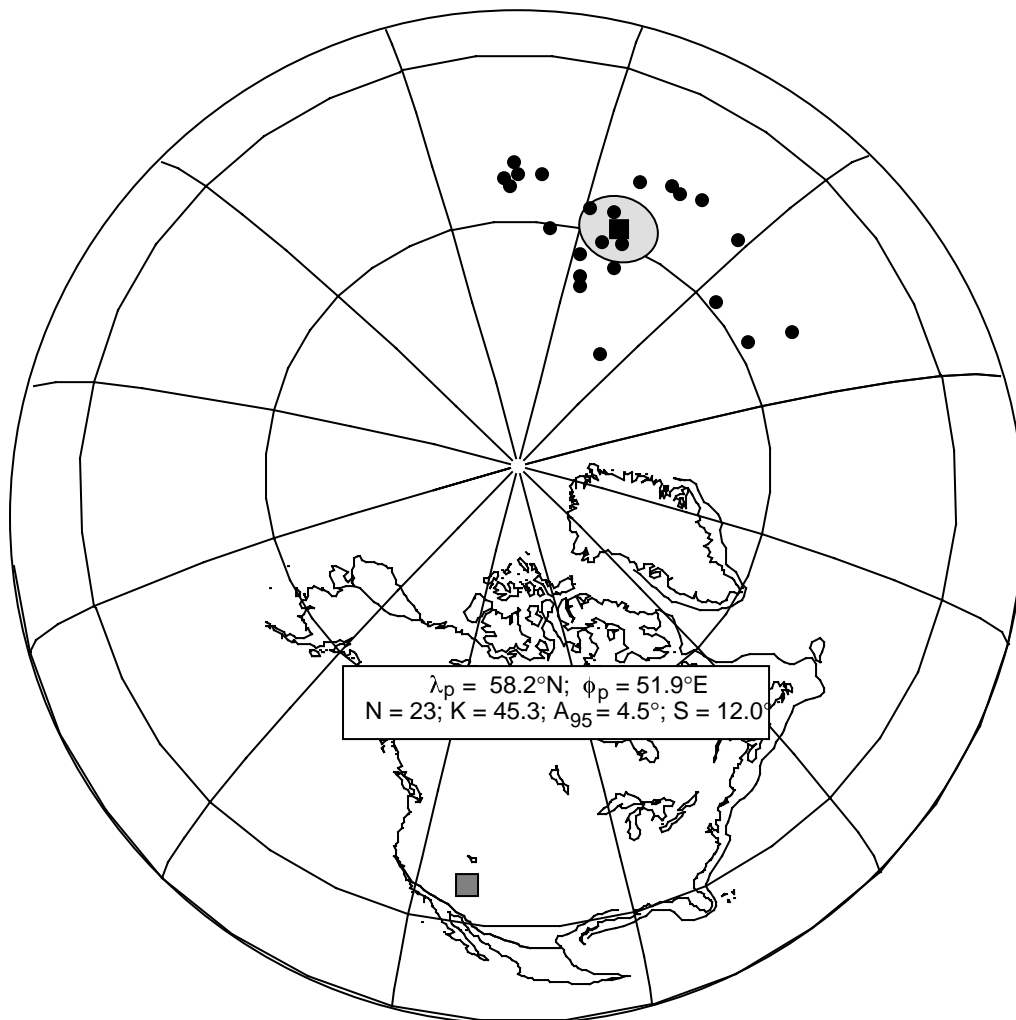


Figure 7.3 Paleomagnetic pole from the Moenave Formation. Solid circles show the 23 site-mean VGPs averaged to determine the paleomagnetic pole shown by the solid square; the stippled circle about the paleomagnetic pole is the region of 95% confidence with radius A_{95} ; the region of sampling is shown by the stippled square; the inset gives the location of the paleomagnetic pole along with statistical parameters.

and southern Utah. This formation is dominated by red and purple-red sediments, and an example of thermal demagnetization behavior was provided in Figure 5.7a. For most of the 23 sites from which a ChRM was successfully isolated, the site-mean α_{95} was $<10^\circ$. Four sites have reversed-polarity ChRM, while 19 sites have normal polarity, and the normal- and reversed-polarity groups pass the reversals test. The mean pole position calculated from the 23 site-mean VGPs is $\lambda_p = 58.2^\circ\text{N}$, $\phi_p = 51.9^\circ\text{E}$. The statistical quantities for this collection of site-mean VGPs are $K = 45.3$, $S = 12.0^\circ$, and $A_{95} = 4.5^\circ$.

SAMPLING OF GEOMAGNETIC SECULAR VARIATION

From the discussion of within-site dispersion in the last chapter, it is clear that tightly clustered ChRM directions from multiple samples within a site are desired. Small within-site dispersion and α_{95} imply that the site-mean direction and site-mean VGP are precisely known. However, the situation for dispersion of site-mean VGPs used for determining a paleomagnetic pole is different because sampling of geomagnetic secular variation is involved. Very low between-site dispersion is usually not the desired result.

For a collection of site-mean VGPs to provide an accurate measure of the time-averaged geomagnetic field, those VGPs must represent a sampling of the geomagnetic field over a time interval that exceeds the dominant periodicities of secular variation. From analyses of the Recent geomagnetic field, we know that the dominant periodicities of secular variation are $\leq 10^5$ yr. Thus a collection of paleomagnetic sites that had randomly sampled the geomagnetic field over 10^5 or 10^6 yr ought to average secular variation. A data set that accomplishes this task will have considerable scatter (see below). It is often difficult or impossible to know the precise time interval represented by collections of ancient rocks. Dating techniques might provide an estimate of the age of the sequence (e.g., 260 ± 15 Ma) but in general cannot provide accurate information about the time interval represented. Thus, judging the adequacy of sampling of geomagnetic secular variation must be done in an indirect fashion.

A considerable amount of information about geomagnetic secular variation has been gathered from examination of (1) the historic geomagnetic field, (2) archeomagnetic data covering the past few thousand years, (3) paleomagnetism of lake sediments, and (4) paleomagnetism of dated igneous rocks. Reasonably detailed records of geomagnetic secular variation are available for the past few thousand years. These provide information about the amplitude, periodicities, and spatial variation of Holocene geomagnetic secular variation. Although of lesser fidelity, considerable information about secular variation during the past 5 m.y. is also available. With still less fidelity, records of geomagnetic secular variation are available for the entire Phanerozoic and even into the Precambrian. From this information, the amount of angular dispersion in a paleomagnetic data set that has adequately sampled secular variation can be estimated.

Paleosecular variation

In an attempt to understand fundamental properties of the geomagnetic field, models of geomagnetic secular variation have been developed. Development and analysis of these models for past geomagnetic fields are referred to as *paleosecular variation*, and this subject has important implications for determination of paleomagnetic poles.

A recent analysis of paleosecular variation for the past 5 m.y. is summarized in Figure 7.4. Paleomagnetic data from 2382 lava flows in the 0 to 5 Ma age range were compiled and analyzed. Sampling sites are distributed spatially and temporally to represent a very thorough sampling of the geomagnetic field during the past 5 m.y. Data were screened to ensure that the individual site-mean results are precisely determined, and data were grouped in bands of site latitude. (For this age range, dispersion introduced by lithospheric plate motion is insignificant.)

There are two fundamental observations from Figure 7.4:

1. The dispersion of VGPs is well constrained to the range $10^\circ < S < 20^\circ$.

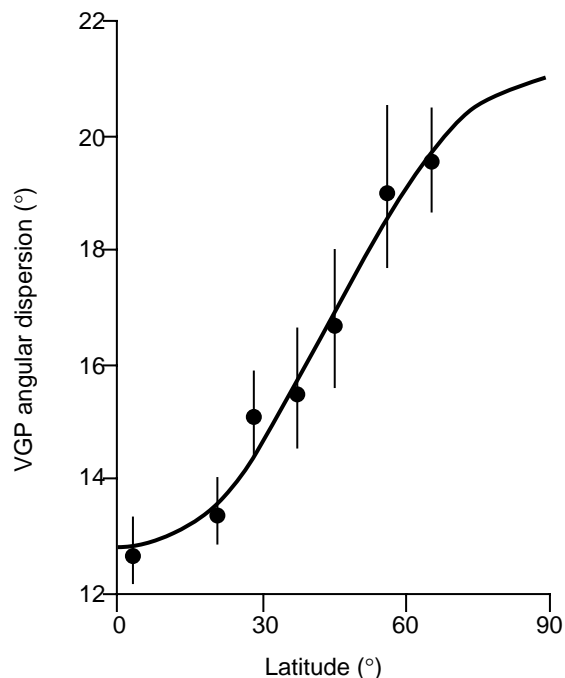


Figure 7.4 Global compilation of paleosecular variation during past 5 m.y. Each data point gives the angular dispersion of VGPs averaged over a band of latitude centered on the data point; the error bars are the 95% confidence limits; the smooth curve is a fit of the observations to a model of paleosecular variation. Redrawn from Merrill and McElhinny (1983).

2. The amount of dispersion of VGPs depends on the site latitude, increasing by almost a factor of two from equator to pole. At least for rocks with ages of 0 to 5 Ma, this analysis provides a powerful and fairly simple method for judging whether a collection of site-mean VGPs from a paleomagnetic study has adequately sampled geomagnetic secular variation.

But what is known about paleosecular variation in more remote geological times? For Late Cretaceous and Cenozoic, seafloor spreading histories allow motion histories of major plates to be reconstructed. The paleomagnetic data available from those plates can be used to construct a “paleoglobal” view of paleosecular variation. For the interval 5 to 45 Ma, the amplitude of VGP dispersion in all latitude bands is slightly greater than for 0 to 5 Ma, whereas for 45 to 110 Ma, dispersion of VGPs is slightly less than for the past 5 m.y. For example, in the band of latitude centered on 10°, VGP dispersion is ~19° for 5 to 45 Ma and ~12° for 45 to 110 Ma as compared to ~13° for 0 to 5 Ma.

With still less certainty than for the last 110 m.y., the amplitude of VGP dispersion produced by geomagnetic secular variation has been investigated for the entire Phanerozoic. The fundamental finding is that the amplitude of paleosecular variation was low during the Cretaceous normal-polarity superchron (~83–118 Ma) and during the Permo-Carboniferous reversed-polarity superchron (~250–320 Ma) (see Chapter 9), two extended intervals during which no reversals of the dipole field occurred. But even during these intervals of unusually low paleosecular variation, VGP dispersion was ~75% of that for the past 5 m.y. So Figure 7.4 can be used as a rough guide in judging the sampling of geomagnetic secular variation afforded by paleomagnetic investigations of rocks of any age (realizing that changes in VGP dispersion of up to ±40% might have occurred during the Phanerozoic).

Testing a paleomagnetic data set for averaging of secular variation is done by comparing observed dispersion of site-mean VGPs with the predicted dispersion. If secular variation has been adequately sampled, the observed angular dispersion of site-mean VGPs should be consistent with that predicted from Figure 7.4 for the paleolatitude of the sampling sites. If the observed dispersion of site-mean VGPs is much less than predicted from Figure 7.4, then the VGPs are more tightly clustered than expected for adequate sampling of secular variation. A likely explanation is that the paleomagnetic sampling sites did not sample a time interval covering the longer periodicities of secular variation. For example, if 20 lava flows were sampled but the flows were all extruded within a 100-yr interval of time, the time interval sampled is too short to afford

complete sampling of geomagnetic secular variation. Accordingly, the VGP dispersion will be much less than would be predicted from Figure 7.4. The implication is that such a paleomagnetic data set has not provided the time averaging of secular variation required for accurate determination of a paleomagnetic pole.

The opposite situation is presented by a VGP dispersion which is substantially larger than predicted from Figure 7.4. Such an observation indicates that there is a source of VGP dispersion in addition to sampling of secular variation. Perhaps there has been tectonic disturbance within the sampling region or there is difficulty in determining the site-mean ChRM directions. In any case, an observed VGP dispersion that substantially exceeds that predicted from Figure 7.4 is a danger signal indicating that the paleomagnetic data are of questionable reliability.

Holocene lavas of western United States

A detailed examination of the paleomagnetism of Holocene lavas in the western United States was made by Champion (see Suggested Readings). A total of 77 lavas were sampled, with site locations primarily in Arizona, Oregon, and Idaho. The large number of samples per lava (11 to 41) and quite straightforward isolation of the ChRM led to site-mean directions with an average $\alpha_{95} \approx 2^\circ$. The dispersion of site-mean VGPs for these 77 lavas is $S = 12.2^\circ$ (95% confidence limits of 11.0° and 13.8°). This is less than the $\sim 16^\circ$ predicted by Figure 7.4 for the average site latitude of 43°N . So the total dispersion of site-mean VGPs is slightly less than typical for the global geomagnetic field during the past 5 m.y.

This collection of accurate data from a particular region for the past 10^4 yr provides an opportunity to examine (1) the dispersion of site-mean VGPs expected for a collection of paleomagnetic sites that have adequately sampled secular variation and (2) the effects of increasing the number of sites sampled. These data were used to simulate sampling of secular variation in the following fashion:

1. Random numbers were used to select five of the 77 site-mean VGPs.
2. This set of VGPs was treated as a "synthetic paleomagnetic data set" and was used to calculate a "paleomagnetic pole," A_{95} , and scatter statistics.
3. Additional sites then were selected randomly to yield synthetic data sets totaling 10, 20, and 30 sites, and the procedures above were repeated for each data set. Results are shown in Figure 7.5.

There are two major realizations to gain from this examination:

1. The dispersion of site-mean VGPs visually appears large but is entirely the result of sampling the geomagnetic secular variation. Dispersion of site-mean VGPs in the range $10^\circ < S < 25^\circ$ is expected (indeed required) for a set of sites that has adequately sampled secular variation. This level of between-site VGP dispersion is desired for reliable determination of a paleomagnetic pole.
2. For a collection of paleomagnetic sites that has randomly sampled secular variation, approximately ten sites will be required to achieve a confidence limit $A_{95} \leq 10^\circ$. For many purposes (including most tectonic applications), this level of precision is desired. Also N (number of sites) ≥ 10 is required for reasonably accurate estimation of the angular dispersion of VGPs.

EXAMPLE PALEOMAGNETIC POLES

In this section, examples of paleomagnetic poles are introduced, starting with poles that are considered very reliable and progressing to poles that are less well determined. These examples put into practice various principles for evaluating paleomagnetic data that have been outlined in this and previous chapters. Emphasis is placed on the paleomagnetic aspects of these example studies with uncertainties about geological interpretation receiving less attention.

Paleocene intrusives of north-central Montana

Diehl and others (see Suggested Readings) conducted a paleomagnetic study that provides a very reliable paleomagnetic pole. In terms of both quantity and quality of paleomagnetic data, the resulting

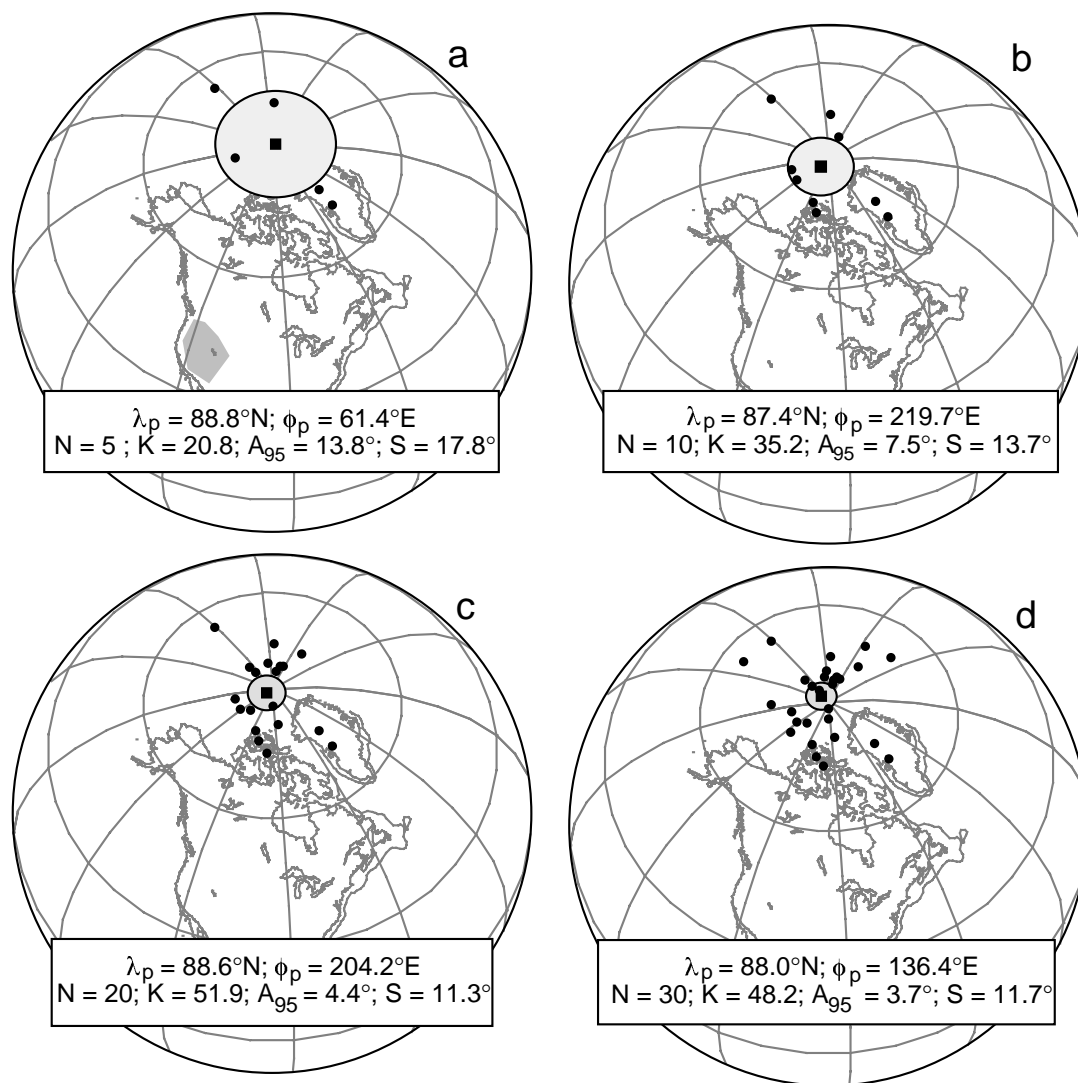


Figure 7.5 “Synthetic paleomagnetic poles” resulting from random sampling of an extensive set of paleomagnetic data from Holocene lavas of the western United States. In each figure, the solid circles show the site-mean VGPs averaged to determine the “paleomagnetic pole” shown by the solid square; the stippled circle about the paleomagnetic pole is the region of 95% confidence with radius A_{95} ; the inset gives the location of the paleomagnetic pole along with statistical parameters. (a) Synthetic paleomagnetic pole resulting from randomly selecting five VGPs; the region of sampling is shown by the stippled polygon. (b) Synthetic paleomagnetic pole resulting from randomly selecting ten VGPs. (c) Synthetic paleomagnetic pole resulting from randomly selecting 20 VGPs. (d) Synthetic paleomagnetic pole resulting from randomly selecting 30 VGPs. Data from Champion (1980).

paleomagnetic pole for the Paleocene of North America is generally regarded as unusually well determined.

Numerous radiometric dates establish the age of shallow level alkalic igneous intrusions in the Judith Mountains, Mocassin Mountains, and Little Rockies Mountains as Paleocene. These rocks intrude essentially flat-lying older sedimentary rocks. Forty-one paleomagnetic sites were collected, with a minimum of eight separately oriented cores per site. Secondary components of NRM were generally easily erased with ChRM isolated over a wide range of AF demagnetizing fields. ChRM was successfully isolated in 36 of the 41 sites, and 32 of these had site-mean ChRM directions with $\alpha_{95} < 10^\circ$. Five sites had reversed polarity

with the normal- and reversed-polarity groups passing the reversals test for paleomagnetic stability. The ChRM is clearly a primary TRM formed during original cooling of these igneous rocks.

The site-mean VGPs are illustrated in Figure 7.6. For reversed-polarity sites, antipodes of site-mean directions were used to calculate VGPs. The resulting paleomagnetic pole is illustrated along with the confidence circle of radius A_{95} about the pole. Statistical quantities calculated from the set of site-mean VGPs are listed on Figure 7.6. The 17.8° dispersion of site-mean VGPs compares favorably with $S \approx 17^\circ$ predicted by Figure 7.4 for the paleolatitude of $\sim 45^\circ$. This observation indicates that the dispersion of site-mean VGPs is consistent with adequate sampling of geomagnetic secular variation. Because both normal- and reversed-polarities of ChRM were observed, the time interval of intrusion must have covered at least parts of two polarity intervals.

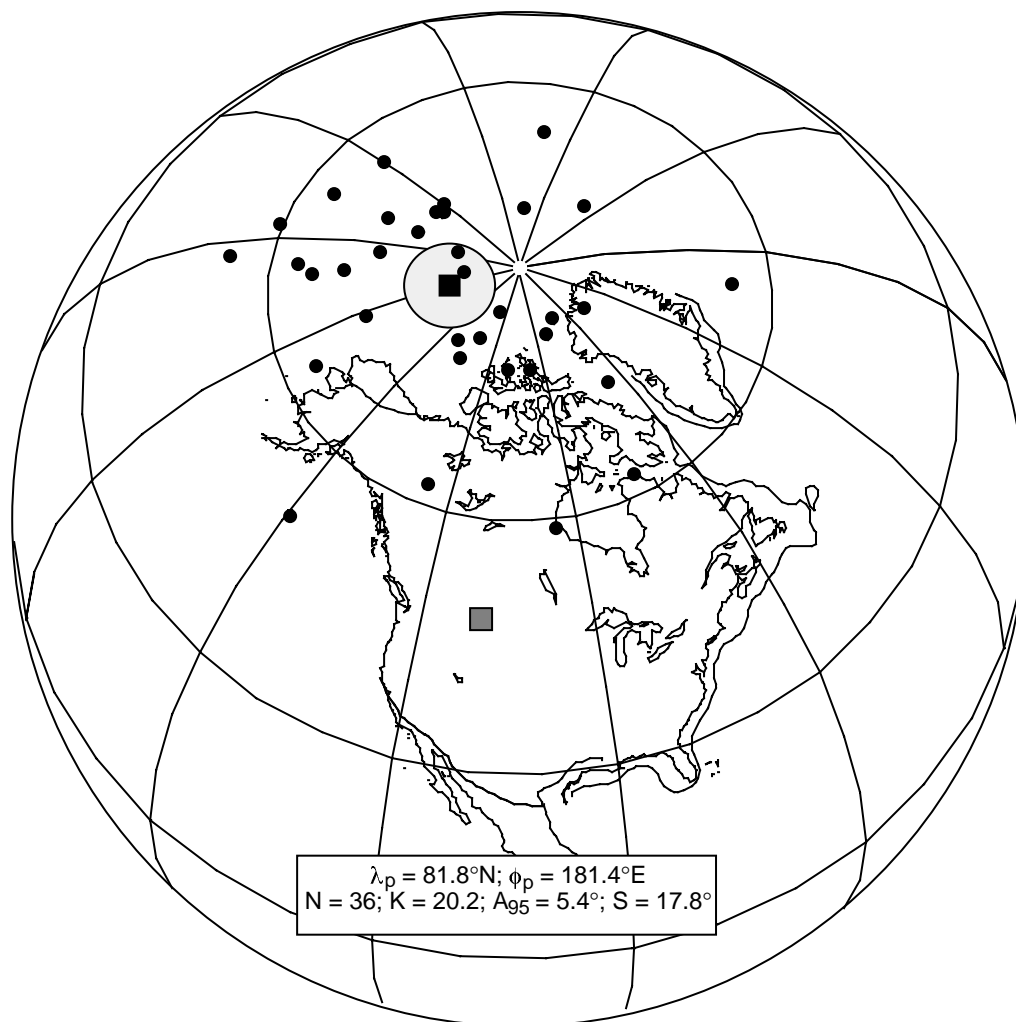


Figure 7.6 Paleomagnetic pole from Paleocene intrusives of north-central Montana. Symbols as in Figure 7.3.

Numerous desirable elements for a paleomagnetic pole determination are present in this investigation. Criteria for accurate determination of site-mean ChRM directions outlined in Chapters 5 and 6 are satisfied. A reversals test for paleomagnetic stability is passed and, along with other data, indicates that the ChRM is a primary TRM, and the large number of sites provides a robust estimation of site-mean VGP dispersion that is consistent with adequate sampling of secular variation. This paleomagnetic study thus provides a reliably determined paleomagnetic pole for the Paleocene of North America, and the A_{95} confidence limit is a realistic assessment of the precision with which that pole has been determined.

Jurassic rocks of southeastern Arizona

A paleomagnetic pole of “intermediate” reliability was determined from Middle Jurassic volcanic and volcanoclastic rocks of southeastern Arizona (reference in Suggested Readings). Nineteen sites with an average of seven cores per site were collected at Corral Canyon in the Patagonia Mountains. Isotopic data indicate an age of 172 ± 6 Ma. Some volcanic units contained magnetite as the dominant ferromagnetic mineral, while hematite dominated in more oxidized volcanic units and there was a single site in red mudstone.

For sites with magnetite as the dominant carrier of NRM, AF demagnetization revealed the same ChRM direction as did thermal demagnetization. For sites with hematite carrying the NRM, thermal demagnetization was generally successful in isolating the ChRM. However, evidence of lightning-induced IRM was found at three sites from which ChRM could not be isolated. Directions of ChRM were isolated from the remaining 16 sites. But four site-mean directions were widely divergent from the other 12 site means (by more than two estimated angular standard deviations). Although only speculative explanations could be provided, these four sites probably do not provide records that are typical of the geomagnetic field during the Middle Jurassic and were not used in the determination of the paleomagnetic pole.

Site-mean ChRM directions of the 12 remaining sites were reasonably well determined; eight site-mean directions had $\alpha_{95} < 10^\circ$. One site had reversed polarity with antipode in the middle of the 11 normal-polarity site-mean directions. But with only one reversed-polarity site, rigorous evaluation of the reversals test is not possible. The site-mean VGPs are shown in Figure 7.7 along with the resulting paleomagnetic pole and statistical quantities. The observed dispersion of site-mean VGPs is 11.5° , in reasonable agreement with $S \approx 13^\circ$ predicted from Figure 7.4 for adequate sampling of secular variation.

This paleomagnetic pole is considered of “intermediate” reliability because there are strengths and weaknesses to the paleomagnetic data used in its determination. On the positive side, several aspects of the data indicate that the ChRM directions in these Middle Jurassic volcanic rocks are primary TRM:

1. There is reasonably clear isolation of ChRM directions from numerous volcanic units of variable deuteric oxidation state and from an interbedded sedimentary unit.
 2. A reversed-polarity site has ChRM direction antipodal to the grouping of normal-polarity site means.
 3. The dispersion of site-mean VGPs is consistent with sampling of geomagnetic secular variation.
- Collectively, these observations indicate that the ChRM of these volcanic rocks is primary TRM.

On the negative side, data from several sites were rejected because a ChRM could not be isolated or the site-mean ChRM direction was divergent from the dominant clustering of site-mean directions. No matter how well founded such data rejection might be, it always causes some uneasiness with the final result. In the end, just 12 sites proved useful for determination of the paleomagnetic pole. Successful isolation of ChRM directions from more sites might have yielded a more confidently determined pole. However, there are sufficient attributes to this paleomagnetic data to regard the “Corral Canyon Pole” as reasonably well determined and the associated $A_{95} \approx 6^\circ$ as a realistic estimate of the precision.

Two problem cases

Figure 7.8 illustrates “paleomagnetic poles” that suffer from two very different inadequacies in the data used for their determination. In Figure 7.8a, site-mean VGPs from 25 sites in a stratigraphic succession of Paleocene lavas at Gringo Gulch (yes, this is a real place name!) near Patagonia, Arizona, are illustrated. Site-mean ChRM directions were all well determined. But all site-mean ChRM directions have reversed polarity. Furthermore, the dispersion of site-mean VGPs (S) is only 4.1° compared with a predicted dispersion $S \approx 14^\circ$ for the paleolatitude of 30° . The obvious problem here is that the VGPs are too tightly clustered. This suggests that the 25 lavas at Gringo Gulch have not adequately sampled geomagnetic secular variation. These flows most likely were extruded in rapid succession during an interval substantially less than the longer periodicities of secular variation, perhaps $<10^3$ yr.

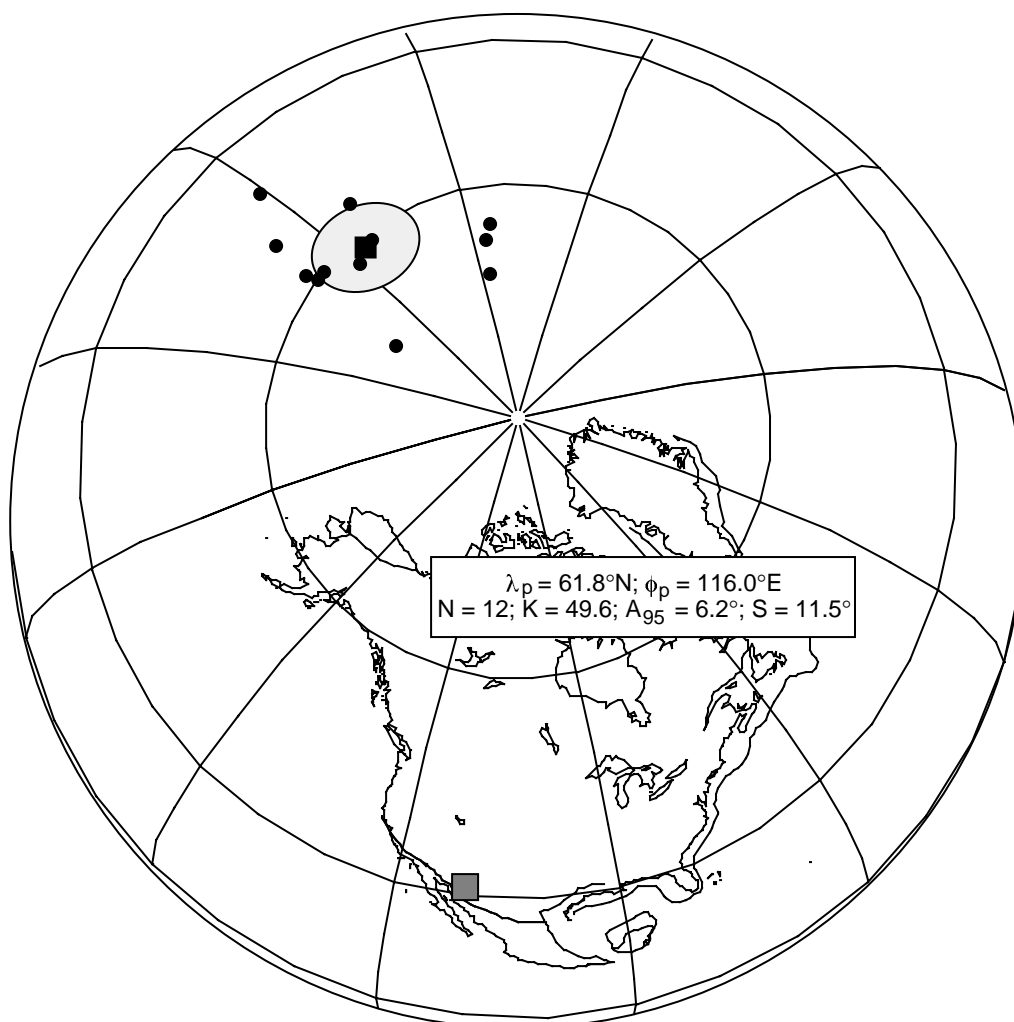


Figure 7.7 Paleomagnetic pole from Middle Jurassic volcanic and volcanoclastic rocks of southeastern Arizona. Symbols as in Figure 7.3.

The small confidence limit ($A_{95} = 1.4^\circ$) for the calculated pole position gives the impression of a highly accurate paleomagnetic pole determination. In this case, however, the small A_{95} is misleading. The Gringo Gulch pole is not more accurate than the paleomagnetic pole from the Paleocene intrusions of north-central Montana discussed above. On the contrary, the Gringo Gulch pole is not nearly as reliably determined as is the pole from the Montana intrusives. This example indicates the importance of careful data examination (at least at the site-mean level) in judging reliability of paleomagnetic poles.

Because of changing experimental techniques and criteria for determination, there are many “paleomagnetic poles” in the literature that would not today be considered reliably determined. So as not to raise the hackles of the original investigators, the following example from the literature is referred to as the “mystery pole.” The paleomagnetic sampling leading to determination of the mystery pole was carried out on volcanic rocks in the southern hemisphere. In the publication reporting the mystery pole, results from 12 sites are listed. However, if one applies data selection criteria requiring three or more samples per site and site-mean $\alpha_{95} \leq 20^\circ$, then data from only three sites remain! Site-mean VGPs for these three sites are illustrated in Figure 7.8b, using the standard convention of showing the paleomagnetic pole closest to the present south geographic pole for observations from the southern hemisphere.

Although the mystery pole has $A_{95} = 8.7^\circ$ and does not at first sight appear poorly determined, again appearances are deceiving. As discussed above, a paleomagnetic data set with only three site-mean direc-



Figure 7.8a Example 1 of a “paleomagnetic pole” based on problematical data. Paleomagnetic pole from Paleocene lavas in southern Arizona. The region of sampling is shown by the stippled square; this paleomagnetic data set has probably not adequately sampled geomagnetic secular variation. Symbols as in Figure 7.3.

tions cannot provide adequate averaging of geomagnetic secular variation. Nor can such a data set provide more than rough estimates of angular standard deviation. Therefore, this paleomagnetic data set does not, in fact, constitute a reliable determination of a paleomagnetic pole. In contrast to earlier examples, the small number of sites prevents rigorous evaluation of the averaging of secular variation.

CAVEATS AND SUMMARY

The principles and discussions above on sampling of geomagnetic secular variation assume that ChRM is acquired within a time interval (generally $\leq 10^2$ yr) that is much shorter than dominant periodicities of secular variation. This assumption is certainly justified for volcanic rocks because they cool through the blocking temperatures of TRM within at most a few years. But for deep-level igneous intrusions (especially plutonic rocks), acquisition of primary TRM may occur over millions of years. This slow cooling can result in time-averaging of the geomagnetic field within-site (even within sample).

An example of this time integration of the geomagnetic field is provided by paleomagnetic studies of Cretaceous plutonic rocks of the Sierra Nevada (see Frei et al. in Suggested Readings). After removing the contribution from within-site dispersion, the between-site dispersion of ChRM directions in three plutonic

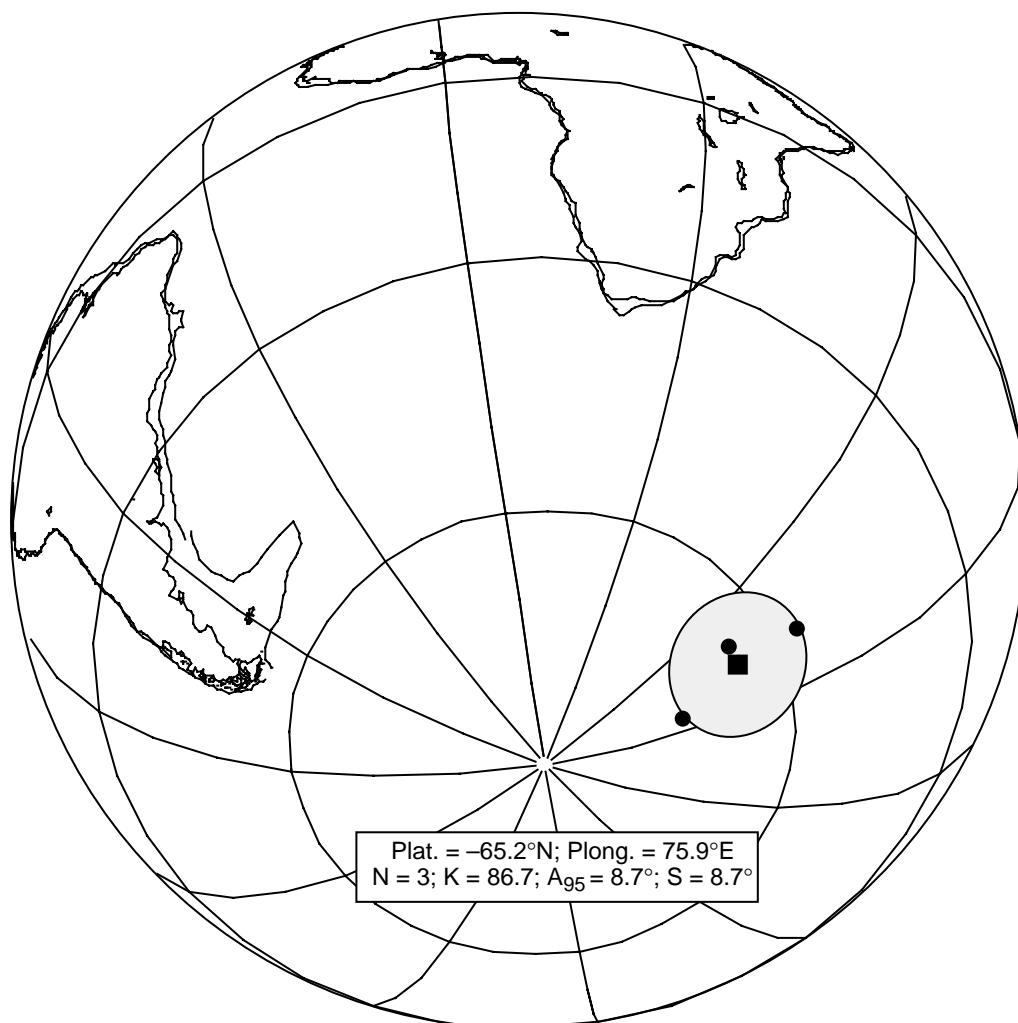


Figure 7.8b Example 2 of a “paleomagnetic pole” based on problematical data. The mystery pole based on just three site-mean VGPs. Symbols as in Figure 7.3.

bodies was found to range from 4.8° to 9.7° . This dispersion is substantially lower than the $\sim 16^\circ$ expected at the Cretaceous paleolatitude of the Sierra Nevada. This low between-site dispersion is not because the rocks were magnetized in a time interval that was too short to provide adequate sampling of secular variation. Instead, the low dispersion results from intra-site or even intra-specimen time averaging of geomagnetic field direction as these rocks were very slowly cooled through their blocking temperature intervals.

A time integration of the geomagnetic field direction may also occur in sedimentary rocks with slow lock-in of pDRM or in red sediments with protracted CRM acquisition. For any rock units in which ChRM acquisition integrates secular variation over $\geq 10^3$ yr, the dispersion of site-mean VGPs may be substantially less than predicted by Figure 7.4. This should be kept in mind in assessing whether a paleomagnetic data set has adequately sampled secular variation.

For paleomagnetic data from stratigraphic successions of volcanic rocks, the episodic nature of volcanic eruption must be considered. If a sequence of flows is erupted in rapid succession so that no significant secular variation takes place between eruptions, the individual flows in the sequence are not independent samples of the geomagnetic field. For adjacent sites in stratigraphic sections, site-mean ChRM directions should be examined to determine whether those directions are statistically distinguishable. In stratigraphic intervals with indistinguishable site-mean directions, those directions should be averaged and treated as a single sample of the geomagnetic field.

The principles and examples presented in this chapter provide some criteria for evaluation of paleomagnetic data, especially data used to determine paleomagnetic poles. Although each case must be separately evaluated and there are no strict rules, the following are some common-sense criteria:

1. Multiple samples per site (three or more, but preferably six to ten) are highly recommended. Site-mean ChRM should be well defined, as discussed in Chapter 6; site-means with $\alpha_{95} \geq 20^\circ$ would generally be considered unacceptable for inclusion in a data set used for determination of a paleomagnetic pole.
2. Application and rigorous evaluation of field tests of paleomagnetic stability can provide crucial information about timing of ChRM acquisition. Especially for ancient rocks in orogenic zones, field tests can be invaluable.
3. The number of site-mean VGPs used to calculate a paleomagnetic pole should be ten or more. This number is required for reasonable averaging of geomagnetic secular variation and for estimating dispersion of site-mean VGPs.
4. Dispersion of site-mean VGPs should be consistent with adequate sampling of geomagnetic secular variation.

SUGGESTED READINGS

- D. E. Champion, Holocene geomagnetic secular variation in the western United States: Implications for the global geomagnetic field, U.S. Geological Survey Open File Report, No. 80-824, 314–354, 1980.
Extensive study of Holocene volcanic rocks in western United States on which results of Figure 7.5 are based.
- A. Cox, Latitude dependence of angular dispersion of the geomagnetic field, *Geophys. J. Roy. Astron. Soc.*, v. 20, 253–192, 1970.
Discusses dispersion of geomagnetic field directions and of VGPs.
- J. F. Diehl, M. E. Beck, Jr., S. Beske-Diehl, D. Jacobson, and B. C. Hearn, Paleomagnetism of the Late Cretaceous–Early Tertiary North-Central Montana Alkalic Province, *J. Geophys. Res.*, v. 88, 10,593–10,609, 1983.
Article reporting the paleomagnetic data used as the basis of Figure 7.6.
- E. J. Ekstrand and R. F. Butler, Paleomagnetism of the Moenave Formation: Implications for the Mesozoic North American apparent polar wander path, *Geology*, v. 17, 245–248, 1989.
Article reporting the paleomagnetic pole illustrated in Figure 7.3.
- L. S. Frei, J. R. Magill, and A. Cox, Paleomagnetic results from the central Sierra Nevada: Constraints on reconstructions of the western United States, *Tectonics*, v. 3, 157–177, 1984.
This paleomagnetic study provides an example of intrasite time integration of geomagnetic secular variation.
- E. Irving and G. Pullaiah, Reversals of the geomagnetic field, magnetostratigraphy, and relative magnitude of paleosecular variation in the Phanerozoic, *Earth Sci. Rev.*, v. 12, 35–64, 1976.
Presents an analysis of magnitude of paleosecular variation as a function of geologic age.
- S. R. May, R. F. Butler, M. Shafiqullah, and P. E. Damon, Paleomagnetism of Jurassic rocks in the Patagonia Mountains, southeastern Arizona: Implications for the North American 170 Ma reference pole, *J. Geophys. Res.*, v. 91, 11,545–11,555, 1986.
Article reporting the paleomagnetic pole illustrated in Figure 7.7.
- P. L. McFadden, Testing a palaeomagnetic study for the averaging of secular variation, *Geophys. J. Roy. Astron. Soc.*, v. 61, 183–192, 1980.
Presents some advanced statistical techniques for evaluating whether a paleomagnetic data set has averaged secular variation.
- R. T. Merrill and M. W. McElhinny, *The Earth's Magnetic Field: Its History, Origin, and Planetary Perspective*, 401 pp., Academic Press, London, 1983.
Chapter 6 presents an in-depth analysis of paleosecular variation.
- R. W. Vugteveen, A. E. Barnes, and R. F. Butler, Paleomagnetism of the Roskrige and Gringo Gulch Volcanics, southeast Arizona, *J. Geophys. Res.*, v. 86, 4021–4028, 1981.
Paleomagnetic results illustrated in Figure 7.8a were reported in this article.

PROBLEMS

- 7.1 A paleomagnetic site from a single Oligocene welded ash flow tuff was collected at site location $\lambda_s = 35^\circ\text{N}$, $\phi_s = 241.2^\circ\text{E}$. The site-mean ChRM data are $N = 8$, $I_m = -17.9^\circ$, $D_m = 232.6^\circ$, $k = 320.0$.
- a. From these data, calculate the site-mean VGP for this site. *Note:* The magnetic colatitude, p , must be a positive number (it is the great-circle distance from the site to the pole). If you obtain a negative number for

$$p = \cot^{-1}\left(\frac{\tan I_m}{2}\right) = \tan^{-1}\left(\frac{2}{\tan I_m}\right)$$

then

$$p = \tan^{-1}\left(\frac{2}{\tan I_m}\right) + 180^\circ.$$

- b. Estimate the semi-axes (dp , dm) of the ellipse of confidence about this VGP.
- 7.2 Data summaries are given below for two (hypothetical) latest Carboniferous formations exposed in central Manitoba, Canada. We are considering the use of these data to determine the latest Carboniferous paleomagnetic pole for the North America craton. Examine the data, assuming that the ChRM directions have been determined by state-of-the-art demagnetization techniques; perhaps plot some observations on an equal-area projection; and come to a conclusion about which of the two data sets is most likely to yield a reliable latest Carboniferous paleomagnetic pole. Explain your reasoning and your choice of the more reliable paleomagnetic data set. *Note:* During the Late Carboniferous through most of the Permian, the geomagnetic field was in a constant state of reversed polarity.

Blue-winged Olive Formation: $N = 22$ sites in flat-lying red sediments; all sites have reversed polarity. Average of the 22 site-mean VGPs:

$$N = 22, \lambda_p = 44.6^\circ\text{N}, \phi_p = 123.4^\circ\text{E}, K = 34.2, A_{95} = 5.1^\circ.$$

Muddler Minnow Formation: $N = 27$ sites in basaltic andesite flows; $N = 13$ normal-polarity sites from flat-lying strata have mean direction:

$$N = 13, I_m = 15.0^\circ, D_m = 309.0^\circ, k = 27.4, \alpha_{95} = 12.1^\circ$$

$N = 14$ reversed-polarity sites from strata with dip azimuth = 317° and dip = 18° have in situ (before structural correction) mean direction:

$$N = 14, I_m = -52.0^\circ, D_m = 169.0^\circ, k = 24.7, \alpha_{95} = 12.8^\circ$$

SPECIAL TOPICS IN ROCK MAGNETISM

In Chapter 3, you discovered the basic mechanisms by which NRM is formed. A variety of special topics in rock magnetism are investigated in this chapter. These topics include (1) special attributes of some types of NRM, such as the ability to retrieve paleointensity of the geomagnetic field from TRM; (2) concerns about effects of chemical changes on primary NRM; (3) questions about the accuracy of NRM records, in particular the questions of inclination error in DRM and possible directional effects of magnetic anisotropy; and (4) the timing of remanence acquisition by red sediments. There are no definitive answers to some of these questions and concerns. But consideration of these topics is important to interpretation of paleomagnetic data in the coming chapters.

PALEOINTENSITY FROM THERMOREMANENT MAGNETIZATION

The development of thermoremanent magnetism in Chapter 3 focused on directional properties of TRM. But TRM is unique among forms of natural remanent magnetism in providing information about past intensities of the geomagnetic field via a technique that is straightforward in principle. Consider Equation (3.28), which describes dependence of TRM on various parameters including strength of magnetizing field, H :

$$\text{TRM}(20^\circ\text{C}) = N(T_B) v j_s(20^\circ\text{C}) \tanh(b) \quad (8.1)$$

where

$$b = \frac{v j_s(T_B) H}{k T_B}$$

For typical values of parameters, b is $\ll 1.0$. This provides a useful simplification because $\tanh(b) \approx b$ for $b \ll 1.0$. Thus from Equation (8.1),

$$\text{TRM}(20^\circ\text{C}) \approx N(T_B) v j_s(20^\circ\text{C}) \left(\frac{v j_s(T_B) H}{k T_B} \right) \quad (8.2)$$

TRM thus depends linearly on the strength of the magnetic field present during cooling through the blocking temperature. The magnetic field dependence can be made more explicit by combining terms that depend on grain-size and shape distribution, blocking temperature, and ferromagnetic properties (e.g., $N(T_B)$, $j_s(T_B)$, etc.) into a proportionality constant, A . Equation (8.2) becomes

$$\text{TRM}(20^\circ\text{C}) = AH \quad (8.3)$$

If the TRM under consideration formed by cooling in the geomagnetic field, this natural TRM ($\text{TRM}_{\text{paleo}}$) is linearly dependent on the intensity of the paleomagnetic field, usually referred to as *paleointensity*. The paleointensity experiment is designed to determine the proportionality constant, A .

Suppose you are attempting to determine the paleointensity of the geomagnetic field from a particular rock sample that contains a primary TRM that we call $\text{TRM}_{\text{paleo}}$. It is an easy matter to measure $\text{TRM}_{\text{paleo}}$,

but neither term on the right side of Equation (8.3) is known. In principal, the proportionality constant A can be determined by giving the same sample a new TRM (TRM_{lab}) in a known field, H_{lab} , so that

$$TRM_{lab} = A H_{lab} \tag{8.4}$$

If the natural TRM, TRM_{paleo} , is an uncomplicated, single-component TRM, the paleointensity can be obtained by combining Equations (8.3) and (8.4) to eliminate the proportionality constant, A . Solving for H_{paleo} yields

$$H_{paleo} = \left(\frac{TRM_{paleo}}{TRM_{lab}} \right) H_{lab} \tag{8.5}$$

In principle, all quantities in Equation (8.5) are easily measurable, and paleointensity can be determined. However, the entire experiment depends on the assumption that no changes occur in the proportionality constant, A . This means that no changes in any properties that determine A (grain size or composition of ferromagnetic grains, etc.) can take place in nature since the original TRM formed or during laboratory heating. In practice, paleointensities of the geomagnetic field are very difficult to determine because the ferromagnetic grains carrying the natural TRM have often undergone alteration and/or the required laboratory heating induces physical or chemical changes. To extract useful paleointensity information at low temperatures before higher temperature alterations occur, the paleointensity experiment is usually done in a series of heating steps to progressively higher temperatures.

The procedure involves a double-heating process:

1. The sample is first heated to a temperature T_i above room temperature but below the Curie temperature. The sample is then cooled to room temperature in zero magnetic field, and the TRM_{paleo} remaining in the sample is measured. The difference between TRM_{paleo} prior to heating and TRM_{paleo} after heating to T_i is the amount of natural TRM with blocking temperatures $\leq T_i$; this difference is the natural partial thermoremanent magnetism (PTRM) carried by grains with blocking temperature $\leq T_i$.
2. Again the sample is heated to T_i but is cooled in a known magnetic field H_{lab} . The amount of PTRM acquired during this cooling is then measured. The TRM_{paleo} remaining after the first heating to T_i is plotted against the PTRM acquired by cooling in H_{lab} following the second heating. This double-heating process is repeated at incrementally higher temperatures; a data point plotting remaining TRM_{paleo} against acquired PTRM is obtained at each temperature. An example plot is shown in Figure 8.1.

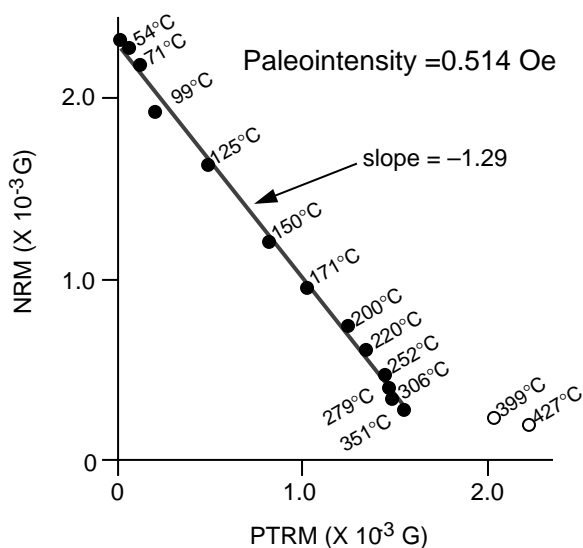


Figure 8.1 NRM remaining versus PTRM acquired. Data points plot NRM remaining after heating to a particular temperature against PTRM acquired by heating to the same temperature followed by cooling in a 0.4-Oe magnetic field; temperatures of heating are shown adjacent to data points; the slope of the line fit to the data points is -1.29 ; the sample is 3790-year-old basalt from Hawaii, and NRM is a primary TRM. Redrawn from Coe et al. (1978), with permission of the American Geophysical Union.

The law of additivity of PTRM (Equation (3.30)) says the PTRM acquired in one interval of blocking temperature is independent of PTRM acquired in other intervals. So Equation (8.5) can be applied at each temperature T_i and each data point on a paleointensity plot (Figure 8.1) provides an estimate of the paleointensity H_{paleo} . If no changes occur in the ferromagnetic grains, the data points obtained at progressively higher temperatures fall on a straight line. The slope of this line is

$$slope = -\frac{H_{paleo}}{H_{lab}} \quad (8.6)$$

In the example of Figure 8.1, the slope is -1.29 , the laboratory field used was 0.4 Oe, and the resulting paleointensity is 0.514 Oe.

If heating above a certain temperature causes changes in the ferromagnetic grains, data points from higher temperatures will not fall on the line described by the data obtained at lower temperatures. Note that data points obtained at 399°C and 427°C in the example of Figure 8.1 fall off the line described by the lower temperature data. This indicates that changes affecting the ferromagnetic minerals have taken place when the sample was heated to $>350^\circ\text{C}$. Only the lower temperature data should be used to determine the paleointensity.

By employing this double-heating procedure, useful paleointensity information can often be obtained at low temperatures before higher-temperature alteration occurs. But the procedure is time consuming, and the success rate is sometimes low. As a consequence, much more is known about past directions of the geomagnetic field than about past intensities. However, knowledge of geomagnetic paleointensities is crucial to evaluation of geomagnetic field models. Accordingly, much effort has been put into development and use of paleointensity techniques.

Merrill and McElhinny (1983) provide a more thorough discussion of paleointensity experiments and results. The book edited by Creer et al. (1983) contains a number of articles on paleointensities. Figure 1.10 showing variations in the geomagnetic dipole moment over the past 10^4 yr was determined from paleointensity experiments compiled by McElhinny and Senanayake (1982). For a discussion of field intensity during a reversal of the geomagnetic dipole, see Prévot et al. (1985).

INCLINATION ERROR OF DRM

In Chapter 3, inclination error (inclination shallowing) of detrital remanent magnetism was discussed in the context of DRM acquisition. Here we investigate how and when inclination error may develop and its likely magnitude in various sedimentary environments. An obvious question is: *Does this inclination error of DRM happen in nature?* The definitive answer is: *Probably, sometimes.*

We have already observed (Figure 3.15) that inclination of depositional DRM, I_o , is systematically shallower than inclination of the magnetic field at the time of deposition, I_H . In a number of redeposition experiments (King, 1955; Griffiths et al. 1960; King and Rees, 1966), the inclinations were found to be related by

$$\tan I_o = f \tan I_H \quad (8.7)$$

and the value of f was found to be ~ 0.4 for redeposited glacial sediments. The corresponding inclination error, ΔI , is

$$\Delta I = I_H - I_o = I_H - \tan^{-1}(f \tan I_H) \quad (8.8)$$

But postdepositional DRM (pDRM) processes dominate magnetization of many sediments, especially fine-grained sediments. And pDRM produces accurate recordings of the direction of the magnetic field (Irving and Major, 1964; Opdyke and Henry, 1969; Kent, 1973; Barton and McElhinny, 1979).

Two natural examples often cited as evidence for absence of inclination error in pDRM are now discussed:

1. *Paleomagnetic records from Holocene lake sediments.* Although exceptions exist, high-quality paleomagnetic records from Holocene lake sediments usually record the inclination of the geomagnetic field at or soon after deposition. The evidence is convincing: (a) many lake sediment paleomagnetic records agree with historic geomagnetic field records; (b) other lake sediment paleomagnetic records agree with directions of thermoremanent magnetism recorded by archeological features or Holocene lava flows; (c) mean inclination observed in sequences of lake sediments spanning $>10^3$ yr usually agree with expected inclination of a geocentric axial dipole (Lund, 1985).
2. *Paleomagnetic records from Plio-Pleistocene deep-sea cores.* Opdyke and Henry (1969) examined paleomagnetism of piston cores of deep-sea sediments collected from a wide variety of locations. These cores allowed collection of only the upper few meters of sediment, which is usually no older than Early Pliocene (ca. 5 Ma). Mean paleomagnetic inclinations are plotted against latitude of collecting site in Figure 8.2; the curve in the diagram is the expected inclination for a geocentric axial dipole field. Fundamental agreement of the observed mean inclination with the predicted inclination argues that no inclination error exceeding about 5° is present.

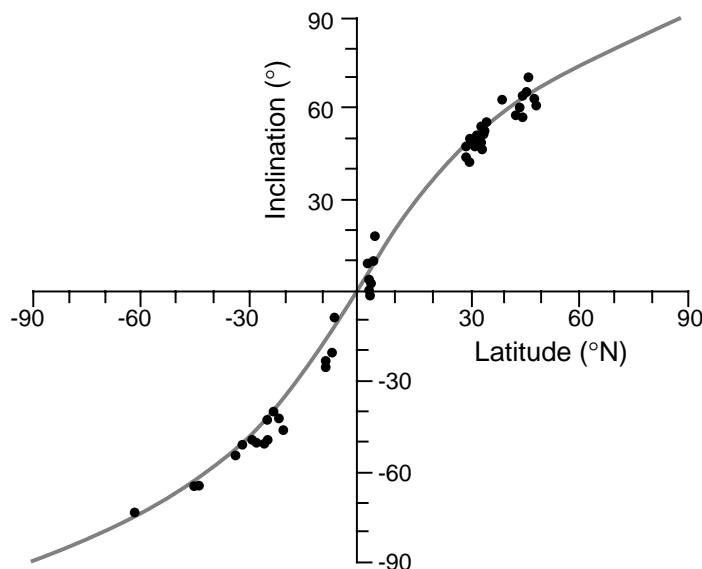


Figure 8.2 Mean inclination of DRM in 52 Plio-Pleistocene deep-sea sediment cores versus latitude of core collection. The solid curve shows the expected inclination for the geocentric axial dipole field; to calculate the mean inclination for each core, the sign of the inclination of DRM in reversed-polarity intervals was changed. Redrawn from Opdyke and Henry (1969).

These examples demonstrate that fine-grained sediments with magnetization dominated by pDRM processes and buried by a few meters of overlying sediments do not possess inclination error. But these results do not demonstrate lack of inclination error in older sediments. Recent examinations indicate that compaction (and possibly deformation) can often shallow the inclination of magnetization.

The potential importance of compaction can be understood by considering changes in porosity resulting from compaction. Clays have typical initial porosity of 50% to 80%. Porosity decreases by about 50% on burial to 1 km; almost complete closure of pores occurs on burial to 2 km. Sands have initial porosity of 20% to 65%, and burial to 4 km decreases porosity to about one half of the initial value. These porosity changes demonstrate the potential for compaction-induced rotation of platy and elongate grains toward the bedding plane. Shallowing of inclination could result in much the same manner shown in Figure 3.15b.

Deep-sea sediments that are older (and more deeply buried) than those of Figure 8.2 sometimes have inclinations of magnetization shallowed by compaction (Blow and Hamilton, 1978; Celaya and Clement, 1988; Arason and Levi, 1990a). Recent advances in ocean floor drilling have allowed the retrieval of cores several hundred meters in length. In some cores up to 500 m in length with oceanic sediments no older than Miocene, inclinations are seen to systematically shallow down core by some 10° to 15° due to compaction. A corresponding gradual decrease in water content is observed, and clay particles are rotated toward the bedding plane. An example is given in Figure 8.3.

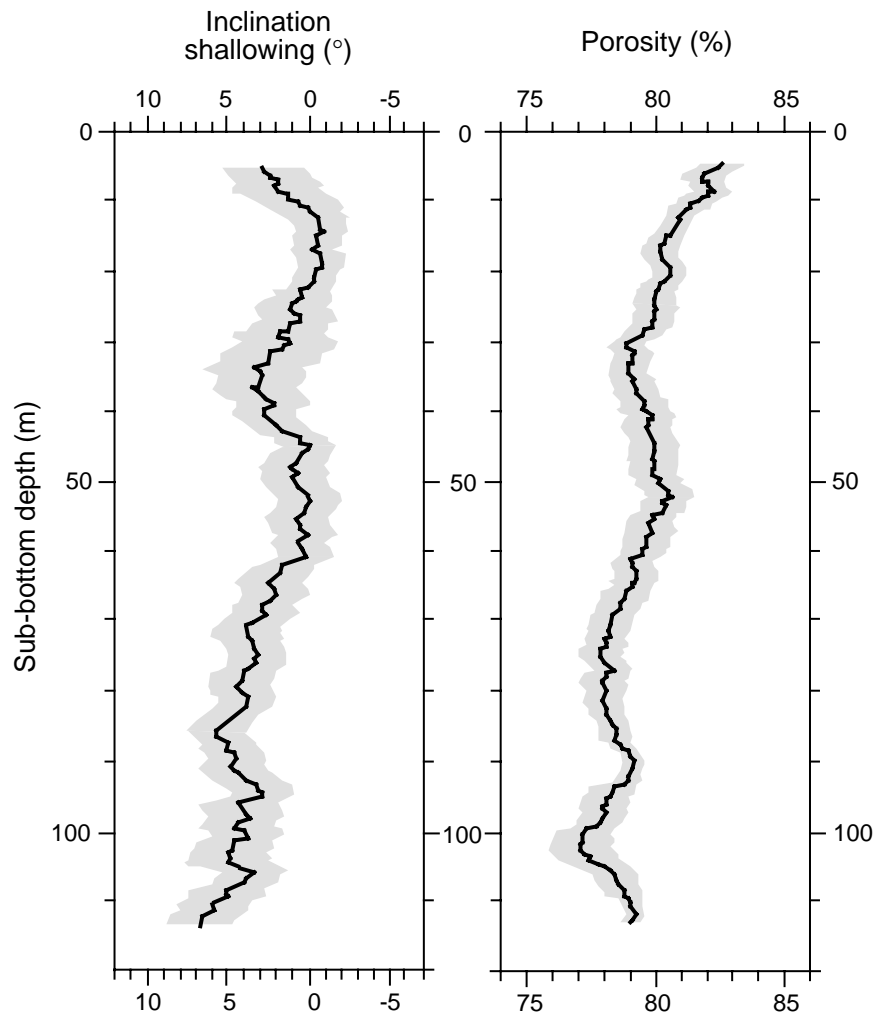


Figure 8.3 Shallowing of DRM inclination and porosity versus depth in a core of deep-sea sediment. The core is from DSDP Site 578 in the northwestern Pacific Ocean; the oldest sediment has an age of 5.6 Ma; the bold line is a 1-m.y. sliding time-window average of inclination shallowing compared with geocentric axial dipole field inclination (corrected for Pacific plate movement); porosities are means calculated every 0.2 m using a 10-m sliding-depth window; stippled envelopes show 95% confidence limits. Redrawn after Arason and Levi (1990), with permission of the American Geophysical Union.

Laboratory experiments suggest that interactions between fine-grained magnetite and clay particles may be important in compaction shallowing of inclination (Anson and Kodama, 1987; Deamer and Kodama, 1990). Small elongate magnetite particles are thought to adhere to clay particles or be trapped inside clusters of clay particles. During compaction, the long axes of magnetite grains are passively rotated toward the bedding plane along with the clay particles. Arason and Levi (1990b) have investigated a variety of models for compaction shallowing of inclination.

For older sedimentary rocks, evidence for or against inclination error becomes less clear. This evidence must come from comparison of paleomagnetic records from sedimentary and igneous rocks of identical age. Such comparisons are not simple because tectonic histories, adequate sampling of geomagnetic secular variation by the igneous rocks, and other complicating factors must be taken into account. Nevertheless, there are a few well-documented examples.

1. *Eocene turbidites of the Oregon Coast Range.* In the Oregon Coast Range, Eocene turbidites of the Tyee and Flounoy formations are overlain by the Tillamook Volcanic Series and underlain by

the Siletz River Volcanics. Both the volcanic rocks and the turbidites have been the subject of extensive paleomagnetic study (Simpson and Cox, 1977; Magill et al., 1981). The inclination of DRM in the Tyee and Flournoy formations closely matches inclinations in the bracketing volcanic sequences. This is clear evidence against significant inclination error in these turbidites.

2. *Alaskan terranes.* Paleomagnetic data from Late Cretaceous and Early Tertiary lavas and oceanic sedimentary rocks are available from several tectonostratigraphic terranes in Alaska. Comparing paleomagnetic data from sediments and lavas of the same terranes, Coe et al. (1985) found that sedimentary rocks yield systematically shallow inclinations. For the Prince William and Chugach terranes, paleomagnetic inclinations from sediments are about 20° shallower than inclinations from lavas. The value of f in Equations (8.7) and (8.8) that best describes the shallowed inclinations in the Alaskan turbidites is $f \approx 0.4$. Many of these sedimentary rocks are deformed, so that shallowed inclinations might have been produced by deformational effects as well as by compaction.
3. *Paleocene continental sediments of San Juan Basin, New Mexico.* Continental claystones and fine siltstones of this Laramide basin were the subject of extensive paleomagnetic study (Butler and Taylor, 1978). The Nacimiento Formation of Paleocene age yielded high-quality paleomagnetic data with many stratigraphic levels investigated. These data were used in Figure 5.16 as an example of the reversals test; means of the normal- and reversed-polarity sites are antipodal to within 1.6°. Yet the mean inclination is $8^\circ \pm 3^\circ$ shallower than predicted by paleomagnetic poles determined from Paleocene igneous rocks in Montana. This shallowing of inclination is almost certainly the effect of compaction.
4. *Late Cretaceous and Early Tertiary pelagic limestones, Umbrian Apennines, Italy.* An extraordinary amount of paleomagnetic data are available from pelagic limestones of northern Italy (see Chapter 9). Inclination of magnetization in these limestones is indistinguishable from the expected inclination predicted for the African plate to which these limestones were formerly attached (Lowrie and Heller, 1982). No inclination error exists in the paleomagnetism of these pelagic limestones.
5. *Pacific Plate Deep Sea Drilling Project Sediments.* Many sediment cores have been collected from the Pacific Ocean Basin by the Deep Sea Drilling Project (DSDP). Paleomagnetic inclinations from these cores have been used to determine the paleolatitude at which these sediments were deposited (using Equation (1.15)). Paleolatitudes can be determined from a variety of other observations, including (1) paleomagnetic data from sequences of lava flows collected at some DSDP sites, (2) analysis of magnetic anomalies produced by seamounts, (3) analysis of the shape of lineated marine magnetic anomalies, and (4) sedimentologic determination of facies deposited near the equator. From all methods of analysis, it is clear that portions of the Pacific Plate moved into the northern hemisphere from Cretaceous paleolatitudes in the southern hemisphere. Tarduno (1990) and Gordon (1990) have shown that the southerly paleolatitudes determined from paleomagnetism of Pacific DSDP sediments are systematically lower (closer to the equator) than paleolatitudes determined from the other techniques.

A shallowing of the paleomagnetic inclination (Equation (8.7)), leads to an error in the paleolatitude (λ) determined from the mean inclination. This paleolatitude error, $\Delta\lambda$, is given by

$$\Delta\lambda = \lambda - \tan^{-1}(f \tan \lambda) \quad (8.9)$$

where λ is the paleolatitude at which the sediments were deposited. For Pacific DSDP sediments, Tarduno (1990) found a best-fit value of $f = 0.52$ with lower and upper confidence limits of $f = 0.23$ and $f = 0.80$.

Thus, it appears that inclination error of about 10° can be documented for some sediments, whereas absence of inclination error can be demonstrated for other sedimentary rocks. We cannot yet predict which rock types contain inclination error. Nevertheless, we can make some generalizations about sources of inclination error and sedimentary rocks that are most likely to contain inclination error.

1. *Depositional inclination error.* Shallowed inclinations during acquisition of depositional DRM (Figure 3.15b) are most likely to occur in larger grain-size sediments. High deposition rate may enhance this effect. For most fine sands and smaller grain-size sediments and any bioturbated sediment, postdepositional alignment dominates and has the effect of erasing depositional inclination error.
2. *Compaction.* Shallowing of inclination can be induced by compaction and is probably a larger effect for fine-grained sediments. Lithologies that undergo substantial compaction (e.g., claystone, mudstone, or sediments with muddy matrix) are probably most susceptible to inclination shallowing through compaction. Lithologies showing minimal compaction such as grain-supported sandstones might not experience compaction shallowing of inclination.
3. *Deformation.* It is likely that deformation can affect inclination. Folding of sedimentary strata involves strain, and high degrees of strain might realign magnetic grains producing magnetic anisotropy. Inclination error might be a result.
4. *Cementation.* While there are many unknowns regarding inclination error, it is clear that early cementation prevents compaction-induced inclination error because cementation essentially halts compaction. Sedimentary rocks that have been cemented soon after deposition are probably immune to shallowing of DRM by compaction.

BIOMAGNETISM: BIRDS DO IT, BEES DO IT

Recent research indicates that magnetite is a biochemical precipitate of major significance. *Biogenic magnetite* has been found in three of the five kingdoms of living organisms, including pigeons and honeybees. Although originally thought to be unrelated to paleomagnetism, biogenic magnetite has been found in a wide variety of sedimentary rocks and might be a major contributor to DRM in marine sediments (Chang and Kirschvink, 1989).

The most celebrated examples of organisms containing biogenic magnetite are *magnetotactic bacteria*. These bacteria contain magnetite crystals arranged in chains and held within a *magnetosome*. Transmission electron microscopy (TEM) has revealed that magnetite grains in magnetotactic bacteria (and in a wide variety of other organisms) are within the stable single-domain (SD) size and shape range (Figure 8.4). Accordingly, individual SD magnetite crystals in bacterial magnetosomes have maximum intensity and stability of magnetization. Furthermore, magnetite crystals are aligned within the magnetosome so that magnetocrystalline easy directions are parallel to the chain with the result that magnetic moments of individual crystals add up to produce a very effective and stable magnet. This magnet serves as a geomagnetic sensor that guides magnetotactic bacteria down magnetic flux lines, helping them to remain within the preferred habitat of oxygen-poor zones within muddy layers of accumulating sediment.

TEM examinations have shown that biogenic magnetite crystals have morphologies that are distinct from magnetite of igneous or authigenic origin. An example is presented in Figure 8.5a. Examination of morphology of magnetite crystals therefore allows identification of biogenic magnetite in sedimentary rocks, and these magnetites are referred to as *magnetofossils*. Biogenic magnetite has been found in marine sedimentary rocks as old as 700 Ma from a wide variety of depositional environments and are especially prevalent in calcareous oozes. Estimates of bacterial abundances and sediment accumulation rates indicate that biogenic magnetite could account for a major percentage of stable DRM in marine sedimentary rocks. The paleomagnetic significance of biogenic magnetite is emphasized by the observation that all sedimentary rocks that are shown to contain biogenic magnetite also contain a stable paleomagnetism formed as a primary DRM.

MARINE SEDIMENTS

Marine sediments are a rich potential source of paleomagnetic data because biostratigraphic data can provide accurate age information and thick sections can encompass large time intervals. In addition, numerous

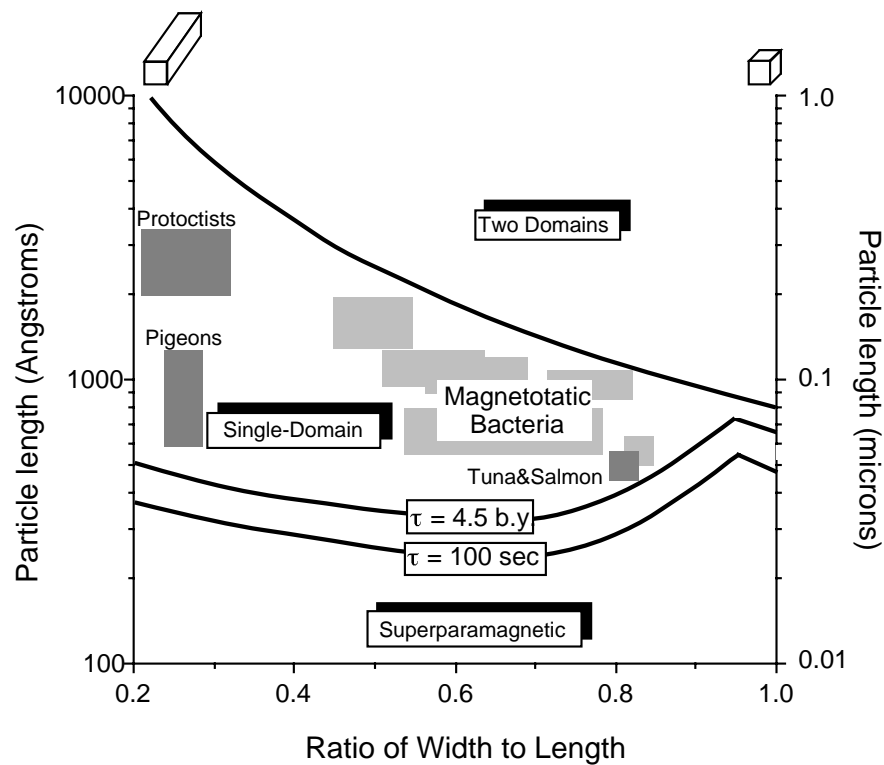


Figure 8.4 Size and shape distribution of biogenic magnetite grains. Distribution of grains in magnetotactic bacteria is shown by lightly stippled fields; distribution of grains in other organisms is shown by darker stippled fields; distribution of two-domain, single-domain, and superparamagnetic fields is from Figure 3.2. Redrawn from Chang and Kirschvink (1989). Reproduced, with permission, from the Annual Reviews of Earth and Planetary Sciences, Vol. 17, copyright 1989 by Annual Reviews Inc.

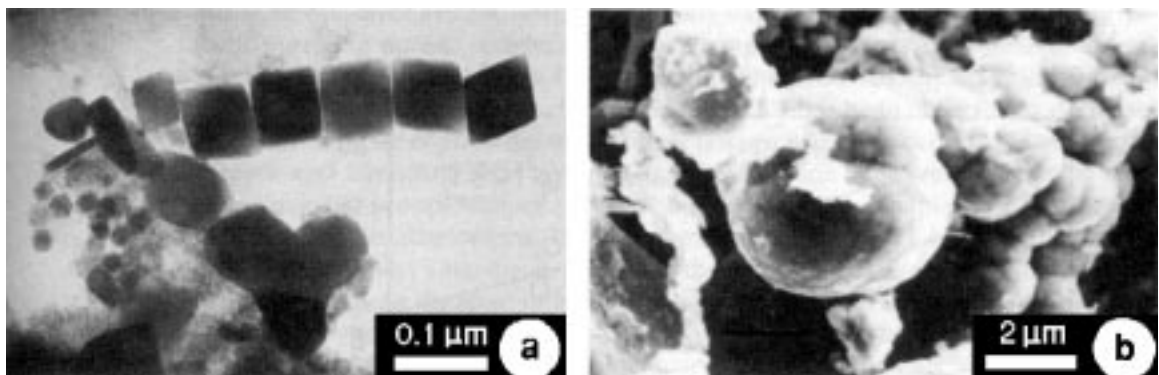


Figure 8.5 (a) Transmission electron micrograph of biogenic magnetite crystals from a deep-sea sediment. Kindly provided by H. Vali. (b) Scanning electron micrograph of botryoidal authigenic magnetite in the Helderberg Group (Devonian) of New York state. Kindly provided by C. McCabe.

subaerially exposed sections of marine sediments (especially shallow-water carbonates) are available. Although intensities of remanent magnetization are low (typically 10^{-6} to 10^{-8} G, 10^{-3} to 10^{-5} A/m), modern magnetometers can measure these weak magnetizations quite accurately.

Some deep-sea cores and subaerial sections of marine sediments yield high-quality paleomagnetic data, while others do not. Destruction of original detrital ferromagnetic minerals and late diagenetic production of ferromagnetic minerals are basic reasons for failure to obtain useful paleomagnetic data. In this section, we consider some fundamental geochemistry of marine sediments. For a more complete discussion, see the excellent review by Henshaw and Merrill (1980).

The first consideration is stability of iron oxides and sulfides in marine sedimentary environments. An equilibrium diagram for the Fe–S–H₂O system is shown in Figure 8.6. The small stippled box in the figure indicates the range of normal seawater conditions. The pH of seawater and marine sediments is controlled within a narrow range ($8.1 < \text{pH} < 8.2$). But oxidizing or reducing conditions vary widely from the nominally oxidizing conditions of seawater to highly reducing conditions within sediments containing abundant organic matter. Figure 8.6 shows that goethite is the Fe-oxide expected to precipitate from solution under normal conditions (if Fe exceeds solubility limits). However, authigenic magnetite and/or pyrite may precipitate if neutral or reducing conditions occur during diagenesis.

Hemipelagic sediments

Hemipelagic sediments have at least 25% of coarse fraction composed of terrigenous, volcanogenic, and/or neritic detritus. These sediments are usually deposited on the continental margin and adjacent abyssal plain. Rates of sediment accumulation are typically 1 m/1000 yr. The dominant detrital ferromagnetic mineral is magnetite with typical concentration 0.05% by volume. Grain size of magnetite is dominantly $\leq 1 \mu\text{m}$. This magnetite is an efficient recorder of primary DRM.

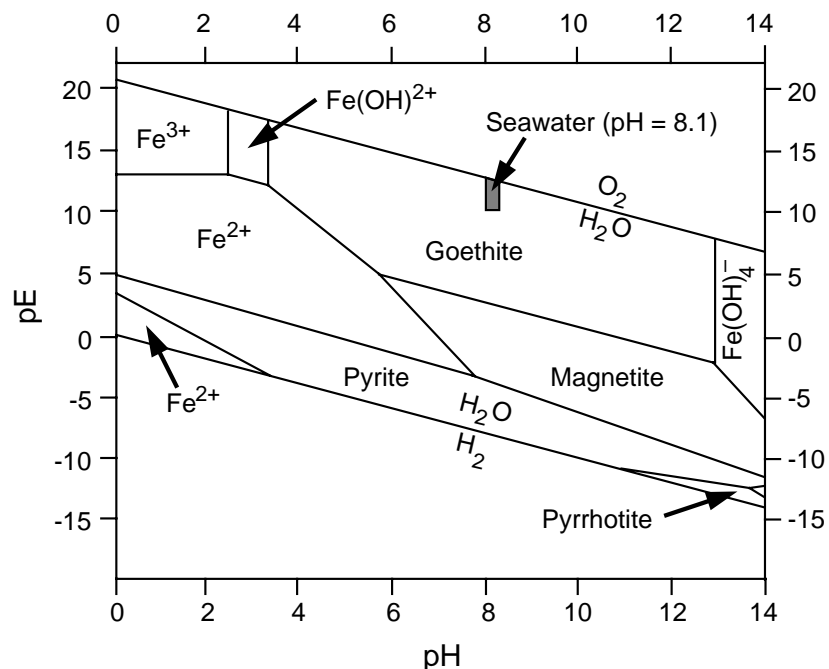


Figure 8.6 Equilibrium diagram of the Fe–S–H₂O system. pH < 7 indicates acidic conditions; pH > 7 indicates basic conditions; pE > 0 indicates oxidizing conditions; pE < 0 indicates reducing conditions; stability fields for precipitation of goethite, magnetite, pyrite, and pyrrhotite are shown; normal seawater conditions are within the stippled region. Redrawn from Henshaw and Merrill (1980) with permission of the American Geophysical Union.

However, diagenetic alteration of detrital ferromagnetic minerals can take place in the upper few meters of hemipelagic sediments (Karlin and Levi, 1985). If a high sedimentation rate prevents complete oxidation of organic matter prior to burial, a two-layer system develops with an oxidizing upper layer less than 1 m thick overlying anoxic sediment below. Figure 8.6 suggests that these reducing conditions could drive the Fe-S-H₂O system into the pyrite stability field. Indeed, the magnetite content of organic-rich hemipelagic muds has been observed to decrease by at least a factor of 10 in the upper meter (Figure 8.7). This decrease in magnetite content and attendant NRM are caused by dissolution of detrital magnetite with accompanying precipitation of pyrite. If this *sulfurization* completely dissolves the detrital magnetite, the original DRM is destroyed.

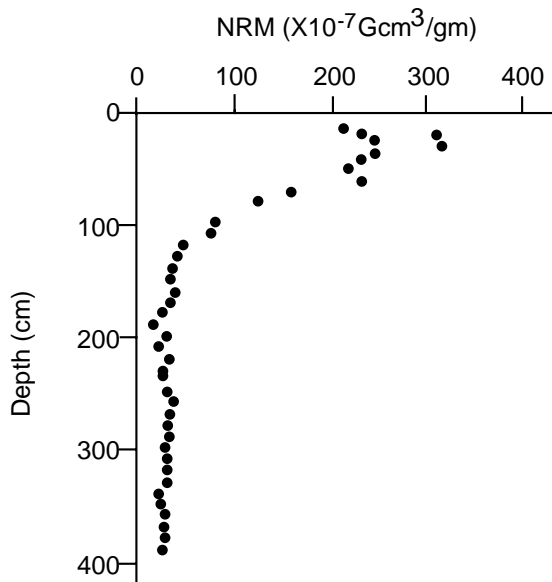


Figure 8.7 NRM intensity versus depth in a core of hemipelagic marine sediment. The core was collected from the lower continental shelf off the coast of Oregon in 1820-m water depth; the sediment is olive green, heavily bioturbated, suboxic hemipelagic mud; the mean sediment accumulation rate was ~120 cm/1000 yr; NRM intensity is after alternating-field demagnetization to peak field of 150 Oe (15 mT). Redrawn from Karlin and Levi (1985), with permission of the American Geophysical Union.

Fortunately, a significant fraction of the detrital magnetite usually survives until anoxic reactions decrease or are halted by cementation or lithification. In strongly reducing environments, however, detrital magnetite may be totally destroyed or survive only within early-formed concretions. Marine sediments with high sulfide content thus are unattractive targets for paleomagnetic study.

Pelagic sediments

Over half the ocean floor is covered by pelagic sediments that are primarily calcareous, diatomaceous, or radiolarian oozes. Gradual lithification and cementation take place by dissolution and recrystallization of foraminifera and coccoliths. Rates of sediment accumulation for pelagic sediments are only a few mm/1000 yr, and conditions are more uniformly oxidizing than for hemipelagic sediments. Detrital magnetite and titanomagnetite constitute about 0.01% by volume.

Fossil-bearing pelagic sediments are commonly reliable paleomagnetic recorders, whereas pelagic sediments without recognizable fossils tend to yield paleomagnetic records that progressively deteriorate in quality down the core (Henshaw and Merrill, 1980). Two diagenetic processes are thought to be responsible:

1. Progressive low-temperature oxidation of detrital magnetite often yields maghemite. This process might be particularly important for pelagic red clays common in the North Pacific. Organic matter in fossil-bearing pelagic sediments might prevent oxidation and account for the superior quality of paleomagnetic records from fossil-bearing sediments.
2. Authigenic precipitation of ferromagnetic ferromanganese oxides produce a slowly acquired CRM that overprints the original DRM.

Ancient Limestones

A detailed review of rock magnetism and paleomagnetism of marine limestones is given by Lowrie and Heller (1982). Only the basic properties are described here.

Some limestones are paleomagnetic recorders of extraordinary fidelity, while others yield little useful paleomagnetic information. Common ferromagnetic minerals in marine limestones included magnetite, goethite, hematite, and maghemite. With the exception of limestones suffering wholesale chemical remagnetization during orogenesis, morphology and chemistry of grains indicate that the magnetite is detrital. The primary paleomagnetism in most limestones is a pDRM carried by detrital magnetite.

Hematite is present as a pigment in red and pink limestones. Some detailed examinations have shown that hematite pigment can form as an early diagenetic product from goethite. In such rocks, CRM carried by the hematite can be essentially contemporaneous with DRM carried by detrital magnetite. However, if significant hematite is present, relative timing of DRM carried by magnetite and CRM carried by hematite must be established on an individual case basis.

Goethite is widespread in limestones and coexists with both magnetite and hematite. The presence of significant goethite is usually ominous for paleomagnetic investigations. Goethite can precipitate directly from solution (Figure 8.6) or result from alteration of pyrite, which is particularly common in white and blue-gray limestone. This alteration may be diagenetic but can also occur during subaerial weathering of porous limestone. Goethite often carries an unstable magnetization and dehydrates to hematite during laboratory heating to 300°C, leading to major complications during thermal demagnetization experiments. Thus, the presence of significant goethite generally leads to difficulties in isolating primary DRM carried by magnetite.

For many limestones, laboratory heating to 450° to 650°C produces new magnetite, either from pyrite or by reduction of hematite. This magnetite has superparamagnetic grain size and rapidly acquires troublesome VRM components that complicate isolation of primary DRM. Limestones with significant detrital magnetite but without significant pyrite or goethite can yield highly reliable paleomagnetic data. However, presence of significant pyrite or goethite usually leads to insurmountable difficulties. The most advantageous sedimentary environment for retaining primary DRM in pelagic limestones is a slightly oxidizing environment in which rapid cementation halts diagenetic changes, preserving detrital magnetite and preventing production of goethite.

Laboratory evidence that the remanent magnetization of a limestone is carried by magnetite is a necessary but not sufficient condition to assert that the magnetization is a primary DRM. As discussed below, secondary authigenic magnetite has been found in some Paleozoic limestones. Especially for ancient limestones that have been subjected to complex geochemical and tectonic history, field tests of paleomagnetic stability are indispensable.

MAGNETIC ANISOTROPY

Rocks in which intensity of magnetization (whether induced or remanent) depends on direction of the applied magnetic field have *magnetic anisotropy*. In such rocks, the direction of magnetization can deviate from that of the magnetizing field. There are two kinds of magnetic anisotropy:

1. *anisotropy of magnetic susceptibility* (AMS), in which susceptibility is a function of direction of the applied field; and
2. *anisotropy of remanent magnetization*, in which acquired remanent magnetization may deviate from the direction of the magnetic field at the time of remanence acquisition. Anisotropy of remanent magnetization has obvious implications for the accuracy of paleomagnetic records.

Studies of anisotropy of magnetic susceptibility have a wide range of applications (Hrouda, 1982; MacDonald and Ellwood, 1987). AMS exceeding 5% is generally observed only in rocks with obvious megascopic fabric, and values exceeding 10% are rare. But AMS of a few percent can be easily measured.

Because AMS can be measured more quickly and easily than, for example, measuring mineral orientations by optical analysis of thin sections, AMS has been used to examine development of petrofabrics.

Anisotropy of magnetic susceptibility is commonly expressed by comparing magnetic susceptibility values in three mutually perpendicular directions: K_1 = maximum susceptibility; K_2 = intermediate susceptibility; K_3 = minimum susceptibility. These values describe the *magnetic susceptibility ellipsoid*. If $K_1 = K_2 = K_3$, the ellipsoid is spherical; if $K_1 \approx K_2$ but $K_2 > K_3$, the ellipsoid is oblate (flattened); if $K_1 > K_2$ and $K_2 \approx K_3$, the ellipsoid is prolate (cigar-shaped). Magnetic susceptibility ellipsoids are usually interpreted as indicating statistical alignment of elongate or platy magnetic grains, usually ferromagnetic grains. For example, elongate magnetite grains in a rock with a pronounced foliation will have long axes rotated toward the foliation plane. The resulting magnetic susceptibility ellipsoid is oblate with K_3 perpendicular to foliation. Conversely, a rock with significant lineation will have a prolate magnetic susceptibility ellipsoid with K_1 parallel to the lineation direction.

AMS applications have been made to sedimentology, igneous processes, and structural geology. Sedimentary rocks generally display a slight AMS of oblate susceptibility ellipsoid with K_3 perpendicular to bedding. AMS of sedimentary rocks can sometimes be used to determine paleocurrent directions (Ellwood, 1980; Flood et al., 1985). AMS has also proved useful in analyses of flow of volcanic rocks. Oblate magnetic susceptibility ellipsoids are often observed in volcanic rocks with flow fabrics; K_3 is found perpendicular to flow surfaces. Prolate magnetic susceptibility ellipsoids are sometimes observed with K_1 parallel to the lines of flow of volcanic rocks. In fact, AMS analyses can be used to locate source areas of volcanic rocks, especially ignimbrites and welded tuffs, by using the direction of the K_1 axis at widely separated sampling locations to triangulate on the source vent (Ellwood, 1982; Knight et al., 1986).

In structural applications, AMS has been used to examine patterns of strain. An oversimplified view is that elongate ferromagnetic grains are passively rotated during straining of rocks. For example, the pattern of AMS in a shear zone might be used to decipher the strain involved. Applications to mylonite zones have been reported by Goldstein and Brown (1988) and Ruf et al. (1988). Quantitative relationships between strain and AMS are needed to infer strain directly from AMS. Kligfield et al. (1983) have developed such a relationship for Permian red sediments of the Maritime Alps.

Rocks with substantial AMS are likely to be anisotropic for acquisition of remanent magnetism and therefore not accurate paleomagnetic recorders. Many rocks that are of interest for AMS studies have obvious petrofabrics, which indicate that they are not appropriate for paleomagnetic analysis. But how much AMS can be tolerated? A useful generality is that paleomagnetic data from rocks with AMS exceeding about 5% should be viewed with particular caution. However, in the case of magnetite-bearing rocks, AMS is dominated by multidomain grains while single-domain and pseudosingle-domain grains are the paleomagnetic recorders. So AMS might not be closely related to anisotropy of remanent magnetization (Stephenson et al., 1986).

Because conditions of primary NRM formation are indirectly inferred and difficult to reproduce, anisotropy of remanent magnetization must be examined indirectly. Some volcanic rocks with pervasive flow fabric have significant deflection of TRM from the direction of the magnetic field present during cooling. However, these cases are rare, and significant anisotropy of remanent magnetization in the vast majority of igneous rocks or in red sediments is demonstrably absent or unlikely.

Most recent attention has focused on sedimentary rocks, especially those with possible inclination error. Some interesting observations have been made by using a form of remanent magnetization that can be easily produced in the laboratory. *Anhyseretic remanent magnetization* (ARM) is produced by superimposing an alternating magnetic field (e.g., Figure 5.1a) on a small direct magnetic field. The ferromagnetic grains that carry ARM are those grains with microscopic coercive force up to the maximum amplitude of the alternating magnetic field used to impart the ARM. As with other forms of remanent magnetization, SD and PSD grains are more effective carriers of ARM than are MD grains. So imparting ARM in different directions within a rock sample allows examination of fabric in the important carriers of remanent magnetism, the SD and PSD grains.

Observed anisotropy of ARM (more or less ARM acquired in some sample directions than in other directions) indicates possible anisotropy in acquiring NRM. This provides a warning that the rock might not be an accurate paleomagnetic recorder. Also ARM can be measured for weakly magnetic rocks (such as limestones), whereas AMS can be measured only for rocks with substantial ferromagnetic content (McCabe et al., 1985; Jackson et al., 1988). Potential applications in deciphering possible inclination error in sedimentary rocks are of major significance.

CHEMICAL REMAGNETIZATION

To this point, secondary CRM components have been discussed only in the section on magnetization of marine sediments. However, many rocks suffer chemical remagnetization in which primary NRM is destroyed and replaced by secondary CRM. In this section, some examples of remagnetization are discussed. This is definitely a “good news and bad news” situation. The bad news is that remagnetized rocks do not retain a primary NRM and many objectives of paleomagnetic study of these rocks cannot be met. The good news is that the timing and processes of remagnetization are providing important insights into orogenic and geochemical processes.

Weathering can affect original ferromagnetic minerals and result in the formation of new ferromagnetic minerals with attendant CRM components. Because surface conditions are predominantly oxidizing, reactions that transform primary ferromagnetic minerals (such as magnetite) to higher oxidation state minerals (such as hematite or goethite) are common. Although the usual concern is for CRM acquired during recent weathering, secondary CRM components may have resulted from ancient weathering. A clear case of remagnetization of older rocks by ancient weathering was presented by Schmidt and Embleton (1976).

Regional lateritization of western Australia in Late Oligocene to Early Miocene time produced chemical remagnetization of Late Paleozoic through Mesozoic strata. Lateritization and acquisition of CRM in resulting hematite occurred over a time interval spanning at least one geomagnetic polarity reversal because both normal- and reversed-polarity CRM is observed. The paleomagnetic pole determined from the direction of chemical remagnetization coincides with the 20 to 25 Ma pole position for Australia. This inferred age of chemical remagnetization in western Australia is supported by independent paleoclimatological and geochronological data indicating a Late Oligocene to Early Miocene interval of peneplanation and lateritization in northern and western Australia.

The most intensely studied remagnetization is that of Early and Middle Paleozoic rocks in the Appalachian region of eastern North America. This remagnetization took place during the Late Carboniferous and Permian, affected a wide variety of rock types, and is clearly related to the Late Paleozoic Alleghenian Orogeny. An excellent review article was provided by McCabe and Elmore (1989).

Creer (1968) observed that many paleomagnetic poles from Early Paleozoic rocks of North America were similar to poles from Late Paleozoic rocks. He suggested that the Early Paleozoic units were chemically remagnetized in the Late Paleozoic by protracted weathering while North America was situated in tropical paleolatitudes (see Chapter 10). As more paleomagnetic data were obtained and more sophisticated demagnetization techniques and analyses were applied, multiple components of NRM were observed in Early Paleozoic units of the Appalachians. For example, Van der Voo and French (1977) found two components of NRM in the Ordovician Juniata Formation. The highest-stability component passed a fold test and is therefore pre-folding. But a lower-stability component was found to fail the fold test, with in situ directions indicating a Late Paleozoic age. Van der Voo and French (1977) argued that this Late Paleozoic component of NRM was the result of remagnetization by thermal and/or chemical effects associated with the Alleghenian Orogeny rather than the result of surface weathering.

Subsequent studies have documented the widespread nature of this remagnetization. Irving and Strong (1984, 1985) observed both pre-folding and post-folding components of NRM in Early Carboniferous red sediments of western Newfoundland. This observation led to significant revision of ideas about tectonic

motions of terranes in the Appalachians, and many of the remagnetizations have been shown to be synfolding (Chapter 5, Figure 5.13), indicating a causal connection with the Alleghenian Orogeny.

Before detailed analysis of remagnetized limestones in the Appalachians, it was commonly believed that only oxidation reactions could lead to remagnetization. But Late Paleozoic remagnetizations of some Appalachian limestones are carried by authigenic magnetite (Scotese et al., 1982; McCabe et al., 1983). Magnetite has been separated from the remagnetized limestones and identified as authigenic by (1) lack of Ti or other Fe-substituting cations that are commonly found in magnetite from igneous or extraterrestrial sources and (2) hollow or botryoidal morphology indicating in situ precipitation (Figure 8.5b). Independent evidence indicates that precipitation occurred at low temperature (<200°C). Recent observations have revealed magnetite crystals with pyrite cores, indicating that authigenic magnetite is an alteration product of preexisting pyrite (Suk et al., 1990).

The geochemistry of this remagnetization is complex; remagnetizations in red sediments are carried by hematite, whereas remagnetizations in most carbonates are carried by magnetite. Furthermore, not all researchers agree that remagnetization is necessarily the result of chemical reactions leading to CRM. Kent (1985) concluded that thermoviscous effects of burial are important (remember TVRM from Chapter 3?). Also van der Pluijm (1987) and Kodama (1988) argue that strain effects during folding play an important role in altering the NRM of some units.

The role of fluids in producing the chemical remagnetizations is also of interest. Lateral migration of "orogenic fluids" may result from motions of thrust sheets driving fluids toward the craton (McCabe et al., 1983; Oliver, 1986). In favorable circumstances, the directions of the remagnetization can be used to date the time of fluid migration and orogeny. This possibility is given economic incentive because the fluids involved include hydrocarbons. Authigenic magnetite has been found in bitumen of remagnetized Paleozoic carbonates in the midcontinent region of North America (McCabe et al., 1987). Evidence for Cretaceous remagnetization carried by authigenic magnetite associated with hydrocarbon migration has been found in the Rocky Mountain region (Benthien and Elmore, 1987). The possible use of remagnetizations carried by authigenic magnetite as a technique for dating hydrocarbon migration is under investigation.

There are several lessons to be gained from this discussion of chemical remagnetization:

1. Detailed demagnetization analyses are essential to resolve the multiple components of NRM that are often encountered in old rocks that have experienced complex histories.
2. Field tests of paleomagnetic stability can provide crucial information about acquisition times for these components of NRM.
3. Geochemical and thermal effects of orogeny can lead to remagnetization by a variety of mechanisms.
4. Rock-magnetic and paleomagnetic analysis of the remagnetization process can lead to new applications of the paleomagnetic technique.

Discovery of secondary CRM is rarely the intent of a paleomagnetic study. But the direction of chemical remagnetization can constitute an important observation potentially allowing determination of the age of geochemical events such as orogenic fluid motions or hydrocarbon migration. As noted by McCabe and Elmore (1989), "Paleomagnetic studies promise to be important in assessing the role of orogeny in driving fluid migrations within sedimentary basins and in constraining the age of the migrations and the nature of the fluids."

THE RED BED CONTROVERSY

Intensity of natural remanent magnetization in red sediments is commonly $\geq 10^{-5}$ G (10^{-2} A/m). These intensities can be measured on a variety of instruments that are available from the early development of paleomagnetism, and red sediments are abundant in the stratigraphic records of most continents. Accordingly, numerous paleomagnetic studies have been undertaken on red sediments. However, there are major

differences of interpretation about magnetization acquisition by red sediments. The resulting debate is the “red bed controversy.”

The extreme views can be summarized as follows:

1. High-stability components of NRM (the ChRM) in red sediments are carried by detrital specular hematite that is magnetized by DRM processes (Elston and Purucker, 1979; Steiner, 1983). This ChRM is penecontemporaneous with deposition and can provide high-fidelity records of the paleomagnetic field, including records of paleosecular variation (Baag and Helsley, 1974) and geomagnetic polarity transitions (Herrero-Bervera and Helsley, 1983; Shive et al., 1984).
2. Multiple components of CRM are acquired during protracted chemical processes occurring up to 10 m.y. after deposition of a red sediment (Roy and Park, 1972; Larson and Walker, 1975; Turner, 1980; Walker et al., 1981; Larson et al., 1982). Neither useful polarity stratigraphy nor records of paleosecular variation or geomagnetic polarity transitions can be retrieved from red sediments.

The fundamental question can be stated as follows: “Is the ChRM in red sediments a DRM acquired penecontemporaneously with deposition, or is it a CRM acquired during protracted chemical change occurring up to 10 m.y. post-deposition?” The answer is a resounding, authoritative “Yes!” Obviously, there would be no controversy if the situation were simple. The discussion below does not provide an answer to the red bed controversy but rather explains the fundamental evidences and arguments. On each aspect of the controversy, the discussion proceeds from generally accepted background information to more controversial interpretations.

The dominant (usually exclusive) ferromagnetic mineral in red sediments is hematite, which occurs in two general categories:

1. Opaque crystals that are generally larger than 1 μm and exhibit silvery, anisotropic reflectance when viewed in polished section. This form is specular hematite, or simply specularite (Figures 8.8a, 8.8b, 8.8c).
2. Fine-grained (< 1 μm) hematite pigment that is translucent and is largely responsible for the red coloration of the sedimentary rock (Figure 8.8d).

Pigmentary hematite often cements detrital grains and is clearly formed by postdepositional chemical processes. Two important reactions probably account for a majority of hematite pigment: (1) dehydration of ferric oxyhydroxides in newly deposited sediment and in soil layers and (2) alteration of Fe-bearing silicates. Textural relationships sometimes allow the sequence of pigment-forming reactions to be determined. However, the rates of these reactions are not sufficiently known to allow secure statements about the time interval required for pigment formation.

Because of the small grain size of many of the pigment crystals, the magnetization of many pigment grains is unstable over geologic time, and these grains tend to acquire viscous magnetization. Usually, this VRM can be erased by either chemical or thermal demagnetization techniques. Pigmentary hematite also can acquire CRM during precipitation and grain growth in the geomagnetic field. But the difficulty in interpretation of this CRM is determining its time of formation. Some experiments indicate that CRM carried by hematite pigment is composed of multiple components of magnetization acquired during protracted chemical precipitation, perhaps millions of years after deposition (Roy and Park, 1972). Although certainly not a universal observation, several studies have shown that the ChRM is carried not by the hematite pigment but rather by the specular hematite (Collinson, 1974; Tauxe et al., 1980). So for most red sediments, the question of the timing of ChRM acquisition becomes a question of time of formation of the specular hematite.

The major question is whether the specular hematite in a red sediment was deposited as a detrital grain of specular hematite and could potentially have acquired a DRM or formed by postdepositional oxidation of magnetite or other Fe-bearing minerals and therefore carries a CRM that could have been acquired long

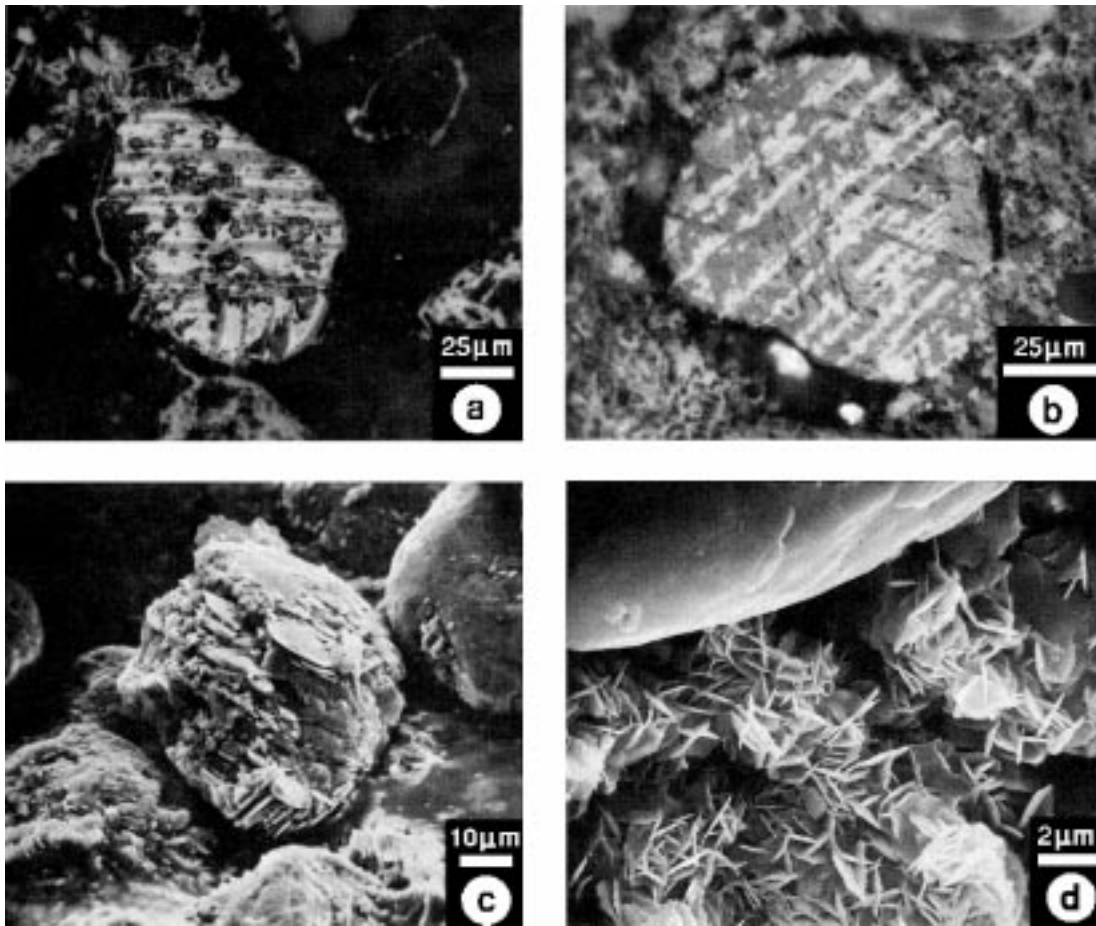


Figure 8.8 Optical and SEM photomicrographs of hematite and associated minerals in red sediments. (a) Detrital grain exhibiting “tiger-striped” ilmenite-hematite intergrowth; darker ilmenite layers alternate with lighter layers of hematite. (b) Polycrystalline martite grain showing crystalline units intersecting along octahedral planes inherited from replacement of parent magnetite; the entire grain is hematite; differing shades of gray result from different crystallographic directions for different portions of the grain; (c) SEM photomicrograph of martite grain with overgrowths of authigenic specular hematite. (d) SEM photomicrograph of interlocking hematite crystals within a sand-size void. All samples are from the Wupatki Member of the Moenkopi Formation. Photomicrographs kindly provided by T. Walker.

after deposition. To appreciate the difficulty of addressing this question, we must consider the possible origins of specular hematite in general.

The forms of specular hematite present in red sediments include the following:

1. *Igneous/metamorphic specular hematite.* As discussed in Chapter 2, hematite can result from igneous processes. Grains that are intergrowths of hematite and ilmenite resulting from high-temperature exsolution are occasionally found in red sediments. These grains often exhibit a “tiger-striped” texture (Figure 8.8a). Such intergrowth grains result from high-temperature processes and must have been eroded from an igneous source terrane and deposited as specular hematite.
2. *Martite.* Grains of specular hematite often show clear evidence of resulting from oxidation of preexisting magnetite. Pseudomorphs of the original magnetite are preserved, and these grains contain ilmenite laths resulting from deuteric oxidation of the original titanomagnetite grain (Figure 8.8b). Composite grains with specular hematite exteriors and magnetite cores are also observed. Grains of specular hematite with clear evidence of formation by oxidation of magnetite are referred to as

martite. But observation of martite grains does not necessarily provide evidence that the grain was martite when deposited; it could have been martitized by in situ postdepositional oxidation of a detrital magnetite grain. Sometimes delicate authigenic overgrowths of specular hematite exist on martite grains (Figure 8.8c). At least the overgrowth portions of these grains must have resulted from postdepositional authigenesis. However, the time of oxidation of most martite grains is indeterminate from petrographic analysis alone.

3. *Specular hematite in Fe-bearing silicates*. Oxidation of Fe-bearing silicates often yields specular hematite that may form in cleavage planes of the host mineral. Textural evidence often indicates sequences of reactions that are the result of in situ oxidation (Walker et al., 1981).
4. *Specular hematite of uncertain origin*. Many grains of specular hematite lack textural patterns that provide information about their origin.

Given the difficulty of determining the origin of specularite grains in red sediments, it is not surprising that disparate interpretations exist. Recent sedimentary deposits do not often contain specular hematite as the dominant ferromagnetic mineral; magnetite is usually dominant (Van Houten, 1968). This observation has been used to argue that most specular hematite must be formed by postdepositional oxidation of detrital magnetite. However, some modern streams do deposit detrital specularite, and these deposits do possess a substantial DRM (Tauxe and Kent, 1984). This DRM is further observed to have a pronounced inclination error, which probably results from the low ratio of magnetic moment to gravitational torque. Paleomagnetic studies of some ancient red sediments has revealed inclinations of magnetization that seem to be systematically shallowed in heavy mineral layers containing high concentrations of specular hematite (Elston and Purucker, 1979; Steiner, 1983). So some evidence favors postdepositional formation of the majority of specularite, while other evidence indicates the possibility of DRM or pDRM acquisition in detrital specularite.

The best evidence for the mode and timing of acquisition of NRM by red sediments comes from field tests (Chapter 5) applied to sedimentary structures. During deposition of stratigraphic sequences of red sediments, rip-up clasts of previously deposited layers are occasionally incorporated within intraformational conglomeratic layers. Oriented samples of these clasts can be used as a conglomerate test. If directions of ChRM in numerous clasts are randomly directed, the magnetization must have been acquired before the layer yielding the clasts was disrupted. This test has been applied to Mesozoic red beds of western North America with mixed results. Some conglomeratic layers pass the conglomerate test, and others appear to fail this test (Purucker et al., 1980; Liebes and Shive, 1982; Larson and Walker, 1982).

Soft-sediment deformational structures such as load casts and slump folds have also been investigated. For the Triassic Moenkopi and Chugwater formations of the Rocky Mountains and Colorado Plateau, magnetizations of most load casts and small-scale slump folds (<1 m amplitude) were found to fail the fold test, while larger-amplitude folds yielded magnetizations that passed the fold test (Liebes and Shive, 1982). These observations indicate that the ChRM of these Mesozoic red sedimentary formations was formed after deposition but prior to burial by about 1 m of sediment. The conclusion was that the ChRM is a CRM acquired predominantly within a few hundred years of deposition.

Examination of the within-site and between-site dispersion of ChRM directions can also provide information about the time interval over which this magnetization was acquired. Acquisition over a time interval exceeding 10^5 yr would yield site-mean ChRM directions with angular dispersion much lower than the dispersion expected for sampling geomagnetic secular variation. However, if dispersion of site-mean ChRM directions between stratigraphically superposed sites substantially exceeds dispersion within individual beds, some directional dispersion from sampling geomagnetic secular variation was probably recorded. Although detailed examinations are not numerous, observed between-site dispersion in some red sediments indicates acquisition of ChRM within 10^2 to 10^3 yr of deposition (Ekstrand and Butler, 1989). Herrero-Bervera and Helsley (1983) and Shive et al. (1984) investigated a polarity transition (~1-m-thick stratigraphic interval deposited while the geomagnetic field was switching polarity) within the Chugwater Formation. They found

that detailed directional changes of ChRM were consistent in multiple stratigraphic sections over a distance of 1 km. They argued that these consistent observations of rapid directional changes of the geomagnetic field require that the ChRM was acquired within $\sim 10^2$ yr of deposition.

So the present situation is that some red sediments appear to contain ChRM that is well defined, without multiple components. The bulk of available evidence suggests that these red sediments acquire a ChRM within 10^2 yr of deposition, most likely as a CRM. However, other red sediments with more complex magnetizations show evidence of components of magnetization acquired long after deposition, although exactly how long is not well constrained.

Figure 8.9 presents a schematic view of magnetization processes in red sediments. The time scale on the ordinate is a “best guess” at the time intervals over which different mechanisms of magnetization may operate. There are two basic categories:

1. *Detrital remanent magnetization.* Depositional or postdepositional DRM could form if a significant portion of the specular hematite is detrital. Mineralogically mature sediment would be more likely to contain detrital specular hematite than would first-generation (mineralogically immature) sedimentary rocks being eroded from a nearby igneous source terrane. Although still a matter of debate, it is a minority view that DRM is the major origin of ChRM in red sediments.
2. *Chemical remanent magnetism.* CRM is acquired during martitization of detrital magnetite, formation of specular hematite from Fe-bearing silicates, and authigenic production of pigmentary hematite. We could divide the CRM field into two subregions: (a) “early” chemical remanence, referring to CRM formed within 10^2 to 10^5 yr of deposition, and (b) “prolonged” chemical remanence, referring to CRM formed over longer time intervals. This subdivision has some paleomagnetic utility because early CRM could be applied to magnetic polarity stratigraphy when acquisition of the characteristic NRM within 10^5 yr of deposition is important. However, CRM formed over intervals up to perhaps 10^7 yr could still be used to determine paleomagnetic poles.

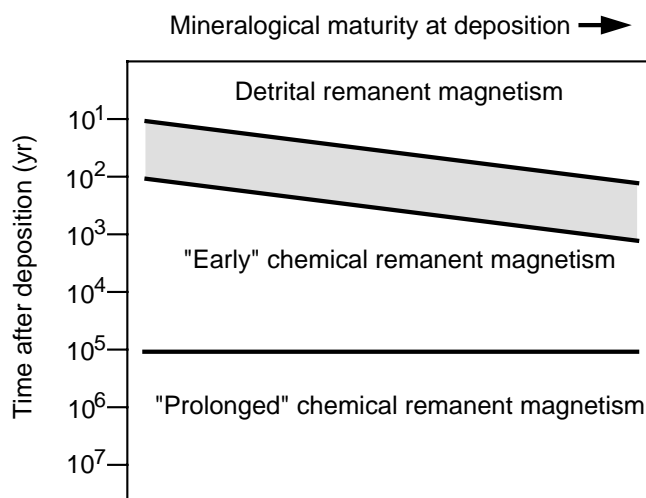


Figure 8.9 Mechanisms of magnetization in red sediments. Mineralogical maturity relates to the oxidation state of the deposited sediment; highly oxidized sediments have higher mineralogical maturity; demarcations between fields of different magnetization mechanisms are highly schematic. Adapted from Turner (1980).

While there are many uncertainties about the magnetization processes in red sediments, there are a number of factors that certainly play a role:

1. *Mineralogical maturity at deposition.* Immature sediments with abundant low-oxidation-state minerals might experience rapid oxidation and acquire the majority of their CRM quickly. More mature sediments might require more time for these postdepositional chemical reactions. This tendency for mineralogically immature sediments to more quickly acquire CRM is indicated schematically in Figure 8.9 by the sloping interface between the DRM and “early” CRM fields.

2. *Grain size of sediment.* Finer-grained sediments have particles with larger surface-to-volume ratio that likely undergo chemical changes more rapidly than larger-grained sediments. Clay diagenesis and cementation occur more rapidly in finer-grained sediments. So CRM in fine-grained, cemented red sediments might be acquired more quickly than in coarse-grained sediments.
3. *Depositional environment and paleoclimate.* A depositional environment that is highly oxygenated will produce more rapid oxidation favoring early formation of CRM. Warm, moist conditions yield more rapid and continual CRM formation than arid, dry conditions.

The bottom line on this discussion of magnetization of red sediments is that the processes are indeed complex and still controversial. Paleomagnetic data obtained from red sediments must be evaluated on a case-by-case basis. The best evidence for timing of remanence acquisition comes from field tests of paleomagnetic stability. The consensus view is that red sediments with uncomplicated, high-stability ChRM probably acquired this magnetization by CRM processes that occurred within 10^3 yr after deposition. Paleomagnetic data from these red sediments are useful for magnetic polarity stratigraphy and for determination of paleomagnetic poles. The timing of magnetization components for red sediments that yield complex, multi-component NRM is poorly constrained; caution must be exercised in interpreting such results.

REFERENCES

- G. L. Anson and K. P. Kodama, Compaction-induced shallowing of the post-depositional remanent magnetization in a synthetic sediment, *Geophys. J. Roy. Astron. Soc.*, v. 88, 673–692, 1987.
- P. Arason and S. Levi, Compaction and inclination shallowing in deep sea sediments from the Pacific Ocean, *J. Geophys. Res.*, v. 95, 4501–4510, 1990a.
- P. Arason and S. Levi, Models of inclination shallowing during sediment compaction, *J. Geophys. Res.*, v. 95, 4481–4499, 1990b.
- C. Baag and C. E. Helsley, Evidence for penecontemporaneous magnetization of the Moenkopi Formation, *J. Geophys. Res.*, v. 79, 3308–3320, 1974.
- C. E. Barton and M. W. McElhinny, Detrital remanent magnetization in five slowly redeposited long cores of sediment, *Geophys. Res. Lett.*, v. 6, 229–232, 1979.
- R. H. Benthien and R. D. Elmore, Origin of magnetization in the Phosphoria Formation at Sheep Mountain, Wyoming: A possible relationship with hydrocarbons, *Geophys. Res. Lett.*, v. 14, 323–326, 1987.
- R. A. Blow and N. Hamilton, Effect of compaction on the acquisition of a detrital remanent magnetization in fine grained sediments, *Geophys. J. Roy. Astron. Soc.*, v. 52, 13–23, 1978.
- R. F. Butler and L. H. Taylor, A middle Paleocene paleomagnetic pole from the Nacimiento Formation, San Juan Basin, New Mexico, *Geology*, v. 6, 495–498, 1978.
- M. A. Celaya and B. M. Clement, Inclination shallowing in deep sea sediments from the North Atlantic, *Geophys. Res. Lett.*, v. 15, 52–55, 1988.
- S. R. Chang and J. L. Kirschvink, Magnetofossils, the magnetization of sediments, and the evolution of magnetite biomineralization, *Ann. Rev. Earth Planet. Sci.*, v. 17, 169–195, 1989.
- R. S. Coe, S. Grommé, and E. A. Mankinen, Geomagnetic paleointensities from radiocarbon-dated lava flows on Hawaii and the question of the Pacific nondipole low, *J. Geophys. Res.*, v. 83, 1740–1756, 1978.
- R. S. Coe, B. R. Globberman, P. W. Plumley, and G. A. Thrupp, Paleomagnetic results from Alaska and their tectonic implications, In: *Tectonostratigraphic Terranes of the Circum-Pacific Region*, ed. D. G. Howell, Amer. Assoc. Petrol. Geol., Circum-Pacific Council for Energy and Mineral Resources Series, v. 1, 85–108, 1985.
- D. W. Collinson, The role of pigment and specularite in the remanent magnetism of red sandstones, *Geophys. J. Roy. Astron. Soc.*, v. 38, 253–264, 1974.
- K. M. Creer, Paleozoic palaeomagnetism, *Nature*, v. 219, 246–250, 1968.
- K. M. Creer, P. Tucholka, and C. E. Barton, ed., *Geomagnetism of Baked Clays and Recent Sediments*, Elsevier, Amsterdam, 324 pp., 1983.
- G. A. Deamer and K. P. Kodama, Compaction-induced inclination shallowing in synthetic and natural clay-rich sediments, *J. Geophys. Res.*, v. 95, 4511–4529, 1990.

- J. F. Diehl, M. E. Beck, Jr., S. Beske-Diehl, D. Jacobson, and B. C. Hearn, Paleomagnetism of the Late Cretaceous-Early Tertiary North-Central Montana Alkalic Province, *J. Geophys. Res.*, v. 88, 10,593–10,609, 1983.
- E. J. Ekstrand and R. F. Butler, Paleomagnetism of the Moenave Formation: Implications for the Mesozoic North American apparent polar wander path, *Geology*, v. 17, 245–248, 1989.
- B. B. Ellwood, Application of anisotropy of magnetic susceptibility method as an indicator of bottom-water flow direction, *Mar. Geol.*, v. 34, M83–M90, 1980.
- B. B. Ellwood, Estimates of flow direction for calc-alkaline welded tuffs and paleomagnetic data reliability from anisotropy of magnetic susceptibility measurements; central San Juan Mountains, Southwest Colorado, *Earth Planet. Sci. Lett.*, v. 59, 303–314, 1982.
- D. P. Elston and M. E. Purucker, Detrital magnetization in red beds of the Moenkopi Formation (Triassic), Gray Mountain, Arizona, *J. Geophys. Res.*, v. 84, 1653–1665, 1979.
- R. D. Flood, D. V. Kent, A. N. Shor, and F. R. Hall, The magnetic fabric of surficial deep-sea sediments in the HEBBLE area (Nova Scotian continental rise), *Mar. Geol.*, v. 66, 149–167, 1985.
- A. G. Goldstein and L. L. Brown, Magnetic susceptibility anisotropy of mylonites from the Brevard zone, North Carolina, U.S.A., *Phys. Earth Planet. Int.*, v. 51, 290–300, 1988.
- R. G. Gordon, Test for bias in paleomagnetically determined paleolatitudes from Pacific Plate Deep Sea Drilling Project sediments, *J. Geophys. Res.*, v. 95, 8397–8404, 1990.
- D. H. Griffiths, R. F. King, A. I. Rees, and A. E. Wright, Remanent magnetism of some recent varved sediments, *Proc. Roy. Soc. London, Ser. A.*, v. 256, 359–383, 1960.
- P. C. Henshaw, Jr., and R. T. Merrill, Magnetic and chemical changes in marine sediments, *Rev. Geophys. Space Phys.*, v. 18, 1980.
- E. Herrero-Bervera and C. E. Helsley, Paleomagnetism of a polarity transition in the Lower(?) Triassic Chugwater Formation, Wyoming, *J. Geophys. Res.*, v. 88, 3506–3522, 1983.
- F. Hrouda, Magnetic anisotropy of rocks and its application in geology and geophysics, *Geophys. Surv.*, v. 5, 37–82, 1982.
- E. Irving and A. Major, Post-depositional detrital remanent magnetization in a synthetic sediment, *Sedimentology*, v. 3, 135–143, 1964.
- E. Irving and D. F. Strong, Paleomagnetism of the Early Carboniferous Deer Lake Group, western Newfoundland: No evidence for mid-Carboniferous displacement of “Acadia,” *Earth Planet. Sci. Lett.*, v. 69, 379–390, 1984.
- E. Irving and D. F. Strong, Paleomagnetism of rocks from the Burin Peninsula, Newfoundland: Hypothesis of late Paleozoic displacement of Acadia criticized, *J. Geophys. Res.*, v. 90, 1949–1962, 1985.
- M. Jackson, W. Gruber, J. Marvin, and S. K. Banerjee, Partial anhysteretic remanence and its anisotropy: Applications and grain-size dependence, *Geophys. Res. Lett.*, v. 15, 440–443, 1988.
- R. Karlin and S. Levi, Geochemical and sedimentological control of the magnetic properties of hemipelagic sediments, *J. Geophys. Res.*, v. 90, 10,373–10,392, 1985.
- D. V. Kent, Post depositional remanent magnetization in deep sea sediments, *Nature*, v. 246, 32–34, 1973.
- D. V. Kent, Thermoviscous remagnetization in some Appalachian limestones, *Geophys. Res. Lett.*, v. 12, 805–808, 1985.
- R. F. King, Remanent magnetism of artificially deposited sediments, *Monthly Notices Roy. Astron. Soc. Geophys. Suppl.*, v. 7, 115–134, 1955.
- R. F. King and A. I. Rees, Detrital magnetism in sediments: An examination of some theoretical models, *J. Geophys. Res.*, v. 71, 561–571, 1966.
- R. Kligfield, W. Lowrie, A. M. Hirt, and A. W. B. Siddans, Effect of progressive deformation on remanent magnetization of Permian redbeds from the Alpes Maritimes (France), *Tectonophys.*, v. 97, 59–85, 1983.
- M. D. Knight, G. P. L. Walker, B. B. Ellwood, and J. F. Diehl, Stratigraphy, paleomagnetism, and magnetic fabric of the Toba Tuffs: Constraints on the sources and eruptive styles, *J. Geophys. Res.*, v. 91, 10,355–10,382, 1986.
- K. P. Kodama, Remanence rotation due to rock strain during folding and the stepwise application of the fold test, *J. Geophys. Res.*, v. 93, 3357–3371, 1988.
- E. E. Larson and T. R. Walker, Development of chemical remanent magnetization during early stages of red-bed formation in Late Cenozoic sediments, Baja California, *Geol. Soc. Amer. Bull.*, v. 86, 639–650, 1975.
- E. E. Larson and T. R. Walker, A rock magnetic study of the Lower Massive Sandstone, Moenkopi Formation (Triassic), Gray Mountain Area, Arizona, *J. Geophys. Res.*, v. 87, 4819–4836, 1982.

- E. E. Larson, T. R. Walker, P. E. Patterson, R. P. Hoblitt, and J. G. Rosenbaum, Paleomagnetism of the Moenkopi Formation, Colorado Plateau: Basis for long-term model of acquisition of chemical remanent magnetism in red beds, *J. Geophys. Res.*, v. 87, 1081–1106, 1982.
- E. Liebes and P. N. Shive, Magnetization acquisition in two Mesozoic red sandstones, *Phys. Earth Planet. Int.*, v. 30, 396–404, 1982.
- W. Lowrie and F. Heller, Magnetic properties of marine limestones, *Rev. Geophys. Space Phys.*, v. 20, 171–192, 1982.
- S. P. Lund, A comparison of the statistical secular variation recorded in some Late Quaternary lava flows and sediments and its implications, *Geophys. Res. Lett.*, v. 7, 251–254, 1985.
- W. D. MacDonald and B. B. Ellwood, Anisotropy of magnetic susceptibility: Sedimentological, igneous, and structural-tectonic applications, *Rev. Geophys.* v. 25, 905–909, 1987.
- J. Magill, A. Cox, and R. Duncan, Tillamook Volcanic Series: Further evidence for tectonic rotation of the Oregon Coast Range, *J. Geophys. Res.*, v. 86, 2953–2970, 1981.
- C. McCabe and R. D. Elmore, The occurrence and origin of Late Paleozoic remagnetization in the sedimentary rocks of North America, *Rev. Geophys.*, v. 27, 471–494, 1989.
- C. McCabe, R. Van der Voo, D. R. Peacor, C. R. Scotese, and R. Freeman, Diagenetic magnetite carries ancient yet secondary remanence in some Paleozoic sedimentary carbonates, *Geology*, v. 11, 221–223, 1983.
- C. McCabe, M. Jackson, and B. B. Ellwood, Magnetic anisotropy in the Trenton Limestone: Results of a new technique, anisotropy of anhysteretic susceptibility, *Geophys. Res. Lett.*, v. 12, 333–336, 1985.
- C. McCabe, R. Sassen, and B. Saffer, Occurrence of secondary magnetite within biodegraded oil, *Geology*, v. 15, 7–10, 1987.
- M. W. McElhinny and W. E. Senanayake, Variations in the geomagnetic dipole, 1: The past 50,000 years, *J. Geomag. Geoelectr.*, v. 34, 39–51, 1982.
- R. T. Merrill and M. W. McElhinny, *The Earth's Magnetic Field: It's History, Origin and Planetary Perspective*, Academic Press, London, 401 pp., 1983.
- J. Oliver, Fluids expelled tectonically from orogenic belts: Their role in hydrocarbon migration and other geologic phenomena, *Geology*, v. 14, 99–102, 1986.
- N. D. Opdyke and K. W. Henry, A test of the dipole hypothesis, *Earth Planet. Sci. Lett.*, v. 6, 138–151, 1969.
- M. Prévot, E. A. Mankinen, R. S. Coe, and C. S. Grommé, The Steens Mountain (Oregon) geomagnetic polarity transition, 2. Field intensity variations and discussion of reversal models, *J. Geophys. Res.*, v. 90, 10,417–10,448, 1985.
- M. E. Purucker, D. P. Elston, and E. M. Shoemaker, Early acquisition of characteristic magnetization in red beds of the Moenkopi Formation (Triassic), Gray Mountain, Arizona, *J. Geophys. Res.*, v. 85, 997–1012, 1980.
- J. L. Roy and J. K. Park, Red beds: DRM or CRM?, *Earth Planet. Sci. Lett.*, v. 17, 211–216, 1972.
- A. S. Ruf, S. J. Naruk, R. F. Butler, and G. J. Calderone, Strain and magnetic fabric in the Santa Catalina and Pinaleno Mountains metamorphic core complex mylonite zones, Arizona, *Tectonics*, v. 7, 235–248, 1988.
- P. W. Schmidt and B. J. J. Embleton, Palaeomagnetic results from sediments of the Perth Basin, Western Australia, and their bearing on the timing of regional lateritisation, *Palaeogeog. Palaeoclim. Palaeoecol.*, v. 19, 257–273, 1976.
- C. R. Scotese, R. Van der Voo, and C. McCabe, Paleomagnetism of the upper Silurian and lower Devonian carbonates of New York State: Evidence for secondary magnetizations residing in magnetite, *Phys. Earth Planet. Int.*, v. 30, 385–395, 1982.
- P. N. Shive, M. B. Steiner, and D. T. Huycke, Magnetostratigraphy, paleomagnetism, and remanence acquisition in the Triassic Chugwater Formation of Wyoming, *J. Geophys. Res.*, v. 89, 1801–1815, 1984.
- R. W. Simpson and A. Cox, Paleomagnetic evidence for tectonic rotation of the Oregon Coast Range, *Geology*, v. 5, 585–589, 1977.
- M. B. Steiner, Detrital remanent magnetization in hematite, *J. Geophys. Res.*, v. 88, 6523–6539, 1983.
- A. Stephenson, S. Sadikun, and D. K. Potter, A theoretical and experimental comparison of the anisotropies of magnetic susceptibility and remanence in rocks and minerals, *Geophys. J. Roy. Astron. Soc.*, v. 84, 185–200, 1986.
- D. Suk, D. R. Peacor, and R. Van der Voo, Replacement of pyrite framboids by magnetite in limestone and implications for palaeomagnetism, *Nature*, v. 345, 611–613, 1990.
- J. A. Tarduno, Absolute inclination values from deep sea sediments: A reexamination of the Cretaceous Pacific record, *Geophys. Res. Lett.*, v. 17, 101–104, 1990.

- L. Tauxe and D. V. Kent, Properties of a detrital remanence carried by haematite from study of modern river deposits and laboratory redeposition experiments, *Geophys. J. Roy. Astron. Soc.*, v. 77, 543–561, 1984.
- L. Tauxe, D. V. Kent, and N. D. Opdyke, Magnetic components contributing to the NRM of Middle Siwalik red beds, *Earth Planet. Sci. Lett.*, v. 47, 279–284, 1980.
- P. Tucker, Magnetization of unconsolidated sediments and theories of DRM, In: *Geomagnetism of Baked Clays and Recent Sediments*, eds. K. M. Creer et al., Elsevier, Amsterdam, pp. 9–19, 1983.
- P. Turner, *Continental Red Beds, Developments in Sedimentology*, v. 29, Elsevier, Amsterdam, 562 pp., 1980.
- B. A. van der Pluijm, Grain-scale deformation and the fold test-Evaluation of syn-folding remagnetization, *Geophys. Res. Lett.*, v. 14, 155–157, 1987.
- R. Van der Voo and R. B. French, Paleomagnetism of the Late Ordovician Juniata Formation and the remagnetization hypothesis, *J. Geophys. Res.*, v. 82, 5796–5802, 1977.
- F. B. Van Houten, Iron oxides in red beds, *Geol. Soc. Amer. Bull.*, v. 79, 399–416, 1968.
- T. R. Walker, E. E. Larson, and R. P. Hoblitt, The nature and origin of hematite in the Moenkopi Formation (Triassic), Colorado Plateau: A contribution to the origin of magnetism in red beds, *J. Geophys. Res.*, v. 86, 317–333, 1981.

GEOCHRONOLOGICAL APPLICATIONS

As discussed in Chapter 1, geomagnetic secular variation exhibits periodicities between 1 yr and 10^5 yr. We learn in this chapter that geomagnetic polarity intervals have a range of durations from 10^4 to 10^8 yr. In the next chapter, we shall see that apparent polar wander paths represent motions of lithospheric plates over time scales extending to $>10^9$ yr. As viewed from a particular location, the time intervals of magnetic field changes thus range from decades to billions of years. Accordingly, the time scales of potential geochronologic applications of paleomagnetism range from detailed dating within the Quaternary to rough estimations of magnetization ages of Precambrian rocks.

Geomagnetic field directional changes due to secular variation have been successfully used to date Quaternary deposits and archeological artifacts. Because the patterns of secular variation are specific to subcontinental regions, these Quaternary geochronologic applications require the initial determination of the secular variation pattern in the region of interest (e.g., Figure 1.8). Once this regional pattern of swings in declination and inclination has been established and calibrated in absolute age, patterns from other Quaternary deposits can be matched to the calibrated pattern to date those deposits. This method has been developed and applied in western Europe, North America, and Australia. The books by Thompson and Oldfield (1986) and Creer et al. (1983) present detailed developments. Accordingly, this topic will not be developed here.

This chapter will concentrate on the most broadly applied of geochronologic applications of paleomagnetism: *magnetic polarity stratigraphy*. This technique has been applied to stratigraphic correlation and geochronologic calibration of rock sequences ranging in age from Pleistocene to Precambrian. Magnetic polarity stratigraphy (or *magnetostratigraphy*) has developed into a major subdiscipline within paleomagnetism and has drawn together stratigraphers and paleontologists working with paleomagnetists to solve a wide variety of geochronologic problems.

To understand the principles of magnetic polarity stratigraphy, it is necessary to understand the development of *geomagnetic polarity time scales*. The first portion of this chapter presents the techniques that are used to develop the geomagnetic polarity time scale (GPTS) and gives examples of the resulting time scales. This discussion necessarily involves the presentation of some classic examples of magnetic polarity stratigraphy; magnetostratigraphy has both required the development of geomagnetic polarity time scales and contributed to that development. In the second half of this chapter, we discuss case histories of applications of magnetic polarity stratigraphy to geochronologic problems. This approach is used because the principles and strategies of magnetostratigraphy are best understood in the context of particular geochronological applications. Topics such as sampling and data analysis and quality are developed as they arise in presentation of the case histories.

DEVELOPMENT OF THE GEOMAGNETIC POLARITY TIME SCALE

The discussion of the development of the geomagnetic polarity time scale presented here is necessarily brief and might not present the details that some readers desire. Detailed accounts of the development of the Pliocene–Pleistocene GPTS are given by Cox (1973) and by McDougall (1979). An excellent and

detailed review of the development of the polarity time scale is given by Hailwood (1989). For a history-of-science approach to the development of the GPTS and its critical role in the evolution of plate tectonic theory, the reader is referred to Glen (1982).

The Pliocene–Pleistocene

Modern development of the geomagnetic polarity time scale was initiated in the 1960s following advances allowing accurate potassium-argon (K-Ar) dating of Pliocene–Pleistocene igneous rocks. In general, igneous rocks with the same age but from widely separated collecting localities were found to have the same polarity. Age and magnetic polarity determinations of increasing numbers of igneous rocks were compiled and led to the development of the first geomagnetic polarity time scales in the 0- to 5-Ma time interval (Figure 9.1).

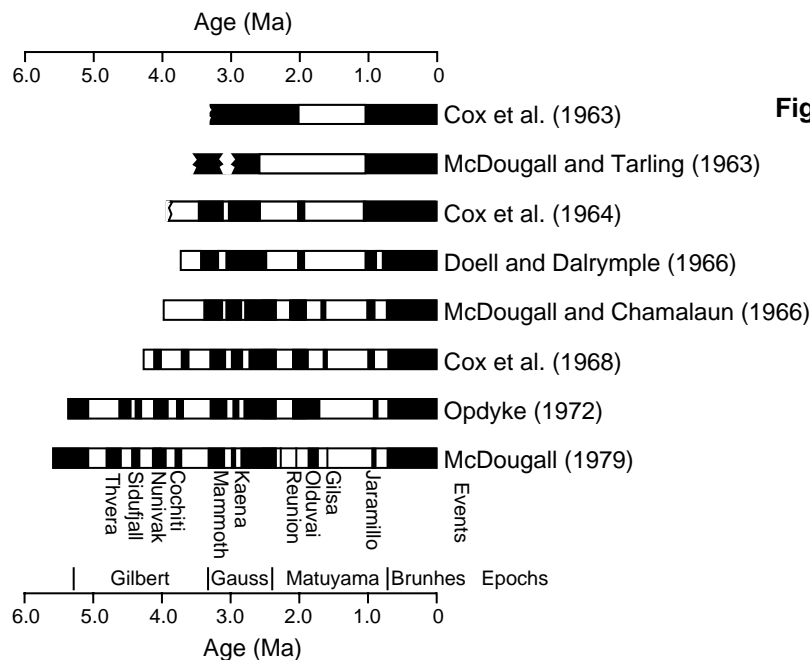


Figure 9.1 Evolution of the Pliocene–Pleistocene geomagnetic polarity time scale between 1963 and 1979. On this and all subsequent polarity columns or time scales, black intervals indicate normal polarity and white intervals indicate reversed polarity; references are given at the right of each time scale; the “event” and “epoch” nomenclature applied to this portion of the time scale is given at the bottom. Adapted from McDougall (1979).

When few age and polarity determinations were available, polarity intervals were thought to have durations of about 1 m.y. These polarity intervals were called *polarity epochs* and were named after prominent figures in the history of geomagnetism. But it soon became clear that shorter intervals of opposite polarity occurred within the polarity epochs. These shorter intervals were called *polarity events* and were named after the locality at which they were first sampled. We now understand that no fundamental distinction exists between polarity epochs and polarity events; polarity intervals of a wide spectrum of durations are possible. The polarity epoch and event nomenclature is basically an accident of history but is retained as a matter of convenience for this portion of the time scale.

During this early development, there were arguments as to whether the reversed-polarity igneous rocks were due to reversed polarity of the geomagnetic field or due to *self-reversal of thermoremanent magnetism*. Nagata et al. (1952) found an igneous rock (the Haruna dacite) that acquired a TRM antiparallel to the magnetic field in which it was cooled. This observation raised the possibility that all reversed-polarity igneous rocks had undergone self-reversal of TRM. The self-reversing TRM of the Haruna dacite was found to be carried by titanohematite of composition $x \approx 0.5$ (remember Chapter 2?). It turns out that self-reversal is a rare occurrence, accounting for perhaps 1% of reversed-polarity igneous rocks; intermediate composition titanohematites are rarely the dominant ferromagnetic minerals in igneous rocks. The internal consistency in geomagnetic polarity time scales derived from igneous rocks distributed worldwide verified that geomagnetic field reversals were the correct explanation for all but a few reversed-polarity igneous rocks.

A Pliocene-Pleistocene geomagnetic polarity time scale based primarily on K-Ar dating and paleomagnetic polarity determinations on igneous rocks is given in Figure 9.2. Some 354 age and polarity determinations were used to construct this time scale. Several important features of geomagnetic polarity history can be appreciated from this figure:

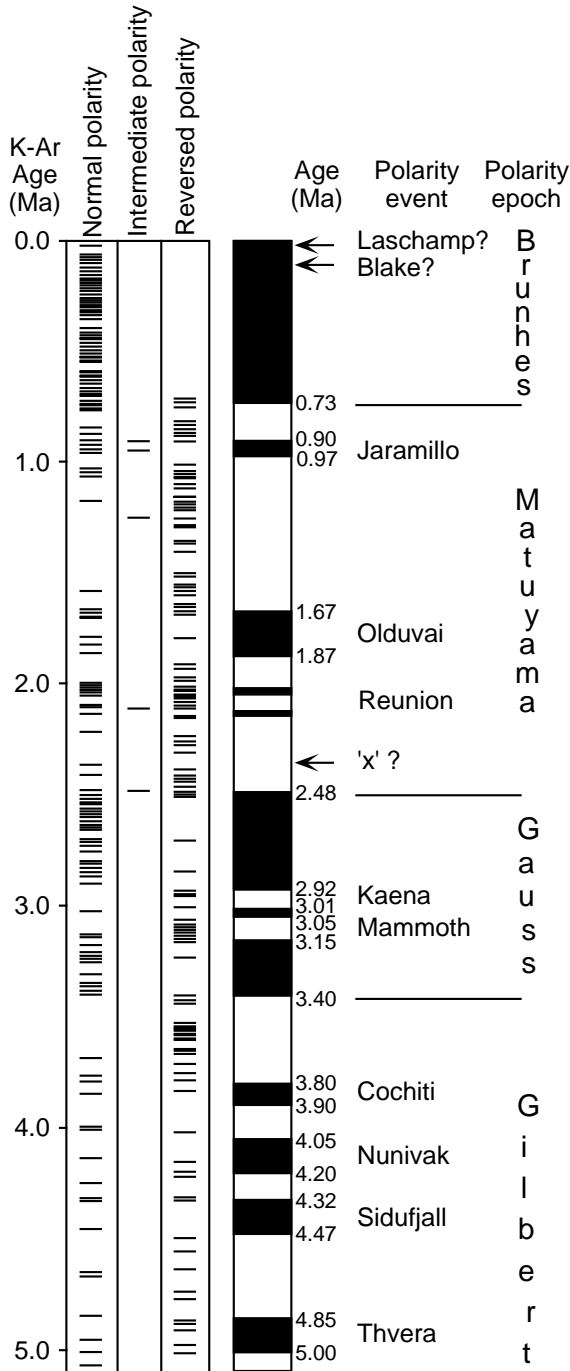


Figure 9.2 Pliocene-Pleistocene geomagnetic polarity time scale of Mankinen and Dalrymple (1979). Each horizontal line in the columns labeled normal polarity, intermediate polarity, or reversed polarity represents an igneous rock for which both K-Ar age and paleomagnetic polarity have been determined; auxiliary information from marine magnetic anomaly profiles and deep-sea core paleomagnetism has also been used to determine the polarity time scale; arrows indicate disputed short polarity intervals or geomagnetic “excursions”; numbers to the right of the polarity column indicate interpreted ages of polarity boundaries. Redrawn from Mankinen and Dalrymple (1979) with permission from the American Geophysical Union.

1. During the past 5 m.y., the average duration of polarity intervals is ~0.25 m.y. But there is a wide range of durations with the shorter duration intervals being more common.
2. Only about 1.5% of the observations are classified as “intermediate polarity.” These intermediate-polarity rocks were probably magnetized while the geomagnetic field was in *polarity transition* between normal and reversed polarities. Polarity transition occurs quickly (probably within about 5000

years), and geomagnetic polarity reversals can be regarded as rapid, globally synchronous events. This feature of polarity reversals is central to many geochronologic applications of polarity stratigraphy.

3. Geomagnetic polarity reversals are randomly spaced in geologic time; they are the antithesis of square-wave or sine-wave behavior, so switches of polarity are not predictable. This means that patterns of four or five successive polarity intervals do not generally recur. Instead, the patterns of long and short intervals can be used as “fingerprints” of particular intervals of geologic time. This type of pattern recognition is essential to most geochronologic applications of polarity stratigraphy.
4. Analytical uncertainties that are inherent in radiometric dating generally limit application of this “dating and polarity determination” technique to the past 5 m.y. At an absolute age of 5 Ma, the typical error in radiometric age determination approaches the typical duration of polarity intervals. With the possible exception of detailed analysis of polarity stratigraphy in thick sequences of volcanic rocks such as in Iceland (McDougall, 1979), other techniques are required to decipher the GPTS for times older than 5 Ma.

Extension into the Miocene

Paleomagnetism of deep-sea cores provided important information about the geomagnetic polarity sequence prior to 5 Ma. An example polarity record in a deep-sea piston core is given in Figure 9.3. Provided that sediment accumulation took place without significant breaks, the DRM of a deep-sea core can allow accurate determination of the magnetic polarity sequence. Paleontological dating of sedimentary horizons is required to determine geologic ages, and correlation to a radiometrically dated polarity sequence is required to estimate absolute ages within individual deep-sea cores. In practice, numbers of deep-sea cores providing high-fidelity paleomagnetic records and paleontologic calibrations of the polarity sequence were required for determination of the geomagnetic polarity time scale. Example time scales determined by this method are those of Opdyke et al. (1974) and Theyer and Hammond (1974).

Marine magnetic anomalies

Marine magnetic anomaly profiles constitute the richest source of information about the sequence of geomagnetic polarity intervals from mid-Mesozoic to the present. The essentials of the seafloor spreading hypothesis (Vine and Matthews, 1963; Morley and Larochele, 1964) explaining the origin of marine magnetic anomalies are presented in Figure 9.4. This hypothesis became a cornerstone of plate tectonic theory.

During seafloor spreading, upper mantle material upwells at a spreading ridge and solidifies onto the trailing edges of the oceanic lithospheric plates that are separating at the ridge. The oceanic crust forms the upper portion of this lithosphere and is composed of mafic igneous rocks including basaltic pillow lavas and feeder dikes. These basaltic rocks contain titanomagnetite and acquire a TRM during cooling in the geomagnetic field. The oceanic crust thus can be viewed as a limited-fidelity tape recording of past polarities of the geomagnetic field. But the polarity record in the oceanic crust is not determined by direct sampling.

The alternating polarities of TRM in the oceanic crust are depicted by the black (normal-polarity) and white (reversed-polarity) crustal blocks in Figure 9.4. These blocks of alternating TRM polarity generate *magnetic anomalies*. At mid to high latitudes, a normal-polarity block generates a magnetic field that adds to the regional geomagnetic field, resulting in a positive magnetic anomaly; the local magnetic field above the normal-polarity block is 100 to 1000 gammas ($1 \text{ gamma} = 10^{-5} \text{ Oe}$) higher than the regional value. For a reversed-polarity block, the resulting magnetic anomaly above the block is negative. By towing a magnetometer behind an oceanographic vessel and observing the magnetic field anomaly profile at the sea surface (the marine magnetic anomaly profile), it is possible to remotely sense the polarity of magnetization in the underlying oceanic crust. From the ridge crest outward to progressively older oceanic crust, observed marine magnetic anomaly profiles allow determination of the polarity of progressively older oceanic crust. The sequence of past geomagnetic polarities thus can be inferred from marine magnetic anomaly profiles.

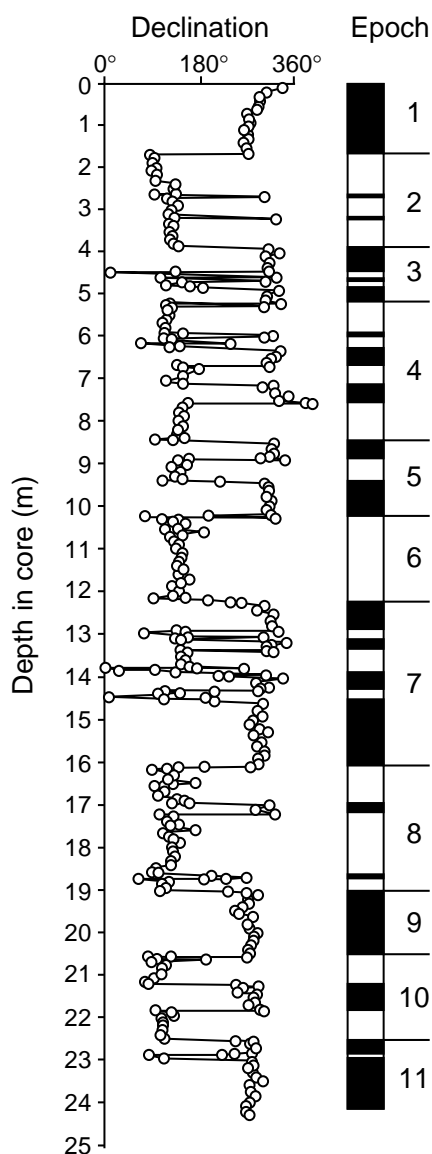


Figure 9.3 Change in paleomagnetic declination with depth in deep-sea piston core RC12-65 collected from the equatorial Pacific Ocean. The absolute declination is arbitrary because the core was not azimuthally oriented (declination at the top of the core was set to 360°); the oldest sediment at the base of the core is early Late Miocene (about 10 Ma absolute age); the interpreted magnetic polarity time scale was divided according to the “magnetic epoch” numbering system, which is now obsolete. Redrawn from Opdyke et al. (1974).

To estimate ages of past polarity intervals determined in this fashion, the rate of seafloor spreading must be determined. Because the Pliocene–Pleistocene GPTS is known independently (e.g., Figure 9.2), the pattern of normal-polarity and reversed-polarity blocks near the ridge crest is also known. This pattern must be linearly scaled according to the rate of seafloor spreading. A *model profile* is computed for an assumed rate of seafloor spreading and is compared with the observed magnetic anomaly profile. The rate of seafloor spreading is determined by matching the model and observed profiles as shown in Figure 9.4.

The first geomagnetic polarity time scale to use marine magnetic anomalies as its primary data base was that of Heirtzler et al. (1968). This GPTS is reproduced in Figure 9.5. Heirtzler et al. used observed magnetic anomaly profiles to infer a block model of the magnetic polarity of the oceanic crust in the South Atlantic. They determined the rate of spreading of the South Atlantic Ridge by matching the observed and model profiles using the independently known GPTS back to 3.35 Ma (the Gauss/Gilbert boundary). Using various marine geophysical evidences, Heirtzler et al. argued that the rate of seafloor spreading of the South Atlantic Ridge had been constant for the past 80 m.y. The age of oceanic crust in the South Atlantic and the age of inferred geomagnetic polarity intervals thus could be predicted. This procedure led to the polarity time scale of Figure 9.5, which must be considered one of the boldest and most accurate extrapolations in the history of Earth science. The subsequent 20 years of research has shown that this time scale was off by only about 5 m.y. at a predicted age of 70 Ma!

Two important features of the Heirtzler et al. (1968) GPTS are easily noticed: (1) During the Cenozoic, the total time in normal-polarity and reversed-polarity states was approximately equal; there was no significant *polarity bias* during the Cenozoic. (2) The rate of reversal of the geomagnetic field increased during the Cenozoic. In the Paleocene and Eocene, the average rate of polarity reversal was about 1/m.y., whereas the rate for the past 5 m.y. was about 4/m.y. Statistical analysis of geomagnetic polarity reversals and reversal rate changes has become a major subject in geomagnetism (see the review by Lowrie, 1989).

About nomenclature

A brief discussion about nomenclature applied to magnetic polarity intervals is required. We noted during dis-

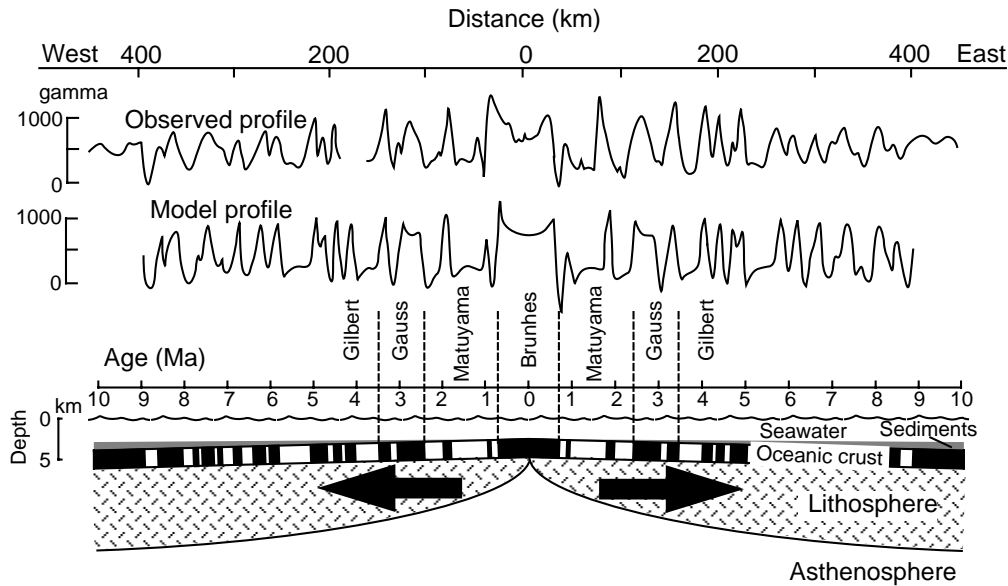


Figure 9.4 Formation of marine magnetic anomalies at an oceanic ridge undergoing seafloor spreading. The oceanic crust is the upper portion of the oceanic lithosphere forming at the ridge crest and being covered by an increasing thickness of oceanic sediments; the black (white) blocks of oceanic crust represent the normal (reversed) polarity TRM acquired during original cooling of the oceanic crust; blocks of crust formed during Pliocene-Pleistocene polarity epochs are labeled, and epoch boundaries are shown by dashed lines; the absolute age of oceanic crust is shown by the horizontal scale; the model profile is the computed sea-level magnetic anomaly profile produced by the block model of TRM polarity in the oceanic crust; the observed profile is the actual observed sea-level magnetic anomaly profile across the Pacific-Antarctic Ridge; the distance scale is given at the top of the figure; model and observed profiles are best matched by a half-spreading rate of 45 km/m.y. Adapted from Pitman and Heirtzler (1966), *Science*, v. 154, 1164–71, ©1966 by the American Association for the Advancement of Science.

cussion of the Pliocene–Pleistocene GPTS that a nomenclature system of polarity epochs and events was developed for this portion of the time scale. This system has been superseded for earlier portions of the time scale but is retained for the Pliocene–Pleistocene because of historical precedent.

The polarity epoch system was extended into the Miocene and Oligocene to describe polarity intervals found in deep-sea cores, but these earlier epochs were denoted by numbers. For example, in Figure 9.3, the Gilbert polarity epoch is designated Epoch 4, the preceding polarity epoch is designated Epoch 5, etc. But use of “epoch” to denote geomagnetic polarity intervals was in conflict with prior usage of “epoch” for a particular subdivision of geologic time.

When marine magnetic anomaly profiles were used to develop geomagnetic polarity time scales, an additional nomenclature problem became apparent. The prominent marine magnetic anomalies had been given numbers increasing away from spreading oceanic ridge crests. These *magnetic anomaly numbers* are noted on the Heirtzler et al. time scale in Figure 9.5. But what nomenclature should be applied to the normal-polarity time interval when the oceanic crust generating magnetic anomaly number 5 was produced? We can’t call it “epoch 5” because that name has already been applied to the polarity epoch preceding the Gilbert epoch. Some new system (not in conflict with previous geological nomenclatures) was required.

A system of geomagnetic *polarity chrons* was developed. Time intervals of geomagnetic polarity are now referred to by a chron designation that is tied to the marine magnetic anomaly numbering system. The normal-polarity time interval discussed in the previous paragraph is referred to as “polarity chron 5” (Cox, 1982). Reversed-polarity time intervals are referred to by using a suffix “r” to denote the reversed-polarity interval preceding a particular normal-polarity chron. For example, the reversed-polarity chron preceding

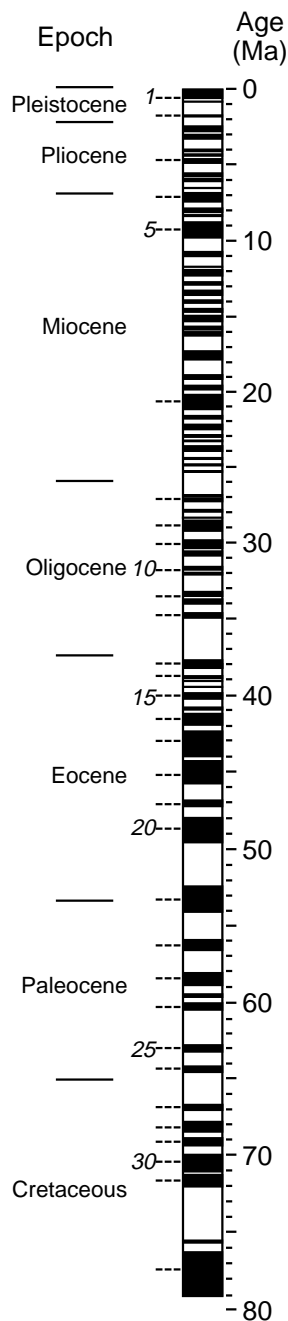


Figure 9.5 The geomagnetic polarity time scale of Heirtzler et al. (1968) determined from analysis of marine magnetic anomalies. Geologic epochs within the Cenozoic are shown at left; the numbers in italics at the left of polarity time scale are magnetic anomaly numbers; the predicted absolute age is given by the scale at the right of polarity column. Redrawn from Heirtzler et al. (1968) with permission from the American Geophysical Union.

chron 25 is designated chron 25r. This nomenclature system takes a little getting used to, but it does work. If you're not burned out by this discussion of nomenclature, detailed accounts are presented by Cox (1982) and Hailwood (1989).

Biostratigraphic calibrations

When the Heirtzler et al. (1968) GPTS was developed, ages of polarity chrons in the Paleogene were predicted by the assumed constant seafloor spreading rate of the South Atlantic Ridge. Testing the predicted ages of these polarity chrons was a major objective of the Deep Sea Drilling Project (DSDP). As shown schematically in Figure 9.4, marine sediments accumulate on newly generated oceanic crust. The age of the oldest sediment thus approximates the age of the oceanic crust.

Hundreds of DSDP cores (and cores drilled during the successor Ocean Drilling Program (ODP)) have been drilled in ocean basins over the past 25 years. To test the prediction of the Heirtzler et al. time scale that magnetic polarity chron 25 is Early Paleocene in age, a core could be drilled through the sediment to igneous basement at a site where marine magnetic anomaly 25 had been identified. Microfossils from that core could be identified by a paleontologist to allow determination of the geologic age of the oldest sediment. In fact the oldest sediment in DSDP cores drilled into oceanic basement formed during chron 25 have been found to be Late Paleocene rather than Early Paleocene in age. In this fashion, definitive sediment ages from numerous DSDP cores have required adjustments to the Heirtzler et al. (1968) polarity time scale. Additional mapping of marine magnetic anomalies has also resulted in some adjustments to the magnetic anomaly pattern itself. Particularly notable examples of geomagnetic polarity time scales developed in this way are those of LaBrecque et al. (1977) and Ness et al. (1980).

Paleontological dating of DSDP sediment cores provided "spot checks" on the polarity time scale. Magnetostratigraphic investigations of marine sedimentary sequences also have provided detailed biostratigraphic calibrations. The most important of these investigations (perhaps the most spectacular of all magnetostratigraphic studies) was that of the Late Mesozoic and Cenozoic pelagic limestone sequences in the Umbrian Apennines of Italy. (It is interesting to note that this paleomagnetic research was initiated by Walter Alvarez and Bill Lowrie to investigate the tectonic devel-

opment of the Apennines. Beyond the important magnetostratigraphic data obtained, subsequent research led to the discovery of iridium-enriched sediment at the Cretaceous/Tertiary boundary and advancement of the impact hypothesis for mass extinctions at this boundary (Alvarez et al., 1980.)

The paleomagnetic data obtained from the pelagic limestone sequence at Gubbio, Italy, are shown in Figure 9.6. Lowrie and Alvarez (1977) analyzed paleomagnetic samples collected at close stratigraphic spacings. The ChRM direction for each sample (corrected for tectonic effects) was used to compute the

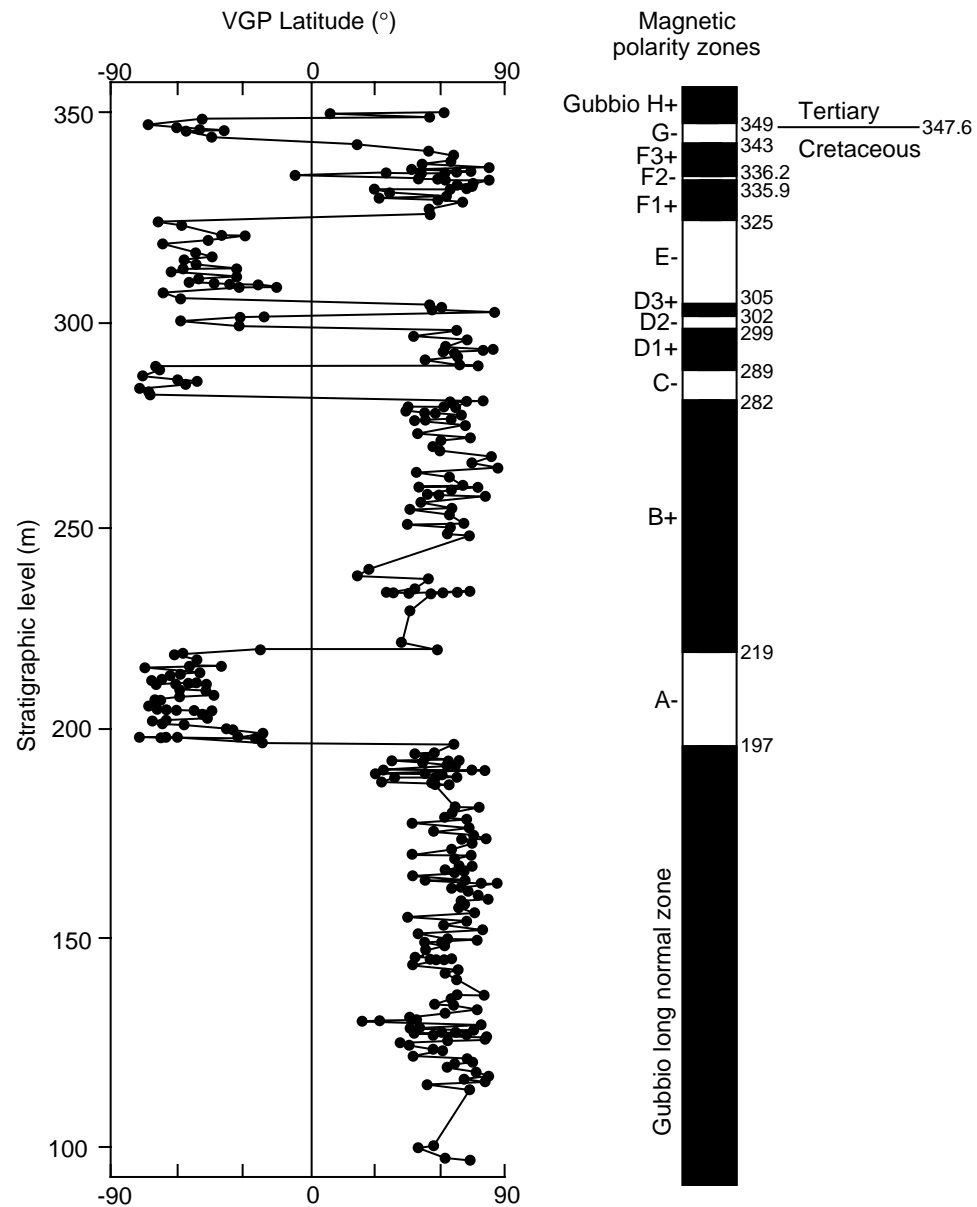


Figure 9.6 Magnetostratigraphic results from the Upper Cretaceous portion of the Scaglia Rossa section in the Umbrian Apennines near Gubbio, Italy. The virtual geomagnetic pole (VGP) latitude determined from the ChRM direction from each paleomagnetic sample is plotted against the stratigraphic level; the sequence of interpreted polarity zones is shown by the polarity column with stratigraphic levels of polarity boundaries (in meters) noted on the right side of the column; polarity zones are designated by the alphabetical system on the left side of column; the position of the Cretaceous/Tertiary boundary is noted at the right. Redrawn from Lowrie and Alvarez (1977) with permission from the Geological Society of America.

virtual geomagnetic pole (VGP) latitude for each stratigraphic horizon. Because VGP latitude is computed from both inclination and declination of ChRM, it is a convenient parameter for displaying results of a magnetostratigraphy investigation. A positive VGP latitude indicates normal polarity of the geomagnetic field at the time of ChRM acquisition, while a negative VGP latitude indicates reversed polarity.

The VGP latitudes from the Gubbio section (Figure 9.6) allow determination of *magnetic polarity zones* in the stratigraphic succession, the term “zone” being used to refer to a particular rock stratigraphic interval. These polarity zones are shown in Figure 9.6 and are labeled by using an alphabetical system. This is now common (and well-advised) practice in magnetostratigraphy. The observed paleomagnetic data (ChRM inclination, declination, VGP latitude, or some combination thereof) are plotted against stratigraphic position. These data are then used to define a *magnetic polarity zonation* for the stratigraphic section. For example, the stratigraphic interval between 219 and 282 m of the Gubbio section has positive VGP latitudes defining normal-polarity zone “Gubbio B+.” The suffix “+” is used to denote normal-polarity zones, while “-” is used for reversed-polarity zones. In the Gubbio section, the Cretaceous/Tertiary boundary occurs within magnetic polarity zone Gubbio G- at the 347.6-m stratigraphic level.

A major contribution from the magnetostratigraphic research at Gubbio was the determination that the Cretaceous/Tertiary boundary occurs within magnetic polarity chron 29r. This determination was reached through the analysis presented in Figure 9.7. Here the magnetic polarity zonation from the Gubbio section is compared with the polarity pattern inferred from analysis of marine magnetic anomaly profiles in three different oceans. Although minor variability exists, the polarity patterns determined from the marine magnetic anomaly profiles can be unambiguously correlated to the Gubbio magnetic polarity zonation. For example, magnetic polarity zone Gubbio D1+ correlates with the normal-polarity interval associated with

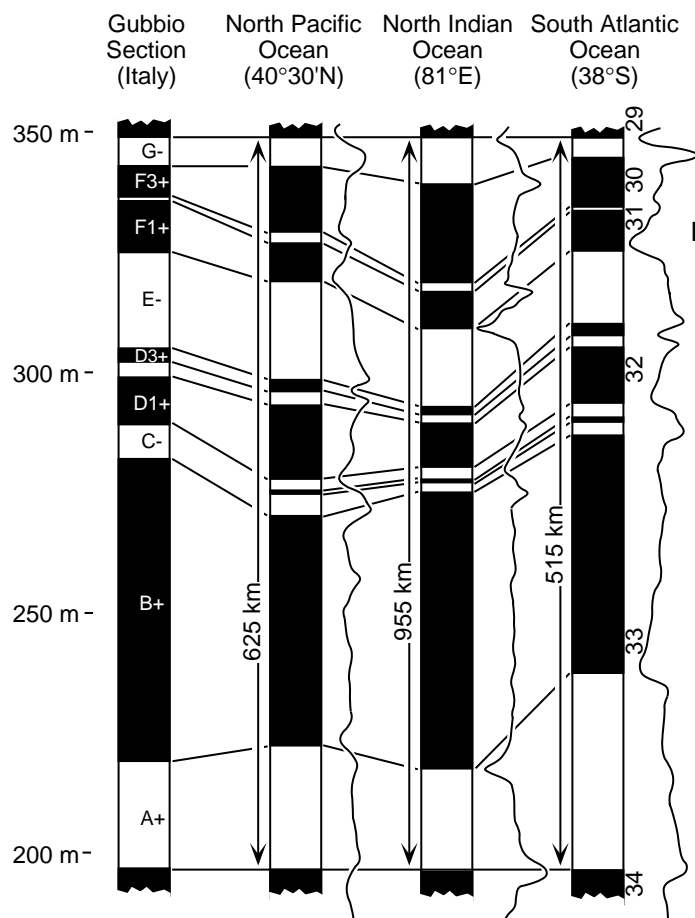


Figure 9.7 Correlation of magnetic polarity zones at the Gubbio section with polarity sequences interpreted from analyses of marine magnetic anomaly profiles in three oceanic areas. Magnetic anomaly numbers and magnetic profiles are shown to the right of each interpreted polarity sequence; linear scales of magnetic profiles are shown to the left of polarity sequences; polarity sequences are scaled so that the polarity boundaries at the beginning and end of the sequence are connected by horizontal lines. Redrawn from Lowrie and Alvarez (1977) with permission from the Geological Society of America.

magnetic anomaly 32. From this correlation, it is evident that the Cretaceous/Tertiary boundary (within polarity zone Gubbio G-) occurred during magnetic polarity chron 29r. Note that the Heirtzler et al. (1968) time scale (Figure 9.5) had predicted that the Cretaceous/Tertiary boundary occurred during chron 26r.

Paleomagnetic analyses of numerous stratigraphic sections in the Umbrian Apennines have allowed additional biostratigraphic calibrations of the GPTS (Figure 9.8). The biostratigraphic zonations of these stratigraphic sections have been determined in great detail, so the stratigraphic position of various geologic time boundaries are well known. The placement of geologic time boundaries within the pattern of polarity intervals thus can be determined. For example, the Paleocene/Eocene boundary occurs within a reversed-polarity zone correlative with magnetic polarity chron 24r.

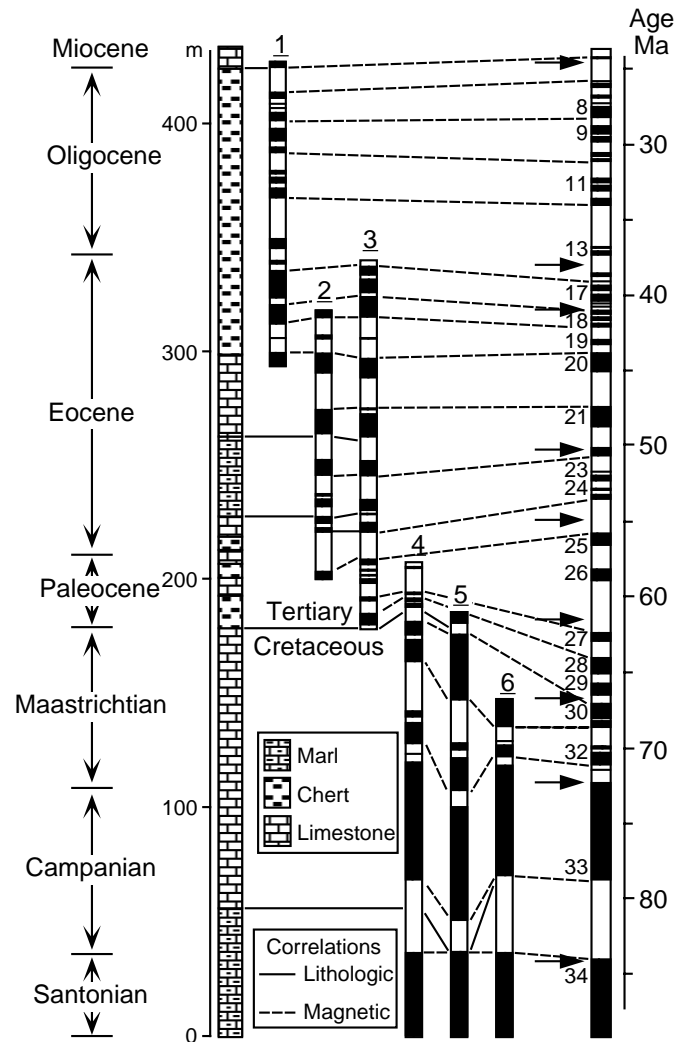


Figure 9.8 Correlations of Late Cretaceous through Cenozoic magnetostratigraphic sections in the Umbrian Apennines with the marine magnetic anomaly sequence. Age from foraminiferal zonation is shown at left; the dominant lithology is noted on the stratigraphic column (scaled in meters); polarity zones in individual columns are correlated with each other and with the marine magnetic anomaly sequence shown by polarity column at the right (magnetic anomaly numbers and paleontological calibration points (shown by the arrows) are noted at the left side of this column); the section numbers noted at the top of the columns are as follows: **1** Contessa quarry; **2** Contessa road; **3** Contessa highway; **4** Bottaccione; **5** Moria; **6** Furlo upper road. Adapted from Lowrie and Alvarez (1981) with permission from the Geological Society of America.

A Late Cretaceous–Cenozoic GPTS

The results from DSDP cores and magnetostratigraphic investigations can allow biostratigraphic calibration of the geomagnetic polarity time scale. But what about absolute age calibration? Development of geologic time scales involves association of isotopically dated horizons with the biostratigraphic zones. There are numerous geologic time scales because evaluating these absolute age calibrations is complex. The process of developing a geomagnetic polarity time scale invariably requires the choice of a geologic time scale. A Late Cretaceous-Cenozoic GPTS developed as part of a larger geological time scale project (and influenced by an effort to minimize changes in seafloor spreading rates) is given in Figure 9.9. This is the time scale of Cox (1982).

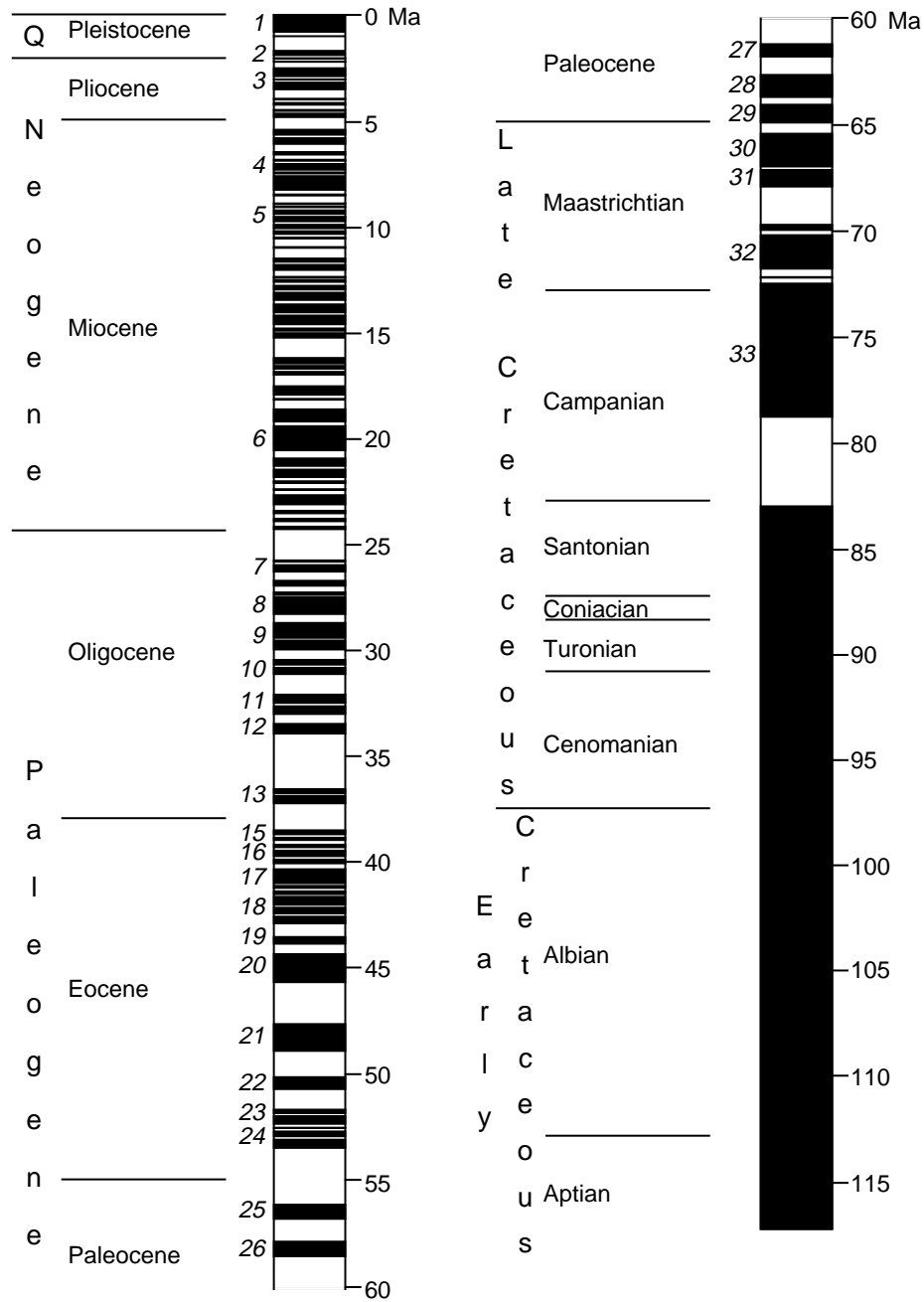


Figure 9.9 Geomagnetic polarity time scale of Cox (1982) from 0 to 118 Ma. Geologic time divisions are shown to the left of the polarity column; magnetic anomaly numbers (polarity chron numbers) are shown in italics at the left of the polarity column; age (in Ma) is shown by the scale to the right of the polarity column. Redrawn from Cox (1982).

Two points should be made about the Late Cretaceous and Cenozoic polarity time scale.

1. Although different approaches have been used in developing polarity time scales, the differences between recent time scales are minor. At least for the Cenozoic, we can conclude that absolute ages of magnetic polarity chrons are known to a precision of ± 2 m.y. It is also important to realize that relative age determinations within a particular polarity time scale are known to much better precision than are the absolute ages. The precision of relative age determinations can approach 10^4 yr.

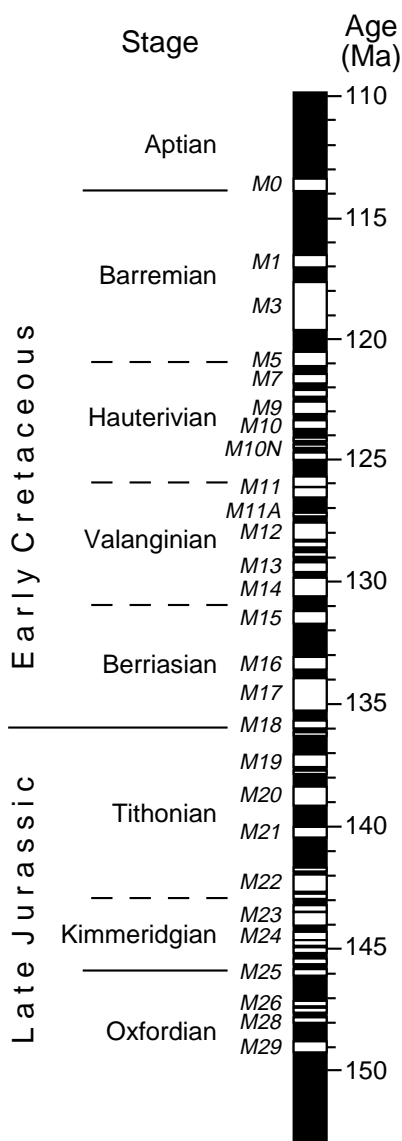


Figure 9.10 Geomagnetic polarity time scale of Lowrie and Ogg (1986) for the Late Jurassic and Early Cretaceous. Geologic time divisions are shown to the left of the polarity column, and the absolute age scale is given to the right of the column; “M anomaly” designations of reversed polarity chrons are given in italics at the left of the polarity column. Redrawn from Lowrie and Ogg (1986).

2. A major feature of the geomagnetic polarity time scale in the Cretaceous is the *Cretaceous normal-polarity superchron*, during which the geomagnetic field was of constant normal polarity. On the Cox (1982) time scale, this interval has absolute age limits of 118 and 83 Ma; the geomagnetic field did not reverse polarity for ~35 m.y.! McFadden and Merrill (1986) present an interesting discussion of polarity superchrons, changes in reversal frequency, and possible links to mantle convection.

The Late Mesozoic

Marine magnetic anomalies have also been mapped above Late Jurassic and Early Cretaceous oceanic crust. These are the “M anomalies,” in which “M” stands for Mesozoic. Again, prominent positive magnetic anomalies have been numbered. Because of large-scale plate motions since the Late Jurassic, the positive M anomalies are produced by underlying oceanic crust with reversed polarity. A recent GPTS for the Late Jurassic and Early Cretaceous is shown in Figure 9.10. Notice that the labeled polarity chrons are reversed-polarity intervals. For example, polarity chron M17 is the reversed-polarity interval in the early portion of the Berriasian stage of the Early Cretaceous.

As with geologic time scales, our knowledge of the GPTS for the Late Jurassic and Early Cretaceous is less precise than for the Cenozoic. Data from primarily three sources are refining biostratigraphic calibration of this portion of the polarity time scale:

1. Analysis of marine magnetic anomaly profiles and paleontological dating of sediment in DSDP and ODP cores have provided important information about the biostratigraphic age of particular polarity chrons.
2. Magnetostratigraphic studies on ODP cores obtained with the advanced piston-coring system have provided critical information about placement of magnetic polarity chrons within biostratigraphic stages of the mid-Mesozoic.
3. Magnetostratigraphic studies of “stratotype sections” in Europe have also provided critical data leading to refinements in the geomagnetic polarity time scale.

In addition to uncertainties in biostratigraphic calibration, absolute age calibration of the Late Jurassic and Early Cretaceous polarity time scale is uncertain. The absolute ages of some stage boundaries in the mid-Mesozoic differ between various geologic time scales by as much as 10 m.y. So the absolute age of polarity chrons in this geologic time interval are known to only about ± 5 m.y. But this is a topic of active

research, and biostratigraphic and absolute age calibrations of the Late Jurassic and Early Cretaceous polarity time scale should be significantly advanced in the coming years.

Early Mesozoic, Paleozoic, and Precambrian

The oldest substantial portions of oceanic crust remaining in ocean basins are Late Jurassic in age. So the determination of the GPTS for older intervals must be done by paleomagnetic studies of exposed stratigraphic sections on land. Accordingly, our knowledge of the polarity time scale for Early Mesozoic and older times is much less refined than for the Late Mesozoic and Cenozoic. The status of knowledge is summarized in Figure 9.11.

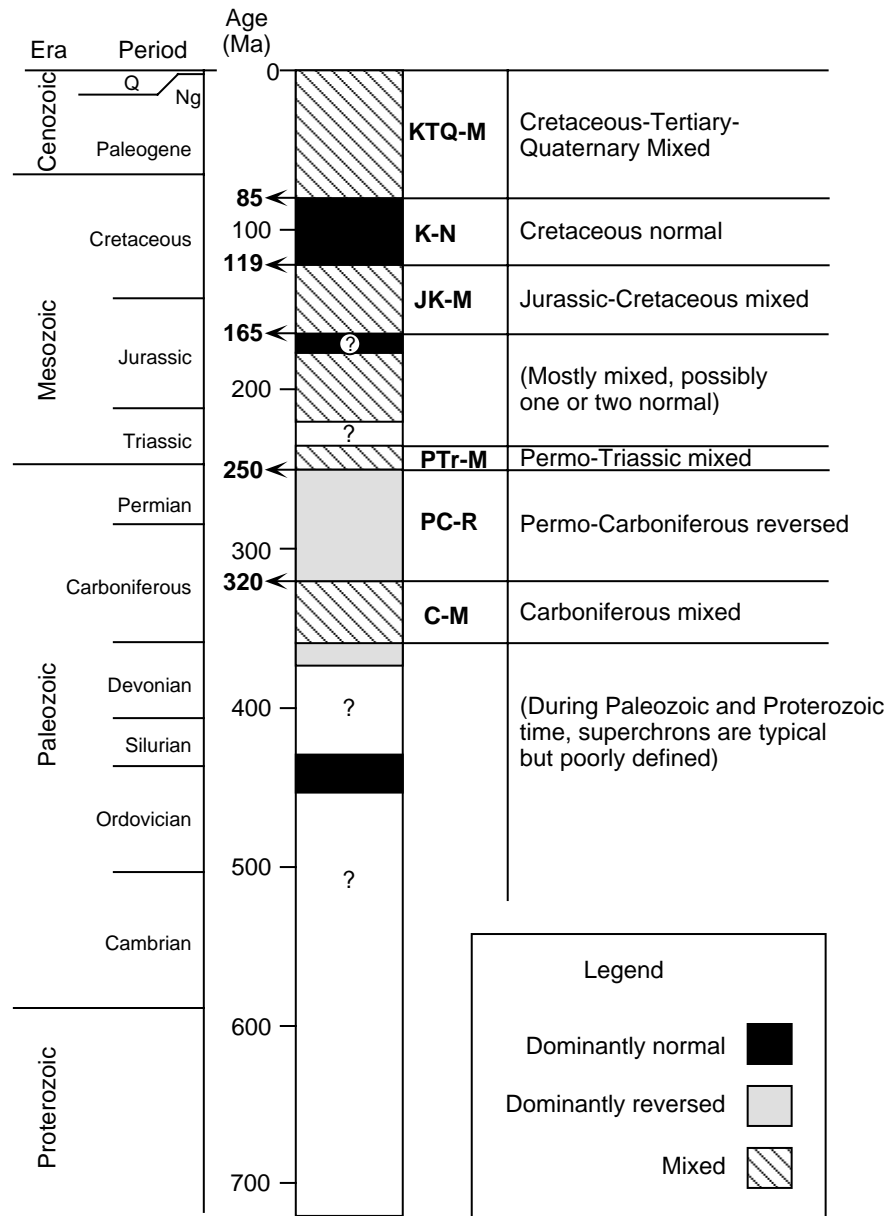


Figure 9.11 Polarity bias superchrons during the Proterozoic and Phanerozoic. Geologic time divisions are shown to the left of the polarity bias column; Q = Quaternary; Ng = Neogene; absolute age is shown to the left of the polarity bias column with age limits of polarity superchrons shown in bold type; names of polarity bias superchrons are given to the right of the column. Redrawn from Cox (1982).

The best-documented feature of the polarity time scale for the Paleozoic is the *Permo–Carboniferous reversed-polarity superchron*, an interval of (almost?) constant reversed polarity lasting for ~70 m.y. from the mid-Carboniferous through most of the Permian. The Permo-Carboniferous reversed-polarity superchron is also known as the *Kiaman interval*. This interval was preceded and followed by intervals of frequent geomagnetic reversals. Stratigraphic correlations between widely separated Paleozoic sections are often difficult to establish by using biostratigraphy. So defining the stratigraphic limits of the Permo-Carboniferous reversed-polarity interval has been used to accomplish intercontinental stratigraphic correlations within the Late Paleozoic.

Aside from a reversed-polarity superchron in the Devonian and a normal-polarity superchron from Late Ordovician through Early Silurian, the pattern of polarity reversals in the Early Paleozoic and Proterozoic is poorly known. Accurate determination of the polarity time scale in this time interval is a major challenge. However, polarity stratigraphy can still serve as a useful stratigraphic correlation technique even though the biostratigraphic and absolute age calibrations are rudimentary (e.g., Kirschvink, 1978).

MAGNETIC POLARITY STRATIGRAPHY

This section starts with discussion of general principles of magnetostratigraphy. In the remainder of the chapter, case histories of magnetic polarity stratigraphy applied to geochronologic problems are presented. The specific examples are applications to Neogene continental sedimentary sequences, but the procedures and principles apply to magnetostratigraphic studies in all sedimentary environments. Through study of these case histories, you will gain an appreciation of strategies used in magnetostratigraphic investigations and of the powers and limitations of magnetic polarity stratigraphy.

Some general principles

In most applications, the primary objective is to provide an age estimate for an event (or series of events) occurring within a sequence of sedimentary rocks. A correlation is usually sought between an observed magnetic polarity zonation in a stratigraphic section and the geomagnetic polarity time scale. In essence, the objective is to determine a pattern of polarity zones that provides a “fingerprint” of a particular interval of the GPTS. The strength of correlation of an observed magnetic polarity zonation to the GPTS depends on several factors including (1) the quality of paleomagnetic data used to define the polarity of each sampled stratigraphic horizon, (2) stratigraphic coverage of sites used to define the magnetic polarity zones, and (3) uniqueness of matching between the pattern of magnetic polarity zones and the sequence of magnetic polarity chrons of the GPTS.

Unambiguous determination of the polarity of the ChRM is the major experimental requirement for magnetic polarity stratigraphy. Consistency of polarity determinations between stratigraphically adjacent sites usually allows clear determination of the polarity zonation. But if a large percentage of sites contain complex magnetizations, the clarity of the polarity zonation is compromised. Normal-polarity sites that are stratigraphically isolated should always be viewed with some suspicion; the NRM could be dominated by an unremoved normal-polarity overprint.

Fine-grained lithologies (claystones, fine siltstones, and mudstones) are generally preferred. These fine-grained sediments acquire DRM more efficiently than coarser lithologies. Also, fine-grained sedimentary layers usually have low permeability and are less susceptible to acquisition of secondary CRM. Collection of a variety of sedimentary rocks (sometimes including unconsolidated lithologies) often requires use of oriented block samples.

Sampling strategies should provide efficient determination of polarity zonation. On the one hand, collecting single samples from closely spaced sedimentary horizons may maximize stratigraphic coverage with a given number of samples. On the other hand, replicate samples from within a horizon can provide critical evaluation of reliability of polarity determinations. For most applications, the compromise strategy of collect-

ing three or four samples from each paleomagnetic site is appropriate. This is the minimum number of samples required for application of statistical analysis (usually Fisher statistics). Often a classification of the quality of site-mean polarity determinations is developed on the basis of multiple samples per site (see the example discussions below).

The stratigraphic separation between paleomagnetic sites depends on the sedimentary environment and the age of the section. For continental sediments in a fluvial environment, sediment accumulation rates are typically 10 to 100 m/m.y. (Sadler, 1981). With a polarity reversal rate of ~ 4 /m.y. during the Neogene, a typical polarity zone is expected to have a thickness of ~ 10 m. So a stratigraphic separation of 3 m between sites generally allows resolution of the polarity zonation. In pelagic environments, sediment accumulation rate is generally < 10 m/m.y., and < 0.5 -m stratigraphic spacing of sites is recommended to allow resolution of important polarity zones.

The uniqueness of correlation between an observed polarity zonation and the GPTS depends on the number and pattern of polarity zones. A useful analogy is identification of crime suspects by fingerprint. A whole thumbprint is likely to hold up in court, but a quarter thumbprint will rarely provide convincing evidence. In the examples presented below, you will see that 10 to 20 polarity zones in a stratigraphic section usually have a pattern that can be unambiguously correlated to the GPTS. Fewer zones may be sufficient if appropriate independent age control is available.

With a reversal rate of ~ 4 /m.y. during the Neogene, the time span represented by a stratigraphic section should be ≥ 2 m.y. to provide effective correlation to the GPTS. For typical sediment accumulation rates, a continental sedimentary sequence ≥ 100 m thick is generally required, but a pelagic sequence that is only a few meters thick may suffice (e.g., Figure 9.3). With the lower rate of polarity reversals in the Late Cretaceous and Paleogene, continental sedimentary sections of ≥ 500 m thickness and pelagic sequences of ≥ 100 m are generally required for convincing correlation to the GPTS. (Note that the Gubbio section of Figures 9.6 and 9.7 has a thickness > 150 m.)

Mathematical cross-correlation techniques have been used to evaluate correlations between magnetic polarity zonations and the GPTS. But correlations are often made convincing by independent age constraints that are difficult to quantify. For example, the fossils at a particular stratigraphic level may be Late Miocene in age. In evaluating alternative correlations, only those placing the fossil level within the Late Miocene portion of the GPTS are reasonable. Isotopic age determinations can also provide tie points, facilitating correlation. In the end, the pattern matching between the observed polarity zonation and the GPTS plus the independent age constraints make a correlation either convincing or ambiguous.

These general principles are brought into focus only by the presentation of specific examples. As we examine the case histories below, keep the general principles in mind by asking the following questions:

1. Do the paleomagnetic data clearly determine the polarity of ChRM at each site?
2. Is the stratigraphic coverage sufficient to delineate the polarity zonation?
3. Considering the independent age constraints, how convincingly does the magnetic polarity zonation correlate to the GPTS?

The Pliocene–Pleistocene St. David Formation

Our first example is an application of magnetostratigraphy to geochronologic calibration of North American land mammal ages. The Cenozoic biostratigraphy of continental deposits is based on mammalian evolution, whereas biostratigraphy in the marine system is based on evolution of invertebrates. Correlation between these biostratigraphic systems depends on stratigraphic intertonguing, occasional isotopic age determinations, and magnetic polarity stratigraphy. Johnson et al. (1975) accomplished an important step in geochronologic calibration of Neogene North American land mammal ages through magnetostratigraphic study of continental deposits in southeastern Arizona. Their pioneering effort led to many similar applications of magnetic polarity stratigraphy to geochronologic problems involving continental sedimentary sequences.

The San Pedro Valley of southeastern Arizona is in the Basin and Range physiographic province, which has experienced crustal extension during the Late Cenozoic. The Miocene to Pleistocene valley fill deposits of the St. David Formation are dominated by lacustrine and fluvial continental deposits. Fossil mammal assemblages include the Benson fauna belonging to the Blancan Land Mammal Age and the Curtis Ranch fauna belonging to the younger Irvingtonian Land Mammal Age. The major objective of the magnetostratigraphic research was to produce a detailed correlation between these Pliocene–Pleistocene land mammal ages and the marine biozonations by defining the position of the Blancan and Irvingtonian land mammal ages within the GPTS.

The 150-m-thick Curtis Ranch section was the major stratigraphic section for which the magnetic polarity zonation was determined (Figure 9.12). Three block samples were collected at each of 81 paleomagnetic sites separated by an average stratigraphic spacing of 3.3 m. Strong-field thermomagnetic analysis of magnetic separates indicated that magnetite and titanomagnetite are the dominant ferromagnetic minerals. Claystones proved to contain the most stable NRM with the ChRM interpreted as detrital in origin. AF demagnetization to peak fields of 100 to 150 Oe (10 to 15 mT) successfully removed secondary VRM, isolating the ChRM, which had an average intensity of 1×10^{-5} G (1×10^{-2} A/m). The mean directions for the normal- and reversed-polarity sites passed the reversals test, adding confidence in the polarity determinations.

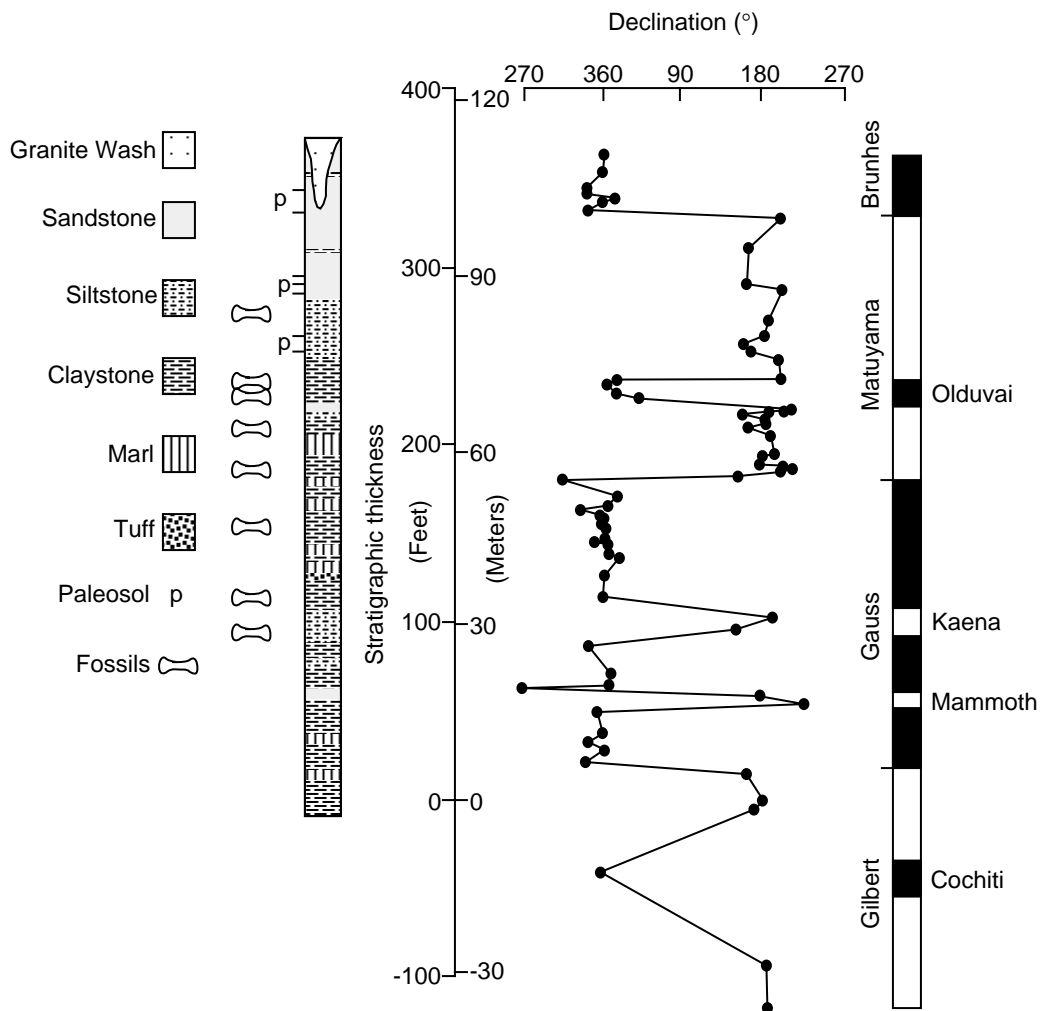


Figure 9.12 Site-mean ChRM declination versus stratigraphic position at Curtis Ranch, San Pedro Valley, Arizona. The interpreted polarity column and correlations to the GPTS are shown at the right. Redrawn from Johnson et al. (1975) with permission from the Geological Society of America.

As seen in Figure 9.12, 12 polarity zones were defined within the Curtis Ranch section. An important age constraint was provided by a K-Ar date of 2.5 ± 0.4 Ma from a volcanic ash within the reversed-polarity zone at the 60- to 70-m stratigraphic level. This reversed-polarity zone thus is best correlated with the early portion of the Matuyama epoch, which has absolute age limits of 2.43 Ma and 1.86 Ma on the GPTS used by Johnson et al. (1975). With that correlation accomplished, the pattern of polarity zones of the Curtis Ranch section convincingly correlates to the GPTS from the late Gilbert epoch into the Brunhes epoch. (Notice that the correlation shown in Figure 9.12 implies that the Reunion events and the Jaramillo event were not detected in the Curtis Ranch section. We will return to this point below.)

In Figure 9.13, fossil levels within the St. David Formation are shown within their respective magnetic polarity zones, which have been correlated to the GPTS. All the absolute age calibration of the GPTS thus can be used to provide absolute age estimates for the faunal levels within this continental sedimentary sequence in which little directly datable material was present. The *Lepus* faunal datum is the first appearance of a definitive Irvingtonian land mammal (rabbit), and the local boundary between the Blancan and Irvingtonian land mammal ages occurs just prior to the Olduvai event. This geochronologic calibration places the Blancan/Irvingtonian boundary very close to the marine Pliocene/Pleistocene boundary (Berggren et al., 1985). Johnson et al. (1975) thus accomplished the detailed correlation between Late Cenozoic land mammal ages and marine biozonations that they sought.

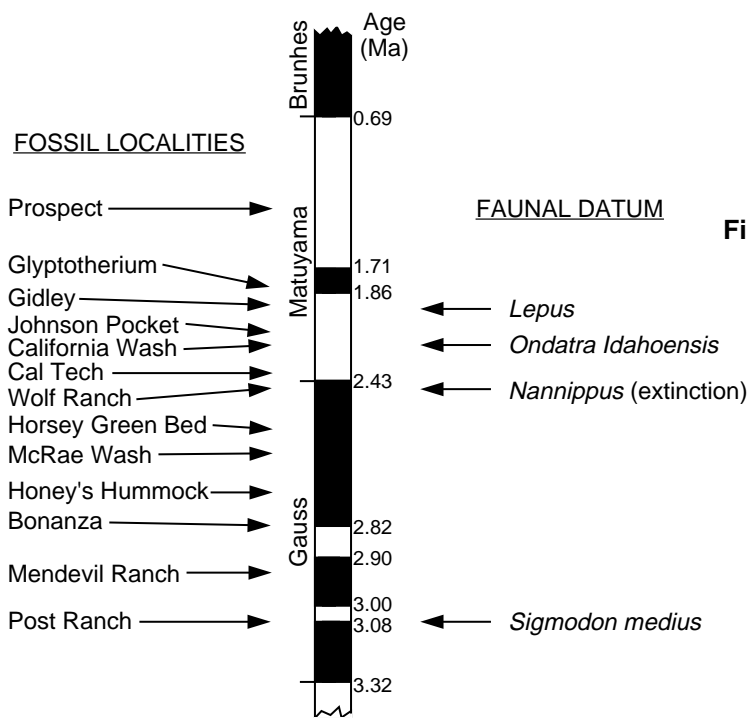


Figure 9.13 Occurrences of fossil-mammal localities in San Pedro Valley with respect to the GPTS. Absolute ages of polarity intervals are indicated on the right side of the polarity column. Redrawn from Johnson et al. (1975) with permission from the Geological Society of America.

As illustrated by the “missing” Curtis Ranch polarity zones corresponding to the Jaramillo and Reunion events (Figure 9.12), polarity stratigraphies often lack polarity zones corresponding to short-duration polarity intervals. Sometimes, as in the Curtis Ranch section, the stratigraphic spacing of sites does not permit detection of short-duration polarity intervals (Johnson and McGee, 1983). It is also possible that a hiatus in sediment accumulation occurred during the time span of a short-duration polarity interval. The discontinuity of sediment accumulation has important implications for magnetostratigraphy and can be quantified by the approach of *stratigraphic completeness*. For discussions of stratigraphic completeness and magnetostratigraphy, see May et al. (1985) and Badgley et al. (1986).

Siwalik Group deposits

The Siwalik Group of northwest India and Pakistan is a sequence of Neogene continental sediments shed from the Himalayas onto the Indian subcontinent during its collision with southern Asia. Because this sequence has been a rich source of Miocene fossil mammals, detailed correlation between fossil localities within the Siwalik deposits and geochronologic calibration of the sedimentary sequence is important to deciphering the evolution of Asian mammals, including primate lineages.

Our next magnetostratigraphic example is part of a large effort to accomplish geochronologic calibration of the Siwalik deposits. Johnson et al. (1985) examined the magnetic polarity stratigraphy of sediments exposed near Chinji Village, Pakistan. In this location, the Siwalik sequence overlies Eocene marine limestone. In stratigraphic order, the formations of the homoclinal sequence are (1) alternating sandstones and mudstones of the Kamli Formation (in some localities called the Murree Formation), (2) greenish-gray sandstones and brown-red mudstones of the Chinji Formation, (3) multistoried green-gray sandstones of the Nagri Formation, and (4) brown silts of the Dhok Pathan Formation. This stratigraphic sequence is exposed in two major drainages: a lower section in Chita Parwala Kas and an upper section in Gabhir Kas.

Although rock colors range from gray to red, Siwalik sediments are “red beds” in the sense that the NRM is carried by hematite. Tauxe et al. (1980) performed detailed rock-magnetic analyses to determine the origin of NRM components. The NRM properties divided the lithologies into two broad categories: “gray sediments” and “red sediments.” Progressive thermal demagnetization showed that gray sediments have a component of NRM with low blocking temperatures (T_B) up to $\sim 400^\circ\text{C}$ and a ChRM component with T_B up to 675°C . Both components are carried by specular hematite, and the low T_B component is quite clearly a VRM. The red sediments have two NRM components in addition to the low T_B VRM. Vector end-point diagrams of progressive thermal demagnetization revealed that the trajectory of vector end points often reversed trend between 525° and 600°C prior to final trajectory to the origin at 680°C . This indicated removal of an NRM component with direction antiparallel to the ChRM.

Tauxe et al. (1980) did coercivity spectrum analysis (Chapter 4) on untreated samples and on samples leached with acid to remove the red pigment. They demonstrated that the pigment had T_B in the 525 to 600°C range and that the ChRM component was carried by specular hematite. The NRM component with direction antiparallel to the ChRM (and with T_B from 525° to 600°C) thus was interpreted as CRM carried by the red pigment. Formation of this NRM component postdates the ChRM formation by at least one polarity reversal.

A conglomeratic layer was located within the Siwalik sequence. The ChRM component of sediment cobbles was shown to be carried by specular hematite and to pass a conglomerate test. Tauxe et al. (1980) thus argued that the ChRM must have been acquired as either a DRM or an early-formed CRM. These important rock-magnetic observations demonstrate that ChRM directions obtained through thermal demagnetization to 600°C can be reliably used to determine the polarity sequence during deposition of Siwalik sediments.

Johnson et al. (1985) collected three block samples at 159 paleomagnetic sites distributed through the two stratigraphic sections and subjected all samples to thermal demagnetization at 600°C . The site-mean results were broken into two classes according to within-site clustering of ChRM directions. Sites with clustering that was significant from random (5% significance level) were designated “class A.” Sites with clustering of ChRM directions that was not significant from random but in which the ChRM polarity of two samples agreed were designated “class B.” In the stratigraphic sections near Chinji Village, there were 99 class A sites, 37 class B sites, and 23 sites that yielded ambiguous results and were rejected. The means of the class A normal- and reversed-polarity groups passed the reversals test.

The magnetic polarity stratigraphies established for the Chita Parwala Kas and Gabhir Kas sections are shown in Figure 9.14. The site-mean VGP latitudes quite cleanly define the polarity zones. Two sandstone layers were traced between the sections and are shown connecting the lithostratigraphic sec-

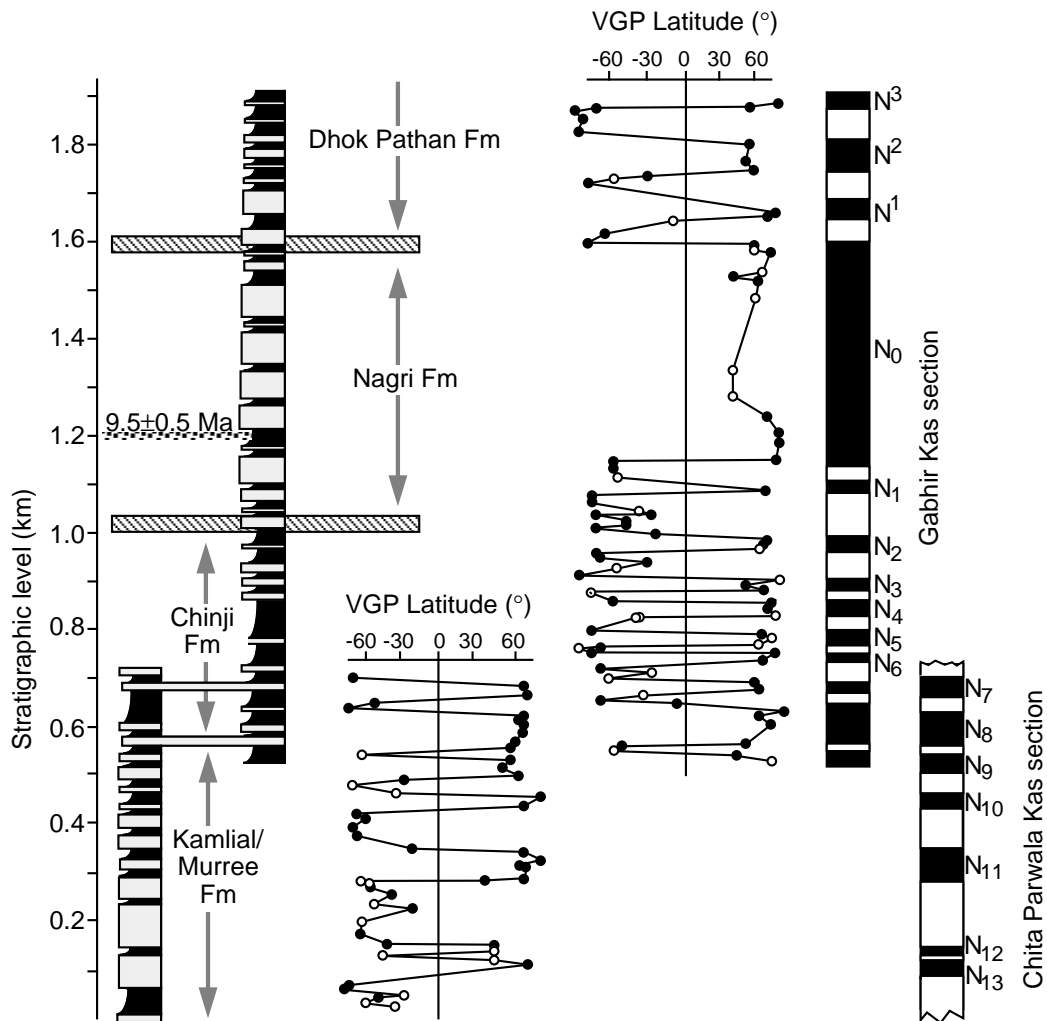


Figure 9.14 Stratigraphic correlation and polarity stratigraphy of Chita Parwala and Gabhir Kas sections. Resistant sandstones are shown by the stippled pattern in the stratigraphic section; finer-grained lithologies are shown in black; tracer sandstone units are shown connecting lithostratigraphic sections; VGP latitudes for class A sites are shown by solid circles; VGP latitudes for class B sites are shown by open circles; the interpreted magnetic polarity zonation is shown at the right. Redrawn from Johnson et al. (1985) with permission from the *Journal of Geology*. Copyright© 1985 by The University of Chicago.

tions in Figure 9.14. The lithologic correlation is corroborated by the magnetic polarity zonation; normal-polarity zones N₇ and N₈ are found in both sections. The magnetic polarity zonation from the two sections were combined into a composite magnetostratigraphic section for Siwalik deposits in this region.

The composite magnetic polarity zonation and its correlation to the GPTS are shown in Figure 9.15. A fission-track date of 9.5 ± 0.5 Ma from an ash deposit within the Nagri Formation allows the thick normal-polarity zone containing the ash to be securely correlated with chron 5 of the GPTS. Also, the polarity pattern and dominance of reversed-polarity within the lower portion of the section correlates well with the polarity pattern of chrons 5Br through 5Cr. Considering the age constraint provided by the fission-track date and the overall matching of the pattern of polarity zones with that of the GPTS in the 18 to 8-Ma interval, the correlation of Figure 9.15 is reasonably convincing. From this magnetostratigraphic analysis, Johnson et al. (1985) estimated absolute ages of formational boundaries and fossil localities within these Siwalik deposits. The Kamliial/Chinji boundary has an estimated

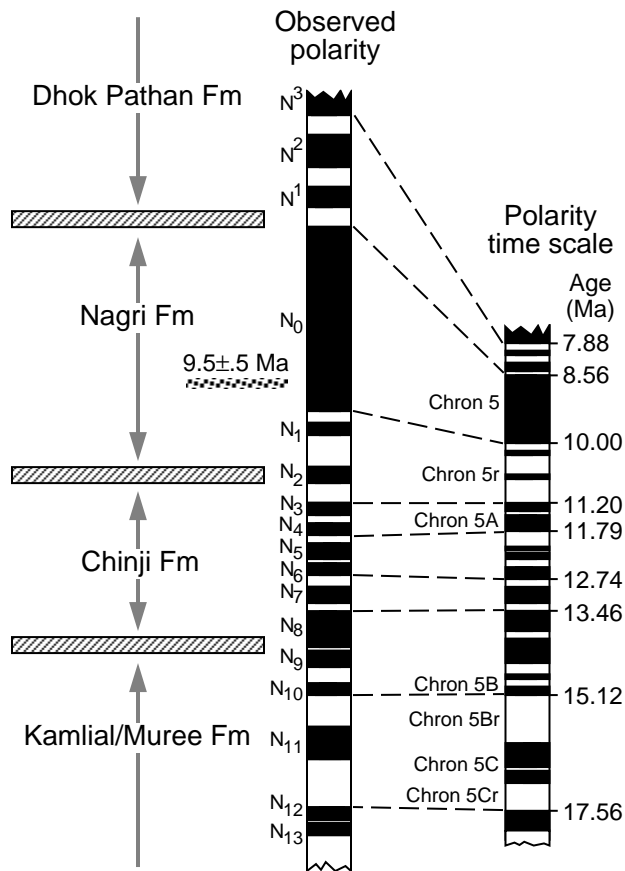


Figure 9.15 Correlation of magnetic polarity zonation of Siwalik deposits near Chinji Village, Pakistan, with the of Mankinen and Dalrymple (1979); the “chron” numbering system is from Cox (1982). Redrawn from Johnson et al. (1985) with permission from the Journal of Geology. Copyright© 1985 by The University of Chicago.

age of 14.3 Ma; the Chinji/Nagri boundary is estimated at 9.8 Ma; and an estimate of 8.5 Ma is made for the Nagri/Dhok Pathan boundary.

An interesting additional observation is shown in Figure 9.16. The age indicated by the magnetostratigraphy and fission-track dating is graphed against stratigraphic level, with slope indicating rate of sediment accumulation. The lower portion of the section has a reasonably constant rate of sediment accumulation of 0.12 m/1000 yr. But the upper portion with age <11 Ma has a higher rate of 0.30 m/1000 yr. This change in sediment accumulation rate also correlates with a marked increase in metamorphic detritus (especially blue-green hornblendes). The tectonic interpretation is that the rate of sediment accumulation accelerated at ~11 Ma because of unroofing of metamorphic rocks in the source region. Indeed, uplift of 10 km since 10 Ma has been documented for the likely source region, the Nanga Parbat-Hunza region of the Himalayas.

The tectonic and sedimentologic implications of the magnetostratigraphic work of Johnson et al. (1985) are best summarized in their concluding paragraph:

In the long-range view then, the Siwalik sequence in the Chinji Village area represents just one ephemeral stage in a dynamic system of landforms, sediments, and tectonics. In the course of its northward drift the Indian Plate has acted like a conveyor belt, bringing a continuous series of depositional sites, including the Chinji Village area, along with it. During its northward ride, the Chinji Village site has been converted slowly from a karst terrane into a depositional terrane, and most recently into a thrust belt and source terrane. Our chronologic data from Chinji Village suggest that the life cycle for each depositional site spans some 20 m.y.

Siwalik sedimentology

The final example application of magnetic polarity stratigraphy is the sedimentological study of Siwalik Group sediments near Dhok Pathan, Pakistan, by Behrensmeier and Tauxe (1982). In this region, shown

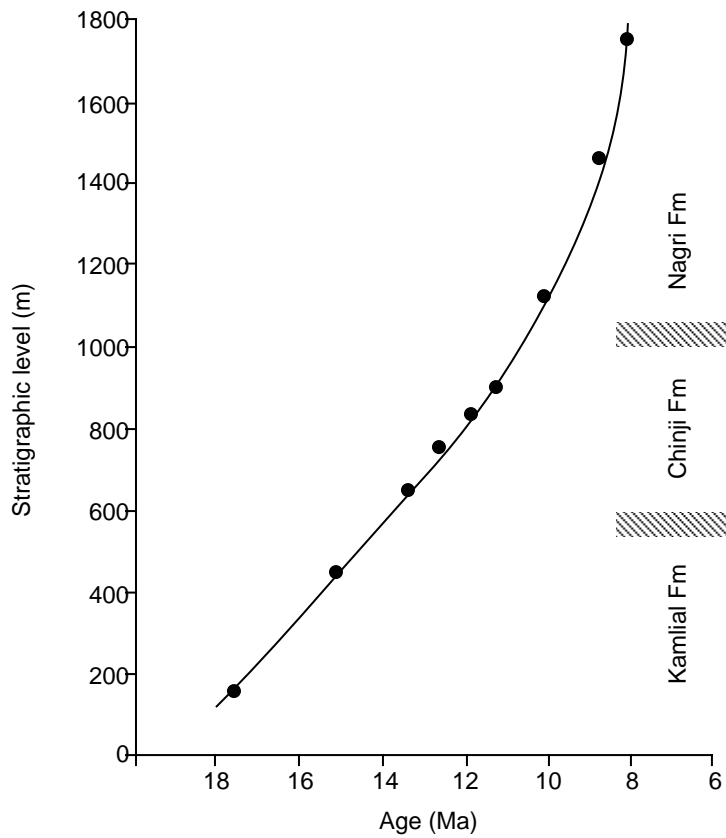


Figure 9.16 Sediment accumulation history of Siwalik deposits near Chinji Village. Data points are boundaries between identified magnetic polarity chrons; the slope of the curve is the sediment accumulation rate. Redrawn from Johnson et al. (1985) with permission from the *Journal of Geology*. Copyright© 1985 by The University of Chicago.

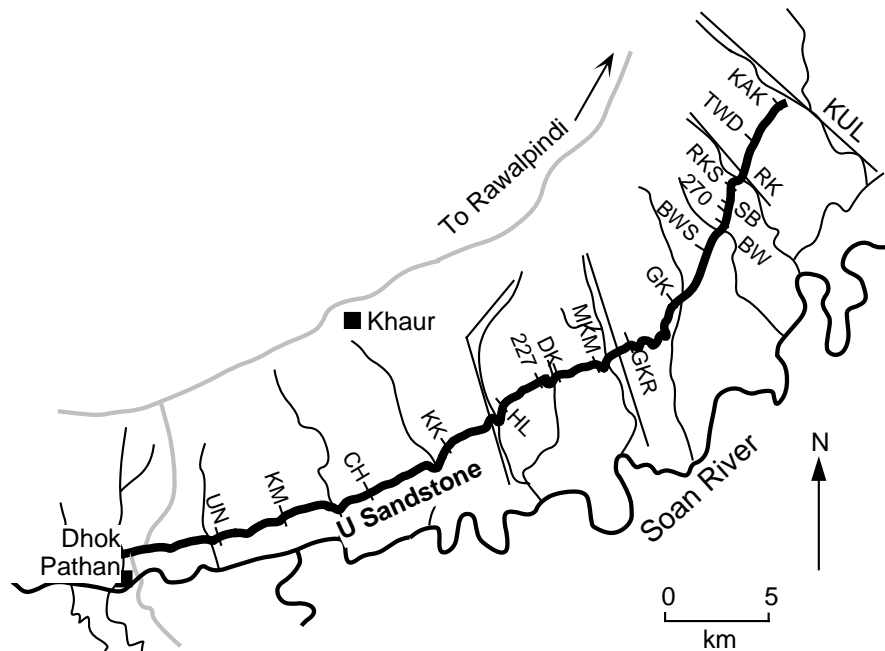


Figure 9.17 Stratigraphic sections of Middle Siwalik deposits near Khaur, Pakistan. The heaviest black line shows the outcrop of U Sandstone; the medium black line shows the course of Soan River; the thin, sinuous black lines show canyons cutting across the strike of deposits; stippled lines indicate roads; initials label stratigraphic sections located by straight black lines and shown in Figure 9.18; the region is within Potwar Plateau. Redrawn from Behrensmeier and Tauxe (1982).

in Figure 9.17, the Nagri Formation is characterized by laterally extensive sheet sandstones, while the Dhok Pathan Formation is characterized by siltstones and claystones. On a gross scale, the Dhok Pathan Formation overlies the Nagri Formation. But using a particular magnetic polarity zone boundary as an isochronous marker, Behrensmeier and Tauxe showed that the formational boundary is a complex interfingering of two fluvial systems.

Previous magnetic polarity studies by Tauxe and Opdyke (1982) provided correlation of the magnetic polarity zonation of the Nagri and Dhok Pathan formations in this region to the GPTS. The paleomagnetic data were similar to those reported by Johnson et al. (1985), and a similar “class” designation was used for reliability of polarity determinations. The correlation provided an absolute age estimate of 8.1 Ma for the boundary between normal-polarity zone DN4 and the overlying reversed-polarity zone DR4. Excellent exposures of the Middle Siwalik group north of the Soan River allowed paleomagnetic sampling of a 40 m stratigraphic interval spanning the DN4-DR4 boundary in closely spaced sections over a distance of 40 km (Figure 9.17). The top of a continuous sheet sandstone body (U Sandstone) was used as a stratigraphic datum for correlation between sections.

A southwest-to-northeast cross section of the major lithologies and the paleomagnetic polarity determinations is shown in Figure 9.18. With an average sediment accumulation rate of 0.52 m/1000 yr and sedimentologic evidence that the boundary is not marked by a hiatus, the DN4-DR4 boundary approximates an isochronous horizon. This cross-sectional mapping of the DN4-DR4 “time line” provides the magnetostratigraphic proof of a basic concept in stratigraphy and sedimentology: the intertonguing of two geologic formations and the time-transgressive nature of the formational contact.

In this particular case, the intertonguing of the Nagri and Dhok Pathan formations is the result of interfingering between two contemporaneous fluvial systems. On the southwest, the dominant system deposited widespread blue-gray sheet sandstones characteristic of the Nagri Formation. To the northeast, the dominant system deposited silt and clay with occasional restricted lenses of buff-colored sandstone. Through use of the DN4-DR4 isochron, Behrensmeier and Tauxe (1982) developed a model for the tectonic and hydrologic influences on the interfingering of the two depositional systems.

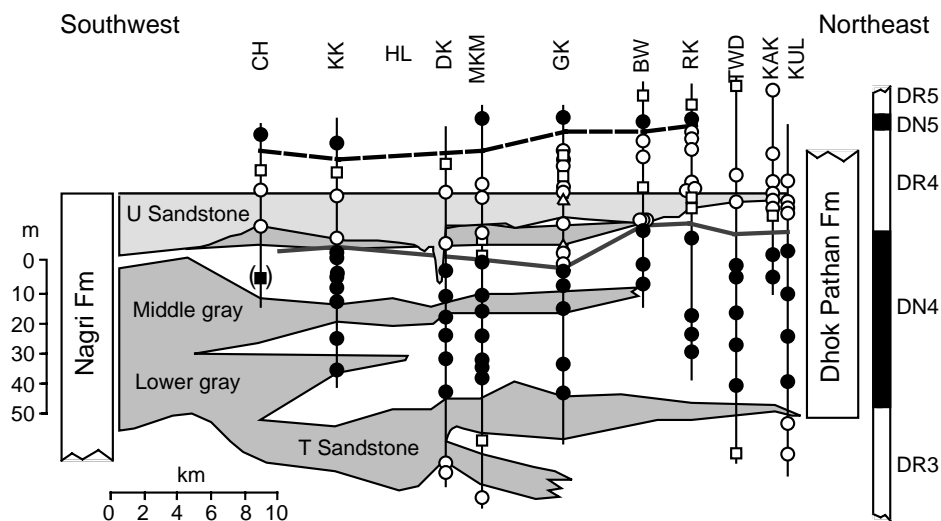


Figure 9.18 Magnetostratigraphic correlation of DN4-DR4 polarity boundary along the strike of the U Sandstone. Sheet sandstones on the southwest side of the cross section are assigned to the Nagri Formation, while silts and clays (shown by white) are characteristic of the Dhok Pathan Formation to the northwest; the top of the U Sandstone is used as a horizontal reference; circles indicate class A paleomagnetic sites; squares indicate class B sites; triangles indicate class C sites (within-site clustering of ChRM significant from random after AF demagnetization); black indicates normal polarity; white indicates reversed polarity; the bold stippled line indicates the position of the DN4-DR4 polarity boundary. Redrawn from Behrensmeier and Tauxe (1982).

REFERENCES

- L. W. Alvarez, W. Alvarez, F. Asaro, and H. V. Michel, Extraterrestrial cause for the Cretaceous–Tertiary extinction, *Science*, v. 208, 1095–1108, 1980.
- C. Badgley, L. Tauxe, and F. L. Bookstein, Estimating the error of age interpolation in sedimentary rocks, *Nature*, v. 319, 139–141, 1986.
- A. K. Behrensmeyer and L. Tauxe, Isochronous fluvial systems in Miocene deposits of northern Pakistan, *Sedimentology*, v. 29, 331–352, 1982.
- W. A. Berggren, D. V. Kent, J. J. Flynn, and J. A. Van Couvering, Cenozoic geochronology, *Geol. Soc. Am. Bull.*, v. 96, 1407–1418, 1985.
- A. Cox, *Plate Tectonics and Geomagnetic Reversals*, W. H. Freeman and Co., San Francisco, 702 pp., 1973.
- A. Cox, Magnetostratigraphic time scale, In: *A Geologic Time Scale*, ed. W. B. Harland et al., Cambridge University Press, Cambridge, England, pp. 63–84, 1982.
- A. Cox, R. R. Doell, and G. B. Dalrymple, Geomagnetic polarity epochs and Pleistocene geochronometry, *Nature*, v. 198, 1049–1051, 1963.
- A. Cox, R. R. Doell, and G. B. Dalrymple, Geomagnetic polarity epochs, *Science*, v. 143, 351–352, 1964.
- A. Cox, R. R. Doell, and G. B. Dalrymple, Radiometric time-scale for geomagnetic reversals, *Quart. J. Geol. Soc.*, v. 124, 53–66, 1968.
- K. M. Creer, P. Tucholka, and C. E. Barton, *Geomagnetism of Baked Clays and Recent Sediments*, Elsevier, Amsterdam, 324 pp., 1983.
- R. R. Doell and G. B. Dalrymple, Geomagnetic polarity epochs: A new polarity event and the age of the Brunhes–Matuyama boundary, *Science*, v. 152, 1060–1061, 1966.
- W. Glen, *The Road to Jaramillo*, Stanford University Press, Stanford, Calif., 459 pp., 1982.
- E. A. Hailwood, *Magnetostratigraphy*, Special Report No. 19, The Geological Society, Blackwell Scientific Publications, Oxford, England, 84 pp., 1989.
- J. R. Heirtzler, G. O. Dickson, E. M. Herron, W. C. Pitman, III, and X. Le Pichon, Marine magnetic anomalies, geomagnetic field reversals, and motions of the ocean floor and continents, *J. Geophys. Res.*, v. 73, 2119–2136, 1968.
- N. M. Johnson and V. E. McGee, Magnetic polarity stratigraphy: Stochastic properties of data, sampling problems, and the evaluation of interpretations, *J. Geophys. Res.*, v. 88, 1213–1221, 1983.
- N. M. Johnson, N. D. Opdyke, and E. H. Lindsay, Magnetic polarity stratigraphy of Pliocene–Pleistocene terrestrial deposits and vertebrate faunas, San Pedro Valley, Arizona, *Geol. Soc. Am. Bull.*, v. 86, 5–12, 1975.
- N. M. Johnson, J. Stix, L. Tauxe, P. F. Cervený, and R. A. K. Tahirkheli, Paleomagnetic chronology, fluvial processes, and tectonic implications of the Siwalik deposits near Chinji Village, Pakistan, *J. Geol.*, v. 93, 27–40, 1985.
- J. L. Kirschvink, The Precambrian–Cambrian boundary problem: Magnetostratigraphy of the Amadeus Basin, Central Australia, *Geol. Mag.*, v. 115, 139–150, 1978.
- J. L. La Brecque, D. V. Kent, and S. C. Cande, Revised magnetic polarity time scale for Late Cretaceous and Cenozoic time, *Geology*, v. 5, 330–335, 1977.
- W. Lowrie, Magnetic polarity time scales and reversal frequency, In: *Geomagnetism and Paleomagnetism*, ed. F. J. Lowes, D. W. Collinson, J. H. Parry, S. K. Runcorn, D. C. Tozer, and A. Soward, Kluwer Academic Publishers, Dordrecht, Netherlands, pp. 155–183, 1989.
- W. Lowrie and W. Alvarez, Upper Cretaceous–Paleocene magnetic stratigraphy at Gubbio, Italy, III. Upper Cretaceous magnetic stratigraphy, *Geol. Soc. Am. Bull.*, v. 88, 374–377, 1977.
- W. Lowrie and W. Alvarez, One hundred million years of geomagnetic polarity history, *Geology*, v. 9, 392–397, 1981.
- W. Lowrie and J. G. Ogg, A magnetic polarity time scale for the Early Cretaceous and Late Jurassic, *Earth Planet. Sci. Lett.*, v. 76, 341–349, 1986.
- E. A. Mankinen and G. B. Dalrymple, Revised geomagnetic polarity time scale for the interval 0–5 m.y. B.P., *J. Geophys. Res.*, v. 84, 615–626, 1979.
- S. R. May, R. F. Butler, and F. A. Roth, Magnetic polarity stratigraphy and stratigraphic completeness, *Geophys. Res. Lett.*, v. 12, 341–344, 1985.
- I. McDougall, The present status of the geomagnetic polarity time scale, In: *The Earth: Its Origin, Structure and Evolution*, ed. M. W. McElhinny, Academic Press, London, pp. 543–566, 1979.

- I. McDougall and F. H. Chamalaun, Geomagnetic polarity scale of time, *Nature*, v. 212, 1415–1418, 1966.
- I. McDougall and D. H. Tarling, Dating of polarity zones in the Hawaiian Islands, *Nature*, v. 200, 54–56, 1963.
- M. W. McElhinny, *Palaeomagnetism and Plate Tectonics*, Cambridge University Press, London, 356 pp., 1973.
- P. L. McFadden and R. T. Merrill, Geodynamo energy source constraints from palaeomagnetic data, *Phys. Earth Planet. Inter.*, v. 43, 22–33, 1986.
- L. W. Morley and A. Larochelle, Palaeomagnetism as a means of dating geological events, In: *Geochronology in Canada*, ed. F. F. Osborne, Roy. Soc. Canada Spec. Publ. No. 8, University of Toronto Press, Toronto, pp. 39–51, 1964.
- T. Nagata, S. Uyeda, and S. Akimoto, Self-reversal of thermoremanent magnetism of igneous rocks, *J. Geomagnet. Geoelect.*, v. 4, 22–38, 1952.
- G. Ness, S. Levi, and R. Couch, Marine magnetic anomaly timescales for the Cenozoic and Late Cretaceous: A precis, critique and synthesis, *Rev. Geophys. Space Phys.*, v. 18, 753–770, 1980.
- N. D. Opdyke, Paleomagnetism of deep-sea cores, *Rev. Geophys. Space Phys.*, v. 10, 213–249, 1972.
- N. D. Opdyke, L. H. Burckle, and A. Todd, The extension of the magnetic time scale in sediments of the central Pacific Ocean, *Earth Planet. Sci. Lett.*, v. 22, 300–306, 1974.
- P. M. Sadler, Sediment accumulation rates and the completeness of stratigraphic sections, *J. Geology*, v. 89, 569–584, 1981.
- L. Tauxe and N. D. Opdyke, A time framework based on magnetostratigraphy for the Siwalik sediments of the Khar area, northern Pakistan, *Paleogeogr. Paleoclimat. Paleoecol.*, v. 37, 43–61, 1982.
- L. Tauxe, D. V. Kent, and N. D. Opdyke, Magnetic components contributing to the NRM of Middle Siwalik red beds, *Earth Planet. Sci. Lett.*, v. 47, 279–284, 1980.
- F. Theyer and S. R. Hammond, Palaeomagnetic polarity sequence and radiolarian zones, Brunhes to polarity epoch 20, *Earth Planet. Sci. Lett.*, v. 22, 307–319, 1974.
- R. Thompson and F. Oldfield, *Environmental Magnetism*, Allen and Unwin, London, 1986, 227 pp.
- F. J. Vine and D. H. Matthews, Magnetic anomalies over ocean ridges, *Nature*, v. 199, 947–949, 1963.

APPLICATIONS TO PALEOGEOGRAPHY

Early paleogeographic applications of fundamental paleomagnetic techniques (primarily by a handful of British scientists) led to one of the most broadly appreciated contributions of paleomagnetism to Earth science: the confirmation of continental drift theory. Here we develop the basic principles of applying paleomagnetism to paleogeography. The geocentric axial dipole hypothesis is a fundamental building block, and we first explore the evidence that this simple form is the first-order behavior of the geomagnetic field. Discussion of paleomagnetic poles and their presentations lead us into development of apparent polar wander paths. Introduction of a few key concepts in comparison of these paths between continents provides the tools for understanding applications to paleogeography. The chapter concludes with several examples that illustrate the powers and limitations of applying paleomagnetism to paleogeographic continental reconstructions.

THE GEOCENTRIC AXIAL DIPOLE HYPOTHESIS

The Geocentric Axial Dipole (GAD) hypothesis was introduced in Chapter 1, where its consistency with a magnetohydrodynamic origin of the geomagnetic field was noted. The GAD hypothesis implies that a paleomagnetic pole indicates the position of the rotation axis with respect to the continent from which the paleomagnetic data were acquired. Through the GAD hypothesis, paleomagnetic poles can be used to determine paleogeographic reconstructions by using the procedures developed below. Because of its crucial role in tectonic applications of paleomagnetism, the GAD hypothesis is further explored in this section.

During the 1950s and early 1960s, paleomagnetic evidence for continental drift was attacked by detractors who questioned the validity of the GAD hypothesis during the Paleozoic and Mesozoic. Irving (1964) discussed this “nondipole hypothesis” and concluded that it was a “hypothesis of desperation, useful at this stage only to those anxious to avoid implications of paleomagnetism.” With subsequent expansion of paleomagnetic data and development of plate tectonics, the fundamental validity of the GAD hypothesis is now quite firmly established.

The past 5 million years

In discussing Figure 1.9, we found that the geomagnetic pole does a random walk about the rotation axis. The average position of the geomagnetic pole over the past 2000 years is indistinguishable from the rotation axis. In Chapter 7, we analyzed paleomagnetic data from Holocene lavas of the western United States. Increasing numbers of VGPs were used to determine the “paleomagnetic poles” shown in Figure 7.5. Resulting poles fell within 3° of the rotation axis, and the confidence limit, A_{95} , decreased to 3.7° when 30 VGPs were averaged. It is apparent that the time-averaged Holocene paleomagnetic field in the western United States was geocentric axial dipolar within a 95% confidence limit of $\sim 3^\circ$. We will return to further discussion of this data set below.

Opdyke and Henry (1969) determined mean paleomagnetic inclinations from 52 Pliocene–Pleistocene deep-sea cores. These mean inclinations are shown in Figure 8.2 and are found to closely match the inclinations predicted by a GAD: $\tan I = 2 \tan \lambda$ (Equation (1.15)). More detailed evaluation of the GAD

hypothesis was made possible by compilation of paleomagnetic data from 4580 lavas with ages in the 0- to 5-Ma interval (Merrill and McElhinny, 1983). The first-order time-averaged geomagnetic field over the past 5 m.y. was found to be axial geocentric dipolar within confidence limits of $\sim 3^\circ$. This data set is sufficiently large to allow resolution of second-order deviations, which are discussed below. The above analyses confirm the validity of the GAD hypothesis for the past 5 m.y. So in the geologic time interval for which the most rigorous tests are available, the GAD hypothesis is confirmed with an uncertainty of $\sim 3^\circ$.

Older geologic intervals

The task of evaluating the GAD hypothesis for geologic time intervals older than 5 m.y. is complicated by motions of lithospheric plates, the phenomena that we're going to use paleomagnetic data to investigate. These evaluations can be divided into tests of (1) the geocentric dipolar nature of the paleomagnetic field and (2) the axial alignment of the geocentric dipole.

From the Late Jurassic to the present, marine magnetic anomalies provide determination of relative plate motions. At least during the Cenozoic, continents can be accurately reconstructed to their relative positions by using these anomalies. The dipolar nature of the time-averaged geomagnetic field can be tested by comparisons of paleomagnetic poles from the different continents as sequential reconstructions to older geologic times are performed. For example, if continents are reconstructed to their relative positions at 30 Ma, paleomagnetic poles from rocks of this age should agree if the time-averaged geomagnetic field was geocentric dipolar; failure of the poles to agree could indicate a nondipolar field. Such analyses have confirmed the geocentric dipolar nature of the geomagnetic field during the Cenozoic and Late Mesozoic to a precision of about 5° (e.g., Livermore et al., 1983, 1984).

Other tests have similarly confirmed the geocentric dipolar nature of the time-averaged paleomagnetic field during Phanerozoic time (e.g., McElhinny and Brock 1975; Evans, 1976). But how do we test whether this geocentric dipole was aligned with the Earth's rotation axis? Comparisons with independent determinations of paleolatitude are required. Although imperfect and of limited precision, *paleoclimatic indicators* are the best available independent measures of paleolatitude with which to compare paleolatitudes determined from paleomagnetism.

Latitudinal zones of climate exist fundamentally because the flux of solar energy strongly depends on latitude. The present mean annual temperature is 25°C at the equator but is only -25°C at the poles. Numerous biologic and geologic phenomena are controlled by climatic zones: Organic reefs (corals), evaporite deposits, and red sediments are predominantly found in equatorial regions or in temperate arid zones symmetric about the equator; and glacial phenomena are found in or surrounding polar regions.

Paleoclimatic spectra are histograms of the latitudinal distribution of these paleoclimatic indicators. Comparison of paleoclimatic spectra in present latitude with spectra in paleolatitude determined from paleomagnetism is the basic method for evaluating the axial alignment of the geocentric dipole for remote geologic times. Irving (1964) presented a thorough discussion of paleoclimatic and paleomagnetic data. The fundamental verification of the GAD hypothesis by favorable comparison with paleoclimatic indicators has not significantly changed since the synthesis by Briden and Irving (1964). The following examples are adapted from their analysis.

In Figure 10.1a, the present latitudinal distribution of modern organic reefs is shown. The observed distribution is symmetric about the equator, and almost all occurrences are within 30° of the equator. But the present latitudinal distribution of fossil organic reefs (Figure 10.1b) shows many fossil reefs at latitudes $>30^\circ\text{N}$, and the distribution is very asymmetric about the equator. It is highly unlikely that this distribution resulted from a drastically different pattern of climatic zones at the time these fossil reefs formed. Furthermore, the distribution of fossil reefs in paleolatitude determined from paleomagnetism (Figure 10.1c) exhibits the anticipated symmetry about the paleoequator. This analysis indicates that the distribution of fossil reef deposits is consistent with the GAD hypothesis.

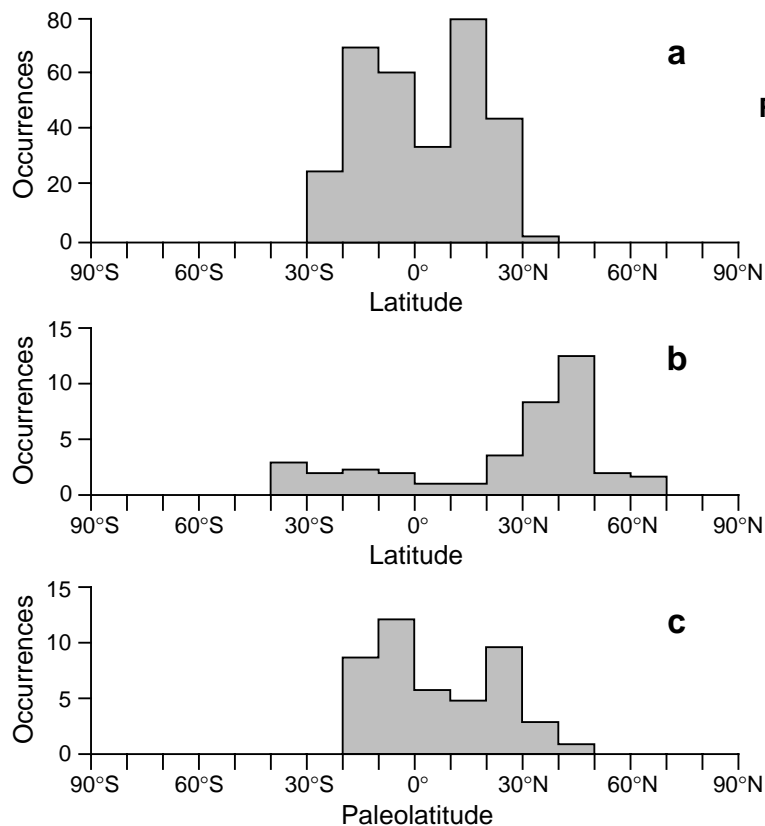


Figure 10.1 Latitudinal distribution of modern and fossil organic reefs. (a) Histogram of modern organic reefs within 10° bands of latitude; note the rough symmetry of modern organic reefs about the equator. (b) Histogram of present latitudinal distribution of ancient organic reefs; note that the majority of ancient organic reefs have present latitudes higher than 30°N. (c) Histogram of fossil organic reefs in paleolatitude determined from paleomagnetism; paleolatitudes of the majority of fossil organic reefs are within 30° of the paleoequator. Redrawn from McElhinny (1973) and Briden and Irving (1964).

Other examinations (e.g., Briden, 1968, 1970; Drewry et al., 1974) have led to the same basic conclusion: Paleomagnetic determinations of paleolatitude are consistent with a variety of paleoclimatic indicators, and the first-order geocentric axial dipolar nature of the time-averaged paleomagnetic field is confirmed. However, the precision of these comparisons is limited and difficult to quantify. Nevertheless, it is reasonable to conclude that the GAD hypothesis is valid at least to $\sim 10^\circ$ precision and perhaps to $\sim 5^\circ$ precision.

Second-order deviations

Acquisition of massive paleomagnetic data sets from rocks with ages < 5 Ma has allowed resolution of small deviations of the time-averaged paleomagnetic field from that of a geocentric axial dipole. Wilson and Ade-Hall (1970) noted a tendency for paleomagnetic poles from Pliocene and younger lavas to be located a few degrees on the opposite side of the rotation axis from the observing locality (sites of paleomagnetic collection). This “far-sided effect” has since been thoroughly investigated (e.g., Coupland and Van der Voo, 1980; Merrill and McElhinny, 1983; Schneider and Kent, 1990).

Although complicated in detail, the basic result is that small nondipole components of the time-averaged paleomagnetic field are evident. Over the past few million years, paleomagnetic poles are far-sided by $\sim 3^\circ$. An example of this far-sided effect is given in Figure 10.2, in which the paleomagnetic pole determined from the entire set of 77 Holocene lavas from the western United States is shown. The pole falls 2.5° on the opposite side of the geographic pole from the collecting location, and the geographic pole is just outside the 95% confidence limit. So while the first-order time-averaged paleomagnetic field confirms the GAD hypothesis to a precision of perhaps $\sim 5^\circ$, second-order deviations amounting to $\sim 3^\circ$ are resolvable during the past few m.y.

Paleomagnetic poles and paleogeographic maps

As discussed in Chapter 7, the usual method of summarizing results of a paleomagnetic study is to determine and display the paleomagnetic pole position computed from the set of site-mean VGPs. If a number of

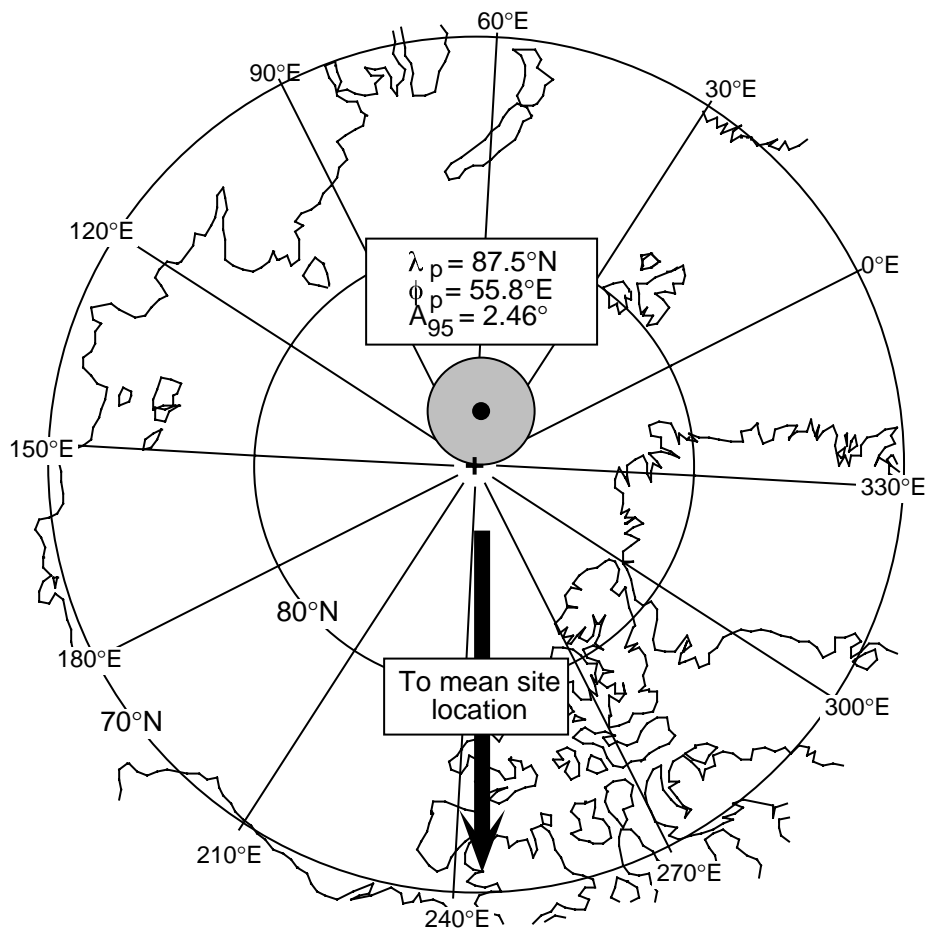


Figure 10.2 Paleomagnetic pole from Holocene lavas of the western United States. The entire data set of 77 VGPs from Holocene lavas was averaged; the paleomagnetic pole is located on the opposite side of the geographic pole from the collecting sites in the western United States; note that the geographic north pole is just outside the 95% confidence limit about the paleomagnetic pole; latitude circles are shown in 10° increments and longitude lines in 30° increments. Modified from Champion (1980).

“reliable” paleomagnetic poles have been determined from rocks of similar age from different areas of a continental interior (basic reliability criteria are discussed in Chapter 7), these poles should ideally be tightly clustered. In practice, even a collection of reliable paleomagnetic poles will have some scatter, owing to imperfect sampling of geomagnetic secular variation, uncertainties in structural correction, or other unknown effects.

In Figure 10.3, four paleomagnetic poles determined from mid-Cretaceous rocks of North America are illustrated. Each of these poles would be judged reasonably reliable by most paleomagnetists. Perhaps the most questionable is from the Niobrara Formation, which is a marine sedimentary formation with attendant uncertainty about possible shallowing of paleomagnetic inclination (Chapter 8). These four mid-Cretaceous poles are reasonably well grouped and represent a typical situation for a geologic time interval during which the paleomagnetic pole is regarded as “well determined.”

For a geologic time interval during which paleomagnetic poles from a continent are reasonably clustered without systematic motion of the pole, it is common to compute a mean pole. The individual paleomagnetic poles are treated as unit vectors, and a mean is computed by using Fisher statistics. The resulting mean mid-Cretaceous paleomagnetic pole for North America is shown in Figure 10.3.

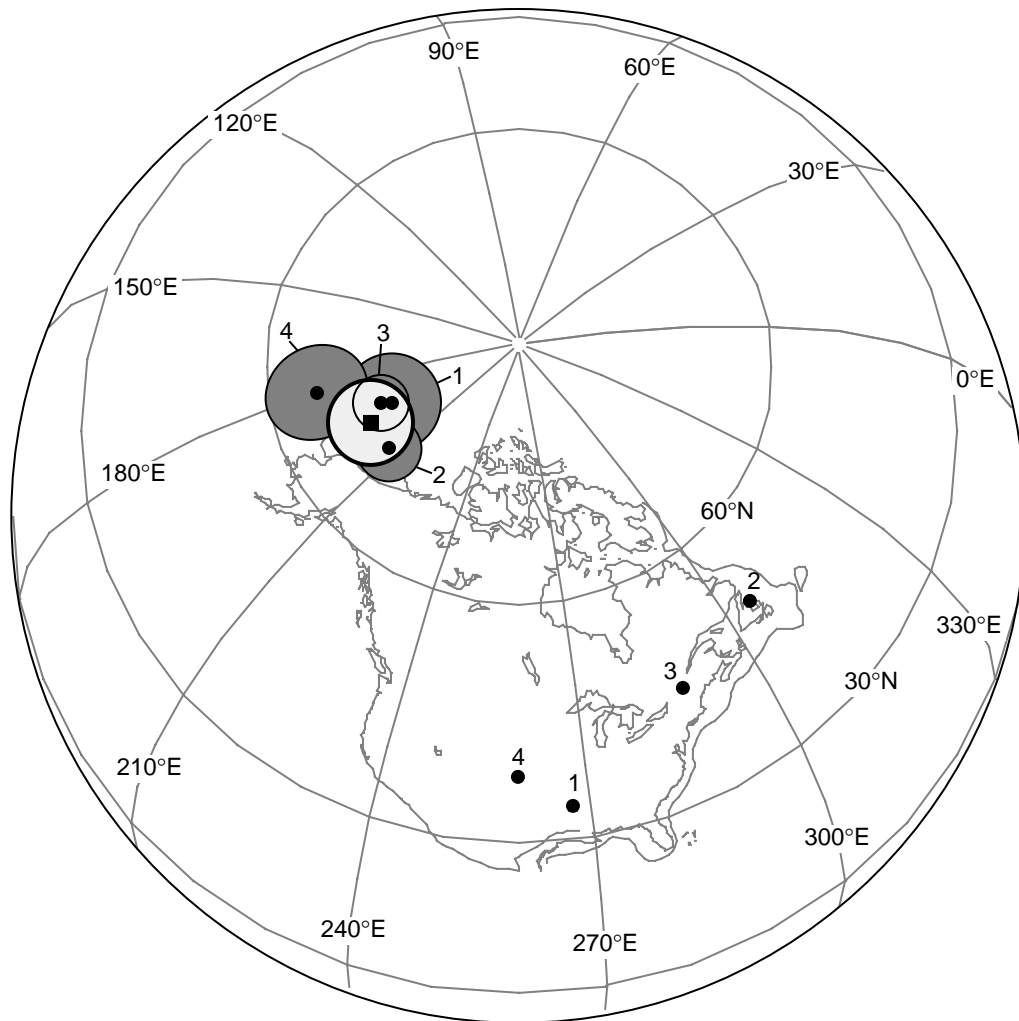


Figure 10.3 Comparison of four mid-Cretaceous paleomagnetic poles for North America. Sampling locations are shown by solid circles; corresponding paleomagnetic poles determined from each sampling location are shown with numbers labeling the stippled 95% confidence limits; 1 = alkalic intrusions, Arkansas (Globerman and Irving, 1988); 2 = lamprophyric dikes, Newfoundland (Prasad, 1981; Lapointe, 1979); 3 = alkalic intrusions, Quebec (Foster and Symons, 1979); 4 = Niobrara Formation, Kansas (Shive and Frerichs, 1974); the mean of these four poles is shown by the solid square with the surrounding lightly stippled 95% confidence region. Modified from Globerman and Irving (1988) with permission from the American Geophysical Union.

The mid-Cretaceous paleomagnetic pole for North America is located in northern Alaska. This pole is illustrated in Figure 10.4a in the usual fashion of plotting the paleomagnetic pole and continent of observation on a projection of the present geographic grid. Through the geocentric axial dipole hypothesis, we know that the mean paleomagnetic pole approximates the paleoposition of the rotation axis with respect to the continent from which the paleomagnetic pole was determined. We can produce a mid-Cretaceous paleogeographic map for North America by rotating the mid-Cretaceous paleomagnetic pole (and North America, to which that pole is rigidly attached) so that the paleomagnetic pole is positioned on the axis of the geographic grid. The resulting mid-Cretaceous *paleogeographic map* for North America is shown in Figure 10.4b. This map shows the distribution of paleolatitudes across North America and the azimuthal orientation of the continent with respect to paleomeridians. Because the time-averaged geomagnetic field is symmetric about the rotation axis, absolute values of paleolongitudes are arbitrary.

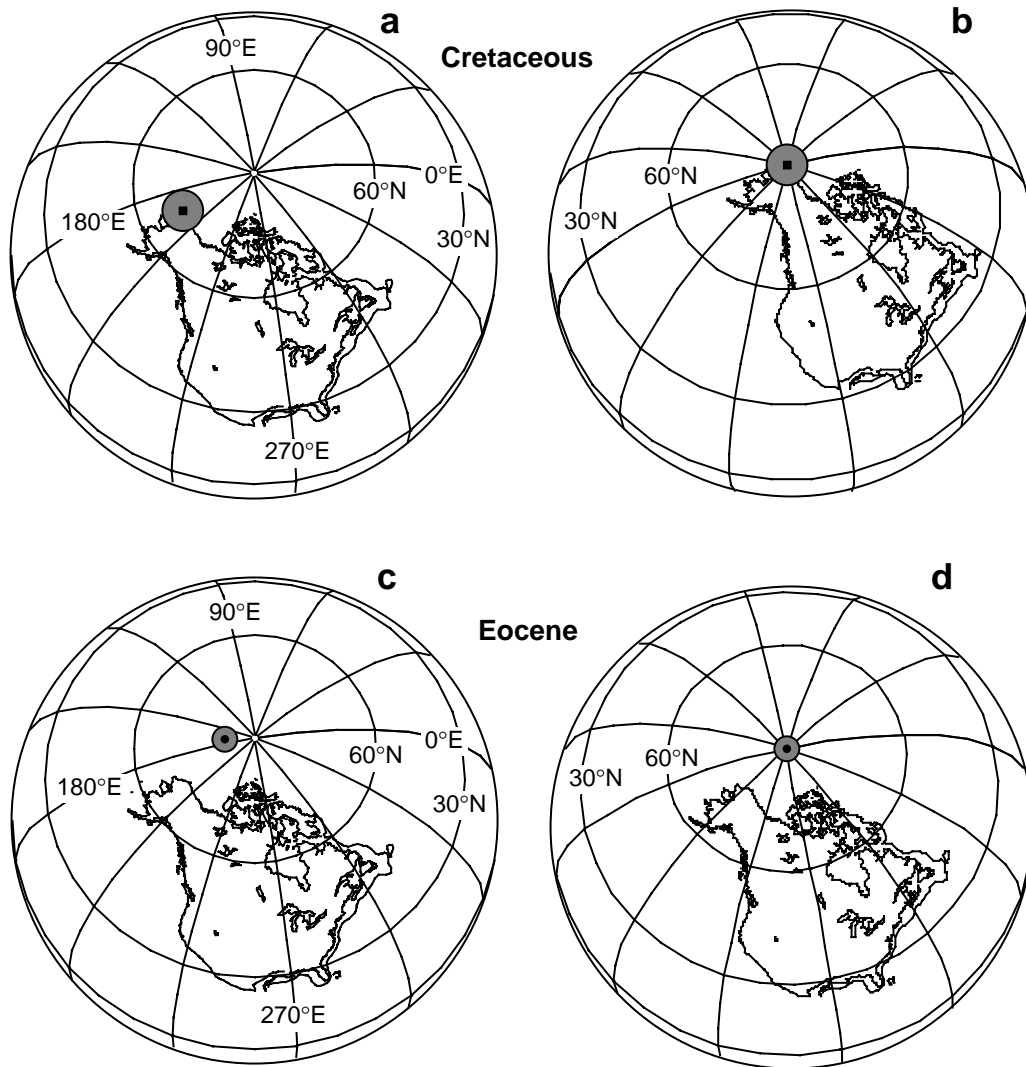


Figure 10.4 North American mid-Cretaceous and Eocene paleomagnetic poles and resulting paleogeographies. (a) Mid-Cretaceous paleomagnetic pole plotted on the present geographic grid; (b) mid-Cretaceous paleogeographic position of North America resulting from rotating the mid-Cretaceous paleomagnetic pole (and North America) so that the paleomagnetic pole coincides with the axis of the grid; (c) Eocene paleomagnetic pole of Diehl et al. (1983) plotted on the present geographic grid; (d) Eocene paleogeographic position of North America.

From the mid-Cretaceous paleogeographic map of Figure 10.4b, we see that locations in western North America were at higher northerly latitudes in the mid-Cretaceous than at present; locations in northeastern North America were at lower mid-Cretaceous latitudes than at present. And during the mid-Cretaceous, North America was clockwise rotated in comparison to its present azimuthal orientation.

The Eocene paleomagnetic pole for North America is shown in Figure 10.4c; the resulting Eocene paleogeographic map is shown in Figure 10.4d. By comparing the paleogeographic maps of Figures 10.4b and 10.4d, you can infer the motion of North America with respect to the rotation axis between mid-Cretaceous and Eocene times. The minimum motion involved counterclockwise rotation of North America about a pivot point located off the southeast coast of North America. Try to visualize how this motion accounts for the changing paleogeography. A basic feeling for continental motions indicated by paleomagnetic poles of that continent will prove immediately useful.

APPARENT POLAR WANDER PATHS

From the above presentation, we understand that sets of paleogeographic maps could be used to summarize paleomagnetic results from a particular continent. But this approach requires construction of a paleogeographic map for every geologic time increment and is cumbersome for large bodies of paleomagnetic data. A more effective approach is to develop an *apparent polar wander (APW) path* for the continent. This technique was introduced by Creer et al. (1954) and has become the standard method of presenting paleomagnetic data covering significant geologic time intervals.

Fundamentally, an APW path is a plot of the sequential positions of paleomagnetic poles from a particular continent, usually shown on the present geographic grid. We have plotted individual North American paleomagnetic poles in Chapter 7 (Figures 7.6 and 7.7) and in this chapter. To develop an APW path, a set of paleomagnetic poles of varying geologic age are presented in a single diagram. As we shall see, paleomagnetic poles for the Neogene are located near the present geographic pole, even for continents that are carried on fast-moving lithospheric plates. For older geologic times, paleomagnetic poles generally fall on a circuitous path leading away from the geographic pole.

Through the geocentric axial dipole hypothesis, an APW path represents the apparent motion of the rotation axis with respect to the continent of observation. Hence the name “apparent polar wander” path. When APW paths were first developed, it was thought that apparent polar wander was largely due to rotation of the whole Earth with respect to the rotation axis (which is fixed with respect to the stars). This whole-Earth rotation is known as *true polar wander*. We now understand that the major portion of apparent polar wander is due to lithospheric plate motions carrying continents over the Earth’s surface (e.g., continental drift).

Constructing APW paths

For continents that are currently in the northern hemisphere, it is convenient to plot the APW path as the sequence of paleomagnetic poles that track away from the north geographic pole. For southern hemisphere continents, the APW path is constructed as a sequence of paleomagnetic poles tracking away from the south geographic pole. Geomagnetic polarity reversals introduce a potential ambiguity in construction of an APW path. But this ambiguity is more apparent than real because the rate of geomagnetic reversals is rapid in comparison to plate motions.

VGPs determined from Cenozoic rocks of normal polarity will be close to the north geographic pole. But VGPs from reversed-polarity rocks will be close to the south geographic pole. For example, the North American Eocene paleomagnetic pole is located less than 10° from the present north geographic pole (Figure 10.4c). This is the position of the Eocene *north paleomagnetic pole*, and normal-polarity Eocene rocks will yield VGPs in this vicinity. Reversed-polarity Eocene rocks will yield VGPs near the south geographic pole. As discussed in Chapter 7, the usual convention (for northern hemisphere continents) is to determine the north paleomagnetic pole by averaging normal-polarity VGPs with the antipodes of reversed-polarity VGPs. For southern hemisphere continents, the convention is to determine the south paleomagnetic pole by averaging reversed-polarity VGPs with the antipodes of normal-polarity VGPs. When abundant paleomagnetic poles are available, the APW path can be unambiguously tracked going away from the present geographic pole. This is now the case for the major continents during Proterozoic and Phanerozoic times.

Methods of analyzing paleomagnetic data to construct APW paths have changed as more data have become available. When few paleomagnetic results were available, average poles were determined for each geologic time period. For example, when only four paleomagnetic poles were available from Jurassic rocks of North America, those poles were averaged to yield the Jurassic pole of the North American APW path (Irving and Park, 1972). As more paleomagnetic poles were determined, more details of APW could be determined by averaging poles within time intervals shorter than geologic time periods. A series of APW paths were produced by using versions of the *sliding-time-window* technique (Van Alstine and deBoer, 1978;

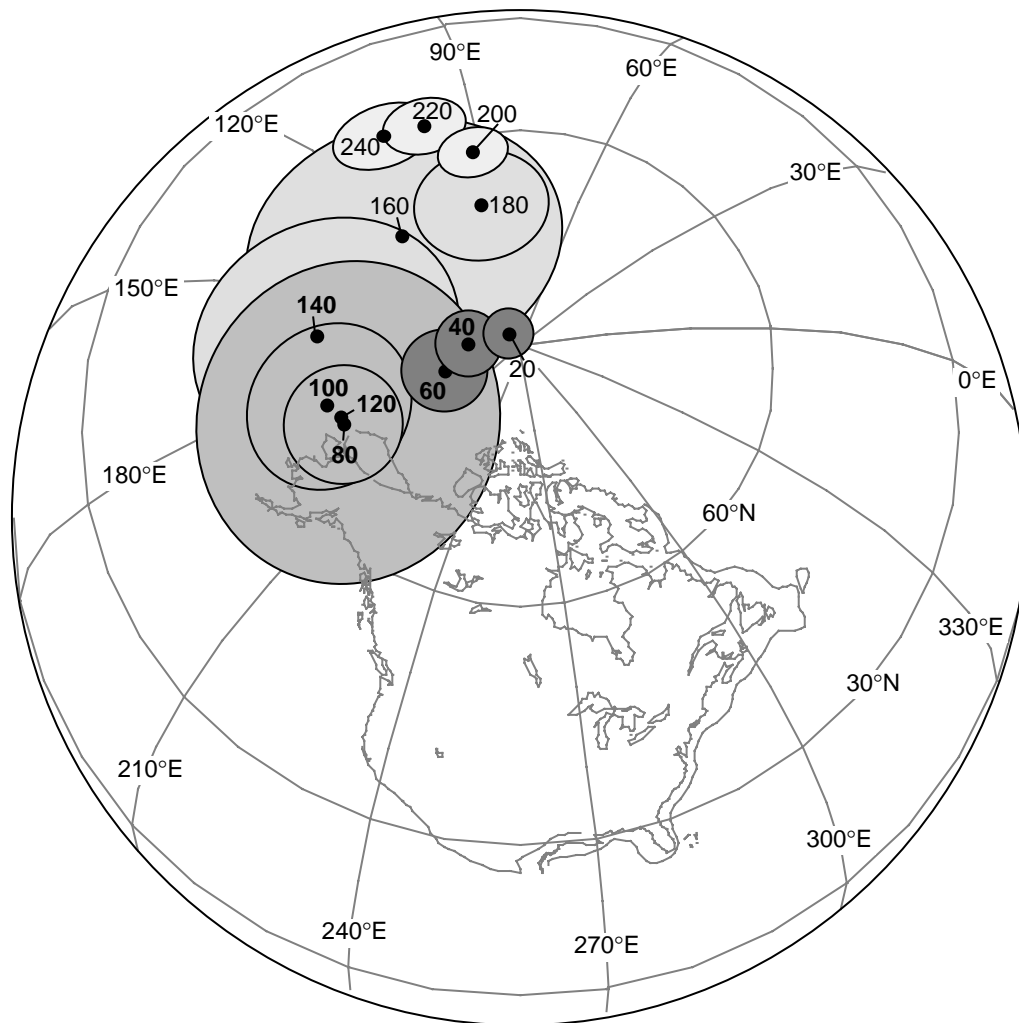


Figure 10.5 North American Mesozoic and Cenozoic apparent polar wander path of Irving and Irving (1982) using the sliding-time-window technique. Ages of mean paleomagnetic poles are labeled in Ma; the time window duration is 30 m.y.; 95% confidence limits are shown surrounding each mean pole.

Irving, 1979b; Harrison and Lindh, 1982; Irving and Irving, 1982). The Mesozoic and Cenozoic portion of the Irving and Irving (1982) North American APW path is shown in Figure 10.5.

The basic sliding-time-window technique is to (1) assign an absolute age to available paleomagnetic poles from a continent, (2) choose a duration (e.g., 30 m.y.) for the time window, and (3) average all paleomagnetic poles with ages falling within the time window centered on a particular absolute age. For example, the time window duration used to construct the APW path of Figure 10.5 was 30 m.y., so the average paleomagnetic pole for 200 Ma was determined from poles assigned absolute ages between 185 and 215 Ma. The sliding-time-window technique is effective in averaging out random noise and allowing the basic pattern of APW to be determined. But if systematic errors are present (e.g., unremoved present-field components of NRM), these errors are reinforced. Also, the sliding-time-window technique limits the detail with which the APW pattern can be determined; meaningful details of APW such as sharp corners in the APW path might not be recognizable in paths constructed by this technique.

Another approach is to construct the APW path from what are interpreted as the “most reliable” paleomagnetic poles, without applying time averaging. The paleomagnetic poles that are judged most reliable are generally those determined most recently by using more rigorous demagnetization analyses and larger

data sets than were previously available. A Mesozoic and Cenozoic APW path for North America constructed in this fashion is shown in Figure 10.6. More rapid variations in the APW path, such as the sharp corner (or *cusps*) in the Late Triassic–Early Jurassic interval, are resolved by this technique. The drawback is that the interpreted pattern of APW is strongly dependent on the accuracy of individual paleomagnetic poles. If some of these poles are inaccurate because of reasons not yet understood, the interpreted pattern of APW is obviously compromised.

Development of APW paths is a topic of active paleomagnetic research. As paleomagnetic techniques become more advanced and more rock units are investigated, older paleomagnetic poles are reevaluated and sometimes discarded. For example, Prévot and McWilliams (1989) have recently questioned the accuracy of the paleomagnetic poles determined from the Newark Trend intrusives (poles NT1 and NT2 of Figure 10.6), and the paleomagnetic pole from the Moenave Formation (pole MO of Figure 10.6) is a recent addition to the set of Mesozoic North American paleomagnetic poles.

The precision of APW paths varies from continent to continent because of differences in the quantity and quality of paleomagnetic data; the Phanerozoic APW path is much better determined for North America than for South America. For a particular continent, the precision of the APW path also depends on geologic age. Comparison of the APW paths of Figures 10.5 and 10.6 indicates that these paths are similar during the Triassic, Cretaceous, and Cenozoic but are different during the Jurassic. The primary reason for this difference is that, until recently, few North American Jurassic paleomagnetic poles were available. To complicate matters, the Jurassic appears to be a geologic time interval of rapid North American apparent polar wander. In evaluating tectonic interpretations that depend on APW paths, you must keep in mind that APW paths are well known for some geologic time intervals and poorly known for other intervals.

Paleomagnetic Euler poles

Some paleomagnetic researchers view apparent polar wander paths as a series of arcuate tracks separated by sharp corners called “cusps” (Gordon et al., 1984). The series of tracks and cusps for the Mesozoic APW path of North America is shown schematically at the top of Figure 10.6. Each track of APW is considered to result from the continent riding on a lithospheric plate that rotated about a fixed *Euler pole* for an extended interval of geologic time (say, 50 m.y.). Different tracks represent rotations about different Euler poles, and cusps represent times of reorganization of the lithospheric plate boundaries and resulting driving forces (Cox and Hart, 1986).

The basics of the *paleomagnetic Euler pole model* (PEP model) are presented in Figure 10.7, in which we consider a planet with only two lithospheric plates. Plate F is fixed, but Plate M is rotating counterclockwise about an Euler pole that is fixed with respect to the underlying mantle and the rotation axis. Transform faults separating the plates are on small circles (latitude circles) centered on the Euler pole. If a hotspot (fixed to the mantle) exists under Plate M, a seamount chain results, with seamounts on a small circle centered on the Euler pole. Paleomagnetic poles determined from young rocks on Plate M are located near the rotation axis. For older rocks, the paleomagnetic poles are located on an APW path, which also describes a small circle about the Euler pole. These paleomagnetic poles are points that were previously at the rotation axis and have subsequently been displaced by rotation of Plate M about the Euler pole.

In PEP analysis, an arcuate track of APW is used to determine the position of an Euler pole (paleomagnetic Euler pole) about which the continent rotated to produce that track of APW. The resulting paleomagnetic Euler pole is used to infer the motion and plate boundary configuration of former lithospheric plates that carried the continent. PEP analysis applied to continental APW paths is relatively new and somewhat controversial. Further refinement of APW paths is required to provide thorough evaluation of this model. The interested reader is referred to Gordon et al. (1984), May and Butler (1986), and Witte and Kent (1990) for further (pro and con) discussion of PEP analysis.

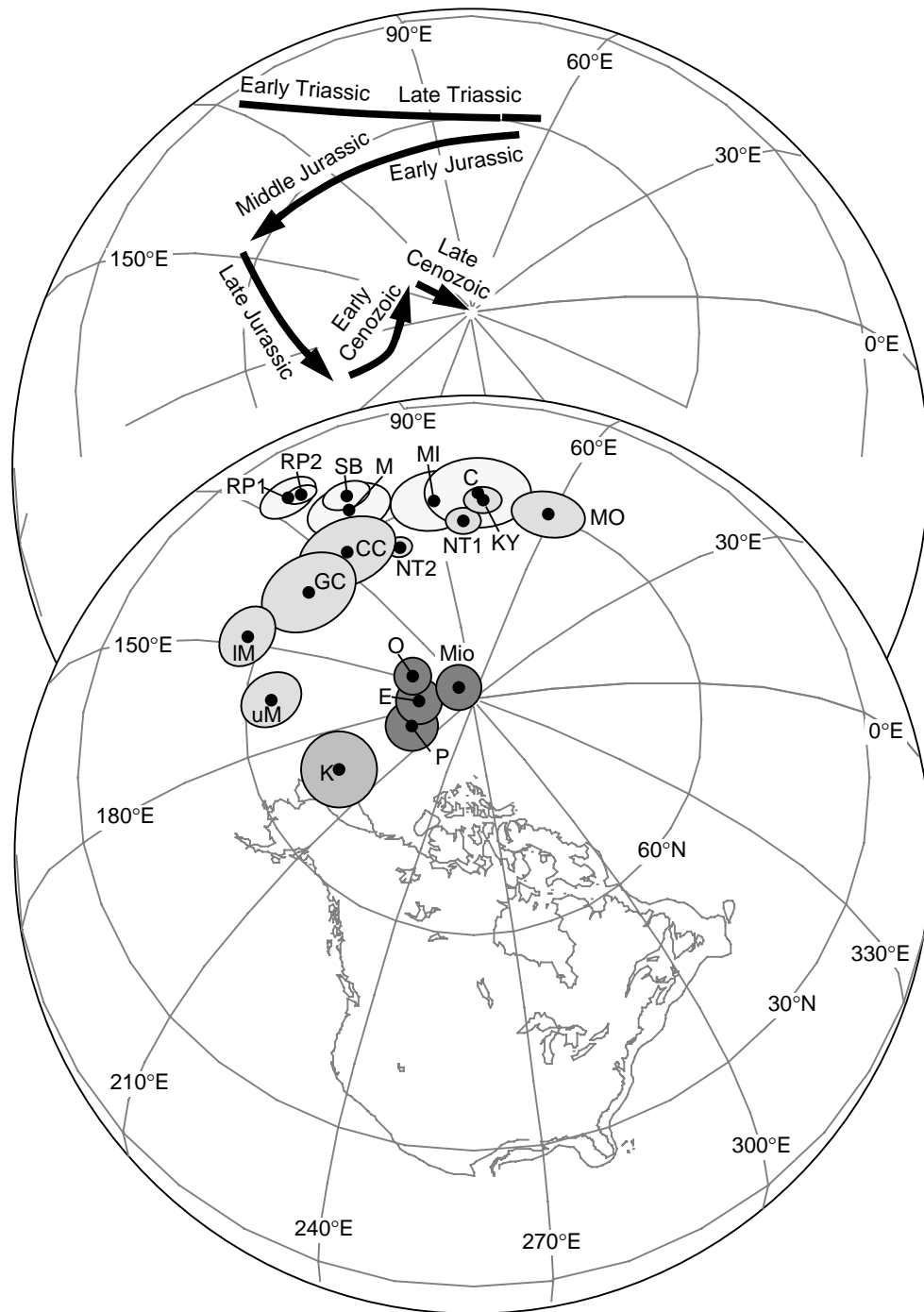


Figure 10.6 North American Mesozoic and Cenozoic apparent polar wander path based on compilation of the most reliable paleomagnetic poles. Stippled regions surrounding each pole are the 95% confidence limits; Triassic poles have the lightest stippling of confidence limits, while Jurassic, Cretaceous, and Cenozoic poles have progressively heavier stippling of confidence limits; Mio = Miocene (Hagstrum et al., 1987); O = Oligocene (Diehl et al., 1988); E = Eocene and P = Paleocene (Diehl et al., 1983); K = mid-Cretaceous (Globberman and Irving, 1988); uM and IM = upper and lower Morrison Fm, respectively; GC = Glance Conglomerate; CC = Corral Canyon; NT2 and NT1 = Newark trend group 2 and group 1 intrusives; KY = Kayenta Fm; MO = Moenave Fm; C = Chinle Fm; MI = Manicogan impact structure; M = Moenkopi Fm; SB = State Bridge Fm; RP1 and RP2 = Red Peak Fm; for references to Jurassic and Triassic poles, see Ekstrand and Butler (1989); arc and cusp interpretation of the APW pattern is shown in the upper diagram.

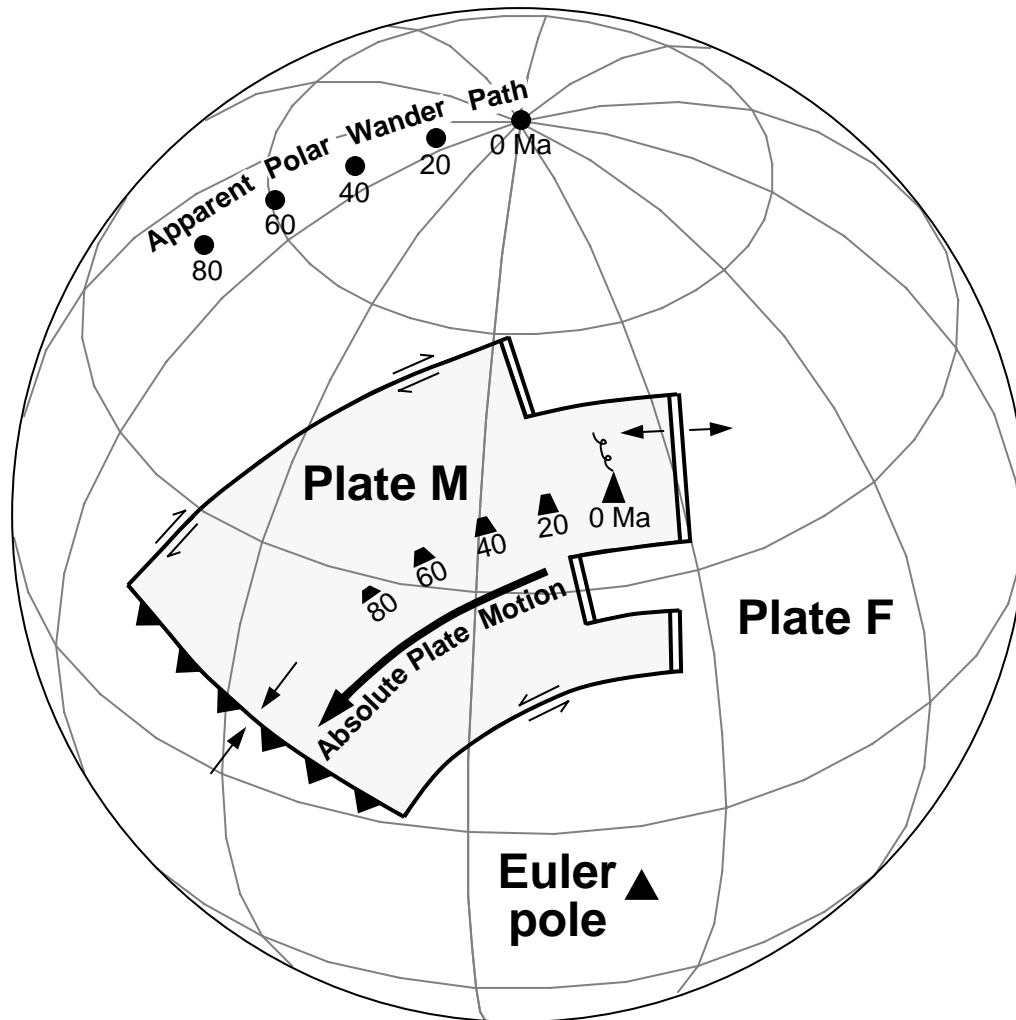


Figure 10.7 Paleomagnetic Euler pole model of apparent polar wander paths. The geographic grid is shown centered on the present rotation axis; Plate F is fixed, while Plate M is rotating about an Euler pole that is fixed in position (with respect to Plate F and the underlying mantle); the direction of absolute motion of Plate M is shown by the bold arrow; directions of relative plate motion along plate boundaries are shown by small arrows; ridge boundaries are shown by double lines; transform fault boundaries are shown by single lines; the convergent plate boundary is shown by the thrust fault symbol with teeth on the overriding plate; a hotspot under the active seamount labeled 0 Ma is fixed to the mantle and produces a seamount chain (hotspot track) with ages indicated; the recent paleomagnetic pole for Plate M is located at the rotation axis, while older paleomagnetic poles fall on the APW path with ages of poles indicated; the APW path, transform faults, and hotspot track all lie on circles of latitude (small circles) centered on the Euler pole. Modified from Gordon et al. (1984) with permission from the American Geophysical Union.

PALEOGEOGRAPHIC RECONSTRUCTIONS OF THE CONTINENTS

The basic confirmation of Wegener's continental drift theory by paleomagnetic research in the late 1950s and early 1960s is clearly a major contribution of paleomagnetism to Earth science (Irving, 1988). This early success of paleomagnetism in paleogeographic reconstruction of the continents is sometimes mistaken to indicate that fundamental Mesozoic and Paleozoic paleogeography is well established and of little current interest. Nothing could be further from the truth. Global paleogeography is an active and exciting (if sometimes mind-boggling) Earth science discipline.

Paleomagnetism is properly viewed as one of several tools in paleogeographic research. Paleoclimatology, paleobiogeography and especially geology are important contributors. In paleogeography, we are faced with the formidable challenge of mapping the Earth in time by fitting available evidence together into a coherent picture. The status of current knowledge was elegantly summarized by Scotese and McKerrow (1990) in a discussion of currently available Paleozoic paleogeographic maps. They stated that “the maps we present here are similar in their precision to the maps of Asia and the New World produced by 16th Century explorers. In the 500 years since the voyages of these early discoverers, we have mapped the Earth ‘in space.’ We are now embarking on a voyage to map the Earth ‘in time.’”

In this section, we first introduce basic principles of applying paleomagnetism to paleogeographic reconstructions. Then the example of North America–Europe reconstruction is used to illustrate a comparatively well-understood example. We then proceed to the reconstruction of Pangea with discussions of alternative reconstructions and timing of formation and dispersal of the supercontinent. To show the rapid evolution of paleogeographic research and the important implications thereof, this section is concluded with an introduction to the current debate about the Paleozoic drift history of Gondwana.

Some general principles

Matching of APW paths of continents is the fundamental paleomagnetic method of proposing and testing past relative positions. For example, any viable paleogeographic reconstruction of Africa and North America for the Permian must result in agreement of the Permian paleomagnetic poles from Africa and North America; these poles must coincide within the uncertainties involved in their determination. This principle is simply a corollary of the GAD hypothesis. A paleomagnetic pole provides the past position of the rotation axis with respect to the continent of observation. There can be only one rotation axis at any particular geologic time. So if two continents are placed in their proper relative positions for a particular geologic time, their paleomagnetic poles for that time must coincide. Furthermore, if these continents had a fixed relative position for a significant interval of geologic time, their paleomagnetic poles during that entire time interval (APW paths) must coincide.

Figure 10.8 presents a hypothetical example to illustrate how matching of APW paths can be used in paleogeographic reconstruction. As detailed in the figure caption, if two continents drift together with respect to the rotation axis prior to undergoing separate drift histories, the portions of their APW paths recording the common drift history can be matched to produce a paleogeographic reconstruction. In this hypothetical example, paleomagnetic poles of perfect accuracy are recorded by rocks of the two continents at set increments of geologic time. With these idealized conditions, any latitudinal motion of the continents during their common drift history results in APW paths that can be matched to yield a unique paleogeographic reconstruction. Such a reconstruction would be ambiguous only if the common drift of the two continents were purely longitudinal, with no resulting common path of APW.

The obvious complication in practice is that APW paths of continents are determined with at best limited precision; the Paleozoic APW paths of some continents are in fact known in only a rudimentary fashion. So from APW paths that are vastly more complex and uncertain than those of Figure 10.8, we must propose and test paleogeographic reconstructions. Inferences drawn from comparisons of continental APW paths also must be balanced against available paleobiogeographic, geologic, and paleoclimatic data.

Knowledge of APW paths in general deteriorates with age, as does the clarity of other forms of paleogeographic data. For Cretaceous and Cenozoic time, a vast array of marine geological and geophysical data are available for reconstruction of ocean basins. These data allow detailed reconstruction of many ocean basins during this time interval. But for geologic times older than Cretaceous, few pieces of former oceanic lithospheric plates are preserved, and this source of paleogeographic information is very limited. Morel and Irving (1978) thus recognized three categories of paleogeographic maps: “Those for the early Jurassic onwards which have reasonably sound basis; those for the Carboniferous, Permian, and Triassic that are less reliable; and those for earlier times with errors of uncertain magnitude.”

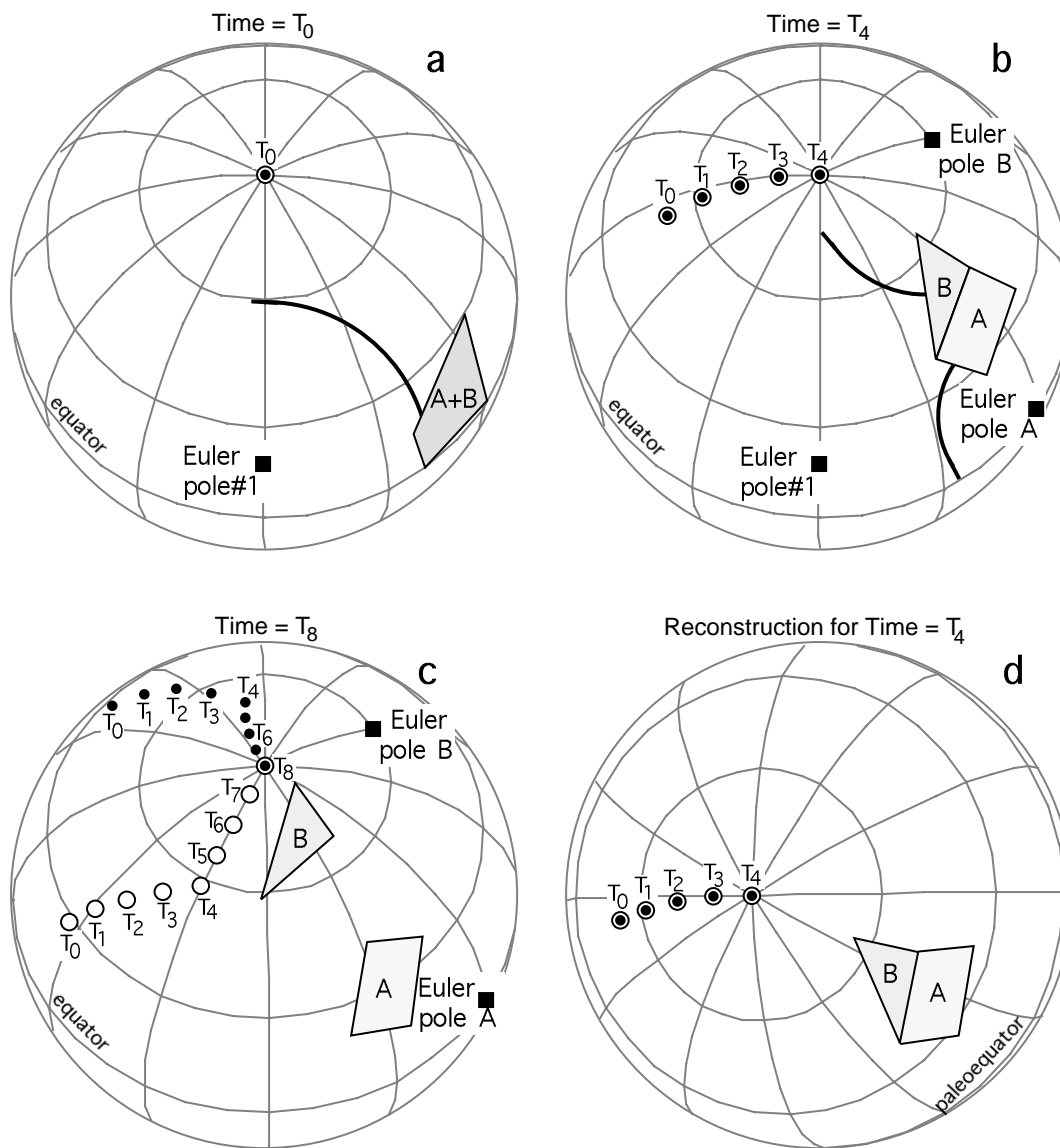


Figure 10.8 Paleogeographic reconstruction from apparent polar wander paths. (a) Continents A and B were joined together at geologic time T_0 ; the paleomagnetic pole for rocks of age T_0 on continents A and B records the position of the rotation axis; during the time interval from T_0 to T_4 , the continents rotate about Euler pole #1 at a rate of 10° per time unit (e.g., T_1 to T_0 = one time unit). (b) The APW paths for continents A and B have recorded the past positions of the rotation axis during the interval T_0 to T_4 ; these APW paths are rotated along with continents A and B during subsequent rotations; at geologic time T_4 , continents A and B rift apart; continent A begins to rotate about Euler pole A (rate = 10° /time unit), and continent B begins to rotate about Euler pole B (rate = 8° /time unit). (c) At geologic time T_8 (present), continent A has the APW path indicated by the open circles while continent B has the APW path indicated by the solid circles; the form of the APW paths during the T_0 through T_4 interval and the geometric relationships between the APW paths and the continents to which they belong are the same as at time T_4 . (d) Paleogeographic reconstruction for time T_4 ; continent A was fixed in position, and continent B was rotated until the APW paths of continents A and B overlapped during the T_0 to T_4 interval; the axis of the geographic grid was then placed on paleomagnetic pole T_4 to produce paleolatitude lines for time T_4 ; the absolute values of the longitude lines are indeterminate; note that the relative placements and paleolatitudes of continents A and B are the same in (b) and (d). Modified from Graham et al. (1964) with permission from the American Geophysical Union.

Europe–North America reconstruction

Comparison of APW paths for North America and Europe provided the initial paleomagnetic confirmation of continental drift (Irving, 1956; Runcorn, 1956); paleomagnetic poles from Paleozoic and Mesozoic rocks of Europe were systematically displaced eastward from poles determined from rocks of North America. Over the past 30 years, there has been a vast increase in the quantity and quality of paleomagnetic data from North America, Greenland, and Europe. Besides securely confirming the necessity of continental drift between these continents, the data now permit detailed tests of alternative paleogeographic reconstructions prior to Cretaceous and younger opening of the North Atlantic. Van der Voo (1990) has provided a detailed analysis of this problem, and the results are summarized in Figure 10.9.

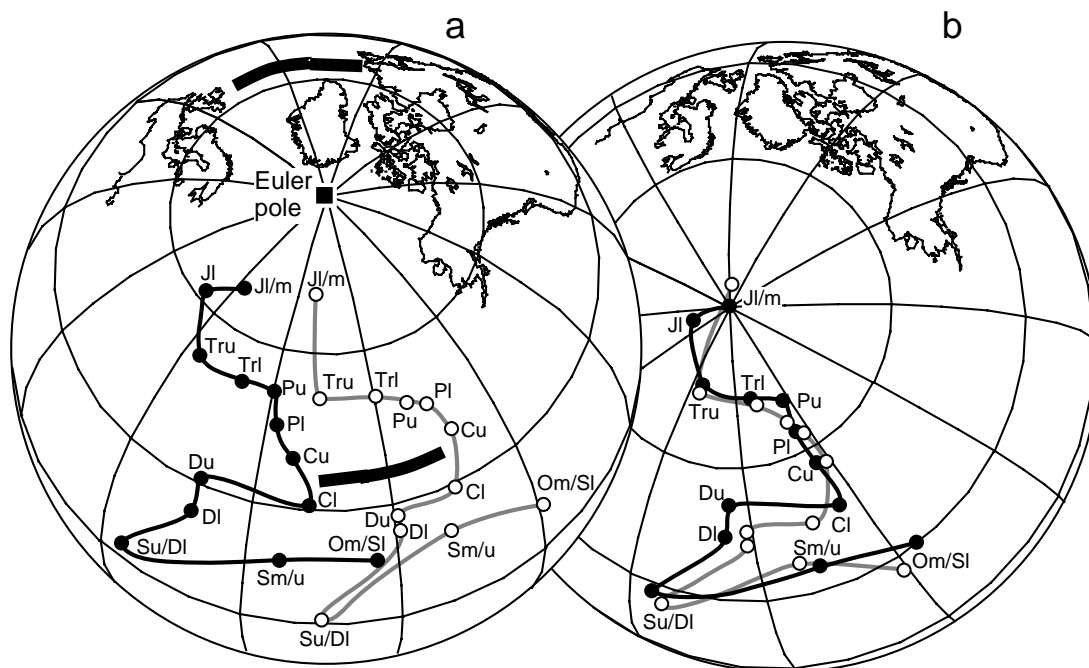


Figure 10.9 (a) Paleozoic and Mesozoic APW paths of North America and Europe. North American poles are shown by solid circles; European poles are shown by open circles; the Euler pole of Bullard et al. (1965) for reconstruction of the North Atlantic prior to Cretaceous and Cenozoic opening is shown by the solid square; the Euler pole location is 88.5°N, 27.7°E; in (b), Europe is rotated 38° clockwise about the Euler pole toward a fixed North America (upper bold arrow); during this rotation, the European APW path also rotates clockwise about the Euler pole (lower bold arrow). (b) Middle Jurassic paleogeographic reconstruction of North America and Europe; O = Ordovician; S = Silurian; D = Devonian; C = Carboniferous; P = Permian; Tr = Triassic; J = Jurassic; l = lower; m = middle; u = upper. Modified from Van der Voo (1990) with permission from the American Geophysical Union.

Van der Voo (1990) compiled and evaluated Phanerozoic paleomagnetic results from Europe and North America (including Greenland). Using paleomagnetic data from appropriate parts of Europe and avoiding poles obtained from major orogenic zones, Van der Voo compiled paleomagnetic poles that can reasonably allow construction of APW paths for the continental interiors. Only results based on testing of paleomagnetic stability through demagnetization experiments were considered. Van der Voo used a checklist of reliability criteria to assign a “quality index” to each paleomagnetic pole. This quality index considered availability and results of fold or conglomerate tests, the reversals test, and other paleomagnetic stability indicators. For Middle Ordovician through Early Jurassic, 111 North American and 110 European paleomagnetic poles satisfied reasonable quality control.

From the selected paleomagnetic poles, mean poles for time intervals of ~25-m.y. duration were determined, and APW paths for Europe and North America were drawn by connecting these mean poles (Figure 10.9a). These APW paths were then used to test Euler pole rotations that had been proposed in alternative paleogeographic reconstructions of North America and Europe. Each Euler pole rotation was applied to the European APW path, and the resulting fit with the North American APW path was examined. The rotation that minimized the misfit between the two APW paths is that proposed by Bullard et al. (1965). The resulting Middle Jurassic paleogeographic reconstruction is shown in Figure 10.9b, in which the agreement of the European and North American APW paths is indeed quite striking.

Two principles of paleomagnetic applications to paleogeography are nicely illustrated by this example:

1. Note that the motion of North America and Europe during opening of the North Atlantic was almost purely longitudinal. A purely longitudinal motion of a continent results in no APW during that geologic time interval. Nevertheless, relative longitudinal motion between two continents can be detected if those continents experienced significant latitudinal motion prior to separation.
2. The fidelity of paleogeographic reconstructions from paleomagnetism depends on the length and clarity of the APW paths that must be matched. The extended Paleozoic through Early Mesozoic drift history of *Laurasia* (North America, Greenland, Europe, and parts of Asia) resulted in long, sinuous APW paths for North America and Europe. So the common drift history of these two continents has provided APW paths that allow accurate tests of paleogeographic reconstructions. For continents with drift histories providing short common segments of APW, tests of paleogeography from paleomagnetism will be much less effective.

Pangea reconstructions

The supercontinent *Pangea* is generally considered to have existed from the Carboniferous through the Triassic. Subsequent Late Mesozoic–Cenozoic Earth history is dominated by lithospheric plate motions resulting from the dispersal of Pangea. The elements of Pangea are the northern supercontinent *Laurasia* and the southern supercontinent *Gondwana*, which are joined by closing the Atlantic Ocean (Figure 10.10).

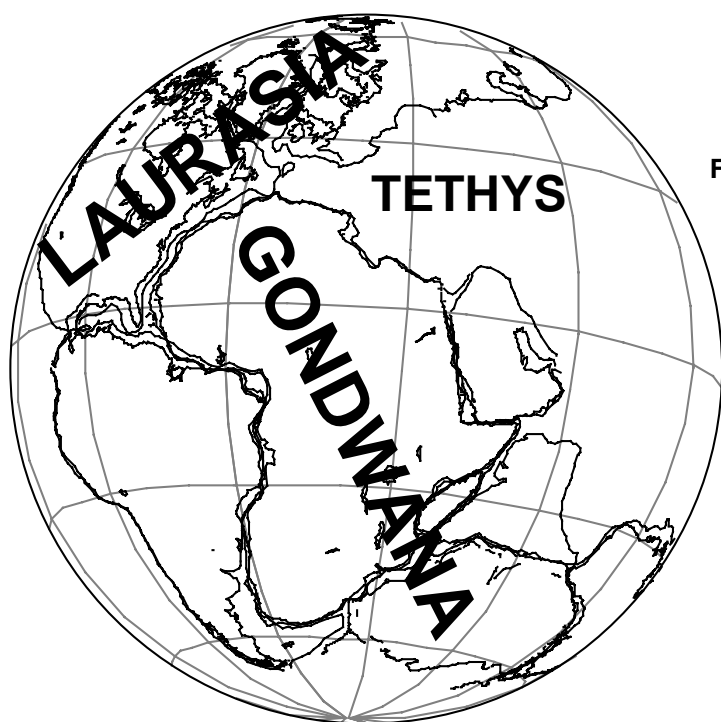


Figure 10.10 Late Triassic reconstruction of Pangea. Northern continents (North America, Greenland, Europe, and parts of present-day Asia) are grouped into the supercontinent Laurasia; southern continents (South America, Africa with Arabia and Madagascar, India, East Antarctica, and Australia) are grouped into supercontinent Gondwana; northeast Gondwana and southeast Laurasia are separated by the Tethys Ocean.

Laurasia and Gondwana are separated on their eastern sides by the intervening Tethys Ocean. The observation that this puzzle of continents could be reconstructed by closing the Atlantic and Indian Oceans was the basis of Wegener's (1924) postulation of continental drift. DuToit (1937) then developed a variety of geological arguments for the existence and configuration of Gondwana. Determining the time and space assembly of Gondwana and Laurasia to form Pangea is perhaps the major challenge of Phanerozoic paleogeography. Only the major features of the Pangean puzzle can be presented here, and even these basic features must be painted with a rather broad brush. Nevertheless, this summary will provide some appreciation for the fundamentals of Phanerozoic paleogeography and the role of paleomagnetism in that discipline.

The continents making up Gondwana were probably assembled by Middle Cambrian time (Piper, 1987). Paleomagnetic tests of alternative reconstructions of Gondwana have been discussed by Irving and Irving (1982). The reconstruction shown in Figure 10.10 is that of DuToit (1937), which was quantified by Smith and Hallam (1970). The major differences between alternative reconstructions are the relative placements of West Gondwana (South America and Africa) and East Gondwana (Antarctica, Australia, and India).

A perceived problem with DuToit's Gondwana was the resulting overlap of the Antarctic Peninsula with the Falkland Plateau (southeastern portion of the South American continental crust). To avoid this problem, several alternative reconstructions were proposed in which East Gondwana was displaced southward so that the Antarctic Peninsula was placed on the western side of southern South America. Irving and Irving (1982) showed that the paleomagnetic data from the Gondwana continents are in better agreement with the DuToit reconstruction than with the alternative fits. The "Antarctic Peninsula problem" is now understood to be more apparent than real; the present Antarctic Peninsula was constructed in part from continental fragments that were assembled after the initial breakup of Gondwana.

By comparison with the simple existence of Gondwana as a supercontinent from essentially the beginning of the Paleozoic, the assembly of Laurasia is complex and much less well understood. At the beginning of the Phanerozoic, there were four major Precambrian "cratonic nuclei": Gondwana, Laurentia, Baltica, and Siberia (Ziegler et al., 1979). Laurentia is North America and Greenland along with the northern portion of the British Isles. Baltica is the interior portion of northeastern Europe. The Siberia cratonic nucleus is the region of the present-day Central Siberian Plateau.

Baltica and Laurentia were joined together by mid-Paleozoic time. In turn, Siberia joined Baltica before the end of the Permian, thus amalgamating the major elements of Laurasia. The fundamental assembly of Pangea occurred during the Carboniferous. Beyond this simplest possible presentation of major events, detailed descriptions of continental distributions, motions, collisions, and resulting orogenies are quite complex and beyond the scope of this treatment. A major source for state-of-the-art Paleozoic paleogeography is McKerrow and Scotese (1990). Kent and May (1987) provide an incisive summary of recent paleomagnetic data; particularly noteworthy are data indicating that major crustal blocks of China were not in place adjacent to Siberia until after the Permian.

While it is generally agreed that Pangea was assembled in the Carboniferous, the exact configuration of the constituent continents is less clear (see the discussion by Kent and May, 1987). The configuration proposed by Wegener (1924) is called *Pangea A* and is generally thought to apply for the Early Jurassic, prior to breakup of the supercontinent. However, the configuration of Pangea for earlier times is a matter of debate.

Van der Voo and French (1974) proposed that Permian and Early Triassic paleomagnetic poles for Gondwana and Laurasia are best grouped by rotating Gondwana ~20° clockwise from the *Pangea A* fit to produce *Pangea A2*. (The reconstruction in Figure 10.10 is a compromise configuration intermediate between *Pangea A* and *Pangea A2*.) In the *Pangea A2* fit, northwestern South America is fit tightly into the Gulf of Mexico.

A larger (~35°) clockwise rotation of Gondwana with respect to Laurasia was proposed by Irving (1977) and Morel and Irving (1981). This *Pangea B* reconstruction placed northwestern South America adjacent to eastern North America. Morel and Irving proposed that *Pangea B* existed during the latest Carboniferous through Early Permian. Then during Late Permian and Triassic, counterclockwise rotation of Gondwana led to the *Pangea A* configuration. However, the *Pangea B* configuration has not been favored in more recent

analyses of the paleomagnetic data (Livermore et al., 1986; Ballard et al., 1986) and is considered at odds with geological and paleobiogeographic data (Hallam, 1983). The most likely scenario is an initial Carboniferous and Permian Pangea A2 configuration that evolves to the Pangea A configuration by Late Triassic (Livermore et al., 1986).

It is evident that more paleomagnetic data and other forms of paleogeographic data are required for a clearer picture of the evolution of Laurasia and Pangea. From this discussion, you should take two general observations:

1. Paleozoic and Mesozoic paleogeography is a vital and active earth science discipline that depends heavily on paleomagnetic observations. Current research will no doubt lead to exciting new realizations about the assembly and evolution of the continents.
2. While many details are different from those presented by the early champions of continental drift, Wegener and DuToit had extraordinary insight into fundamental paleogeography.

Paleozoic drift of Gondwana

The existence of Gondwana as a supercontinent from the Early Paleozoic through the Early Mesozoic is substantiated by a variety of geologic, paleontologic, and paleomagnetic data. But the drift history, latitudinal positions, and possible collisions of Gondwana with the northern continents are matters of widely differing interpretations and much interest. We conclude our examination of global paleogeography with an introduction to the current debate concerning the mid-Paleozoic drift history of Gondwana.

Figure 10.11a shows two alternative interpretations of the APW path for Gondwana from the Ordovician to the Carboniferous. An Ordovician paleomagnetic pole position in the present-day Sahara Desert region of northwest Africa has been known for some time (McElhinny, 1973). The implied location of northern Africa at the south pole in the Ordovician is confirmed by Late Ordovician glaciation of northern Africa (Caputo and Crowell, 1985). Carboniferous and Permian paleomagnetic poles for Gondwana are located in or near southern Africa, consistent with widespread Late Paleozoic glaciation of southern Gondwana. A major difficulty in constructing a Paleozoic APW path for Gondwana occurs for the mid-Paleozoic. Where is the Silurian paleomagnetic pole for Gondwana?

Until recently, the only Silurian paleomagnetic poles from the Gondwana continents were determined from rocks of the Tasman foldbelt in southeast Australia. These poles fall near southwest South America. But McElhinny and Embleton (1974) suggested that southeast Australia did not accrete to Australia until the Late Paleozoic. So it is unclear whether mid-Paleozoic poles from southeast Australia should be used to construct the Gondwana APW path. This ambiguity led to discussions of alternative mid-Paleozoic Gondwana APW paths (Schmidt and Morris, 1977; Morel and Irving, 1978). The conservative view was to interpolate between the Ordovician pole in northern Africa and the Carboniferous pole in southern Africa, thus producing an APW path that simply tracks across Africa during the Paleozoic. This option is the dashed line of Figure 10.11a. The alternative view was to argue that the Silurian poles from southeast Australia do pertain to Gondwana. In this option, there is a large loop of APW from northwest Africa in the Ordovician to southwest South America in the Silurian and then back to Africa. This path is shown by the solid line in Figure 10.11a.

Recently, Hargraves et al. (1987) have obtained paleomagnetic data from Silurian intrusive rocks of cratonic Africa (Niger). The resulting paleomagnetic pole is located in southern South America. Hurley and Van der Voo (1987) determined a Late Devonian paleomagnetic pole from rocks in cratonic western Australia. This Late Devonian pole falls in central Africa. These two mid-Paleozoic poles lend considerable support to the interpretation that the Paleozoic APW path for Gondwana includes a large mid-Paleozoic loop. This APW path for Gondwana must still be considered controversial because it is based on only a few paleomagnetic studies. However the possible implications are major.

Van der Voo (1988) has explored the paleogeographic and tectonic implications of the mid-Paleozoic loop in the Gondwana APW path. The major features are shown in the reconstructions of Figure 10.11.

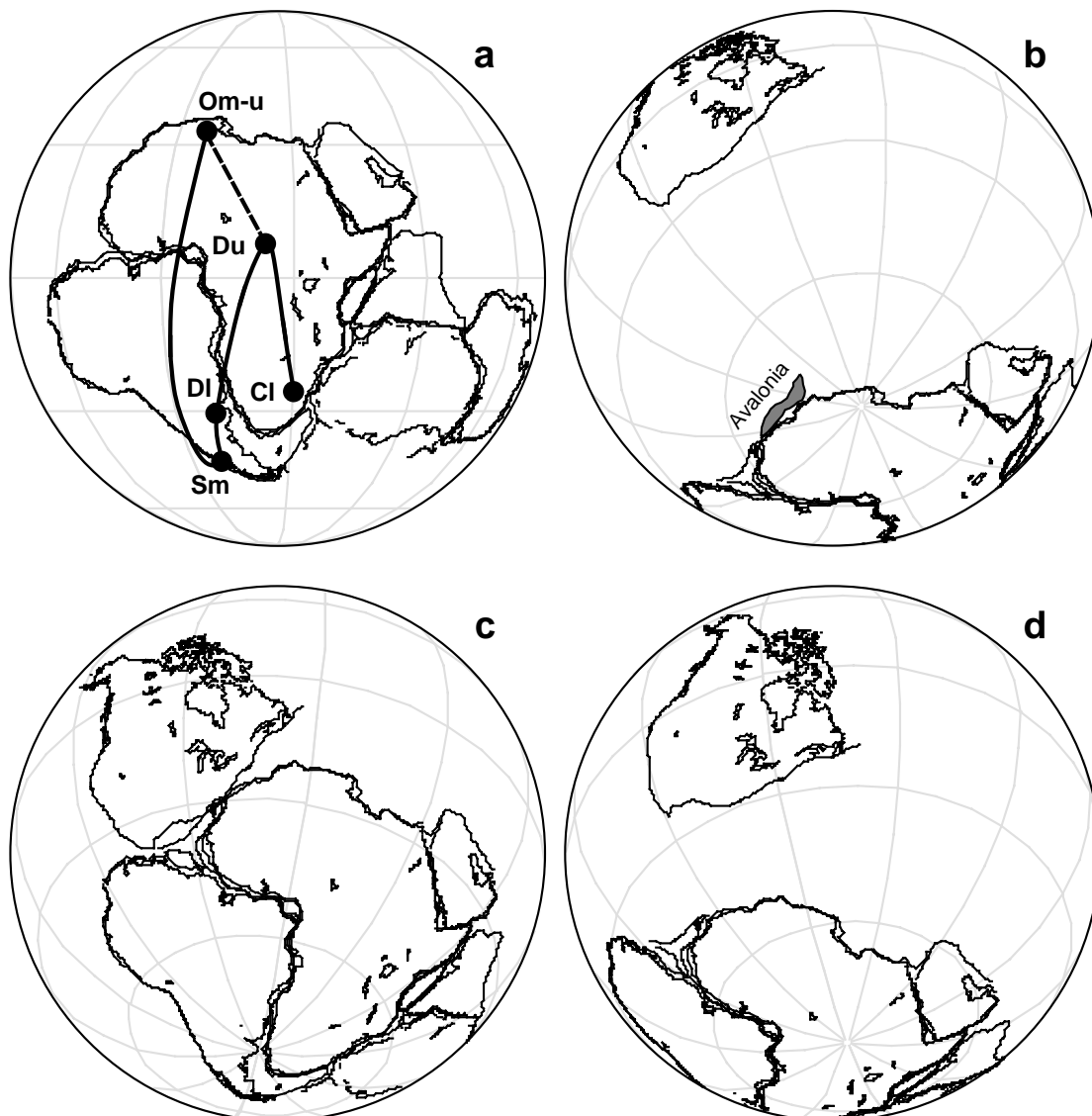


Figure 10.11 Paleozoic APW paths and paleogeographies for Gondwana. (a) The APW path shown by the bold curve contains a loop in the Silurian through Early Devonian; “traditional” interpolation of the Silurian through Early Devonian portion of the APW path is shown by the dashed line; the paleomagnetic south poles are plotted on the present geographic grid fixed to Africa; labels on paleomagnetic poles are as in Figure 10.9. (b) Ordovician paleogeography of Gondwana and North America; the Avalon terrane is adjacent to northwest Africa; the paleogeographic grid is centered on the Gondwana paleomagnetic pole. (c) Early Devonian paleogeography of Gondwana and North America; northern Africa has moved rapidly north into subtropical to equatorial paleolatitudes during latest Ordovician–Early Silurian; the Africa–North America collision causes the Acadian orogeny and transfers the Avalon terrane to North America; the paleogeographic grid is centered on the Early Devonian paleomagnetic pole for Gondwana. (d) Late Devonian paleogeography of Gondwana and North America; during the Devonian, a medium-width ocean opens between North America and northern Gondwana; the paleogeographic grid is centered on the Late Devonian paleomagnetic pole for Gondwana. Modified from Van der Voo (1988) with permission from the Geological Society of America.

Throughout the Early Paleozoic, North America is in equatorial paleolatitudes. In the Ordovician, northwest Africa is situated at the south pole with Gondwana and North America separated by a wide ocean. Several terranes that later become parts of the northern continents are thought to have been adjacent to northern Gondwana during the Early Paleozoic. These terranes include the Avalon terrane (now part of the Appalachians) and the Armorica terrane (portions of southern Europe). The position of the Avalon terrane adjacent to northwest Africa in the Ordovician is shown schematically in Figure 10.11b.

The loop in the Paleozoic APW path of Gondwana implies that Gondwana moved rapidly northward during latest Ordovician–Early Silurian time. The resulting Early Devonian paleogeography of Gondwana and North America is shown in Figure 10.11c. This northward motion of Gondwana allows the possibility that northwest Africa was adjacent to eastern North America in the Early Devonian. Thus the Africa–North America collision might have caused the Caledonian–Acadian orogeny and transferred the Avalon and Armorica terranes to North America. During the Devonian, a medium-width ocean opened between North America and northern Gondwana with the resulting Late Devonian paleogeography shown in Figure 10.11d. This new ocean closed during the Carboniferous with the collision of Gondwana and Laurasia, producing the Hercynian–Alleghanian orogenies and forming Pangea.

Scotese and Barrett (1990) have argued against portions of the motion history of Gondwana implied by the mid-Paleozoic loop in the APW path. They agree that the Gondwana paleomagnetic pole moves to southern South America in the Silurian, but they do not accept a central Africa position for the Late Devonian pole. Instead, they favor a progression of the Gondwana APW path from southern South America in the Silurian to southern Africa in the Early Carboniferous. The Scotese and Barrett (1990) interpretation accepts the rapid northward motion of Gondwana during the latest Ordovician–Early Silurian but does not accept the subsequent southward Devonian motion outlined above. The implications of these alternative drift histories for Gondwana are of great importance to Paleozoic paleogeography and tectonics. It will be interesting to see what new data, arguments, and interpretations are offered in the coming years.

REFERENCES

- M. Ballard, R. Van der Voo, and I. W. Haelbich, Remagnetizations in Late Permian and Early Triassic rocks from southern Africa and their implications for Pangea reconstructions, *Earth Planet. Sci. Lett.*, v. 79, 412–418, 1986.
- J. C. Briden, Paleoclimatic evidence of a geocentric axial dipole field, In: *The History of the Earth's Crust*, ed. R. A. Phinney, Princeton University Press, Princeton, N. J., pp. 178–194, 1968.
- J. C. Briden, Palaeolatitude distribution of precipitated sediments, In: *Palaeogeophysics*, ed. S. K. Runcorn, Academic Press, New York, pp. 437–444, 1970.
- J. C. Briden and E. Irving, Palaeoclimatic spectra of sedimentary palaeoclimatic indicators, In: *Problems in Palaeoclimatology*, ed. A. E. M. Nairn, Interscience, New York, pp. 199–250, 1964.
- E. C. Bullard, J. E. Everett, and A. G. Smith, A symposium on continental drift. IV. The fit of the continents around the Atlantic, *Phil. Trans. Roy. Soc. London*, v. A258, 41–51, 1965.
- M. V. Caputo and J. C. Crowell, Migration of glacial centers across Gondwana during the Phanerozoic Era, *Geol. Soc. Amer. Bull.*, v. 96, 1020–1036, 1985.
- D. E. Champion, Holocene geomagnetic secular variation in the western United States: Implications for the global geomagnetic field, *U.S. Geol. Surv. Open File Rep. 80-824*, p. 314, 1980.
- D. H. Coupland and R. Van der Voo, Long-term nondipole components in the geomagnetic field during the last 130 m.y., *J. Geophys. Res.*, v. 85, 3529–3548, 1980.
- A. Cox, Frequency of geomagnetic reversals and the symmetry of the nondipole field, *Rev. Geophys.*, v. 13, 35–51, 1975.
- A. V. Cox and R. B. Hart, *Plate Tectonics: How It Works*, Blackwell Scientific Publications, Palo Alto, Calif., 392 pp., 1986.
- K. M. Creer, E. Irving, and S. K. Runcorn, The direction of the geomagnetic field in remote epochs in Great Britain, *J. Geomagn. Geoelectr.*, v. 6, 163–168, 1954.

- J. F. Diehl, M. E. Beck, Jr., S. Beske-Diehl, D. Jacobson, and B. C. Hearn, Paleomagnetism of the Late Cretaceous–Early Tertiary north-central Montana alkalic province, *J. Geophys. Res.*, v. 88, 10,593–10,609, 1983.
- J. Diehl, K. M. McClannahan, and T. J. Bornhorst, Paleomagnetic results from the Mogollon–Datil volcanic field, southwestern New Mexico, and a refined mid-Tertiary reference pole for North America, *J. Geophys. Res.*, v. 93, 4869–4879, 1988.
- G. E. Drewry, A. T. S. Ramsay, and A. G. Smith, Climatically controlled sediments, the geomagnetic field, and trade wind belts in Phanerozoic time, *J. Geol.*, v. 82, 531–553, 1974.
- A. L. DuToit, *Our Wandering Continents*, Oliver and Boyd, Edinburgh, 336 pp., 1937.
- E. J. Ekstrand and R. F. Butler, Paleomagnetism of the Moenave Formation: Implications for the Mesozoic North American apparent polar wander path, *Geology*, v. 17, 245–248, 1989.
- M. E. Evans, Test of the dipolar nature of the geomagnetic field throughout Phanerozoic time, *Nature*, v. 262, 676, 1976.
- J. Foster and D. T. A. Symons, Defining a paleomagnetic polarity pattern in the Montereian intrusives, *Can. J. Earth Sci.*, v. 16, 1716–1725, 1979.
- B. R. Globerman and E. Irving, Mid-Cretaceous paleomagnetic reference field for North America: Restudy of 100 Ma intrusive rocks from Arkansas, *J. Geophys. Res.*, v. 93, 11,721–11,733, 1988.
- R. G. Gordon, A. Cox, and S. O'Hare, Paleomagnetic Euler poles and the apparent polar wander and absolute motion of North America since the Carboniferous, *Tectonics*, v. 3, 499–537, 1984.
- K. W. T. Graham, C. E. Helsley, and A. L. Hales, Determination of the relative positions of continents from paleomagnetic data, *J. Geophys. Res.*, v. 69, 3895–3900, 1964.
- J. T. Hagstrum, M. G. Sawlan, B. P. Hausback, J. G. Smith, and C. S. Grommé, Miocene paleomagnetism and tectonic setting of the Baja California Peninsula, Mexico, *J. Geophys. Res.*, v. 92, 2627–2639, 1987.
- A. Hallam, Supposed Permo–Triassic megashear between Laurasia and Gondwana, *Nature*, v. 301, 499–502, 1983.
- R. B. Hargraves, E. M. Dawson, and F. B. Van Houten, Palaeomagnetism and age of mid-Palaeozoic ring complexes in Niger, West Africa, and tectonic implications, *Geophys. J. Roy. Astron. Soc.*, v. 90, 705–729, 1987.
- C. G. A. Harrison and T. Lindh, A polar wandering curve for North America during the Mesozoic and Cenozoic, *J. Geophys. Res.*, v. 87, 1903–1920, 1982.
- N. F. Hurley and R. Van der Voo, Paleomagnetism of Upper Devonian reefal limestones, Canning Basin, western Australia, *Geol. Soc. Am. Bull.*, v. 98, 138–146, 1987.
- E. Irving, Palaeomagnetic and palaeoclimatological aspects of polar wandering, *Geofis. Pura Appl.*, v. 33, 23–41, 1956.
- E. Irving, *Paleomagnetism and Its Applications to Geological and Geophysical Problems*, John Wiley, New York, 399 pp., 1964.
- E. Irving, Drift of the major continental blocks since the Devonian, *Nature*, v. 270, 304–309, 1977.
- E. Irving, Pole positions and continental drift since the Devonian, In: *The Earth: Its Origin, Structure and Evolution*, ed. M. W. McElhinny, Academic Press, London, pp. 567–593, 1979a.
- E. Irving, Paleopoles and paleolatitudes of North America and speculations about displaced terrains, *Can. J. Earth Sci.*, v. 16, 669–694, 1979b.
- E. Irving, The paleomagnetic confirmation of continental drift, *Eos Trans. AGU*, v. 69, 994–1014, 1988.
- E. Irving and G. A. Irving, Apparent polar wander paths Carboniferous through Cenozoic and the assembly of Gondwana, *Geophys. Surv.*, v. 5, 141–188, 1982.
- E. Irving and J. K. Park, Hairpins and superintervals, *Can. J. Earth Sci.*, v. 9, 1318–1324, 1972.
- D. V. Kent and S. R. May, Polar wander and paleomagnetic reference pole controversies, *Rev. Geophys.*, v. 25, 961–970, 1987.
- P. L. Lapointe, Paleomagnetism of the Notre Dame lamprophyre dikes, Newfoundland, and the opening of the North Atlantic Ocean, *Can. J. Earth Sci.*, v. 16, 1823–1831, 1979.
- R. A. Livermore, F. J. Vine, and A. G. Smith, Plate motions and the geomagnetic field. I. Quaternary and late Tertiary, *Geophys. J. Roy. Astron. Soc.*, v. 73, 153–171, 1983.
- R. A. Livermore, F. J. Vine, and A. G. Smith, Plate motions and the geomagnetic field. II. Jurassic to Tertiary, *Geophys. J. Roy. Astron. Soc.*, v. 79, 939–962, 1984.

- R. A. Livermore, A. G. Smith, and F. J. Vine, Late Paleozoic to early Mesozoic evolution of Pangea, *Nature*, v. 322, 162–165, 1986.
- S. R. May and R. F. Butler, North American Jurassic Apparent polar wander: Implications for plate motions, paleogeography and Cordilleran tectonics, *J. Geophys. Res.*, v. 91, 11,519–11,544, 1986.
- M. W. McElhinny, *Palaeomagnetism and Plate Tectonics*, Cambridge University Press, London, 358 pp., 1973.
- M. W. McElhinny and B. J. J. Embleton, Australian palaeomagnetism and the Phanerozoic plate tectonics of eastern Gondwana, *Tectonophys.*, v. 22, 1–29, 1974.
- M. W. McElhinny and A. Brock, A new palaeomagnetic result from east Africa and estimates of the Mesozoic palaeoradius, *Earth Planet. Sci. Lett.*, v. 27, 321–328, 1975.
- M. W. McElhinny and R. T. Merrill, Geomagnetic secular variation over the past 5 m.y., *Rev. Geophys.*, v. 13, 687–708, 1975.
- W. S. McKerrow and C. R. Scotese, eds., *Palaeozoic Palaeogeography and Biogeography*, Geol. Soc. London Mem. No. 12, 1990.
- R. T. Merrill and M. W. McElhinny, Anomalies in the time-averaged paleomagnetic field and their implications for the lower mantle, *Rev. Geophys.*, v. 15, 309–323, 1977.
- R. T. Merrill and M. W. McElhinny, *The Earth's Magnetic Field: Its History, Origin and Planetary Perspective*, Academic Press, San Diego, 401 pp., 1983.
- P. Morel and E. Irving, Tentative paleocontinental maps for the early Phanerozoic and Proterozoic, *J. Geol.*, v. 86, 535–561, 1978.
- P. Morel and E. Irving, Paleomagnetism and the evolution of Pangea, *J. Geophys Res.*, v. 86, 1858–1872, 1981.
- N. D. Opdyke and K. W. Henry, A test of the dipole hypothesis, *Earth Planet. Sci. Lett.*, v. 6, 139–151, 1969.
- J. D. A. Piper, *Palaeomagnetism and the Continental Crust*, John Wiley, New York, 434 pp., 1987.
- J. N. Prasad, Paleomagnetism of the Mesozoic lamprophyric dikes in north-central Newfoundland, M.S. thesis, 119 pp., Mem. Univ. of Newfoundland, St. John's, 1981.
- M. Prévot and M. McWilliams, Paleomagnetic correlation of Newark Supergroup volcanics, *Geology*, v. 17, 1007–1010, 1989.
- S. K. Runcorn, Paleomagnetic comparisons between Europe and North America, *Proc. Geol. Assoc. Canada*, v. 8, 77–85, 1956.
- P. W. Schmidt and W. A. Morris, An alternative view of the Gondwana Paleozoic apparent polar wander path, *Can. J. Earth Sci.*, v. 14, 2674–2678, 1977.
- D. A. Schneider and D. V. Kent, The time-averaged paleomagnetic field, *Rev. Geophys.*, v. 28, 71–96, 1990.
- C. R. Scotese and S. F. Barrett, Gondwana's movement over the south pole during the Palaeozoic: Evidence from lithological indicators of climate, In: *Palaeozoic Palaeogeography and Biogeography*, ed. W. S. McKerrow and C. R. Scotese, Geol. Soc. London Mem. No. 12, pp. 75–85, 1990.
- C. R. Scotese and W. S. McKerrow, Revised world maps and introduction, In: *Palaeozoic Palaeogeography and Biogeography*, ed. W. S. McKerrow and C. R. Scotese, Geol. Soc. London Mem. No. 12, pp. 1–21, 1990.
- P. N. Shive and W. E. Frerichs, Paleomagnetism of the Niobrara Formation in Wyoming, Colorado, and Kansas, *J. Geophys Res.*, v. 79, 3001–3007, 1974.
- A. G. Smith and A. Hallam, The fit of the southern continents, *Nature*, v. 225, 139–149, 1970.
- D. R. Van Alstine and J. deBoer, A new technique for constructing apparent polar wander paths and revised Phanerozoic path for North America, *Geology*, v. 6, 137–139, 1978.
- R. Van der Voo, Paleozoic paleogeography of North America, Gondwana, and intervening displaced terranes: Comparisons of paleomagnetism with paleoclimatology and biogeographical patterns, *Geol. Soc. Am. Bull.*, v. 100, 311–324, 1988.
- R. Van der Voo, Phanerozoic paleomagnetic poles from Europe and North America and comparisons with continental reconstructions, *Rev. Geophys.*, v. 28, 167–206, 1990.
- R. Van der Voo and R. B. French, Apparent polar wandering for the Atlantic-bordering continents: Late Carboniferous to Eocene, *Earth Sci. Rev.*, v. 10, 99–119, 1974.
- A. Wegener, *The Origin of Continents and Oceans* (English translation by J. G. A. Skerl), Methuen, London, 212 pp., 1924.
- R. L. Wilson, Permanent aspects of the Earth's non-dipole magnetic field over upper Tertiary times, *Geophys. J. Roy. Astron. Soc.*, v. 19, 417–437, 1970.

- R. L. Wilson, Dipole offset—The time-average palaeomagnetic field over the past 25 million years, *Geophys. J. Roy. Astron. Soc.*, v. 22, 491–504, 1971.
- R. L. Wilson and J. M. Ade-Hall, Paleomagnetic indications of a permanent aspect of the non-dipole field, In: *Paleogeophysics*, ed. S. K. Runcorn, Academic Press, San Diego, pp. 307–312, 1970.
- W. K. Witte and D. V. Kent, The paleomagnetism of red beds and basalts of the Hettangian extrusive zone, Newark Basin, New Jersey, *J. Geophys Res.*, v. 95, 17,533–17,545, 1990.
- A. M. Ziegler, C. R. Scotese, W. S. McKerrow, M. E. Johnson, and R. K. Bambach, Paleozoic paleogeography, *Ann. Rev. Earth Planet. Sci.*, v. 7, 473–502, 1979.

APPLICATIONS TO REGIONAL TECTONICS

Plate tectonics has taught us to view the Earth's lithosphere as a dynamic system of spreading oceanic ridges, transform faults, and subduction zones. Continental drift is now accepted as a corollary of plate tectonics, and the complexity of orogenic belts is leading to an appreciation of the mobility of continental crust. The margins of continents are often tectonically active, especially above subduction zones. Portions of continental crust can rift from a continent and move, as Baja California is doing today. Continental fore-arc regions may also be displaced during intervals of oblique subduction. Paleomagnetism has played a central role in this developing view of continental geology.

Lithospheric plates carrying continents have experienced intervals of rapid motion, and oceanic plateaus, seamounts, and island arcs have been *accreted* (become attached) to continental margins. Although details are hotly disputed, many geologists now view much of the western Cordillera of North America as a collage of *tectonostratigraphic terranes* (Coney et al., 1980). These terranes are generally fault-bounded regions (dimensions up to hundreds of kilometers) with geologic histories that are distinct from those of neighboring regions. Some terranes are composed of rocks that originated in oceanic basins far from their present locations; others have experienced little or no motion with respect to the continental interior. Paleomagnetism is one of the primary methods of deciphering motion histories of terranes.

This chapter is devoted to applications of paleomagnetism to regional tectonics. We start by introducing general principles and techniques for applying paleomagnetism to regional tectonic problems. Case examples of specific applications are then developed to illustrate how paleomagnetism has been used to decipher continental margin tectonics and motion histories of accreted terranes. The examples are taken from paleomagnetic studies of the western margin of North America, but the principles are generally applicable. Through study of these examples, you will gain insight into the effectiveness and limitations of paleomagnetism in regional tectonics.

SOME GENERAL PRINCIPLES

Throughout this discussion, the term "crustal block" or simply "block" is used to denote a subcontinental-scale region that may have moved with respect to the continental interior. A crustal block may be composed of rocks of continental or oceanic origin. A crustal block may or may not also comprise a tectonostratigraphic terrane that has a specific geologic definition.

The fundamentals of how paleomagnetism can be used to detect motions of crustal blocks are illustrated in Figure 11.1. With paleomagnetism, we can detect only motions with respect to a paleomagnetic pole; purely longitudinal motions cannot be detected because of the geocentric axial dipole nature of the geomagnetic field. In Figure 11.1a, a cross section of the Earth is shown in the plane containing a paleomagnetic pole at location *PP*. The arrows at the Earth's surface show the inclination of the dipolar magnetic field with pole at *PP*; these are the magnetic field *expected inclinations*. If a crustal block is magnetized at intermediate latitude and then moved (angular distance *p*) to high latitude, the *observed inclination* of paleomagnetism in this crustal block will be less than the expected inclination at its new location. So latitudinal motion toward a paleomagnetic pole produces *flattening of inclination* shown by the angle *F* in Figure 11.1a.

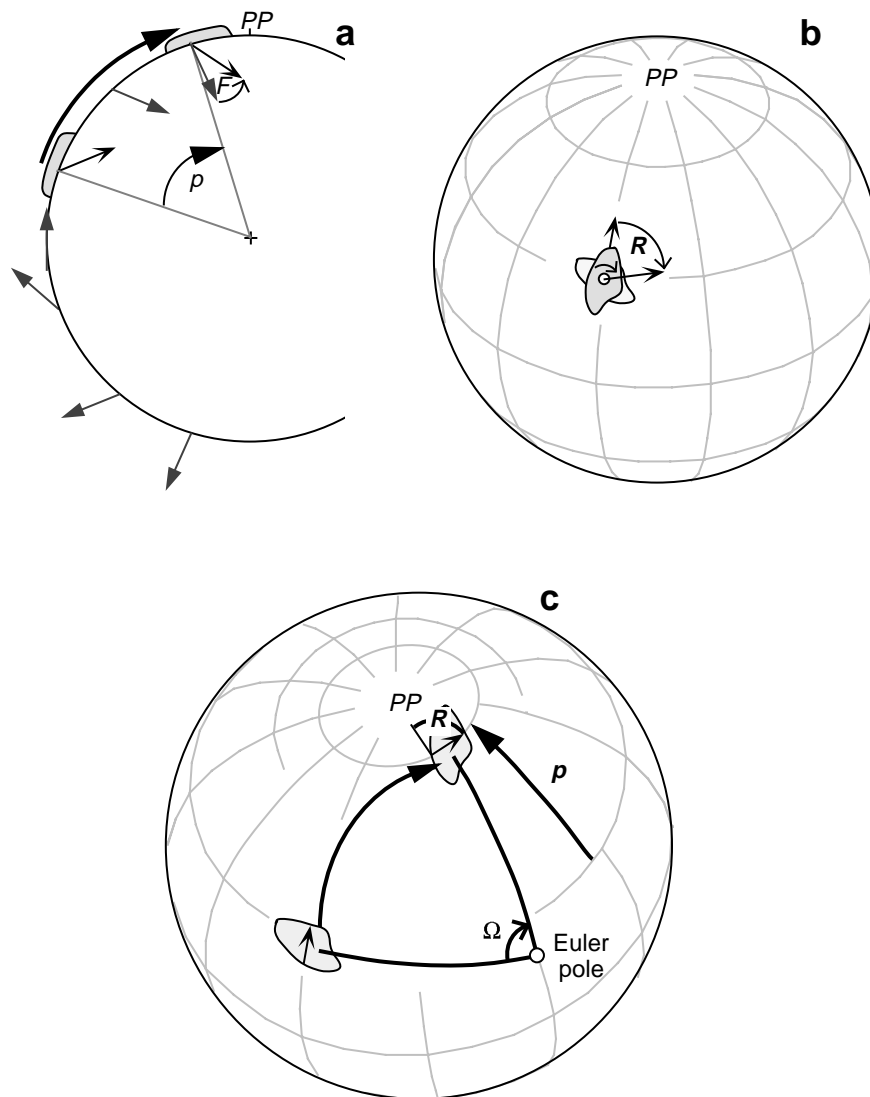


Figure 11.1 Discordant paleomagnetic directions resulting from tectonic movements. *PP* = paleomagnetic pole. **(a)** Meridional cross section of the Earth showing the directions of a dipolar magnetic field with magnetic pole at *PP*; the expected magnetic field directions are shown by the stippled arrows; a terrane magnetized at low paleolatitude acquires a magnetization in the direction of the black arrow; transport of the terrane toward the paleomagnetic pole by the angle p results in its magnetization being shallower than the expected direction by the angle F (flattening); note that the angle of flattening F does not equal the angle of poleward transport p . **(b)** Rotation of the paleomagnetic declination by tectonic rotation about a vertical axis internal to the crustal block. The original orientation of the block is shown by the partially hidden outline; the present orientation is shown by the outline filled with the heavier stippling; the crustal block was magnetized along the paleomeridian in the direction of the partially hidden arrow; vertical-axis rotation has caused the paleomagnetic declination to rotate clockwise by the angle R to the direction indicated by the arrow drawn from the center of the block; the projection (for this and all global projections to follow) is orthographic, with the latitude and longitude grid in 30° increments. **(c)** Rotation of a crustal block about an Euler pole external to the block. Rotation by the angle Ω about an external Euler pole results in rotation of the paleomagnetic declination by the angle R and a poleward translation by the angle p .

In Figure 11.1b, a crustal block rotates about a vertical axis located within its boundary; little or no net latitudinal motion occurs during this vertical-axis rotation. The paleomagnetism of rocks of this crustal block would originally have pointed along the *expected declination* toward the paleomagnetic pole PP . But the vertical-axis rotation produces a *rotation*, R , of the *observed declination* from the expected declination.

Motions of lithospheric plates are described by rotations about an *Euler pole* (Cox and Hart, 1986). The tectonic motion of a crustal block (e.g., far-traveled oceanic plateau) can similarly be described by a rotation about an Euler pole that in general is located outside the boundaries of the block. This is illustrated in Figure 11.1c, in which a crustal block is rotated by the angle Ω about an Euler pole. The rotation transports the block in latitude (angular distance = p) and produces a vertical-axis rotation (angle = R); both a flattening of inclination and a rotation of declination result from this motion.

There are two basic methods of analyzing vertical-axis rotations and latitudinal motions from paleomagnetic directions: the *direction-space* and *pole-space* approaches. These methods have been developed by Beck (1976, 1980), Demarest (1983), and Beck et al. (1986). Derivations of the necessary equations are given in the Appendix. At this point, we are concerned only with developing an intuitive appreciation of the direction-space and pole-space approaches.

For most applications, we want to determine motion of a crustal block with respect to a continental interior. The apparent polar wander (APW) path of the continent indicates how that continent has moved with respect to the rotation axis. The set of paleomagnetic poles that make up the APW path also serve as *reference poles* for determining motions of crustal blocks. Each reference pole was determined by paleomagnetic analysis of rocks of a particular age from the continental interior. So in principle the reference pole can be used to calculate the expected paleomagnetic direction for rocks of that age at any point on the continent. Equations (A.53) through (A.61) in the Appendix are used for this calculation.

The direction-space approach is illustrated in Figure 11.2a and developed in the Appendix (Equations (A.62) to (A.67)). The expected direction (I_x, D_x) is simply compared with the observed paleomagnetic direction (I_o, D_o). The inclination flattening, F , is given by

$$F = I_x - I_o \quad (11.1)$$

and the rotation of declination is given by

$$R = D_o - D_x \quad (11.2)$$

R is defined as positive when D_o is clockwise of D_x . The expected and observed directions both have associated confidence limits, so F and R have 95% confidence limits ΔF and ΔR , respectively. The required equations are derived as Equations (A.66) and (A.67) in the Appendix. Results of direction-space analyses are usually reported by listings of $R \pm \Delta R$ and $F \pm \Delta F$. An observed direction that deviates significantly from the expected direction ($F > \Delta F$ and/or $R > \Delta R$) is a *discordant paleomagnetic direction*. An observed direction that is not statistically distinguishable from the expected direction is a *concordant paleomagnetic direction*.

The pole-space approach is illustrated in Figure 11.2b, and the attendant mathematics are derived as Equations (A.68) to (A.78) in the Appendix. In this approach, the comparison is between the reference pole (RP) of the continent and the *observed pole* (OP) determined from a crustal block located at geographic location S . The pole-space method involves analysis of the spherical triangle with corners at S , OP , and RP (Figure 11.2b). The angular distance from S to OP is p_o , while the angular distance from S to RP is p_r ; comparison of these distances indicates whether the block has moved toward or away from the reference pole. The *poleward transport*, p , is given by

$$p = p_o - p_r \quad (11.3)$$

and p is positive if the block has moved toward the reference pole (as shown in Figure 11.2b). The vertical-axis rotation, R , indicated by deviation of the observed pole from the reference pole is the angle of the spherical triangle at apex S (Equation (A.72)). Confidence limits on the reference and observed poles lead

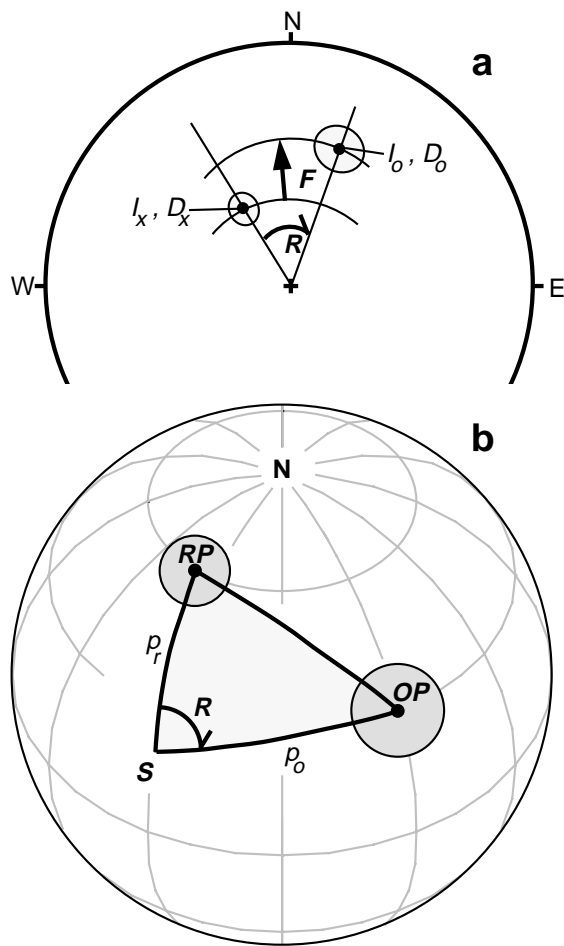


Figure 11.2 Direction-space versus pole-space analysis of paleomagnetic discordance. (a) Equal-area projection of an observed discordant paleomagnetic direction with inclination I_o and declination D_o compared to an expected direction with inclination I_x and declination D_x ; the observed direction is shallower than the expected direction by the flattening angle $F (= I_x - I_o)$; observed declination is clockwise from the expected declination by the rotation angle R . (b) Comparison of observed and reference paleomagnetic poles. The discordant paleomagnetic pole OP (observed pole) was determined from paleomagnetic analysis of rocks at the collection location labeled S ; RP is the reference paleomagnetic pole; the spherical triangle with apices at S , OP , and RP is shown by the heavy lines; p_r = great-circle distance from S to RP ; p_o = great-circle distance from S to OP ; poleward transport $p = p_o - p_r$; vertical-axis rotation R = angle of spherical triangle at S .

to confidence limits Δp and ΔR on p and R , respectively. So results of pole-space analyses are given by $p \pm \Delta p$ and $R \pm \Delta R$, and the observed pole is discordant if statistically significant from the reference pole.

A significant positive flattening of inclination, $F \pm \Delta F$, indicates motion toward the paleomagnetic pole. However, the amount of motion is only indirectly given by the angle F because the inclination is related to paleolatitude through the dipole equation (Equation (1.15)). But a significant positive poleward transport, $p \pm \Delta p$, is a direct measure of motion toward the reference pole. Accordingly, we will use the pole-space approach to determine poleward transport, $p \pm \Delta p$, when analyzing paleolatitudinal motions. For tectonic rotations about a nearby vertical axis, the amount of vertical-axis rotation, $R \pm \Delta R$, can be determined by either the direction-space or pole-space method. Most students find the direction-space approach to vertical-axis rotations intuitively appealing, so that method is used in presenting examples of vertical-axis tectonic rotations. In this way, you will gain experience in both methods.

Before proceeding to the examples, it is important to emphasize the importance of the paleomagnetic data from the crustal block and the importance of the reference pole. All the concerns emphasized in previous chapters about quality and quantity of paleomagnetic data apply to evaluating paleomagnetic data from a crustal block. Important questions include the following:

1. What is the lithology of the rocks sampled, and are those rocks accurate paleomagnetic recorders?
2. Have thorough demagnetization experiments demonstrated isolation of a high-stability characteristic component (ChRM)?
3. What structural corrections are required, and what uncertainties accompany those corrections?
4. What do field tests indicate about the stability and age of the ChRM?
5. Does the set of site-mean directions provide adequate sampling of geomagnetic secular variation?

Your knowledge of rock magnetism and paleomagnetism gained through study of the previous chapters should allow you to effectively address these questions. The quality and quantity of paleomagnetic data used to determine the motion history of a crustal block should be no less than that required for determination of a paleomagnetic pole from the continental interior.

Because all determinations of crustal block motion are with respect to a reference paleomagnetic pole (or expected direction calculated from the reference pole), accuracy of the reference pole is crucial. Inaccuracy in the reference pole leads directly to inaccurate estimates of motion of the crustal block. As discussed earlier in this chapter, development of APW paths (reference poles) for continents is an ongoing process. New data and new methods of analysis sometimes result in significant changes to APW paths. So evaluation of reference poles is equal in importance to evaluation of paleomagnetic data from a crustal block. A case in point is provided by recent analyses of North American Mesozoic APW and resulting implications for motion histories of Cordilleran terranes (Gordon et al., 1984; May and Butler, 1986).

THE TRANSVERSE RANGES, CALIFORNIA: A LARGE, YOUNG ROTATION

The Transverse Ranges of southern California trend east-west, cutting across the dominant northwest-southeast trends of the Coast Ranges and San Andreas fault system (Figure 11.3). Some geological observations suggested that the Transverse Ranges had undergone a major vertical-axis rotation. For example, Jones et al. (1976) noted that structures in Mesozoic rocks of the Transverse Ranges are aligned east-west, whereas similar structures in Mesozoic rocks from Oregon to Baja California are oriented north-south. They concluded that the Transverse Ranges had been affected by a major vertical-axis rotation during the Cretaceous or Tertiary. Paleomagnetism has dramatically confirmed this suggestion, and the magnitude, young age, and rate of rotation are indeed startling. Our first example application of paleomagnetism to regional tectonics is the pioneering work of Kamerling and Luyendyk (1979), who demonstrated major clockwise rotation of the western Transverse Ranges.

The Conejo Volcanics are a sequence of volcanic breccias, tuff breccias, pillow lavas, and massive andesitic and basaltic flows intruded by dikes, sills, and hypabyssal intrusives. These volcanic rocks have

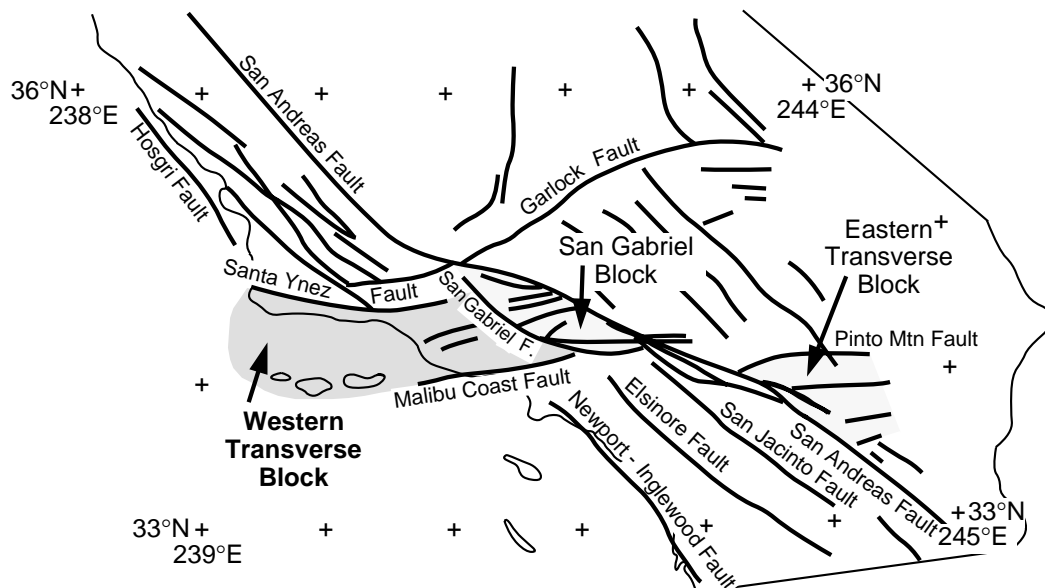


Figure 11.3 Map of southern California. Major Neogene faults are shown by heavy lines; the state boundary of California is shown by the thin line; the Transverse Ranges are shown by the stippled pattern. Redrawn from Luyendyk et al. (1985) with permission from the American Geophysical Union.

been dated by the K-Ar method, and ages range from 13.1 to 16.1 Ma. Kamerling and Luyendyk (1979) collected paleomagnetic samples from the Conejo Volcanics exposed in the Santa Monica Mountains and the Conejo Hills, western Transverse Ranges (mean location approximately 34°N, 241°E).

Five to nine samples were collected from each site (individual flow or dike); secondary components of NRM were generally removed by AF demagnetization to peak fields in the 100- to 600-Oe (10- to 60-mT) range; and the majority of site-mean ChRM directions were determined with $\alpha_{95} < 8^\circ$. The 15 site-mean directions from the Conejo Volcanics of the Santa Monica Mountains and Conejo Hills are illustrated in Figure 11.4a. The five normal-polarity sites have mean direction $I = 43.9^\circ$, $D = 74.9^\circ$, while ten reversed-polarity sites have mean direction $I = -50.1^\circ$, $D = 247.1^\circ$. These mean directions are not significant from antipodal (5% significance level), so the site-mean ChRM directions pass the reversals test. The dispersion of site-mean ChRM directions suggests that geomagnetic secular variation has been adequately sampled. Available rock-magnetic and paleomagnetic analyses indicate that the Conejo Volcanics provide a reliable paleomagnetic record of the geomagnetic field direction at ~15 Ma.

Taking the antipodes of the reversed-polarity site-mean directions and averaging the 15 site-mean directions yields a formation-mean direction $I_o = 47.6^\circ$, $D_o = 70.9^\circ$, $\alpha_{95} = 7.7^\circ$ (Figure 11.4b). The Miocene reference pole for North America is well determined at $\lambda_r = 87.4^\circ\text{N}$, $\phi_r = 129.7^\circ\text{E}$, $A_{95} = 3.0^\circ$ (Hagstrum et al., 1987). Using the site location in the Western Transverse Ranges, Equations (A.53) to (A.61) yield the expected Miocene direction: $I_x = 52.4^\circ \pm 3.2^\circ$, $D_x = 357.1^\circ \pm 3.6^\circ$. Comparison of the expected and observed

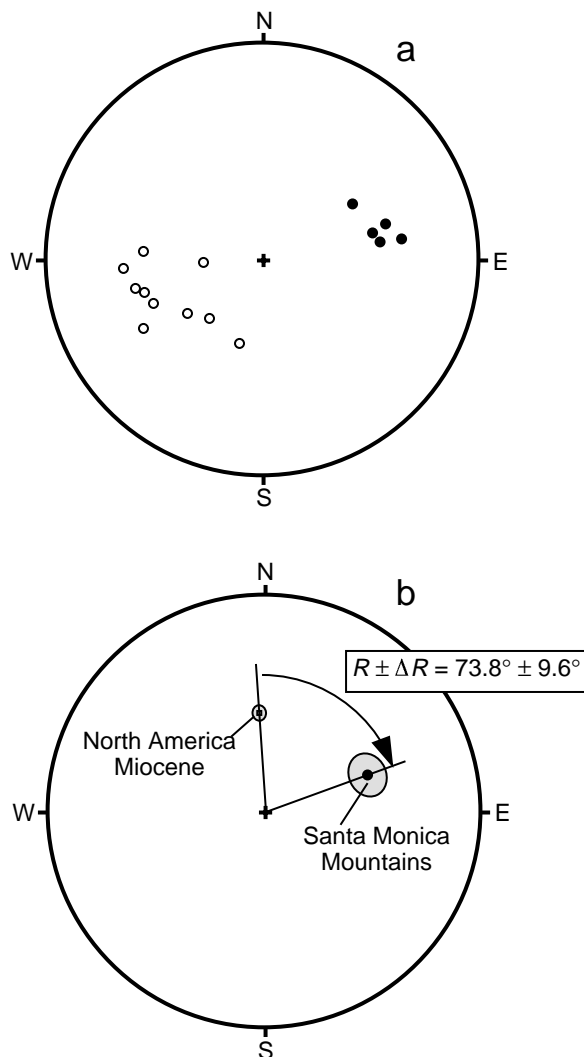


Figure 11.4 (a) Equal-area projection of site-mean ChRM directions from the Conejo Volcanics of the Santa Monica Mountains, western Transverse Ranges. Directions in the lower hemisphere are shown by solid circles; directions in the upper hemisphere are shown by open circles. (b) Comparison of discordant formation-mean ChRM direction from the Conejo Volcanics of the Santa Monica Mountains with the expected direction calculated from the Miocene reference pole for North America. Data from Kamerling and Luyendyk (1979) with permission from the Geological Society of America.

paleomagnetic directions using Equations (A.62) to (A.67) yields $R \pm \Delta R = 73.8^\circ \pm 9.6^\circ$ (Figure 11.4b). Kamerling and Luyendyk (1979) thus quite conclusively demonstrated that the western Transverse Ranges had indeed rotated. The truly surprising result was that $\sim 70^\circ$ of clockwise rotation occurred during the past 15 m.y.

Subsequent paleomagnetic investigations by Bruce Luyendyk and other researchers have extended paleomagnetic sampling to older rocks and other regions of the Transverse Ranges and Mojave Desert. These results were summarized by Luyendyk et al. (1985) and reveal an interesting pattern of post-20-Ma vertical-axis rotations: (1) San Clemente, Santa Barbara, and San Nicolas islands have not rotated, whereas Santa Catalina Island has rotated $\sim 100^\circ$ clockwise; (2) the Northern Channel Islands have rotated clockwise by 70° to 80° ; (3) the Santa Ynez Range has rotated clockwise by $\sim 90^\circ$; and (4) the crustal block between the San Gabriel and San Andreas faults has rotated clockwise $\sim 35^\circ$. The Late Oligocene reconstruction of southern California in Figure 11.5 illustrates the interpretation of this pattern of rotations advanced by Luyendyk et al. (1985). The Transverse Ranges are reconstructed to a north-south orientation and are surrounded by a system of northwest-southeast-oriented right-lateral strike-slip faults. Panels of crust within the Transverse Ranges are separated by left-lateral strike-slip faults, and these panels rotated clockwise as the entire region underwent right shear caused by interaction between the Pacific and North American plates.

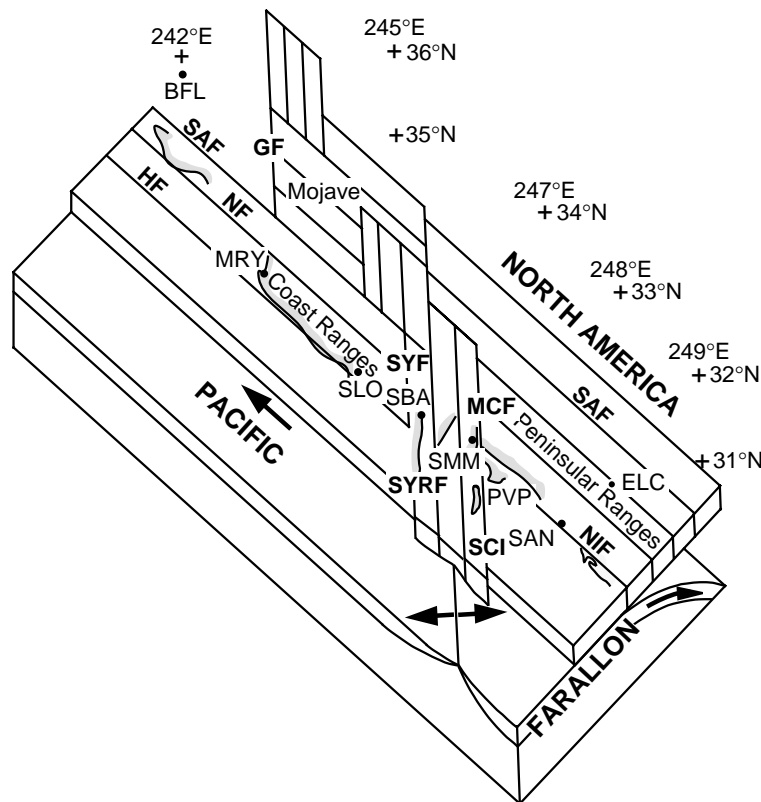


Figure 11.5 Schematic reconstruction of southern California in the Late Oligocene. The Pacific Plate is moving northwest, and the Farallon Plate is subducting beneath the North America plate; separation of the Pacific and Farallon plates at the East Pacific Rise is shown by diverging arrows; crustal panels are separated by strike-slip faults, including SAF = San Andreas fault; NF = Nacimiento fault; HF = Hosgri fault; GF = Garlock fault; SYF = Santa Ynez fault; SYRF = Santa Ynez River fault; MCF = Malibu Coast fault; SCI = Santa Cruz Island fault; NIF = Newport-Inglewood fault; place names are BFL = Bakersfield; MRY = Monterey; SLO = San Luis Obispo; SBA = Santa Barbara; SMM = Santa Monica Mountains; PVP = Palos Verdes Peninsula; SAN = San Diego; ELC = El Centro. Redrawn from Luyendyk et al. (1985) with permission from the American Geophysical Union.

Certainly many questions about the kinematics and dynamics of crustal rotations in southern California remain and will be debated for some time. But paleomagnetic determinations of Neogene rotations have dramatically focused these questions and are a major advance in understanding the tectonic development of this complex region.

THE GOBLE VOLCANICS: AN OLDER, SMALLER ROTATION

Figure 11.6 illustrates the pattern of discordant paleomagnetic declinations observed in the U.S. Pacific Northwest. Cox (1957) observed a paleomagnetic declination in the Eocene Siletz River Volcanics of the Oregon Coast Range that was east of the anticipated direction. But at that time, the expected Eocene direction was poorly known, and the tectonic significance of this early result was not fully appreciated. Subsequently, Simpson and Cox (1977) confirmed that the Oregon Coast Range had rotated clockwise by $\sim 70^\circ$ since the Eocene. In subsequent years, paleomagnetic investigations have determined in considerable

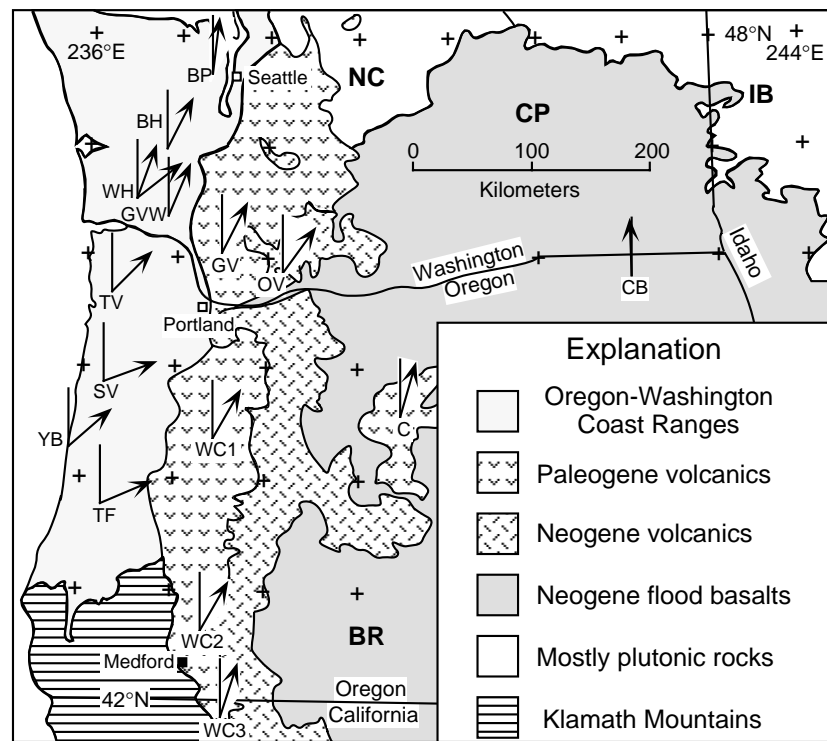


Figure 11.6 Geologic and physiographic provinces of the Pacific Northwest. Expected and observed paleomagnetic declinations are compared at sites of paleomagnetic studies of Cenozoic layered rocks; expected declinations are shown by the north-directed line; observed declinations are shown by arrows; references to paleomagnetic studies are CB = Columbia River Basalt Group (data compiled by Grommé et al., 1986); C = Clarno Formation (Grommé et al., 1986); OV = Ohanapecosh Volcanics (Bates et al., 1981); GV = Goble Volcanics (Beck and Burr, 1979); GVV = Goble Volcanics (Wells and Coe, 1985); WH = Crescent Formation (Wells and Coe, 1985); BH = Crescent Formation (Globerman et al., 1982); BP = Crescent Formation (Beck and Engebretson, 1982); TV = Tillamook Volcanics (Magill et al., 1981); SV = Siletz River Volcanics (Simpson and Cox, 1977); YB = Yachats Basalt (Simpson and Cox, 1977); TF = Tye and Flournoy formations (Simpson and Cox, 1977); WC1&WC2 = Western Cascades Volcanics (Magill and Cox, 1980); WC3 = Western Cascades Volcanics (Beck et al., 1986); geologic/physiographic provinces include NC = North Cascades; IB = Idaho batholith; CP = Columbia Plateau; BR = Basin and Range. Modified from Grommé et al. (1986) with permission from the American Geophysical Union.

detail the spatial and temporal pattern of clockwise rotations in the Pacific Northwest. Attendant tectonic models have become more sophisticated and better constrained as increasing numbers of paleomagnetic results have become available. Recent tectonic syntheses are provided by Wells and Coe (1985), Grommé et al. (1986), and Wells and Heller (1988). Our next example application of paleomagnetism to regional tectonics is the paleomagnetic study by Beck and Burr (1979) of the Goble Volcanics in southwest Washington (labeled GV in Figure 11.6).

The Goble Volcanics consist of subaerial andesitic and basaltic flows with minor pyroclastic and sedimentary deposits, which are part of a volcanic arc ancestral to the present Cascade arc. K-Ar ages range from 32 to 45 Ma (Late Eocene to Early Oligocene). Beck and Burr (1979) reported paleomagnetic results from 392 samples collected from 42 flows. The sampled flows are mostly massive flows 1 m to 30 m thick. Some flows have dips up to 25°, but most dip at less than 10°. Limited sedimentary interbeds and limited outcrops lead to an interesting complication. Are the observed dips due to flows having erupted onto sloping topography and therefore original? Or were the flows originally horizontal with present dips resulting from subsequent tectonic disturbance? The geologic observations do not provide clear evidence as to whether the observed paleomagnetic directions should be structurally corrected for the local dip of the sampled flows. The paleomagnetic data do not solve the problem either. The clustering of site-mean ChRM directions is improved by applying the structural corrections, but the improvement is not statistically significant (k increases from 27.45 to 30.54). Fortunately, the observed dips are generally small, and the sampling region is sufficiently large that observed dips are randomly directed. So no systematic bias is introduced by the structural corrections, and in the final analysis, Beck and Burr (1979) used structurally corrected site-mean directions.

The rock magnetism of the Goble Volcanic Series was fairly straightforward with AF demagnetization successfully isolating the ChRM direction for most flows. Results from four sites were rejected because site-mean ChRM directions had $\alpha_{95} > 15^\circ$. Results from another site were rejected because of its aberrant direction and petrologic character suggesting that it belongs to a younger volcanic series. The resulting 37 site-mean ChRM directions are shown in Figure 11.7a, with reversed-polarity directions inverted through the origin of the equal-area projection.

The 28 normal-polarity sites have mean direction $I = 58.7^\circ$, $D = 19.0^\circ$, $\alpha_{95} = 5.4^\circ$. The mean of the nine reversed-polarity sites ($I = -54.6^\circ$, $D = 197.7^\circ$, $\alpha_{95} = 7.8^\circ$) indicates that the site-mean ChRM directions pass the reversals test. The observed formation-mean direction is $I_o = 57.5^\circ$, $D_o = 18.5^\circ$, $\alpha_{95} = 4.3^\circ$ (Figure 11.7a). An analysis of site-mean VGPs yields an observed pole $\lambda_o = 75.5^\circ\text{N}$, $\phi_o = 345.5^\circ\text{E}$, $A_{95} = 5.5^\circ$, with estimated angular standard deviation ($S = 19.2^\circ$) consistent with adequate sampling of geomagnetic secular variation.

For calculation of the expected direction, we use the mid-Tertiary (20 to 40 Ma) reference pole compiled by Diehl et al. (1988) at $\lambda_r = 81.5^\circ\text{N}$, $\phi_r = 147.3^\circ\text{E}$, $A_{95} = 2.4^\circ$. For the sampling location (46°N , 237.5°E), the resulting expected mid-Tertiary direction is $I_x = 63.7^\circ \pm 1.9^\circ$, $D_x = 347.9^\circ \pm 3.4^\circ$. In Figure 11.7b, this expected mid-Tertiary direction is compared to the observed formation-mean direction from the Goble Volcanic Series. The major result is that the observed declination is clearly discordant, with $R \pm \Delta R = 30.6^\circ \pm 6.9^\circ$. This paleomagnetic study thus provided another important constraint on the spatial and temporal pattern of vertical-axis tectonic rotations in the Pacific Northwest.

An interesting additional observation from the paleomagnetic analysis of the Goble Volcanic Series is that a statistically significant poleward transport is indicated; the direction-space analysis yields $F \pm \Delta F = 6.2^\circ \pm 3.8^\circ$, while the pole-space analysis yields $p \pm \Delta p = 5.3^\circ \pm 4.8^\circ$. We will discuss this result in the Caveats and Summary section.

A further observation illustrated by this example is the limited precision of determining vertical-axis rotations from a formation-mean direction. Fundamentally, because of the dispersion of site-mean directions intrinsic in the required sampling of geomagnetic secular variation, even the best formation-mean direction can rarely be determined with $\alpha_{95} < 5^\circ$. Further considering the confidence limit on the expected direction leads to the conclusion that a formation-mean direction rarely can allow determination of a vertical-axis rotation with confidence limit, ΔR , less than 10° .

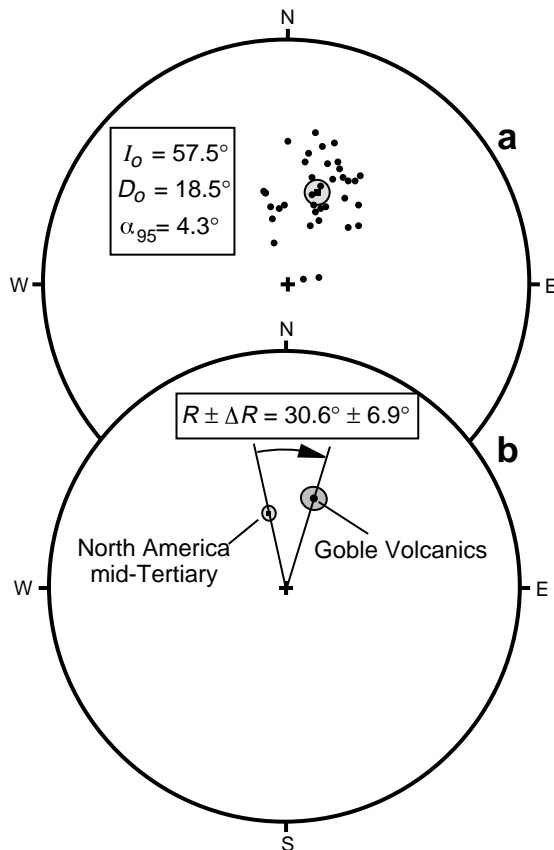


Figure 11.7 (a) Equal-area projection of site-mean ChRM directions from the Goble Volcanic Series of southwest Washington. Directions of reversed-polarity sites have been inverted through the origin of the projection; all directions are in the lower hemisphere; the formation-mean ChRM direction is listed and is shown by the solid square with surrounding stippled α_{95} confidence limit. (b) Comparison of discordant formation-mean ChRM direction from the Goble Volcanic Series with the expected direction calculated from the mid-Tertiary reference pole for North America. Data provided by M. Beck.

Widespread individual flows sometimes serve as accurate recorders of differential vertical-axis rotation across the region that they cover. Magill et al. (1982) reported paleomagnetic results from the Pomona Member of the Saddle Mountains Basalt. This flow erupted at ~12 Ma from a source in western Idaho and flowed >400 km to the Pacific Coast. In the Coast Ranges of southwestern Washington, this flow is also known as the Basalt of Pack Sack Lookout. This “single-flow” method avoids the necessity of averaging geomagnetic secular variation and has allowed resolution of rotations approaching 5° to be determined. Magill et al. (1982) were able to detect a 15° clockwise tectonic rotation of the Coast Range with respect to the Columbia Plateau had occurred since 12 Ma.

Wells and Heller (1988) combined additional results of the single-flow method with an analysis of geologic and paleomagnetic constraints on the rotation history of the Pacific Northwest. They concluded that:

1. The rotation of oceanic microplates during accretion to the continental margin (Figure 11.8a) was not a major mechanism for vertical-axis rotation in the Pacific Northwest.
2. Distribution of right shear between oceanic plates and the North American plate over a 100- to 200-km-wide zone contributes at least 40% of the post-15-Ma rotation of the Coast Ranges. Mechanisms similar to those of Figure 11.8b and 11.8c are involved. The dimensions of the coherently rotating crustal blocks (e.g., balls in the ball-bearing model of Figure 11.8b) are ~20 km (Wells and Coe, 1985).
3. Northwards decreasing amount of extension in the Basin and Range Province east of the Cascade Arc (Figure 11.8d) contributes the remainder (up to 60%) of the post-15-Ma rotation of the Coast Ranges.

It is clear from these examples that paleomagnetism is effective in determining vertical-axis tectonic rotations. This tectonic process is quite difficult to detect by other methods. The growing list of examples indicates that vertical-axis tectonic rotations are a major tectonic process in continental deformation.

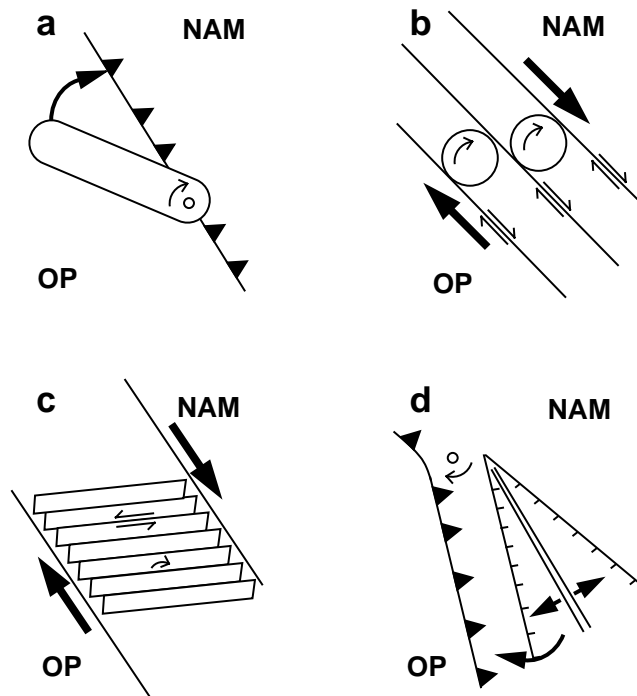


Figure 11.8 Schematic tectonic models for rotation of crustal blocks along the western continental margin of North America. OP = oceanic plate; NAM = North American plate. (a) Rotation during oblique collision; the pivot point is shown by the small circle; barbs are on the overriding plate. (b) Ball-bearing model of right shear distributed between en-echelon right-lateral strike-slip faults. (c) Rotating-panels model of right shear distributed between en-echelon right-lateral strike-slip faults; the small arrow shows clockwise rotation of panels. (d) Rotation by asymmetric extension of the continent inboard of the subduction zone; the zone of extension is shown by diverging arrows; the pivot point is shown by the small circle. Redrawn from Wells and Heller (1988) with permission from the Geological Society of America.

WRANGELLIA IN ALASKA: A FAR-TRAVELED TERRANE

Wrangellia is a tectonostratigraphic terrane exposed along the western Cordillera from eastern Oregon to Alaska (Figure 11.9). Jones et al. (1977) defined Wrangellia to include Late Carboniferous to Early Permian andesitic volcanic arc rocks, Middle to Late Triassic tholeiitic basalt flows and pillow lavas (including the Nikolai Greenstone in Alaska), and Late Triassic platform carbonates. Wrangellia is interpreted to be an ancestral island arc and/or oceanic plateau that was dismembered and dispersed along the North American continental margin. Wrangellia has been the subject of intense paleomagnetic research. Published reports include Hillhouse (1977), Yole and Irving (1980), Hillhouse et al. (1982), Hillhouse and Grommé (1984), and Panuska and Stone (1981, 1985).

To determine motion history in detail, a complete APW path for Wrangellia would be required. But terranes usually represent limited geologic time intervals, and the rocks often are deformed or have suffered chemical or thermal remagnetization. So we rarely have more than one or two paleomagnetic poles from which to decipher the motion history. Our final example application of paleomagnetism to regional tectonics is representative of paleomagnetic studies of displaced terranes. This example is the original paleomagnetic investigation of Wrangellia by Hillhouse (1977).

Paleomagnetism of the Nikolai Greenstone

The Nikolai Greenstone is exposed along the southern flank of the Wrangell Mountains in south-central Alaska (Figure 11.9). This sequence of mostly subaerial tholeiitic basalt flows reaches a stratigraphic thickness of 3000 m. The basalt flows are bracketed by sedimentary rocks containing fossils that indicate a Middle–Late Triassic (Ladinian/Carnian) age for the Nikolai Greenstone. Hillhouse (1977) reported paleomagnetic results from 126 core samples collected at five locations of the Nikolai Greenstone. The samples were collected in 1962, and the collection scheme was somewhat unconventional by present-day standards; just two cores were collected from each individual basalt flow. However, a sufficient number of cores was collected, and stability tests indicate that the resulting data are reliable. Also, subsequent paleomagnetic analysis of nearby portions of Wrangellia have confirmed the original findings.

The rock magnetism of the Nikolai Greenstone was investigated in some detail. Strong-field thermomagnetic experiments revealed Curie temperatures of 570° to 580°C, indicating that Ti-poor titanomagnetite

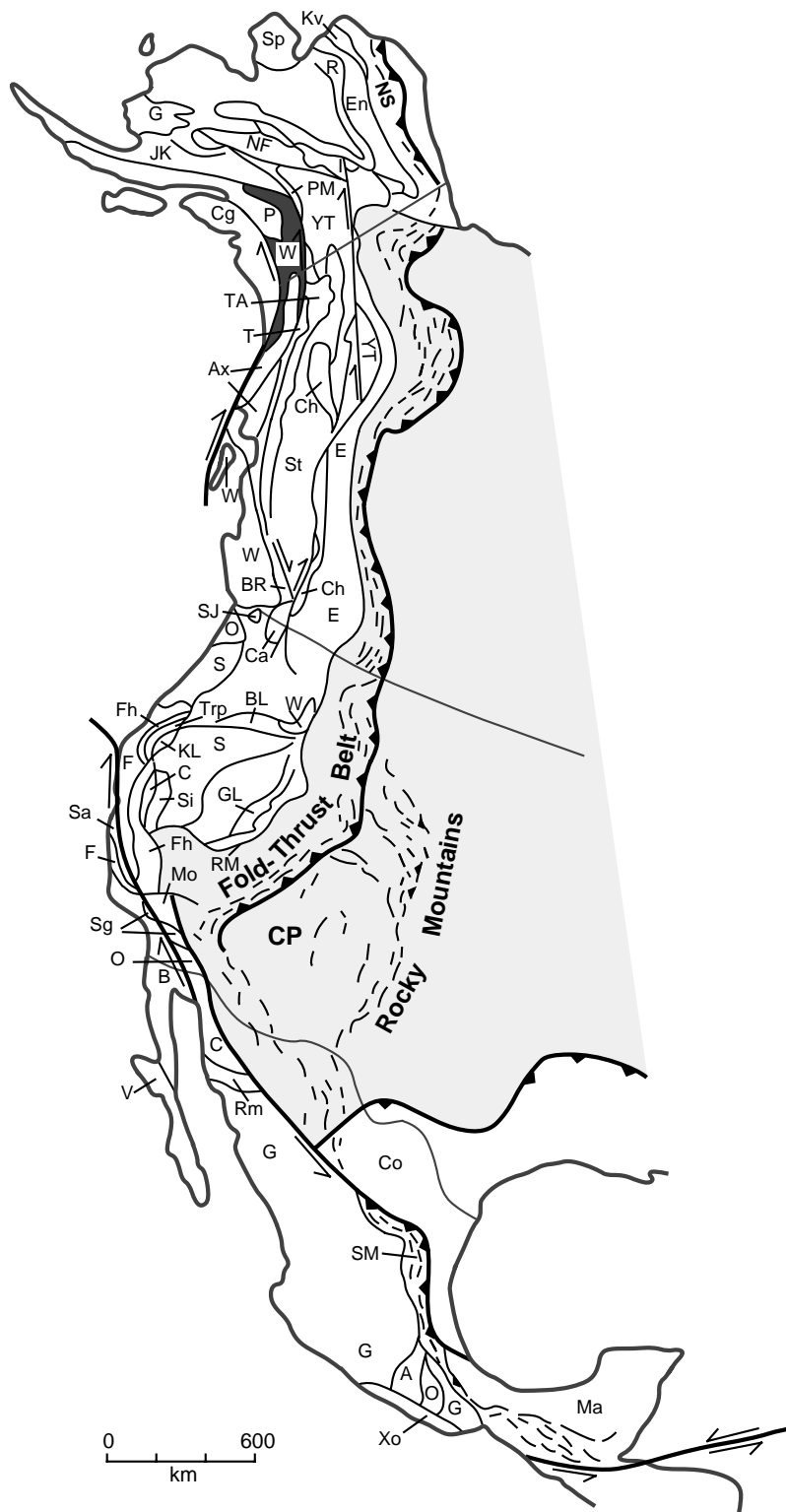


Figure 11.9 Tectonostratigraphic terranes of the North American Cordillera. The area of dark stippling in southern Alaska is the Wrangellia terrane containing the Nikolai Greenstone locality. Definitions and descriptions of terranes can be found in Coney (1981). Redrawn from Coney (1981).

is the dominant ferromagnetic mineral (Chapter 4). Progressive thermal demagnetization experiments indicated two NRM components: a secondary component with blocking temperature (T_B) $< 250^\circ\text{C}$, and a ChRM with T_B in the 505° to 580°C interval. Later work by Hillhouse and Grommé (1984) revealed ChRM blocked above 580°C in samples containing deuteritic hematite. AF demagnetization was used for the majority of samples; demagnetization to peak fields of 400 Oe (40 mT) generally removed a secondary NRM component subparallel to the present geomagnetic field direction. The secondary NRM was interpreted as a VRM, while the ChRM was interpreted as primary TRM.

Because of failure to definitively isolate a ChRM, results from ~30 samples were rejected. At one location, both normal- and reversed-polarity flows were observed in a succession of 27 flows; the ChRM directions from this location passed the reversals test. Changes in bedding attitude between the locations allowed a fold test. In fact, the locality-mean ChRM directions from the Nikolai Greenstone were used in Figure 5.12 to illustrate the fold test. These directions were used again in Chapter 6 as an example of statistical evaluation of the fold test. The ChRM directions pass the fold test (5% significance level), and the structurally corrected locality-mean ChRM directions are shown in Figure 5.12. So the rock-magnetic and paleomagnetic evidence strongly supports the interpretation that the ChRM of the Nikolai basalt flows is a primary TRM.

To determine the paleomagnetic pole for the Nikolai Greenstone, Hillhouse (1977) averaged VGPs from 50 flows. The resulting observed pole ($\lambda_o = 2.2^\circ\text{N}$, $\phi_o = 146.1^\circ\text{E}$, $A_{95} = 4.8^\circ$) is shown in Figure 11.10. An appropriate reference pole for the Late Triassic is the pole from the Chinle Formation (Reeve and Helsley, 1972; Figure 11.10). (The Chinle Formation is younger than the Nikolai Greenstone, but not by an amount that alters the major conclusions.) Using the pole-space method of analysis (Equations (A.68) to (A.78)), the vertical-axis rotation is $R \pm \Delta R = -80.3^\circ \pm 7.8^\circ$. This result indicates that $\sim 80^\circ$ of counterclockwise vertical-axis rotation accounts for the counterclockwise deflection of the observed pole (Nikolai Greenstone pole) from the reference pole (Chinle pole). But correcting for this vertical-axis rotation does not bring the observed pole into coincidence with the reference pole.

The great-circle distance from the Wrangell Mountains to the reference pole ($p_r = 56.5^\circ$) is less than the distance to the observed pole ($p_o = 79.3^\circ$). The poleward transport of the Nikolai Greenstone is simply the 22.8° difference between p_o and p_r (Equation (11.3)). To produce coincidence of the observed and reference poles, you must move the Nikolai Greenstone (to which the observed pole is attached) southward down the western edge of North America by 22.8° . This result indicates that the Nikolai Greenstone must have been magnetized in the Middle–Late Triassic at a lower paleolatitude than its present location. Between the Middle–Late Triassic and the present, the Nikolai Greenstone was transported toward the Chinle pole (\sim northward) by 22.8° (~ 2500 km).

Consideration of the confidence limits on the reference and observed poles leads to $p \pm \Delta p = 22.8^\circ \pm 6.8^\circ$ (Equations (A.76) to (A.78)). The basic conclusion that the Nikolai Greenstone originated far south of its present location seems quite clear. However, $22.8^\circ \pm 6.8^\circ$ is not necessarily the amount of poleward transport experienced by the Nikolai Greenstone. In fact, this is the minimum transport required!

The hemispheric ambiguity

Figure 11.11 illustrates what is referred to as the *hemispheric ambiguity*. The Middle–Late Triassic is a time of frequent geomagnetic polarity reversals (Figure 9.11), and the Nikolai Greenstone contains both normal- and reversed-polarity flows. For Upper Paleozoic or younger rocks of northern North America, we know that rocks of normal polarity have positive inclination and rocks of reversed polarity have negative inclination. But for a far-traveled terrane, this distinction is not clear. As shown in Figure 11.11, a positive inclination results from magnetization in the northern hemisphere during a normal-polarity interval (Figure 11.11a) or from magnetization in the southern hemisphere during a reversed-polarity interval (Figure 11.11b). So it is ambiguous whether flows of the Nikolai Greenstone with positive inclinations are normal-polarity flows magnetized in the northern hemisphere or reversed-polarity flows magnetized in the southern hemisphere.

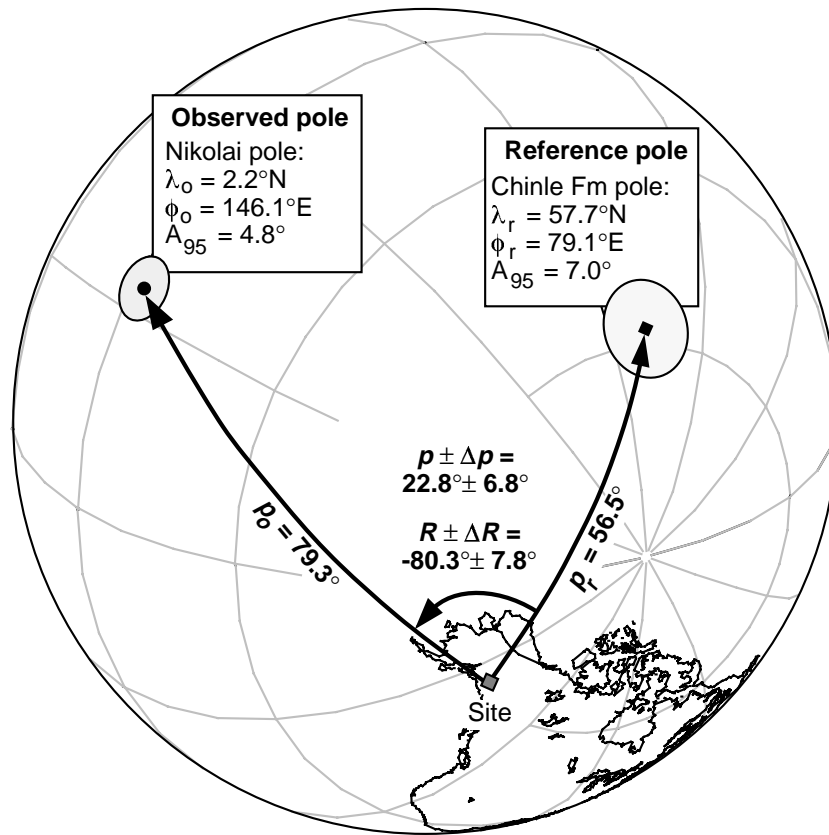


Figure 11.10 Comparison of the paleomagnetic pole from the Middle–Late Triassic Nikolai Greenstone with the reference paleomagnetic pole from the Chinle Formation. The paleomagnetic pole from Nikolai Greenstone is shown by the solid circle; the paleomagnetic pole from the Chinle Formation is shown by the solid square; locations of poles and radii of 95% confidence (A_{95} , shown by the stippled circles) are listed; the collecting site in Alaska is shown by the small stippled square; p_o = great-circle distance from the site to the observed paleomagnetic pole; p_r = great-circle distance from the site to the reference paleomagnetic pole; implied poleward transport, $p \pm \Delta p$, of the Nikolai Greenstone is $p_o - p_r = 22.8^\circ \pm 6.8^\circ$; implied vertical-axis rotation, $R \pm \Delta R$, is counter-clockwise by $80.3^\circ \pm 7.8^\circ$.

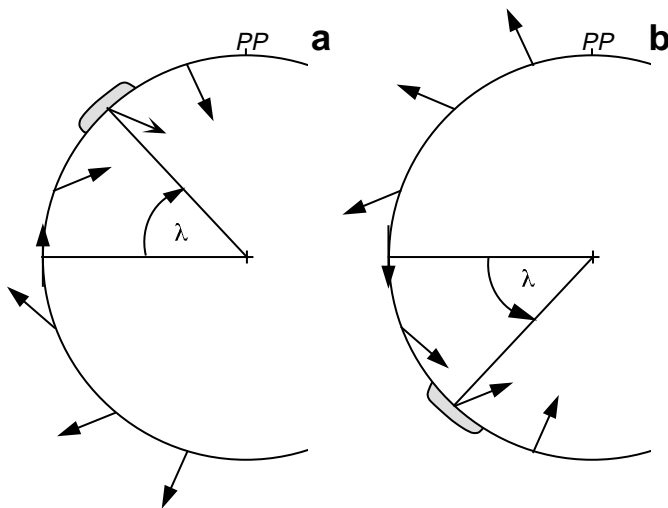


Figure 11.11 The hemispheric ambiguity. Positive inclination of ChRM can indicate either (a) magnetization in the northern hemisphere during a normal-polarity interval or (b) magnetization in the southern hemisphere during a reversed-polarity interval.

The paleogeographic map shown by Hillhouse (1977) places the Nikolai Greenstone in the northern hemisphere. This option requires the minimum poleward transport. Hillhouse (1977) illustrated the northern hemisphere option because of the “principle of least astonishment.” The conclusion of 2500 km of poleward transport of the Nikolai Greenstone is a sufficiently startling result; it is best not to further astonish the reader with the possibility that the Nikolai Greenstone might have originated in the southern hemisphere and been transported >5000 km to its present location. In the specific case of Wrangellia, most researchers have favored a northern hemisphere origin (e.g., Panuska and Stone, 1981).

A Middle–Late Triassic paleogeographic map is shown in Figure 11.12 with North America, South America, and the Nikolai Greenstone placed in their Middle–Late Triassic positions. This map was constructed by using the following steps:

1. North America and South America were placed in their proper relative positions by closing the Atlantic Ocean to reconstruct this portion of Pangea.
2. The pole of the geographic grid was rotated to the reference pole (Chinle pole). This operation produces the Middle–Late Triassic distribution of paleolatitudinal lines across North America and South America. Remember that we have no direct control on paleolongitude, so absolute values of paleolongitude are not known.
3. The great-circle distance from the Nikolai Greenstone to its paleomagnetic pole ($p_o = 79.3^\circ$; Figure 11.10) is its *paleocolatitude*. Through the geocentric dipole hypothesis, this is also the paleolatitudinal distance from the Nikolai Greenstone to the paleogeographic pole. So the paleolatitude of the Nikolai Greenstone is $90^\circ - p_o = 10.7^\circ$. Recalling the hemispheric ambiguity, this paleolatitude could be either 10.7°N or 10.7°S . These paleolatitudes are shown in Figure 11.12. As discussed in the Appendix, the confidence limit on the relative paleolatitudinal position of the Nikolai Greenstone and North America is $\Delta p = 6.8^\circ$, and these limits are shown by the stippled paleolatitude bands in Figure 11.12.

With this paleogeographic map, we get a picture of the minimum distance traveled by the Nikolai Greenstone. We cannot determine the amount of longitudinal motion. Notice that the Middle–Late Triassic paleolatitude of the Wrangell Mountains is 33.5°N ; this is the *expected paleolatitude*. The minimum difference between the expected and observed paleolatitudes is $33.5^\circ\text{N} - 10.7^\circ\text{N} = 22.8^\circ$. This of course is the amount of poleward displacement determined above. The paleomagnetic study of Hillhouse (1977) thus provides a realistic, practical example of how paleomagnetism is used to determine poleward transport of terranes with respect to the continents to which they are now attached.

CAVEATS AND SUMMARY

This discussion of paleomagnetic applications to regional tectonics concludes with a few comments on special problems and concerns. One special consideration is the potential solution of the hemispheric ambiguity provided by polarity superchrons. If rocks of a potentially far-traveled crustal block have ages within a polarity superchron, the polarity of these rocks is known. For example, consider rocks of a particular crustal block with ages within the Cretaceous normal-polarity superchron (~118 to ~83 Ma; Figure 10.11). A formation-mean ChRM direction with positive inclination would indicate a northern hemisphere paleolatitude for these rocks, while a negative inclination would indicate a southern hemisphere origin. The opposite situation holds for the Permo-Carboniferous reversed-polarity superchron, the other well-established polarity superchron during the Phanerozoic.

Resolution of the hemispheric ambiguity for far-traveled crustal blocks by this “superchron method” has proved difficult. Alvarez et al. (1980) and Tarduno et al. (1986) found negative inclinations in the Cretaceous Laytonville Limestone of the Franciscan Complex in northern California. Because the biostratigraphic ages fell within the Cretaceous normal-polarity superchron, these investigators concluded that the Franciscan

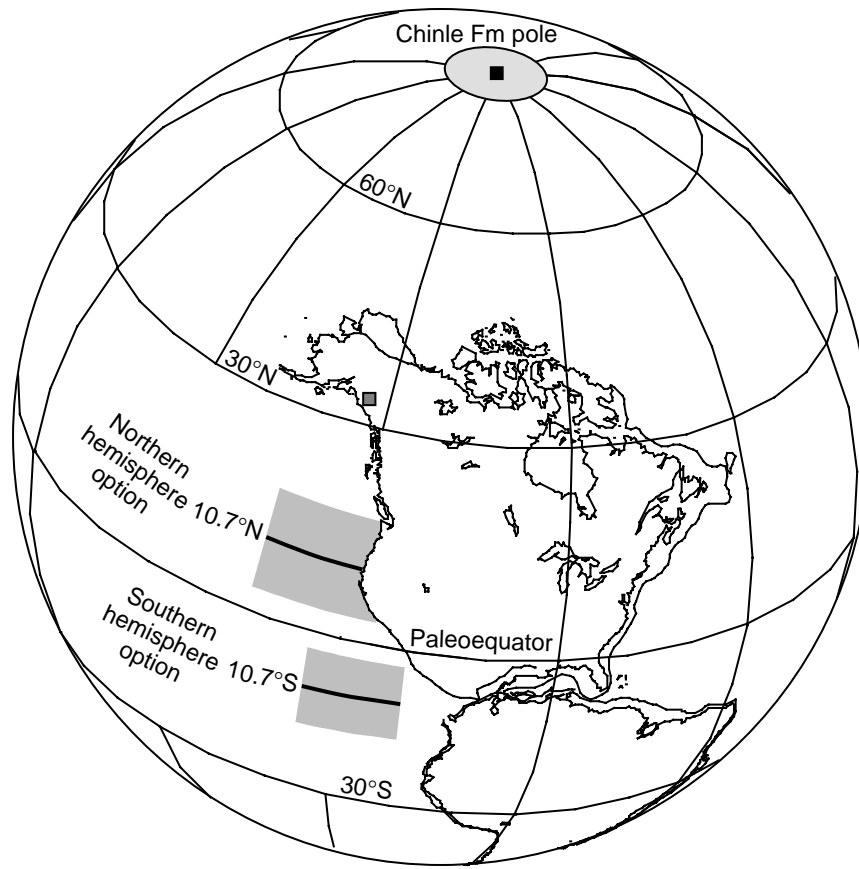


Figure 11.12 Paleogeographic position of the Nikolai Greenstone in the Middle–Late Triassic. The paleomagnetic pole from the Chinle Formation is used as the North American reference pole for the Carnian/Norian stage of the Late Triassic; the Chinle pole is used as the pole of the paleogeographic grid; South America is placed in its Late Triassic paleogeographic position with respect to North America; the Nikolai Greenstone paleolatitude (10.7° north or south) is shown by the heavy line with confidence limits ($\pm 6.8^\circ$) shown by the stipple band of latitudes.

limestones were formed in the southern hemisphere. However, Courtillot et al. (1985) investigated other Franciscan limestones of similar age but different lithology and concluded a northern hemisphere origin. From detailed paleomagnetic analysis of the Laytonville Limestone, Tarduno et al. (1990) have presented a strong case for a southern hemisphere origin of those limestone blocks in the Franciscan mélangé. Apparently, the Franciscan Complex contains some limestone blocks of northern hemisphere origin and other blocks of southern hemisphere origin. The fundamental basis of the superchron method is sound, and it will no doubt be used successfully in the future.

A question that is often asked about tectonic conclusions based on paleomagnetic results concerns the confidence limits ΔR and Δp . What is the real limit on the magnitude of tectonic transport that can be resolved by paleomagnetism? Do the confidence limits ΔR and Δp tell the whole story? If $\Delta p = 5^\circ$ for a particular paleomagnetic study, does this mean that poleward tectonic transport of 550 km is resolvable? In the examples given above, the observed paleomagnetic directions or poles were highly discordant and clearly have important tectonic implications. However, when the rotation of declination (R) or poleward transport (p) just meets or only slightly exceeds the confidence limit, it is not clear what inferences should be drawn. Different methods of data analysis (and even the philosophy of the investigator) can lead to different conclusions.

Let's consider the result from the Goble Volcanic Series discussed above. The clockwise vertical-axis rotation ($R \pm \Delta R = 30.6^\circ \pm 6.9^\circ$) of the sampling region is clearly a statistically significant and geologically

meaningful result. But we also calculated $p \pm \Delta p = 5.3^\circ \pm 4.8^\circ$ for the Goble Volcanic Series. Should we conclude that southwest Washington was transported toward the mid-Tertiary reference pole (~north) by 550 km during the past 30 m.y.? Although I might be unfairly representing the views of some paleomagnetists, I don't think many researchers would use the results of an individual paleomagnetic investigation to conclude a poleward transport of <1000 km (~8°), no matter how solid the data from that investigation might appear. Perhaps if numerous investigations in the same region consistently yield results such as $p \pm \Delta p = 6^\circ \pm 4^\circ$, a conclusion of several hundred kilometers of poleward transport might be justified (Beck, 1984).

The following sage and lucid passage about confidence limits and tectonic displacements (poleward transport) is taken from a discussion of paleomagnetic results from Alaska by Coe et al. (1985):

Three of the displacements appear to be statistically significant at marginally greater than 95% confidence. . . . It is important to note, however, that the formal confidence limits are always minimum estimates for two reasons. First, they are often based on overestimates of the number of independent samplings of the geomagnetic field, especially in the case where a sequence of lava flows is sampled. . . . Second, the formal confidence limits do not take account of possible sources of systematic geological errors. The most serious of these for lava flows is usually uncertainty in the structural correction. For instance, typical initial dips for lava flows on the flanks of shield volcanoes are 5° to 7°, and they may be considerably steeper than this. Such initial dips are difficult to distinguish in ancient environments from tectonic dip and thus undoubtedly lead to spurious estimates of latitudinal displacement. Since 5° error in inclination corresponds to 8° or 9° of apparent latitudinal displacement at the high paleolatitudes of these studies, it is entirely possible that any or all of the paleomagnetically inferred displacements that appear statistically significant (e.g., $-9^\circ \pm 8^\circ$) are artifacts of the initial dip.

Other special considerations that are worthy of mention are discordant paleomagnetic poles observed from plutonic rocks and from magnetite-bearing sedimentary rocks. The special problem with plutonic rocks is that paleohorizontal is not directly known and must be inferred. This ambiguity has led to differing interpretations of discordant paleomagnetic poles observed from Cretaceous plutonic rocks of the North Cascades and British Columbia (Irving et al., 1985; Butler et al. 1989). In Chapter 8, we discussed the possibility of compaction shallowing of paleomagnetic inclinations in magnetite-bearing sedimentary rocks. Paleomagnetically determined paleolatitudes from sedimentary rocks that have suffered inclination shallowing will be biased toward low paleolatitudes. If poleward transport of terranes is determined from rocks with this systematic bias, overestimates of latitudinal transport are likely to result.

REFERENCES

- W. Alvarez, D. V. Kent, I. P. Silva, R. A. Schweickert, and R. A. Larson, Franciscan limestone deposited at 17° south paleolatitude, *Geol. Soc. Am. Bull., Pt. 1*, v. 91, 476–484, 1980.
- R. B. Bates, M. E. Beck, Jr., and R. F. Burmester, Tectonic rotations in the Cascade range of southern Washington, *Geology*, v. 9, 1984–189, 1981.
- M. E. Beck, Jr., Discordant paleomagnetic pole position as evidence of regional shear in the western Cordillera of North America, *Am. J. Sci.*, v. 276, 694–712, 1976.
- M. E. Beck, Jr., Paleomagnetic record of plate-margin tectonic processes along the western edge of North America, *J. Geophys. Res.*, v. 85, 7115–7131, 1980.
- M. E. Beck, Jr., Has the Washington–Oregon Coast Range moved northward?, *Geology*, v. 12, 737–740, 1984.
- M. E. Beck, Jr., and C. D. Burr, Paleomagnetism and tectonic significance of the Goble Volcanic Series, southwestern Washington, *Geology*, v. 7, 175–179, 1979.
- M. E. Beck, Jr., and D. C. Engebretson, Paleomagnetism of small basalt exposures in the west Puget Sound area, Washington, and speculations on the accretionary origin of the Olympic Mountains, *J. Geophys. Res.*, v. 87, 3755–3760, 1982.

- M. E. Beck, Jr., R. F. Burmester, D. E. Craig, C. S. Grommé, and R. E. Wells, Paleomagnetism of middle Tertiary volcanic rocks from the Western Cascade series, northern California: Timing and scale of rotation in the southern Cascades and Klamath Mountains, *J. Geophys. Res.*, v. 91, 8219–8230, 1986.
- R. F. Butler, G. E. Gehrels, W. C. McClelland, S. R. May, and D. Klepacki, Discordant paleomagnetic poles from the Canadian Coast Plutonic Complex: Regional tilt rather than large-scale displacement? *Geology*, v. 17, 691–694, 1989.
- R. S. Coe, B. R. Globerman, P. W. Plumley, and G. A. Thrupp, Paleomagnetic results from Alaska and their tectonic implications, In: *Tectonostratigraphic Terranes of the Circum-Pacific Region*, ed. D. G. Howell, Am. Assoc. Petrol. Geol., Houston Circum-Pacific Council for Energy and Mineral Resources Series, 1, pp. 85–108, 1985.
- P. J. Coney, Accretionary tectonics in western North America, In: *Relations of Tectonics to Ore Deposits in the Southern Cordillera*, ed. W. R. Dickinson and W. D. Payne, *Ariz. Geol. Soc. Digest*, v. XIV, 23–37, 1981.
- P. J. Coney, D. L. Jones, and J. W. H. Monger, Cordilleran suspect terranes, *Nature*, v. 288, 329–333, 1980.
- V. Courtillot, H. Feinberg, J. P. Ragaru, R. Kerguelon, M. McWilliams, and A. Cox, Franciscan Complex limestone deposited at 24°N, *Geology*, v. 13, 107–110, 1985.
- A. V. Cox, Remanent magnetization of lower middle Eocene basalt flows from Oregon, *Nature*, v. 179, 685–686, 1957.
- A. Cox, Frequency of geomagnetic reversals and the symmetry of the nondipole field, *Rev. Geophys.*, v. 13, 35–51, 1975.
- A. V. Cox and R. B. Hart, *Plate Tectonics: How It Works*, Blackwell Scientific Publications, Palo Alto, Calif., 392 pp., 1986.
- H. H. Demarest, Error analysis of the determination of tectonic rotation from paleomagnetic data, *J. Geophys. Res.*, v. 88, 4321–4328, 1983.
- J. Diehl, K. M. McClannahan, and T. J. Bornhorst, Paleomagnetic results from the Mogollon–Datil volcanic field, southwestern New Mexico, and a refined mid-Tertiary reference pole for North America, *J. Geophys. Res.*, v. 93, 4869–4879, 1988.
- B. R. Globerman, M. E. Beck, Jr., and R. A. Duncan, Paleomagnetism and tectonic significance of Eocene basalts from the Black Hills, Washington Coast Range, *Geol. Soc. Am. Bull.*, v. 93, 1151–1159, 1982.
- R. G. Gordon, A. Cox, and S. O'Hare, Paleomagnetic Euler poles and the apparent polar wander and absolute motion of North America since the Carboniferous, *Tectonics*, v. 3, 499–537, 1984.
- C. S. Grommé, M. E. Beck, Jr., R. E. Wells, and D. C. Engebretson, Paleomagnetism of the Tertiary Clarno Hills Formation of central Oregon and its significance for the tectonic history of the Pacific Northwest, *J. Geophys. Res.*, v. 91, 14,089–14,103, 1986.
- J. T. Hagstrum, M. G. Sawlan, B. P. Hausback, J. G. Smith, and C. S. Grommé, Miocene paleomagnetism and tectonic setting of the Baja California Peninsula, Mexico, *J. Geophys. Res.*, v. 92, 2627–2639, 1987.
- J. W. Hillhouse, Paleomagnetism of the Triassic Nikolai Greenstone, McCarthy quadrangle, Alaska, *Can. J. Earth Sci.*, v. 14, 2578–2592, 1977.
- J. W. Hillhouse and C. S. Grommé, Northward displacement and accretion of Wrangellia: New paleomagnetic evidence from Alaska, *J. Geophys. Res.*, v. 89, 4461–4477, 1984.
- J. W. Hillhouse, C. S. Grommé, and T. L. Vallier, Paleomagnetism and Mesozoic tectonics of the Seven Devils volcanic arc in northeastern Oregon, *J. Geophys. Res.*, v. 87, 3777–3794, 1982.
- E. Irving, G. J. Woodsworth, P. J. Wynne, and A. Morrison, Paleomagnetic evidence for displacement from the south of the Coast Plutonic Complex, British Columbia, *Can. J. Earth Sci.*, v. 22, 584–598, 1985.
- D. L. Jones, M. C. Blake, and C. Rangin, The four Jurassic belts of northern California and their significance to the geology of the Southern California borderland, In: *Aspects of the Geologic History of the California Continental Borderland*, ed. D. G. Howell, Misc. Publ. 24, Am. Assoc. Petrol. Geol., Tulsa, Okla., pp. 343–362, 1976.
- D. L. Jones, N. J. Silberling, and J. Hillhouse, Wrangellia—A displaced terrane in northwestern North America, *Can. J. Earth Sci.*, v. 14, 2565–2577, 1977.
- M. J. Kamerling and B. P. Luyendyk, Tectonic rotations of the Santa Monica Mountains region, western Transverse Ranges, California, suggested by paleomagnetic vectors, *Geol. Soc. Am. Bull.*, v. 90, 331–337, 1979.
- B. P. Luyendyk, M. J. Kamerling, R. R. Terres, and J. S. Hornafius, Simple shear of southern California during Neogene time suggested by paleomagnetic declinations, *J. Geophys. Res.*, v. 90, 12,454–12,466, 1985.

- J. R. Magill and A. Cox, Tectonic rotation of the Oregon Western Cascades, Special Paper 10, Oregon Dept. Geol. Min. Ind., Portland, 67 pp., 1980.
- J. R. Magill, A. Cox, and R. Duncan, Tillamook volcanic series: Further evidence for tectonic rotation of the Oregon Coast Range, *J. Geophys. Res.*, v. 86, 2953–2970, 1981.
- J. R. Magill, R. E. Wells, R. W. Simpson, and A. V. Cox, Post-12 m.y. rotation of southwest Washington, *J. Geophys. Res.*, v. 87, 3761–3776, 1982.
- S. R. May and R. F. Butler, North American Jurassic Apparent polar wander: Implications for plate motions, paleogeography and Cordilleran tectonics, *J. Geophys. Res.*, v. 91, 11,519–11,544, 1986.
- B. C. Panuska and D. B. Stone, Late Paleozoic paleomagnetic data for Wrangellia: Resolution of the polarity ambiguity, *Nature*, v. 293, 561–563, 1981.
- B. C. Panuska and D. B. Stone, Latitudinal motion of the Wrangellia and Alexander terranes and southern Alaska superterrane, In: *Tectonostratigraphic Terranes of the Circum-Pacific Region*, ed. D. G. Howell, Am. Assoc. Petrol Geol., Houston Circum-Pacific Council for Energy and Mineral Resources Series, 1, pp. 579, 1985.
- S. C. Reeve and C. E. Helsley, Magnetic reversal sequence in the upper portion of the Chinle Formation, Montoya, New Mexico, *Geol. Soc. Am. Bull.*, v. 83, 3795–3812, 1972.
- R. W. Simpson and A. Cox, Paleomagnetic evidence for tectonic rotation of the Oregon Coast Range, *Geology*, v. 5, 585–589, 1977.
- J. A. Tarduno, M. McWilliams, W. V. Sliter, H. E. Cook, M. C. Blake, Jr., and I. Premoli-Silva, Southern hemisphere origin of the Cretaceous Laytonville Limestone of California, *Science*, v. 231, 1425–1428, 1986.
- J. A. Tarduno, M. McWilliams, and N. Sleep, Fast instantaneous oceanic plate velocities recorded by the Cretaceous Laytonville Limestone: Paleomagnetic analysis and kinematic implications, *J. Geophys. Res.*, v. 95, 15,503–15,527, 1990.
- R. E. Wells and R. S. Coe, Paleomagnetism and geology of Eocene volcanic rocks of southwest Washington: Implications for mechanisms of rotation, *J. Geophys. Res.*, v. 90, 1925–1947, 1985.
- R. E. Wells and P. L. Heller, The relative contribution of accretion, shear, and extension to Cenozoic tectonic rotation in the Pacific Northwest, *Geol. Soc. Am. Bull.*, v. 100, 325–338, 1988.
- R. W. Yole and E. Irving, Displacement of Vancouver Island: Paleomagnetic evidence from the Karmutsen Formation, *Can. J. Earth Sci.*, v. 17, 1210–1288, 1980.

APPENDIX: DERIVATIONS

This appendix provides details of derivations referred to throughout the text. The derivations are developed here so that the main topics within the chapters are not interrupted by the sometimes lengthy mathematical developments.

DERIVATION OF MAGNETIC DIPOLE EQUATIONS

In this section, a derivation is provided of the basic equations describing the magnetic field produced by a magnetic dipole. The geometry is shown in Figure A.1 and is identical to the geometry of Figure 1.3 for a geocentric axial dipole. The derivation is developed by using spherical coordinates: r , θ , and ϕ . An additional polar angle, p , is the *colatitude* and is defined as $\pi - \theta$. After each quantity is derived in spherical coordinates, the resulting equation is altered to provide the results in the convenient forms (e.g., horizontal component, H_h) that are usually encountered in paleomagnetism.

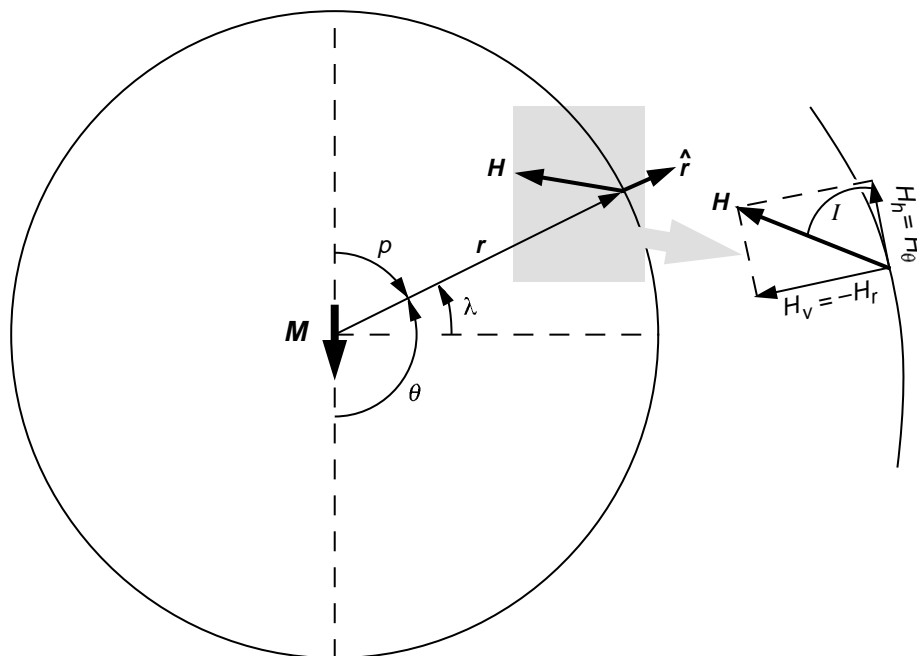


Figure A.1 Geocentric axial dipole. The large arrow is the magnetic dipole moment, \mathbf{M} ; θ is the polar angle from the positive pole of the magnetic dipole; p is the magnetic colatitude; λ is the geographic latitude; r is the radial distance from the magnetic dipole; \mathbf{H} is the magnetic field produced by the magnetic dipole; \hat{r} is the unit vector in the direction of r . The inset figure in the upper right corner is a magnified version of the stippled region. Inclination, I , is the vertical angle (dip) between the horizontal and \mathbf{H} . The magnetic field vector \mathbf{H} can be broken into (1) vertical component, $H_v = -H_r$, and (2) horizontal component, $H_h = H_\theta$.

The starting point is the scalar magnetic potential of a magnetic dipole:

$$V = \frac{\mathbf{M} \cdot \hat{\mathbf{r}}}{r^2} = \frac{M \cos \theta}{r^2} \quad (\text{A.1})$$

The magnetic field, \mathbf{H} , is derived from the scalar magnetic potential by taking the gradient of the potential:

$$\mathbf{H} = -\nabla V = -\left(\frac{\partial}{\partial r} \hat{\mathbf{r}} + \frac{1}{r} \frac{\partial}{\partial \theta} \hat{\boldsymbol{\theta}}\right) \left(\frac{M \cos \theta}{r^2}\right) \quad (\text{A.2})$$

Separating the differentials yields

$$\mathbf{H} = -\frac{\partial}{\partial r} \left(\frac{M \cos \theta}{r^2}\right) \hat{\mathbf{r}} - \frac{1}{r} \frac{\partial}{\partial \theta} \left(\frac{M \cos \theta}{r^2}\right) \hat{\boldsymbol{\theta}} \quad (\text{A.3})$$

Performing the required differentiations leads to

$$\mathbf{H} = \frac{2M \cos \theta}{r^3} \hat{\mathbf{r}} + \frac{M \sin \theta}{r^3} \hat{\boldsymbol{\theta}} = H_r \hat{\mathbf{r}} + H_\theta \hat{\boldsymbol{\theta}} \quad (\text{A.4})$$

The horizontal component, H_h , of \mathbf{H} is then given by

$$H_h = H_\theta = \frac{M \sin \theta}{r^3} = \frac{M \sin(\pi - \theta)}{r^3} = \frac{M \sin p}{r^3} \quad (\text{A.5})$$

To get this expression in terms of geographic latitude, λ , substitute

$$p = \frac{\pi}{2} - \lambda \quad (\text{A.6})$$

to yield

$$H_h = \frac{M \cos \lambda}{r^3} \quad (\text{A.7})$$

This is Equation (1.12) in Chapter 1.

Now returning to Equation (A.4), the vertical component, H_v , of \mathbf{H} is

$$H_v = -H_r = -\frac{2M \cos \theta}{r^3} = \frac{2M \cos p}{r^3} \quad (\text{A.8})$$

Again using Equation (A.6), H_v in terms of geographic latitude, λ , is

$$H_v = \frac{2M \sin \lambda}{r^3} \quad (\text{A.9})$$

This is Equation (1.13).

The inclination, I , can be determined by

$$\tan I = \frac{H_v}{H_h} = \left(\frac{2M \cos p}{r^3}\right) \left(\frac{r^3}{M \sin p}\right) = 2 \cot p \quad (\text{A.10})$$

Using Equation (A.6), the inclination is given as a function of geographic latitude by

$$\tan I = 2 \tan \lambda \quad (\text{A.11})$$

This is Equation (1.15), “the dipole equation.”

For the total intensity, H , of the magnetic field, we find

$$H = \sqrt{H_h^2 + H_v^2} = \frac{M}{r^3} \sqrt{1 + 3\cos^2 p} = \frac{M}{r^3} \sqrt{1 + 3\sin^2 \lambda} \quad (\text{A.12})$$

which is Equation (1.14).

ANGLE BETWEEN TWO VECTORS (AND GREAT-CIRCLE DISTANCE BETWEEN TWO GEOGRAPHIC LOCATIONS)

The dot product (scalar product) of two vectors \mathbf{A} and \mathbf{B} is given by

$$\mathbf{A} \cdot \mathbf{B} = AB \cos \theta \quad (\text{A.13})$$

where A is the length of vector \mathbf{A} , B is the length of vector \mathbf{B} , and θ is the angle between \mathbf{A} and \mathbf{B} .

In terms of the components of the vectors in Cartesian coordinates,

$$\mathbf{A} \cdot \mathbf{B} = A_x B_x + A_y B_y + A_z B_z \quad (\text{A.14})$$

where B_x is the x component of \mathbf{B} , etc.

The angle θ can be determined by

$$\theta = \cos^{-1} \left(\frac{\mathbf{A} \cdot \mathbf{B}}{AB} \right) \quad (\text{A.15})$$

Now instead of dealing with Cartesian coordinates, express the directions in terms of north, east, and down components on a sphere. For example, a unit vector $\hat{\mathbf{A}}$ can be expressed as

$$\hat{\mathbf{A}} = A_N \hat{\mathbf{N}} + A_E \hat{\mathbf{E}} + A_V \hat{\mathbf{V}} \quad (\text{A.16})$$

where A_N is the north component of $\hat{\mathbf{A}}$, etc.

The unit vector $\hat{\mathbf{A}}$ can be written in terms of its inclination and declination by

$$A_N = \cos I_A \cos D_A, \quad A_E = \cos I_A \sin D_A, \quad \text{and} \quad A_V = \sin I_A \quad (\text{A.17})$$

where I_A is the inclination of unit vector $\hat{\mathbf{A}}$, etc.

Now the angle between two directions (unit vectors) can be written as

$$\theta = \cos^{-1} \left(\frac{\hat{\mathbf{A}} \cdot \hat{\mathbf{B}}}{\hat{A} \hat{B}} \right) = \cos^{-1} (\hat{\mathbf{A}} \cdot \hat{\mathbf{B}}) \quad (\text{A.18})$$

In terms of the inclinations and declinations of the two vectors, the angle θ is given by

$$\theta = \cos^{-1} (\cos I_A \cos D_A \cos I_B \cos D_B + \cos I_A \sin D_A \cos I_B \sin D_B + \sin I_A \sin I_B) \quad (\text{A.19})$$

So given the inclinations and declinations of any two vectors, one can use Equation (A.19) to determine the angle between those two directions.

Equation (A.19) also can be used to determine the great-circle distance (angular distance) between any two geographic locations. Instead of viewing directions as being points on a sphere of unit radius, we now use the unit sphere to view geographic locations. Consider two geographic locations, one at latitude λ_a and longitude ϕ_a and another at latitude λ_b and longitude ϕ_b . The great-circle distance from (λ_a, ϕ_a) to (λ_b, ϕ_b) is determined by substituting λ_a for I_A , ϕ_a for D_A , etc. in Equation (A.19). The result is

$$\theta = \cos^{-1} (\cos \lambda_a \cos \phi_a \cos \lambda_b \cos \phi_b + \cos \lambda_a \sin \phi_a \cos \lambda_b \sin \phi_b + \sin \lambda_a \sin \lambda_b) \quad (\text{A.20})$$

An alternative expression for the great-circle distance between two locations is introduced below and is sometimes the more convenient form.

LAW OF SINES AND LAW OF COSINES

Two fundamental relationships of spherical trigonometry can be illustrated by using the spherical triangle ABC in Figure A.2, and these relationships will be used often in the derivations to follow. The spherical triangle has corners A , B , and C ; and A , B , and C stand for the angles between the sides of the triangle at the respective corners. The distances a , b , and c are angular distances of the sides of the triangle that are opposite the corners A , B , and C , respectively. These angular distances are the angle subtended by a side of the triangle at the center of the sphere (see the inset in Figure A.2).

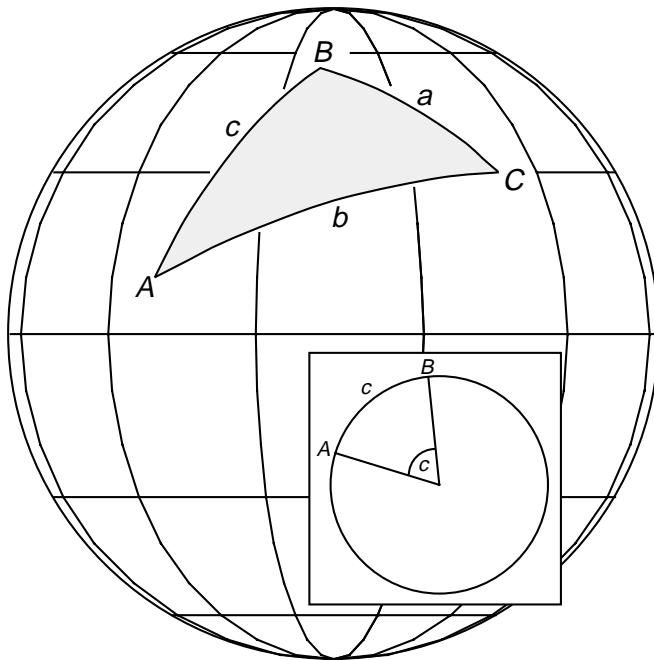


Figure A.2 Spherical triangle with apices at A , B , and C and sides a , b , and c . The inset figure shows the plane containing A , B , and the center of the sphere; the angular distance c is the angle subtended by side c at the center of the sphere. The projection (for this and all global projections to follow) is orthographic with the latitude and longitude grid in 30° increments.

The *Law of Cosines* states that

$$\cos a = \cos b \cos c + \sin b \sin c \cos A \quad (\text{A.21})$$

The Law of Cosines can be applied to any side of a spherical triangle by simply rearranging the labels on the sides and at the corners. For example, in the triangle of Figure A.2,

$$\cos b = \cos c \cos a + \sin c \sin a \cos B \quad (\text{A.22})$$

The second relationship is the *Law of Sines*, for which the governing equation is

$$\frac{\sin a}{\sin A} = \frac{\sin b}{\sin B} = \frac{\sin c}{\sin C} \quad (\text{A.23})$$

We will apply the Law of Cosines and the Law of Sines frequently in the coming derivations.

CALCULATION OF A MAGNETIC POLE FROM THE DIRECTION OF THE MAGNETIC FIELD

The trigonometry involved in deriving the expressions for calculating a magnetic pole from a magnetic field direction is shown in Figure A.3a. The site is at geographic latitude λ_s and longitude ϕ_s and the pole is at geographic latitude λ_p and longitude ϕ_p . We form a spherical triangle with apices at (λ_s, ϕ_s) , (λ_p, ϕ_p) , and the

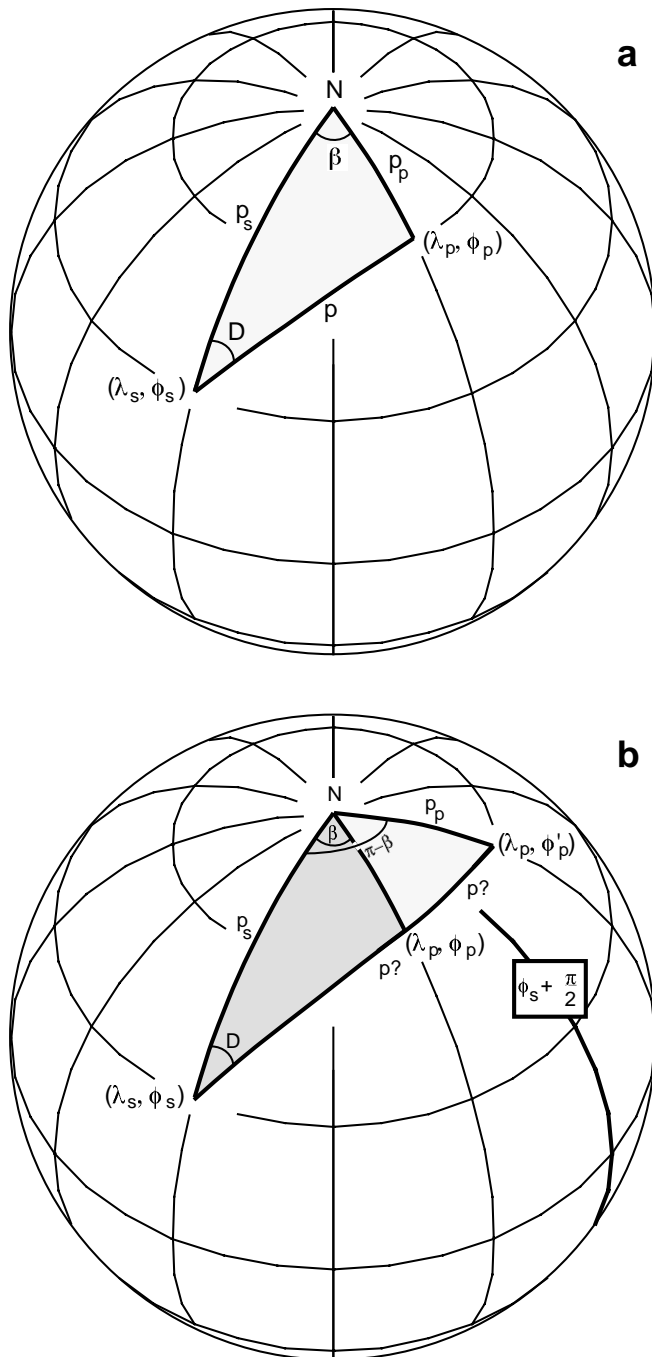


Figure A.3 (a) Determination of a magnetic pole from a magnetic field direction. The site is at (λ_s, ϕ_s) ; the magnetic pole is at (λ_p, ϕ_p) ; the north geographic pole is at point N ; the colatitude of the site is p_s ; the colatitude of the magnetic pole is p_p ; β is the longitudinal difference between the magnetic pole and the site. (b) Ambiguity in magnetic pole longitude. The pole may be at either (λ_p, ϕ_p) or (λ_p, ϕ_p') ; the longitude at $\phi_s + \pi/2$ is shown by the heavy line.

north geographic pole, N . The colatitude (angular distance from the north geographic pole) of the site is p_s , while the colatitude of the magnetic pole is p_p .

The magnetic colatitude, p , is the great-circle angular distance of the site from the magnetic pole. This angular distance is determined from the dipole formula (Equation (A.10)):

$$p = \cot^{-1}\left(\frac{\tan I}{2}\right) = \tan^{-1}\left(\frac{2}{\tan I}\right) \tag{A.24}$$

Now we need to find p_p by using the Law of Cosines:

$$\cos p_p = \cos p_s \cos p + \sin p_s \sin p \cos D \tag{A.25}$$

Using the definition of the colatitude,

$$p_p = \frac{\pi}{2} - \lambda_p \quad \text{and} \quad p_s = \frac{\pi}{2} - \lambda_s \quad (\text{A.26})$$

Substituting these expressions for p_p and p_s in Equation (A.25) leads to

$$\cos\left(\frac{\pi}{2} - \lambda_p\right) = \cos\left(\frac{\pi}{2} - \lambda_s\right) \cos p + \sin\left(\frac{\pi}{2} - \lambda_s\right) \sin p \cos D \quad (\text{A.27})$$

Using

$$\cos\left(\frac{\pi}{2} - x\right) = \sin x \quad \text{and} \quad \sin\left(\frac{\pi}{2} - x\right) = \cos x$$

in Equation (A.27) yields

$$\sin \lambda_p = \sin \lambda_s \cos p + \cos \lambda_s \sin p \cos D \quad (\text{A.28})$$

and

$$\lambda_p = \sin^{-1}(\sin \lambda_s \cos p + \cos \lambda_s \sin p \cos D) \quad (\text{A.29})$$

which is Equation (7.2).

The next step is to determine the angle β , which is the difference in longitude between the pole and the site (Figure A.3a). Applying the Law of Sines to the spherical triangle in Figure A.3 yields

$$\frac{\sin p}{\sin \beta} = \frac{\sin p_p}{\sin D} \quad (\text{A.30})$$

Rearrange Equation (A.30) to give

$$\sin \beta = \frac{\sin D}{\sin p_p} \sin p \quad (\text{A.31})$$

Now substitute $p_p = (\pi/2) - \lambda_p$ to yield

$$\sin \beta = \frac{\sin D}{\sin\left(\frac{\pi}{2} - \lambda_p\right)} \sin p \quad (\text{A.32})$$

and

$$\sin \beta = \frac{\sin D}{\cos \lambda_p} \sin p \quad (\text{A.33})$$

Now solve for β to give

$$\beta = \sin^{-1}\left(\frac{\sin p \sin D}{\cos \lambda_p}\right) \quad (\text{A.34})$$

which is Equation (7.3).

As given by Equation (A.34), β is limited to the range $-\pi/2$ to $+\pi/2$. But this raises an important ambiguity in the derivation. Simply adding β to the site longitude would not allow the pole longitude to differ from the site longitude by more than $\pi/2$. This ambiguity is shown schematically in Figure A.3b. As viewed from the site at λ_s, ϕ_s , the above expression for β would not allow the pole to be in the longitudinal hemisphere opposite from the site (beyond the longitude shown by the heavy line in Figure A.3b).

The ambiguity is whether the pole longitude is given by (1) $\phi_p = \phi_s + \beta$ (as shown in Figure A.3a) or (2) $\phi_p = \phi_s + (\pi - \beta)$. These two possibilities are shown by the two spherical triangles in Figure A.3b. The

smaller triangle has apices at (λ_s, ϕ_s) , (λ_p, ϕ_p) , and N ; the larger triangle has apices at (λ_s, ϕ_s) , (λ_p, ϕ'_p) , and N . Because λ_p is the same for either of the two possible poles, ρ_p is the same angular distance for either triangle. So we must devise a test to determine which of the two possible spherical triangles applies to a particular calculation of a magnetic pole position.

Apply the Law of Cosines to the two triangles in Figure A.3b. For the smaller triangle,

$$\cos p = \cos p_p \cos p_s + \sin p_p \sin p_s \cos \beta \quad (\text{A.35})$$

while for the larger triangle,

$$\cos p = \cos p_p \cos p_s + \sin p_p \sin p_s \cos(\pi - \beta) \quad (\text{A.36})$$

Now substitute

$$p_p = \left(\frac{\pi}{2} - \lambda_p\right), \quad p_s = \left(\frac{\pi}{2} - \lambda_s\right), \quad \cos(\pi - \beta) = -\cos \beta, \quad \cos\left(\frac{\pi}{2} - \lambda_p\right) = \sin \lambda_p, \\ \text{and } \sin\left(\frac{\pi}{2} - \lambda_p\right) = \cos \lambda_p \quad (\text{A.37})$$

into Equations (A.35) and (A.36) to yield

$$\cos p = \sin \lambda_p \sin \lambda_s + \cos \lambda_p \cos \lambda_s \cos \beta \quad (\text{A.38})$$

for the smaller triangle and

$$\cos p = \sin \lambda_p \sin \lambda_s - \cos \lambda_p \cos \lambda_s \cos \beta \quad (\text{A.39})$$

for the larger triangle.

At this point we realize that λ_p , λ_s , and β are all limited to the range $-\pi/2$ to $+\pi/2$. Within this range, the product $\cos \lambda_p \cos \lambda_s \cos \beta$ will always be positive. So if we find $\cos p \geq \sin \lambda_p \sin \lambda_s$, this indicates that we must be dealing with the smaller spherical triangle in Figure A.3b, and pole longitude is given by

$$\phi_p = \phi_s + \beta \quad (\text{A.40})$$

But if we find $\cos p < \sin \lambda_p \sin \lambda_s$, we must be dealing with the larger triangle in Figure A.3b, for which

$$\phi_p = \phi_s + \pi - \beta \quad (\text{A.41})$$

This development explains the conditional tests and alternative methods of calculating ϕ_p given by Equations (7.4) through (7.7).

CONFIDENCE LIMITS ON POLES: dp AND dm

From the previous section, we know how to map an observed magnetic field direction I and D observed at site (λ_s, ϕ_s) into a magnetic pole position (λ_p, ϕ_p) . Now we consider the confidence limits on (λ_p, ϕ_p) resulting from circular confidence limits on the direction.

We start by determining the confidence limits, ΔI , on the inclination and on the declination, ΔD , from I , D , and α_{95} (the usual confidence limit on the direction). At this point, this is a direction space problem as schematically represented on the lower hemisphere of the equal-area projection in Figure A.4a. Two examples of directions and confidence limits are shown in this diagram. Note how a steep inclination results in a large confidence limit ΔD on the declination.

Now consider the spherical triangle ABC of Figure A.4a. The angular distance $b = (\pi/2) - I$ and $c = \alpha_{95}$. The angle B is $\pi/2$, and the angle C is ΔD . Apply the Law of Sines to this triangle to give

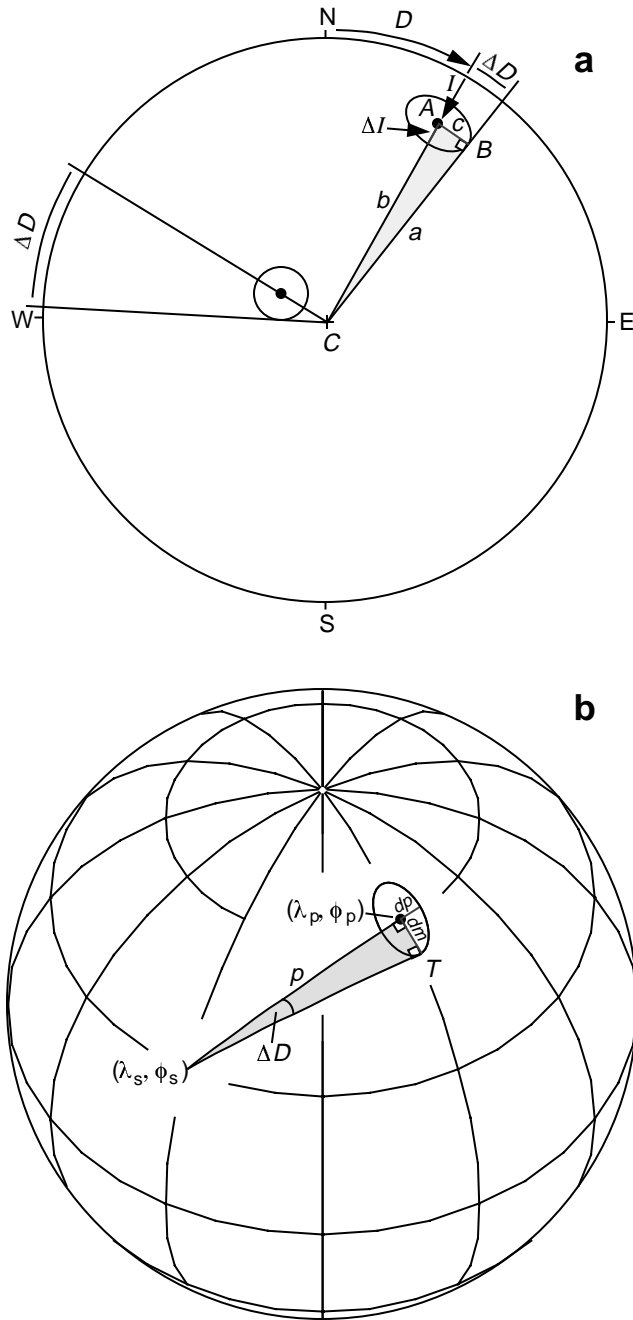


Figure A.4 (a) Equal-area projection of direction I , D and attendant confidence limits ΔI , ΔD . The confidence limit surrounding the direction is circular in direction space but is mapped into an ellipse by the equal-area projection. (b) Magnetic pole at (λ_p, ϕ_p) and attendant confidence limits dp and dm . The site location is (λ_s, ϕ_s) ; p is the magnetic colatitude; the dark stippled region is a spherical triangle with apices (λ_s, ϕ_s) , (λ_p, ϕ_p) , and T ; the light stippled region is a confidence oval about the magnetic pole with semi-major and semi-minor axes dm and dp , respectively; ΔD is the angle at apex (λ_s, ϕ_s) .

$$\frac{\sin c}{\sin C} = \frac{\sin b}{\sin B} \tag{A.42}$$

which rearranges to

$$\sin C = \frac{\sin c \sin B}{\sin b} \tag{A.43}$$

Substituting the above quantities for b , c , B , and C yields

$$\sin \Delta D = \frac{\sin \alpha_{95} \sin \frac{\pi}{2}}{\sin \left(\frac{\pi}{2} - I \right)} = \frac{\sin \alpha_{95}}{\cos I} \tag{A.44}$$

from which ΔD can be determined. By inspection of Figure A.4a,

$$\Delta I = \alpha_{95} \quad (\text{A.45})$$

Now we turn our attention to Figure A.4b, which illustrates mapping a magnetic field direction I , D observed at (λ_s, ϕ_s) into a magnetic pole at (λ_p, ϕ_p) . Consider the spherical triangle with apices at (λ_s, ϕ_s) , (λ_p, ϕ_p) , and T . The angle at apex (λ_s, ϕ_s) is ΔD . The angles at apices (λ_p, ϕ_p) and T are both $\pi/2$. The angular distance from (λ_s, ϕ_s) to (λ_p, ϕ_p) is the magnetic colatitude p . The angular distance from (λ_p, ϕ_p) to T is dm , the confidence limit perpendicular to the great-circle path from (λ_s, ϕ_s) to (λ_p, ϕ_p) .

Apply the Law of Sines to get

$$\frac{\sin dm}{\sin \Delta D} = \frac{\sin p}{\sin T} \quad (\text{A.46})$$

Now substitute

$$T = \frac{\pi}{2} \text{ and } \sin \Delta D = \frac{\sin \alpha_{95}}{\cos I}$$

(from Equation (A.44)) and rearrange to get

$$dm = \sin^{-1} \left(\frac{\sin \alpha_{95} \sin p}{\cos I} \right) \quad (\text{A.47})$$

This is the general expression for the confidence limit dm . But because dm and α_{95} are usually small angles and $\sin(x) \approx x$, for small x , Equation (A.47) is usually given as

$$dm = \alpha_{95} \frac{\sin p}{\cos I} \quad (\text{A.48})$$

which is Equation (7.9).

From Equation (A.10), we know that

$$p = \tan^{-1} \left(\frac{2}{\tan I} \right) = \cot^{-1} \left(\frac{\tan I}{2} \right) \quad (\text{A.49})$$

Now we use

$$d(\cot^{-1} x) = -\frac{dx}{1+x^2} \text{ and } d(\tan x) = \sec^2 x dx$$

to get

$$dp = d \left[\cot^{-1} \left(\frac{1}{2} \tan I \right) \right] = -\frac{\frac{1}{2} \sec^2 I dI}{1 + \frac{1}{4} \tan^2 I} = -\frac{2 \sec^2 I dI}{4 + \tan^2 I} \quad (\text{A.50})$$

Use of the trigonometric identities

$$\sec^2 x = \frac{1}{\cos^2 x}, \tan x = \frac{\sin x}{\cos x}, \text{ and } \sin^2 x + \cos^2 x = 1$$

in Equation (A.50) yields

$$dp = \frac{-2 \frac{dI}{\cos^2 I}}{4 + \frac{\sin^2 I}{\cos^2 I}} = \frac{-2dI}{4 \cos^2 I + \sin^2 I} = \frac{-2dI}{1 + 3 \cos^2 I} \quad (\text{A.51})$$

Recalling that $dl = \alpha_{95}$ and observing that dp is symmetrical about (λ_p, ϕ_p) give the end result

$$dp = 2\alpha_{95} \left(\frac{1}{1 + 3\cos^2 I} \right) \tag{A.52}$$

which is Equation (7.8).

EXPECTED MAGNETIC FIELD DIRECTION

The problem here is to derive expressions that allow determination of the magnetic field direction expected at an observing site (λ_s, ϕ_s) due to a geocentric dipole with pole position (λ_p, ϕ_p) . We also derive expressions for the confidence limits on the expected direction that result from circular confidence limits (usually A_{95}) on the pole. The geometry of the problem is illustrated in Figure A.5.

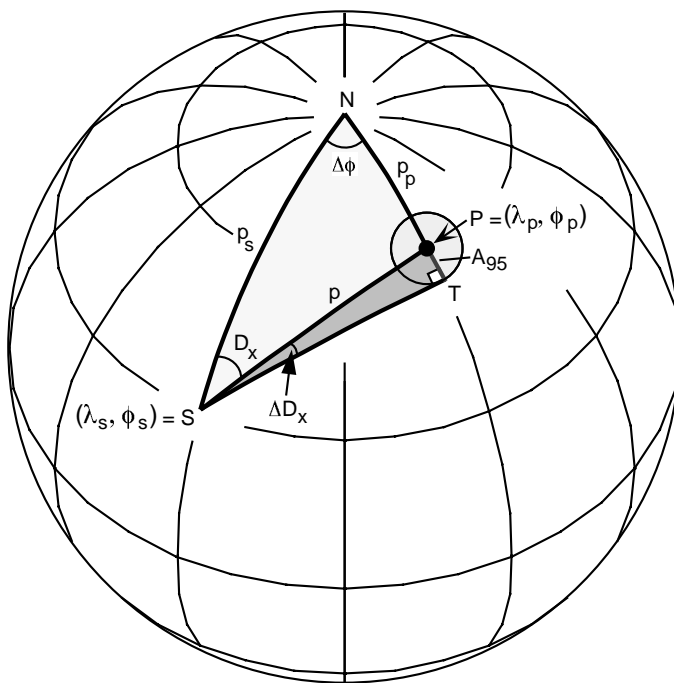


Figure A.5 Geometry used to determine the expected magnetic field direction from a magnetic pole. The magnetic pole is at $P(\lambda_p, \phi_p)$ with circular confidence limit A_{95} ; the site location is at $S(\lambda_s, \phi_s)$; N is the geographic north pole; p is the magnetic colatitude of the site; p_s is the geographic colatitude of the site; p_p is the geographic colatitude of the magnetic pole; $\Delta\phi$ is the longitudinal difference between the magnetic pole and the site; D_x is the expected magnetic field declination at the site with confidence limit $= \Delta D_x$.

A spherical triangle SPN is constructed with N at the geographic pole, P at the magnetic pole (λ_p, ϕ_p) , and S at the site (λ_s, ϕ_s) . Having gone through a similar problem before, we realize that the declination of the expected magnetic field direction, D_x , at site (λ_s, ϕ_s) is the angle at apex S .

The first step in the derivation is to determine the angular distance, p , from (λ_p, ϕ_p) to (λ_s, ϕ_s) . Apply the law of sines to triangle SPN in Figure A.5 to get

$$\cos p = \cos p_p \cos p_s + \sin p_p \sin p_s \cos \Delta\phi \tag{A.53}$$

Now substitute

$$p_p = \frac{\pi}{2} - \lambda_p, \quad p_s = \frac{\pi}{2} - \lambda_s, \quad \text{and} \quad \Delta\phi = \phi_p - \phi_s$$

into Equation (A.53) and use

$$\cos\left(\frac{\pi}{2} - \lambda_p\right) = \sin \lambda_p \quad \text{and} \quad \sin\left(\frac{\pi}{2} - \lambda_p\right) = \cos \lambda_p$$

to find

$$\cos p = \sin \lambda_p \sin \lambda_s + \cos \lambda_p \cos \lambda_s \cos(\phi_p - \phi_s) \quad (\text{A.54})$$

from which you can determine p .

The expected inclination, I_x , can be determined from p by using the dipole equation (Equation (A.10)):

$$I_x = \tan^{-1}(2 \cot p) \quad (\text{A.55})$$

The confidence limit on I_x is defined as ΔI_x and can be determined from the equation that we derived to get dp from ΔI ($= \alpha_{95}$ in Equation (A.52)) and substituting A_{95} for dp :

$$A_{95} = 2\Delta I_x \left(\frac{1}{1 + 3\cos^2 I_x} \right) \quad (\text{A.56})$$

which rearranges to give

$$\Delta I_x = \frac{A_{95}}{2} (1 + 3\cos^2 I_x) = A_{95} \left(\frac{2}{1 + 3\cos^2 p} \right) \quad (\text{A.57})$$

To determine the expected declination, D_x , we can use Equation (A.28) derived above:

$$\sin \lambda_p = \sin \lambda_s \cos p + \cos \lambda_s \sin p \cos D \quad (\text{A.28})$$

and rearrange to solve for D_x :

$$\cos D_x = \frac{\sin \lambda_p - \sin \lambda_s \cos p}{\cos \lambda_s \sin p} \quad (\text{A.58})$$

from which D_x can be determined.

The confidence limit on D_x is ΔD_x , which can be derived by applying the Law of Sines to the spherical triangle STP (Figure A.5):

$$\frac{\sin A_{95}}{\sin \Delta D_x} = \frac{\sin p}{\sin T} \quad (\text{A.59})$$

Now note that $T = \pi / 2$ (thus $\sin T = 1$) and rearrange to give

$$\Delta D_x = \sin^{-1} \left(\frac{\sin A_{95}}{\sin p} \right) \quad (\text{A.60})$$

If you actually go through some calculations of ΔI_x and ΔD_x , you will find that these confidence limits change with I_x (and p) in a systematic fashion. For small p (steep inclination), $\Delta D_x > \Delta I_x$; $\Delta I_x \approx \Delta D_x$ at about $p = 60^\circ$ ($I_x \approx 50^\circ$); for $60^\circ < p \leq 90^\circ$ ($I_x < 50^\circ$), $\Delta I_x > \Delta D_x$.

This determination of the confidence limits ΔI_x and ΔD_x produces a confidence *oval* (not circle) about I_x, D_x . ΔI_x is the semi-axis of the confidence oval in the vertical plane through I_x, D_x . But the other semi-axis of the confidence oval is not ΔD_x . Remember that ΔD_x is the projection of the direction space confidence limit onto the periphery of the equal-area projection (Figure A.4a). The required dimension of the confidence limit about I_x, D_x can be determined from Equation (A.44) by substituting the desired angular distance c (Figure A.4a) for α_{95} . This leads to

$$c = \sin^{-1}(\cos I_x \sin \Delta D_x) \quad (\text{A.61})$$

ROTATION AND FLATTENING IN DIRECTION SPACE

Here, we derive the equations to evaluate the vertical axis rotation that is required to align an observed declination with an expected declination. In addition, we develop equations to determine the *flattening of inclination* indicated by comparison of the observed and expected inclination.

The equal-area projection of Figure A.6 illustrates the problem. In this example, the observed direction has inclination $I_o = 40^\circ$, and declination $D_o = 20^\circ$. The confidence limit is $\alpha_{95} = 8^\circ$. This observed direction is compared to an expected direction at the sampling site, $I_x = 60^\circ$ and $D_x = 330^\circ$. The confidence limits on the expected direction are $\Delta I_x = 5.3^\circ$ and $\Delta D_x = 8^\circ$.

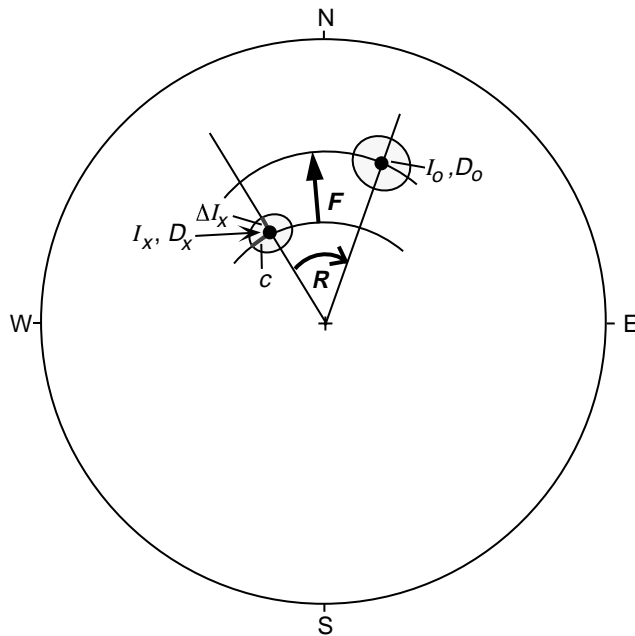


Figure A.6 Equal-area projection of vertical axis rotation, R , and inclination flattening, F . The observed direction is I_o, D_o ; the expected direction is I_x, D_x ; the confidence regions about the directions are shown by stippling; c is the angular distance of the confidence limit from the vertical plane through I_x, D_x .

The vertical-axis rotation is R and is defined as positive for an observed direction clockwise from the expected direction as shown in Figure A.6. The vertical-axis rotation is simply given by

$$R = D_o - D_x \tag{A.62}$$

The flattening of inclination is labeled F and is defined as positive when the observed inclination is less than (“flatter” than) the expected inclination. Thus F is given simply by

$$F = I_x - I_o \tag{A.63}$$

We need a method to evaluate confidence limits on R and F , which are labeled ΔR and ΔF , respectively. The original method of assigning confidence limits to R and F was to treat the errors in the observed and expected directions as independent errors. This approach led to

$$\Delta R = \sqrt{\Delta D_o^2 + \Delta D_x^2} \tag{A.64}$$

and

$$\Delta F = \sqrt{\Delta I_o^2 + \Delta I_x^2} \tag{A.65}$$

The confidence limits ΔD_o , and ΔI_o can be determined from Equations (A.44) and (A.45). ΔI_x and ΔD_x can be determined from Equations (A.57) and (A.60). Subsequent to derivation of the above equations, a rigorous statistical analysis of the confidence limits on R and F by Demarest (1983; reference in Chapter 11) has shown that the confidence limits should be calculated by using the following equations:

$$\Delta R = 0.8\sqrt{\Delta D_o^2 + \Delta D_x^2} \tag{A.66}$$

and

$$\Delta F = 0.8\sqrt{\Delta I_o^2 + \Delta I_x^2} \tag{A.67}$$

ROTATION AND POLEWARD TRANSPORT IN POLE SPACE

Rotation about a vertical axis and (paleo)latitudinal transport are sometimes more effectively addressed by comparing an observed paleomagnetic pole with a reference paleomagnetic pole. This situation is shown in Figure A.7. The reference pole is at point $RP (\lambda_r, \phi_r)$ with $A_{95} = A_r$; the observed pole is at point $OP (\lambda_o, \phi_o)$ with $A_{95} = A_o$; the site location from which the observed pole was determined is at point $S (\lambda_s, \phi_s)$. The problem is to determine the vertical axis rotation, R , and the poleward transport (motion toward the reference pole) indicated by the discordance between the observed pole and the reference pole.

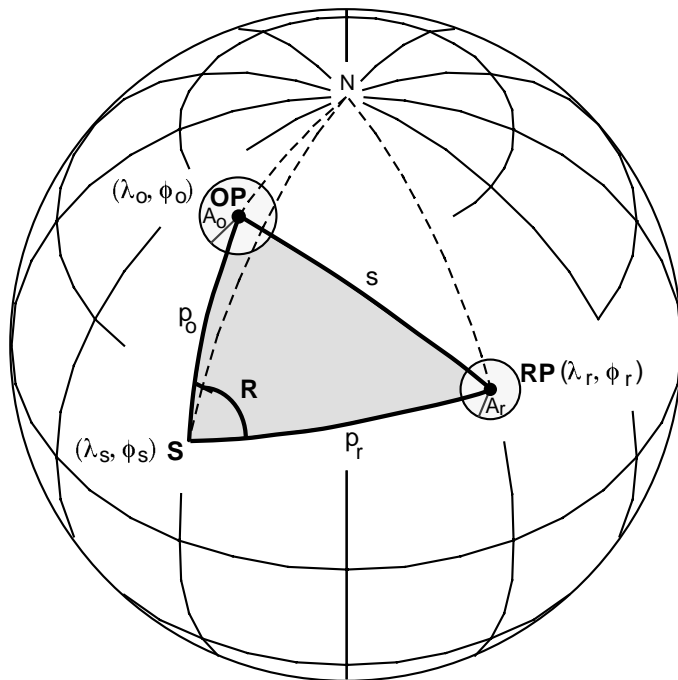


Figure A.7 Geometry required to determine vertical axis rotation and poleward displacement by comparing observed and reference paleomagnetic poles. RP is the reference paleomagnetic pole at (λ_r, ϕ_r) with $A_{95} = A_r$; OP is the observed paleomagnetic pole at (λ_o, ϕ_o) with $A_{95} = A_o$; the site location S is (λ_s, ϕ_s) ; N is the north geographic pole; the dashed longitudinal lines connect S , OP , and RP to N ; the dark stippled region is a spherical triangle with apices S , OP , RP and sides p_o , p_r , and s ; the light stippled circles are confidence circles about observed and reference poles; the vertical axis rotation is angle R .

We form the spherical triangle shown in Figure A.7 with apices at S , OP , and RP . The first step is to determine the angular distances p_r , p_o , and s . There are two approaches: (1) Use the formula developed for determining the great-circle distance between two locations (Equation (A.20)); or (2) use the formula developed for determining the angular distance from observation location to the observed paleomagnetic pole (Equation (A.38)). For the second approach, we form three spherical triangles ($N-OP-S$, $N-S-RP$, and $N-OP-RP$) by connecting the three apices of $S-OP-RP$ with the geographic pole. Equation (A.38) is then applied to each of these three triangles to determine the unknown angular distances p_r , p_o , and s . The results are

$$p_r = \cos^{-1}(\sin \lambda_r \sin \lambda_s + \cos \lambda_r \cos \lambda_s \cos[\phi_r - \phi_s]) \tag{A.68}$$

$$p_o = \cos^{-1}(\sin \lambda_s \sin \lambda_o + \cos \lambda_s \cos \lambda_o \cos[\phi_s - \phi_o]) \tag{A.69}$$

$$s = \cos^{-1}(\sin \lambda_r \sin \lambda_o + \cos \lambda_r \cos \lambda_o \cos[\phi_r - \phi_o]) \tag{A.70}$$

Knowing these angular distances, we can determine the rotation, R , by realizing that R is the angle at apex S and applying the Law of Cosines to the spherical triangle $S-OP-RP$:

$$\cos s = \cos p_o \cos p_r + \sin p_o \sin p_r \cos R \quad (\text{A.71})$$

Solving for R gives

$$R = \cos^{-1} \left(\frac{\cos s - \cos p_o \cos p_r}{\sin p_o \sin p_r} \right) \quad (\text{A.72})$$

Note that Equation (A.72) will not tell you whether R is positive (clockwise rotation) or negative (counterclockwise rotation). But inspection of Figure A.7 indicates that R is negative in this example.

The poleward transport, p , is simply

$$p = p_o - p_r \quad (\text{A.73})$$

The confidence limit on R can be determined from Equation (A.66):

$$\Delta R = 0.8 \sqrt{\Delta D_o^2 + \Delta D_x^2} \quad (\text{A.66})$$

where from Equation (A.60):

$$\Delta D_x = \sin^{-1} \left(\frac{\sin A_r}{\sin p_r} \right) \quad (\text{A.74})$$

and

$$\Delta D_o = \sin^{-1} \left(\frac{\sin A_o}{\sin p_o} \right) \quad (\text{A.75})$$

The confidence limit on p is Δp and is given by

$$\Delta p = 0.8 \sqrt{\Delta p_r^2 + \Delta p_o^2} \quad (\text{A.76})$$

From inspection of Figure A.7, we can see that

$$\Delta p_o = A_o \quad (\text{A.77})$$

and

$$\Delta p_r = A_r \quad (\text{A.78})$$

PALEOLATITUDES AND CONFIDENCE LIMITS

A paleogeographic map is often used to compare the paleomagnetically determined paleolatitude of an accreted terrane with the paleolatitude of the continent to which the terrane was accreted. The confidence limits on the paleolatitude of the terrane are illustrated by showing the upper and lower paleolatitudinal limits. An example is shown in Figure 11.13. In this section, we derive the equations that are used to determine paleolatitudes and the attendant confidence limits.

Two basic approaches to this problem have been used in the paleomagnetic literature. As with the rotation and transport problem, one approach uses the observed paleomagnetic direction, while the other uses the observed paleomagnetic pole. We'll first derive the equations for the direction-space approach then address the pole-space approach.

If we observe a mean paleomagnetic inclination I_o at a particular site, the dipole equation (Equation A.11) can be used to determine the paleolatitude:

$$\lambda_o = \tan^{-1} \left(\frac{\tan I_o}{2} \right) \quad (\text{A.79})$$

The confidence limit on I_o is $\Delta I_o = \alpha_{95}$. Because of the nonlinearity of Equation (A.79), the resulting confidence limits on λ_o are not symmetric about λ_o . Adding $\Delta I_o = \alpha_{95}$ to I_o will yield the higher latitude confidence limit, which we can label λ_o^+ :

$$\lambda_o^+ = \tan^{-1} \left[\frac{\tan(I_o + \alpha_{95})}{2} \right] \quad (\text{A.80})$$

The lower confidence limit λ_o^- is determined by subtracting $\Delta I_o = \alpha_{95}$ from I_o :

$$\lambda_o^- = \tan^{-1} \left[\frac{\tan(I_o - \alpha_{95})}{2} \right] \quad (\text{A.81})$$

These confidence limits on paleolatitude λ_o will be symmetric about λ_o only for $\lambda_o = 0^\circ$ or $\lambda_o = 90^\circ$.

This derivation explains why paleolatitudes determined from paleomagnetic inclinations are sometimes listed with asymmetric confidence limits. For example, “The Cretaceous paleolatitude of the Macintosh Terrane is 42.3° with upper and lower 95% confidence limits of 50.0° and 35.7° , respectively.”

In the pole-space approach, the paleogeographic map for a continent is produced as described in Chapter 10. The confidence limit for the reference pole is A_r , which directly gives the paleolatitude confidence limit for any point on the continent. As explained in the development of rotation and poleward displacement of a crustal block (and illustrated in Figure A.7), the angular distance from the site location to the observed pole is p_o , the observed paleocolatitude. From p_o , the observed paleolatitude is easily determined by

$$\lambda_o = 90^\circ - p_o \quad (\text{A.82})$$

The confidence limit on λ_o is simply A_o , the confidence limit on the observed pole (= confidence limit on p_o ; Equation (A.77)). So there are confidence limits on the paleolatitude of the crustal block and on the continent to which the terrane is now attached.

The simplest way to make a paleogeographic map that encompasses these paleolatitudinal confidence limits is to use the results derived for poleward transport. You want to show how far the crustal block has moved latitudinally with respect to the continent. So you place the continent in its paleogeographic position; then use Equation (A.82) to determine the paleolatitude of the crustal block and place the block at that paleolatitude. The confidence limit on paleolatitudinal position of the crustal block with respect to the continent is the confidence limit Δp on poleward transport (Equation (A.76)). This confidence limit accounts for uncertainties in the paleolatitudes of both the crustal block and the continent. But to make the paleogeographic map, we fix the continent in the paleogeographic grid and ascribe all the paleolatitudinal uncertainty to the crustal block. The confidence limits on paleolatitude of the block are shown as $\lambda_o \pm \Delta p$ on the paleogeographic map. This procedure was used to construct the Middle–Late Triassic paleogeographic map of Figure 11.13 showing the paleolatitude of the Nikolai Greenstone.